Dissertation
submitted to the
Combined Faculty of Natural Sciences and Mathematics
of Heidelberg University, Germany
for the degree of
Doctor of Natural Sciences

Put forward by
Stefan Felix Paul
born in Siegen

Oral examination: 09-01-2023

Precision mass measurements for the astrophysical *rp*-process and electron cooling of trapped ions

Referees: Prof. Dr. Klaus Blaum

Prof. Dr. Ulrich Uwer

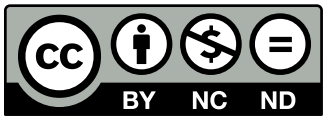

Precision mass measurements for the astrophysical *rp*-process and electron cooling of trapped ions

Precision mass measurements of rare isotopes with decay half-lives far below one second are of importance to a variety of applications including studies of nuclear structure and nuclear astrophysics as well as tests of fundamental symmetries. The first part of this thesis discusses mass measurements of neutron-deficient gallium isotopes in direct vicinity of the proton drip line. The reported measurements of $^{60-63}$Ga were performed with the multiple-reflection time-of-flight mass spectrometer of TRIUMF's Ion Trap for Atomic and Nuclear Science (TITAN) in Vancouver, Canada. The measurements mark the first direct mass determination of ^{60}Ga and yield a ^{61}Ga mass value three times more precise than the literature value from AME2020. Our ^{60}Ga mass value constrains the location of the proton dripline in the gallium isotope chain and extends the experimentally evaluated isobaric multiplet mass equation for isospin triplets up to $A = 60$. The improved precision of the ^{61}Ga mass has important implications for the astrophysical rapid proton capture process (*rp*-process). Calculations in a single-zone model demonstrate that the improved mass data substantially reduces uncertainties in the predicted light curves of Type I X-ray bursts.

TITAN has demonstrated that charge breeding provides a powerful means to increase the precision and resolving power of Penning trap mass measurements of radioactive ions. However, the charge breeding process deteriorates the ion beam quality, thus mitigating the benefits associated with Penning trap mass spectrometry of highly charged ions (HCI). As a potential remedy for the beam quality loss, a cooler Penning trap has been developed in order to investigate the prospects of electron cooling the HCI prior to the mass measurement. The second part of this thesis reports exploratory studies of electron cooling of singly charged ions in this cooler Penning trap. Comparison of measured ion energy evolutions to a cooling model provides a detailed understanding of the underlying cooling dynamics. Extrapolation of the model enables the deduction of tentative estimates of the expected cooling times for radioactive HCI.

Präzisionsmassenmessungen für den astrophysikalischen rp-Prozess und Elektronenkühlung von gefangenen Ionen

Präzisionsmassenmessungen an seltenen Isotopen mit Zerfallshalbwertszeiten weit unter einer Sekunde sind relevant für eine Vielzahl von wissenschaftlichen Anwendungen, wie zum Beispiel Untersuchungen zur Atomkernstruktur und im Bereich der nuklearen Astrophysik sowie Tests von fundamentalen Symmetrien. Der erste Teil dieser Dissertation diskutiert Massenmessungen an neutronenarmen Galliumisotopen in direkter Nähe der Protonenabbruchkante. Die hier präsentierten Messungen an $^{60-63}$Ga wurden mit dem Multireflektionsflugzeitspektrometer von TRIUMF's Ion Trap for Atomic and Nuclear Science (TITAN) in Vancouver, Kanada durchgeführt. Die Messungen stellen die erste direkte Massenmessung des Grundzustands von ^{60}Ga dar und liefern einen ^{61}Ga Massenwert, der dreimal genauer ist als der Literaturwert in AME2020. Der neue ^{60}Ga Massenwert ist von Bedeutung für die Position der Protonenabbruchkante in der Gallium-Isotopenkette und erweitert die experimentell-evaluierte isobarische Multiplet-Massengleichung für Isospintripletts zur Massenzahl $A = 60$. Die verbesserte Genauigkeit der Masse von ^{61}Ga hat wichtige Implikationen für den astrophysikalischen, schnellen Protoneinfangprozess (engl.: *rp*-process). Berechnungen mit einem Ein-Zonen-Modell demonstrieren die substantzielle Reduktion von Ungenauigkeiten in Modellvorhersagen der Lichtkurven kosmischer Röntgenstrahlenblitze des ersten Typs (engl.: Type I X-ray bursts).

Das TITAN-Experiment hat demonstriert, dass Ladungsbrütung eine Möglichkeit bietet, die Präzision und das Auflösungsvermögen von Penningfallenmassenspektrometrie an radioaktiven Ionen zu verbessern. Der Ladungsbrütungsprozess verringert allerdings die Ionenstrahlqualität, was wiederum die genannten Vorteile von Massenmessungen an hochgeladenen Ionen abschwächt. Als mögliche Gegenmaßnahme für den Strahlqualitätsverlust wurde eine Kühlfalle entwickelt, um die Machbarkeit von Elektronenkühlung der kurzlebigen, hochgeladenen Ionen vor der Massenmessung zu testen. Der zweite Teil dieser Dissertation beschreibt Untersuchungen der Elektronenkühlung von einfachgeladenen Ionen in dieser Kühl-Penningfalle. Der Vergleich gemessener Zeitverläufe der Ionenenergien mit einem vereinfachten Kühlmodell liefert ein detailiertes Verständnis der zugrundeliegenden Kühlungsdynamik. Extrapolation der Modellrechnungen erlaubt die grobe Abschätzung der erwartbaren Kühlzeiten für radioaktive, hochgeladene Ionen.

Contents

List of Figures

List of Tables

List of Acronyms

***rp*-process** rapid proton capture process

***r*-process** rapid neutron capture process

AC alternating current

ADC analog-to-digital converter

AME2020 2020 Atomic Mass Evaluation

ARIEL Advanced Rare Isotope Laboratory

CCD charge-coupled device

CDE Coulomb displacement energy

CERN-ISOLDE Isotope mass Separator On-Line at the European Organization for Nuclear Research

COM centre-of-mass

CPET cooler Penning trap

CSRe experimental Cooler Storage Ring (at HIRFL)

DAC digital-to-analog converter

DAQ data acquisition

DC direct current

DR dielectronic recombination

EBIT electron beam ion trap

ECR electron cyclotron resonance

ES electron-injection side

ESR Experimental Storage Ring (at GSI)

FAIR Facility for Antiproton and Ion Research

FC Faraday cup

FEBIAD forced electron-beam-induced arc discharge

FRIB Facility for Rare Isotope Beams

FRS Ion Catcher Fragment Separator (FRS) Ion Catcher

FT-ICR Fourier transform ion cyclotron resonance

FWHM full width at half maximum

GANIL Large Heavy Ion National Accelerator

GSI GSI Helmholtz Centre for Heavy Ion Research

HCI highly charged ion

HFB Hartree-Fock-Bogolyubov (variational approach)

HIE-ISOLDE high-intensity and -energy upgrade for CERN-ISOLDE

HITRAP Facility for decceleration and trapping of highly charged ions (at GSI)

HV high voltage

hyper-EMG hyper-exponentially modified Gaussian

IAS isobaric analogue state

IG-LIS ion-guide laser ion source

IMME isobaric multiplet mass equation

IMP Institue of Modern Physics (in Lanzhou)

IMS isochronous mass spectrometry

INC isospin-nonconserving

IOI ion of interest

IS ion-injection side

ISAC Isotope Separator and Accelerator

ISOL isotope separation on-line

ISOLTRAP ISOLTRAP (mass measurement facility at CERN-ISOLDE)

IT isochronous turn

JSON JavaScript Object Notation (file format)

JYFLTRAP Penning trap setup coupled to the IGISOL facility at the University of Jyväskylä

KATRIN Karlsruhe Tritium Neutrino experiment

LEBIT Low Energy Beam and Ion Trap (at NSCL)

MAc Mass Acquisition software

MCMC Markov-chain Monte Carlo

MCP micro-channel plate

MCS multichannel scaler

MIDAS Maximum Integrated Data Acquisition System

MLE maximum likelihood estimation

MLLTRAP Maier-Leibnitz-Laboratory trap

MPET measurement Penning trap

MPIK Max-Planck-Institute for Nuclear Physics (in Heidelberg)

MR-TOF-MS multiple-reflection time-of-flight mass spectrometer

MRS mass range selector

MSU Michigan State University

NIM Nuclear Instrumentation Module standard

NSCL National Superconducting Cyclotron Laboratory

PI-ICR phase-imaging ion cyclotron resonance

PIC particle in-cell

PPG programmable pulse generator

PTMS Penning trap mass spectrometry

QED quantum electrodynamics

R3 Rare-RI Ring (in the Rare Ion Beam Facility at RIKEN)

RF radiofrequency

RFA retarding field analysis

RFQ radiofrequency quadrupole

RIB rare isotope beam

RIKEN Institute of Physical and Chemical Research

RMS root-mean-square

RR radiative recombination

SCI singly charged ion

SHIPTRAP ion trapping facility coupled to the SHIP velocity filter at GSI

SIMION SIMION Ion Optics Simulator

SMS Schottky mass spectrometry

SPI serial-peripheral interface

SPIRAL1 Production System of Radioactive Ion and Acceleration On-Line facility at GANIL

SPIRAL2 Expansion of the Production System of Radioactive Ion and Acceleration On-Line facility at GANIL

TBR three-body recombination

TDC time-to-digital converter

TFS time-focus shift

TITAN TRIUMF's Ion Trap for Atomic and Nuclear Science

TOF time-of-flight

TOF-ICR time-of-flight ion cyclotron resonance

TRC time-resolved calibration

TRILIS TRIUMF's Resonant Ionization Laser Ion Source

TRIUMF Canada's national particle accelerator centre

TTL transistor-transistor logic

VME Versa Module Europa

WITCH Weak Interaction Trap for Charged Particles

Chapter 1

Introduction – from the masses of single nuclei to the physics of neutron stars

The mass of an atomic nucleus is one of its fundamental properties. Through the binding energy, i.e. the energy equivalent of the mass difference between the bound nucleon system and the sum of its isolated constituents, the nuclear mass provides a sensitive measure of the interactions between its underlying protons and neutrons. Giving access to the valuable information decoded in nuclear binding energies, precision measurements of atomic masses form a key technique for nuclear structure studies [1, 2], tests of fundamental symmetries [3, 4] and nuclear astrophysics [5–7].

Atomic mass measurements have long emerged as a major driving force for studies of nuclear structure. Substantial efforts in this field evolve around questions such as: How do interactions between nucleons arise from the underlying quark-gluon dynamics of quantum chromodynamics? What happens to the structure of a nucleus as one successively changes its proton or neutron content? Where lie the limits of nuclear existence?

In search for answers to these questions, a variety of algebraic mass relations [8–11] have been formulated that combine the mass values of multiple, close-by nuclides with the goal to isolate certain nuclear structure aspects or features of the underlying nuclear interactions. Arguably the most fundamental mass relations are given by the one-proton and one-neutron separation energies, which are denoted S_p and S_n, and measure the minimal energy required to release a proton or neutron from the nucleus, respectively. Successively following an isotopic chain to regions far away from the valley of β-stability, the backbone of the Segrè chart of nuclides formed by all non-radioactive isotopes, one eventually reaches an isotope for which S_p or S_n become negative. Isotopes where this is the case are energetically unstable and decay by emission of a nucleon [12]. The zero-crossing of S_p and S_n thus delineate the so-called proton and neutron drip line, respectively — two fundamental bounds of nuclear stability [13].

The advent of accelerator-based isotope production techniques [14–16] in the second half of the last century has enabled physicists to synthesize and probe radioactive isotopes that are not naturally occurring on earth and therefore referred to as rare isotopes. As the isotope production capabilities and the sensitivity of experimental techniques advanced, ex-

perimentalists have been able to access rare isotopes increasingly far from the valley of stability [17]. In many cases, studies of rare isotopes far from stability have revealed exotic phenomena that find no counterpart in stable nuclides and whose description poses a challenge — or rather opportunity of growth — for nuclear structure theory. The prime example of such exotic behavior is the emergence of unexpectedly tight binding in some rare isotopes whose proton number Z and neutron number N differ from the canonical magic numbers [18, 19] predicted by the nuclear shell model [20].

Of special interest to this thesis are neutron-deficient isotopes in the vicinity of the proton drip line at mass numbers $A \approx 40$–70, a region of the nuclear chart that hosts a rich set of interconnected physics [12, 17]. Due to the Coulomb repulsion between protons, the proton drip line lies substantially closer to stability than the neutron drip line. While neutron-unbound nuclides ($S_n < 0$) are known to decay on times scales far below one nanosecond [21], the Coulomb barrier allows nuclides beyond the proton drip line ($S_p < 0$) to exist in metastable states that, in exceptional cases, exhibit half-lives of several $100\,\mathrm{ms}$ against proton emission [22]. The comparatively long half-lives of some proton-unbound nuclides introduce subtleties in the experimental localization of the proton drip line and demand accurate mass measurements to stringently map out the, in many isotopic chains unknown, position of this important limit of nuclear stability [17, 23].

Another topic that has seen large interest in this region of the nuclear chart is the symmetric structure of isobars (i.e. nuclides of the same mass number) on either side of the $N = Z$ line. These nuclides can be interconverted by exchange of their proton and neutron numbers and are thus referred to as mirror nuclei. Assuming that nucleon-nucleon forces conserved isospin symmetry and correcting for the mass difference of the proton and neutron, the mass difference of mirror nuclei would be expected to be fully explained by the Coulomb interaction. The experimental observation that mirror nuclei do not adhere to this expectation became known as the Nolen-Schiffer anomaly [24] and was explained by the fact that isospin symmetry in nuclei is not only broken by the Coulomb interaction but to a lesser degree also violated by nucleon-nucleon forces [25, 26]. Studies of the mass differences of isobaric nuclides around the $N = Z$ line therefore provide important information for the development of isospin nonconserving corrections to nuclear shell models [27, 28]. A powerful tool to test and refine such isospin nonconserving corrections is the isobaric multiplet mass equation (IMME) [8] which relates the masses of isobaric analog states in nuclei near $N = Z$, as will be detailed in the subsequent chapter. Isospin-symmetry-breaking corrections find important application in tests of fundamental symmetries of the electroweak interaction [4, 29] which are based on superallowed Fermi β-decays of nuclides with $N \approx Z$ such as ^{62}Ga [30].

Atomic mass measurements also provide essential inputs for nuclear astrophysics since they determine the Q-values and thus the absolute rates and temperature sensitivity of nuclear reactions underlying explosive cosmic nucleosynthesis scenarios such as supernovae and Type I X-ray bursts [5, 31]. A key objective of the nuclear astrophysics community [32] is to understand the structure of neutron stars and the wealth of exotic physics assumed to occur within them [33]. Their extreme gravity and density conditions make neutron stars

valuable tools to constrain the equation of state of dense nuclear matter [34–36] or to elucidate phenomena such as neutron superfluidity and proton superconductivity [32, 37]. As I will lay out in chapter 2, the quest to unravel details about the internal structure and the exotic physics of neutron stars [32, 38] is a multi-disciplinary endeavour that requires contributions from astronomy, nuclear astrophysics and nuclear physics.

A promising way to extract information about neutron stars lies in Type I X-ray bursts [39], recurring, thermonuclear explosions that are frequently observed on the surface of accreting neutron stars. By modelling the nuclear reaction sequences that power these cosmic events nuclear astrophysicists may predict the light curves of X-ray bursts [40] and, by comparing their predictions to astronomical observation, deduce critical information about the parameters of the underlying neutron star [41–45].

The primary energy source of Type I X-ray bursts is the rapid proton capture process (*rp*-process) [46, 47], a sequence of fast proton capture reactions and slower β-decays that may synthesize neutron-deficient isotopes up to the $A \approx 100$ region [48]. The *rp*-process is known to critically affect the shape of the X-ray burst light curve [49]. Sensitivity studies [50, 51] have demonstrated that X-ray burst model predictions depend critically on nuclear properties of nuclides along the *rp*-process path, especially those near so-called waiting point nuclei whose comparatively small proton capture Q-values and long β-decay half-lives may slow down the thermonuclear energy generation. Although many of the relevant model inputs, in particular masses and β-decay half-lives, have been measured over the last two decades, a number of critical masses and other nuclear properties remain unmeasured or are not known accurately enough [51]. Chapter 2 gives a more detailed description of the mentioned interplay between astronomy, nuclear astrophysics and nuclear physics in the quest to constrain the properties of neutron stars. It further discusses the special role played by nuclear masses in pinning down the *rp*-process flow and presents a detailed motivation for the mass measurements reported in this thesis.

This thesis covers two main topics and is thus effectively split into two parts. The major goal of the first part of thesis is to reduce prediction uncertainties of X-ray burst models deriving from ill-constrained nuclear properties near the ^{60}Zn *rp*-process waiting point. To this end, precision mass measurements of neutron-deficient gallium isotopes were conducted at TRIUMF's Ion Trap for Atomic and Nuclear Science (TITAN) [52, 53] in Vancouver, Canada. The measurements were performed with a multiple-reflection time-of-flight mass spectrometer (MR-TOF-MS) [54], a comparatively new type of mass spectrometer that, over the last decade, has extended the reach of precision mass measurement facilities worldwide closer to the nuclear drip lines. To provide context for the discussion of the measurement results, the central techniques for mass measurements of rare isotopes as well as the primary isotope production methods are reviewed in chapter 3. Chapter 4 gives an overview of the TITAN experiment and introduces the experimental components of relevance to this thesis. Chapter 5 presents the results and implications of the gallium mass measurements. After a description of the data analysis procedure, the obtained mass values are reported and compared to pre-existing data. Subsequently, the implications of the new data with respect to the location of the proton drip line, the isobaric multiplet mass equation and X-ray burst

model predictions are discussed.

While the addition of an MR-TOF-MS has substantially extended the sensitivity limit for mass measurements at TITAN, parallel efforts have been focused on further improving the precision limit of the facility [55–57]. These technical developments will enable high-precision measurements for fundamental-symmetry tests and Q-value determinations for neutrino physics [57]. A key feature that distinguishes TITAN [58] from other mass measurement setups at rare isotope beam facilities, is its combination of an electron beam ion trap (EBIT) charge breeder [59] with a Penning trap mass spectrometer [60] which allows for the charge of the radioactive ions of interest to be raised prior to the mass measurement. Exploiting the linear increase of a trapped ion's cyclotron frequency with the charge state, TITAN has demonstrated that charge breeding of radioactive ions can substantially increase the achievable mass precision and resolving power [61–63], or alternatively reduce the overall measurement time needed to reach a given precision level [61]. However, charge breeding in an EBIT deteriorates the ion beam quality [64], which, in turn, negatively affects the mass measurement and mitigates the benefits of high charge states. In order to access the full potential of Penning trap mass spectrometry with radioactive HCI, it is desirable to cool the charge bred ions prior to the mass measurement [65]. Cooling of radioactive HCI is an experimental challenge, as established cooling techniques such as buffer gas cooling are not applicable [65] due to the short decay half-lives or the HCI's tendency to undergo charge exchanging collisions with neutral gas particles. Electron cooling of HCI in a cooler Penning trap has been proposed as a promising alternative [65] but remains to be demonstrated experimentally. To investigate the prospects of this cooling method in regards to cooling of short-lived radioactive HCI, a cooler Penning trap was developed at TITAN [55, 65].

As the second main topic of this thesis, exploratory studies of electron cooling of singly charged ions were performed with TITAN's cooler Penning trap (CPET). These investigations and the technical developments that enabled them are reported in chapter 6. The systematic studies of electron cooling of singly charged ions are analyzed in a cooling model that is adjusted to the experimental results. Extrapolation of the model results to HCI enables us to comment on the prospects of the technique for cooling of charge-bred, radioactive ions.

The thesis closes with conclusions and an outlook in chapter 7.

Chapter 2

Background - X-ray bursts and nuclear physics near the proton drip line

Precision measurements on rare isotopes near the proton drip line are important to a rich set of interconnected physics, ranging from the macroscopic properties of neutron stars down to the microscopic interactions of individual nucleons. The first half of this chapter gives an overview of our understanding of type I X-ray bursts and outlines how these cosmic scenarios can serve as unique probes of explosive nucleosynthesis, the exotic physics of neutron stars and the properties of matter under extreme density conditions. The discussion highlights the importance of accurate nuclear properties for X-ray burst models and emphasizes the special role played by nuclear masses. The gradually narrowing focus leads into a detailed astrophysical motivation of the mass measurements of neutron-deficient gallium isotopes presented in this thesis.

In regions where nuclear properties have not yet been measured, predictions from nuclear theory become essential ingredients of nucleosynthesis models. The second half of this chapter thus introduces some of the most common theoretical tools for predictions of masses and other nuclear structure observables of astrophysical interest. After a brief review of global mass models, the discussion turns to local mass extrapolation methods and shell-model studies of nuclides near the $N = Z$ line. A focus is placed on the subtle but often critical role of isospin-symmetry breaking in nuclear interactions.

2.1 Type I X-ray bursts

Type I X-ray bursts[1] are the most frequently observed thermonuclear explosions in the universe [66]. They take place on the surface of accreting neutron stars and are fuelled by the typically hydrogen- and helium-rich matter accumulated from the outer layers of a faint, low-mass ($M < 1M_{\odot}$, where $M_{\odot}$ denotes the solar mass) companion star [39].

The matter transfer between both stars is not necessarily continuous but may occur in intermittent episodes [67]. During these so-called outbursts, the matter from the companion

[1] The classification as type I indicates that the X-ray burst arises from a thermonuclear runaway instead of accretion instabilities as is the case for the much less common Type II X-ray bursts [66].

star overflows from its Roche lobe and forms an accretion disk around the neutron star. As the material spirals inward and reaches the neutron star surface, pressure gradients cause it to distribute evenly across the stellar surface and form a thin (~ 1–10 m) spherical shell [68]. In its approach to the neutron star surface, the accreted matter releases significant amounts of gravitational binding energy (≈ 200 MeV per nucleon [37]). The released gravitational energy heats the stellar environment and results in the emission of blackbody radiation which can be detected by distant telescopes as a persistent flux of X-rays. As more accreted material piles up, the extreme surface gravity of the neutron star ($g_{\mathrm{NS}} \approx 10^{12}\,\mathrm{m/s^2}$ [69]) compresses the matter deeper in the accretion layer, resulting in a gradual increase in pressure and temperature. Eventually, suitable conditions are reached to trigger a thermonuclear runaway through a thin-shell instability [70]. The ensuing thermonuclear explosion releases enormous amounts of energy (10^{32}–10^{33} J [71]) over typically 10–100 s and results in a bright X-ray flash that is $\approx$ 10-100 times more luminous than the persistent X-ray emission during the accretion phase [69]. Despite the enormous energy release, the X-ray burst is not powerful enough to affect the integrity of the neutron star; once the unstable nuclear burning ceases, a new cycle of accretion and subsequent thermonuclear ignition may follow. X-ray bursts can thus be observed as series of bright, recurring flashes.

Besides being fascinating objects of study in their own right, X-ray bursts further allow us to refine our understanding of explosive nucleosynthesis [31, 42] and can act as sensitive probes of the underlying neutron star [72]. The primary energy source of most X-ray bursts is the *rp*-process [46, 47] which synthesizes increasingly heavy, proton-rich nuclides up to the $A \approx 100$ region [48]. After the thermonuclear burning ceases, these nuclides and their decay products stay behind as the burst ashes. It has been conjectured [47, 73] that the burst ashes might contribute to the solar elemental abundances and thus help to explain the unexpectedly large abundance of certain proton-rich isotopes, the so-called light p-nuclei, in the solar system [47, 74]. However, it remains unclear whether substantial amounts of material can be ejected out of the extreme gravitational field of the neutron star [67, 71].

Over the last decade, an increasing emphasis has been placed on using X-ray bursts to probe the hosting neutron star [75]. Comparing astrophysical model predictions to X-ray burst observations enables the extraction of system parameters [40, 42, 43, 71, 76–79] such as the accretion rate, the fuel composition or neutron star mass and radius. Section 2.1.1, will introduce some of the exotic neutron star physics that can, in principle, be elucidated through X-ray burst model-observation comparisons. However, the quantitative extraction of system parameters requires robust astrophysical models and accurate nuclear physics inputs. Model-observation comparisons are therefore inherently collaborative and interdisciplinary endeavours. Sections 2.1.2, 2.1.3 and 2.1.4 outline the respective roles that astronomy, theoretical astrophysics and nuclear physics play in the collective effort to understand X-ray burst phenomena and constrain the properties of neutron stars. Section 2.1.4 highlights the special importance of masses in determining the nuclear reaction paths that power X-ray bursts. Section 2.1.5 details the astrophysical motivation for the gallium mass measurements presented in this thesis.

2.1.1 Neutron stars as laboratories of ultradense matter

Neutron stars are among the most extreme environments in the observable universe. Compressing a mass of 1–2 $M_\odot$ into a sphere with a radius of about 10 km [80], they contain matter at densities more than three times higher than the typical interior density of heavy nuclei ($\rho_0 = 2.8 \times 10^{14}$ g cm^{-3} [81]) and exhibit a surface gravity roughly 11 orders of magnitude stronger than that of the earth. The behaviour of matter under such extreme conditions is poorly understood and its theoretical description poses a major challenge for modern fundamental physics. While terrestrial studies of dense matter with heavy ion colliders [82] inherently involve high temperatures, neutron stars provide a unique avenue to study ultradense matter at comparatively low temperatures ($T \sim 10^8$ K), where macroscopic quantum phenomena such as superfluidity and superconductivity are expected to occur [32, 72, 83].

Neutron stars can therefore serve as distant laboratories for studies of cold, ultradense matter as well as for tests of general relativity [32, 80, 84]. One of the major questions concerning the physics of ultradense matter is that of its equation of state [35, 36, 85], i.e. the relation between pressure and energy density. The most direct way to constrain the dense matter equation of state lies in measuring the neutron star's mass and radius [34, 72, 86, 87]. While neutron star masses are comparatively well constrained from pulsar timing measurements [88], observational radius determinations are challenging and still involve significant uncertainties [86, 88]. The recent addition of radius constraints from gravitational wave astronomy [44] has improved the situation [88]. However, since all radius determination methods rely on astrophysical model assumptions, it is important to pursue multiple, independent approaches to minimize the risk of model-dependent systematic uncertainties [86].

Already early theoretical studies pointed out the possibility to use X-ray burst observations to extract the mass, radius and other global properties of the underlying neutron star [89–91]. In recent years, constraints derived from X-ray burst observations have been showing an increasing level of convergence with detailed observations [34, 72, 86, 88, 92] and reinforced the interest in using these events as probes of the interior of neutron stars and dense matter in general. Comparisons of X-ray burst model predictions to astronomical observations can, in principle, provide detailed constraints on many of the astrophysical parameters of interest [42, 43, 79]. However, such constraints are presently still hampered by astrophysical model uncertainties and insufficient knowledge of nuclear physics inputs [43, 50, 51, 93]. The following sections will provide selected examples of how burst observations can be used to constrain neutron star properties and how these constraints are affected by nuclear physics uncertainties.

Although X-ray bursts take place in the outermost layers of neutron stars, they crucially affect the thermal structure and matter composition of deeper stellar regions. This is best seen by considering the journey of accreted material through the different radial layers of the neutron star, as illustrated in Fig. 2.1. The outermost layers of the accreting neutron star are given by a gaseous atmosphere on top of an optically-thick, liquid ocean [67]. Together, they are referred to as the neutron star envelope and form the hosting environment for all types of X-ray bursts. The *rp*-process in X-ray bursts [47, 94] (see section 2.1.4 for details)

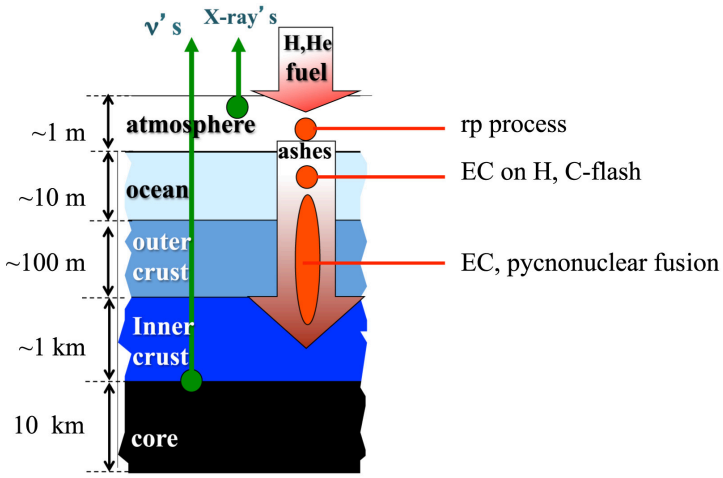

Figure 2.1. Radial structure of a neutron star in a logarithmic scale. The large arrows indicate the inward transport and the processing of the accreted fuel and the X-ray burst ashes through nuclear reactions. Figure adapted from [38] (Courtesy of H. Schatz), ©2016, with permission from Elsevier.

synthesizes the accreted hydrogen- and helium-rich fuel in the atmosphere into heavier, proton-rich isotopes. The latter stay behind as the burst ashes once the unstable burning ceases. As new material accretes on top of them, the burst ashes are successively incorporated into the ocean. There, they may provide a sufficient carbon enrichment to cause the ignition of a powerful carbon-flash referred to as superburst [95].

If not consumed by a superburst, the burst ashes migrate deeper into the neutron star and enter its ~ 1 km-thick, solid crust. The outer crust is composed of a Coulomb lattice of fully ionized nuclei and a degenerate electron gas. The inner crust is characterized by sufficiently high densities ($\rho > 4.3 \times 10^{11}$ g cm^{-3} [85]) for some neutrons to "drip" out of the nuclei, thus adding a superfluid of free neutrons to the electron gas and the crystal lattice. The degenerate electron gas induces electron capture reactions that successively convert the proton-rich ashes into neutron-rich nuclei. The high electron densities further screen the Coulomb barriers to such a degree that zero-point oscillations around the crystal lattice sites can induce fusion reactions [37, 96]. In contrast to thermonuclear fusion, these pycnonuclear fusion reactions are pressure driven and essentially temperature insensitive [38]. The electron capture and fusion reactions cause the processed ashes to become progressively more neutron-rich as the depth and density increases. Some neutron star crusts [97] (and oceans [98]) contain pairs of neighbouring neutron-rich nuclei that undergo repeated cycles of electron captures and β-decays which remove substantial amounts of energy from the crust through neutrino emission. Shells of nuclei undergoing these so-called urca cooling cycles may act as thermal barriers [97] between different layers of the neutron star. Crustal heating and neutrino cooling processes affect the temperature conditions in the envelope [71, 97–99], which in turn influence the ignition of X-ray bursts [5, 100]. A comprehensive understanding of these processes requires reliable crust models which in turn depend on accurate mass values for neutron-rich nuclei [5].

At the transition region from the inner crust to the neutron star core, some theories predict nuclear matter to re-arrange into complex, non-spherical topologies, termed "nuclear pasta" [37, 101]. Since the burst ashes define the initial material for the nuclear processing within the crust [99], X-ray bursts are critical in understanding the matter composition and the exotic physics of the neutron star crust [71, 99].

Although it makes up most of the neutron star's volume and holds roughly 99% of its bulk mass [75], little is known about the neutron star core. It is assumed to consist of uniform nuclear matter compressed to a multiple of the nuclear saturation density ρ_0 [85]. It has further been conjectured that the pressure in the inner core might be high enough to cause nucleons to disintegrate into exotic phases of quark matter [35]. Questions concerning the phases of matter in the inner core of the neutron star will only find definitive answers with tighter constraints on the dense matter equation of state.

2.1.2 Astronomical observations

Due to their brightness and recurring nature, X-ray bursts have been extensively studied by observational astronomy. Since their discovery in 1975 [102], more than 7000 bursts from more than 110 different sources have been observed with space-based X-ray telescopes [39]. These observations provide essential data for the study and modelling of X-ray burst phenomena.

Particularly detailed observations have been obtained with the Proportional Counter Array installed on the Rossi X-ray Timing Explorer (RXTE) satellite [67], which recorded more than 1100 bursts with timing resolutions as low as $1\,\mu s$ [103]. Since the decommissioning of RXTE in 2012, a new generation of X-ray telescopes has taken over. It includes instruments such as the Nuclear Spectroscopic Telescope Array (NuSTAR) [104], AstroSat [105] and The Neutron star Interior Composition Explorer (NICER) [106], which are presently mapping the X-ray sky with expanded spectral range [67] and unprecedented sensitivity. These astronomical efforts have resulted in extensive observational catalogues [103, 107, 108] that make high-quality data available for benchmarking of X-ray burst models [40, 42, 43].

The most important observables of an X-ray burst are the recurrence time and the shape of the light curve, i.e. the time evolution of the observed photon flux. These observational features are sensitive to parameters of the binary system such as the accretion rate, the fuel composition and the neutron-star spin frequency [66]. X-ray bursts can be broadly categorized by their duration [39].

The light curves of the most common class of Type I X-ray bursts are characterized by a fast rise of the luminosity over typically ≈ 1–$10\,s$ followed by a slower decay over timescales of ≈ 10–$100\,s$ [66]. The recurrence times typically range from hours to days [39]. Through astrophysical modelling, this class of X-ray bursts has been associated with hydrogen and helium burning in the neutron star atmosphere [109–111]. Different fuel composition upon ignition give rise to systematic variations in the observational features [103]. These variations are a result of the complicated interplay between hydrogen and helium burning and up

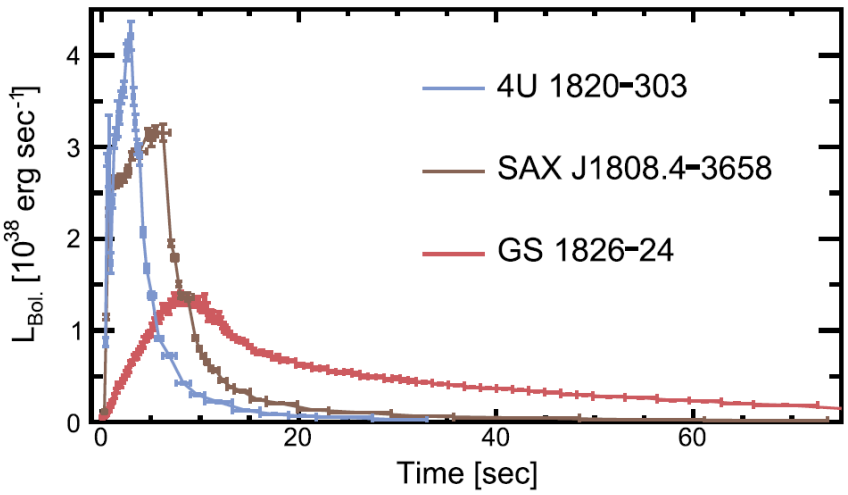

Figure 2.2. Representative light curves for observed Type I X-ray bursts with different fuel compositions. The light curves observed from the sources 4U 1820-303, SAX J1808.4-3658 and GS 1826-24 are typical for a pure He, a He-rich and a mixed H/He burst, respectively. The former two bursts exhibit photospheric radius expansion (see text for details). Figure adapted from [67]. ©IOP Publishing. Reproduced with permission. All rights reserved.

to seven distinct burst ignition regimes have been theoretically predicted [39, 107].

Fig. 2.2 shows examples of observed light curves of H and/or He powered X-ray bursts with different fuel compositions. The light curve from the source 4U 1820-303 shows the rapid rise and the high peak luminosity typical for a pure He Type I X-ray burst. The less bright light curve observed from SAX J1808.4-3658 is accorded to a He-rich ignition environment. The light curve from GS 1826-24 is characterized by a moderate peak luminosity and an extended tail – typical characteristics of a mixed H/He Type I X-ray bursts [111]. The longer durations of hydrogen-burning bursts are the result of an extended *rp*-process which includes slow nuclear β-decays that delay the cooling of the neutron star envelope (see section 2.1.4 for details). Due to its regular recurrence times, GS 1826-24 has been the prime target of model-observation comparisons [40–43] and is often referred to as the "clocked burster" or the "textbook burster".

Two other classes of bursts with longer durations have been identified [39]. So-called superbursts exhibit durations of many hours to days and are about 1000 times more energetic than regular Type I X-ray bursts [112]. These events are thought to be triggered by carbon burning in the neutron star ocean [113]. Intermediate duration bursts fall between regular bursts and superbursts in terms of both their duration and their energy release [114]. These bursts are believed to arise from helium ignition in deeper layers of the neutron star envelope [113]. We will not discuss the less common intermediate bursts and superbursts any further and focus on H/He-fuelled bursts from here on.

Several methods for neutron star mass and radius determinations [75, 83] exploit that most burst emission spectra resemble that of a black body [110, 115]. Of particular interest [34, 83, 86] are bursts exhibiting photospheric radius expansion [116]. These events are sufficiently intense to exceed the Eddington luminosity, at which point the radiation pres-

sure exceeds the gravitational compression at the stellar surface, causing the photosphere[2] to lift off from the stellar surface. This effect is most commonly seen in powerful He-fuelled bursts [39], such as the ones from 4U 1820-303 and SAX J1808.4-3658 in Fig. 2.2. The expansion is accompanied by a decrease in the observed black body temperature. After sufficient radial expansion, the luminosity drops below the Eddington limit, causing the photosphere to contract and its temperature to rise again. The observed photon flux at the moment the photosphere touches back down on the stellar surface, $F_{\mathrm{TD},\infty}$, is assumed to equal the Eddington flux [86]

$$F_{\mathrm{TD},\infty} = \frac{1}{4\pi d^2}\frac{4\pi GMc}{\kappa}\left(1-\frac{2GM}{Rc^2}\right)^{1/2}, \tag{2.1}$$

where d is the distance to the observer, κ is the opacity of the atmosphere, M and R are the neutron star mass and radius, respectively, G is the gravitational constant, c is the speed of light. The touchdown is followed by a gradual cool-down of the atmosphere [75]. Throughout this cooling tail of the light curve, the apparent emission area A stays constant and can be determined by simultaneous measurement of the flux F_∞ and the black body temperature T_∞ using the relation [86]

$$A = \frac{F_\infty}{\sigma T_\infty^4} = \frac{R^2}{d^2 f_c^4}\left(1-\frac{2GM}{Rc^2}\right)^{-1}, \tag{2.2}$$

where σ is the Stefan-Boltzmann constant, and the color correction factor $f_c = {}^{T_\infty}/_{T_{\mathrm{eff}}}$ accounts for absorption-induced deviations between the observed black body temperature T_∞ and the effective surface temperature T_{eff}. When d, κ and f_c are sufficiently well known, these two equations can be used to determine the stellar mass M and radius R.

Such observational mass-radius determinations require detailed modelling of the neutron star atmosphere and robust knowledge of its chemical composition. The opacity κ arises from Thompson scattering and can be estimated from the atmospheric hydrogen mass fraction X_H via $\kappa = 0.2(1+X_H)\mathrm{cm}^2\,\mathrm{g}^{-1}$ [66]. The color correction factor f_c is determined from atmosphere models [81, 117, 118] and depends on the metallicity[3] of the atmosphere. Since the predicted burst ashes affect the chemical composition of the atmosphere [119], reliable X-ray burst models are therefore critical for neutron star mass and radius determinations from observed photospheric radius expansion bursts.

2.1.3 X-ray burst models and model-observation comparisons

Computational models have been instrumental in shaping our current understanding of X-ray bursts. They allow astrophysicists to interpret burst observations in terms of the underlying nuclear reaction sequences and enable the extraction of system parameters such as the accretion rate, and the matter composition of the neutron star envelope. While this has facilitated

[2] The photosphere refers to the innermost optically-thin layer of a stellar atmosphere.

[3] Metallicity here refers to the mass fraction of elements heavier than hydrogen and helium - a common definition used in astronomy and astrophysics.

detailed deductions of many astrophysical parameters, such as the accretion rate and the fuel composition [40], the reliable extraction of neutron star properties is more challenging and presently still hampered by nuclear uncertainties, as will be illustrated below. X-ray burst models are therefore also important to guide experimental efforts by identifying the most critical nuclear input uncertainties [42, 43, 50, 51].

Already shortly before the first observations of X-ray bursts in 1975 [102, 120], numerical studies had indicated the high likelihood of unstable nuclear burning in the outer layers of neutrons stars [70]. Extending this pioneering work, further modelling efforts [91, 109, 121] could confirm the first X-ray bursts observations as results of thermonuclear explosions on the surface of accreting neutron stars. While these early models succeeded in qualitatively reproducing the gross observational features of X-ray bursts [110], the computationally-limited size of the underlying nuclear reaction networks prevented a more quantitative theoretical description. Subsequent studies steadily increased the size of the modelled reaction networks [122–124].

In 2001, a landmark study by Schatz et al. [48] used a single-zone model with a reaction network of more than 600 isotopes to cover, for the first time, the full range of X-ray burst nucleosynthesis. The model approximated the neutron star envelope as a single spherically symmetric layer. The astrophysical density and temperature evolution within this layer was tracked self-consistently, accounting for their interplay with the nuclear energy generation. This study established that, even under the most favourable conditions, the *rp* process ultimately terminates in a cyclic reaction flow pattern, the SnSbTe cycle [48], suggesting $A \approx 107$ as the upper mass limit of the produced burst ashes.

Another milestone was reached in 2007, when Heger at al. [40] reproduced large parts of the observed light curve of the clocked burster GS 1826-24 in one-dimensional multi-zone simulations[4] with the hydrodynamics code KEPLER [94, 125]. Due to further computational advances and improved nuclear input data, multi-zone models are now able to closely match observed features of GS 1826-24 [42, 43, 126], as illustrated in Fig. 2.3. At first glance, these successes indicate that model-observation comparisons might soon be able to yield important constraints on neutron star properties.

However, the close agreement between models and observation should be taken with caution since many possible sources of systematic uncertainties remain unquantified. To verify the numerical fidelity of the models, they have to be tested against each other [77]. First direct comparisons [42, 68] have shown unexplained discrepancies and call for more systematic cross checks between different multi-zone models [42]. Within the variety of bursting behaviours, there are also still a number of astrophysical phenomena that cannot be reproduced by the models. Some examples are superbursts and the flame spreading across the neutron star surface during burst ignition. So far, attempts to model superbursts [95, 127] have not been able to match all observational features. Flame spreading [128] refers to the assumption that the unstable thermonuclear burning first ignites at localized hot spots and subsequently spreads across the entire neutron star surface. Numer-

[4] 1D multi-zone simulations approximate the neutron star envelope as a stack of spherically symmetric shells and can thus resolve radial gradients in temperature, density and matter composition. [94]

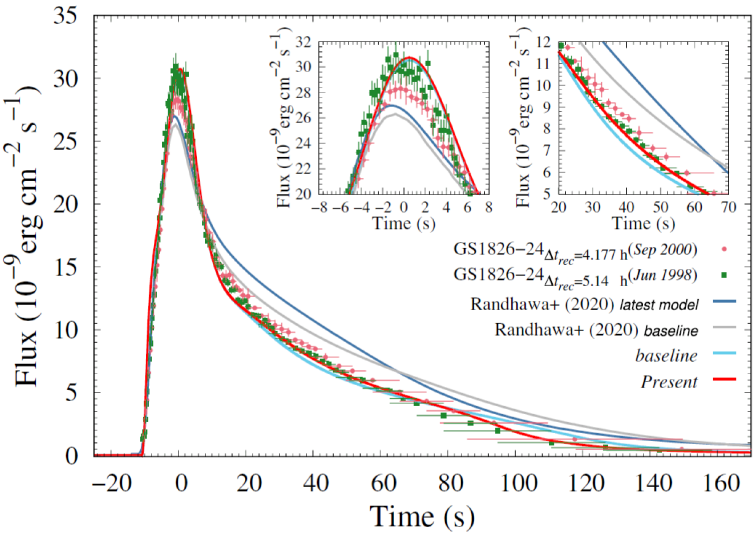

Figure 2.3. Model-observation comparison of the light curve of the clocked burster GS 1826-24. Averaged observational data from the 1998 and 2000 bursting epochs of GS 1826-24 (data points) were fitted with predictions from the multi-zone model KEPLER (lightblue and red lines) and MESA (darkblue and grey lines), respectively. The difference between the light curves from a given model result from variation of the $^{22}\mathrm{Mg}(\alpha,\mathrm{p})$ reaction rate. Reprinted with permission from [126]. ©2021 by the American Physical Society.

ical studies of the lateral propagation of the burning front inherently require 2D (or 3D) hydrodynamic models, which can presently not be coupled to large reaction networks due to computational limitations [129]. Even more importantly, ill-constrained nuclear inputs can substantially alter the calculated light curves, the ash computation and other predicted observables [50, 51, 93, 130].

Recent X-ray burst model-observation comparisons by Meisel et al. [43] explored, for the first time for a specific astronomical source, to which extent nuclear input uncertainties affect predictions of neutron star properties. Building on an earlier study [42], they performed MESA multi-zone simulations to model burst sequences from GS 1826-24 and varied ill-constrained nuclear reaction rates. The simulated luminosity $L(t)$ of the light curve was converted to an observable flux F using the relation

$$F(\tilde{t}) = \frac{L(\tilde{t})}{4\pi\xi_b d^2(1+z)}, \tag{2.3}$$

where $(1+z)$ is the gravitational redshift, $\tilde{t} = (1+z)t$ is the dilated time, and flux variations due to the burst emission anisotropy ξ_b are accounted for by replacing the true distance between neutron star and observer d with the observed distance $d\sqrt{\xi_b}$. Using Eqn. 2.3 to match the simulated luminosity $L(t)$ to the observed lightcurve $F(\tilde{t})$ allowed Meisel et al. to extract constraints on the surface gravitational redshift $(1+z)$ and the observed distance $d\sqrt{\xi_b}$. To evaluate the sensitivity of these constraints to uncertainties of nuclear inputs, they re-performed their analysis after varying single critical reaction rates. Fig. 2.4 a) illustrates how the reaction rate variations shift the associated confidence regions with respect to the

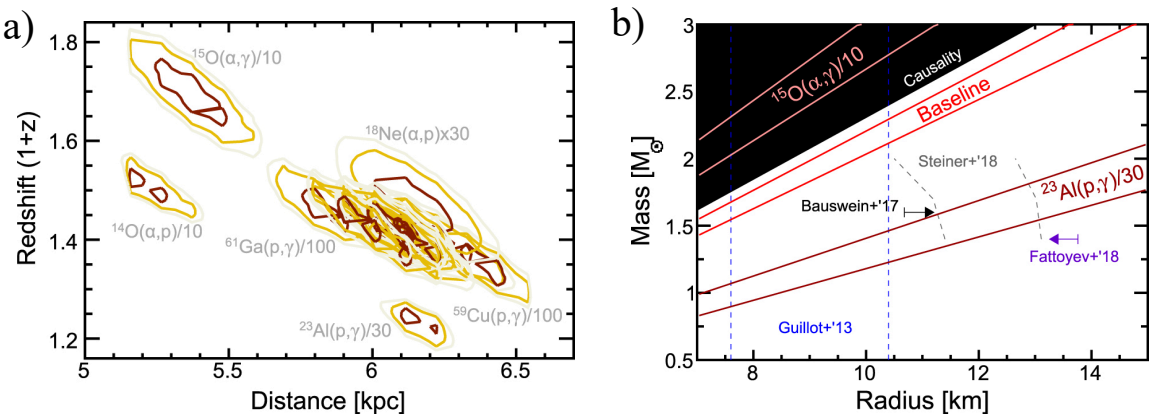

Figure 2.4. a) Neutron star redshift-distance constraints extracted from X-ray burst model-observation comparisons after variation of different reaction rates [43]. Lines indicate the corresponding 68% (red), 95% (orange) and 99% (gray) confidence regions. b) Neutron star mass-radius constraints derived from the 68% confidence intervals of selected $(1+z)$ from a). Radius constraints from other astrophysical observables [84, 131–133] are also shown and the region excluded by causality [134] is indicated in black. Variation of the nuclear model inputs induced large prediction uncertainties. Figures reproduced with permission from [43]. ©AAS.

baseline result.

With the gravitational redshift constrained, the following general relativistic relation was used to place bounds on the neutron star mass-to-radius ratio $^{M}/_{R}$:

$$1 + z = \left(1 - \frac{2GM}{Rc^2}\right)^{-1/2} . \tag{2.4}$$

The mass-radius prediction bands resulting from the baseline result and from variation of the two most critical reaction rates are shown in Fig. 2.4 b). The baseline prediction shows that, in principle, X-ray burst model-observation comparisons have great potential to constrain neutron star properties. When combined with independent determinations of M_{NS}, these constraints could yield R_{NS} estimates and help to constrain the equation of state of neutron star matter. However, at present, ill-constrained nuclear model inputs can evidently induce substantial prediction uncertainties. In fact, the 10-fold reduction of the $^{15}O(\alpha,\gamma)$ rate compared to the baseline rate from [135] contradicts constraints derived from causality [134].

This example illustrates that critical nuclear uncertainties have to be addressed before neutron star properties can be reliably constrained by X-ray burst model-observation comparisons. Meisel et al. also noted [43] that additional systematic uncertainties might arise from neglected astrophysical effects such as flame spreading. Further exploration of these effects and detailed evaluations of the sensitivity of model-observation comparisons to other nuclear inputs such as masses are desirable. As nuclear mass uncertainties have shown significant impact on predicted light curves and burst ashes [51, 93, 136], model-observation comparisons can also be assumed to be sensitive to nuclear mass inputs. Nuclear masses are further important inputs for calculations of unmeasured reaction rates and can therefore also

indirectly induce reaction rate uncertainties [5]. More experimental work is needed to eliminate the impact of nuclear uncertainties on model-observation comparisons. This would mark an important step towards the long-term goal of using neutron stars as laboratories of ultradense matter.

2.1.4 The *rp*-process and the importance of nuclear masses

The energy generation and the nucleosynthesis in X-ray bursts is determined by the underlying nuclear reaction sequences. Burst observables such as the light curve or the composition of the burst ashes are sensitive to nuclear input uncertainties. Therefore, nuclear physics plays an important role in understanding the variety of observed burst phenomena and accurate nuclear properties are essential inputs for X-ray burst models.

Mixed H/He bursts are frequently observed and exhibit the most extensive nucleosynthesis, making them ideally suited to probe the impact of nuclear inputs on model predictions [137]. The reaction flow in these bursts is determined by the 3α-process, the hot CNO cycles, the αp-process and the *rp*-process [67]. The interplay between these processes has been described in detail in [94] and [138]. The presentation here first gives a broad overview of the main reaction sequences underlying a H/He-fuelled X-ray burst before focusing on the role of the *rp*-process.

Fig. 2.5 shows the simulated reaction flow of a mixed H/He X-ray burst, indicating the extent of the different reaction sequences and the respective parts of the light curve that they power. Since the hydrogen-burning, hot CNO cycles become temperature independent at $T \gtrsim 0.7\,\mathrm{GK}$, they alone cannot induce a thermonuclear runaway [139]. Instead, He burning through the temperature-sensitive 3α-process provides the trigger for burst ignition, resulting in sufficiently high temperatures to activate breakout reactions from the hot CNO cycles [39].

The breakout reactions form the start of the αp-process [46], a series of (α,p) reactions and proton captures (p,γ). These reactions boost the nuclear energy generation rate, causing the sharp initial rise of the burst light curve. Due to the increasing height of the Coulomb barriers, (α,p)-reactions become successively less likely at higher masses, eventually causing the αp-process to fade out. The extent of the αp-process strongly depends on the specific astrophysical temperatures [5] but never reaches beyond the Sc region [6]. The proton-rich nuclei it produces form the seeds for the rapid proton capture process (*rp*-process).

The *rp*-process [46, 109, 137] acts as the main energy source of mixed H/He bursts [138]. Through a sequence of rapid proton captures and slower β-decays it synthesizes increasingly heavy neutron-deficient isotopes, under ideal conditions up to the mass $A \approx 100$ [48] region (see Fig. 2.5).

The reaction path of the *rp*-process is primarily fought out in a competition of proton captures, (p,γ), photodisintegrations, (γ,p), and β-decays [46]. The rates of the reverse process of photodisintegration, $\lambda_{(\gamma,\mathrm{p})}$, can be calculated from the corresponding proton capture

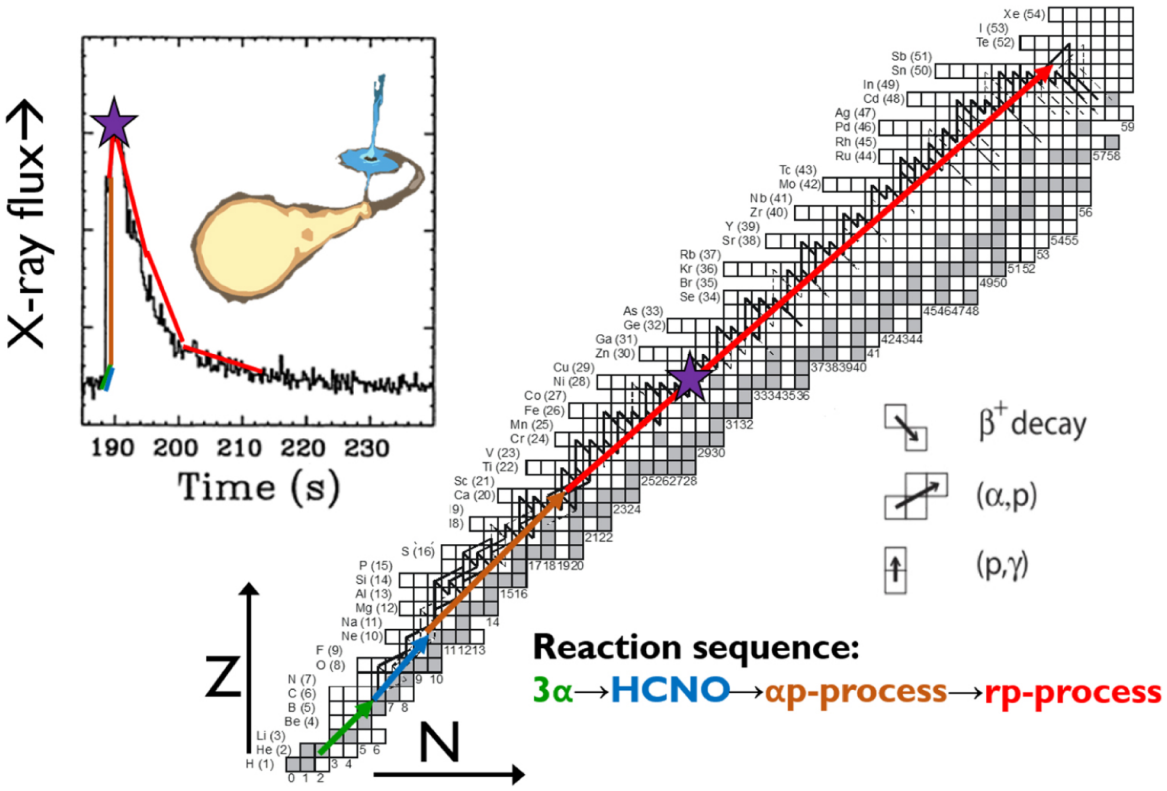

Figure 2.5. Nuclear reaction sequences powering Type I X-ray bursts. The black line shows the main reaction flow predicted by a simulation of a mixed H/He burst. The coloured lines indicate the extent of the underlying reaction sequences on the nuclear chart and the respective parts of the light curve that they drive are marked in the inset. See text for details. Figure from [67]. ©IOP Publishing. Reproduced with permission. All rights reserved.

rates, $\langle \mathrm{p}, \gamma \rangle$, using the principle of detailed balance [47]:

$$\lambda_{(\gamma,\mathrm{p})} = \frac{(2J_p+1)G_f}{G_i} \left(\frac{\mu k_B T}{2\pi\hbar^2}\right)^{\frac{3}{2}} \exp\left(-\frac{Q_{(\mathrm{p},\gamma)}}{k_B T}\right) \langle \mathrm{p}, \gamma \rangle, \tag{2.5}$$

where G_i and G_f denote the partition functions of the initial and the final nucleus, respectively, μ is the reduced mass of a proton and the final nucleus (after photodisintegration), J_p is the proton spin, T is the temperature, k_B is the Boltzmann constant, $\hbar$ is the reduced Planck constant, and $\langle \mathrm{p}, \gamma \rangle$ and $Q_{(\mathrm{p},\gamma)}$ denote the proton capture rate and Q-value, respectively. At the typical proton densities and temperatures during an X-ray burst, the proton capture rates are generally much higher than the competing β-decay and photodisintegration rates, causing matter to be transferred upwards along an isotone[5] to increasingly proton-rich nuclei. As the proton drip line is approached, the $Q_{(\mathrm{p},\gamma)}$-values decrease and the exponential function in Eqn. 2.5 causes the inverse photodisintegration events to become increasingly competitive with proton captures. Eventually, the photodisintegration rates become high enough to hamper further forward flow through proton captures, resulting in a local (p,γ)-(γ,p) equilibrium [51]. This forces the *rp*-process to proceed through a slow β-decay into

[5] An isotone refers to nuclides with identical neutron number N but differing proton numbers Z and forms a vertical line in the Segrè chart of nuclides (when plotting Z over N).

the next isotonic chain. There, the reaction flow can continue through rapid proton captures again. At typical X-ray burst conditions with temperatures of $T \approx 1\,\mathrm{GK}$, densities of $\rho \approx 10^6\,\mathrm{g/cm^3}$ and an initial hydrogen mass fraction of $X_H \approx 0.7$, local equilibrium is achieved if $Q_{(\mathrm{p},\gamma)} \lesssim 1\,\mathrm{MeV}$ [47, 67].

Nuclides with such a small positive or negative $Q_{(\mathrm{p},\gamma)}$-value and a long β-decay half-life with respect to the overall burst duration can considerably delay the forward reaction flow and act as so-called waiting points. In a typical mixed H/He burst, the first major waiting point is given by ^{56}Ni [73] (terrestrial half-life of $t_{1/2} = 6.1\,\mathrm{d}$). The reaction flow impedance imposed by ^{56}Ni reduces the nuclear energy generation rate and causes the temperature and luminosity to peak, as indicated by the star in Fig. 2.5. Further *rp*-process waiting points at higher masses (^{60}Zn, ^{64}Ge, ^{68}Se and ^{72}Kr) may subsequently delay the nuclear energy release, resulting in a light curve with an extended cooling tail [111] (see e.g. the GS 1826-24 burst light curve in Fig. 2.2).

The slow β-decay of a waiting point nucleus a can be bypassed through the sequential two-proton capture reaction $a(\mathrm{p},\gamma)b(\mathrm{p},\gamma)c$ [140]. At temperatures $T \lesssim 1.4\,\mathrm{GK}$, the net forward reaction flow is then essentially determined by the rate for two-proton capture on nucleus a [47]

$$\langle 2\mathrm{p},\gamma\rangle_a = \frac{2G_b}{(2J_p+1)G_a}\left(\frac{2\pi\hbar^2}{\mu k_B T}\right)^{\frac{3}{2}} \exp\left(\frac{Q_{a(\mathrm{p},\gamma)}}{k_B T}\right)\langle \mathrm{p},\gamma\rangle_b\,, \tag{2.6}$$

which depends linearly on the rate for proton capture on the intermediate nucleus, $\langle \mathrm{p},\gamma\rangle_b$, and exponentially on the Q-value for proton capture on the waiting point nucleus, $Q_{a(\mathrm{p},\gamma)}$.

A reliable determination of the *rp*-process path, and in extension the burst light curve and the ash composition, requires accurate β-decay half-lives, and proton capture rates and Q-values [32, 66]. The proton capture Q-values are fully determined by nuclear masses via the relation

$$Q_{(\mathrm{p},\gamma)} = m(A,Z) + m_p - m(A+1,Z+1), \tag{2.7}$$

where $m(A,Z)$ denotes the mass of the nuclide with mass number A and proton number Z, and m_p denotes the mass of the proton. Due to the exponential dependence on the Q-value in Eqn. 2.6, nuclear masses thus sensitively affect the *rp*-process flow near waiting point nuclei. Consequentially, accurate mass values, especially near waiting points, are crucial inputs for X-ray burst models [5, 31, 93]. Since masses enter Eqn.s 2.5 and 2.6 through a Boltzmann factor, the required mass precision depends on the astrophysical temperatures. At typical thermal energies of $k_B T \approx 86\,\mathrm{keV}$ in an X-ray burst, masses should be measured to a precision on the order of $10\,\mathrm{keV}$ to remove mass-induced uncertainties from burst model predictions [5].

Large efforts (see e.g. [137]) at rare isotope beam facilities have been devoted to constraining the relevant nuclear inputs for modelling the astrophysical *rp*-process. The β-decay half-lives of the contributing nuclides have essentially all been measured [32]. Many of the nuclear masses have been experimentally determined but some critical ones remain to be measured or are not known accurately enough [51]. Direct measurements of reaction

rates are particularly challenging since they often require higher beam intensities than currently available at rare isotope beam facilities [137]. Consequently, most proton capture rates along the *rp*-process path have so far escaped direct measurements [32]. The upcoming next-generation rare isotope beam facilities will substantially extend the experimental reach [67]; but even then, many of the relevant capture rates will likely not be directly measurable.

In the absence of direct measurements, capture rates have to be theoretically estimated. Reaction rate estimates are typically performed using a statistical Hauser-Feshbach [141, 142] approach or a narrow-resonance approximation [143–145] . The widely used Hauser-Feshbach calculations determine reaction rates as an average over many close-lying reaction resonances. At temperatures above 1 GK, this approach is valid for most nuclei along the path of the *rp*-process [47]. However, for nuclei close to the proton drip line or near nuclear shell closures, the reaction cross sections may be dominated by only a few isolated resonances, rendering the high-level density assumption of the Hauser-Feshbach approach invalid [142, 143, 146]. In these cases, reaction rates are more appropriately approximated as a sum over a few narrow resonances [147]:

$$\langle \mathrm{p},\gamma \rangle \propto \sum_j (\omega\gamma)_j \exp(-E_j/kT), \tag{2.8}$$

where $E_j = E_j^x - Q$ is the energy of the resonance leading to the level with excitation energy E_j^x in the compound nucleus. The resonance strengths $\omega\gamma$ are given by [147, 148]

$$\omega\gamma = \frac{2(J+1)}{(2J_p+1)(2J_g+1)} \frac{\Gamma_p \Gamma_\gamma}{\Gamma_p + \Gamma_\gamma}, \tag{2.9}$$

where J is the resonance spin, J_g is the ground-state spin of the initial nucleus, Γ_p is the proton partial width, Γ_γ is the γ partial width. Narrow-resonance rate estimates thus require detailed knowledge of the spins, parities, level energies and partial widths of the contributing states in the target nucleus [143]. This nuclear structure information is ideally obtained through indirect measurements [149], or otherwise deduced from nuclear structure models, typically the nuclear shell model (see e.g. [143]).

Through the exponential dependence on the resonance energies E_j, and thus the Q-value, reaction rate estimates are also critically affected by nuclear masses and again mass uncertainties of the order of 10 keV are desirable [5]. This is true for the Hauser-Feshbach [150, section 5.4.2] as well as for the narrow-resonance formalism. In the latter case, the sensitivity to nuclear masses is even stronger since the proton widths Γ_p in Eqn. 2.9 are also a function of resonance energies E_j [5].

2.1.5 Nuclear uncertainties near the ^{60}Zn *rp*-process waiting point

This thesis presents mass measurements of $^{60-63}$Ga that address nuclear uncertainties near the important ^{60}Zn waiting point. The *rp*-process flow in this region of the nuclear chart is indicated in Fig. 2.6. At temperatures of $T \approx 1$ GK, the small proton capture Q-value of ^{60}Zn ($Q_{(\mathrm{p},\gamma)} = 250(40)$ keV [151]) induces a (p,γ)-(γ,p) equilibrium between ^{60}Zn and

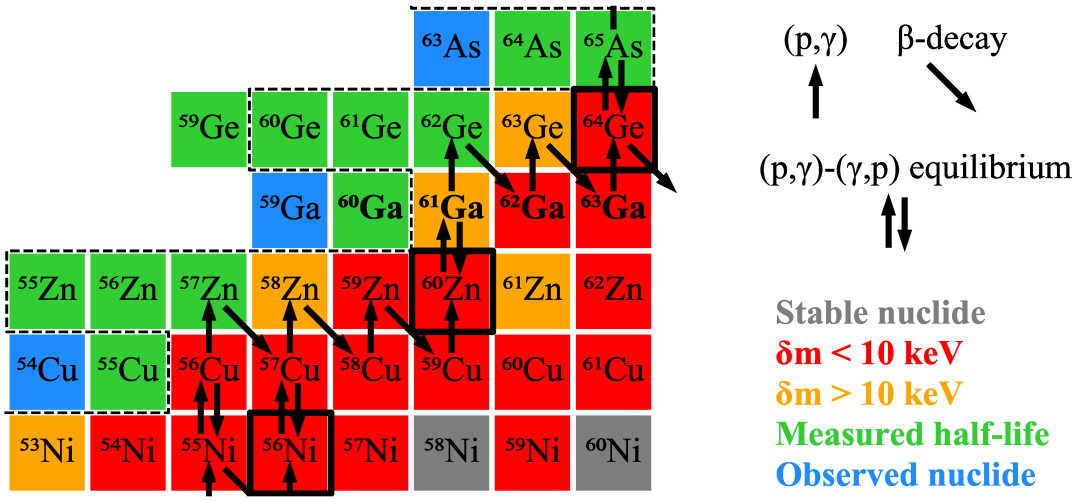

Figure 2.6. Status of nuclear data and the predicted *rp*-process path [32] near the ^{60}Zn waiting point. The gallium isotopes measured in this thesis are labelled with bold font. Waiting points are enclosed by black boxes. The dashed line indicates the proton drip line as predicted by AME2020 [151]. The color code indicates stable nuclides (grey), nuclides with a literature mass uncertainty [152] of less (red) or more (orange) than 10 keV, and nuclides with no detailed experimental data except for a measured decay half-life (green) or a lower half-life limit (blue).

^{61}Ga. Due to the long β-decay half-life of ^{60}Zn ($t_{1/2} = 2.4$ min), the equilibrium cannot be left efficiently via β-decay to ^{60}Cu. However, the *rp*-process flow can bridge the ^{60}Zn waiting point via the sequential two-proton capture ^{60}Zn(p,γ)^{61}Ga(p,γ)^{62}Ge. According to Eqn. 2.6, the effective delay imposed by the ^{60}Zn waiting point then depends exponentially on the ^{60}Zn(p,γ) Q-value and linearly on the ^{61}Ga(p,γ) reaction rate. While the ^{60}Zn mass is accurately measured, the uncertainty of the ^{60}Zn(p,γ) Q-value has been limited by the 40 keV literature mass uncertainty of ^{61}Ga (see color code in Fig. 2.6). Together with the unmeasured mass of ^{62}Ge, the ^{61}Ga mass further affects theoretical estimates of the unmeasured ^{61}Ga(p,γ) rate through the corresponding Q-value, as detailed in the previous section.

Multiple sensitivity studies have stressed the need to reduce these nuclear uncertainties near the ^{60}Zn waiting point in order to improve X-ray burst model predictions [50, 51, 93, 130, 153]. Most noteworthy are two complementary, large-scale sensitivity studies by Cyburt et al. [50] and Schatz et al. [51] that evaluated the influence of reaction rate and mass uncertainties, respectively. Cyburt et al. [50] assessed the impact of reaction rate uncertainties on the burst light curve and the ash composition by individually varying a large set of reaction rates. They demonstrated that variation of the unmeasured ^{61}Ga(p,γ) rate within the assumed uncertainty had a significant effect on the predicted light curve. Schatz et al. [51] evaluated the effect of mass uncertainties on burst model predictions by individually varying nuclear mass inputs by $\pm 3\sigma$. They found the 40 keV literature mass uncertainty [151] of ^{61}Ga to induce departures from the typical power-law decay of the burst luminosity [111]

and categorized it as one of only a few nuclear mass uncertainties that substantially affected the model predictions for a typical mixed H/He burst. Due to the astrophysical importance of the ^{61}Ga mass and due to concerns about potentially underestimated systematic uncertainties in earlier measurements, they strongly recommended a re-measurement of this mass value.

Analogous to the secondary bypass of ^{56}Ni via ^{57}Zn [154] (see Fig. 2.6), the ^{60}Zn waiting point could, in principle, also be partially bypassed through the sequential two-proton capture ^{59}Zn(p, γ)^{60}Ga(p, γ)^{61}Ge. This hypothesis was first expressed by Blank et al. in 1995 [155]. In 2001, *rp*-process simulations based on a semi-empirical estimate of the ^{60}Ga mass indicated [156] that this branching only redirects a minor fraction of the reaction flow around ^{60}Zn. This indication was supported by a 2007 decay study [157] which found ^{61}Ge to undergo β-delayed proton emission leading to ^{60}Zn with a branching ratio of at least 62(4)%. To definitively determine the strength of this branching, a robust determination of the Q value for the ^{59}Zn(p,γ) reaction [or equivalently of the one-proton separation energy of ^{60}Ga, $S_p(^{60}\mathrm{Ga})$] has been needed.

2.2 Nuclear mass and structure predictions for astrophysics

Despite extensive experimental efforts, many nuclear inputs of relevance to nucleosynthesis models such as masses, half-lives and excitation energies are still unmeasured or not constrained accurately enough by experiment. As we have seen in the previous sections, many properties of the neutron-deficient nuclei along the *rp*-process path remain experimentally unknown. Since the rapid neutron capture process (*r*-process) proceeds even further from nuclear stability than the *rp*-process, involving many isotopes with particularly short half-lives and low production yields, the lack of experimental data is even more severe on the neutron-rich side of the nuclear chart. Nuclear theory is therefore essential to provide accurate predictions of unmeasured masses and other nuclear properties for astrophysical models.

The following sections review the most popular methods for mass predictions of rare isotopes, with a focus on proton-rich nuclides along the *rp*-process path. Accurate mass measurements of rare isotopes offer important benchmarks and add valuable anchor points for the refinement of the various theoretical approaches. As a fundamental boundary of nuclear stability, the proton drip line offers particularly well-suited testing grounds for mass prediction methods. The mass measurements presented in chapter 5 of this thesis constrain the location of the proton drip line in the gallium isotope chain, allowing us to test the extrapolation power of the various mass prediction methods discussed in the following. Section 2.2.1 gives an overview over global mass models that enable mass predictions across the entire nuclear chart. Local mass relations based on the symmetric structure of nuclides along the $N = Z$ line are discussed in section 2.2.2.

Relations describing the mass splitting of isobaric nuclides near the $N = Z$ line are of special interest since they further serve as sensitive probes of isospin-symmetry breaking and

the nature of nucleon-nucleon interactions inside nuclei. Section 2.2.3 outlines how such measures of the isobaric mass splitting enable the description of isospin-forbidden processes within the nuclear shell model and extend our understanding of nuclear interactions.

2.2.1 Global mass models

Global nuclear mass models aim to describe all bound nuclei and are therefore the most universal frameworks for predictions of masses and other nuclear properties. An inherent advantage of such universal frameworks lies in the guaranteed consistency of the model predictions which prevents ambiguities that can arise when nuclear quantities of astrophysical interest are deduced using nuclear structure inputs from different sources. The development of nuclear mass models has been driven by an interplay between nuclear theory and experiment. Therein, the continual increase of experimental data far from nuclear stability provides testing grounds for current models, creates stimuli for their refinements and adds anchor points to expand their extrapolation power. A comprehensive discussion of the wide variety of available mass models can be found in [10]. Generally, global mass models are based on one of the following approaches:

1. *Macroscopic mass models* aim to phenomenologically describe the bulk properties of nuclei while neglecting a detailed description of the underlying nucleon-nucleon interactions. The classic example is the Bethe-Weizsäcker mass formula [158, 159] which models the nucleus as an incompressible, liquid drop and predicts its nuclear binding energy as [160]

$$E_B(A,Z) = a_{\text{vol}}A - a_{\text{sur}}A^{2/3} - a_C\frac{Z(Z-1)}{A^{1/3}} - a_{\text{sym}}\frac{(A-2Z)^2}{A} \tag{2.10}$$

   where the parameters a_{vol}, a_{sur}, a_{C} and a_{sym} are typically determined by fits to experimental data. The first and second term correspond to the volume and surface-tension contributions to the energy of a spherical liquid drop, respectively. They are manifestations of the short-range character of the nuclear force and the essentially incompressible nature of nuclear matter – a consequence of the Pauli principle. The third term accounts for the reduced binding due to the Coulomb repulsion between protons. The final term is based on the Pauli principle and accounts for the empirical fact that large asymmetries in the proton and neutron numbers are energetically unfavourable.

   Despite it's simplicity, the Bethe-Weizäcker mass formula reproduces experimental binding energies with surprising accuracy (relative deviations from experiment below 2% for $A \geq 50$) and correctly predicts a number of nuclear phenomena such as the curvature of the valley of β-stability and the parabolic form of the mass excesses within an isobaric chain (the "mass parabola"). However, as seen in Fig. 2.7, the formula fails to reproduce the binding energies of light nuclei and the exceptionally strong binding of nuclei with specific proton and neutron numbers, the so-called magic numbers which are associated with closed-shell nucleon configurations. While the first of these two shortcomings can be remedied by inclusion of a surface symmetry

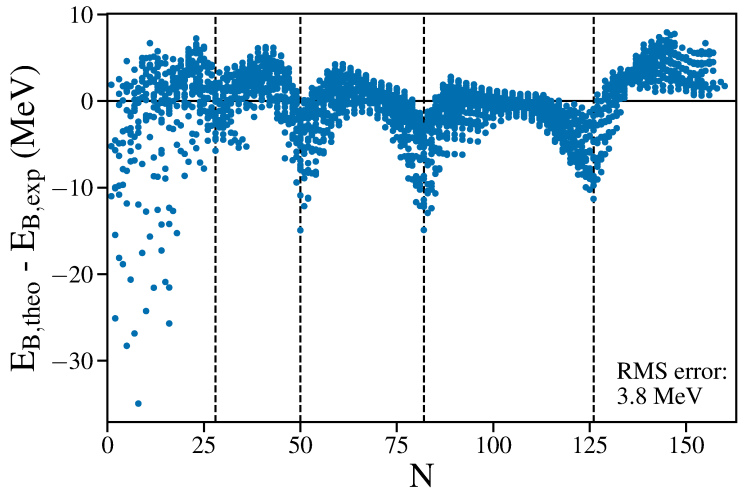

Figure 2.7. Discrepancy between predictions of the Bethe-Weizäcker mass formula and measured binding energies from [151]. The data was calculated with Eqn. 2.10, adopting the parametrization of Ref. [161]. Increased discrepancies are found at low masses and near magic neutron numbers $N = 28, 50, 80, 126$ (dashed lines).

term (see e.g. [10]), even more modern macroscopic drop models such as the liquid drop model are inherently incapable of describing shell effects and other phenomena deriving from the internal quantum structure of nuclei (see top panel of Fig. 2.8).

2. *Microscopic-macroscopic models* address these issues with a hybrid approach by adding microscopic corrections to a liquid-drop-type mass formula. The foundation for successful microscopic-macroscopic models was laid by Strutinsky [162] who presented a rigorous formalism to apply shell corrections to a macroscopic model. The Strutinsky method involves solving a single-particle Schrödinger equation assuming a nuclear potential that depends on the shape of the nucleus [163]. The resulting spectrum of single-particle energies is then used to estimate the required correction due to the non-uniform level density. The second important correction that requires a microscopic single-particle treatment is the pairing energy which derives from the tendency of like nucleons to form pairs with anti-aligned nuclear spins. The macroscopic-microscopic mass models tested in this thesis are dubbed FRDM(2012) [164] and WS4 [165].

   The macroscopic part of FRDM(2012) is based on the finite-range droplet model [166], a generalization of the liquid drop model that is based on the droplet model [167] and additionally accounts for the finite compressibility and surface diffuseness of nuclei as well as for the finite range of the nuclear interaction. The microscopic corrections are given by pairing and shell energies derived on a single-nucleon level with the Strutinsky method. Fig. 2.8 illustrates that inclusion of the microscopic energy correction in the FRDM(2012) model removes the systematic deviations near magic numbers and yields quite impressive agreement with experimental data, as evidenced by a global

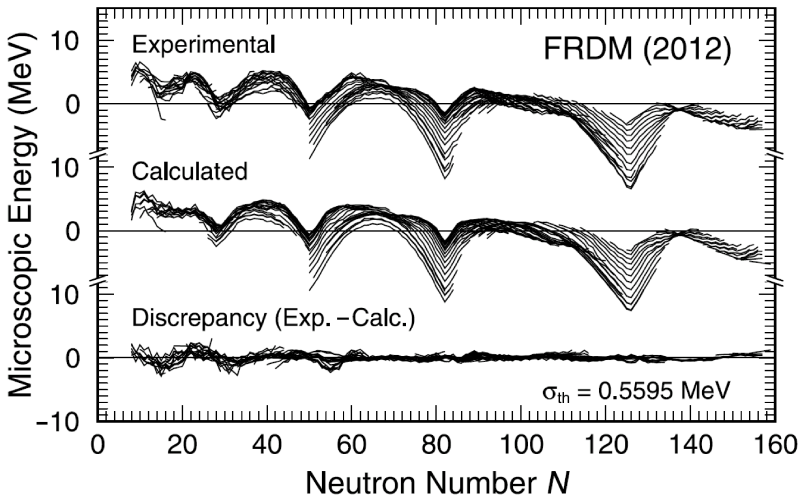

Figure 2.8. Calculated microscopic energies in the FRDM(2012) mass model compared to experimental values. The top and bottom panel show the respective discrepancies obtained with the macroscopic part of FRDM(2012) and with the full model including shell effects and other microscopic corrections. Figure reprinted from [164], ©2016, with permission from Elsevier.

accuracy of $\approx$ 560 keV [164]. A potential shortcoming of the FRDM(2012) mass model lies in the fact that, for reasons of computational efficiency, the parameters adopted in the microscopic and the macroscopic calculations are not fully consistent [164].

Upon conception, the Weizäcker-Skyrme (WS) mass model aimed to address this potential issue through a self-consistent treatment of the microscopic and macroscopic calculations [168]. Additionally, the WS model placed special emphasis to account for isospin-symmetry-breaking effects (see section 2.2.3). The upgraded variant WS4 [165] investigated here includes additional corrections for the surface diffuseness of the nuclear fluid. The WS4 model contains a total of 18 fit parameters [165] compared to 38 parameters in FRDM(2012) [164]. Despite the smaller number of fit parameters, the WS4 model has enabled fits of all measured masses with an RMS deviation on the order of only 300 keV. It should be noted that, although the global RMS deviation from all measured masses is the most commonly used metric to compare the performance of different mass models, it does not necessarily correlate with a model's extrapolation power to unknown masses [169], especially when one aims to extrapolate to exotic isotopes far outside the experimentally known territory. Mass measurements of unmeasured nuclides far from stability are therefore critical for mass model validation.

3. *Microscopic mass models* aim to derive mass predictions from principles as fundamental as possible. This aspiration is complicated by significant mathematical and computational hurdles arising from the complex nature of the nuclear force. Nev-

ertheless, significant efforts have been directed at the development of microscopic mass models since they are assumed to provide, at least in principle, higher extrapolation power than more phenomenological approaches [170]. So far, predictions from ab-initio theories [171, 172] that solve the nuclear many-body problem with realistic nucleon-nucleon forces have either not shown the required accuracy for astrophysical applications ($\delta m \leq 10$–$100\,\mathrm{keV}$) or been computationally restricted to light nuclei.

To overcome these limitations and enable predictions for all bound nuclei, microscopic mass models treat nucleons as the relevant degrees of freedom but use phenomenological effective forces to approximate the interactions between them. These effective forces contain microscopically-motivated phenomenological terms whose parameters are adjusted in fits to experimental data. The so-called microscopic mass models are therefore clearly not fully microscopic [10]. Once an effective force has been specified, the nuclear many-body problem is solved non-relativistically in a Hartree-Fock-Bogolyubov (HFB) variational approach, an extension of the Hartree-Fock method with pairing correlations built into the trial wavefunctions [170]. The most widely used effective interactions are non-relativistic, zero-range forces of Skyrme type [173]; but, despite the higher computational costs, also non-relativistic, finite-range forces of Gogny type [174] and relativistic forces [175] have been used to construct mass models. With an effective force specified, the nuclear many-body problem is solved by self-consistently minimizing the total energy functional of the system in a variational mean-field approach [176]. In the latter, the many-body problem is effectively simplified to a single-particle problem by assuming that each nucleon moves in a mean field created by all other nucleons.

The two microscopic mass models tested in this thesis are both based on Skyrme-type forces and use the non-relativistic HFB variational approach [170]. The first model is a mass table calculated [13, 177] using the HFB solver HFBTHO [178] and the SkM* force [179]. The second model, dubbed HFB-30 [180], is a recent variant of a series of Skyrme-HFB models optimized for astrophysical applications [181]. From HFB-9 on, the Skyrme forces underlying these models have not only been fitted to mass data but also to calculations of the equation of state of pure neutron matter using realistic nuclear forces. As a result, these microscopic models can in principle also provide unified frameworks for predictions of the matter composition and the equations of state throughout all layers of a neutron star [182]. Such predictions have in turn been shown to rely on precise mass measurements of neutron-rich isotopes [183].

Empowered by advances in high-performance computing, microscopic models have seen impressive progress over the last two decades and have started to reach similar accuracy as microscopic-macroscopic models. This is evidenced by an RMS deviation of $\approx 570\,\mathrm{keV}$ [180] between HFB-30 predictions and all measured masses (see also [184]). These developments are of special interest to the astrophysics community since the effective forces underlying microscopic mass models enable predictions beyond ground-state properties such as level densities and β-decay strengths [181].

2.2.2 Local mass predictions and the isobaric multiplet mass equation

With typical uncertainties of several 100 keV [169], mass predictions from global mass models are oftentimes not accurate enough to eliminate mass-induced uncertainties from astrophysical models. Local extrapolations of known masses can provide more accurate mass estimates but are only applicable a few isotopes beyond experimentally explored territory. For this reason, simulations of *r*-process nucleosynthesis are presently forced to rely almost exclusively on inputs from global mass models. The situation is different on the neutron-deficient side of the nuclear chart since many isotopes near the proton dripline have already been studied experimentally. In this region, local mass extrapolations are powerful tools to estimate nuclear masses for *rp*-process simulations, mappings of the proton dripline and other nuclear structure applications.

Some local extrapolation methods such as the Audi-Wapstra systematics [185], the Garvey-Kelson relations [186–188] and mass relations based on the residual proton-neutron interaction [189–191] are applicable near all experimentally explored regions of the nuclear chart. A different class of local extrapolation methods is founded on the concept of isospin symmetry and can only be applied near the $N = Z$ line. These methods are of special interest to this thesis, as they enable particularly accurate mass estimates and provide sensitive probes of nucleon-nucleon interactions.

Isospin symmetry is an approximate symmetry that ignores the Coulomb interaction, and treats protons and neutrons as different states of the same particle: The nucleon with an isospin of $T = 1/2$. Adopting the convention where the proton and the neutron carry isospin projections $T_z(p) = -1/2$ and $T_z(n) = +1/2$, respectively, the total isospin projection of a nucleus with N neutrons and Z protons is given by $T_z = (N - Z)/2$. Isospin follows the same mathematical formalism as the intrinsic spin of a quantum particle.

Each nuclear state with isospin T is part of an isospin multiplet formed by $2T + 1$ so-called isobaric analogue states with the same mass number A, identical total angular momentum (also "nuclear spin") J, same parity π and similar excitation energy. If isospin was an exact symmetry, the isobaric analogue states in a multiplet would exhibit identical masses and binding energies as hypothetically illustrated in Fig. 2.9 a).

However, as a result of the different masses and electric charges of u and d quarks, isospin symmetry is broken by three distinct effects [25]: (1) the Coulomb interaction which only affects the protons, (2) the neutron-proton mass difference ($(m_n - m_p)/m_p \approx 0.14\%$ [192]), and (3) the charge dependence (i.e. isospin nonconservation) of nuclear forces. Although the Coulomb interaction is by far the most dominant symmetry-breaking contribution, the much smaller isospin-nonconserving (INC) forces of nuclear origin can also not be neglected in certain applications, as will be discussed in the subsequent section. The symmetry breaking lifts the mass degeneracy of isobaric analogue states (see Fig. 2.9 b)) and causes them to contain small admixtures of states with different isospin. Fortunately, in most multiplets, such isospin mixing is sufficiently small for T and T_z to remain useful quantum numbers.

The binding energies E_B and mass excesses ME of two mirror nuclei in a multiplet

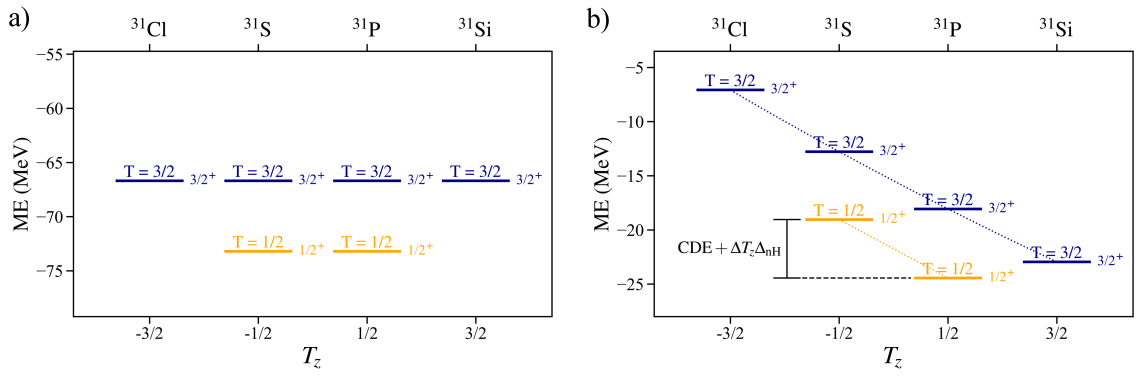

Figure 2.9. Mass excesses of the lowest-lying $T = 1/2$ and $T = 3/2$ multiplets at $A = 31$: (a) Hypothetical situation neglecting isospin-symmetry-breaking effects, and (b) realistic situation with experimental mass excesses. The corresponding spin-parity J^π is indicated next to each energy level. IMME (Eqn. 2.13) fits to the data (dotted lines) and the relation between the mass splitting and the Coulomb displacement energy (CDE) of the $T = 1/2$ multiplet are also indicated in (b). Data from [193].

characterized by a given isospin T and a set of other quantum numbers $\alpha = \{A, J^\pi, ...\}$ are related through the so-called Coulomb displacement energy (CDE) [194]:

$$\mathrm{CDE}(\alpha, T) = E_\mathrm{B}(\alpha, T, T_z^>) - E_\mathrm{B}(\alpha, T, T_z^<) \tag{2.11}$$

$$= \mathrm{ME}(\alpha, T, T_z^<) - \mathrm{ME}(\alpha, T, T_z^>) - \Delta T_z \Delta_\mathrm{nH}\,, \tag{2.12}$$

where $T_z^<$ and $T_z^>$ denote the isospin projection of the proton-rich and neutron-rich nucleus in the mirror pair, respectively, $\Delta T_z = T_z^> - T_z^<$ and $\Delta_\mathrm{nH} = 782.347\,\mathrm{keV}$ [151] is the neutron-hydrogen mass difference. With $\mathrm{CDE}(T)$ known from theory [195–197] or from experimental systematics [198], Eqn. 2.11 can be used to estimate the mass of a proton-rich nucleus from the typically well-known mass of its neutron-rich mirror nucleus. Binding energy differences (and hence CDEs) depend primarily on Coulomb effects and can therefore be calculated more accurately than absolute binding energies [196]. As a result, the method of Coulomb displacement energies has enabled mass predictions of various proton-rich mirror nuclides with uncertainties down to $\approx$100 keV [195, 199]. The term Coulomb displacement energy is historically motivated and obscures the fact that the Coulomb interaction and the neutron-hydrogen mass difference Δ_{nH} alone cannot explain the magnitude of experimental CDEs. This discrepancy, known as the Nolen-Schiffer anomaly [24], has been resolved by the inclusion of INC interactions into the nuclear Hamiltonian [200, 201].

Another powerful framework for mass predictions of nuclides along the $N = Z$ line and studies of isospin symmetry breaking is given by Wigner's isobaric multiplet mass equation (IMME) [8]. Wigner originally deduced this relation by treating the Coulomb interaction as a first-order perturbation to an isospin-conserving nuclear Hamiltonian. The derivation, however, also remains valid for two-body INC interactions of nuclear origin [193, 202]. The IMME describes the mass excesses (ME) of members of an isobaric multiplet with isospin

T and other quantum numbers α through a quadratic function of their isospin projection T_z:

$$\mathrm{ME}(\alpha, T, T_z) = a(\alpha, T) + b(\alpha, T)\, T_z + c(\alpha, T)\, T_z^2, \tag{2.13}$$

where the coefficients a, b and c are either theoretically predicted or deduced from fits to experimental data (see e.g. the dotted lines in Fig. 2.9).The IMME can enable mass predictions of proton-rich nuclides near the $N = Z$ line with an accuracy down to a few 10 keV [203]. It has further been used to predict level energies as well as nuclear spins and parities of excited isobaric analogue states [204–206].

The T_z and T_z^2 terms in Eqn. 2.13 depend on the isovector and isotensor parts of the INC nuclear Hamiltonian, respectively [193]. Extensive experimental work has been dedicated to test the validity of the quadratic form of the IMME. Most of these tests confirmed its validity [207–209] but in a few multiplets a need for cubic or quartic terms in T_z, was found [210–212]. These higher-order correction terms are thought to arise from isospin mixing [203, 213], three- or higher-body components in the nuclear interaction [193, 202], or density-dependent INC terms in the nuclear Hamiltonian [214]. The IMME can therefore serve as a probe of the fundamental nature of nuclear forces. It also plays an important role in the construction of isospin-nonconserving nuclear forces for shell-model predictions of nuclear structure properties, as will be detailed in the following section.

2.2.3 The shell model and isospin-nonconserving interactions

The nuclear shell model is one of the most successful tools for nuclear structure predictions. The model was conceived independently by Maria Goeppert-Mayer and Hans Jensen in 1949 in close analogy to the atomic shell model. The most striking feature of the nuclear shell model is that it correctly reproduces the exceptionally high binding energies of nuclei with magic neutron or proton numbers (see Fig 2.7). In contrast to many global mass models, it not only predicts ground-state properties but also provides detailed information of excited states. Among other applications, it can therefore yield crucial ingredients for reaction rate calculations based on the narrow-resonance formalism such as excitation energies, nuclear spins J, proton partial widths Γ_p and γ partial widths Γ_γ (see section 2.1.4) and has been used to predict various thermonuclear reaction rates of relevance for *rp*-process simulations [143, 144, 204, 206, 215, 216]. Before discussing the role of INC interactions in shell-model calculations, a brief account of the central features of the shell model is given. For comprehensive reviews, the reader is referred to [217] and [218].

In its most basic form, the shell model treats each nucleon as moving independently under the influence of a spherically symmetric mean-field potential $U(r)$ jointly created by all nucleons. Assuming a two-body-type nucleon-nucleon interaction V, the full Hamiltonian of the nuclear many-body problem,

$$H = \sum_{i}^{A} K_i + \sum_{i>j}^{A} V(\vec{r_i} - \vec{r_j}), \tag{2.14}$$

is then approximated as

$$H = \underbrace{\sum_{i}^{A}(K_i + U(r_i))}_{H_0} + \underbrace{\sum_{i>j}^{A} V(\vec{r_i} - \vec{r_j}) - \sum_{i}^{A} U(r_i)}_{V_{\text{res}}} \approx \sum_{i}^{A}(K_i + U(r_i)), \tag{2.15}$$

where $\vec{r_i}$ and K_i denote the position vector and the kinetic energy of the i-th nucleon, respectively. This approximation effectively reduces the nuclear many-body problem to a set of single-particle problems. Solving the single-particle Schrödinger equation $H_0\psi = \varepsilon_i\psi$, results in a set of single-particle orbitals with an associated spectrum of single-particle energies ε_i. The full nuclear wavefunction is then given by the Slater determinant of the single-particle wavefunctions. Due to the Pauli principle, each orbital can only hold a finite number of fermionic nucleons that therefore successively populate higher-energy orbitals. The harmonic oscillator potential $U_{\text{HO}}(r) = m\omega^2 r^2/2$ with nucleon mass m and angular frequency ω is a popular ansatz for the mean-field potential but, taken alone, it fails to reproduce the magic nucleon numbers [see leftmost level scheme in Fig. 2.10 a)].

A more appropriate description is obtained by additionally including a centrifugal term with a quadratic angular moment operator $\hat{l}^2$ and a spin-orbit coupling term $\vec{l} \cdot \vec{s}$. The single-particle energies then form the rightmost level scheme shown in Fig. 2.10 (a) and each level is $(2j + 1)$-fold degenerate (with j being the respective total angular momentum quantum number). The centrifugal and the spin-orbit coupling terms in the average potential break the equidistant spacing and the degeneracy of the harmonic oscillator levels and cause orbitals to form clusters known as the (major) shells. The increased energy spacings between these clusters, also known as the shell gaps, are found at the magic nucleon numbers. As a direct consequence, this independent-particle variant of the shell model correctly describes the outstanding stability of nuclei with magic proton or neutron configurations. For nuclei that deviate from a magic configuration by no more than one nucleon, the model also correctly predicts other nuclear properties such as spins and parities [219].

For nuclei that differ from a closed-shell configuration by more than one nucleon, the residual interaction $V_{\text{res}} = \sum_i (V_i - U(r_i))$ between the valence nucleons becomes important. It leads to a mixing of different single-particle configurations and shifts the single-particle energies relative to each other. Within the interacting shell model, residual interactions are treated as particle-hole excitations across the Fermi surface [217]. They enter the nuclear Hamiltonian in the form of two-body matrix elements. The many-body problem then consists in diagonalizing the full Hamiltonian $H = H_0 + V_{\text{res}}$ in a basis of the eigenstates of the independent-particle Hamiltonian H_0. However, the matrix size and the computation time grow rapidly with the number of contributing orbitals [220]; shell-model calculations of all but the lightest nuclei are therefore performed in a truncated model space that only permits interactions between nucleons in a few valence orbitals, while higher- and lower-lying orbitals are considered inert and not included in the diagonalization (see Fig. 2.10 b). To correctly reproduce a subset of the eigenvalues of the full Hamiltonian, calculations in the model space have to be performed using an effective Hamiltonian H_{eff} that absorbs the excluded interactions with nucleons in core orbitals as well as three- and higher-body

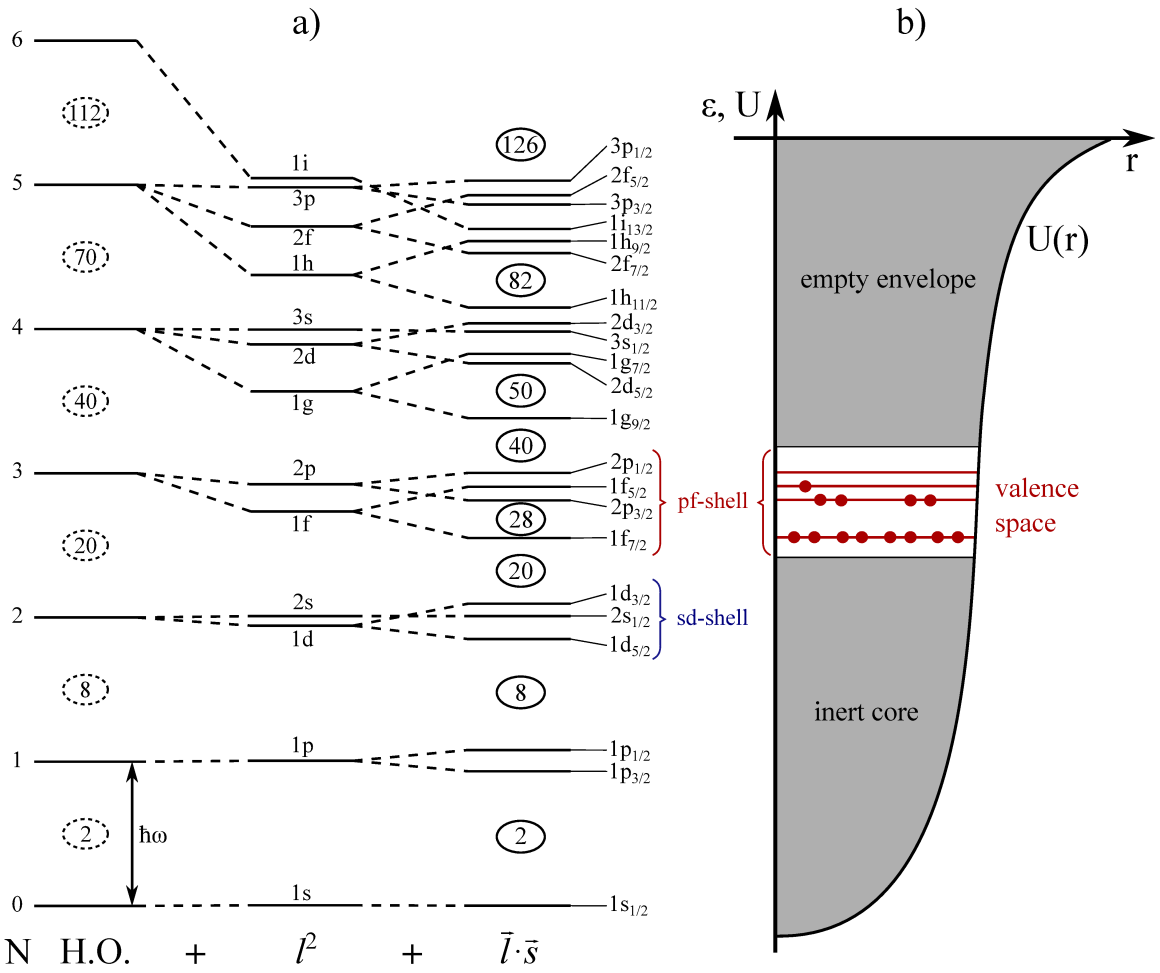

Figure 2.10. The nuclear shell model: a) Single-particle energies (ε) arising from a spherical harmonic oscillator potential (H.O.), a H.O. with a centrifugal term (l^2) added, and a full shell-model potential with both a centrifugal term and a spin-orbit term ($\vec{l} \cdot \vec{s}$), respectively. The encircled numbers indicate the total number of neutrons or protons up to a given orbital. Level scheme adapted from [219]. b) Average shell-model potential $U(r)$ with the single-particle energy levels of the partially filled *pf*-shell valence space indicated (see text for details).

components of the nuclear force [221].

Although microscopic effective interactions from ab-initio theory have seen remarkable progress over the last two decades (see [222] for a review), empirical effective Hamiltonians presently still provide the most precise shell-model predictions [223]. A successful approach to obtain an empirical effective Hamiltonian is to start with a microscopic Hamiltonian derived from realistic free nucleon-nucleon interactions and to iteratively adjust its single-particle energies and two-body matrix elements to experimental binding and excitation energies [220]. This philosophy formed the foundations of two successful families of empirical shell-model Hamiltonians, namely USD [224] for the *sd*-shell model space ($16 \leq A \leq 40$) and GXPF1 [225] for the *pf*-shell model space ($40 \leq A \leq 80$).

In order to reduce the number of fit parameters, most shell-model Hamiltonians are

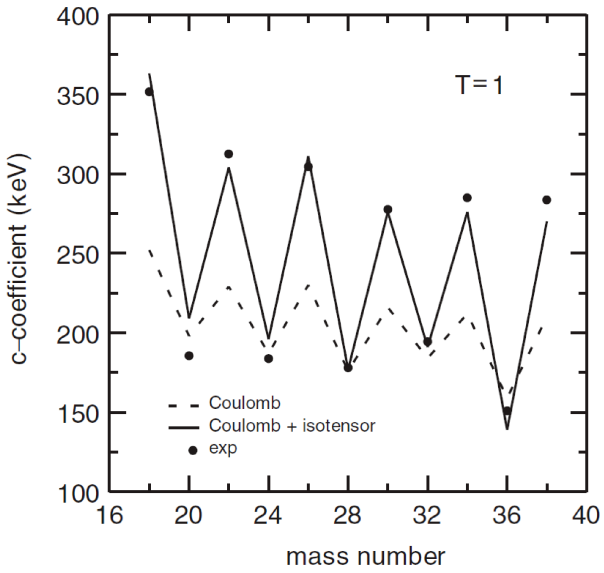

Figure 2.11. Experimental IMME c coefficients compared to shell model calculations with and without isospin-nonconserving (INC) forces of nuclear origin. Reprinted with permission from [223]. ©2020 by the American Physical Society.

constructed to conserve isospin symmetry. A mass splitting between isobaric analogue states is then usually only introduced through a simplistic Coulomb correction [220]. In this approach, the nucleon-nucleon interaction is assumed to be both charge symmetric, i.e. $V_{nn} = V_{pp}$, and charge independent, i.e. $(V_{nn} + V_{pp})/2 = V_{pn}$, where n and p indicate the neutron and proton, respectively. However, nucleon-nucleon scattering experiments revealed that charge symmetry is slightly broken, with V_{pp} and V_{nn} differing by $\approx 0.6\%$ [226], and charge independence is violated by V_{pn} being $\approx 2\%$ larger than $(V_{pp}+V_{nn})/2$ [25]. Accounting for charge symmetry breaking of nuclear forces enabled a correct reproduction of the experimental mass differences between mirror nuclei, thus providing a widely accepted resolution of the Nolen-Schiffer anomaly [25].

A particularly sensitive measure of isospin symmetry breaking is given by the IMME c coefficients in isospin triplets. The experimental c coefficients exhibit a strong staggering between odd-odd and even-even nuclei that cannot be explained by the Coulomb interaction alone. However, as illustrated for *sd*-shell nuclei in Fig. 2.11, inclusion of an isotensor nuclear interaction consistent with the nucleon-nucleon scattering data enables a detailed reproduction of the experimental data. Clearly, a proper account of INC forces is needed to describe the mass splitting of isobaric analogue states. A correct description of isospin symmetry breaking is further important to model isospin-forbidden decays [227] and to obtain isospin-breaking corrections for the calculation of $\mathcal{F}t$-values for superallowed β-decays [29, 228, 229] (e.g. for ^{62}Ga). The $\mathcal{F}t$-values are crucial for tests of the conserved-vector-current hypothesis and the unitarity of the Cabibbo–Kobayashi–Maskawa quark mixing matrix [4, 230].

Recognizing the need to properly account for isospin symmetry breaking in shell-model calculations, a pioneering 1989 study by Ormand and Brown presented a set of effective

shell-model Hamiltonians with INC terms of nuclear as well as Coulomb origin [27]. Their procedure to obtain the charge-dependent (or INC) Hamiltonians involved adding empirical INC forces as perturbations to an isospin-conserving Hamiltonian. The strength parameters of the INC terms were adjusted in fits to experimental b and c coefficients. The INC forces deduced by Ormand and Brown have been widely used to model isospin-forbidden processes, particularly in *sd*-shell nuclei [195, 204, 231]. Motivated by the increase in computational power and the much expanded experimental data, Lam et al. presented an updated version of Brown and Ormand's charge-dependent *sd*-shell Hamiltonian [28]. While this Hamiltonian has enabled precise predictions of excitation energies, it only poorly matches the experimental ground-state binding energies [223]. This shortcoming has recently been addressed through the development of a new set of effective INC Hamiltonians for the *sd*-shell. Instead of posthumously applying INC corrections to a pre-determined isospin-conserving Hamiltonian, these Hamiltonians were based on a consistent adjustment of isospin-conserving and charge-dependent terms [223, 232]. One of these Hamiltonians produced the remarkable agreement between experimental and theoretical c coefficients seen in Fig. 2.11.

Similarly well adjusted shell-model frameworks for the *pf* shell are actively being pursued [232] but not available yet. This is due both to the limited availability of experimental binding and excitation energy data in this region and to the computational complexity arising from the significant size of the *pf*-shell valence space. Although Ormand and Brown also presented an INC Hamiltonian for the *pf* shell, this framework is likely less well-tuned since the lack of experimental data prevented a local fit to c coefficients.

The role of charge-dependent nuclear forces in the *pf* shell has been debated in the literature. Studies of Coulomb energy differences, i.e. the shifts between excitation energies of isobaric analogue states have indicated that isospin-symmetry breaking of nuclear interactions is indispensable to explain the Coulomb energy differences in the $f_{7/2}$ shell but becomes less critical towards the upper *pf*-shell region [200, 233, 234]. Other work [235] has challenged this assertion and suggested nuclear INC forces to have a universal strength across the entire *pf* shell. More binding and excitation energy data is required to resolve these questions [201]. Microscopic INC shell-model Hamiltonians deduced from realistic nucleon-nucleon interactions could greatly help to clarify the roles of the different sources of isospin-symmetry breaking. However, microscopic frameworks have so far failed to describe the experimental binding energy differences of isobaric analogue states [236–238]. Empirical interactions therefore continue to be the tools of choice for shell-model studies of isospin-mixing and isospin-forbidden processes.

Experimental data on $T = 1/2$ and $T = 1$ multiplets are also important for adjustments of effective forces for mean-field calculations (such as those performed within the microscopic mass models mentioned in section 2.2.1). This was demonstrated in a recent study on isospin-nonconservation in the masses of nuclei along the $N = Z$ line [239]. In that study, the inclusion of empirical INC terms with only two fit parameters enabled a correct reproduction of the experimental mirror and triplet displacement energies (equivalent to IMME b and c coefficients, respectively). These results are in line with the earlier find-

ings of shell-model studies and highlight the universal relevance of INC forces in effective nuclear interactions [239].

In aggregate, all these results point to the importance of high-quality experimental data on isobaric analogue states both to test and construct INC forces for studies of isospin-forbidden processes. The most recent comprehensive evaluations of experimental data on isobaric analogue states and the associated IMME coefficients were given by Lam et al. in 2013 [193] and by MacCormick et al. in 2014 [203]. Due to a lack of experimental data, the $T = 1$ isospin triplets evaluated in these studies only extended up to $A = 58$. Additional experimental data at higher masses is needed to test the importance of INC forces in the upper *pf* shell and, if necessary, to re-tune the associated strength parameters [240]. A well-adjusted empirical INC Hamiltonian for the *pf* shell would be of relevance both to nuclear structure as well as nuclear astrophysics. The first direct mass measurement of ^{60}Ga presented in chapter 5 allows us to re-evaluate and extend the $T = 1$ IMME coefficients in the *pf* shell. The obtained trends are compared to shell-model predictions obtained with a charge-dependent version of the GXPF1A Hamiltonian [241] with INC terms from the early work by Ormand and Brown [27, 228]. Details of the evaluation procedure and the emerging trends in the IMME coefficients are discussed in chapter 5.4.2.

Chapter 3

Fundamentals of mass spectrometry of rare isotopes

Through the binding energy, the mass of a nucleus provides a sensitive measure of the interactions between its constituent nucleons. In experimental practice, the atomic mass is, however, often the more convenient quantity as most precision mass measurements have so far been performed on singly charged atomic ions rather than bare nuclei [242]. In these cases, the measured atomic (or rather ionic) mass is readily converted into the nuclear mass by correcting for the mass and the atomic binding energy of the bound electrons (see e.g. [151] for details). To access the valuable nuclear structure information decoded in the masses of nuclei far from stability, a range of complementary techniques have been developed for mass spectrometry of rare isotopes. These mass measurement techniques can be subdivided into direct and indirect methods.

Indirect mass measurements are based on measuring the Q-values for nuclear reactions or decays, i.e. the mass difference between the initial and the final states involved in the process. Assuming the energies of all other contributing states are known, the mass of a nuclide partaking in a reaction can be reconstructed from the measured Q-value [152]. Indirect mass determinations can provide high-precision mass determinations [243] but may be prone to systematic mass shifts [244]. This is particularly true for cases where excited nuclear states are involved and the relevant level structure information is limited, or when the reaction kinematics become ambiguous [245]. Such complications may, for example, be encountered in studies of β-decays, where the energy released in the reaction is distributed among three reaction products (the daughter nuclide, a β-particle and a (anti)neutrino). In this case, the reaction Q-value has to be deduced in a detector-response-corrected extrapolation [246] of the measured β-particle energy spectrum to the zero-crossing of the underlying energy distribution, the so-called β-endpoint energy. In multiple instances, such mass determinations have shown substantial deviations of several $100\,\mathrm{keV}$ from the mass values later accepted in the literature [244, 247–250].

Direct mass measurements are based on probing the motion of ions under the influence of well-controlled electromagnetic fields. Since the equations of motion in such fields depend on the ions' mass-to-charge ratios and the electromagnetic field strength along the

ion path, these techniques provide direct access to the ions' inertial mass. While the ion charge is usually known upfront or straightforward to determine due to its discrete nature, the strength of the electromagnetic fields must be precisely determined through calibration measurements with reference ions of well-known mass. The mass of the ions of interest is then measured in relation to the mass of the reference ions and oftentimes expressed as a ratio or a difference of the respective mass-to-charge ratios [152]. Generally, the measurement precision increases with the time over which the ions are stored inside the electromagnetic fields. The ion storage can be realized at a wide range of length and energy scales. In storage rings and MR-TOF-MS the ions are guided onto closed macroscopic orbits with respective revolution path lengths of $\approx 100\,\mathrm{m}$ [251] and $\approx 1\,\mathrm{m}$ [252] and typical kinetic energies of several $100\,\mathrm{MeV/u}$ [253] and a few keV [254], respectively. In Penning traps, the ions are restricted to microscopic trajectories with motional amplitudes below $1\,\mathrm{mm}$ [255] and kinetic energies of less than a few eV [58]. Combining particle storage in well-controlled environments with single-ion-sensitive detection schemes, direct mass measurements enable high-precision and high-accuracy determinations of the masses of rare isotopes [1].

A few words should be devoted to the general conventions adopted to report mass measurements for nuclear science. Experimental mass results are usually tabulated [152] as atomic mass values m in units of the unified atomic mass unit[1] u, or as (atomic) mass excesses

$$\mathrm{ME}(A, Z) = m(A, Z) - A\,\mathrm{u}, \tag{3.1}$$

in units of keV. Note that, exploiting Einstein's mass-energy equivalence, the term $1/c^2$ has been omitted in the unit of the mass excess value. This shorthand notation is commonly used in the particle and nuclear physics communities and will also be followed throughout this thesis.

This chapter focuses on direct techniques for mass measurements of rare isotopes. The first challenge in realizing such measurements is oftentimes the production of the nuclides of interest. To provide the necessary context, section 3.1 thus first introduces the primary methods for production and separation of rare isotopes. Subsequently, the different techniques used for direct mass measurements in storage rings (section 3.2), in Penning traps (section 3.3) and in multiple-reflection time-of-flight mass spectrometers (section 3.4) are reviewed. Section 3.5 concludes the chapter with a direct comparison of the different techniques.

3.1 Production and separation of rare isotopes

Over the last decades rare isotope science has primarily been driven by two complementary approaches of producing rare isotope beams (RIBs) [15], namely the in-flight separation method and the isotope separation on-line (ISOL) method. Both techniques are based on bombarding production targets with energetic ion beams to induce nuclear reactions that can synthesize radioisotopes far from stability. These primary beams have to be generated

[1] 1 u is defined as $1/12$ of the mass of an isolated, neutral ^{12}C atom.

by large particle accelerators which form the core of every RIB facility. Since the radiation background induced by the reactions in the target area (up to ≈ 15 TBq for ISOL targets at TRIUMF [256]) is too high for most experiments, the isotopes of interest are formed into secondary ion beams (the RIBs) and delivered to separate experimental areas, usually located at a distance of more than 10 m from the radiation-shielded production region. The production and study of isotopes farther from nuclear stability becomes increasingly challenging, since, generally, both the production cross sections and the decay half-lives drop as one moves closer to the limits of nuclear stability. At the time of writing, more than 3000 of the about 7000 particle-bound isotopes assumed to exist [13] across the nuclear chart have been produced and identified at RIB facilities [16].

The in-flight separation method

In the in-flight separation method [257], a heavy ion beam (e.g. ^{84}Kr, ^{132}Xe or ^{238}U) [258] is accelerated to very high energies ($\approx 50\,\mathrm{MeV/u} - 2\,\mathrm{GeV/u}$) and impinged onto a production target, thus triggering projectile fragmentation and induced fission reactions that generate a wide array of radioisotopes. The target is thin (typical areal density $\sim 1\,\mathrm{g/cm^2}$ [259]), in the sense that it cannot stop the recoiling reaction products. Instead, the high projectile momenta cause the reaction products to be forward scattered out of the target. With suitable ion optics, nearly 100% of the highly ionized reaction products can be collected [257] and shaped into a secondary beam. Before the beam is delivered to experimental setups, unreacted primary beam particles and undesired reaction products are suppressed in a fragment separator, resulting in a purified rare isotope beam. The isotopic separation [258] is based on the mass-to-charge ratio dependence of the particles' magnetic rigidity $B\rho$ in bending magnets and the element-specific energy loss ΔE in an energy degrader.

A principal advantage of the in-flight method is that the rare isotope beam formation proceeds independent of the chemical properties of the isotopes of interest [257] as the relativistic reaction products are not stopped inside the target. The minimal half-life of the isotopes accessible at an in-flight facility is dictated by their flight time through the fragment separator and lies on the order of only 100 ns. Since the produced nuclides emerge from the target at typically $\approx 90\%$ of the primary beam energy [257], a post-acceleration of the rare isotopes is generally not necessary. This makes the method well-suited for high-energy studies ($> 100\,\mathrm{MeV/u}$) of rare isotopes with half-lives down into the µs-range [260]. However, the inherent momentum spread arising from the reaction kinematics results in secondary beams of poor beam quality, with transverse emittances of $\epsilon_\perp \sim 40\,\pi$ mm mrad [258, 261] and longitudinal momentum spreads of several percent [257]. The delivery of these beams to experiments at low energies ($<15\,\mathrm{MeV/u}$), requires complex preparation steps, such as the capture in a gas stopping cell, cooling for phase space reduction and post-acceleration to the desired energy [262]. These steps involve considerable efficiency losses [263, 264] and typically take several 10 ms [265], resulting in prohibitive decay losses for isotopes with half-lives below 20 ms. Nevertheless, the in-flight technique remains the production method of choice for the discovery of new isotopes and studies of extremely exotic nuclides

with sub-ms half-lives. As such, it is presently used at a number of RIB facilities [15], including GSI [266], NSCL [267] and RIKEN [268], and will see continued usage in the next-generation facilities FAIR [269] and FRIB [270].

The ISOL method

In the isotope separation on-line (ISOL) method [271] a thick target of a high-Z material is bombarded with an intense ($\approx$ 1–100 µA), high-energy ($\sim 100\,\mathrm{MeV/u}$) beam of light ions, generating radioisotopes in fission, spallation and fragmentation reactions. Due to the target thickness ($\sim$ 10–100 $\mathrm{g/cm^2}$ [272]) and the reaction kinematics, the generated nuclides are stopped inside the target and neutralize. For delivery to experiments, they are extracted from the target, ionized by a surface, laser or plasma ion source, re-accelerated and magnetically mass separated to form a secondary beam.

The resulting rare isotope beams exhibit a high beam quality with transverse emittances of $\epsilon_\perp \approx 10\,\pi\,\mathrm{mm\,mrad}$ and beam energies of $\leq 10\,\mathrm{keV}$ [273]. Thus, they can be directly delivered to low-energy experiments. This makes the ISOL method particularly attractive for precision measurements with stopped beams, such as ion-trap-based mass spectrometry. The needs of experiments at energies $\geq 60\,\mathrm{keV}$ are met via post-acceleration. The yields of isotopes produced with the ISOL method depend not only on the in-target production cross sections, but also on the diffusion through the target and the desorption from its surface [274]. To quicken these processes, the target is heated to temperatures on the order of 2000 °C. Typical release times range from a few milliseconds in ideal cases to multiple hours for non-volatile elements such as the refractory metals. As a result, the latter have remained largely inaccessible at ISOL facilities. For the many elements with suitable release properties, however, the ISOL method can provide some of the most intense rare isotope beams available today [275]. These benefits are presently being exploited at a number of ISOL facilities around the world [15], such as CERN-ISOLDE [276], SPIRAL1 [277] at GANIL and ISAC [275] at TRIUMF. To meet the increasing demand for rare isotope beams, the former is presently undergoing the HIE-ISOLDE upgrade [278] and the latter two will soon get expanded by the upcoming SPIRAL2 [279] and ARIEL [280] facilities, respectively.

3.2 Storage ring mass spectrometry

Heavy-ion storage rings provide a versatile tool [281–283] for mass spectrometry and half-life measurements with rare isotope beams. Able to store and optionally cool relativistic beams of highly charged ion, they are well-suited to couple directly to a fragment separator. It is therefore not suprising that all storage rings presently operated with radioactive beams are found at in-flight facilities, namely the Experimental Storage Ring (ESR) [251] at GSI, the experimental Cooler Storage Ring (CSRe) [284] at the Institue of Modern Physics (IMP) in Lanzhou and the Rare-RI Ring (R3) [285] at RIKEN. However, efforts are underway [286] to add the first storage ring to an ISOL facility. Allowing to guide radioactive ion beams many times through a gaseous target, storage rings also have large potential for measuring

nuclear reactions of astrophysical relevance [287, 288]. They can further act as preparation stages for precision experiments with stable highly-charged ions at rest, as foreseen at the HITRAP facility [289] at GSI. The following will only focus on the basic principles of mass measurements with storage rings.

Storage ring mass spectrometry relies on the fact that the revolution frequency ν of an ion circulating at a velocity v depends on its mass-to-charge ratio $\frac{m}{q}$. The revolution frequency in a storage ring can be shown to obey the following differential relationship [290]:

$$\frac{\Delta\nu}{\nu} = -\frac{1}{\gamma_t^2}\frac{\Delta(m/q)}{(m/q)} + \left(1 - \frac{\gamma^2}{\gamma_t^2}\right)\frac{\Delta v}{v}, \tag{3.2}$$

where $\gamma = (1 - (v/c)^2)^{-\frac{1}{2}}$ is the Lorentz factor, v is the particle velocity and γ_t is an ion-optical parameter, referred to as the transition point. A direct proportionality between the revolution frequency and the mass-to-charge ratio of stored ions is obtained by making the second term in Eqn. 3.2 negligible. This can be achieved in the following two ways:

1. **Schottky mass spectrometry (SMS)**: This method [291] relies on minimizing the beam velocity spread via electron cooling: $\frac{\Delta v}{v} \rightarrow 0$. To this end, a cold electron beam is accelerated to the nominal ion beam energy and merged with the ion beam over a straight subsection of the ring, as indicated on the left in Fig. 3.1. In the centre-of-mass frame, the ions are thus subjected to a cold electron plasma that sympathetically cools them through Coulomb interactions. As a result, both the longitudinal and the transversal ion velocity spread are gradually compressed [292]. A more detailed description of the electron cooling mechanism can be found in section 6.2, or in Ref. [293] along with technical details of electron coolers. Electron cooling can reduce the beam's velocity spread from typically a few percent after fragment separation to $\frac{\Delta v}{v} < 1 \times 10^{-6}$ [283, 294].

   The revolving ions are non-destructively detected by recording the current induced on a pair of pick-up electrodes placed around the beam path. The pick-up signals exhibit periodic fluctuations due to the beam's non-uniform line charge density arising from the discrete number of stored ions. By amplifying and Fourier analyzing this so-called Schottky noise [295] over many thousand revolutions, one obtains a revolution frequency spectrum with up to single-ion sensitivity [296].

   Using simultaneously stored ion species of well-known mass as calibrants, the spectrum can be used for precise mass determinations with mass uncertainties down to $\frac{\delta m}{m} \approx 1 \times 10^{-7}$ and mass resolving powers[2] approaching $R = \frac{m}{\Delta m} = 1\,000\,000$ [294]. A drawback of Schottky mass spectrometry is the long duration of the cooling process, which usually takes 1–10 s [281, 290], even when combining electron cooling with stochastic pre-cooling [297]. As a result, the technique is not applicable to short-lived nuclides with half-lives < 1 s.

[2] The resolving power quantifies a spectrometers capability to distinguish two close-lying peaks. Following the most common convention used in mass spectrometry, throughout this thesis, the smallest discernible mass difference Δm is taken as the full width at half maximum (FWHM) of a peak. The ability to resolve two peaks not only depends on their spacing but also on other factors including their amplitude ratio and their shapes.

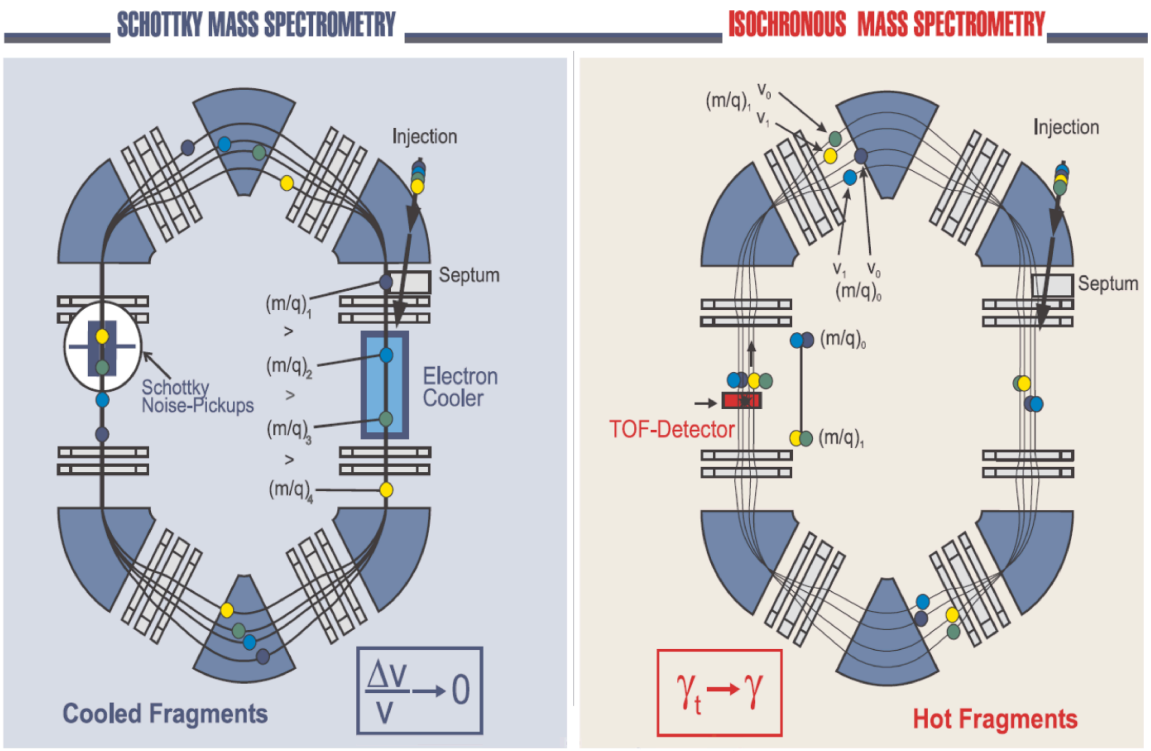

Figure 3.1. Principles of the two variants of storage ring mass spectrometry. In Schottky mass spectrometry (left), electron cooling is used to minimize the velocity spread $\frac{\Delta v}{v}$ of the stored ion beam and ion revolution frequencies are detected via induced image currents in Schottky pick-up electrodes. Isochronous mass spectrometry (right) circumvents the need for beam cooling by operating the storage ring at its transition point, such that $\gamma_t \rightarrow \gamma$. Measuring the revolution periods with a non-destructive time-of-flight (TOF) detector then allows mass and lifetime measurements of nuclides with half-lives of only several 10 µs. Figure adapted from [298]. Used with permission of IOP Publishing Ltd., from [298], ©2003; permission conveyed through Copyright Clearance Center, Inc.

2. **Isochronous mass spectrometry (IMS):** In IMS [290], the second term on the right-hand side of Eqn. 3.2 is minimized by adjusting the storage ring's ion-optical tune and the beam energy such that $\gamma_t \rightarrow \gamma$ for a single $\frac{m}{q}$ of interest. In isochronous operation (see Fig. 3.1 right), the longitudinal velocity spread is compensated by forcing faster ions of a given species onto slightly longer orbits through the ring's bending magnets (consult section 3.4.1 for a more detailed explanation of isochronicity).

   The ion revolution periods are measured with the following time-of-flight (TOF) detection scheme. The beam is passed through a thin carbon foil, releasing secondary electrons. These are subsequently guided onto a nearby electron multiplier creating a time stamp [290]. In contrast to Schottky noise detection, the TOF detection scheme allows to determine the revolution periods of single ions within only $\approx$ 20 passes through the detector which require about 10 µs [294].

   Since IMS circumvents the need for beam cooling and provides rapid ion detection,

it enables mass measurements of nuclides as short-lived as a few $10\,\mu s$. Typically, relative mass uncertainties of $\frac{\delta m}{m} \approx 10^6 - 10^7$ and resolving powers of $R \approx 100\,000 - 200\,000$ are achieved [283]. As an example, IMS at the CSRe provided the first direct mass measurement of ^{65}As [299] with a mass uncertainty of 85 keV, thus constraining the *rp* process flow near the ^{64}Ge waiting point.

Over the last decade, the introduction of resonant pick-up cavities [296] has greatly improved the speed and sensitvity of Schottky pick-up detection, thus enabling precise revolution frequency measurements of single ions within only a few $10\,ms$. The improved pick-up detection facilitates Schottky mass spectrometry of uncooled beams in an isochronously-tuned storage ring. This hybrid-approach holds prospects for high-resolution mass measurements of isotopes with half-lives $> 10\,ms$ [294] but still requires more experimental exploration.

3.3 Penning trap mass spectrometry

Developed by Hans Dehmelt in the 1950s based on early ideas by Michel Penning [300] and John R. Pierce [301] and recognized with the 1989 Nobel Prize in Physics, Penning traps have developed into the most accurate mass spectrometers available at present. As such they are used for ultra-high precision ($\frac{\delta m}{m} < 10^{-10}$) tests of fundamental physics with stable nuclides [1, 3, 302]. Enabling mass measurements of short-lived isotopes with half-lives below $100\,ms$ at 10 ppb-level accuracy [1], they have also emerged as an indispensable tool for studies with rare isotopes [302, 303] and have been installed at almost every major radioactive beam facility [3].

Penning traps combine a strong magnetic field with a weak electrostatic field to confine ions to a small volume in space, typically much below $1\,cm^3$. The ion confinement to such a small volume offers a number of advantages. It allows to engineer the electric and magnetic fields probed by trapped ions to extreme levels of precision and stability. By creating an ultra high vacuum in the trapping region, ions can be confined in a well-controlled environment over extended periods of time (from seconds up to more than a year in extreme cases [304]). The result is a near-ideal setup for precision measurements on single particles.

An additional advantage of Penning traps is their conceptual simplicity. With an appropriately shaped electrostatic field, the motion of a single ion in a Penning trap is described by a small set of analytical equations, as will be detailed in section 3.3.1. Experimenters have exploited the simplicity of the equations of motion to develop powerful techniques to manipulate and probe the microscopic motions of trapped ions. These techniques form the basis of Penning trap mass spectrometry.

A complication of precision measurements in ion traps lies in the fact that the rare isotopes have to be brought to kinetic energies of no more than a few $10\,eV$ [1, 65]. Even for ISOL beams with typical transport energies of several $10\,keV$, the efficient transport of rare isotopes into ion traps therefore requires elaborate preparation steps for deceleration, bunching and phase-space cooling. Introducing additional ion losses and delaying the time

between isotope production and measurement, these preparations can hamper or prohibit studies of particularly short-lived or rare isotopes. Some of the typical preparation stages are described in chapter 4 in the context of the TITAN ion trapping facility.

All variants of Penning trap mass spectrometry are based on determining the true cyclotron frequency

$$\nu_c = \frac{1}{2\pi}\frac{q}{m}B \tag{3.3}$$

of an ion with charge q and mass m circulating in a strong, homogeneous magnetic field. To accurately extract an ion's mass from its true cyclotron frequency, one needs exact knowledge of the magnetic field strength B. The latter is calibrated by measuring the true cyclotron frequency $\nu_{\mathrm{c,ref}}$ of reference ions with a well-known mass m_{ref} and charge q_{ref}. The mass of the ion of interest is then obtained from the following frequency ratio:

$$r = \frac{\nu_{\mathrm{c,ref}}}{\nu_{\mathrm{c}}} = \frac{q_{\mathrm{ref}}}{q}\frac{m}{m_{\mathrm{ref}}} \tag{3.4}$$

After a brief theoretical account of the ion motion in a Penning trap in section 3.3.1, the principal ion manipulation and frequency detection schemes of relevance to nuclear mass measurements are discussed in sections 3.3.2 and 3.3.3, respectively.

3.3.1 Confinement and motion of ions in an ideal Penning trap

Consider a single ion of charge q and mass m moving in a perfect vacuum. Subjecting the ion to a uniform magnetic field of the form $\vec{B} = B\vec{e_z}$ will cause it to circulate around the field lines at the true (angular) cyclotron frequency

$$\omega_c = 2\pi\,\nu_c = \frac{q}{m}B \tag{3.5}$$

and thus confine it radially. To trap the ion in all three dimensions, an axially-confining electric potential is superimposed upon the magnetic field. The most simple axisymmetric configuration that achieves this [305] is a quadrupolar potential of the form

$$\phi(r,z) = \frac{V_0}{2d^2}\left(z^2 - \frac{r^2}{2}\right), \tag{3.6}$$

where we have adopted cylindrical coordinates (r, φ, z). Such a potential can be created by a set of three electrodes whose shapes follow hyperboloids of revolution around the z-axis: a central "ring" electrode biased to a potential V_0 with respect to the two "end-caps". This type of electrode geometry is shown in Fig. 3.2 a) and characterized by the single parameter $d^2 = \frac{1}{2}(z_0^2 + \frac{r_0^2}{2})$. Near the trap's symmetry axis, a quadrupole potential can also be well approximated by a set of cylindrical trap electrodes with well-chosen length ratios, the electrode geometry of such a cylindrical Penning trap is shown in Fig. 3.2 b).

The quadrupole potential from Eqn. 3.6 gives rise to the following electric field components:

$$E_z = \frac{V_0 z}{d^2} \qquad \text{and} \qquad \vec{E_r} = -\frac{V_0 r}{2d^2}\vec{e_r}. \tag{3.7}$$

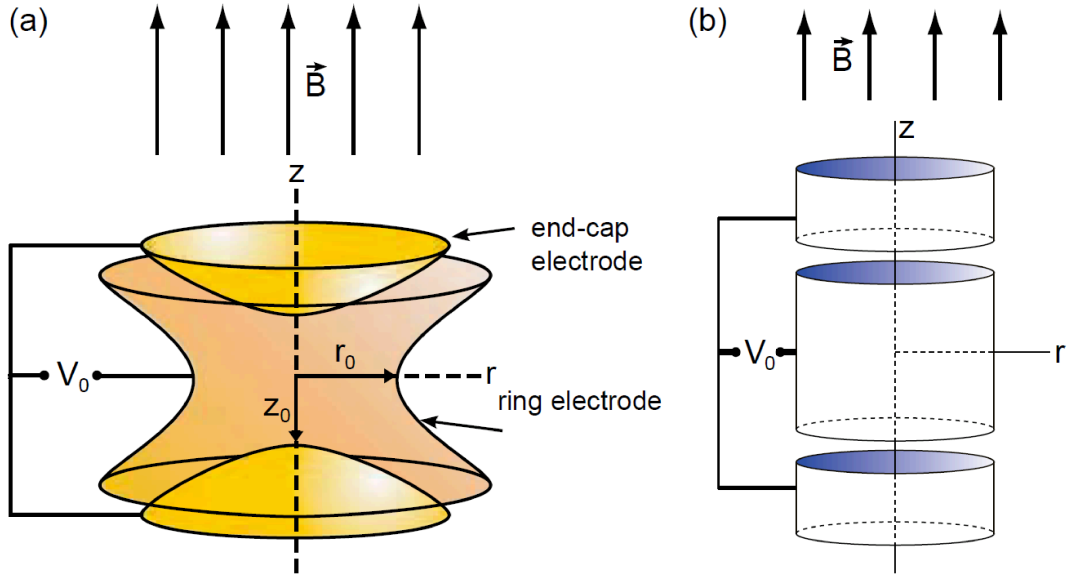

Figure 3.2. Basic types of Penning trap geometries: a) Hyperbolical and b) cylindrical Penning trap. Both electrode configurations create an approximately quadrupolar potential near the trap centre when a voltage V_0 is applied between the ring and the endcap electrodes. Figure adapted from [306].

While axially confining, the electric field acts repulsive in the radial plane. Therefore, care must be taken to keep the electric field sufficiently weak to not destroy the radial confinement provided by the strong magnetic field.

The combination of such fields forms an ideal Penning trap and gives rise to the following equations of motion:

$$\ddot{z} = -\frac{q}{m}E_z \qquad \text{and} \qquad \ddot{\vec{r}} = \frac{q}{m}(\vec{E}_r + \dot{\vec{r}} \times \vec{B}). \tag{3.8}$$

Solving these equations one finds that the ion motion in an ideal Penning trap is composed of three de-coupled, harmonic motions [307], described by the following angular eigenfrequencies [308] :

$$\omega_z = \sqrt{\frac{qV_0}{md^2}} \tag{3.9}$$

$$\omega_\pm = \frac{\omega_c}{2} \pm \sqrt{\left(\frac{\omega_c}{2}\right)^2 - \frac{\omega_z^2}{2}} \tag{3.10}$$

In the z-direction, the ion performs a simple harmonic oscillation at the angular axial frequency ω_z. In the radial plane, the addition of the repulsive electric field causes two superimposed circular motions: a fast circulation at the reduced angular cyclotron frequency ω_+ and a slow drift around the saddle point of the quadrupole potential at the angular magnetron frequency ω_-. At typical trap parameters [303] of $B \approx 5\,\mathrm{T}$, $V_0 \approx 10\,\mathrm{V}$ and $d \approx 1\,\mathrm{cm}$, the three angular eigenfrequencies follow the hierarchy

$$\omega_- \ll \omega_z \ll \omega_+. \tag{3.11}$$

They can further be shown to obey the following relations [308]:

$$\omega_c = \omega_+ + \omega_- \tag{3.12}$$

$$\omega_c^2 = \omega_+^2 + \omega_-^2 + \omega_z^2, \tag{3.13}$$

the second of which is also referred to as the Brown-Gabrielse invariance theorem [308]. These relations have important implications for precision mass measurements in Penning traps. They imply that, although the true cyclotron frequency ω_c cannot be directly measured, it can still be determined by measuring individual eigenfrequencies or combinations thereof. How exactly these relations are exploited for precision mass measurements of short-lived isotopes will be detailed further below.

The real Penning trap

Many of the idealized assumptions underlying the above treatment are, at least to a small degree, violated in real Penning traps.

For example, the exact creation of the potential in Eqn. 3.6 would require hyperbolically-shaped electrodes of infinite extension. Field imperfections introduced by the finite electrode size can, however, be compensated by introducing additional correction electrodes. Moreover, many contemporary Penning traps consist of easier-to-machine cylindrical electrodes, as schematically shown in Fig. 3.2. With a sufficient number of correction electrodes, these configurations can still closely approximate the ideal quadrupole potential near the trap centre [308].

Other imperfections of real Penning traps include spatial inhomogeneities and temporal fluctuations of the magnetic field, mechanical imperfections in the electrode surfaces, misalignment between the electrode structure and the magnetic field axis, and Coulomb interactions among multiple stored ions. If uncompensated, all these effects may induce systematic shifts of the measured eigenfrequencies, and thus negatively affect a mass measurement. Detailed evaluations of how such systematic effects impact mass measurements with TITAN's precision Penning trap have been presented in [309, 310].

An important foundation of Penning trap mass spectrometry is the fact that both Eqn. 3.12 and 3.13 are to first order unaffected by small trap misalignment and anharmonic distortions in the axial trap potential [308, 311]. Penning trap mass measurements of rare isotopes are based on Eqn. 3.12 which enables mass determinations with uncertainties down to a few parts in 10^{10} [3, 311]. Mass measurements with even higher accuracy are presently only achievable with stable or long-lived nuclides ($T_{1/2} \gtrsim 1$ h) and rely on the Brown-Gabrielse invariance theorem [311] (Eqn. 3.13).

3.3.2 Radiofrequency excitation of ion motions

Precision measurements in Penning traps require fine control over the motion of trapped ions. This can be achieved by creating radiofrequency (RF) fields inside the trap [312]. To this end, the static electrode voltages for trapping are mixed with oscillating voltages of the

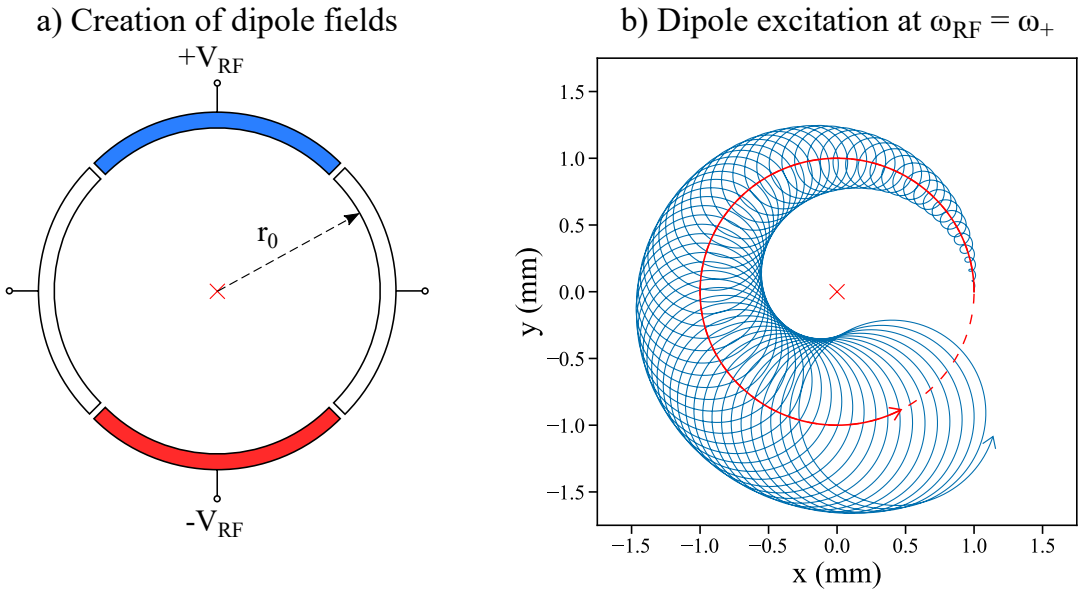

Figure 3.3. Dipole RF excitation of an ion stored in a Penning trap: a) Applying an alternating voltage $V_{\mathrm{RF}}(t) = V_{\mathrm{RF},0}\cos(\omega_{\mathrm{RF}}t + \phi_{\mathrm{RF}})$ with the indicated polarities to the segments of an azimuthally-split ring electrode creates a dipole RF field near the trap centre. b) Trajectory of an ion (blue line) under dipole excitation at $\omega_{\mathrm{RF}} = \omega_+$. The resonant excitation gradually increases the amplitude of the reduced cyclotron motion while leaving the underlying magnetron orbit (solid red line) on its initial trajectory (dashed red line).

form

$$V_{\mathrm{RF}}(t) = V_{\mathrm{RF},0}\cos(\omega_{\mathrm{RF}}t + \phi_{\mathrm{RF}}). \tag{3.14}$$

An RF field applied at an eigenfrequency, or at sums or differences of eigenfrequencies can resonantly transfer energy into the ion motion. Hence, these ion manipulations are referred to as RF excitations.

Dipole excitations

Dipole RF excitations provide control over the amplitude of individual eigenmotions [1]. They are regularly used to centre ions in the trap or to remove contaminant ions [1, 313].

To manipulate the radial eigenmotions, one of the trap electrodes (usually the ring electrode) is azimuthally split into four (or more) segments. Applying the alternating voltage $V_{\mathrm{RF}}(t)$ with a $180°$ phase shift to two opposing electrodes, as indicated in Fig. 3.3 a), creates a dipolar RF field near the trap centre and induces a periodic force on the ion [1]:

$$F_y = qE_y = q\frac{V_{r,0}}{r}\cos(\omega_{\mathrm{RF}}t + \phi_{\mathrm{RF}}), \tag{3.15}$$

where $V_{r,0}$ is the RF amplitude at a distance r from the trap centre. When the frequency of the RF drive ω_{RF} matches one of the radial eigenfrequencies, the respective eigenmotion is either resonantly excited or damped, depending on the relative phase between the RF field and the ion motion.

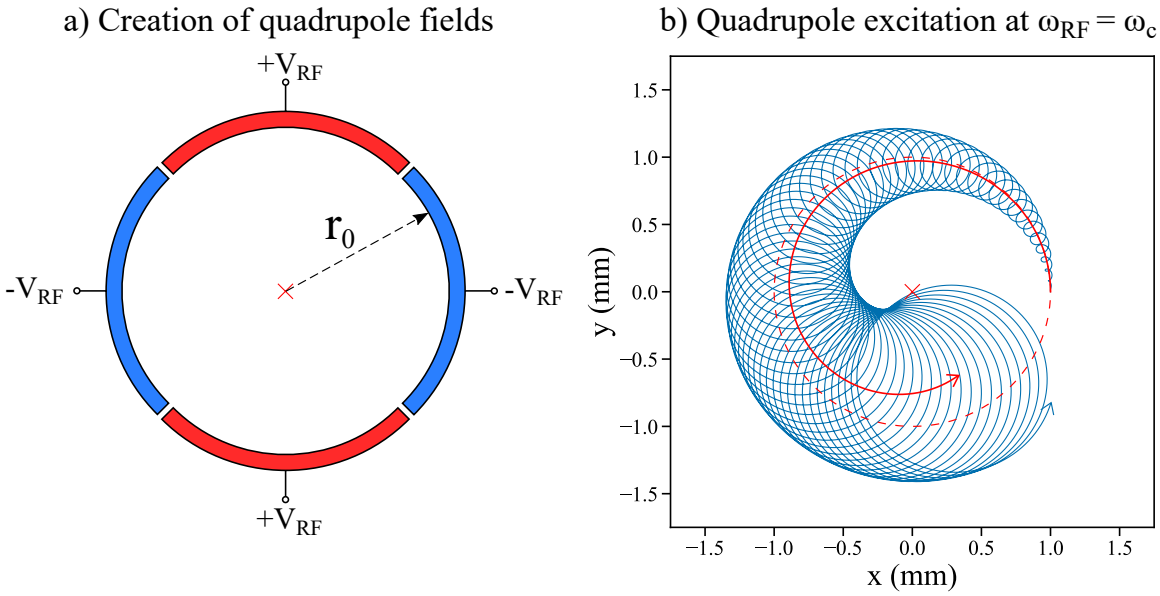

Figure 3.4. Quadrupole excitation of an ion stored in a Penning trap: a) Applying an alternating voltage $V_{\mathrm{RF}}(t) = V_{\mathrm{RF},0}\cos(\omega_{\mathrm{RF}}t+\phi_{\mathrm{RF}})$ with the shown polarities to the segments of a four-fold split electrode creates a quadrupole RF field near the trap centre. b) Trajectory of an ion (blue line) under quadrupole excitation at $\omega_{\mathrm{RF}} = \omega_+ + \omega_- = \omega_c$. The excitation gradually converts the initial pure magnetron motion (dashed red line) into reduced cyclotron motion, causing a widening of the reduced cyclotron orbit while decreasing the magnetron amplitude (solid red line).

Since the amplitude of the reduced cyclotron motion grows with increasing energy, an excitation at $\omega_{\mathrm{RF}} = \omega_+$ can be used to gradually widen the cyclotron orbit [see Fig. 3.3 b)], eventually leading to ion loss against an electrode surface. By exploiting the mass dependence of ω_+, such dipole excitations can be used to selectively remove unwanted ion species from the trap [1, 313].

Quadrupole excitations

Quadrupole excitations are used to couple the different eigenmotions of an ion [1]. They form the basis for multiple of the mass measurement schemes described in the next section and are also of relevance for buffer-gas cooling in Penning traps [314].

Applying the alternating voltage V_{RF} from Eqn. 3.14 with opposite polarity to neighboring segments of a fourfold-split ring electrode, as shown in Fig. 3.4 a), creates a quadrupole RF field near the trap centre and exerts the following periodic force on the ion:

$$F_x = qE_x = q\frac{V_{r,0}}{2r^2}\sin(\omega_{\mathrm{RF}}t + \phi_{\mathrm{RF}})y \tag{3.16}$$

$$F_y = qE_y = q\frac{V_{r,0}}{2r^2}\sin(\omega_{\mathrm{RF}}t + \phi_{\mathrm{RF}})x, \tag{3.17}$$

where $V_{r,0}$ is the RF amplitude at a distance r from the trap centre.

Applied at the sum frequency $\omega_{\mathrm{RF}} = \omega_c = \omega_+ + \omega_-$, the quadrupole RF field resonantly couples the radial eigenmotions, periodically transferring energy between the magnetron

and the reduced cyclotron motion. An ion initially on a pure magnetron orbit is thus forced onto a trajectory with a gradually increasing reduced cyclotron amplitude and a simultaneously decreasing magnetron amplitude. The first half of such an interconversion is shown in Fig. 3.4 b). After the so-called conversion time T_{conv}, an initial pure magnetron motion of amplitude $r_- = 1\,\text{mm}$ is fully converted into a pure reduced cyclotron motion of identical amplitude $r_+ = 1\,\text{mm}$. Excitation slightly off resonance only induces a partial conversion of both eigenmotions. Since the reduced cyclotron motion is significantly faster than the magnetron motion ($\omega_+ \gg \omega_-$), the conversion results in a detectable increase in the ion's radial kinetic energy [1]. The RF-induced gain in radial energy is exploited in the time-of-flight ion cyclotron resonance (TOF-ICR) method [312] to determine the ion's pure cyclotron frequency, as will be detailed below.

3.3.3 Frequency measurement techniques

Every Penning trap mass measurement is based on a determination of the true (angular) cyclotron frequency $\omega_c = \frac{qB}{m}$. This section introduces the three major techniques used to access ω_c experimentally.

To accurately extract an ion's mass from its true cyclotron frequency, one needs exact knowledge of the magnetic field strength B. The latter is obtained by determining the true cyclotron frequency of calibrant ions with a well-known mass. To minimize the influence of temporal drifts of the magnetic field strength, the magnetic field calibration is repeated periodically.

The time-of-flight ion cyclotron resonance (TOF-ICR) method

Over most of the past three decades, the time-of-flight ion cyclotron resonance (TOF-ICR) technique [312, 315] has been the primary method for Penning trap mass measurements of short-lived isotopes. It is based on the resonant coupling of the magnetron and the reduced cyclotron motions due to quadrupole excitation at the sideband $\omega_c = \omega_+ + \omega_-$. The technique has been shown to produce relative mass uncertainties of $\frac{\delta m}{m} \approx 10^{-7} - 10^{-9}$.

In a TOF-ICR measurement, ions of interest are initially prepared in a pure magnetron motion, either by applying suitable dipole excitations or via direct injection onto a magnetron orbit with a Lorentz steerer [316]. Applying a quadrupole excitation at $\omega_{\text{RF}} = \omega_c$ with a well-chosen amplitude and duration T_{RF} yields a full conversion of the magnetron into reduced cylotron motion. As discussed in section 3.3.2, the conversion significantly increases the ion's radial kinetic energy E_r. On-resonance excitation ($\omega_{\text{RF}} = \omega_c$) results in the maximal gain in radial energy. Off-resonance excitation can only produce a partial conversion, and therefore yields a smaller radial energy gain [312]. As a result, the ion's final radial energy becomes a measure of the degree of conversion and depends on the applied excitation frequency: $E_r = E_r(\omega_{\text{RF}})$.

Changes in radial energy are monitored by extracting the ions axially onto a TOF detector placed $\approx 1\,\text{m}$ outside the trap in a region of weak magnetic field ($B \leq 100\,\text{mT}$). The magnetic field gradient along the extraction flight path interacts with the ion's orbital

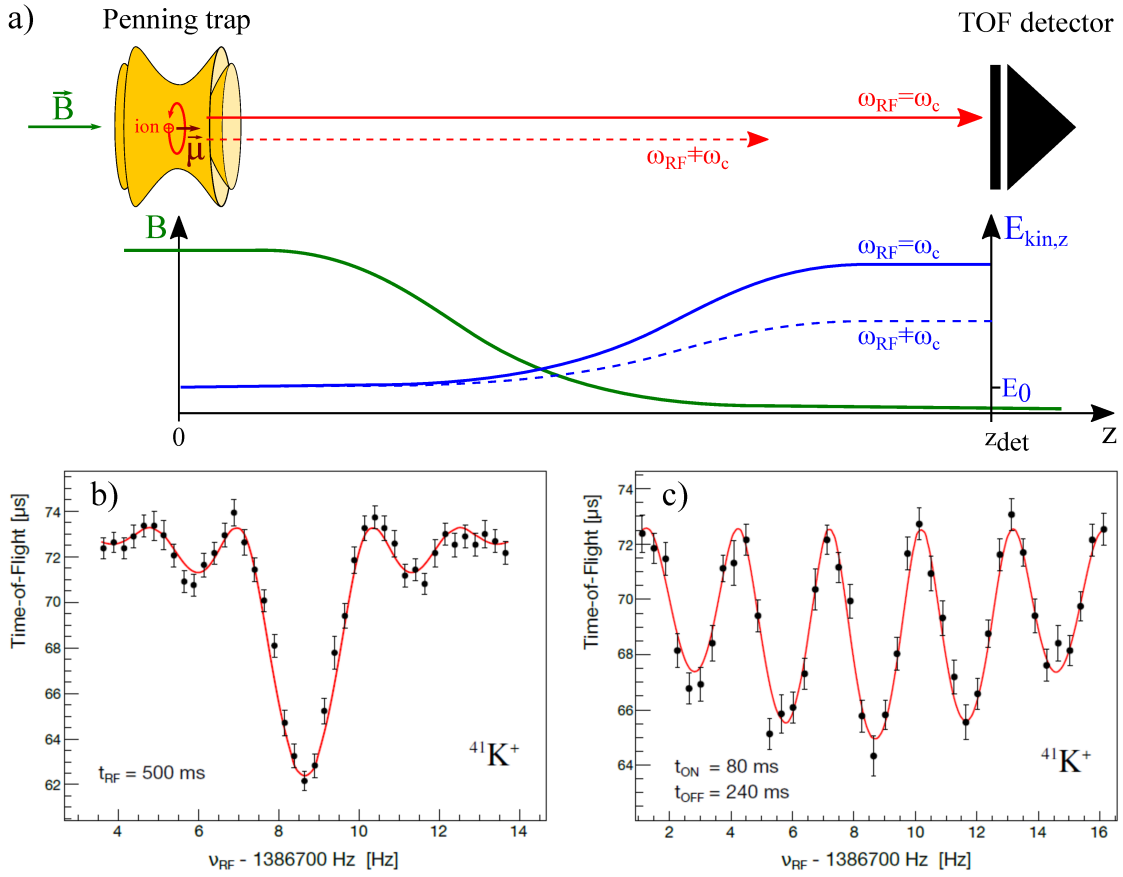

Figure 3.5. The TOF-ICR technique: a) After quadrupole excitation in the trap, ions are extracted onto a TOF detector. The magnetic field gradient converts radial into axial kinetic energy ($E_{\mathrm{kin,z}}$), thus reducing the flight time of resonantly excited ions ($\omega_{\mathrm{RF}} = \omega_c$) to the detector. b) TOF resonance obtained with a conventional single-pulse excitation. c) TOF resonance obtained with a two-pulse Ramsey excitation. The red lines indicate fits with the respective theoretical line shape. Both resonances were recorded with TITAN's measurement Penning trap (MPET). b) & c) adapted from [56].

magnetic moment $\vec{\mu} = \frac{E_r(\omega_{\mathrm{RF}})}{B}\vec{e_z}$ and exerts the following accelerating force on the ion [317]:

$$\vec{F} = -\vec{\nabla}\left(\vec{\mu}(\omega_{\mathrm{RF}})\vec{B}\right) = -\frac{E_r(\omega_{\mathrm{RF}})}{B}\frac{\partial B}{\partial z}\vec{e_z}. \tag{3.18}$$

Since the force increases proportionally with E_r, ions starting with a large radial energy in the trap attain higher velocities and arrive earlier at the detector [see Fig. 3.5 a)]. The TOF is described by the following expression [312]:

$$T(\omega_{\mathrm{RF}}) = \int_0^{z_{\mathrm{det}}} \sqrt{\frac{m}{2(E_0 - qV(z) - \mu(\omega_{\mathrm{RF}})B(z))}}dz, \tag{3.19}$$

where z_{det} is the distance from the trap centre to the detector, E_0 is the ion's axial kinetic energy in the trap, and $V(z)$ and $B(z)$ are the electric potential and the magnetic field strength along the extraction flight path, respectively.

Repeating this procedure for various excitation frequencies ω_{RF} near ω_c yields a TOF resonance curve with a characteristic line shape [312], as exemplified in Fig. 3.5 b). Since

resonant excitation yields the maximal radial energy, the minimal TOF is found at $\omega_{\mathrm{RF}} = \omega_c$. A precise determination of ω_c is obtained by fitting the theoretical line shape [312] to the TOF resonance data. The FWHM of the central lobe of the resonance is Fourier limited to $\Delta\nu_c \approx {}^{0.9}/_{T_{\mathrm{RF}}}$ [318]. Hence, the achievable resolving power is given by:

$$R = \frac{\nu_c}{\Delta\nu_c} \approx 1.1\,\nu_c T_{\mathrm{RF}}. \tag{3.20}$$

Typical excitation times of several $100\,\mathrm{ms}$ and true cyclotron frequencies on the order of $1\,\mathrm{MHz}$ result in resolving powers of up to $R \approx 10^6$. For mass measurements of very short-lived nuclides, excitation times as short as a few $10\,\mathrm{ms}$ have been realized [319, 320].

A variant of the TOF-ICR technique is the Ramsey excitation scheme [321, 322]. Instead of a single excitation pulse of duration T_{RF}, the Ramsey scheme uses two phase-coherent excitation pulses of the same amplitude and identical durations t_{ON}, separated by a waiting time t_{OFF}. This results in a modified TOF resonance curve with narrow lobes of near-identical amplitude, as displayed in Fig. 3.5 c). The FWHM of the central lobe is given by $\Delta\nu_c \approx {}^{0.6}/_{T_{\mathrm{RF}}}$ [318] and scales with the total length of the two-pulse excitation pattern $T_{\mathrm{RF}} = t_{\mathrm{ON}} + t_{\mathrm{OFF}} + t_{\mathrm{ON}}$. Due to the smaller $\Delta\nu_c$ and the larger number of pronounced TOF lobes available to constrain a fit, the Ramsey TOF-ICR method yields a roughly three times higher precision [322] compared to a one-pulse excitation with identical T_{RF}. In principle, it also provides a higher resolving power. In practice, however, the one-pulse excitation scheme is oftentimes preferable for the resolution of close-lying nuclear isomers because its prominent central lobe is easier to distinguish from the side lobes of an overlapping TOF resonance [318, 323].

The phase-imaging ion cyclotron resonance (PI-ICR) method

Developed roughly 10 years ago, the phase-imaging ion cyclotron resonance (PI-ICR) method [324] has enabled direct measurements of the radial eigenfrequencies by projection of the radial ion motion onto a position-sensitive detector. Again exploiting Eqn. 3.12, the true cyclotron frequency is then determined from the sum of the radial eigenfrequencies: $\omega_+ + \omega_- = \omega_c$. Compared to the TOF-ICR method, the PI-ICR technique offers a more than 10-times higher resolving power [318, 325] and is 5 times more precise or alternatively 25 times faster [318]. Due to these advantages, all Penning trap experiments at rare isotope beam facilities are presently either planning to or have already adopted this technique [3].

The principle of the PI-ICR method is displayed in Fig. 3.6. Dipole excitations are used to prepare an ion in an (ideally) pure radial eigenmotion. After an excitation-free phase accumulation time T, the ion is extracted onto a position-sensitive micro-channel plate (MCP) detector [326] placed in a region of weak magnetic field ($B \leq 10\,\mathrm{mT}$). The diverging magnetic field lines expand extracted ion clouds, resulting in magnified images of the radial ion positions in the trap. These images are used to monitor the radial ion motion in the trap. The frequency of the given eigenmotion ν is extracted from the total phase φ_{tot} acquired over the phase accumulation time T [318]:

$$\nu = \frac{\varphi_{\mathrm{tot}}}{2\pi T} = \frac{2\pi N + \varphi}{2\pi T}, \tag{3.21}$$

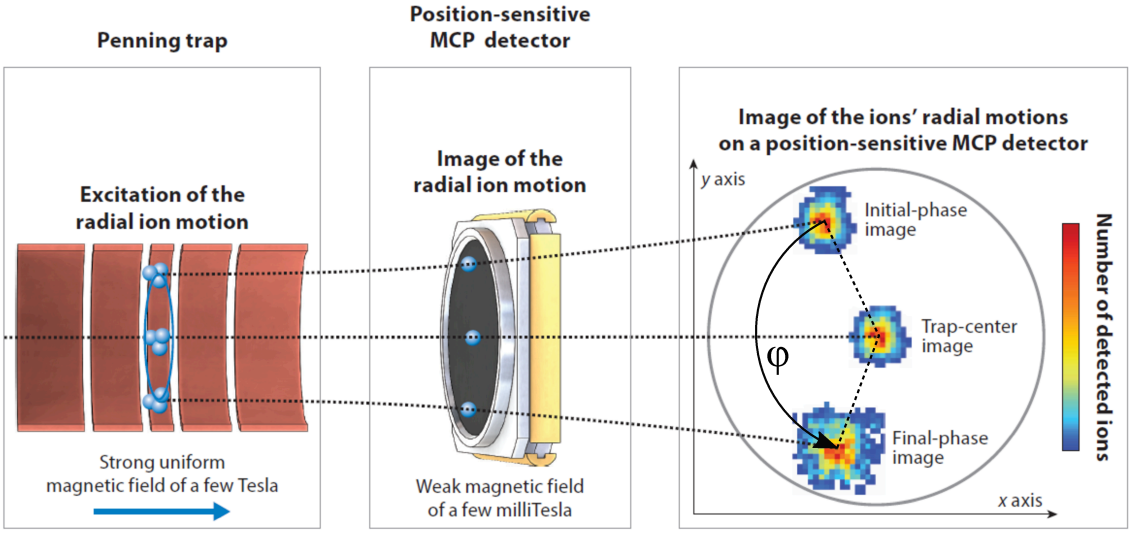

Figure 3.6. The PI-ICR technique: Projection of the radial ion motions onto a position-sensitive detector enables precise determinations of the radial eigenfrequencies in the trap. See text for details. Adapted with permission of Annual Reviews, Inc., from [3], ©2018; permission conveyed through Copyright Clearance Center, Inc.

where N is the integer number of completed revolutions and φ is the measured azimuthal angle between the ion projections before and after the accumulation period (see Fig. 3.6). Determining N requires a rough prior knowledge of the frequency ν, which is obtained by performing a TOF-ICR resonance in advance.

The ions' axial energy spread in the trap causes a dispersion in their TOF to the detector. A typical TOF distribution with a FWHM of a few 100 ns substantially smears out direct projections of the fast reduced cyclotron motion ($\nu_+ \sim 1$ MHz) [318, 327], resulting in large frequency uncertainties. To determine ν_+ precisely, the accumulated cyclotron phase is indirectly measured by imprinting it onto the slow magnetron motion [318]. To this end, an suitable quadrupole excitation at ν_c is applied before extraction to fully convert the reduced cyclotron into magnetron motion. As the conversion preserves the magnitude of the accumulated phase, a subsequent projection of the magnetron motion onto the detector gives access to the reduced cyclotron phase. More details on the technical implementation of the PI-ICR technique can be found in [318].

Since the magnetron frequency is to first order independent of the ion mass, the resolution of ion species with close-lying masses depends primarily on the ability to resolve their respective reduced cyclotron frequencies. Therefore, the resolving power of the method can be estimated as [324]:

$$R = \frac{\nu_c}{\Delta\nu_c} \approx \frac{\nu_+}{\Delta\nu_+} = \pi\nu_+ T \frac{r_+}{\Delta r_+}. \tag{3.22}$$

In contrast to the TOF-ICR technique, the resolution of a PI-ICR measurement is not only determined by the (reduced) cyclotron frequency and the observation time but also depends on the radial offset r_+ and the radial spread Δr_+ of the ion projection on the detector. The resolving power can therefore be enhanced by increasing r_+, e.g. through use of higher ion

charges [57], or by reducing Δr_+ through cooling prior to the frequency measurement [324]. Under typical trapping conditions resolving powers of up to 5×10^6 are achievable, making the PI-ICR technique a powerful tool for the resolution of low-lying nuclear isomers with excitation energies of a few $10\,\mathrm{keV}$ [327].

Due to its non-scanning nature, the PI-ICR technique is also more sensitive than the TOF-ICR method. While the latter usually requires several 100 ions for a reliable frequency determination, a PI-ICR measurement may be performed with only a few 10 ions [325]. This makes the PI-ICR methods well-suited for mass measurements of low-yield nuclides with production rates below 100 particles per hour.

The Fourier transform ion cyclotron resonance (FT-ICR) method

In contrast to the two previous techniques, the FT-ICR method [328] provides a means to determine the true cyclotron frequency non-destructively, i.e. without losing the ion. As a result, a precision mass measurement can in principle be performed with a single ion.

The ion eigenfrequencies are measured by picking up the minuscule image currents ($\sim 1\,\mathrm{fA}$) that oscillating ions induce on the trap electrodes. The signal amplitude is raised to a detectable level using a narrow-band RLC resonance circuit and a low-noise amplifier. To achieve single-ion sensitivity, the trap electrodes and the detection circuit must be cooled to cryogenic temperatures ($T \approx 5\,\mathrm{K}$) to suppress otherwise overwhelming Johnson noise [302]. For a frequency measurement, the oscillating signal in the time domain is Fourier transformed. Hence, the measurement precision increases linearly with the ion observation time. Usually, the axial oscillation is monitored while the radial eigenmotions are indirectly probed by coupling them to the axial eigenmotion [1]. A high-precision frequency determination usually relies on time-consuming ($\geq 1\,\mathrm{s}$ long) pre-cooling [329] of the ion motion and requires observation times on the order of $1\,\mathrm{s}$ to several $10\,\mathrm{s}$ [330].

Due to the resulting measurement timescales and the technical challenges involved in achieving single-ion sensitivity, FT-ICR mass spectrometry has so far only been used for measurements of non-radioactive and long-lived particles ($T_{\frac{1}{2}} > 1\,\mathrm{h}$). Exploiting the Brown-Gabrielse invariance theorem, these measurements have achieved mass uncertainties as low as $\frac{\delta m}{m} \approx 10^{-11}$ [331].

Two on-line ion trapping facilities are presently striving to extend the FT-ICR technique to rare isotopes for mass measurements of nuclides with extremely low production yields below 1 particle per day. The SHIPTRAP facility [332, 333] plans to exploit it for mass measurements of single trans-uranium isotopes [334] with typical half-lives $> 1\,\mathrm{s}$, while the LEBIT experiment will explore the applicability of the technique to low-yield isotopes with half-lives far below $1\,\mathrm{s}$ [335].

3.4 Multiple reflection time-of-flight mass spectrometry

Roughly a decade ago, MR-TOF-MS emerged as competitive instruments [336] for precision mass measurements of rare isotopes [254] and applications within analytical chem-

istry [337]. A key feature of these devices is their fast measurement cycles with typical durations of about 10 ms. Achieving mass uncertainties on the order of $\frac{\delta m}{m} \approx 10^{-7}$ [338, 339] in such short time frames, MR-TOF-MS are particularly well suited for mass measurements of very short-lived isotopes. Additionally, they can also serve as high-resolution isobar separators, with typical resolving powers of several 100 000. Their non-scanning measurement cycles combined with single-ion detection provide high sensitivity. Their broad mass range and isobar-separation capability make them useful tools for diagnosing and optimizing the composition of rare isotope beams [340]. Due to these benefits, they have quickly been adopted by on-line ion trapping facilities worldwide [336], and are now in operation or planned to be installed at almost every major RIB facility [183, 252, 339, 341–343].

Before addressing specifics of MR-TOF-MS in section 3.4.2, the basic principles of TOF mass spectrometry are introduced in the context of simpler systems in section 3.4.1. Technical details of TITAN's MR-TOF-MS [54] which was used for the gallium mass measurements reported in this thesis will be discussed in section 4.2.5.

3.4.1 Principles of time-of-flight mass spectrometry

The basic equation exploited in TOF mass spectrometers is readily derived from the equation for the total energy E_{tot} of a non-relativistic ion of charge q and mass m travelling along a path C through an electrostatic optical system:

$$E_{\text{tot}} = qV_0 = \frac{m\,v(z)^2}{2} + qV(z) \tag{3.23}$$

where V_0 and $V(z)$ denote the electrostatic potentials at the starting position and along the flight path, respectively. Re-arranging for $v = \frac{dz}{dt}$, we find the time of flight to obey the following relation:

$$t = \int_C \frac{dz}{v(z)} = \sqrt{\frac{m}{2q}} \int_C \frac{dz}{\sqrt{V_0 - V(z)}} \propto \sqrt{\frac{m}{q}}. \tag{3.24}$$

Since $t \propto \sqrt{\frac{m}{q}}$, ions with different mass-to-charge ratios will take different times to fly through the system. Recording the ions on a time-sensitive detector at the end of the flight path, one obtains a time-of-flight spectrum with distinct peaks. The mass-to-charge ratios corresponding to the different TOF peaks are then extracted using an equation of the type:

$$\frac{m}{q} = a\,t^2 = a\,(t_{\text{obs}} - t_0)^2, \tag{3.25}$$

where we have introduced a system-dependent constant of proportionality a and a small time-offset t_0, which accounts for electronic delays in a realistic TOF measurement. The constants a and t_0 are calibrated using ions of well-known mass.

Since $m \propto t^2$, the mass resolving power of a TOF mass spectrometer is given by:

$$R = \frac{m}{\Delta m} = \frac{t}{2\Delta t}, \tag{3.26}$$

where Δt denotes the FWHM of a TOF peak. To achieve the maximal resolving power, one therefore has to realize long flight times while keeping the width of the TOF peaks Δt minimal.

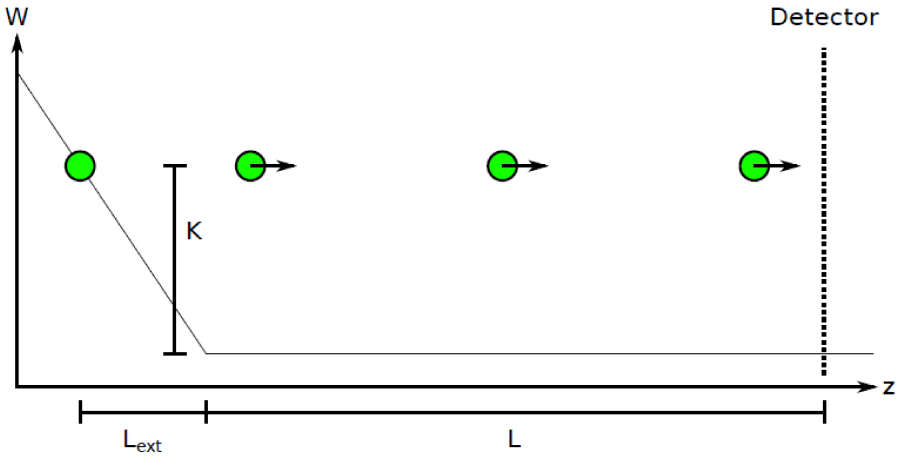

Figure 3.7. Electric potential along the axis of a simplistic linear TOF mass spectrometer. Ions start at a distance L_{ext} from the end of the acceleration region. They cross a field-free drift section of length L with a kinetic energy K and are registered on a TOF detector. Figure from [344].

A simple linear time-of-flight mass spectrometer

Let us first consider the most simple configuration for a TOF measurement: A linear TOF spectrometer comprised of an acceleration region followed by a field-free drift section of length L and a time-sensitive detector, as schematically shown in Fig. 3.7. The acceleration region is formed by a planar electrode and a mesh at a common spacing d, both initially kept at ground potential. Ions of mass m start at rest, at a distance L_{ext} from the mesh. Pulsing the planar electrode to a voltage V creates a uniform electric field $E = \frac{V}{d}$ that accelerates the ions towards the mesh. They cross the drift region with a constant kinetic energy K_{ref} and are eventually recorded at the detector. Inserting the corresponding potential $V(z)$ into Eqn. 3.24 and integrating over the path one obtains the following flight time to the detector:

$$t = \sqrt{\frac{2m}{K_{\text{ref}}}} \left(L_{\text{ext}} + \frac{L}{2} \right) . \tag{3.27}$$

In the ideal case of initially resting ions, perfectly localized to the nominal starting position, this spectrometer would yield an infinite resolving power and a perfect correlation between ion mass m and the measured time of flight t. In reality, however, deviations from the nominal ion starting conditions are far from negligible and severely limit the performance of such a simple mass spectrometer. Let us therefore separately evaluate the impact of an initial spread in the ion positions and energies.

Initial position spread and time focussing

A spread ΔL_{ext} in the initial ion positions affects the time of flight in two opposing ways. Ions starting farther from the detector take more time to reach the drift region. On the other hand, they acquire a larger kinetic energy K due to the longer acceleration and fly

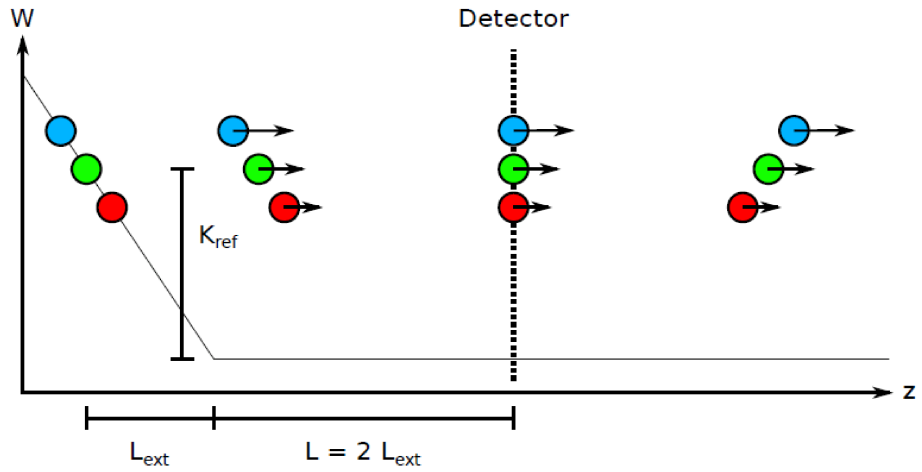

Figure 3.8. The concept of time focussing. The colored circles indicate ions of identical mass starting a different positions in the acceleration region of a linear TOF mass spectrometer. The TOF dispersion due to the initial position spread is compensated to first order by placing the detector at the time focus plane (see text for details). Figure from [344].

faster through the drift section. As a result, there is a drift distance at which the faster ions overtake the slower ones. Despite their different starting points, the ions reach this position at approximately the same time. It is therefore referred to as a time focus (plane). While the position spread ΔL_{ext} generally induces a widening of the TOF peaks, the dispersion can be minimized by matching the time focus with the detector plane. This concept is illustrated in Fig. 3.8.

More formally, an offset ΔL_{ext} from the nominal starting position translates into the following kinetic energy in the drift section:

$$K = qE(L_{\text{ext}} - \Delta L_{\text{ext}}) = qEL_{\text{ext}}\left(1 - \frac{\Delta L_{\text{ext}}}{L_{\text{ext}}}\right) = K_{\text{ref}}(1-\delta), \tag{3.28}$$

where $\delta = \frac{\Delta K}{K_{\text{ref}}} = \frac{\Delta L_{\text{ext}}}{L_{\text{ext}}}$ measures the relative deviation from the energy and the starting position of the reference ion. With the transformations $L_{\text{ext}} \rightarrow L_{\text{ext}}(1-\delta)$ and $K_{\text{ref}} \rightarrow K_{\text{ref}}(1-\delta)$, Eqn. 3.27 becomes:

$$t = t_a + t_d = \sqrt{\frac{2m}{K_{\text{ref}}}}\left(L_{\text{ext}}\sqrt{1-\delta} + \frac{L}{2}\frac{1}{\sqrt{1-\delta}}\right). \tag{3.29}$$

Taylor expanding this expression around $\delta = 0$ and eliminating the first order yields the following condition for the first-order time focus:

$$0 \stackrel{!}{=} \left.\frac{\partial t}{\partial \delta}\right|_{\delta=0} \Leftrightarrow \; L = 2L_{\text{ext}} \tag{3.30}$$

A spread in the initial ion positions is thus to first order compensated by placing the detector at a distance $2L_{\text{ext}}$ from the end of the acceleration region (see Fig. 3.8). To achieve a better compensation, one could, in principle, try to also eliminate higher orders in the Taylor

expansion. A lack of degrees of freedom prevents higher-order time focussing in the simplistic spectrometer considered here. However, the additional degrees of freedom available in a TOF spectrometer with two acceleration stages [345] would already allow one to either freely shift the position of the first-order time focus within the drift section or to realize a time focus up to second order [344].

Initial velocity spread and turn-around time

The second critical cause of TOF aberrations is a spread of the initial ion velocities. An ion initially travelling away from the detector with velocity $-v_0$ is decelerated by the electric field until it comes to rest at its turning point after the turn-around time $t_{\text{ta}} = \frac{mv_0}{qE}$. From this point on, it will behave identical to a particle started at zero velocity but with a corresponding displacement from the reference position, i.e. it acts equivalent to the blue particle in Fig. 3.8. Assuming the first-order time focus falls onto the detector plane, the particle will thus to first order acquire the same flight time as the reference particle plus a time lag $t_0 = +t_{\text{ta}}$ [346]. Analogously, a particle starting at the nominal position with velocity $+v_0$, will to first order acquire the same flight time as a reference particle started at time $t_0 = -t_{\text{ta}}$. Assuming a thermalized ion sample at temperature T, the FWHM of the TOF peak resulting from the initial particle velocities is thus given by [347]:

$$\Delta t_{\text{ta}} = \frac{m\Delta v_0}{qE} = \frac{\sqrt{8ln(2)mk_BT}}{qE}. \tag{3.31}$$

Consequentially, there is two ways to reduce the peak broadening induced by the initial ion velocities: (1) Cooling to reduce the ion temperature T prior to acceleration into the TOF analyzer or (2) the use of a strong acceleration gradient E. For an ion bunch with a spatial spread Δz_0 the second option comes at the price of an increased energy spread $\Delta K = qE\Delta z_0$. Relative energy spreads beyond a few permille quickly deteriorate the quality of a low-order time focus, thus resulting in peak broadening. One therefore faces a trade-off between the turn-around time Δt_{ta} and the ion energy spread ΔK.

For ions of mass $m = 100\,\text{u}$ at $T = 300\,\text{K}$ and a typical acceleration gradient of $E = 100\,\text{V}\,\text{mm}^{-1}$, the induced time spread amounts to $\Delta t_{\text{ta}} \approx 4\,\text{ns}$. Using $\Delta z_0 = 0.5\,\text{mm}$ as a realistic approximation for the initial spatial spread of the ion positions, the above conditions result in an energy spread of $\Delta K \approx 50\,\text{eV}$. At typical ion energies of $K_{\text{ref}} \approx 5\,\text{keV}$, this translates into a substantial relative ion energy spread of $\delta \approx 1\%$. Such large energy spreads cause peak broadening due to higher-order aberrations. One therefore needs TOF analyzers with excellent time-focussing capabilities with respect to the ion energies.

Isochronicity and energy focussing

Electrostatic ion mirrors provide a suitable means to reduce TOF aberrations arising from ion energy spread. The energy-spread compensation is based on the fact that faster ions penetrate deeper into the repulsive mirror potential and thus acquire a longer flight path than slower ions, as illustrated in Fig. 3.9. This enables the creation of a secondary time focus

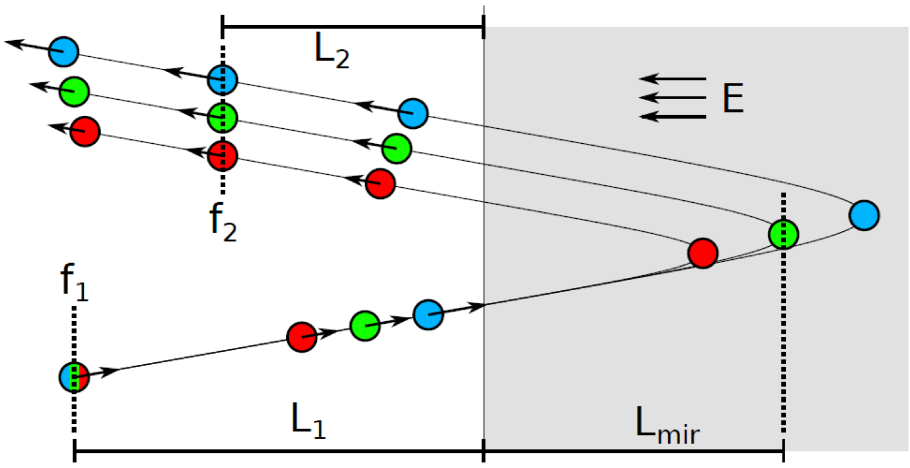

Figure 3.9. Time-energy focusing with an electrostatic ion mirror. Ions of same mass but different kinetic energies disperse after a primary time focus f_1. Faster ions (blue circles) penetrate deeper into the repulsive mirror potential and acquire a longer path length, resulting in a secondary time focus f_2 after the mirror. Figure from [344].

with respect to energy after the mirror. Placing a detector at the position of the secondary time focus results in a TOF mass spectrometer referred to as a reflectron [348]. Since the detector has to be transversally offset from the acceleration region, the ions have to enter the mirror at a small angle ($\approx 2°$ [348]) with respect to the mirror axis.

Consider the ion mirror shown in Fig. 3.9. The ion mirror is used to form a uniform electric field E. The primary time focus f_1 lies at a distance L_1 in front of the mirror surface. The reference ion penetrates the mirror to a depth L_{mir}. Ions of different energy acquire different path lengths inside the mirror resulting in the formation of a secondary time focus f_2 at a distance L_2 after the mirror surface. The flight times from the primary to the secondary time focus plane is given by:

$$t_{12} = \sqrt{\frac{m}{K_{\text{ref}}}} \left(\frac{L_1 + L_2}{\sqrt{1+\delta}} + 4L_{\text{mir}}\sqrt{1+\delta} \right), \tag{3.32}$$

where $\delta = \frac{\Delta K}{K}$ is again the relative ion energy spread. Requiring $\frac{\partial t_{12}}{\partial \delta}\big|_{\delta=0} \stackrel{!}{=} 0$ yields the following condition for the secondary time focus of first order with respect to energy:

$$L_1 + L_2 = 4L_{\text{mir}}. \tag{3.33}$$

When the detector position matches a time focus plane, the total ion flight path is said to be isochronous, i.e. approximately independent from the specific ion energy. By tuning the potential inside the mirror, the secondary time focus can be shifted along the flight path of the reflected ions. Analogous to the compensation of spatial spreads with the acceleration potential, higher-order time foci (and thus a higher level of isochronicity) can be accomplished by splitting the ion mirror into multiple stages with different electric field strengths [349].

3.4.2 Multiple-reflection time-of-flight mass spectrometers

Let us estimate the required dimensions for a TOF mass spectrometer for applications in rare-isotope science. Typical nuclear structure studies demand relative mass uncertainties of $\frac{\delta m}{m} \approx 10^{-6}$ or below. In order to target very low-yield isotopes, one may aim to achieve this uncertainty level with as few as $N_{\text{ions}} = 20$ detected ions. The relative statistical uncertainty of a TOF mass measurement obeys the following relation with the mass resolving power and the measurement statistics N_{ions} [254, 350]:

$$\frac{\delta m}{m} = C\frac{1}{R\sqrt{N_{\text{ions}}}}, \tag{3.34}$$

where the constant of proportionality C depends on the specific shape of the TOF peaks produced by the spectrometer [350]. Assuming Gaussian peaks, one finds $C \approx 0.42$. The mass resolving power required for the aforementioned measurement is thus on the order of $R \approx 110\,000$. The minimal width of the TOF peaks can be estimated as $\Delta t \approx 4\,\text{ns}$ since reducing the turnaround time much below this level is technically challenging [346]. Plugging these numbers into Eqn. 3.26 yields a minimal flight time of $t \approx 0.9\,\text{ms}$. Assuming ions of mass $100\,\text{u}$ and a kinetic energy of $K_{\text{ref}} = 1\,\text{keV}$, the demanded resolution would be achieved after a flight path of $\approx 39\,\text{m}$. A linear TOF mass spectrometer or a reflectron of this size are impractical.

A convenient way to realize mass resolving powers $R \geq 100\,000$ is to fold the flight path up by reflecting ions many times between two opposing electrostatic mirrors. Such a multiple-reflection time-of-flight mass spectrometer (MR-TOF-MS) can either be realized as an open- or a closed-path system [254], as illustrated in Fig. 3.10. An open-path system provides an, in principle, unlimited mass range at the expense of a limited path length. A closed-path system is generally more compact and offers an incrementable, theoretically unlimited path length, since ions can be sent onto arbitrarily many closed loops inside the device. Due to these advantages, all MR-TOF-MS installed at rare isotope beam facilities presently use closed-path TOF analyzers. The following discussion will therefore only consider closed-path systems.

The mass resolving power of an MR-TOF-MS is given by [252]:

$$R = \frac{t_l + N_a t_a}{2\sqrt{(\Delta t_l)^2 + (N_a \Delta t_a)^2}}, \tag{3.35}$$

where N_a is the number of revolutions completed in the TOF analyzer, t_l denotes the flight time without any reflections, Δt_l is the peak broadening arising from the non-ideal ion starting conditions, t_a is the flight time for one revolution and Δt_a is mean time spread acquired per revolution in the TOF analyzer. In the limit $N_a \to \infty$, the resolving power becomes independent of the initial bunch conditions and asymptotically approaches $R_\infty = \lim_{N_a \to \infty}(R) = \frac{t_a}{2\Delta t_a}$. A long flight path inside a well-designed TOF analyzer with minimal TOF aberrations Δt_a is thus an effective way to overcome the limitations imposed by the turn-around time. For an MR-TOF-MS, the calibration equation (Eqn. 3.25) is modified to [350]:

$$\frac{m}{q} = \frac{c\,(t - t_0)^2}{(1 + N_a b)^2}, \tag{3.36}$$

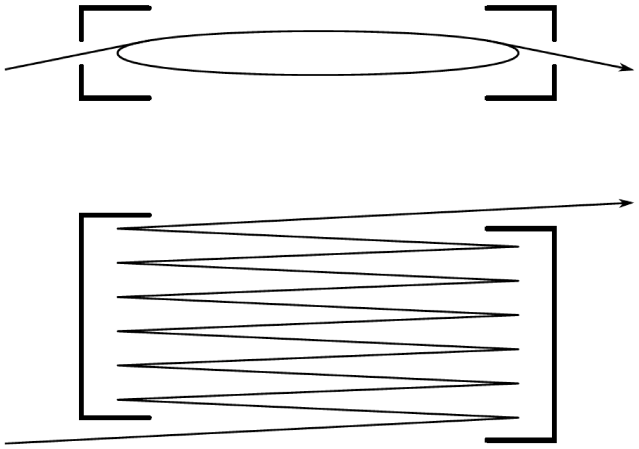

Figure 3.10. Schematics of multiple-reflection TOF analyzers with closed (top) and open (bottom) path configuration. Figure from [344].

where c, b, and t_0 are calibration constants which are determined by TOF measurements of reference ions with well-known mass.

An MR-TOF-MS measurement cycle is divided into the following stages: (1) ion bunch preparation, (2) mass separation in the TOF analyzer, and (3) ion detection or isobar separation. The following sections reviews the main demands imposed by these stages and discusses how they are met by different technical approaches.

Ion bunch preparation

As illustrated for the simple linear TOF mass spectrometer above, both the initial position and velocity spreads of the ion bunches have to be minimized to avoid broadening of the TOF peaks. As we have just seen, the maximum achievable resolving power of an MR-TOF-MS theoretically only depends on the TOF aberrations acquired in the TOF analyzer. However, the real situation is more complicated since ion losses due to radiaoctive decays, imperfect vacuum conditions and ion optical aberrations limit the achievable path lengths and thus the revolution number N_a. In order to closely approach the asymptotic limit R_∞ within the achievable flight times, Δt_l has to be limited to no more than a few $10\,\mathrm{ns}$ as it determines the speed of convergence. Even well-designed TOF analyzers can only compensate TOF aberrations due to percent-level deviations from the nominal ion energy and injection angle. Larger energy and angular spreads result in substantial increases of Δt_a and deteriorate the mass resolving power.

Suitable ion bunch conditions are achieved by initially storing the ions in a buffer-gas-filled linear Paul trap [351]. As will be detailed in section 4.2.1, these ion traps use a combination of an electrostatic axial potential and radiofrequency fields to achieve three-dimensional ion confinement. The addition of a buffer gas sympathetically cools the stored ions, reducing their thermal velocity spread and causing them to accumulate in the trap's potential minimum. Rapidly switching the axial trapping potential to an acceleration gradient with $E \approx 100\,\mathrm{V\,m^{-1}}$ allows one to create compressed ion bunches with suitable properties

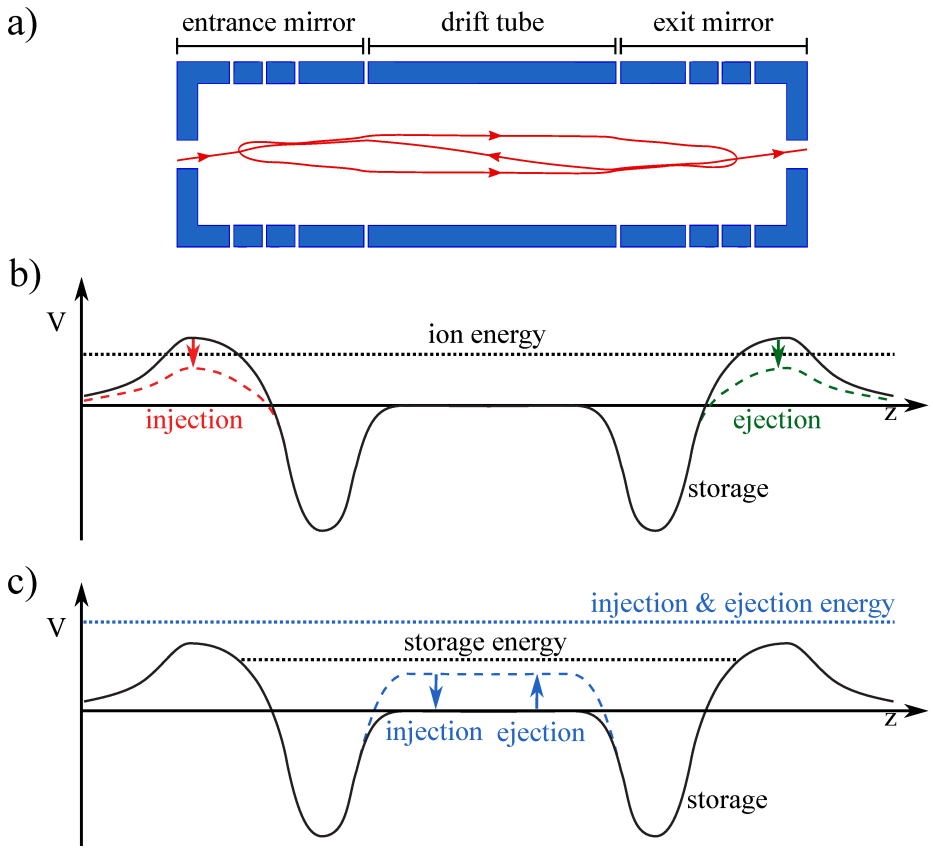

Figure 3.11. a) Cross section of a multiple-reflection time-of-flight analyzer (blue, not to scale) with an example trajectory of an ion undergoing a single revolution in the analyzer (red, not to scale). b) On-axis potentials during storage and injection/ejection in a pulsed-mirror scheme. c) On-axis potentials during storage and injection/ejection with an in-trap lift. See text for details. Figure adapted from [252].

for high-resolution TOF analysis. The acceleration potential can further be tailored to form a primary time focus. To realize measurement cycles with durations on the order of ≈ 10 ms, the cooling time should not exceed a few milliseconds. This usually necessitates buffer gas pressures on the order of 10^{-2}–10^{-3} mbar [252, 339].

TOF analysis

A multiple-reflection TOF analyzer is generally composed of two opposing ion mirrors and a central drift region formed by a drift tube, as shown in Fig. 3.11 a). To enable several 100 m-long flight paths with ion losses of no more than a few 10%, the TOF analyzer has to be kept under high vacuum with pressures of $p \lesssim 1 \times 10^{-7}$ mbar [339]. To achieve such vacuum levels, the TOF analyzer usually has to be isolated from the buffer-gas-filled preparation trap with a differential pumping stage.

The ion injection and ejection is realized either by temporarily lowering the mirror voltages or by pulsing the potential of the drift tube. The pulsed-mirror scheme [347] leaves the total energy of injected ions unchanged and allows the ions to enter or leave the TOF

analyzer by temporarily lowering the otherwise reflective potential of one of the ion mirrors [see Fig. 3.11 b)]. In the second scheme, the mirror voltages remain static whereas the drift tube is switched to lower (or raise) the ion energies to a level below (or above) the maxima of the mirror potential. To prevent an increase in energy spread, the drift tube is pulsed when the ions are localized in its field-free central region [see Fig. 3.11 c)]. Since the drift tube essentially acts as an elevator in energy space, this injection/ejection scheme is referred to as an in-trap lift [352]. The two schemes come with distinct benefits and challenges, and both are currently in use at MR-TOF-MS at RIB facilities (see e.g. [252, 254, 352]). While the pulsed-mirror scheme provides a larger mass range (see below for details), the switching of the mirror potentials complicates the stabilization of the mirror voltages during the TOF analysis. Stable mirror voltages are a prerequisite to achieving high mass resolving powers, as voltage fluctuations add up over the typically several 100 ion reflections and expand the ion phase space beyond what can be compensated with the ion mirrors. As detailed in section 4.2.5, TITAN's MR-TOF-MS [54] uses the pulsed-mirror scheme for ion injection.

The ion-optical design of the ion mirrors should fulfil the following criteria [346]:

- stable ion trajectories over flight paths of several 100 m
- minimal TOF aberrations due to the initial spatial, angular and energy spread of the ion bunches
- grid-less electrodes to avoid transmission loss over the large numbers of reflections.

These demands are met by using ion mirrors composed of a stack of gridless, concentric electrodes. To provide enough degrees of freedom for higher-order time focussing with respect to the ion energies and their longitudinal position spread, the ion mirrors typically consist of 4–6 electrodes (see e.g. [183, 341, 342, 346, 353]). Four-electrode mirrors as used in TITAN's MR-TOF-MS enable third-order time focusing with respect to the ion energy and second-order time focusing with respect to spatial spreads of the ion bunches [346]. While the outer mirror electrodes are kept at retarding potentials, the innermost mirror electrodes are usually biased to an accelerating potential to provide transversal focussing. A schematic of a TOF analyzer is shown in Fig. 3.11, along with a point-to-parallel focused ion trajectory and typical mirror potentials.

Ion detection and isobar separation

After a sufficient amount of TOF separation has been acquired, ions are ejected from the TOF analyzer and either guided onto a time-sensitive detector for mass measurement or isobar separated by discarding undesired ion species. To make the total flight path isochronous, the time-focus has to be matched with the detector plane. This can either be achieved by applying carefully tuned mirror voltages or by installing a reflectron at the ejection end of the TOF analyzer [254]. Present MR-TOF-MS use a number of different schemes for time-focus matching as detailed in [354].

Besides mass measurements, an MR-TOF-MS may also be used for isobar separation. Several schemes have been developed to discard undesired isobaric contaminants after TOF

separation. A so-called Bradbury-Nielsen ion gate [355] uses a harp-like arrangement of wires alternatingly biased to opposite polarities to deflect ions outside the accepted beam path. Placing the ion gate close to a time-focus plane and pulsing the wire voltages with a well-chosen timing allows one to only deflect undesired ion species while letting the ions of interest pass with near-unit efficiency [252, 254]. Since many passes through the wires result in non-negligble ion losses, the ion gate should be placed outside the TOF analyzer. Pulsing an in-trap lift with a well-chosen timing allows to selectively eject a specific ion species and thus provides an alternative way to isolate the ions of interest [356]. The third approach presently used for isobar separation is to guide the mass-separated ions back to the injection Paul trap where they are then selectively re-captured. This so-called mass-selective retrapping [357] is used for isobar separation in TITAN's MR-TOF-MS. Since the re-captured ion samples can also be re-cooled and re-injected into the TOF analyzer, this scheme allows one to operate the spectrometer as its own isobar separator. The mass-selective retrapping technique proved essential for the first direct mass measurement of ^{60}Ga and is described in more detail in section 4.2.5.

Unambiguous mass range

A drawback of closed-path TOF analyzers is their limited mass range. As ions successively separate in time, lighter ions will eventually lap heavier ones. Subsequently extracting the ions onto the detector, the light ions will have completed more revolutions inside the TOF analyzer and thus have acquired a longer flight path than the heavier ones. This introduces ambiguities in the spectrum since peaks at a larger TOF do not necessarily correspond to larger mass-to-charge ratios anymore. Assuming a pulsed-mirror ejection scheme and a large number of revolutions N_a, the non-ambiguous mass range can be estimated from [358]:

$$\frac{m_{\text{max}}}{m_{\text{min}}} \approx 1 + \frac{2(1-\lambda_{\text{mir}})}{N_a}, \tag{3.37}$$

where N_a denotes the number of completed revolutions and λ_{mir} is the fraction of a revolution period that ions spent inside one mirror.

In the case of TITAN's MR-TOF-MS, $1-\lambda_{\text{mir}} \approx 0.68$ [359]. Even after several 100 revolutions, the mass acceptance is thus sufficiently wide to ensure an identical number of revolutions for isobaric species. To achieve a non-ambiguous spectrum, a pulsed deflector installed inside the TOF analyzer can be used to selectively remove ions that deviate from the nominal number of revolutions. Such a mass-range selector [252] is installed in TITAN's MR-TOF-MS, as detailed in section 4.2.5. In principle, a mass measurement can even be performed when the calibrant species and the species of interest have completed different revolution numbers [350]. However, in such multi-turn calibrations care must be taken that none of the analyzed species has been affected by switched electric fields and the analysis must include careful checks for additional systematic uncertainty contributions [350]. Due to these complications, it is usually preferable to use an isobaric mass calibrant, if available.

For MR-TOF-MS using an in-trap lift for ion ejection, the term $(1-\lambda_{\text{mir}})$ Eqn. 3.37 has to be replaced by half the fraction of a revolution period that the ions spent inside the field-

Table 3.1. Comparison of typical performance figures of different techniques for direct precision mass measurements. In measurements of short-lived isotopes the given performance figures may not be simultaneously achievable.

Technique	Observation time	Required ion number	Precision $\frac{\delta m}{m}$	Resolving power R	Mass range
SMS	1–10 s	1–10 ions	10^{-7}	1×10^6	Broad
IMS	10–300 µs	1–10 ions	$10^{-6} - 10^{-7}$	$1 - 2 \times 10^5$	Moderate
MR-TOF-MS	10 ms	>10 ions	10^{-7}	$10^5 - 10^6$	Moderate
TOF-ICR-MS	10–1000 ms	>100 ions	$10^{-7} - 10^{-9}$	1×10^6	Narrow
PI-ICR-MS	10–1000 ms	>10 ions	$10^{-8} - 10^{-10}$	$10^6 - 10^7$	Narrow
FT-ICR-MS	1–1000 s	1 ion	$10^{-7} - 10^{-11}$	$10^7 - 10^{11}$	Narrow

free region of the central drift tube [358]. This number is usually not larger than 0.3 [358], causing even the flight paths of isobars to become ambiguous after a few 100 revolutions.

3.5 Comparison of mass spectrometry techniques

An overview of the performance characteristics of the different approaches discussed in this chapter is given in table 3.1. In many regards, the different techniques are complementary. For direct mass measurements of rare isotopes with sub-ms half-lives, isochronous mass spectrometry (IMS) in storage rings is the only applicable technique. On the other hand, Penning trap mass spectrometers hold a monopoly for high-precision measurements of longer-lived or stable isotopes with half-lives above[3] 50 ms and relative mass uncertainties distinctly below $\frac{\delta m}{m} = 10^{-7}$.

For mass measurements of rare isotopes with less stringent precision requirements, MR-TOF-MS have started to challenge Penning traps as the unrivalled work horses. Due to their fast measurement cycles and their high sensitivity, MR-TOF-MS are particularly well suited for measurements of short-lived isotopes with $5\,\text{ms} \leq t_{1/2} \leq 50\,\text{ms}$ or species with low production yields below 100 particles per hour. Due to impressive technical progress over the last years, MR-TOF-MS now regularly achieve mass uncertainties of $\frac{\delta m}{m} \leq 10^{-7}$ [338, 339, 360], thus making them powerful tools not only for nuclear structure studies but also for nuclear astrophysics. The fact that MR-TOF-MS are now regularly used as high-resolution beam purifiers for Penning trap mass spectrometers highlights the complementarity of both instrument types.

[3] As an exception to this general rule, the TITAN facility has demonstrated that magnetron orbit preparation by ion injection with a Lorentz steerer [316] enables Penning trap mass measurements of nuclides with half-lives below 10 ms [320].

Chapter 4

Mass measurements of rare isotopes at TITAN

The mass measurements of neutron-deficient gallium isotopes discussed in this thesis were performed at TRIUMF's Ion Trap for Atomic and Nuclear Science (TITAN) [52]. The TITAN facility is an array of charged particle traps specialized on mass measurements and in-trap decay spectroscopy of exotic isotopes. It is located in the low-energy section of the Isotope Separator and Accelerator (ISAC) facility [256] in Vancouver, Canada.

This chapter gives an overview of the scientific program and the experimental components of the TITAN facility. Building on the review of the primary methods for the production of rare isotope beams in section 3.1, specifics of exotic isotope generation at ISAC, as well as the available yields for neutron-deficient gallium isotopes are discussed in section 4.1. Section 4.2 proceeds with an overview of the mass measurement program at the TITAN facility and introduces its various ion traps.

4.1 Production of rare isotopes at ISAC

The Isotope Separator and Accelerator (ISAC) facility [256] at TRIUMF delivers radioactive beams to a variety of experimental setups for studies in nuclear physics, nuclear astrophysics, fundamental symmetries and material science [275, 361]. An overview of the rare isotope beam production at ISAC is shown in Fig. 4.1. Radioisotopes are generated by impinging a high current (up to $100\,\mu$A), 480 MeV proton beam from TRIUMF's H^- cyclotron [362] on a set of target foils housed inside a target/ion source assembly. Possible target materials include Nb, Ta as well as composites such as UC_x, SiC and ZrC [363]. For fast diffusion and effusion of the produced nuclides out of the target into the ionization tube, the target assembly is resistively heated to high temperatures of up to $2300\,^\circ$C [363]. Depending on the element of interest and experimental requirements, the produced isotopes are either ionized with a Re surface ion source, a forced electron-beam-induced arc discharge (FEBIAD) plasma ion source [364], TRIUMF's Resonant Ionization Laser Ion Source (TRILIS) [365] or a surface-ion rejecting ion-guide laser ion source (IG-LIS) [366]. The ionized particles are electrostatically accelerated and undergo mass-to-charge ratio ($^A/_q$)

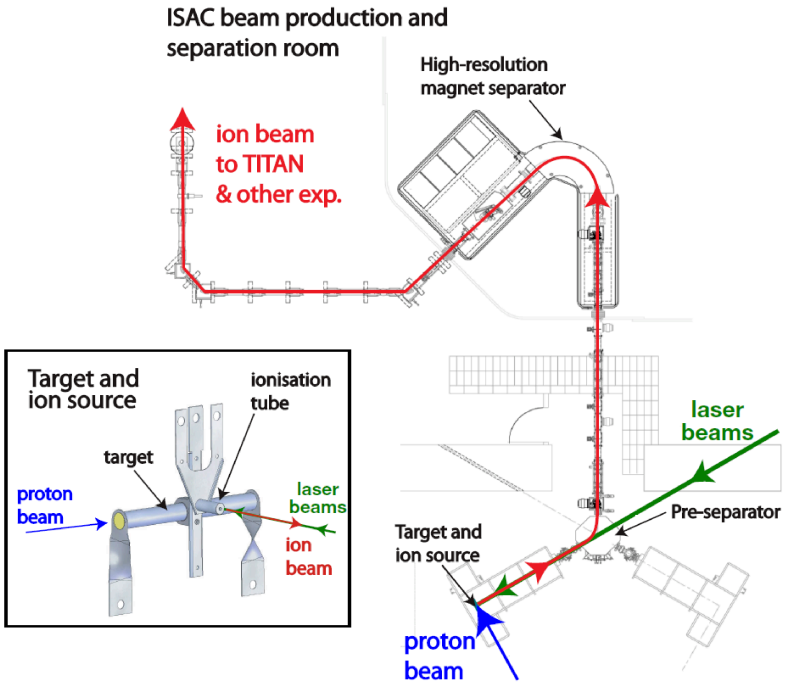

Figure 4.1. Schematic of rare isotope beam production with the isotope separation on-line method at TRIUMF's ISAC facility. The inset shows a zoomed view of a target/laser ion source assembly. Figure from [56].

selection in a pre-separator and a subsequent high-resolution separator magnet. With a maximal mass separation power of $\frac{m}{\Delta m} \approx 2000$ for typical beams at ISAC, the separator magnets can only provide isobarically-pure beams at very low masses of $A < 30$ [256]. Higher-mass beams often contain significant amounts of surface- or plasma-ionized isobaric contamination – a potential challenge for experiments. Assuming the species of interest can be laser ionized, the IG-LIS enables contaminant suppression by up to 6 orders of magnitude, at the cost of a typically 50-100x lower efficiency as compared to the regular laser ion source [366]. Two symmetric on-line target stations allow target replacements with nearly uninterrupted radioactive beam delivery. Additionally, an off-line ion source terminal [367] can supply non-radioactive atomic and molecular beams for machine commissioning and optimization or for stable beam experiments. Beam delivery to low-energy experiments such as TITAN proceeds through a series of electrostatic beamlines [368] at transport energies of 20–60 keV. A chain of post-accelerators [369] alternatively provides fast beams to experimental stations [370, 371] at a medium-energy ($0.12\,\mathrm{MeV/u} \leq {}^{E}/_{A} \leq 1.8\,\mathrm{MeV/u}$ [372]) and a high-energy ($1.5\,\mathrm{MeV/u} \leq {}^{E}/_{A} \leq 6.5\,\mathrm{MeV/u}$ for ${}^{A}/_{q} \leq 6$ [369]) area.

Fig. 4.2 depicts historic yields [373] for neutron-deficient gallium isotopes obtained with different target/ion source combinations and proton beam currents at ISAC. Based on this data, a ZrC target and the TRILIS laser ion source were selected for the gallium mass measurements reported in this thesis. For these measurements, a higher proton current of $55\,\mu\mathrm{A}$ on target was used to further increase the isotope production rates. The element-selective, multi-step laser ionization was found to boost the gallium yield by more than a factor of

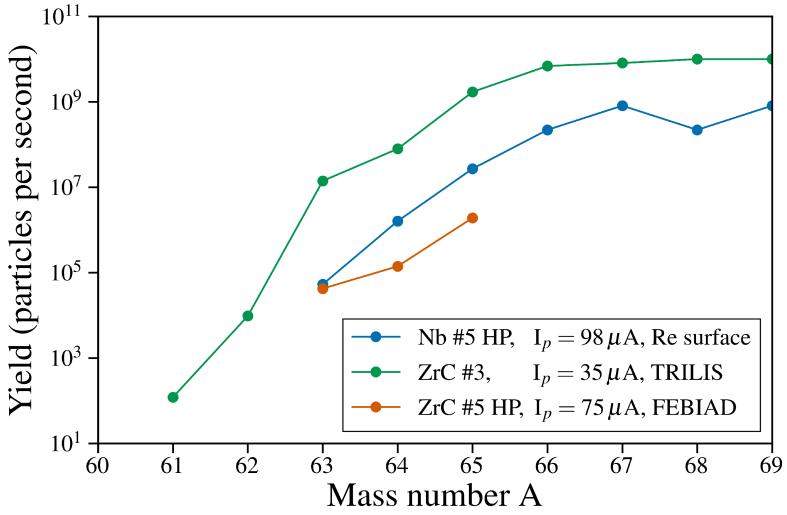

Figure 4.2. Yields for neutron-deficient gallium isotopes measured at the ISAC yield station [256]. The legend indicates the respective production target, the proton current on target I_p and the used ion source. The measurements discussed in chapter 5 were performed using a ZrC target. Data taken from the ISAC Yield Database [373].

five, while leaving the yields of (surface-ionized) contaminants unaffected. This indicates the effectiveness of resonant laser ionization in optimizing the signal-to-contaminant ratios of ISOL beams. After mass separation, the product nuclides were delivered to the TITAN facility as a continuous beam at a transport energy of ≈20 keV.

4.2 The TITAN facility

First proposed in 2003 [52] and commissioned in 2006, the TITAN facility has been in successful operation for more than 15 years. During this time, mass measurements and decay studies at TITAN have yielded important contributions to a variety of fields including nuclear physics, nuclear astrophysics, neutrino physics and tests of fundamental symmetries. Highlights of TITAN's science program include mass measurements that challenged ab-initio theory descriptions of exotic halo nuclei [320, 374–377], elucidated the emergence of new magic numbers in nuclides far from stability [19, 378] and constrained models of r-process nucleosynthesis [379–381].

TITAN's continual success is noteworthy since precision studies with rare isotope beams involve unique experimental challenges. Some of the primary complications are: small production yields and short half-lives of the nuclides of interest, overwhelming isobaric beam contamination and limited access to high in-demand radioactive beams. The following characteristics of the TITAN setup can help experimenters to overcome these challenges:

- **Fast measurement cycles** – Rapid ion preparation techniques such as the use of a Lorentz steerer [316] for ion injection into the measurement Penning trap limit ra-

dioactive decay losses and give access to nuclides with half-lives of only a few milliseconds. This capability was highlighted in a precision mass measurement of the halo nucleus ^{11}Li [320] with a half-life of only 8.8 ms – the fastest Penning trap mass measurement to date.

- **Increased mass precision and resolution through charge breeding –** A dedicated on-line charge breeder provides TITAN with the unique ability to perform Penning trap mass measurements of short-lived, highly charged ions [58]. This approach has the demonstrated potential [382] to significantly boost the achievable mass precision and resolving power, thereby opening new pathways to high-precision tests of fundamental symmetries [61] or the resolution of low-lying nuclear isomers [63].

- **Versatility –** The interconnected array of ion traps installed at TITAN provides high flexibility. This allows experimenters to tailor the beam preparation steps to the specific demands of a given measurement. Moreover, it enables uninterrupted readiness for on-line measurements, even when one of the measurement traps is undergoing technical upgrades or off-line development.

- **Sensitivity –** Efficient mass measurement schemes and single-ion sensitive detection allows TITAN to leverage the intense radioactive beams available at the ISAC facility. The addition of an multiple-reflection time-of-flight mass spectrometer (MR-TOF-MS) and isobar separator [54] in 2017 has strongly increased the sensitivity and background-handling capability of the TITAN setup [339].

Fig. 4.3 shows an overview of the core components of the TITAN facility. To accommodate spatial constraints, the TITAN setup was mounted on an elevated platform in the ISAC-I experimental hall. The first stage of the system is formed by a radiofrequency quadrupole (RFQ) cooler & buncher which prepares incoming beams for efficient transfer into the downstream ion traps. When no radioactive beam is injected from ISAC, a surface ion source can provide stable beams for testing and technical development. An electrostatic beamline links all ion traps and is used to transport ion bunches between them. The measurement Penning trap (MPET) (see section 4.2.4 for details) enables mass measurements on short-lived, singly charged ions with relative uncertainties of $\frac{\delta m}{m} \approx 10^{-8}$. Alternatively, the ion charge state can first be raised in an electron beam ion trap (EBIT) charge breeder, thereby enabling PTMS of highly charged radioisotopes. The benefits and challenges of this unique approach as well as the potential of decay spectroscopy in TITAN's EBIT are discussed in section 4.2.2. A multiple-reflection time-of-flight mass spectrometer (MR-TOF-MS) and isobar separator can either serve as a high-resolution beam purifier for the other ion traps or act as a standalone mass spectrometer. The gallium mass measurements reported in this thesis were performed with the MR-TOF-MS after beam preparation in the RFQ cooler & buncher. Section 4.2.5 gives a technical overview of the MR-TOF-MS and discusses how it has extended TITAN's reach to more exotic nuclides. Fig. 4.3 also shows the tentative position of a possible cooler Penning trap (CPET) upgrade for electron cooling of highly charged

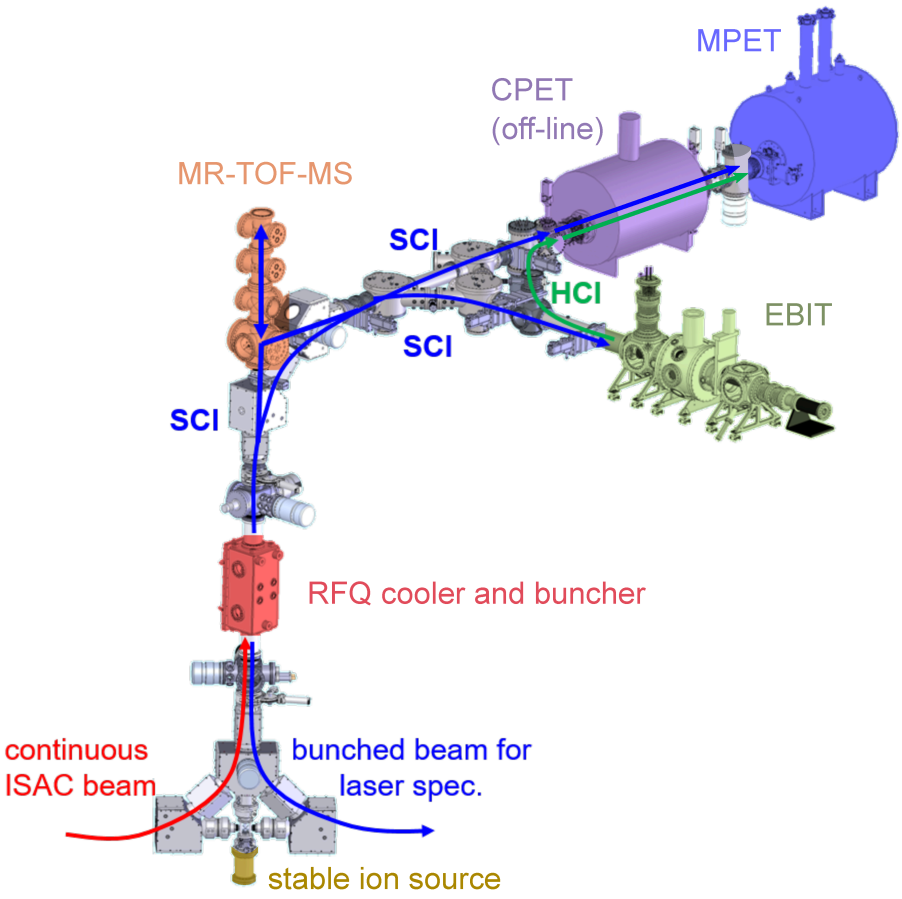

Figure 4.3. Overview of the TITAN facility. Continuous ion beams from ISAC (red arrow) or from a stable ion source are injected into the RFQ cooler & buncher and then passed on to the other ion traps through electrostatic beamlines. Possible paths for bunched transport of singly charged ions (blue) or highly charged ions (green) between the different ion traps are indicated by arrows. See text for details.

ions (HCI) prior to mass measurement in MPET. The prospects of this upgrade were investigated as part of this thesis. To this end, tests of electron cooling of singly charged ions (SCI) were performed with CPET installed in an off-line setup and the results of these studies are reported in chapter 6.

4.2.1 RFQ cooler & buncher

Since ion beams in ISAC's low-energy section are continuous, and exhibit beam energies of several 10 keV and typical energy spreads of ≈10 eV, they are unsuited for direct injection into ion traps for precision measurements. To adapt the properties of incoming beams to the acceptance requirements of the downstream ion traps, a gas-filled radiofrequency quadrupole (RFQ) cooler & buncher [383] acts as the first stage of the TITAN system.

After pioneering work [384–386] at the ISOLTRAP [387] and JYFLTRAP [388] facilities, RFQ coolers & bunchers have emerged as standard tools for preparing radioactive ion beams for precision mass measurements [389–392] or collinear laser spectroscopy [393–

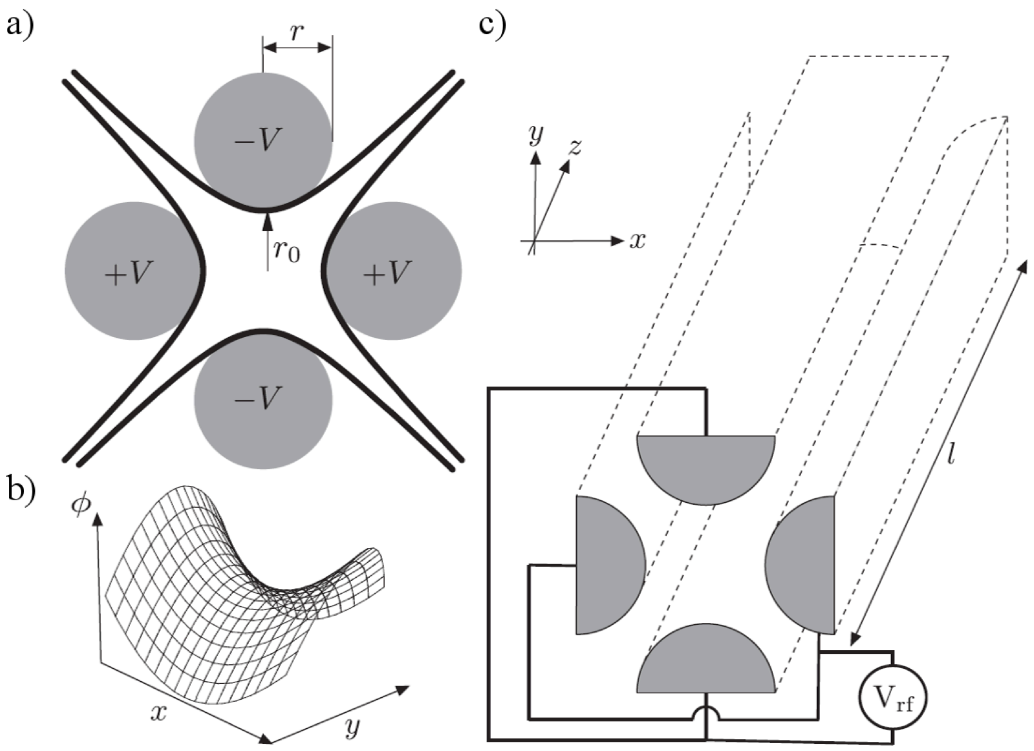

Figure 4.4. Operating principle of an radiofrequency quadrupole ion guide. a) Cross section of four circular RFQ rods approximating the equipotential lines of an ideal quadrupole field. b) Shape of the corresponding electric potential in the radial plane. c) Geometry of an RFQ ion guide with pairwise alternating potentials for ion confinement in all radial directions. Adapted from [383], ©2012, with permission from Elsevier.

395]. All RFQ coolers & bunchers rely on the combination of two basic principles: (1) three-dimensional ion confinement in a linear Paul trap [351] and (2) the use of a buffer gas to sympathetically cool injected ions.

Since this concept will be relevant repeatedly throughout this chapter, it is worth to introduce the idea of ion trapping in radio-frequency fields. Consider an electrode configuration with four parallel circular rods at even spacing and a common distance r_0 to the symmetry axis, as depicted in Fig. 4.4 a). With neighbouring rods biased to static voltages of identical magnitude V but opposite polarity, the configuration approximates a (saddle-shaped) quadrupolar potential in the radial plane [see Fig. 4.4 b)]. An ion beam travelling along the symmetry axis of this system is focussed in one radial direction but diverges along the perpendicular dimension and would eventually get lost against the quadrupole rods. This situation can be prevented by periodically inverting the polarity of the applied voltages at an appropriate frequency. Such an oscillating driving field creates an effective harmonic potential (also called "pseudo-potential") in the radial plane and results in a net confinement in all radial directions. A device of this kind, sketched in Fig. 4.4 c), permits efficient ion transport and is referred to as a radiofrequency quadrupole ion guide [396]. Assuming a sinusoidal drive amplitude of the form $V(t) = V_{\mathrm{RF}} \sin(\omega_{\mathrm{RF}} t)$ and solving the equations of motion for an ion of charge $z \cdot e$ and mass m, one finds [351] that radial ion confinement may

only be achieved if the stability parameter $q = \frac{2zeV_{\text{RF}}}{m\omega_{\text{RF}}r_0^2}$ lies in the range $0 < q < q_{\text{max}} = 0.92$. To ensure optimal confinement, the frequency and amplitude of the RF drive therefore have to be tuned to the given ion mass.

Starting from an ion guide, three-dimensional ion trapping is a straightforward extension. It only requires the superposition of a confining electrostatic potential along the symmetry axis, for example created by repelling endcap electrodes on either end of the ion guide, or by axially segmenting the RFQ rods and applying suitable DC voltage offsets. This type of device is the aforementioned linear Paul trap [351], as first conceived by nobel laureate Wolfgang Paul[1].

A light buffer gas injected into a linear Paul trap sympathetically cools stored ions, causing them to accumulate in the trap's potential minimum. The result is in an efficient setup for cooling and bunching ion beams [397]. When too heavy buffer-gas atoms are used, ion-atom collisions in high-field regions can transfer significant amounts of energy from the RF field into the ion motion, resulting in a net heating effect [398–400]. This so-called RF heating is minimized by using a buffer gas of low-mass atoms. It is further advisable to use inert gases to prevent ion loss through chemical reactions.Therefore, helium is usually the buffer gas of choice for TITAN's and other coolers & bunchers, and was also used for the gallium measurement campaign reported on in this thesis.

TITAN's RFQ cooler & buncher [401] is a linear Paul trap comprised of four 70 cm-long quadrupole rods, each lengthwise split into 24 segments to allow the application of axial drag fields. The electrode structure of the device is schematically depicted in Fig. 4.5 a) and c). In contrast to RFQ coolers and bunchers at other RIB facilities [384, 386, 391, 392], the radial confinement in TITAN's cooler & buncher is provided by a digital, i.e. square-wave, RF drive. The square-wave driver offers advantages over conventional sinusoidal RF generators since it provides a more than 1.5 times deeper pseudo-potential at a given RF amplitude and can deliver high RF amplitudes ($V_{\text{pp}} \leq 800$ V) over a wide range of frequencies ($\nu_{\text{RF}} \approx 200$–$1200$ kHz) [383]. This high bandwidth enables efficient trapping of ions over an extremely wide range of masses ($A \approx 4 - 220$).

The RFQ cooler & buncher is floated to a high voltage carefully adjusted such that the incoming ions enter the system with kinetic energies of only a few 10 eV. After a few milliseconds of buffer gas cooling, the ions accumulate in the potential minimum near the trap exit. To eject them from the trap, the DC voltages of electrode segments 22 and 24 are switched to form an extraction gradient [red dashed line in Fig. 4.5 b)]. Helium gas at pressures of the order of 1×10^{-2} mbar generates cold ion bunches with energy spreads of $\approx$5 eV which can be extracted at rates as high as 100 Hz. The extraction rate used in a specific experiment is dictated by the requirements of the used measurement trap and the half-lives of the species of interest.

After ejection from the RFQ cooler & buncher, the ion bunch is accelerated into a pulsed drift tube initially kept at a high voltage V_{DT}, typically a few kV below V_{TRFC}. Once the ions are centred in the drift tube, it is pulsed to earth ground, thereby removing potential energy

[1] Regrettably, the author cannot claim any family relations with this pioneer in the field of ion trapping – and has certainly never done so to test the gullibility of his colleagues.

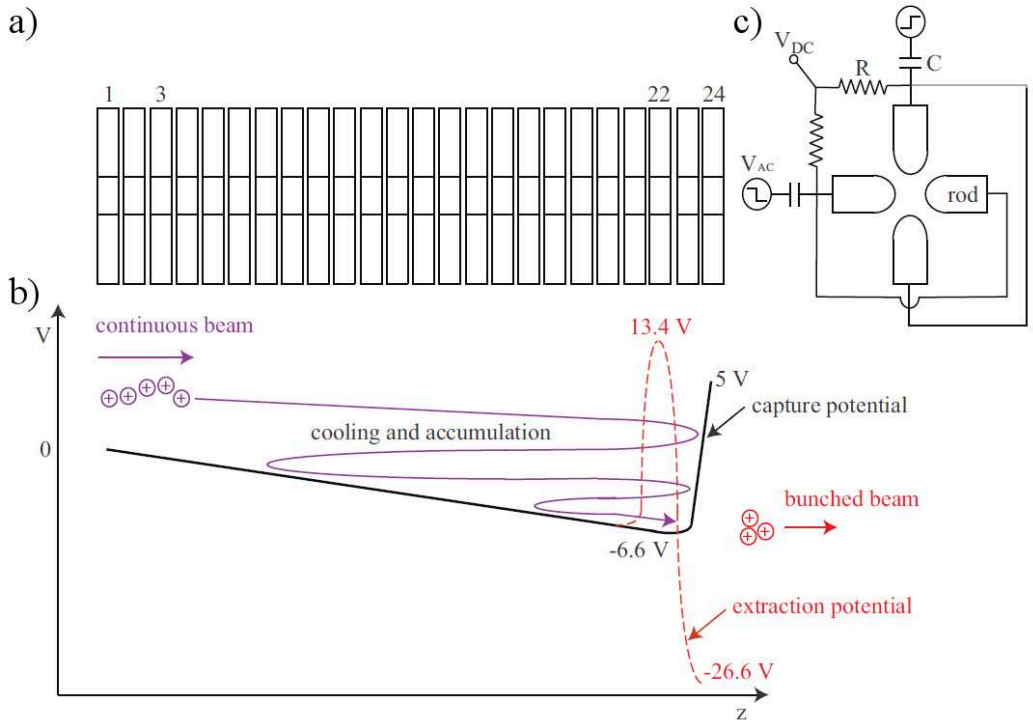

Figure 4.5. Schematic of the TITAN RFQ cooler & buncher depicting the axial segmentation of the RFQ rods (a) along with typical axial potentials during the ion cooling and ejection phases (b). The radial cross section and the biasing scheme of the quadrupole rods is shown in (c). The injected ions are buffer-gas cooled, accumulate in the potential minimum, and are eventually ejected as cold ion bunches suited for capture in downstream ion traps. Adapted from [383], ©2012, with permission from Elsevier.

from the ions. In this way, the voltage difference between the RFQ cooler & buncher and the initial drift tube bias, $V_{\mathrm{TRFC}} - V_{\mathrm{DT}}$, defines the final beam energy for transport to one of other ion traps at TITAN. The MR-TOF-MS measurements reported in chapter 5 were performed with a 50 Hz extraction cycle and a transport energy of ≈ 1.3 keV.

4.2.2 Electron beam ion trap

TITAN's array of ion traps includes an electron beam ion trap [59] for on-line charge breeding of radioactive ions. The primary motivations for charge breeding at TITAN are high-precision mass measurements with highly charged ions (HCI) and in-trap decay spectroscopy. Before discussing the advantages and challenges of on-line charge breeding for PTMS, I will introduce the device and its basic operating principles.

The TITAN EBIT [59] was designed and built [402] at the Max-Planck-Institute for Nuclear Physics (MPIK) in Heidelberg. After installation at TITAN, it was commissioned with first radioactive ion beams in 2008. A simplified schematic of the device is shown in Fig. 4.6. Two superconducting coils in a Helmholtz-like configuration create a strong magnetic field (up to 6 T) that confines ions radially. Voltages applied to a set of drift tubes

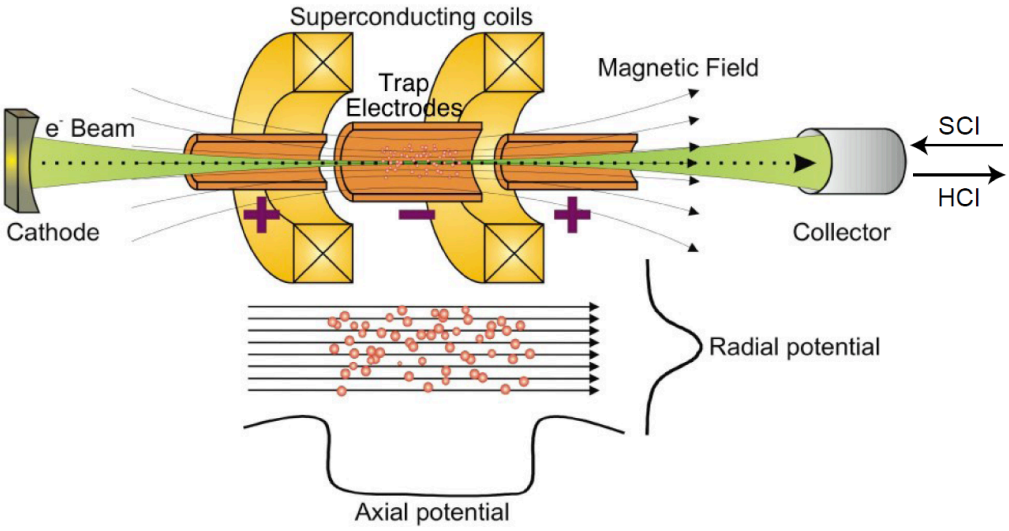

Figure 4.6. Simplified schematic of TITAN EBIT. For clarity, the superconducting coils and the cylindrical trap electrodes confining the ions are shown in a cross sectional view. A magnetically-compressed, energetic electron beam successively raises the charge states of trapped ions via electron-impact ionization. Figure from [310].

centred between the magnet coils form an electrostatic potential which traps the ions axially. By overlapping the trapped ion cloud with an electron beam with currents of the order of $100\,\mathrm{mA}$ [403] and energies of up to $62\,\mathrm{keV}$ [404], the ion charge states are successively raised via electron-impact ionization. To prevent electron-ion recombination via charge exchange with residual gas, the trap electrodes are cooled to cryogenic temperatures, resulting in pressures below $1 \times 10^{-11}\,\mathrm{mbar}$ in the trapping region.

The electron beam is generated by a hot-cathode electron gun, electrostatically accelerated through the trap electrodes and finally dumped onto a hollow electron collector on the opposite end of the trap. The magnetic field gradient between the electron gun and the magnet coils strongly compresses the entering electron beam, thereby increasing the electron current density at the trap centre by several orders of magnitude. The high electron current density in the trapping region ($\approx 1 \times 10^4\,\mathrm{A/cm^2}$) boosts the ionization rate and enables charge breeding times of only a few $10\,\mathrm{ms}$ [59] – a necessity for charge breeding of short-lived radioisotopes ($t_{1/2} < 100\,\mathrm{ms}$). Additionally, it creates a strong space-charge potential that enhances the radial ion confinement. To further optimize the charge breeding efficiency, the EBIT's electron gun is currently being upgraded for higher beam currents and improved beam compression.

Precision mass measurements require the preparation of ions in a specific and known charge state. However, the charge breeding process inherently populates a range of charge states. By appropriate choice of the charge breeding time, the fraction of ions in a given charge state can be maximized [382]. Upon transport to the MPET mass spectrometer, ions with the charge state of interest are isolated by A/q-selection with a Bradbury-Nielsen ion gate [405].

The central drift tube of TITAN EBIT is azimuthally segmented, thereby providing optical access to the ion trapping region through a set of 25 µm-thin beryllium windows. This enables the collection of X- and γ-rays transversally-emitted from trapped, charge-bred ions. This feature has been exploited for in-trap decay spectroscopy campaigns [406–408] at TITAN. Such measurements benefit from a strong suppression of background from emitted β-particles [409] because the axial magnetic field guides charged particles onto spiralling trajectories around the field lines and causes them to leave the trap axially, hence preventing β-particles from reaching the radiation detectors.

A recent proof-of-principle experiment [410] has demonstrated that TITAN EBIT can further be used to create high-quality beams composed of recoil ions from β-decays of trapped HCI. The efficient recapture of recoil ions is facilitated by the strong confinement provided by the electron space charge and the high magnetic field. Assuming a beam of the progenitor nuclide is available, this technique can give access to isotopes for which direct production is hampered at an ISOL facility, for example by target chemistry restrictions (see section 3.1).

The benefits of charge breeding

Since the ion cyclotron frequency increases linearly with the charge state, charge breeding has the potential to increase the achievable mass precision in PTMS. For instance, the relative statistical uncertainty of a mass measurement performed with the TOF-ICR technique[2] (see section 3.3.3) scales as

$$\frac{\delta m}{m} \propto \frac{m}{qBT_{\text{exc}}\sqrt{N_{\text{ions}}}}, \tag{4.1}$$

where m is the ion mass, B is the magnetic field strength, T_{RF} is the RF excitation time and N_{ions} is the number of detected ions. The field strength of superconducting magnets for precision measurements is technically limited to $\lesssim$10 T, the excitation time is constrained by the half-life of the species of interest and the measurement statistics ($\sqrt{N_{\text{ions}}}$) are often restricted by low production yields. The most practical path to higher mass precision is therefore to raise the ions' charge before the mass measurement [58]. TITAN has pursued this avenue and successfully performed high-precision mass measurements of short-lived HCI [61]. On-line charge breeding is especially beneficial for tests of fundamental symmetries which demand mass precisions of $\frac{\delta m}{m} \leq 1 \times 10^{-8}$ [2].

For many cases in nuclear astrophysics and nuclear structure, the required mass uncertainties of $1 \times 10^{-6} > \frac{\delta m}{m} > 1 \times 10^{-8}$ [2] are readily achieved with SCI. In these instances, charge breeding may alternatively shorten the measurement time, since it allows to reach a given precision level with quadratically lower statistics. Faster measurements due to charge breeding not only shorten the required radioactive beam time. They can further reduce the impact of system instabilities such as power supply drifts due to day-night-temperature

[2]Charged-particle simulations indicate [57] that similar gains in precision and resolving power can be expected when using HCI with the more recent PI-ICR technique [318]. The latter is currently being implemented for TITAN's precision Penning trap MPET.

variation, thus resulting in smaller systematic uncertainties and a potentially higher mass accuracy.

The use of HCI further increases the resolving power of PTMS [63, 382]. Again considering the TOF-ICR technique, the mass resolving power obeys the scaling

$$R = \frac{\nu_c}{\Delta\nu_c} \propto \frac{qBT_{\mathrm{RF}}}{m}, \tag{4.2}$$

where $\Delta\nu_c$ denotes the FWHM of the central lobe of the TOF resonance. As seen from Eqn. 4.2, the only practical path to higher resolution with singly charged ions is longer RF excitation times. However, for short-lived isotopes, T_{RF} is often severely limited since decay losses degrade the quality of the TOF resonance, and thus the achievable resolving power. Charge breeding therefore offers an alternative path to higher resolution and thereby provides a powerful tool to resolve low-lying nuclear isomers with half-lives $t_{1/2} \geq 50\,\mathrm{ms}$. This was demonstrated in a TITAN mass measurement of ^{78}Rb [63], where charge breeding to $q = 10\,e$ and an excitation time of $T_{\mathrm{RF}} = 197\,\mathrm{ms}$ enabled the separation of a $110\,\mathrm{keV}$ isomer from the corresponding ground state ($R \approx 650\,000$).

Moreover, charge breeding can lend a way to isobarically purify radioactive ion beams via so-called threshold charge breeding [382]. This technique was first demonstrated by the separation of $^{71}\mathrm{Ga}^{21+}$ and $^{71}\mathrm{Ge}^{22+}$ ions in a Q-value measurement at TITAN [411]. The Ga and Ge ions were predominantly bred into neon-like charge states by adjusting the electron beam energy to $2\,\mathrm{keV}$, i.e. just below the respective ionization-energy thresholds for breeding beyond the atomic shell closure, $E_{\mathrm{IP}}(\mathrm{Ga}^{21+}) = 2.01\,\mathrm{keV}$ and $E_{\mathrm{IP}}(\mathrm{Ge}^{22+}) = 2.18\,\mathrm{keV}$. Due to their different charges, the two isobars were then easily separated during transport to the MPET.

Challenges of on-line charge breeding

Besides the aforementioned benefits, on-line charge breeding of rare isotopes introduces a number of practical challenges.

The above discussion has not taken efficiency considerations into account. However, charge breeding in an EBIT is accompanied by non-negligible losses of the available amount of the ions of interest. Primary causes for a reduced efficiency as compared to a mass measurement with singly charged ions are additional decay losses and the population of multiple charge states inherent to the charge breeding process. Further efficiency losses occur in the injection into and extraction from the EBIT as well as the transport and capture into the MPET. If the reduced system efficiency cannot be compensated by increasing the rare isotope beam intensity (as is often the case for low-yield isotopes), the lower measurement statistics mitigate the effective precision gain from charge breeding. In practice, it is therefore necessary to assess the expected benefits from charge breeding on a case-by-case basis in the experiment planning stage. The detailed treatment presented in [62] enables a quantitative evaluation of the expected precision gain from charge breeding.

An additional complication resulting from charge breeding is an increased probability for charge exchange with residual gas in the MPET. These reactions cause losses of the

charge state of interest and deteriorate the quality of TOF resonances. To prevent this, the MPET has recently been upgraded to a cryogenic trap for improved vacuum conditions.

In addition to efficiency losses, charge breeding reduces the ion beam quality.Whereas singly charged ion bunches from the RFQ cooler & buncher typically exhibit longitudinal energy spreads of $\approx$5 eV [412], measurements of $^{85}Rb^{13+}$ ions extracted from the EBIT have shown longitudinal energy spreads of $\Delta E(\mathrm{FWHM}) \approx 20\,\mathrm{eV}/q$ [64]. The charge breeding process also is accompanied by an increase in the transverse emittance. The increased longitudinal energy spread as well as the larger transverse emittance reduce the capture efficiency into the MPET and enlarge the volume the HCI occupy inside the trap. As a result they are subjected to larger magnetic field inhomogeneity, increasing systematic frequency shifts. To mitigate these issues and preserve a high mass accuracy, the phase space of the HCI needs to be compressed.

4.2.3 Cooler Penning trap

Electron cooling in a Penning trap has been proposed [65] as a promising way to counteract the beam quality losses due to charge breeding in TITAN EBIT. To explore the prospects of this technique, we have performed detailed studies of electron cooling in a designated cooler Penning trap (CPET). Details on the electron cooling process, the CPET off-line test setup and the results of these tests are reported in chapter 6.

4.2.4 Measurement Penning trap

The MPET is a Penning trap mass spectrometer for precision measurements of short-lived radioisotopes. It is TITAN's tool of choice for science cases that require mass precisions of $\frac{\delta m}{m} < 1 \times 10^{-7}$. The Penning trap's hyperbolical electrode structure is housed inside a 3.7 T superconducting magnet with a highly homogeneous field throughout the trapping region (with manufacture specifications of $\frac{\Delta B_z}{B} \leq 1 \times 10^{-9}$ throughout a cylindrical volume of 2 cm-length and 1 cm diameter [60]). The Penning trap is framed by ion optics for injection and extraction. A Lorentz steerer [316] enables direct and precise injection of ions into an initial magnetron orbit and circumvents the need to prepare the initial radial ion motion with a typically several 10 ms-long dipole RF excitations. This makes the MPET capable of rapid Penning trap mass spectrometry (PTMS), as evidenced by the first Penning trap mass measurement of the halo nucleus ^{11}Li [320] with a half-life of only 8.8 ms. Since the trap electrodes are operated at low voltages (≤ 36 V) with respect to earth ground, the injection optics further include a pulsed drift tube to lower the energy of the incoming ion bunches from typical transport energies of $\approx$ 2 keV to a level suitable for dynamic capture into the trap (ideally no more than a few eV inside the MPET). A schematic and a photograph of the original trap structure are shown in Fig. 4.7. Azimuthal segmentation of the correction electrodes enables RF excitation of the radial ion motions. A Chevron-type micro-channel plate (MCP) detector [413] outside the cryomagnet is used to count extracted ions and record their time-of-flight. MCP detectors enable single-ion detection with sub-ns time resolution.

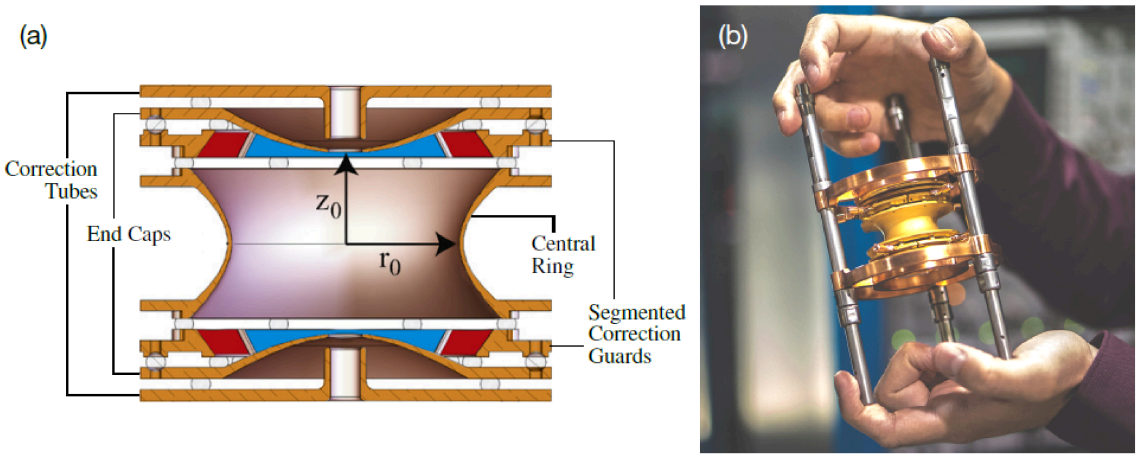

Figure 4.7. TITAN's original measurement Penning trap. a) Cross-sectional schematic of the trap electrode structure. b) Photograph of the trap electrodes and the surrounding support structure. Figure from [56].

Their light-ion detection efficiency at impact energies of a few keV typically ranges from 50% to 70% [414], and generally increases with the ions' impact velocity [415] and thus (under electrostatic acceleration) with the charge state.

So far, all Penning trap measurements at TITAN have been performed with a room-temperature trap (Fig. 4.7) and using the TOF-ICR technique [312] (see section 3.3.3). This has enabled mass measurements at ppb-level accuracy [60, 309].

With the original room-temperature Penning trap, charge-exchange effects limited the excitation times of HCI to a few 100 ms. To achieve the required vacuum levels ($p \leq 1 \times 10^{-11}$ mbar [56]) for longer measurements with HCI, the trap has recently been upgraded to a cryogenic Penning trap [56]. To enable future measurements with the PI-ICR technique [324] (see section 3.3.3), the upgrade also included modifications of the extraction optics and the installation of a larger, position-sensitive MCP [416]. The new precision trap is currently being commissioned and first mass measurements are planned for 2023. The combination of HCI with the more powerful PI-ICR technique is expected to yield relative mass uncertainties below $\frac{\delta m}{m} \approx 1 \times 10^{-9}$ [57], thereby opening up new science opportunities for tests of fundamental symmetries at TITAN.

4.2.5 Multiple-reflection time-of-flight mass spectrometer

The most recent addition to the TITAN trap array is a multiple-reflection time-of-flight mass spectrometer (MR-TOF-MS) and isobar separator [54]. The MR-TOF-MS was designed and built at Justus-Liebig-University Gießen [54, 344] and has been fully operational at TITAN since 2017 [339, 417]. Primarily installed as a beam purifier for the other ion traps at TITAN, it has quickly proven valuable as a stand-alone mass spectrometer that complements the characteristics of the MPET.

While the MPET remains the tool of choice for high-precision mass measurements at TI-

TAN, the MR-TOF-MS has demonstrated a precision level suitable for many science cases within nuclear structure and astrophysics. Moreover, due to fast measurement cycles and its high sensitivity (see below for details), the MR-TOF-MS has extended the reach of mass measurements at TITAN towards more exotic isotopes with shorter half-lives and lower production yields. This capability was first showcased in a direct comparison with the MPET in on-line mass measurements of neutron-rich titanium isotopes [19]. Along this isotopic chain, the MR-TOF-MS was abled to reach two nuclides farther from stability than the Penning trap mass spectrometer.

More comprehensively, the TITAN MR-TOF-MS is characterized by the following set of performance metrics:

- **Broadband measurement:** The large mass acceptance enables simultaneous measurement of all species contained in a cocktail beam. This makes the device a powerful tool for beam diagnostics and optimization of rare isotope yields [340].
- **Rapid measurement:** With typical measurement cycles of 10–100 Hz, isotopes with half-lives on the order of 10 ms can be targeted.
- **Sensitivity:** Efficient ion transport and single-ion detection result in an overall system efficiency of $\approx 30\%$ [339]. In contrast to TOF-ICR-MS, MR-TOF-MS is a non-scanning technique and enables precision mass measurements with less than 50 detected ions, as demonstrated in the ^{60}Ga measurement reported in chapter 5.
- **High resolution:** An optimized ion optical design combined with stabilization against short-term fluctuations of the mirror voltages and correction of long-term drifts with time-resolved mass calibrations [350] enable resolving powers of up to $R \approx 400\,000$ [339].
- **High accuracy and precision:** The instrument enables mass measurements with relative mass uncertainties of the order of $\frac{\delta m}{m} \approx 1 \times 10^{-7}$ [339].
- **Background-handling capability:** The device can handle signal-to-background ratios of 1:10^4 [339]. Using the mass-selective re-trapping technique [357] to deploy the MR-TOF-MS as its own isobar separator can provide up 4 additional orders of magnitude in dynamic range [339].

A cross-sectional view of the device is shown in Fig. 4.8. The MR-TOF-MS is comprised of a buffer-gas-filled RFQ transport system ($p \sim 10^{-2}$ mbar) and a TOF analyzer under high vacuum ($p \sim 10^{-7}$ mbar).

RFQ transport system

The RFQ transport system uses helium gas-filled RFQ ion guides [252] (see section 4.2.1) for efficient ion transfer at low energies ($\sim$ 1 eV). Each ion guide is composed of four resistive plastic rods ($\approx 5\,\Omega\,\mathrm{mm}^{-1}$) [339], allowing the creation of linear axial drag fields

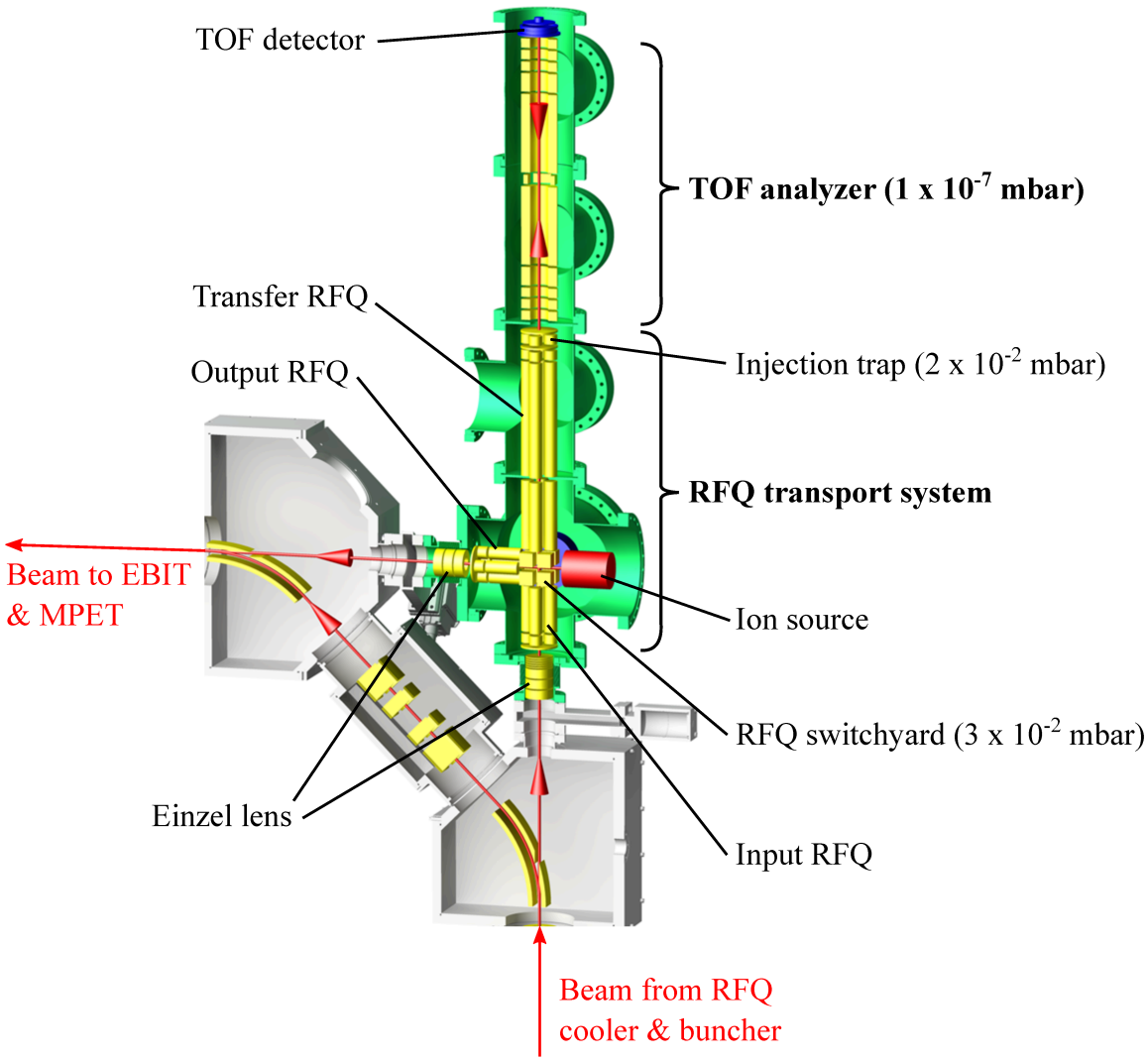

Figure 4.8. Cross-sectional schematic of TITAN's MR-TOF-MS. Ion bunches from TITAN's cooler and buncher are guided through a helium-gas-filled RFQ transport section and buffer-gas cooled in a linear injection Paul trap. After mass separation in the TOF analyzer, they are either analyzed on the TOF detector or isobarically purified via re-capture in the injection trap. Purified bunches are either re-injected into the TOF analyzer for mass measurement, or transported to one of the other ion traps at TITAN. Adapted from [344].

by applying DC voltages to the rod endings. The DC voltages are mixed with sinusoidal RF signals with amplitudes of several 100 V and frequencies of 1–1.6 MHz to form transversally confining pseudopotentials with depths of $\approx$ 5–20 eV [339]. Biased apertures between the different ion guides allow the accumulation and storage of ions in various places. An RFQ switchyard [336] at the centre of the transport system can transport ions between any of its six ports and enables the merging of injected ion bunches with stable calibrant ions from a surface ion source (Heatwave #101139). The entire transport system is floated at 1.3 kV above earth ground to match the transport energy of incoming ions from the TITAN RFQ cooler & buncher.

Ion bunches from the RFQ cooler & buncher enter the input RFQ through a pulsed aperture which is used as an ion gate. Switching the aperture potential between an open and a reflective setting only allows ions in a specific mass-to-charge range to enter the system. The selected ions accumulate inside the input RFQ and are then transported through the switchyard and the transfer RFQ into an injection trap system. The latter consists of two linear Paul traps: a pre-trap for ion accumulation and initial cooling, and an injection trap for final ion bunch preparation and injection into the TOF analyzer. For ion injection, a strong accelerating gradient ($\approx 80\,\mathrm{V\,mm^{-1}}$) [339] is formed inside the injection trap by rapidly switching the potentials of the planar end-cap electrodes. The strong extraction gradient reduces the ions' turn-around times in the injection trap, thereby minimizing the initial time spread of ion samples in the TOF analyzer. The temporal bunch compression comes at the price of a large energy spread of ≈ 17 eV [339], which has to be compensated by ion mirrors with a high isochronicity (see section 3.4.1).

TOF analyzer

The TOF analyzer [344] is a scaled version of the MR-TOF-MS [252] installed at the FRS Ion Catcher [347] at GSI. A cross-sectional view of the TOF analyzer is shown in Fig. 4.9 a). It consists of a stack of concentric stainless steel electrodes forming two opposing, gridless ion mirrors [358] connected by a grounded drift tube. The schematic also displays the injection Paul trap and the set of ion optics used to steer and focus ions onto stable trajectories inside the TOF analyzer. A differential pumping stage with two narrow apertures between the injection trap and the entrance-side mirror isolates the analyzer vacuum chamber from the buffer-gas-filled sections. The resulting vacuum level of $\approx 1 \times 10^{-7}$ mbar reduces the likelihood of collisional ion losses and translates into transmission efficiencies of $\approx 60\%$ after 350 revolutions inside the TOF analyzer [339].

A pulsed quadrupole steerer at the centre of the drift tube can optionally be used as a mass range selector (MRS) [252]. By applying steering voltages during well-defined subperiods of the first 30–50 revolutions inside the TOF analyzer, it gradually deflects non-isobaric contaminants onto unstable trajectories, eventually causing them to get lost on the baffles inside the drift tube [see Fig. 4.9 a)]. The steering voltages are toggled on and off in phase with the ion motion such that only non-isobaric contaminants are deflected, while the ions of interest remain unaffected [418]. The MRS can greatly simplify the identification of TOF peaks as it ensures that all ions in a spectrum have completed the same number of revolutions.

Mass measurement operation

The different mirror potentials applied throughout a mass measurement cycle are depicted in Fig. 4.9 b). The inner-most mirror electrodes are kept at negative voltages to focus the ion samples through the baffle apertures.

At the beginning of an analysis cycle, the potential of the entrance-mirror end cap is pulsed to ground, allowing ions to enter the TOF analyzer. On the first pass, the MRS

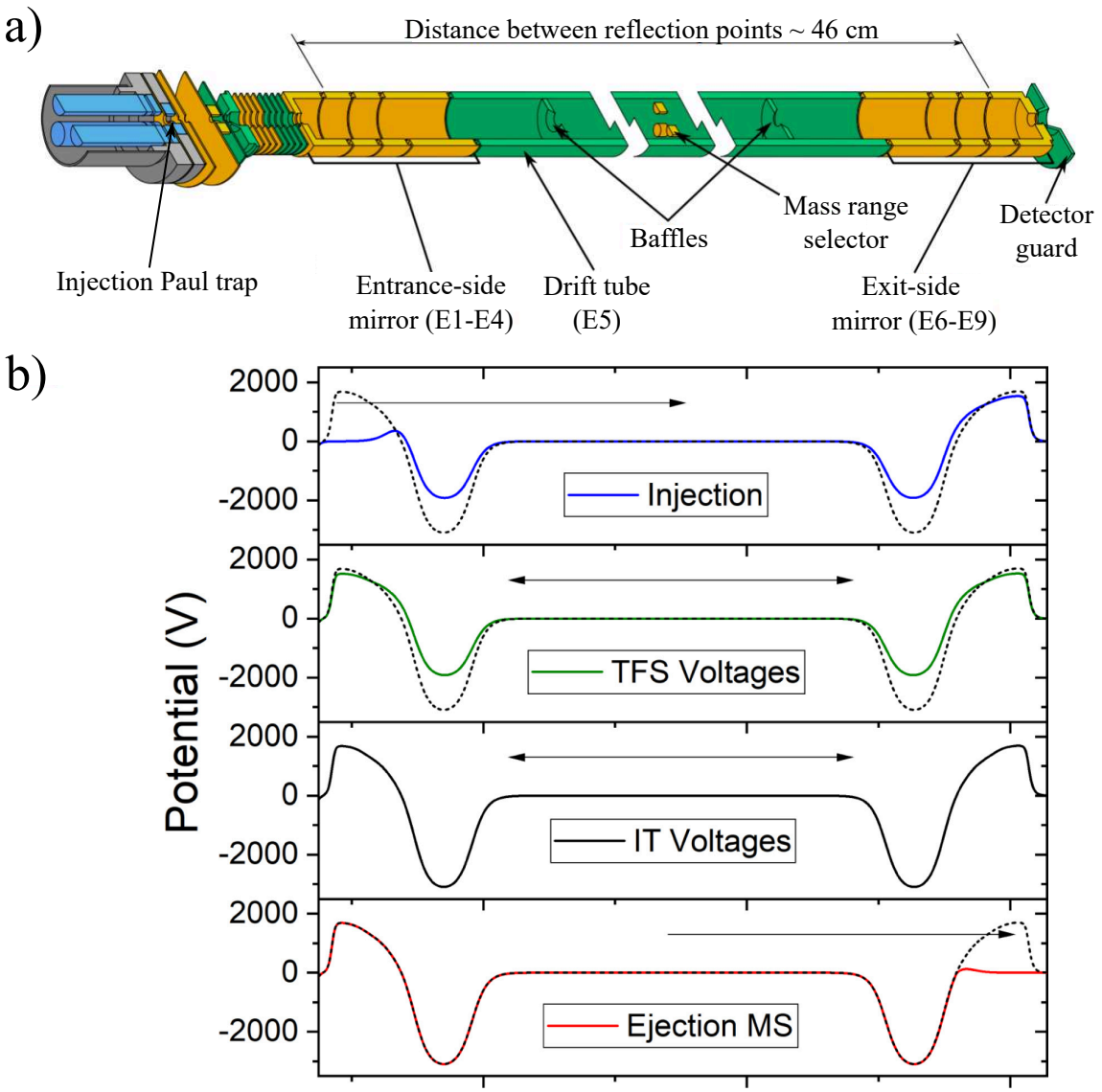

Figure 4.9. a) Cross-sectional view of the of the MR-TOF-MS injection trap system and the time-of-flight analyzer. Adapted from [359]. b) Respective on-axis potentials inside the TOF analyzer during the ion injection, the initial time-focus-shift (TFS) turn, isochronous turns (IT) and the ejection to the TOF detector. The black arrows indicate the direction of ion travel and the mean ion energy of 1.3 keV. Reprinted from [339], ©2021, with permission from Elsevier.

electrodes are used to align the ion trajectories with the optical axis of the TOF analyzer.

During the first two reflections, a dynamic time-focus shift (TFS) [354] is performed by applying special mirror voltages which define TOF foci both on the detector and near the injection trap.

Subsequently, the potentials of both mirrors are switched into an isochronous state and the ions are gradually mass separated by many revolutions inside the analyzer. These revolutions will subsequently be referred to as isochronous turns (IT). Due to the isochronous mirror potentials, the time foci defined by the dynamic TFS remain preserved irrespective

of the number of reflections. Thus, the experimenter is free to change between different IT numbers without the need to re-tune the instrument for optimal resolving power [347].

After a pre-defined number of IT, the endcap voltage of the exit-side mirror is pulsed to ground to eject the ions towards the detector. Due to its high single-ion detection efficiencies of $\approx$ 60–80% [339], a MagneTOF detector [419] placed behind the exit-side ion mirror is used as the sub-nanosecond TOF detector. The ion arrival times on the detector are recorded using a time-to-digital converter (TDC) [420] typically operated with a timing resolution of $1.6\,\mathrm{ns}$.

Stable mirror voltages are an essential prerequisite to achieve high mass resolving powers with an MR-TOF-MS. In order to preserve the ion energies throughout a measurement cycle, the mirror voltages have to be switched rapidly (within $\sim 100\,\mathrm{ns}$), with well-defined timings and minimal electronic ringing. These technical demands are met [344] by using custom solid-state HV switches [421]. The HV inputs for the switches are derived from low-noise precision power supplies [422]. Since the ions sample the IT voltages up to several 100 times, the respective power supply outputs are additionally stabilized against sub-second-scale fluctuations with passive low-pass filters [344].

Long-term drifts due to temperature-related changes of the mirror voltages and the analyzer length can be compensated with time-resolved mass calibrations [350] in the dedicated Mass Acquisition software (MAc) [423]. In this approach, the calibration parameter b in Eqn. 3.36 is periodically re-determined using an isobaric calibrant peak (see the description of the data analysis procedure in section 5.2 for more details). Combined, these measures prevent peak broadening and enable high mass resolving powers up to $R \approx 400\,000$ [339].

Isobar separation via mass-selective re-trapping

Experiments with exotic nuclides at ISOL facilities are often complicated by a large amount of isobaric beam contamination. To address this challenge within the tight spatial bounds of the TITAN platform, a novel technique referred to as mass-selective retrapping [357] was developed for the TITAN MR-TOF-MS.

For isobar separation, the ions are first mass separated in the TOF analyzer and subsequently selectively re-captured in the injection trap. The mass separation cycle is identical to that of a mass measurement [see Fig. 4.9 b)], except that the ions are finally ejected towards the injection trap instead of the detector. In the injection trap, initially the same potential gradient already used for ion injection is applied. Once the ions of interest are near the trap centre, they are selectively re-captured by switching the potential gradient to a shallow trapping configuration. The pre-determined timing for the switching of the injection trap potential, referred to as the re-trapping time, has to be well adjusted to within a few $10\,\mathrm{ns}$ for successful re-capture [424]. Ions of a different mass that have acquired a sufficient TOF separation from the ions of interest to be outside the injection trap region at re-trapping time are obviously not re-captured and fly back into the TOF analyzer. There, they are easily discarded via deflection with the MRS.

Even closer lying contaminants that are in the injection trap region at the re-trapping

time can potentially be suppressed. The mechanism underlying the suppression of these contaminants is less trivial and requires a detailed explanation. Since the trap depth U_r for re-trapping is typically chosen to be in the range of 3–15 eV, only ions within a narrow range of energies are re-captured. The high mass selectivity of the re-trapping method relies on the fact that the switching operation changes the energy of any ion located in the injection trap region except those at the trap centre. This concept is visualized in Fig. 4.10. After a period of mass separation in the TOF analyzer, the entrance-side mirror is opened to guide ions of a common charge q back towards the injection trap. There, they are decelerated by the same potential gradient that was initially used to accelerate them into the TOF analyzer. As a result, they come to rest when returning to their starting positions near the trap centre and are then reflected back towards the TOF analyzer. The re-trapping time is chosen such that the retarding gradient is switched to the re-trapping configuration just when a species of interest with a mass m_1 reaches the trap centre. At this time, contaminant ions with a slightly heavier mass $m_2 > m_1$ are still located in the end-cap region. Therefore, they gain energy from the switching operation and are elevated above the energy acceptance of the trap, causing them to get lost. At the same point in time, ions with a slightly lower mass $m_3 < m_1$ (not shown in Fig. 4.10) have already been reflected by the potential gradient and are leaving the trap again. The switching operation also raises their energy above the acceptance of the trap, likewise causing them to get discarded. Only ions whose kinetic energy K at the re-trapping time satisfies the condition $K < qU_r$ are re-trapped. The condition for re-trapping is only fulfilled for ions within a narrow mass range.

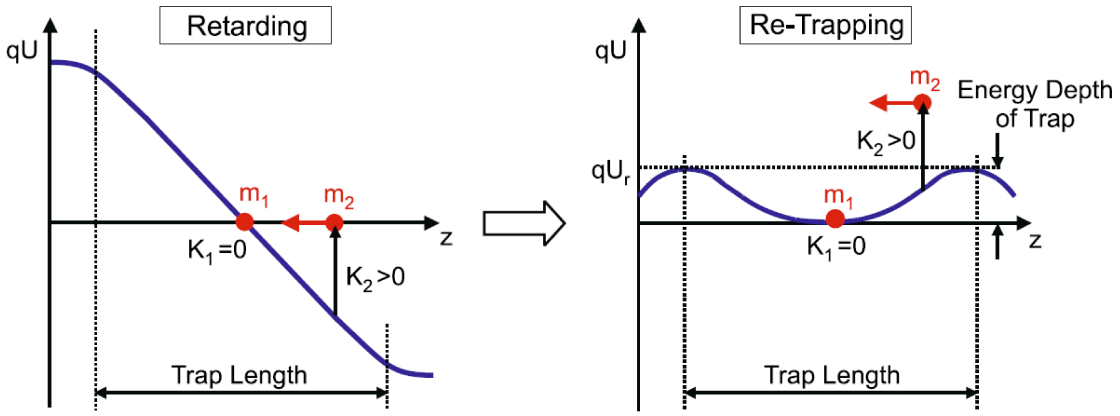

Figure 4.10. Principle of isobar separation with the mass-selective re-trapping technique. After TOF separation, ions of charge q are guided back towards the injection trap. When the ions of interest with mass m_1 reach their turning point near the trap centre the axial potential is switched from a retarding gradient (left) to a shallow trapping configuration (right). Heavier (or lighter) ions of mass m_2 gain energy in the switching operation, causing them to escape capture into the shallow trap. Only ions whose kinetic energy at the switching time (K) is smaller than the energy depth of the trap (qU_r) are re-trapped. Reprinted with permission from [357].

The width of the re-captured mass window can be adjusted by varying either the injection trap depth or the number of IT used for the mass separation prior to re-trapping. Since high IT numbers and very shallow trap depths result in increased losses of the ions of interest, one faces a trade off between the achievable mass separation power and the re-capture efficiency. At a trap depth of 3.2 V and after 320 IT for mass separation, the re-trapping technique has enabled mass separation powers up to $R \approx 100\,000$ with a re-trapping efficiency of $\approx$ 15% [339]. At greater trap depths, separation powers up to $40\,000$ with re-capture efficiencies of $\approx 70\%$ can be realized.

After mass-selective re-trapping, purified ion samples are re-cooled and then either re-injected into the TOF analyzer for mass measurement, or guided back through the RFQ transport section and passed on to the other ion traps at TITAN. The re-trapping technique has enabled TITAN to perform mass measurements with extreme signal-to-background ratios, as exemplified by the first direct mass measurement of ^{60}Ga [425] discussed in chapter 5.

Mass measurement operation with prior isobar separation

Depending on the specific requirements of a given experiment, the MR-TOF-MS can be operated at repetition rates of 10–100 Hz. Most measurements, including the gallium mass measurements presented in chapter 5, have been performed with a repetition rate of 50 Hz. To obtain a usable spectrum, the TOF histograms recorded in single experimental cycles are added up until sufficient statistics are reached.

To enable quick changes between measurement cycles with and without initial isobar separation, each MR-TOF-MS cycle is divided into two subcycles of identical length. The first is dedicated to optional isobar separation by mass-selective re-trapping and the second is used for the mass measurement. The device is then operated in either of the two following modes [339]:

1. Regular mass measurement: The ions are simply kept inside the injection trap during the first half cycle. In the second half cycle, they are injected into the TOF analyzer for mass measurement following the procedure described above.

2. Mass measurement with prior isobar separation: With re-trapping activated, the ions are already injected during the first half cycle. Once a sufficient TOF separation has been acquired, they are mass-selectively re-trapped and re-cooled in the injection trap. The second half cycle then proceeds identical to that in regular mass measurement operation.

Chapter 5

Mass measurements of neutron-deficient gallium isotopes

This chapter discusses the mass measurements of $^{60-63}$Ga performed with TITAN's MR-TOF-MS. The results of these measurement have been published in [425]. Specifics of the measurements and the data analysis procedure are described in sections 5.1 and 5.2, respectively. Section 5.3 reports the obtained mass values and discusses them in the context of the pre-existing data. The implications of the obtained mass data for the location of the proton drip line in the gallium chain, the $T = 1$ IMME in the *pf* shell and the *rp*-process in X-ray bursts are discussed in section 5.4. Conclusions are given in section 5.5.

5.1 Measurement procedure

The mass measurements of $^{60-63}$Ga were performed over a total time period of 58 hours with radioactive ion beam. Throughout the entire experiment, the MR-TOF-MS was operated at a repetition rate of 50 Hz. The radioactive ion beam provided by the ISAC facility was produced as detailed in section 4.1 and the ISAC mass-separator magnet was optimized for maximum yield of the respective isotope of interest.

At each mass unit, at first, a broadband mass spectrum without mass-selective re-trapping was recorded to assess the beam composition. This enabled the identification of a suitable species for the mass calibration and informed whether additional isobar separation through mass-selective re-trapping was necessary. Toggling the MRS on and off further allowed for a differentiation between isobaric and non-isobaric contaminant species.

In the subsequent precision mass measurements, the average count rate on the TOF detector was kept below ≈ 0.95 particles per measurement cycle in order to limit systematic uncertainties due to ion-ion interactions in the TOF analyzer. The measurements were performed by letting the ions of interest revolve in the TOF analyzer for 327–400 isochronous turns (IT), resulting in total flight times in the range of 5.1–6.2 ms.

The mass measurements of ^{62,63}Ga were performed in the regular mass measurement mode without additional isobar suppression. For the mass measurements of ^{60}Ga and ^{61}Ga, mass-selective re-trapping (see section 3.4.2 for details) was used to suppress isobaric beam

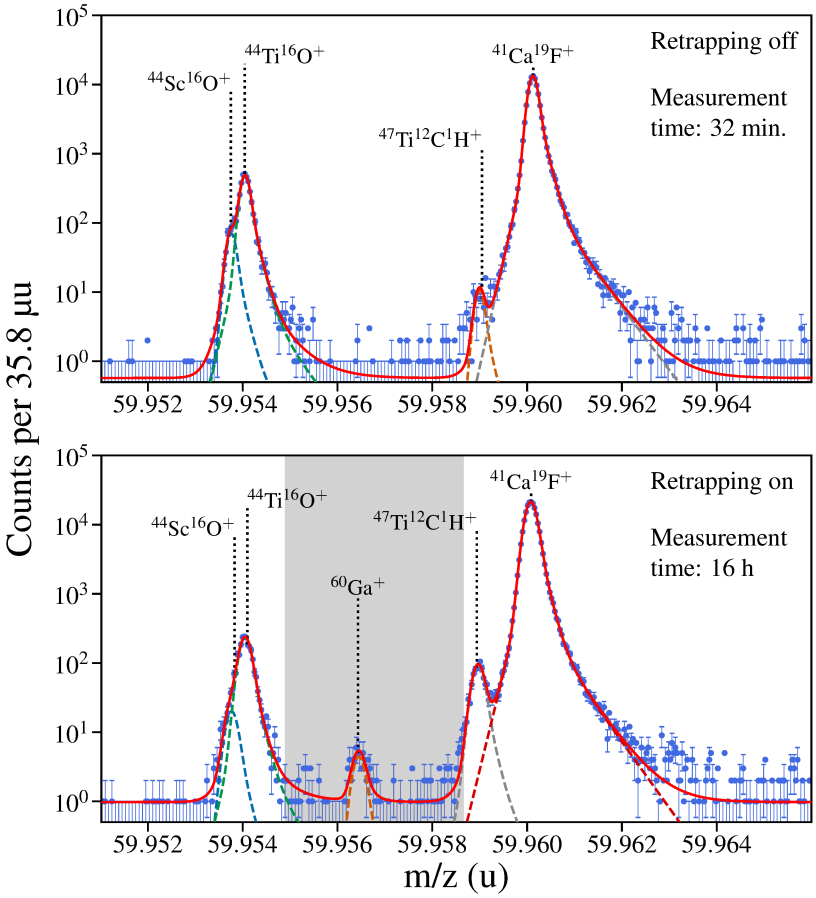

Figure 5.1. Mass spectra acquired at $A = 60$ with mass-selective re-trapping off (top) and on (bottom). The spectra were drift-corrected with a time-resolved calibration (TRC). In re-trapping operation, the intensities of peaks outside the re-trapping acceptance window (grey-shaded area) were suppressed by up to two orders of magnitude, thus enabling the detection of the peak of interest, ^{60}Ga. Multi-peak fits to the data (solid red line) and the underlying single-peak fit components (dashed lines) are indicated. For clarity, only every second error bar is shown. The respective measurement time is indicated in each spectrum. Figure reprinted from [425].

contamination by several orders of magnitude. The improved signal-to-contaminant ratios allowed for the total incoming beam intensity to be raised by factors of 50 and 5, respectively, while keeping the overall count rate at $\ll 1$ pps. As a result, the required measurement times were reduced substantially without introducing additional systematic uncertainties due to ion-ion interactions. The re-trapping technique proved instrumental in realizing the first direct mass measurement of ^{60}Ga, as it lifted the minute ^{60}Ga signal (detected rate of 7×10^{-4} pps) above an otherwise overwhelming background induced by close-lying contaminant peaks with several orders of magnitude higher intensity (see Fig. 5.1). Out of every 400 000 particles entering the TITAN system, on average only one corresponded to a gallium ion. These numbers showcase the effectiveness of the mass-selective re-trapping technique.

At each mass unit, the identification of the gallium peak was verified by recording a

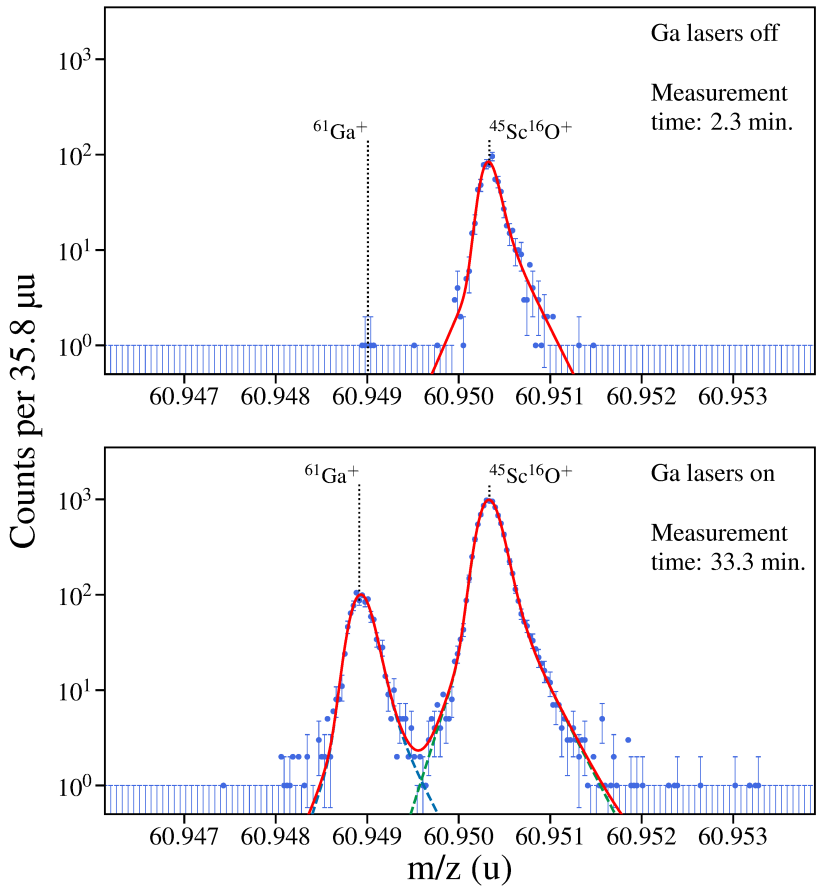

Figure 5.2. Mass spectra acquired at $A = 61$ with resonant laser ionization of gallium atoms on (top) and off (bottom). The spectra were drift-corrected with a time-resolved calibration (TRC). Multi-peak fits to the data (solid red line) and the underlying single-peak fit components (dashed lines) are indicated. For clarity, only every second error bar is shown. The respective measurement time is indicated in each spectrum. Figure reprinted from [425].

reference spectrum with the ionizing TRILIS laser beam blocked. The resulting, more than five-fold reduction in the gallium count rate provided unambiguous confirmation of the peak-of-interest identification (see Fig. 5.2 for an example). Identifications of molecular contaminant peaks were confirmed by tracing these ion species over multiple mass units.

5.2 Data analysis

The analysis of the mass data was generally based on the methodology developed for the analysis of MR-TOF mass data from fragment-separated RIBs at GSI's FRS Ion Catcher, as extensively described in Ref. [350]. The procedures outlined in Ref. [350] were adapted to the specific (and often simpler) requirements of mass measurements with ISOL beams at ISAC. The acquisition of the TOF data, the species identification and the initial mass calibration were performed in the mass data acquisition software MAc [423]. The resulting mass

spectra were then further processed with the open-source Python package EMGFIT [426], a dedicated library for peak fitting of MR-TOF mass data with hyper-exponentially modified Gaussian (hyper-EMG) line shapes [427]. The fitting package was developed as part of this thesis and extensively tested in studies with simulated Monte-Carlo spectra. A selection of these tests is presented in appendix A. The following section outlines the data analysis procedure and highlights noteworthy deviations from the methodology presented in [350].

5.2.1 Time-resolved mass calibration (TRC)

Within the MAc software, the acquired flight times t were converted to mass-to-charge-state ratios $\frac{m}{z}$ using the following calibration equation:

$$\frac{m}{z} = \frac{c\,(t - t_0)^2}{(1 + N_{\mathrm{IT}}\,b)^2}, \tag{5.1}$$

where N_{IT} denotes the number of completed isochronous turn (IT), and c, t_0 and b are calibration parameters. Since the ion-optical tune remained unchanged throughout the experiment, the parameters c and t_0 could be treated as constants and were pre-determined through off-line measurements with multiple non-radioactive ion species of well-known mass [350]. In the analysis of a given spectrum, only isobaric peaks that underwent the same number of isochronous turns were considered. With c and t_0 pre-determined, the calibration parameter b could hence be determined using only a single reference peak in each spectrum.

Long-term TOF drifts, e.g. due to temperature-related power-supply instabilities, induce a broadening of the mass peaks and degrade the resolving power. These effects were compensated by allowing the parameter b to vary over the measurement duration. In this so-called time-resolved calibration (TRC) [350], a given TOF data set is split into blocks of identical length. Within each block, the calibration parameter b is assumed to be constant and re-determined through a Gaussian fit to the isobaric mass calibrant peak. Finally, all calibration blocks are added up to obtain a drift-corrected mass spectrum, as illustrated in Fig. 5.3.

The length of the calibration blocks (typically 1–100 s) is user-defined and has to be adapted to the respective reference-ion count rate. On the one hand, the calibration block length should be chosen as short as possible to correct for drifts on shorter time-scales. On the other hand, the block length should ensure a sufficient amount of statistics for a robust centroid determination in each Gaussian peak fit. In the analysis of the presented gallium mass data, the block lengths were chosen such that each calibration block contained at least 100 reference ion counts. In spectra with an ideal reference ion count rate, the TRC almost doubled the achieved spectral resolution, enabling mass resolving powers of the order of $R \approx 250\,000$ (see top right in Fig. 5.3).

5.2.2 Fit models

Ion-optical aberrations and collisions with residual-gas atoms distort the shape of TOF mass peaks, oftentimes leading to highly asymmetric line shapes. The accurate determination of

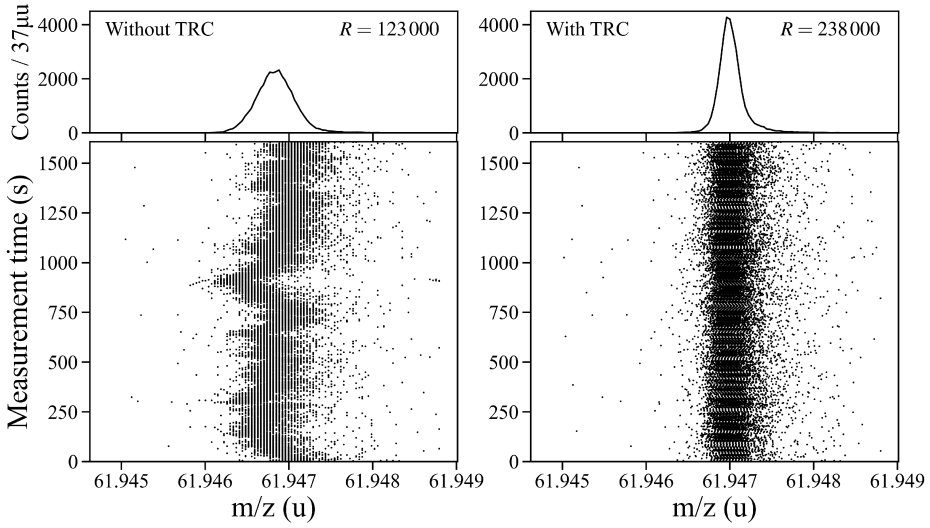

Figure 5.3. Effect of the time-resolved calibration (TRC) on the $^{46}Ti^{16}O^{+}$ peak used as mass calibrant in the ^{62}Ga mass measurement. The waterfall plots (bottom) show the same ion events with the calibration parameter b temporally fixed (left) and with b varied in a TRC (right). After the TRC, the summed mass spectrum (top) exhibited an almost two times higher resolving power (see text insets).

peak positions and areas poses a challenge in such scenarios and requires the best-possible description of the line shape. Exponentially-modified Gaussians have been demonstrated to be powerful tools in the analysis of spectroscopic data from different fields, obtained with various techniques such as TOF mass spectrometry [427], chromatography [428] and alpha-particle spectrometry [429]. Hyper-exponentially modified Gaussian (hyper-EMG) distributions [427] are mixture models that allow an arbitrary number of positively- and negatively-skewed exponential tails to be added to a Gaussian distribution, thus providing highly flexible model functions for fits of peaks with asymmetric line shapes. The probability density function of a hyper-EMG distribution is defined as [427]

$$h_{\text{emg}}(x;\mu,\sigma,\Theta,\eta_-,\tau_-,\eta_+,\tau_+)\doteq\Theta h_{-\text{emg}}(x;\mu,\sigma,\eta_-,\tau_-)+(1-\Theta)h_{+\text{emg}}(x;\mu,\sigma,\eta_+,\tau_+), \tag{5.2}$$

where Θ is a mixing weight that determines the relative contribution of the negatively- and positively-skewed exponential tails, denoted by $h_{-\text{emg}}$ and $h_{+\text{emg}}$, respectively and defined as

$$h_{-\text{emg}}(x;\mu,\sigma,\eta_-,\tau_-)\doteq\sum_{i=1}^{N_-}\frac{\eta_{-i}}{2\tau_{-i}}\exp\left(\left(\frac{\sigma}{\sqrt{2}\tau_{-i}}\right)^2+\frac{x-\mu}{\tau_{-i}}\right)\operatorname{erfc}\left(\frac{\sigma}{\sqrt{2}\tau_{-i}}+\frac{x-\mu}{\sqrt{2}\sigma}\right), \tag{5.3}$$

$$h_{+\text{emg}}(x;\mu,\sigma,\eta_+,\tau_+)\doteq\sum_{i=1}^{N_+}\frac{\eta_{+i}}{2\tau_{+i}}\exp\left(\left(\frac{\sigma}{\sqrt{2}\tau_{+i}}\right)^2-\frac{x-\mu}{\tau_{+i}}\right)\operatorname{erfc}\left(\frac{\sigma}{\sqrt{2}\tau_{+i}}-\frac{x-\mu}{\sqrt{2}\sigma}\right), \tag{5.4}$$

where positive (negative) indices refer to individual positively-skewed (negatively-skewed) exponential tails, $N_\pm$ denote the respective numbers of positively-skewed and negatively-skewed exponential tails, $\eta_\pm \doteq \{\eta_{\pm 1}, \eta_{\pm 2}, ..., \eta_{\pm N_\pm}\}$ and $\tau_\pm \doteq \{\tau_{\pm 1}, \tau_{\pm 2}, ..., \tau_{\pm N_\pm}\}$ are the sets of tail weights and exponential decay constants, respectively, and μ and σ denote the centroid and standard deviation of the underlying Gaussian distribution, respectively. The tail weights obey the following normalizations:

$$\sum_{i=1}^{N_-} \eta_{-\mathrm{i}} = 1, \tag{5.5}$$

$$\sum_{i=1}^{N_+} \eta_{+\mathrm{i}} = 1. \tag{5.6}$$

At certain distances from the peak maximum, numerical implementations of hyper-EMG functions tend to suffer from numerical accuracy loss. As detailed in appendix A, the EMGFIT fitting package prevents these issues by dynamically switching between different, mathematically-equivalent formulations of the right-hand sides of Eqn.s 5.3 & 5.4.

EMGFIT can be used to fit an entire mass spectrum containing an, in principle, arbitrary number of hyper-EMG peaks with a common peak shape defined by the shape parameters $\sigma, \Theta, \eta_-, \tau_-, \eta_+$ & τ_+. The total model function for a multi-peak fit of a continuous mass range containing N_{peaks} peaks is given by

$$f(x) \doteq \sum_{i=1}^{N_{\text{peaks}}} a_i \, h_{\text{emg}}(x; \mu_i, \sigma, \Theta, \eta_-, \tau_-, \eta_+, \tau_+) + c_{\text{bkg}}, \tag{5.7}$$

where a_i, μ_i denote the amplitude, and the mean and standard deviation of the underlying Gaussian of the i-th peak, respectively. The constant c_{bkg} defines the amplitude of a uniform background and allows to account for detector dark counts and ions registered after scattering with residual gas particles.

5.2.3 Model selection and peak-shape calibration

The resolving power of an ideal MR-TOF-MS is constant as a function of m/z. The shape parameters of peaks centred at different m/z are thus identical after scaling them to the respective peak centroid position [344]. Simultaneous fits of peaks differing by more than one mass unit usually require a re-scaling of the shape parameters to the respective peak centroids [350]. For isobaric mass peaks measured with TITAN's MR-TOF-MS, however, the m/z-dependent changes of the shape parameters (typically $< 0.1\%$) are negligible compared to the typical shape parameter uncertainties of $1 - 10\%$. Fits of isobaric species were therefore performed using a fixed, pre-determined peak shape, without re-scaling the shape parameters to the peaks of interest. The fixed peak shape was pre-determined by fitting an isobaric and ideally baseline-separated peak (or alternatively multiple, overlapping peaks) in the same spectrum as the peaks of interest. This peaks is then referred to as the shape-calibrant peak. Fixing the peak shape reduces the number of free parameters, and thus in-

creases the robustness and sensitivity of multi-peak fits that include overlapping peaks with limited statistics.

In each analyzed spectrum, a high-statistics and ideally well-separated isobaric reference peak was selected as the peak-shape calibrant and individually fitted by minimizing Pearson's chi-squared statistics [430, 431], defined as

$$\chi^2_P \doteq \sum_{i=1}^{N} \frac{(f(x_i) - y_i)^2}{f(x_i) + \epsilon}, \tag{5.8}$$

where the sum runs over all N mass bins and y_i is the number of counts in the i-th bin. The small constant $\epsilon = 10^{-10}$ was added to the denominator to prevent numerical instabilities for $f(x_i) \to 0$. To find the ideal peak-shape model, the peak-shape calibrant was fitted using hyper-EMG models with successively higher numbers of exponential tails, N_+ and N_-, starting from a pure Gaussian ($N_+ = N_- = 0$) up to a distribution with $N_+ = N_- = 3$. Overfitting was prevented by excluding all models from the selection for which any of the best-fit tail-weight parameters $\eta_{\pm i}$ or decay constants $\tau_{\pm i}$ agreed with 0 within the respective 1σ confidence intervals. Among the remaining models, the one which produced the smallest χ^2_P per degree of freedom was selected as the best-fit model. The subsequent fits of the mass calibrant and the ions of interest were performed using the so determined peak-shape model and the corresponding best-fit peak-shape parameters.

The peak-shape calibrant should ideally be baseline-separated from other peaks to ensure maximal accuracy in the determination of the peak-shape parameters. In the ^{60,61}Ga mass spectra, no fully separated peak was available as a peak-shape calibrant (see the lower subplots in Fig.s 5.1 and 5.2). The peak shape at $A = 60$ was thus calibrated by simultaneously fitting the ^{47}Ti^{12}C^{1}H$^+$ & ^{41}Ca^{19}F$^+$ peaks. As isobaric peaks acquire non-distinguishable shape parameters within our statistical measurement uncertainties (see above), in the simultaneous fit, identical line shapes were enforced for both peaks. The peak shape at $A = 61$ was calibrated analogously by fitting the ^{61}Ga$^+$ & ^{45}Sc^{16}O$^+$ doublet. In both cases, the result can be expected to be a sufficiently accurate approximation of the true peak shape since the more prominent shape-calibrant peaks were separated over a dynamic range larger than the total amplitude of the respective gallium peak.

5.2.4 Mass-calibrant and ion-of-interest fits

To obtain accurate peak positions and areas, all peaks of interest were simultaneously fitted through a binned maximum likehood estimation by minimizing the following (negative) log-likelihood ratio [432, 433]:

$$\mathcal{L} \doteq 2 \sum_{i=1}^{N} \left[f(x_i) - y_i + y_i \ln\left(\frac{y_i}{f(x_i)}\right) \right]. \tag{5.9}$$

As opposed to a chi-squared statistic, this cost function respects the Poisson nature of counting statistics and hence remains applicable for fitting low-statistics peaks. It further asymptotically converges to a chi-squared distribution and thus provides a convenient goodness-

of-fit measure which may remain applicable even in low-statistics scenarios [433]. Numerical implementation details and a comparison of fits with $\mathcal{L}$, χ^2_P and a number of other cost functions can be found in appendix A. As the peak-shape parameters were fixed to the predetermined values, only the peak positions, peak amplitudes and the uniform background parameter were varied in the fit. Example maximum-likelihood fits of the mass spectra obtained at $A = 60, 61$ are shown as red lines in Fig.s 5.1 and 5.2, respectively.

To validate that the multi-peak fits robustly converged to a maximum in the likelihood surface, the spectrum analysis was re-performed by fitting baseline-separated (groups of) peaks individually. For all reported results, such individual ion of interest (IOI) fits resulted in negligible mass shifts ($\frac{\delta m}{m} < 4 \times 10^{-8}$) with respect to the results from a simultaneous fit of all peaks.

5.2.5 Precision calibration and calculation of final mass values

We recall that the m/z-scale established in the TRC is based on peak positions from Gaussian least-squares fits, whereas the ion-of-interest peak positions $(m/z)_{\text{fit}}$ are determined through a maximum likelihood estimation with hyper-EMG model functions. To avoid systematic mass shifts arising from these differences, a precision mass calibration was performed by scaling the peak positions obtained in the maximum likelihood fit with the recalibration factor

$$\gamma_{\text{recal}} \doteq \frac{(m/z)_{\text{cal,lit}}}{(m/z)_{\text{cal,fit}}}, \tag{5.10}$$

where $(m/z)_{\text{cal,fit}}$ is the peak position of the chosen mass-calibrant species and $(m/z)_{\text{cal,lit}}$ is the corresponding literature mass-to-charge ratio deduced from AME2020 [151]. The final (ionic) mass values m_{ion} and the corresponding atomic mass excesses ME were then calculated as

$$m_{\text{ion}} = \gamma_{\text{recal}} \cdot (m/z)_{\text{fit}} \cdot z, \tag{5.11}$$

$$\text{ME} = m_{\text{ion}} + z m_e - A\,\text{u}. \tag{5.12}$$

In converting an ionic mass to an atomic mass or an atomic mass excess (which both presume a neutral atom in the atomic ground state), one must, in principle, correct for the ionization potentials I of the removed electrons. However, for singly-charged atomic ions ($I \leq 24.6\,\text{eV}$), this correction is only relevant at a precision level $\ll$1 keV and was thus neglected in the calculations of the atomic mass excess values. The final mass values were validated in an independent analysis performed with a different code for least-squares fitting with hyper-EMG models [434]. In all cases, the final mass values agreed within their uncertainties.

Combination of independent measurement results

The final mass values for ^{60,61,62}Ga were each deduced from fits of a single mass spectrum obtained by summing TOF data acquired with identical instrument settings; no combination of separate measurement results was necessary. For ^{63}Ga, separate mass measurements

were performed with 327, 337 & 347 isochronous turns, respectively, and required a special treatment. The ionic mass values m_i resulting from the three independent ^{63}Ga measurements agreed within their total mass uncertainties δm_i and were combined into a single, final value using a variance-weighted mean,

$$m = \frac{\sum_{i=1}^{3} {m_i}/{(\delta m_i)^2}}{\sum_{i=1}^{3} {1}/{(\delta m_i)^2}}. \tag{5.13}$$

Since the uncertainties of the different ^{63}Ga mass measurements, δm_i, were fully dominated by systematic contributions (see table 5.1 below), the uncertainty of the combined mass value was calculated as the weighted mean of the individual uncertainties:

$$\delta m = \frac{\sum_{i=1}^{3} {\delta m_i}/{(\delta m_i)^2}}{\sum_{i=1}^{3} {1}/{(\delta m_i)^2}}. \tag{5.14}$$

5.2.6 Uncertainty contributions

The total relative uncertainties of the final mass values were calculated by summing the following uncertainty contributions in quadrature:

$$\left(\tfrac{\delta m}{m}\right)_{\text{ion}} = \left[\left(\tfrac{\delta m}{m}\right)^2_{\text{stat}} + \left(\tfrac{\delta m}{m}\right)^2_{\text{recal}} + \left(\tfrac{\delta m}{m}\right)^2_{\text{PS}} + \left(\tfrac{\delta m}{m}\right)^2_{\text{NIE}} + \left(\tfrac{\delta m}{m}\right)^2_{\text{ion-ion}} + \left(\tfrac{\delta m}{m}\right)^2_{\text{TRC}}\right]^{1/2}. \tag{5.15}$$

Each of the terms on the right-hand side of Eqn. 5.15 is discussed in detail below. Special attention was taken to quantify possible systematic uncertainties arising in the fitting process. The magnitudes of mass shifts due to the finite bin size, and due to variations in the user-defined fit ranges for the peak-shape calibration and the ion-of-interest fits were evaluated and all found to be negligible (see appendix A for details). An overview of the uncertainty budget for each analyzed mass spectrum is given in a table at the end of this section.

Statistical uncertainty

The statistical mass uncertainty of a hyper-EMG fit is related to the FWHM of the given peak through [350]

$$\delta m_{\text{stat}} = A_{\text{stat}} \frac{\text{FWHM}}{\sqrt{N_{\text{events}}}}, \tag{5.16}$$

where N_{events} denotes the number of events in the peak. For a regular Gaussian, the constant of proportionality is simply given by $A_{\text{stat}} = 1/(2\sqrt{2\ln 2}) \approx 0.425$. For a hyper-EMG distribution, however, A_{stat} becomes dependent on the specific peak shape and has to be evaluated numerically. EMGFIT includes a parametric bootstrap routine for calibrating A_{stat} to the shape of a reference peak. Once A_{stat} has been calibrated, Eqn, 5.16 enables quick estimates of the statistical uncertainties of any peak with the same shape as the reference peak.

In the analysis of the presented gallium mass data, the statistical mass and peak-area uncertainties were, instead, estimated through a parametric bootstrap procedure following

the approach outlined in [350]. In this Monte-Carlo approach, 1000 simulated spectra were created by randomly sampling as many events from the best-fit model obtained in the maximum likelihood estimation as contained in (the relevant subsection of) the measured spectrum. The ion-of-interest fit was then re-performed for each simulated spectrum and the corresponding final mass values were calculated. Finally, the statistical mass uncertainty was estimated as the sample standard deviation of the resulting 1000 mass values. This procedure yields robust estimates of the statistical uncertainties, even for strongly overlapping peaks. It is particularly well-suited in low-statistics situations, as it also accounts, to some degree, for the sensitivity of the fit results to outlier events (e.g. due to detector dark counts) and will correspondingly increase the statistical mass and peak-area uncertainties.

Mass calibrant uncertainty

The mass calibrant uncertainty accounts for both the literature mass uncertainty of the calibrant species taken from [151] and the statistical uncertainty of the mass calibrant fit. Both contributions were added in quadrature to obtain the (relative) mass calibrant uncertainty

$$\left(\frac{\delta m}{m}\right)_{\text{recal}} = \left(\frac{\delta \gamma}{\gamma}\right)_{\text{recal}} = \sqrt{\left(\frac{\delta m_{\text{cal,lit}}}{m_{\text{cal,fit}}}\right)^2 + \left(\frac{\delta m_{\text{cal,fit}}}{m_{\text{cal,fit}}}\right)^2}. \tag{5.17}$$

Peak-shape uncertainty

The peak-shape uncertainty δm_{PS} quantifies the impact of uncertainties in the pre-determined shape parameters on the final mass value obtained from an ion-of-interest fit. A simple procedure to estimate this uncertainty contribution has been outlined in [350] and entails re-performing the ion-of-interest and mass-calibrant fits while individually varying each shape parameter by $+1\sigma$ and -1σ, respectively. The peak-shape uncertainty is then obtained by adding the larger of the two mass shifts[1] obtained from the variation of each shape parameter in quadrature. This approach implicitly assumes that the posterior distributions of all shape parameters follow Gaussian distributions and that the shape parameters are uncorrelated, i.e. statistically independent. In most practical cases, one or both of these assumptions are violated.

To obtain more refined estimates of the peak-shape uncertainty a dedicated Monte Carlo procedure has been developed as an alternative and implemented as a routine in EMGFIT. The procedure uses Markov-chain Monte Carlo (MCMC) sampling [435] to obtain a large number[2] of peak-shape parameter sets supported by the mass data used for the peak-shape calibration. These representative sets of peak-shape parameters approximate the posterior distributions of the shape parameters and naturally respect the corresponding parameter correlations. By re-performing the IOI fit with these many different peak shapes, the peak-shape

[1] Note that only peak-position shifts relative to the mass-calibrant position affect the final mass values. Therefore, both a new ion-of-interest peak position $(m/z)_{\text{fit}}$ and a new re-calibration factor γ_{recal} has to be determined to calculate a new ionic mass value for each variation in peak shape.

[2] All cases considered here were performed with 1000 sets of peak-shape parameters.

uncertainty can be estimated as the root-mean-square (RMS) deviation of the resulting mass values. A detailed description of the procedure is given in appendix A.

In the analyzed $^{60-63}$Ga mass spectra, the peak-shape uncertainties obtained with the Monte-Carlo method were all smaller than the corresponding estimates from the simple $\pm 1\sigma$-variation method, and were found to be on a negligible level of $\left(\frac{\delta_m}{m}\right)_{\text{PS}} < 1 \times 10^{-8}$ in all cases. Additional studies with other mass spectra suggest that the Monte-Carlo method indeed only yields non-negligible peak-shape uncertainties in cases of strongly overlapping peaks.

Uncertainty from the time-resolved calibration

Generally, uncertainties in all three calibration parameters (b, c & t_0) can induce uncertainties in the final mass values. For the measurements reported here, the situation is greatly simplified since only isobaric species that undergo the same number of isochronous turns are considered. In this case, the parameters c and b are fully correlated (see Eqn. 5.1) and the uncertainty arising from the calibration parameter c becomes zero [350]. Further, the mass uncertainty induced by an uncertainty in t_0 can safely be neglected.[3]

The mass uncertainty deriving from the determination of the calibration parameter b in the time-resolved calibration (TRC) was estimated using the following relation[4]

$$\left(\frac{\delta m}{m}\right)_{\text{TRC}} \approx 2\frac{\delta b}{b}, \tag{5.18}$$

where δb was calculated as the standard error of the mean variation of b between successive calibration blocks.

Uncertainty from non-ideal ejection

In order to release the ions from the TOF-analyzer onto the detector, the exit-mirror potential is rapidly switched into a non-reflecting state. Ions that are subjected to the resulting time-varying electric potential experience a change in their kinetic energy that may cause a shift in their TOF to the detector. If the calibrant ions and the ions of interest experience different time-varying potentials, this results in a systematic mass shift. In order to minimize this effect, the exit-mirror opening time was optimized in off-line measurements prior to the beamtime such that the ions were at a maximal distance from the second mirror when the switching occurs. Nevertheless, the mirror switching may induce non-negligible systematic mass shifts referred to as the non-ideal ejection (NIE) uncertainty.

Following the procedure described in [350], this uncertainty contribution was estimated in off-line measurements by varying the opening time of the exit-side ion mirror while recording the respective TOF of reference ions (see Fig. 5.4). After truncating the TOF

[3] Conservatively assuming $\delta t_0 = 10\% \times t_0$ and following the evaluation procedure detailed in [350] resulted in t_0-induced mass uncertainties $< 5 \times 10^{-11}$ for the cases reported here. See also [338].

[4] This relation is only valid for large numbers of isochronous turns, $N_{\text{IT}} \gg 1/b$, where $b \approx 0.5$ for TITAN's MR-TOF-MS.

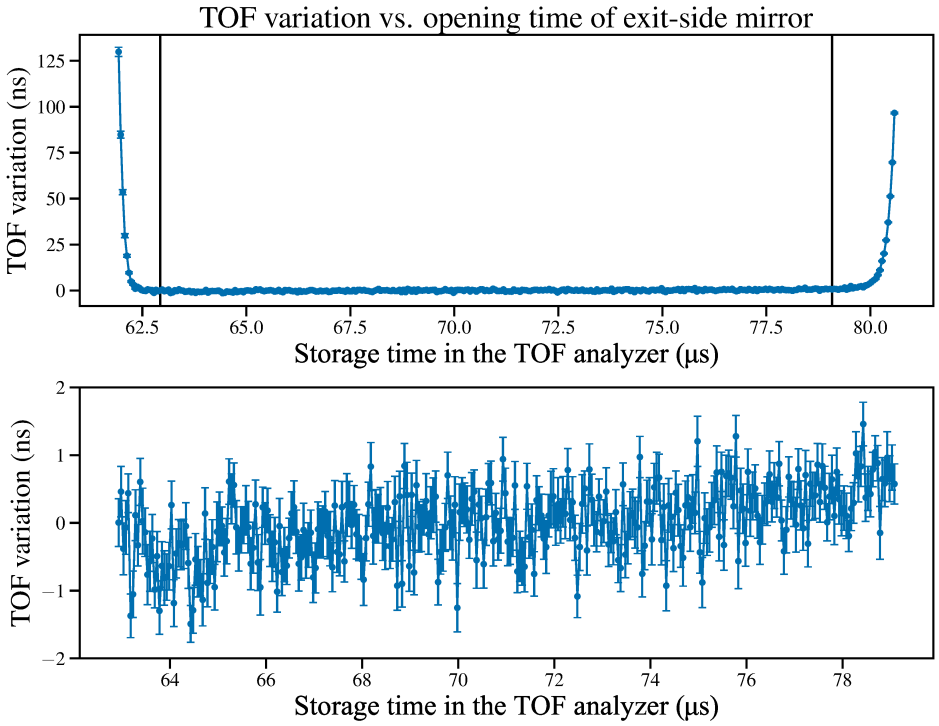

Figure 5.4. Variation of the TOF centroid of $^{133}Cs^{+}$ ions as function of the storage time in the TOF analyzer. The latter was varied by scanning the delay for opening the exit-side ion mirror. All measured ions fell well into the range indicated by the vertical lines in the top plot. Hence, only the data within this range (bottom plot) was considered for the evaluation of the TOF uncertainty from non-ideal ejection, δ_{NIE}. See text for details.

variation data to the relevant range (see Fig. 5.4 bottom), the TOF uncertainty due to non-ideal ejection, δt_{NIE}, was estimated as the standard deviation obtained in a Gaussian fit to a histogram of the TOF variations shown in the bottom plot of Fig. 5.4, resulting in $\delta t_{\mathrm{NIE}} \approx 0.54\,\mathrm{ns}$. The mass uncertainty from non-ideal ejection was then calculated using the relation [350]

$$\left(\frac{\delta m}{m}\right)_{\mathrm{NIE}} = \frac{2\delta t_{\mathrm{NIE}}}{t_{\mathrm{IOI}}}\sqrt{\frac{(m/z)_{\mathrm{IOI}}}{(m/z)_{\mathrm{ref}}}}, \tag{5.19}$$

where t_{IOI} is the total flight time of the ions of interest.

Uncertainty from ion-ion interactions

Coulomb interactions between ions stored simultaneously in the TOF analyzer may induce systematic mass shifts. The impact of such ion-ion interactions on a measured mass value depends on many factors including the ion-optical tune of the TOF analyzer, the ion storage time inside the TOF analyzer, the transmission and detection efficiencies, and the specific composition of the analyzed ion samples. Test measurements [436] of ion-ion interactions in the isobar pair $^{40}Ar_2^{+}$ and $^{80}Kr^{+}$ derived from non-radioactive ion beams from the off-line

Table 5.1. Uncertainty budget of the reported gallium mass measurements. The lowest row contains the total mass uncertainties calculated with Eqn. 5.15.

Nuclide	^{60}Ga	^{61}Ga	^{62}Ga	^{63}Ga		
N_{IT}	350	400	347	327	337	347
$\left(\frac{\delta m}{m}\right)_{\mathrm{stat}}$ / 10^{-7}	5.12	0.69	0.66	0.17	0.21	0.12
$\left(\frac{\delta m}{m}\right)_{\mathrm{recal}}$ / 10^{-7}	0.06	0.25	0.12	0.86	0.27	0.60
$\left(\frac{\delta m}{m}\right)_{\mathrm{PS}}$ / 10^{-7}	0.06	0.04	0.02	0.02	0.01	0.02
$\left(\frac{\delta m}{m}\right)_{\mathrm{TRC}}$ / 10^{-7}	0.75	1.55	0.92	1.01	1.07	0.83
$\left(\frac{\delta m}{m}\right)_{\mathrm{NIE}}$ / 10^{-7}	1.35	1.19	1.37	1.45	1.41	1.37
$\left(\frac{\delta m}{m}\right)_{\mathrm{ion-ion}}$ / 10^{-7}	0.14	0.23	1.69	1.62	1.79	1.56
$\left(\frac{\delta m}{m}\right)_{\mathrm{ionic}}$ / 10^{-7}	5.35	2.10	2.45	2.55	2.54	2.32

ion source terminal [367] for ISAC yielded an effect of $(\delta m/m)_{\mathrm{ion-ion}} \approx 1.9 \times 10^{-7}$ per detected ion per measurement cycle. The mass uncertainties from ion-ion interactions were estimated by scaling this number to the total ion count rate in each analyzed mass spectrum. In all reported measurements, the average count rate registered on the TOF detector was ≤ 0.95 ions per cycle.

Resulting uncertainty budget

The aforementioned uncertainty contributions were separately evaluated for each analysed mass spectrum. The total uncertainty budget including all considered error contributions is given in table 5.1. For ^{62,63}Ga, the systematic uncertainty from ion-ion interactions formed the dominant uncertainty contribution. In the ^{60,61}Ga measurements, the impact of ion-ion interactions was insignificant due to the low total ion count rates and the total mass uncertainty was dominated by the statistical uncertainty.

5.3 Mass results

The $^{60-63}$Ga mass excess values obtained in this study are reported along with literature values in table 5.2. Fig 5.5 illustrates the respective deviations from literature and earlier mass determinations. Separately for each isotope, the following sections discuss our new experimental results in the context of the previously available data.

Table 5.2. Mass excess values obtained for $^{60-63}$Ga in the TITAN mass measurements compared to literature values from 2020 Atomic Mass Evaluation (AME2020) [151]. The respective half-lives $T_{1/2}$, event numbers N_{events} and mass-calibrant species are also listed.

Nuclide	$T_{1/2}$ (ms)	N_{events}	Calibrant species	Mass excess (keV)	
				TITAN	AME2020
^{60}Ga	70	41	$^{41}Ca^{19}F^{+}$	$-40005(30)$	$-39590^{\#}(200^{\#})$
^{61}Ga	167	1001	$^{45}Sc^{16}O^{+}$	$-47114(12)$	$-47130(40)$
^{62}Ga	116	954	$^{46}Ti^{16}O^{+}$	$-51992(14)$	$-51987.0(6)$
^{63}Ga	3240	48099	$^{47}Ti^{16}O^{+}$	$-56563(14)$	$-56547.1(13)$

$^{\#}$ Extrapolated values based on trends of the mass surface [152].

^{63}Ga

The mass of ^{63}Ga had already been precisely determined in a Penning trap measurement [440] at ISOLTRAP and is listed in the 2020 Atomic Mass Evaluation (AME2020) [151] with an uncertainty of 1.3 keV. The new mass result obtained with TITAN's MR-TOF-MS does not match this precision level but agrees with the literature value within 1.2σ. With an average count rate of 0.8–0.9 ions per cycle, the leading uncertainty contribution is given by the uncertainty from ion-ion interactions, $(\delta m/m)_{\text{ion-ion}} \approx 1.6 - 1.8 \times 10^{-7}$, closely followed by the uncertainty due to non-ideal ion ejection, $(\delta m/m)_{\text{NIE}} \approx 1.4 - 1.5 \times 10^{-7}$ (see table 5.1).

^{62}Ga

Due to its superallowed β-decay, ^{62}Ga has been extensively studied in earlier experiments (see e.g. [30, 442–444]). Its literature mass value had already been well-established with an uncertainty of 0.6 keV in AME2020, based on a Penning trap measurement [439] at JYFLTRAP. Our mass result of ME $= -47\,114(12)$ keV is less precise than the earlier measurement but confirms the preexisting data with an agreement within 0.4σ. With an average count rate of ≈ 0.9 detected ions per cycle, the estimate of the uncertainty from ion-ion interactions, $(\delta m/m)_{\text{ion-ion}} \approx 1.7 \times 10^{-7}$, forms the dominant uncertainty contribution in this measurement.

^{61}Ga

The AME2020 literature mass value of ^{61}Ga is based on an indirect β-endpoint measurement [437] and a direct mass measurement at the CSRe storage ring in Lanzhou [438]. The literature mass excess of ME $= -47\,130(40)$ keV does not exhibit the required precision for *rp*-process simulations ($\delta m \leq 10$ keV) and has been found to induce significant uncertainties in light curve calculations for hydrogen-rich X-ray bursts [51] (see section 2.1.5). Due to concerns about the reliability of the existing experimental results [51], an independent and more precise measurement of the ^{61}Ga mass has long been outstanding.

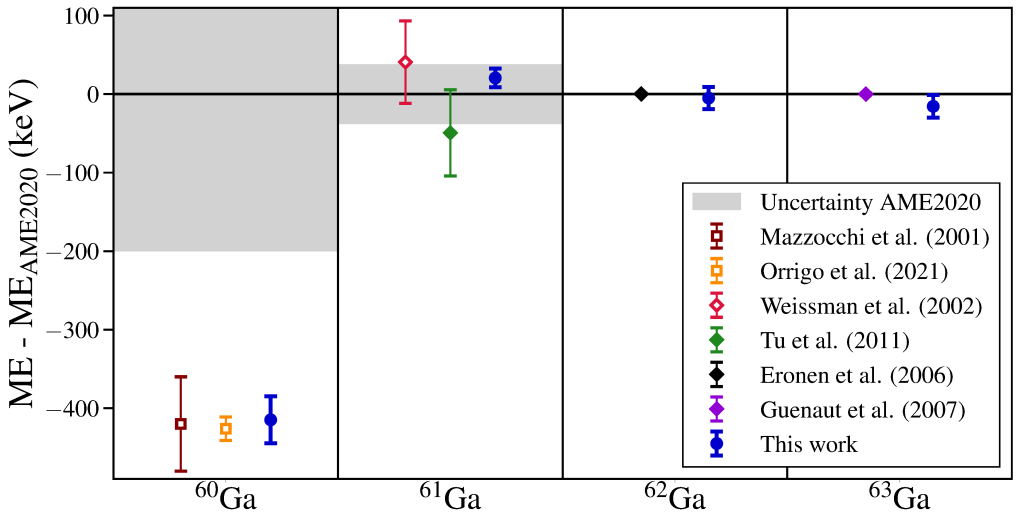

Figure 5.5. $^{60-63}$Ga mass excess values obtained in this work (blue dots) relative to literature values from AME2020 [151] ($ME_{AME2020}$). The earlier experimental results [437–440] that formed the input data for AME2020 are shown as diamonds. For ^{60}Ga, squares indicate a semi-empirical mass estimate from Mazzocchi et al. [156] and the recent, indirect mass determination by Orrigo et al. [441]. All directly measured values are marked by solid symbols.

Our new ^{61}Ga mass value of ME $= -47\,114(12)$ keV confirms the earlier experimental results, thus diffusing concerns about their accuracy. The uncertainty of our result is dominated by the systematic uncertainty from the time-resolved calibration, $(\delta m/m)_{\mathrm{TRC}} \approx 1.6 \times 10^{-7}$. With an average of ≈ 0.12 detected ions per cycle, systematic effects from to ion-ion interactions are negligible. Our result is three times more precise than the current literature mass value and four times more precise than the storage ring result (see Fig. 5.5).

^{60}Ga

Previous to our study, the mass of ^{60}Ga had not been directly measured. The literature value listed in AME2020 is therefore an extrapolation based on trends of the mass surface (see [152] for details on Audi-Wapstra mass extrapolations). In the absence of a direct mass determination, a number of mass estimates have been derived based on theoretical Coulomb displacement energies (CDEs) [195, 199, 445].

The first detailed experimental work on ^{60}Ga was a spectroscopy study of its β-decay and charged particle emission performed by Mazzocchi et al. [156] in 2001. Mazzocchi et al. measured the half-life of the ^{60}Ga ground-state for the first time, identified its $T = 1$ isobaric analogue state (IAS) in ^{60}Zn and measured the corresponding excitation energy. Combining the latter result with a CDE deduced from global experimental systematics [198], they extracted semi-empirical estimates for the ^{60}Ga ground-state mass and proton separation

energy of ME(^{60}Ga) $= -40010(60)$keV and $S_p(^{60}\text{Ga}) = 40(70)$ keV, respectively.

Another indirect determination of the ^{60}Ga ground-state mass was recently obtained in a study of the β-decay of ^{60,62}Ge by Orrigo et al. [441]. In that study, β-decays of ^{60}Ge were found to populate the (excited) isobaric analogue state (IAS) in ^{60}Ga. The IAS then either de-excited through a γ cascade to the ^{60}Ga ground state, or decayed to states in ^{59}Zn via emission of a proton (β-delayed proton emission). Combining the measured energy for proton emission leading to the ground state with the well-known literature mass of ^{59}Zn allowed Orrigo et al. to extract the mass of the IAS in ^{60}Ga. They further constructed a level scheme for ^{60}Ga assuming that the IAS de-excites through the successive emission of the observed 1775 keV and 837 keV γ rays. This hypothesis provided them with the excitation energy of $E_x = 2611.8(0.9)$keV for the IAS in ^{60}Ga. Combining this excitation energy with their measured mass for the IAS, Orrigo et al. indirectly deduced a ^{60}Ga ground-state mass excess of ME(^{60}Ga) $= -40016(15)$ keV and a corresponding proton separation energy of $S_p(^{60}\text{Ga}) = 90(15)$ keV. Their underlying assumptions about the de-excitation of the IAS in ^{60}Ga were strengthened by the agreement with the excitation energy of the mirror level in ^{60}Zn. However, the Fermi transition strength obtained for the decay of the IAS in ^{60}Ga, $B(F) = 3.1(1)$), fell short of the theoretical expectation of $B(F) = 4$. This discrepancy could indicate that γ-ray transitions de-exciting the IAS were misassigned or remained undetected, thus raising questions about the reliability of the proposed level scheme and the obtained ^{60} ground-state mass excess. Orrigo et al. themselves called for an additional decay study with higher statistics to resolve the apparent inconsistencies in their observations.

Our MR-TOF-MS measurements provide the first direct determination of the ^{60}Ga ground-state mass. With 41(8) ^{60}Ga events accumulated over a total of 16 h, the measurement uncertainty is dominated by the statistical error of $(\delta m/m)_{\text{stat}} \approx 5.1 \times 10^{-7}$. Our result of ME(^{60}Ga) $= -40005(30)$ keV deviates from the extrapolated value in AME2020 by almost 400 keV but agrees with the semi-empirical estimate by Mazzocchi et al. [156] and the more precise, indirect determination by Orrigo et al [441] within the quoted uncertainties (see Fig. 5.5). The agreement with our mass value lends further credibility to the assumptions of Orrigo et al. concerning the de-excitation of the IAS in ^{60}Ga. Additional decay studies are still desirable to obtain a more comprehensive understanding of the level structure of ^{60}Ga. While our mass value disagrees with the AME2020 value, it is compatible with the extrapolated value[5] of ME(^{60}Ga) $= -40000^{\#}(110^{\#})$ keV listed in AME2003 [446]. Several other studies [441, 447–449] have found similar discrepancies with extrapolations in mass evaluations after AME2003. Our mass value could act as an anchor point for future atomic mass evaluations but additional mass measurements in the region are desirable. Our mass value is further in close agreement with an estimate based on a theoretical CDE from Brown et al. [220], ME(^{60}Ga) $= -40005(10)$ keV.

[5] Values extrapolated based on trends from the mass surface [152] are marked with a hash ($^{\#}$).

5.4 Discussion

The new mass data allows us to constrain the location of the proton drip line in the gallium isotope chain, extend the $T = 1$ IMME in the *pf* shell, deduce an estimate for the mass of ^{61}Ge and investigate implications for the *rp*-process in X-ray bursts. These applications are discussed separately in the subsequent sections.

5.4.1 Location of the proton drip line in the gallium chain

The proton drip line is defined as the point along an isotope chain where the (one-)proton separation energy,

$$S_p(A, Z) = \mathrm{ME}(A-1, Z-1) - \mathrm{ME}(^1\mathrm{H}) - \mathrm{ME}(A, Z), \tag{5.20}$$

becomes negative [17]. Nuclides beyond the proton (neutron) drip line are said to be proton-(neutron-)unbound and decay through emission of a proton (neutron). As a fundamental boundary of nuclear stability, the proton drip line provides ideal testing grounds for nuclear mass models. Here, we use our new mass data to benchmark the global and local mass prediction methods introduced in sections 2.2.1 and 2.2.2, respectively, and to investigate the location of the proton drip line in the gallium chain.

In contrast to the near-instantaneous decay of neutron-unbound nuclei ($t_{1/2} \lesssim 1$ ps [17]), the additional confinement due to the Coulomb barrier causes some proton-unbound nuclei to exhibit surprisingly long half-lives against proton emission (up to multiple seconds [12]). The existence of such long-lived proton emitters makes the exact localization of the proton drip line an experimental challenge [12]. The detection of ground-state proton emission immediately establishes the proton-unbound nature of a nucleus. However, as detailed in [23], the non-observation of emitted protons in a charged-particle spectrometer is generally not sufficient to conclude that a nucleus is stable against proton emission. This is due to two reasons. (1) In the case of a small, negative S_p value, the partial half-life against proton emission can exceed the half-life against competing β-decay by several orders of magnitude, resulting in a undetectably small branching ratio for proton emission (see also [12]). Adopting the barrier-penetration model of [450], the proton-emission half-life of ^{60}Ga was calculated as a function of the respective decay Q-value, Q_p, and is plotted for different proton angular momenta in Fig. 5.6. Already within the literature uncertainty of $S_p(^{60}\mathrm{Ga})$ (grey-shaded area), the proton-emission half-life could exceed the β-decay half-life (red line) by more than 7 orders of magnitude, implying a branching ratio below the sensitivity of conventional charged-particle decay spectrometers. (2) The detection of a proton peak in decay spectrometers without charged-particle identification is further hampered by the low-energy background induced by the β-particles (see e.g. Fig. 2 in [441]) which falls into the same energy range as the emitted protons. These complications are circumvented by informing the particle bound nature of a nuclide based on reliable mass data and the requirement that $S_p < 0$. Precision mass measurements are therefore essential to stringently determine the location of the proton drip line. This is especially true in such challenging

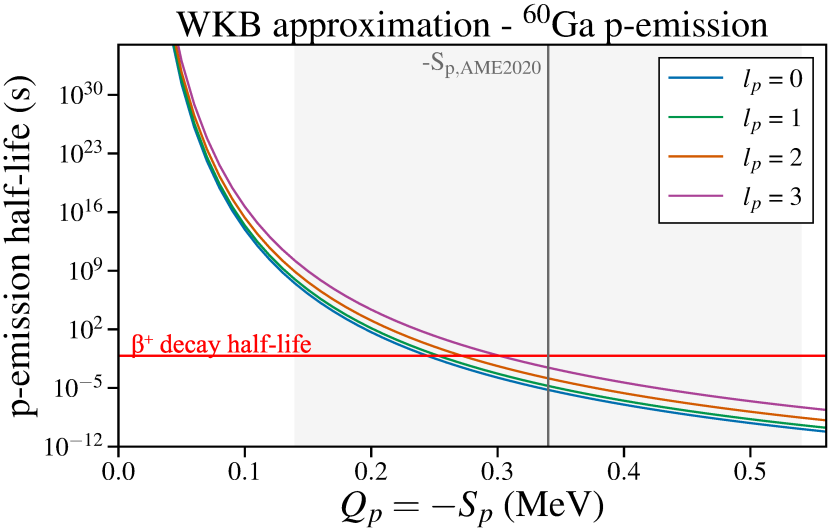

Figure 5.6. Partial half-life of ^{60}Ga against proton emission calculated as function of the proton-emission Q-value, Q_p, and for different proton angular momenta, l_p. The grey-shaded area indicates the 1σ confidence interval of the S_p-value listed in AME2020 [151]. The red line marks the experimental β-decay half-life adopted in [451].

cases as the gallium chain, where both ^{60}Ga and ^{61}Ga are expected to lie very close to the proton drip line.

Combining our $^{60-63}$Ga mass values with the well-established literature masses of the neighbouring zinc isotopes enables us to extract the proton separation energies along the gallium chain. The resulting S_p values are listed in table 5.3, in comparison to AME2020 values and the results from earlier indirect experimental determinations.

The S_p values obtained with the new mass data from TITAN's MR-TOF-MS are shown in Fig. 5.7 along with the values from AME2020 and predictions from various theoretical approaches. The predictions from the representative set of global mass models introduced

Table 5.3. Proton separation energies, S_p, deduced from the new $^{60-63}$Ga mass data and AME2020 values for the neighbouring zinc isotopes. AME2020 literature values and the results for ^{60}Ga from the indirect experimental deductions by Mazzocchi et al. [156] and Orrigo et al. [441] are also listed.

Nuclide	S_p (keV)			
	TITAN	AME2020	Ref. [156]	Ref. [441]
^{60}Ga	78(30)	$-340^{\#}(200^{\#})$	40(70)	90(15)
^{61}Ga	229(12)	250(40)		
^{62}Ga	2932(21)	2927(16)		
^{63}Ga	2684(14)	2668.0(14)		

$^{\#}$ Extrapolated values based on trends of the mass surface [152].

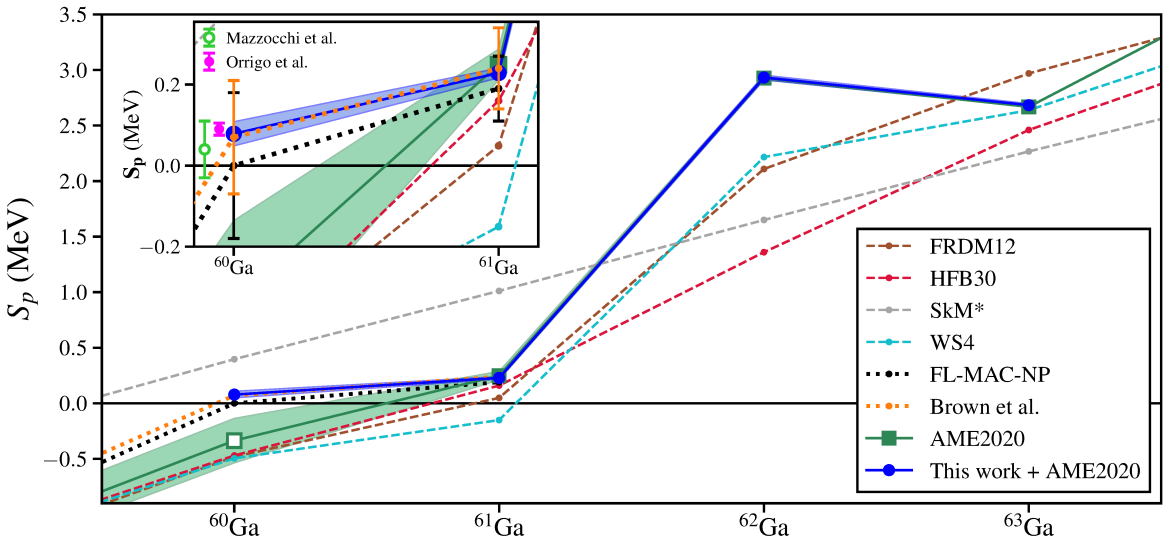

Figure 5.7. Proton separation energies S_p of $^{60-63}$Ga from this work (blue dots) in comparison to literature values from AME2020 (green squares), and predictions from global mass models (dashed lines) and from local mass extrapolations (dotted lines). For clarity, the indirect experimental determinations of $S_p(^{60}\mathrm{Ga})$ by Mazzocchi et al. [156] and Orrigo et al. [441] and theory error bars are only shown in the inset. Figure reprinted from [425].

in section 2.2.1 (FRDM12 [452], HFB30 [180], WS4 [165] and the mass model [13] based on the SkM* interaction [179]) all fail to closely match the experimental trend. None of the models reproduces the exceptionally strong binding of the odd-odd $N = Z$ nucleus ^{62}Ga, possibly due to an improper description of the Wigner energy [453]. Except for SkM*, all models considered underbind ^{60}Ga. The spread between the model predictions illustrates the typical prediction accuracy of global mass models which has been found to be ≈ 400–$700\,\mathrm{keV}$ in this region of the nuclear chart [169]. In terms of drip line predictions, this translates into a dispersion by roughly one nuclide.

Multiple studies [454–456] have recently deployed Bayesian inference and machine learning to improve the predictive power of global mass models. The Bayesian model averaging approach presented in [457] combined various mass models, weighing each model according to its agreement with experimental mass data in a certain region of the nuclear chart. In agreement with our experimental data, this approach predicted ^{60}Ga to be proton-bound with ≈80% probability. More comparisons to experimental data are desirable to evaluate the extrapolation power of these novel approaches.

The dotted lines in Fig. 5.7 display mass extrapolations based on CDEs (see section 2.2.2). Klochko et al. [197] recently mapped the proton drip line using CDEs derived from theoretical IMME b coefficients. The latter were deduced from FL-MAC-NP, a modified version of the macroscopic part of the finite-range liquid drop model (FRLDM) [458]. According to the FL-MAC-NP predictions (black dotted lines) ^{60}Ga falls right onto the proton drip line, with $S_p(^{60}\mathrm{Ga}) = 0(180)\,\mathrm{keV}$. Brown et al. [199] performed an earlier mapping of the proton drip line using CDEs from Hartree-Fock calculations with a Skyrme-type interaction. Mass predictions from these CDEs have been used as X-ray burst model inputs in

multiple studies [48, 51, 199, 459], including the investigations presented in section 5.4.4. The S_p values based on the CDEs by Brown et al. (orange dotted line) are seen to be in excellent agreement with our experimental data and suggest ^{60}Ga to be proton-bound with $S_p = 70(140)$ keV. Both CDE approaches considered here closely reproduce our new experimental trends. However, due to the small proton separation energy of ^{60}Ga, the prediction uncertainties prevent a detailed localization of the proton drip line.

Our direct mass measurement of ^{60}Ga yields a ^{60}Ga proton separation energy of $S_p = 78(30)$ keV, implying ^{60}Ga to be proton-bound with 2.6σ confidence. This is in strong tension with the extrapolated AME2020 result, which lists ^{60}Ga as proton-unbound with $S_p = -340^{\#}(200^{\#})$ keV. Our new S_p value for ^{60}Ga is in decent agreement with the semi-empirical value by Mazzocchi et al [156] and the recent result by Orrigo et al. [441] (see table 5.3 or the inset of Fig. 5.7). The compatibility with our direct mass measurement confirms the reliability of the more precise, indirect determination by Orrigo et al. Combining both values yields a variance-weighted mean of $S_p(^{60}\text{Ga}) = 88(18)$ keV, thereby establishing the proton-bound nature of ^{60}Ga with more than 3σ significance.

To pin down the location of the proton drip line in an isotopic chain also requires an experimental confirmation of the proton-unbound nature of the first nuclide beyond the drip line, i.e. ^{59}Ga in the case of the gallium chain. The non-observation of ^{59}Ga in an isotope search at the A1900 fragment separator at NSCL provided strong evidence that ^{59}Ga is indeed proton-unbound [460]. Combining this finding with the results by Orrigo et al. [441] and those from our study, we find strong evidence that ^{60}Ga is the last proton-bound nuclide in its isotopic chain and marks the location of the proton drip line.

5.4.2 Extending the T=1 isobaric multiplet mass equation

The most recent global evaluations of IMME coefficients were presented by Lam et al. in 2013 [193] and MacCormick et al. in 2014 [203]. Due to a lack of experimental input data, the evaluated $T = 1$ triplets in these surveys only reached up to $A = 58$ and contained gaps at $A = 44, 52, 56$. These gaps have, by now, all been filled through precision mass measurements of ^{44g,m}V [240], ^{52g,m}Co [461], ^{56}Cu [462].

Our ^{60}Ga mass measurement completes the IAS data for the lowest-lying isospin triplet at $A = 60$, allowing us to extend the high-mass end of the evaluated $T = 1$ IMME. To study the trends of the b and c coefficients in the *pf* shell, we evaluated the lowest-lying triplets at $A = 42 - 62$. The selection of the input data on the relevant IASs proceeded according to the procedures detailed in [203]. The mass excesses of excited IAS were calculated by combining ground-state masses with the corresponding excitation energies. Unless otherwise noted, ground-state masses were taken from AME2020 [151], and IAS assignments and excitation energies were adopted from ENSDF [463]. The corresponding IMME coefficients were extracted through least-squares fits of the evaluated IAS mass excesses with the quadratic IMME (Eqn. 2.13).

The data selection for the triplet at $A = 60$ was complicated by ambiguities in the assignment of the lowest-lying $T = 1$ IAS in ^{60}Zn, ^{60}Zn^{i}. ENSDF suggests two levels with

excitation energies of $E_x = 4852.2(7)$ keV and $E_x = 4913.3(9)$ keV, respectively, as probable candidates for ^{60}Zn^i [451]. Neither of the two reaction studies [464, 465] that measured the higher-lying candidate level could assign it a spin-parity or provide other conclusive evidence for the identification of this level as the IAS. The lower-lying level was first observed in a study of ^{58}Ni(^{16}O,^{14}C)^{60}Zn reactions [466] and assigned as the IAS on the grounds of the close agreement with a CDE prediction. Later, this level was re-measured in the decay spectroscopy studies by Mazzocchi et al. [156] and Orrigo et al. [441], which both assigned it as the $T = 1$ IAS. The assignment by Mazzocchi et al. was informed by the coincident detection of β-delayed γ rays attributed to the cascading de-excitation of the IAS. The agreement of the corresponding decay strength with the theoretical expectation further indicated that, if any, only a small fraction of γ rays de-exciting the IAS remained unobserved. In accordance with NUBASE2020 [467], we hence identified the lower-lying candidate level as ^{60}Zn^i and used the literature excitation energy of 4852.2 keV to evaluate the IAS mass excess.

To compare the trends of the b and c coefficients to theory predictions, shell-model calculations were performed within the full *pf*-shell valence space using the NuShellX@MSU code [468] and the isospin-nonconserving (INC) interaction cdGX1A. The latter is a charge-dependent (cd) version of the phenomenological effective interaction GXPF1A [225, 241] with the Coulomb two-body interaction, the nuclear isospin-symmetry breaking terms from [27], and isovector single-particle energies from [228]. The two-body Coulomb interaction and the isovector single-particle energies were scaled with a factor proportional to $\sqrt{\hbar\omega(A)}$ to account for their mass dependence throughout the *pf* shell (see [193] for details).

The IMME b and c coefficients obtained in our evaluation are shown in Fig. 5.8 along with the results from the survey by MacCormick et al. [203] and the shell-model predictions. The comparison of our results to the 2014 survey by MacCormick et al. illustrates the substantial expansion of the experimental IAS data due to recent measurements on rare isotopes, including dramatic uncertainty reductions at $A = 48, 50, 54$. Our expanded set of experimental b coefficients seamlessly continue the near-linear decrease observed towards higher masses. The c coefficients exhibit the characteristic staggering attributed to Coulomb pairing and INC forces of nuclear origin (see section 2.2.3). The new c coefficients are compatible with a gradually decreasing staggering amplitude. All lowest-lying $T = 1$ multiplets up to $A = 60$ are now well-constrained by experiment, except for the triplet at $A = 58$. In the latter, the precision of the c coefficients is not known accurately enough to exclude a possible anomaly. Generally, such an anomaly could indicate isospin mixing or misidentification of an IAS [203]. The precision of the triplet at $A = 58$ is currently limited by the 50 keV uncertainty of the ^{58}Zn mass which is based on a measurement of the ^{58}Ni(π^+,π^-)^{58}Zn reaction Q-value. A direct, precision mass measurement of ^{58}Zn is desirable to rule out a possible anomaly at $A = 58$.

The experimental b and c coefficients at $A = 42 - 60$ are found to be in reasonable agreement with the shell-model predictions, as evidenced by RMS deviations of 59 keV and 23 keV, respectively. However, we observe increasing discrepancies at masses

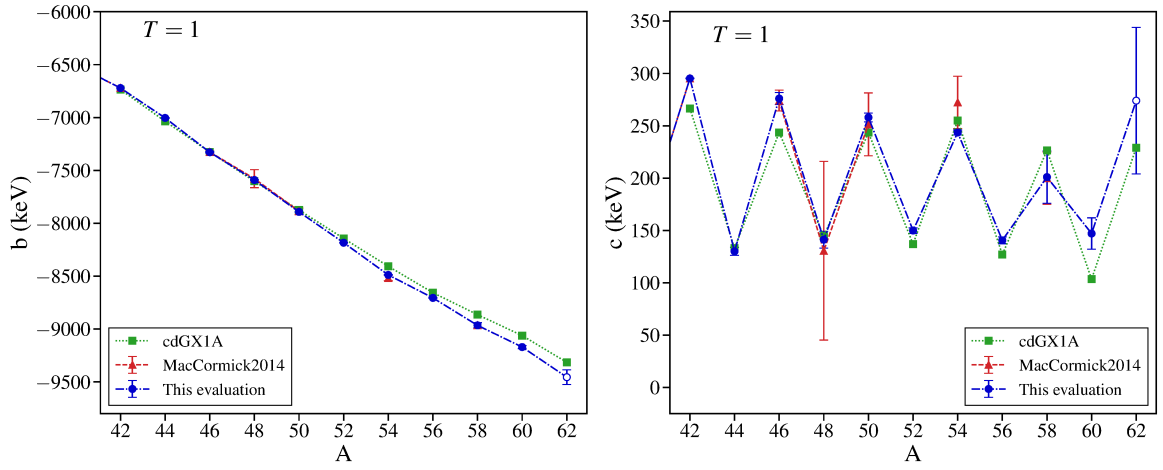

Figure 5.8. Trends of the IMME b and c coefficients of the $T = 1$ multiplets in the *pf* shell. The results from our evaluation (blue dots) are contrasted to those from the earlier compilation by MacCormick et al. [203] (red triangles) and theoretical predictions from shell-model calculations with the isospin-nonconserving cdGX1A interaction (green squares).

$A > 56$. These deviations could indicate a need to re-adjust the INC terms in the shell-model Hamiltonian to the much expanded sets of experimental b and c coefficients as compared to the data available for the original adjustment of the force parameters. However, the observed deviations could also, at least partially, arise from a gradual decline in the predictive power of the underlying isospin-conserving GXPF1A interaction. In fact, cross-shell excitations to the excluded $g_{9/2}$ orbital are expected to become relevant beyond $A \sim 60$ [202]. More experimental data is desirable to evaluate these trends and clarify the role of INC forces in the upper *pf* shell.

5.4.3 IMME prediction of the ^{61}Ge mass

The mass of ^{61}Ge has never been measured and enters calculations of the unmeasured ^{60}Ga(p,γ) reaction rate. Reasonable estimates of this rate are critical to investigate whether the two-proton capture sequence ^{59}Zn$(p,\gamma)^{60}$Ga$(p,\gamma)^{61}$Ge provides a secondary bypass of the ^{60}Zn *rp*-process waiting point (see section 5.4.4). Calculations of this reaction rate require decent knowledge of the ^{60}Ga and ^{61}Ge masses to pin down the corresponding reaction Q-value. Since the ^{61}Ge mass is experimentally unknown, rate calculations have been forced to rely on theoretical mass estimates.

To verify these estimates, we deduce an IMME prediction for the unmeasured ^{61}Ge mass. To this end, we combined our improved ^{61}Ga mass value with pre-existing experimental data on the $T = 3/2$ IAS, ^{61}Ga^{i}, ^{61}Zn^{i} and ^{61}Cu. Adding our ^{61}Ga ground-state mass excess with the literature excitation energy of the IAS ($E_x = 3162(30)$ keV [469]), we obtained a mass excess of $-43723(30)$ keV for the lowest-lying $T = 3/2$ IAS in ^{61}Ga. The excitation energy of ^{61}Zn^{i} listed in ENSDF [463] ($E_x = 3380$ keV) is based on a Q-value measurement [470] that did not provide uncertainty estimates. We therefore deduced this excitation energy from

Table 5.4. Prediction of the unmeasured mass excess of ^{61}Ge from an IMME fit to the other $T = 3/2$ multiplet members, ^{61}Ga^{i}, ^{61}Zn^{i} and ^{61}Cu. The extrapolated AME2020 [151] mass excess of ^{61}Ge and a mass estimate [51] based on a theoretical CDE from Brown et al. [199] are also listed.

	IMME input data			IMME prediction
IAS	^{61}Cu	^{61}Zn^{i}	^{61}Ga^{i}	^{61}Ge
T_z	$+3/2$	$+1/2$	$-1/2$	$-3/2$
Mass excess (keV)	$-61984(1)$	$-53001(25)$	$-43723(30)$	$-34150(117)$
			AME2020 mass excess (keV):	$-33790^{\#}(300^{\#})$
			CDE estimate (keV):	$-34065(100)$

$^{\#}$ Extrapolated values based on trends from the mass surface [152].

a different reaction study by Weber et al. [471]. Measuring the energy spectra of reaction products from two different heavy-ion transfer reactions, Weber et al. observed a ^{61}Zn level at an excitation energy of $3345(20)$ keV and $3370(60)$ keV, respectively. Both excitation energies agree with the value quoted in [470] and likely belong to the same level. We thus identified this level as the IAS and estimated its excitation energy as the variance-weighted mean of the two energies measured by Weber et al., resulting in $E_x(^{61}\text{Zn}^{i}) = 3348(19)$ keV. None of the aforementioned experimental values for $E_x(^{61}\text{Zn}^{i})$ agree closely with the shell-model prediction of 3097 keV obtained with the cdGX1A interaction. A confirmation of our IAS assignment through a decay spectroscopy study would be desirable.

Fitting the obtained mass excesses for ^{61}Ga^{i}, ^{61}Zn^{i}, and ^{61}Ni with the quadratic IMME, we deduce a ^{61}Ge mass estimate of ME(^{61}Ge) $= -34150(117)$ keV (see table 5.4). Within the uncertainties, this result is compatible with the AME2020 extrapolation of ME(^{61}Ge) $= -33790^{\#}(300^{\#})$ keV and a mass estimate of ME(^{61}Ge) $= -34065(100)$ keV based on the theoretical CDEs by Brown et al. [199]. The latter have been used to deduce a ^{60}Ga(p,γ) Q-value of $Q = 1349.47$ keV, which was used to calculate the literature rate listed for this reaction in the JINA REACLIB database [135]. Inserting our measured ^{60}Ga mass excess and our IMME prediction for ME(^{61}Ge) into Eqn. 5.20, we obtain an estimate of $Q = 1434(121)$ keV for the same Q-value. Our estimate confirms the Q-value used in the calculation of the literature rate within the uncertainties. We further recall that the ^{60}Ga mass estimate based on the CDEs by Brown et al. is in perfect agreement with our direct mass measurement (see section 5.3). For consistency with earlier studies [50, 51], we hence opt to use the CDE estimate of the ^{61}Ge mass rather than our IMME prediction as input for the X-ray burst simulations presented in the subsequent section.

5.4.4 Implications for the *rp* process in X-ray bursts

We investigate the impact of the reduced ^{60,61}Ga mass uncertainties on X-ray burst model predictions and the *rp*-process flow near the ^{60}Zn waiting point using a one-zone model.

X-ray burst light curves were simulated using model A from Ref. [51]. This self-consistent one-zone model has been shown to reproduce multi-zone model results sufficiently well to study the sensitivity of model predictions to nuclear input uncertainties [50]. The model is characterized by a high initial hydrogen mass fraction of $X_H = 0.66$, resulting in peak temperatures of ≈ 2 GK and a strong *rp*-process that extends up to the $A = 100$ region. Nuclear reaction rates were adopted from JINA REACLIB [135]. Nuclear masses were generally taken from AME2020 [151]. The masses of unmeasured, proton-rich nuclides were obtained from the theoretical CDEs from Brown et al. [220]. To evaluate the sensitivity of model predictions to the new mass inputs, simulation runs were performed with the masses of ^{60,61}Ga and ^{59,60}Zn varied by $\pm 3\sigma$.The mass variations resulted in updated proton capture Q-values, (or equivalently one-proton separation energies, S_p), where the signs of the mass variations were chosen such as to either minimize or maximize $S_p(^{60}\text{Ga})$ and $S_p(^{61}\text{Ga})$. New Hauser-Feshbach estimates of the relevant proton capture rates were calculated from the updated Q-values using the TALYS package [146]. The reverse photodisintegration rates were also re-calculated from the updated capture rates and Q-values using the principle of detailed balance (Eqn. 2.5).

The first direct mass measurement of ^{60}Ga allows us to investigate the possibility of a secondary bypass of the ^{60}Zn waiting point through the sequential two-proton capture reaction $^{59}\text{Zn}(p,\gamma)^{60}\text{Ga}(p,\gamma)^{61}\text{Ge}$. Under the modelled astrophysical conditions a (p,γ)-(γ,p) equilibrium is established between ^{59}Zn and ^{60}Ga. According to Eqn. 2.6, the forward reaction flow then depends exponentially on the $^{59}\text{Zn}(p,\gamma)$ Q-value, or equivalently on $S_p(^{60}\text{Ga})$. Although we find ^{60}Ga to be proton bound, our new result of $S_p(^{60}\text{Ga}) = 78(30)$ keV causes only a negligible fraction of 10^{-4} of the total reaction flow from ^{59}Zn to branch out into this capture sequence. Even $\pm 3\sigma$ variation of $S_p(^{60}\text{Ga})$ does not alter this finding. A secondary bypass of ^{60}Zn through sequential two-proton capture on ^{59}Zn, as hypothesized in Ref. [155], can therefore now be excluded with certainty.

The impedance imposed by the ^{60}Zn waiting point on the *rp*-process reaction flow is primarily bypassed through the $^{60}\text{Zn}(p,\gamma)^{61}\text{Ga}(p,\gamma)^{62}\text{Ge}$ proton capture sequence. Due to the (p,γ)-(γ,p) equilibrium between ^{60}Zn and ^{61}Ga, the efficiency of this bypass, and thus the effective half-life of ^{60}Zn, is determined by $S_p(^{61}\text{Ga})$ and the $^{61}\text{Ga}(p,\gamma)^{62}\text{Ge}$ reaction rate (see Eqn. 2.6 again).

The literature uncertainty of $S_p(^{61}\text{Ga})$ has been limited by the 40 keV mass uncertainty of ^{61}Ga, resulting in substantial prediction uncertainties in the light curves of hydrogen-rich X-ray bursts [51]. Our new ^{61}Ga mass value yields a three times more precise value of $S_p(^{61}\text{Ga}) = 229(12)$ keV (see table 5.3). The effect of $\pm 3\sigma$ variation of the $S_p(^{61}\text{Ga})$ values from AME2020 and from this work on the predicted light curve is shown in Fig. 5.9. One observes the characteristic deviation from the standard power-law decay of the burst luminosity that can be caused by the ^{60}Zn waiting point. The new ^{61}Ga mass value is seen to substantially constrain the predicted light curve.

For a more quantitative evaluation, the ratio of the varied light curves is plotted in Fig. 5.10. The more precise ^{61}Ga mass value is found to reduce the prediction uncertainty of the burst luminosity by more than a factor of two. The 12 keV uncertainty of the $S_p(^{61}\text{Ga})$

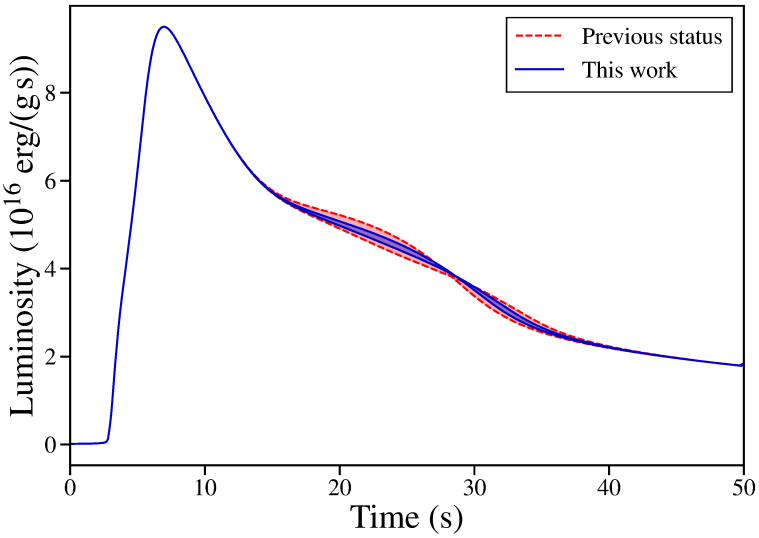

Figure 5.9. Effect of 3σ variation of $S_p(^{61})$Ga on predicted X-ray burst light curves. The light curves obtained after 3σ variation of $S_p(^{61}\text{Ga})$ from AME2020 (red dashed line) and from this work (blue dashed line). The areas between the varied light curves are filled for clarity. Figure reprinted from [425].

value still induces a small effect on the light curve, indicating that, at the chosen astrophysical conditions, a measurement to $\sim$1 keV uncertainty would be needed to fully eliminate the mass-induced light curve uncertainty. Traditionally reserved to Penning trap mass spectrometry, such precision levels have recently become achievable with MR-TOF-MS as demonstrated in Ref. [360]. This encourages a re-measurement of this nuclide in the near future.

However, the most critical nuclear input uncertainty remaining near the ^{60}Zn waiting point is now the unmeasured $^{61}\text{Ga}(p,\gamma)$ rate. Our more precise ^{61}Ga mass value also affects $S_p(^{62}\text{Ge})$ which is critical for reliable estimates of the $^{61}\text{Ga}(p,\gamma)$ rate. However, at the present, the precision of $S_p(^{62}\text{Ge})$ remains limited by the 200 keV literature uncertainty of the unmeasured ^{62}Ge mass. A direct mass measurement of this nuclide is highly desirable to further pin down the *rp*-process flow near the ^{60}Zn waiting point.

5.5 Conclusion

The mass measurements of $^{60-63}$Ga performed with TITAN's MR-TOF-MS have yielded a ^{61}Ga mass value three times more precise than the AME2020 value and provided the first direct mass measurement of ^{60}Ga. Our new mass data has a variety of implications for both nuclear structure and nuclear astrophysics. Combining our first-time measurement of ^{60}Ga with earlier experimental results provides very strong evidence that ^{60}Ga is the last proton-bound nuclide in its isotopic chain and marks the location of the proton drip line. Our ^{60}Ga mass result disagrees with the current literature value in AME2020 but agrees with

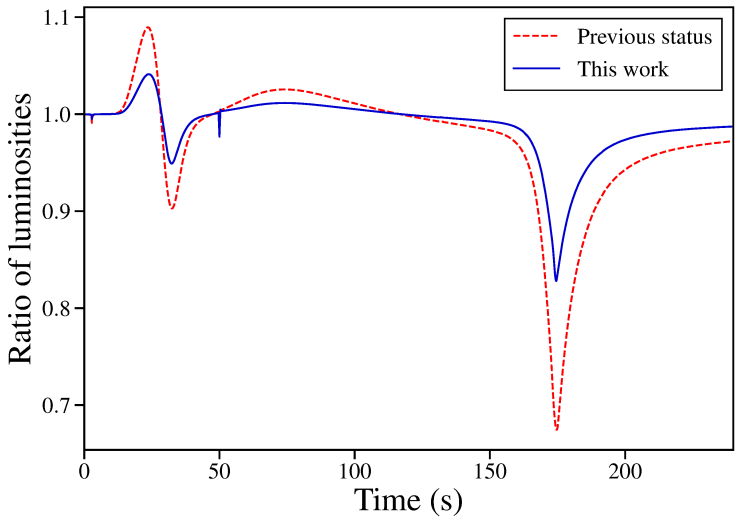

Figure 5.10. Ratio of the varied X-ray burst light curves shown in Fig. 5.9. Figure reprinted from [425].

values from earlier indirect measurements and extrapolations in atomic mass evaluations before AME2003. In this region of the nuclear chart, earlier studies [441, 447–449] have found similar discrepancies with mass evaluations after AME2003. Our measurement adds an important anchor point for mass extrapolations and will help to resolve the observed discrepancies in future mass evaluations.

Our ^{60}Ga mass completes the IAS data for the lowest-lying isospin triplets up to $A = 60$ and allowed us extend the high-mass end of the evaluated $T = 1$ IMME. Studying the trends of the resulting IMME coefficients in the *pf* shell, we found a smooth continuation of the experimental trends and generally decent agreement with the predictions of the INC shell-model interaction, cdGX1A. However, increasing discrepancies with the shell-model predictions appear towards the high-mass end of the studied multiplets. These discrepancies could indicate a need to re-adjusted the phenomenological INC terms in the Hamiltonian to nuclides in the upper *pf* shell. Alternatively, they could be a result of a general degradation in the predictive power of the isospin-conserving part of the Hamiltonian due to the increasing importance of cross-shell excitations to the $g_{9/2}$ orbital. More experimental and theoretical work on IASs in the upper *pf* shell is needed to assess the role of INC forces at $A \geq 60$ in detail.

The new mass data refines our knowledge of the *rp*-process flow in X-ray bursts. Studying the effects of the new mass data in a one-zone model of a hydrogen-rich X-ray burst, we could rule out a hypothesized secondary bypass of the ^{60}Zn waiting point through the ^{59}Zn$(p,\gamma)^{60}$Ga(p,γ) proton capture sequence. The three times more precise ^{61}Ga mass constrains the efficiency of the primary ^{60}Zn bypass through the ^{60}Zn$(p,\gamma)^{61}$Ga(p,γ) sequence, leading to a more than twofold reduction in the light curve prediction uncertainty. The remaining 12 keV mass uncertainty still produces a small effect on the light curve. However, the most critical nuclear input uncertainty near ^{60}Zn is now given by the unmeasured rate of the ^{61}Ga(p,γ) reaction. Estimates of this key reaction rate require decent knowledge of the

corresponding Q-value. Our ^{61}Ga mass measurement marks an important step towards a reliable experimental determination of this Q-value, but presently its uncertainty is dominated by the $200\,$keV uncertainty of the unmeasured ^{62}Ge mass.

Chapter 6

Electron cooling of singly charged ions in a Penning trap

This chapter discusses experimental studies of electron cooling of singly charged ions (SCI) in a Penning trap. Using a test setup with a dedicated cooler Penning trap (CPET), we experimentally studied the sympathetic cooling of stable, singly-charged alkali ions by a co-trapped electron plasma. Technical challenges imposed by the simultaneous storage of electrons and positively charged ions in a nested trapping potential are discussed, and the applied countermeasures that enabled the observation of electron cooling of SCI are presented. We present a model of the cooling dynamics and benchmark it against the experimental findings. Matching the model predictions to the experimental data obtained with SCI, estimates of the crucial system parameters are deduced, enabling an extrapolation to the expected performance for electron cooling of highly charged ions (HCI).

The chapter sets out with a motivation for cooling of HCI at TITAN and other ion trapping facilities and briefly discusses the benefits and drawbacks of electron cooling in comparison to other cooling techniques in section 6.1. Section 6.2 gives an general overview of the investigated cooling scheme and presents the expectations from theoretical studies of the electron cooling process. The cooler Penning trap and the test setup used for the experimental studies are discussed in section 6.3. As important prerequisites for studies of electron cooling of trapped ions, the preparation of electron plasmas in CPET is examined in section 6.4.3, and the trapping of stable SCI from a surface ion source as well as the first tests of co-trapping of ions and electrons are discussed in section 6.4.4. Section 6.4.5 first introduces the experimental procedures developed to probe the energy evolution of trapped ions and gives an overview of the experimental cycles used in the ion-electron interaction studies. Subsequently, it reports the results of the interactions studies and presents a simplified model of the observed cooling dynamics. Section 6.5 concludes with a summary of the obtained results and comments on the prospects of electron cooling of short-lived, radioactive HCI.

6.1 Motivation

Since the cyclotron frequency increases linearly with the ion's charge state, the use of highly charged ions (HCI) provides an effective way to boost the achievable mass precision and resolving power of Penning trap mass spectrometry (PTMS) (see section 4.2.2 for details). This fact is routinely exploited in ultra-high precision studies with stable or very long-lived radioactive isotopes [255]. For example, mass measurements for tests of fundamental symmetries or Q-value determinations for neutrino science demand relative uncertainties well below $\frac{\delta m}{m} = 10^{-10}$ [331, 472]. These studies heavily rely on the use of HCI since such mass precisions are hardly attainable with SCI, whose smaller cyclotron frequencies ν_c cause a given absolute frequency uncertainty $\delta\nu_c$ (typically limited by systematic uncertainties) to result in a substantially larger fractional mass uncertainty $\delta m/m \sim \delta\nu_c/\nu_c$. The high cyclotron frequencies and the strong internal electric fields associated with trapped HCI are also frequently exploited in g-factor measurements for tests of bound-state quantum electrodynamics (QED) [473, 474]. The mentioned high-precision applications additionally benefit from high ion charge states as they increase the coupling between trapped ions and resonant detection circuits, thus increasing the signal-to-noise ratio of eigenfrequency determinations with the FT-ICR technique (consult section 3.3.3). HCI further offer a unique set of advantages for PTMS within the realm of rare isotope science, where they can potentially reduce the measurement time by up to an order of magnitude [63], enable the resolution of low-lying nuclear isomers [63] or can be used to isobarically purify rare isotope beams [382] (see section 4.2.2 for details).

The creation of HCI, whether through charge breeding in an EBIT [475] or an electron cyclotron resonance (ECR) cell [476], or by electron stripping in a heavy-ion accelerator [477], is based on energetic particle collisions and thus inherently reduces the ion beam quality. The impact of ion storage and charge breeding in TITAN EBIT on the longitudinal ion energy spread is illustrated by the data from measurements with a retarding-field energy analyzer [64] in Fig. 6.1. In retarding field analysis (RFA), the ion count rate $N(\phi_r)$ is recorded as function of a repulsive potential ϕ_r in the beam path. The longitudinal ion energy distribution is then given by the derivative of the measured count profile: $n(E_\parallel) = -\frac{\partial N}{\partial \phi_r}$. In principle, the underlying energy distribution can be extracted directly from an RFA count profile using finite-difference methods. However, this approach is oftentimes hampered by statistical fluctuations in the count data. It it is therefore often more practical to presume a certain functional form for the ion energy distribution and then determine its parameters by fitting the complement of the respective cumulative distribution to the RFA count data. For the data presented in Fig. 6.1, assuming a Gaussian energy distribution (orange dashed lines) is seen to yield good fits to the measured RFA count data. The fit results revealed that storing and charge breeding $^{85}Rb^{+}$ ions to $q = +3e$ in TITAN EBIT increased the energy spread of the bunched ion beam from $20\,^{eV}/_{q}$ to $44\,^{eV}/_{q}$. More extensive studies of the beam properties of charge-bred ion bunches ejected from TITAN EBIT found that, even under optimized conditions, the charge breeding and extraction from EBIT resulted in beam energy spreads of several $10\,^{eV}/_{q}$ and a transverse emittance of $\epsilon_{\text{RMS}} = 5.27(73)\,\pi$ mm mrad [64].

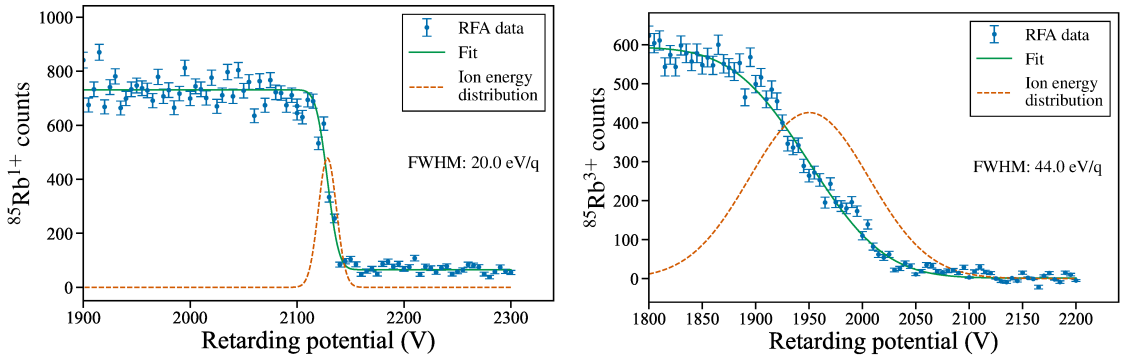

Figure 6.1. Retarding field analysis (RFA) of the energy spread of ^{85}Rb ion bunches without storage and charge breeding in TITAN EBIT (left) and after 1 ms-long charge breeding to $q = +3e$ (right).

The beam quality reduction resulting from charge breeding is detrimental to precision measurements in ion traps which usually demand a high level of reproducibility in terms of the initial ion conditions. In the case of PTMS, an increased phase space volume occupied by the trapped ions degrades the achievable measurement precision in several ways. A larger longitudinal energy spread upon injection results in increased axial oscillation amplitudes in the measurement Penning trap. This, in turn, subjects ions to a larger magnetic field inhomogeneity and induces systematic shifts in the measured cyclotron frequency. Similarly, an increased transverse beam emittance causes ions to attain larger radial motion amplitudes in the precision Penning trap, again introducing systematic shifts in a cyclotron frequency measurement. In mass measurements with the PI-ICR method, an excessive spread in the radial ion velocities smears out the projected phase images on the position-sensitive detector and thereby degrades the achievable mass precision.

To access the full potential of PTMS with HCI, it is desirable to counteract the charge-breeding-induced loss in beam quality by cooling the ions prior to the mass measurement. However, conventional and widely-used cooling techniques are not universally applicable to short-lived, radioactive HCI. Sympathetic cooling with a neutral buffer gas [397] would cause excessive losses of the charge state of interest since cross sections for charge-exchange reactions increase rapidly with the ion charge state. While direct laser cooling is regularly used to cool trapped SCI into the millikelvin regime [329], it cannot be universally applied to HCI since suitable laser schemes are often not readily available [478]. This limitation has been overcome by sympathetic laser cooling [329, 479], where a trapped ensemble of laser-cooled SCI acts as a sympathetic coolant for co-confined HCI [480]. In principle, sympathetic laser cooling could provide suitable energy-loss rates to be applied for cooling of short-lived, radioactive HCI, as had orginally been proposed for the MLLTRAP mass measurement facility [481]. However, after a relocation of the MLLTRAP setup to a different laboratory, the plans to test this cooling scheme have, to the author's knowledge, not been further pursued and the technique remains experimentally unexplored in regards to cooling of short-lived, radioisotopes. A potential drawback of this cooling scheme lies in its in-

compatiblity with experimental repetition rates ≥ 1 Hz, which in turn limits the achievable data accumulation rates; since the laser-cooled ion plasma is destroyed upon extraction of the ions of interest, it has to be regenerated and re-cooled in each experimental cycle — a process which typically requires multiple seconds [482]. Resistive cooling is an attractive option for cooling of stable HCI because the technique is, in principle, directly applicable to any element and the coupling between ions and the external RLC circuit increases with the ion charge state. Nevertheless, typical time constants for resistive cooling of HCI lie in the range of seconds [483], making this technique unsuited for cooling short-lived radioactive isotopes with half-lives < 1 s.

Based on calculations with an unmagnetized[1] two-component plasma model [484] (see section 6.2), electron cooling in a dedicated cooler Penning trap has been identified as a promising alternative for cooling radioactive HCI at TITAN [65]. In storage rings, electron cooling has been widely used to reduce the phase space of heavy, highly charged ion beams [293]. As discussed in section 3.2, electron cooling forms a cornerstone for precision measurements in storage rings and has been widely studied in theory and experiment (see [293] for a review).

Electron cooling of charged particles stored in a Penning trap was pioneered by Gabrielse et al. in 1989 [485], who succeeded in cooling antiprotons to energies below 100 meV. The use of electron cooling was motivated by the excessive annihilation losses that antiproton samples would suffer when subjected to a neutral buffer gas. This is in close analogy to the situation for HCI, where charge-exchange losses prevent the application of buffer gas cooling. Since the early work by Gabrielse et al., in-trap electron cooling has further been applied to protons [486], Au^- ions and C_{70}^- clusters [487]. In recent years, antimatter trapping experiments have been extensively using electron cooling for the preparation of cold antiprotons [304], or electron and subsequent positron cooling for the synthesis of antihydrogen [488, 489]. Nevertheless, cooling with trapped lepton plasmas has remained less well explored than electron cooling in storage rings and questions remain concerning the applicability of the technique to multiply charged ions. Systematic experimental studies with different ion species and over a range of plasma properties (density, temperature, degree of magnetization) would provide important data to test existing theory descriptions of the cooling process as well as the plasma dynamics in the high-magnetic field regime.

As part of this thesis, the prospects of in-trap electron cooling of radioactive HCI at TITAN were investigated in off-line tests with a dedicated cooler Penning trap (CPET). Similar efforts are under way within the HITRAP project [289, 490] at the GSI Helmholtz Centre for Heavy Ion Research (GSI) which plans to use an array of ion traps to perform precision studies on heavy, stable HCI up to fully-stripped uranium. The science program at HITRAP [491, 492] includes laser spectroscopy of Coulomb crystallized ions [482], tests

[1] A plasma species with charge q, mass m, number density n and temperature T is regarded as *magnetized* when its thermal Larmor radius $r_c = \frac{mv_\perp}{qB}$ with $v_\perp = \sqrt{2k_BT_e/m_e}$ is smaller than the Debye length $\lambda_D = \sqrt{\frac{\epsilon_0 k_B T}{nq^2}}$. In collisions of charged particles with $r_c < \lambda_D$ the ambient magnetic fields starts to affect the collision dynamics. In contrast, for $r_c > \lambda_D$, external magnetic fields can essentially be neglected in calculations of the plasma collision dynamics.

of bound-state QED [493] and ion-surface interaction studies [289]. Since the HCI are produced through in-flight electron stripping, they have to be decelerated from energies of several $100\,\mathrm{MeV/u}$ to less than $1\,\mathrm{eV}$ [494]. Ion bunches are first decelerated to a few $\mathrm{keV/u}$ in the Experimental Storage Ring (ESR) and a downstream linear decelerator. For the final deceleration and cooling before injection into the precision ion traps, a cooler Penning trap [494] for electron cooling and subsequent resistive cooling of HCI is being developed at HITRAP. In contrast to CPET, the time constraints imposed on the electron cooling process in HITRAP's cooler trap are less restrictive since only cooling of stable or very long-lived HCI is foreseen. However, electron cooling has, to date, not been demonstrated in HITRAP's cooler trap and in-trap electron cooling of HCI remains experimentally untested.

6.2 The cooling scheme

This section gives a general overview of the electron cooling scheme employed in CPET. After a brief outline of the cooling scheme, I discuss the key results from simulation of the cooling process in a two-component plasma model. Preceding studies in such a model provided the original motivation to pursue cooling of radioactive HCI at TITAN and helped to identify the parameters that most critically affect the cooling dynamics. The updated simulations with refined input parameters presented here help to illustrate the key aspects of the cooling process and provided guidance during the experimental work discussed later in this chapter.

The general scheme for electron cooling of ions in a Penning trap is schematically illustrated in Fig. 6.2 and consists of the following stages:

a) *Plasma preparation:* Electrons are loaded into the trap. As they are stored in a high magnetic field region, they self-cool by emission of cyclotron radiation and settle into inverted wells within the axial trap potential, forming a near-room temperature electron plasma[2].

b) *Ion injection:* By suitable switching of the endcap potentials, ions are injected into the trap and co-confined with the prepared electron plasma. The simultaneous storage of oppositely charged particles necessitates a nested electric trap potential with inverted wells for electron storage ("electron nests") framed by non-inverted wells where cold ions may accumulate ("ion wells").

c) *Electron cooling of trapped ions:* The ions perform axial oscillations in the trap potential and lose kinetic energy through Coulomb collisions with electrons upon each pass through the plasma. While the initial cooling stage primarily dissipates energy from the

[2] Strictly speaking, the term non-neutral plasma would be more accurate since any plasma confined under non-perfect vacuum conditions will contain a certain fraction of impurity ions, resulting e.g. from electron impact ionization of rest gas particles. I use the term electron plasma throughout this work, both for simplicity and to indicate the typically > 3 orders of magnitude difference between the numbers of electrons and impurity-ions in the considered plasmas.

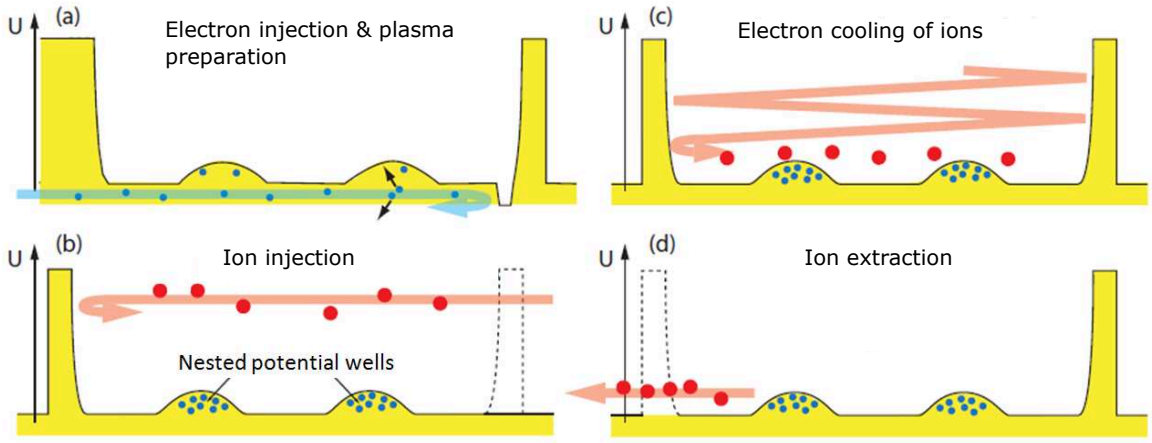

Figure 6.2. The general scheme for electron cooling of ions in CPET. The upper border of the yellow shaded region indicates the on-axis trap potential during the different stages. Figure adapted from [306].

ions' centre-of-mass motion, the energy exchange with the much colder plasma electrons eventually also reduces the energy spread of the trapped ion sample.

d) *Ion extraction:* After sufficient cooling, the ions are extracted through the exit-side end-cap either for diagnosis on an external detector or for transport to downstream systems, e.g. to TITAN's precision Penning trap for mass measurement. The electron plasma may be kept in the trap and re-used in a subsequent cooling cycle, or can likewise be ejected and re-generated at the beginning of the next cooling cycle.

An actual machine cycle is naturally more elaborate than this simplified picture. A detailed overview of a typical cooling cycle along with the corresponding trap potentials applied at different stages will be given in section 6.4.5.

The magnetic-field-induced breaking of isotropy, the large numbers of interacting particles and the often more than 9 orders-of-magnitude wide range of relevant time scales[3] make the theoretical description of electron cooling in a Penning trap a challenge and render a fully microscopic treatment of the many-body dynamics underlying the cooling process numerically intractable.

Analytic expressions for the stopping power exerted on HCI in magnetized electron plasmas have been deduced mainly based on two complementary approaches [495]. The first one exploits dielectric theory and models the cooling force exerted on an ion as its interaction with the polarization field created in its wake as it passes through the plasma [496, 497]. The second approach is based on binary ion-electron collisions under the influence of an effective interaction potential and the net cooling force is deduced as an integral of the two-body force over all possible impact parameters and the electron velocity distribution [498]. In recent theoretical work, approximate cooling forces based on binary ion-electron collisions

[3] The shortest relevant timescale is set by the electron cyclotron period, of e.g. $T_c = 2\pi m_e/(eB) \approx 5\,\mathrm{ps}$ in a magnetic field of strength $B = 7\,\mathrm{T}$, whereas the electron cooling of singly charged ions and other relevant processes such as radial diffusion of ions inside the plasma proceed at typical timescales $> 0.1\,\mathrm{s}$.

have been deduced using a Fokker-Planck formalism [499, 500]. The expressions given for the cooling force exerted on ions in a magnetized plasma in the literature have either been deduced in the limit of infinite magnetic field, or contain integrals without closed analytic solutions which make ion-trajectory tracing calculations numerically expensive.

Various authors have bypassed the mentioned complications by using variants of a simple two-component plasma model to explore the feasibility and characteristics of in-trap electron cooling. In 1989, Rolston and Gabrielse [501] used this approach to describe the cooling of trapped antiprotons by a co-confined electron plasma. Bernard et al. [502] later deployed a two-component plasma model to study electron and positron cooling of HCI and to obtain estimates of the cooling timescale. In 2006, Ke et al. [65] used a similar model to study the prospects of electron cooling of radioactive HCI. Their findings motivated the development of a cooler Penning trap at TITAN and informed the conceptual design of CPET. At the time, some of the input parameters for the model, such as the typical energy spread of HCI from EBIT or the achievable electron densities in CPET, were unknown and had to be conservatively estimated by Ke et al.

Since several of these parameters have by now been informed by measurements, I here present an updated set of calculations with a near-identical model. The calculations not only convey a qualitative understanding of the cooling process but also helped us to identify suitable parameters for its experimental realization. To this end, model calculations are presented both for cooling of a set of fully stripped ions (C^{12+}, Kr^{36+} & U^{92+}) as well as for the singly charged alkali ions used in the exploratory measurements presented in this chapter (Na^+, K^+ & Rb^+).

The two-component plasma model describes the time evolution of the ion and electron temperatures, denoted T_e and T_i respectively, through the following set of coupled differential equations:

$$\frac{dT_e}{dt} = \frac{\kappa}{\tau_{ie}}\frac{N_i}{N_e}\left(T_i - T_e\right) - \frac{1}{\tau_e}\left(T_e - T_{e,\infty}\right), \tag{6.1}$$

$$\frac{dT_i}{dt} = -\frac{\kappa}{\tau_{ie}}\left(T_i - T_e\right), \tag{6.2}$$

where $T_{e,\infty}$ is the equilibrium electron plasma temperature, $\kappa \leq 1$ is a correction factor that accounts for the possibility of only partially overlapping plasma components, and N_i and N_e are the total number of ions and electrons in the plasma, respectively. The electron-temperature relaxation time constant, τ_e, sets the rate at which cyclotron cooling drives the electron plasma towards its equilibrium temperature $T_{e,\infty}$, which is set by the microwave radiation environment and ideally equals the ambient temperature of the surrounding electrodes [503]. In principle, the relaxation of T_e must be thought of as a two-stage process since the emission of cyclotron radiation directly cools only the transversal electron motions, with an exponential energy-loss time constant given by

$$\tau_{e,\perp} = \frac{3\pi\epsilon_0 m_e^3 c^3}{e^4 B^2}, \tag{6.3}$$

whereas the relaxation of the longitudinal motion requires subsequent equipartition through electron-electron collisions. However, since, under typical CPET conditions, the collisional

equipartition time (see e.g. [504]) is ~ 3 orders of magnitude faster than $\tau_{e,\perp}$, it is fair to assume instantaneous equilibration of the transversal and longitudinal electron temperatures and the overall electron-plasma temperature relaxation time can be estimated as $\tau_e = \frac{3}{2}\tau_{e,\perp}$. For the case of CPET's magnetic field, with a strength of $B = 7\,\mathrm{T}$, this relation yields $\tau_e \approx 79\,\mathrm{ms}$.

The time constant for energy exchange through ion-electron collisions, τ_{ie}, is estimated from the following expression from Spitzer's theory of unmagnetized plasma [484]:

$$\tau_{ie} = \frac{3(4\pi\epsilon_0)^2 m_e m_i c^3}{8\sqrt{2\pi} n_e q^2 e^2 \ln(\Lambda)} \left(\frac{k_B T_i}{m_i c^2} + \frac{k_B T_e}{m_e c^2}\right)^{\frac{3}{2}}, \tag{6.4}$$

where m_e and m_i denote the electron and ion masses, respectively, n_e is the electron number density, $q = ze$ is the ion charge and $\ln(\Lambda)$ is the Coulomb logarithm. The Coulomb logarithm imposes appropriate limits on the range of Coulomb interactions under the influence of Debye screening and can be calculated as [502]

$$\ln(\Lambda) = \ln\left(4\pi \left(\frac{\epsilon_0 k_B}{e^2}\right)^{\frac{3}{2}} \frac{1}{z}\sqrt{\frac{T_e}{n_e}} \left(T_e + \frac{m_e}{m_i} T_i + 2\sqrt{\frac{m_e}{m_i}}\sqrt{T_e T_i}\right)\right). \tag{6.5}$$

A possible complication of in-trap electron cooling of HCI is the potential loss of the charge state of interest through electron-ion recombination. Since precision instruments such as a TITAN's mass measurement Penning trap can typically only be tuned to accept or measure ions in a specific charge state, charge-altering reactions may reduce the achievable statistics in measurements of low-yield ion species and should ideally be limited to a level of no more than a few 10%. In this regard, the processes of concern are radiative, dielectronic and three-body recombination.

In radiative recombination (RR), an ion of charge state z non-resonantly captures a free electron, radiating away excess energy through emission of a photon and reducing the ion charge state to $z - 1$. The rate coefficient for radiative recombination of HCI may be estimated as [505]

$$\alpha_{\mathrm{RR}} = 5.2 \times 10^{-14} Z_{\mathrm{eff}} \sqrt{\frac{E_\infty}{T_{\mathrm{eff}}}} \left(0.43 + \frac{1}{2}\ln\left(\frac{E_\infty}{T_{\mathrm{eff}}}\right) + 0.469\left(\frac{E_\infty}{T_{\mathrm{eff}}}\right)^{-\frac{1}{3}}\right)\ \mathrm{cm}^3/\mathrm{s}, \tag{6.6}$$

where $Z_{\mathrm{eff}} = z$ for fully stripped ions, the ionization potential is estimated as $E_\infty \approx R_y z^2$ with $R_y = 13.6\,\mathrm{eV}$, and $T_{\mathrm{eff}} \approx T_e + \frac{m_e}{m_i} T_i$ is the effective collision temperature in the centre-of-mass system. Since Eqn. 6.6 only applies to HCI, the role of RR for the SCI considered here was judged based on temperature-averaged fits to theoretical RR coefficients from [506]. Multiplying the RR rate coefficients of Na^+ and K^+ in Fig. 6.3 by the expected electron number densities of $n_e \sim 1 \times 10^8\,\mathrm{cm}^{-3}$ yields negligible recombination probabilities of $< 0.1\%$ per second. Due to its analog atomic structure, similar results can be expected for Rb^+. Hence, RR could be neglected for the SCI of interest.

Dielectronic recombination (DR) is a two-step process and involves the resonant capture of a free electron with simultaneous excitation of a bound electron inside the same ion into

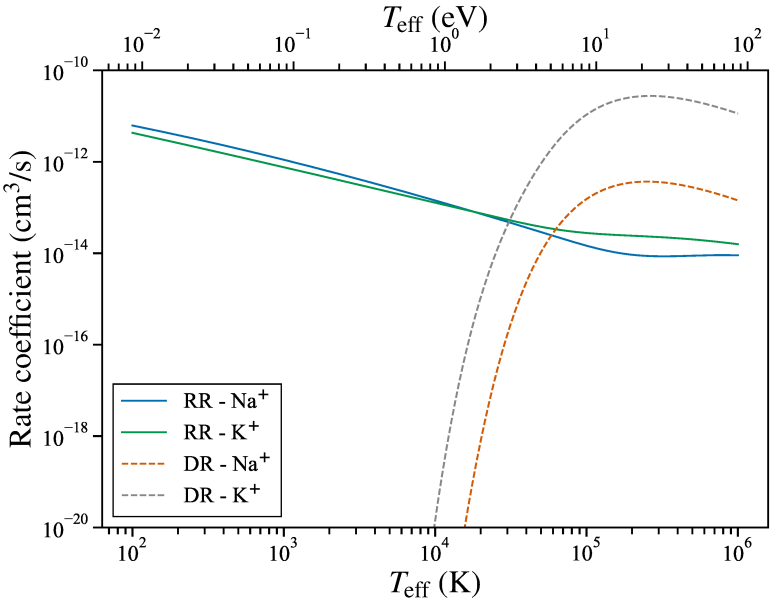

Figure 6.3. Maxwellian-averaged, theoretical rate coefficients for radiative recombination (RR; solid lines) and dielectronic recombination (DR; dashed lines) of Na^+ and K^+. The coefficients were calculated with parametrizations from Ref. [506].

a higher-lying orbit. Subsequently, the ion de-excites through the emission of a photon. Due to its resonant nature, DR is strongly dependent on an ion's atomic structure and rate estimates cannot be deduced from a simple, universal formula. For fully stripped ions, the DR channel is blocked and did not have to be considered. The DR rates of the singly charged alkali ions were again evaluated based on theoretical rate coefficients from Ref. [506]. As seen from the dashed lines in Fig. 6.3, the DR coefficients of Na^+ and K^+ are negligible at the relevant temperatures for an equilibrated electron plasma in a room-temperature Penning trap ($T_{\mathrm{eff}} \approx T_e < 1\,\mathrm{eV}$).

In three-body recombination (TBR), the excess kinetic energy of a recombining electron is absorbed by a nearby, unbound electron. The rate coefficient for this process is given by [507]:

$$\alpha_{\mathrm{TBR}} = 2 \times 10^{-27} z^3 T_{\mathrm{eff}}^{-\frac{9}{2}} n_e \ \mathrm{cm}^6/\mathrm{s}, \tag{6.7}$$

where T_{eff} is in units of eV. As the recombined electron usually ends up bound in a Rydberg state that is readily re-ionized by the trap potential [65], TBR will typically have to be followed by radiative de-excitation in order to lead to a permanent loss of the charge state of interest. However, to be conservative neither field ionization nor any other charge state re-populating processes were included in the present calculations.

Taking into account all mentioned recombination processes, the evolution of the survival fraction of ions in the initial charge state, P_z, is determined by

$$\frac{dP_z}{dt} = (\alpha_{\mathrm{RR}} + \alpha_{\mathrm{DR}} + \alpha_{\mathrm{TBR}})\, \kappa\, n_e. \tag{6.8}$$

Of course, HCI may also undergo charge-altering reactions with neutral residual gas parti-

Table 6.1. Input parameters for the calculations with the two-component plasma model based on typical experimental conditions in CPET. The parameter value are conservative estimates informed by measurements from Ref. [508] and the present work; only for the equilibrium electron temperature, no detailed experimental information was available.

Parameter	Symbol	Value
Initial ion energy	$E_{i,0}$	$100\,\mathrm{eV/q}$
Initial electron temperature	$T_{e,0}$	$300\,\mathrm{K}$
Equilibrium electron temperature	$T_{e,\infty}$	$300\,\mathrm{K}$
Electron number density	n_e	$1 \times 10^8\,\mathrm{cm}^{-3}$
Effective electron cyclotron cooling time	τ_e	$79\,\mathrm{ms}$
Ion-plasma overlap fraction	κ	0.5
Total number of ions	N_i	1×10^3
Total number of electrons	N_e	1×10^7

cles. As will be detailed in section 6.3.4, the rates of ion-neutral reactions can, however, be reduced to insignificant levels by realizing suitable ultra high vacuum conditions.

Integrating the coupled Eqn.s 6.1, 6.2 & 6.8 with the Euler method and using parameters similar to experimental conditions in CPET (see table 6.1), resulted in the ion and electron energy evolutions shown in Fig. 6.4 a) and b), respectively. Within less than $100\,\mathrm{ms}$, the different HCI have cooled from initially $100\,\mathrm{eV/q}$ to below $1\,\mathrm{eV/q}$, the desirable level for precision mass measurements in TITAN's measurement Penning trap. Due to the energy deposited by the hot HCI, the respective mean electron energies exhibit a rapid initial rise by more than one order of magnitude for the heavier HCI. Subsequently, the electron plasma recools to its equilibrium temperature. As the ion-electron collision time scales as $\tau_{ie} \propto 1/q^2$, the cooling of SCI proceeds much slower than that of HCI and SCI only reach the $1\,\mathrm{eV/q}$ level after $\geq 400\,\mathrm{ms}$. Since τ_{ie} takes values larger than the effective cyclotron cooling time constant τ_e, the SCI only induce a small rise in the electron temperature and their energies decay approximately exponentially over the full calculation time range of $700\,\mathrm{ms}$.

The role of recombination losses of the initial charge state can be assessed from Fig. 6.4 c). While the SCI and C^{6+} exhibit negligible recombination losses over the duration of the cooling process, Kr^{36+} and U^{92+} show sizable losses of $> 20\%$ after a few $100\,\mathrm{ms}$. The increased recombination losses for these ions are a consequence of the linear scaling of the RR rate coefficient with the effective nuclear charge (see eqn. 6.6). More detailed investigations of the contribution from TBR by Ke et al. [65] showed that these losses only become significant for plasmas stored in cryogenic Penning traps, as is expected from the scaling $\alpha_{\mathrm{TBR}} \propto T_{\mathrm{eff}}^{-9/2}$. However, even for U^{92+}, the recombination loss rate is slow compared to the cooling rate. According to the model, only a few percent of the ions would loose their initial charge state if they were immediately separated from the plasma once the $1\,\mathrm{eV/q}$ level is reached. The rapid initial energy loss could therefore provide a window of opportunity for

[3]The low-temperature enhancement of the TBR rate is, in fact, exploited in antihydrogen experiments which use TBR of antiprotons and positrons at plasma temperatures $< 100\,\mathrm{K}$ to synthesize antihydrogen [509].

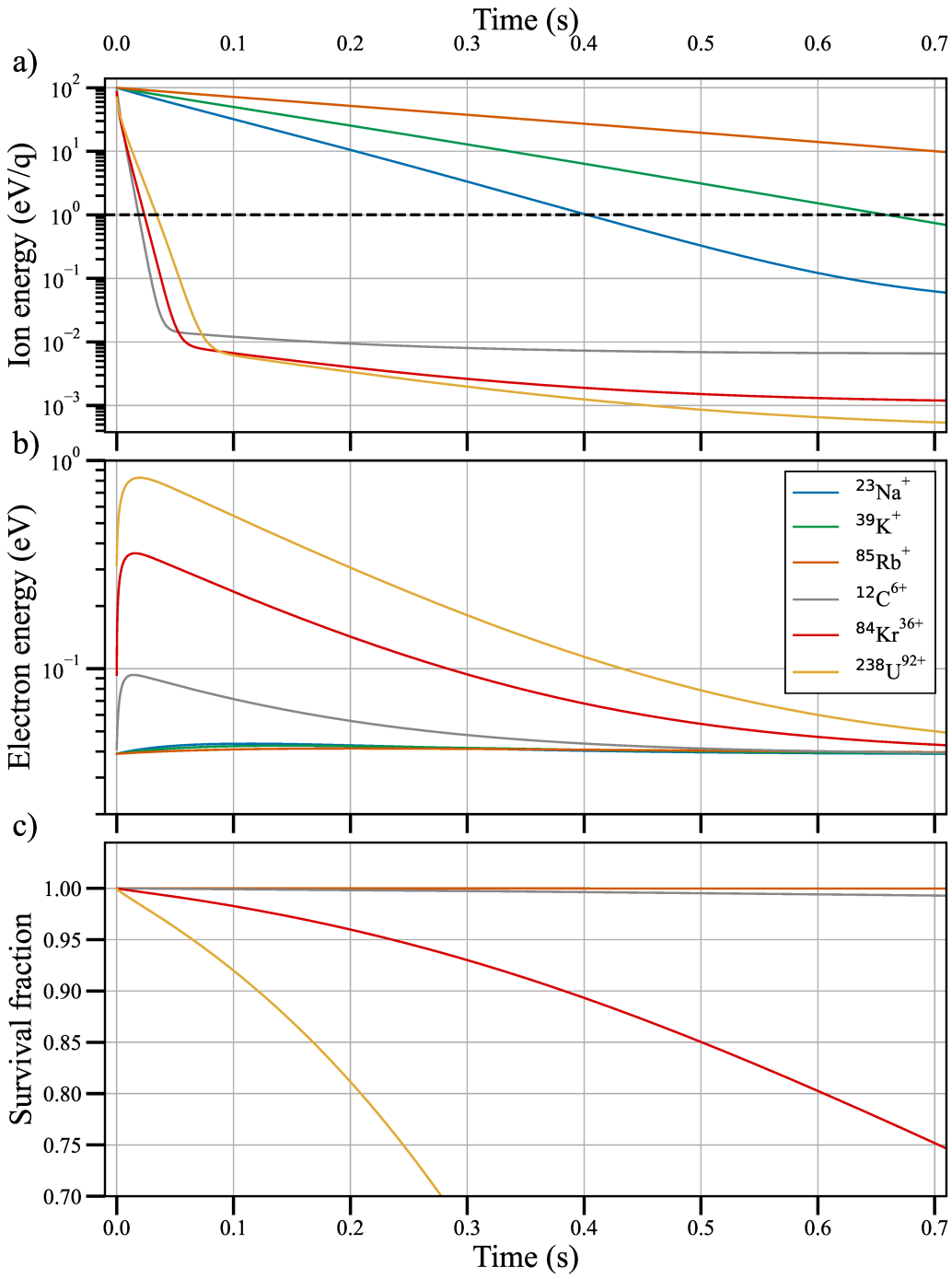

Figure 6.4. Electron cooling calculations for different ion species with a two-component plasma model. a) Evolution of the mean kinetic energy per ion $E_i = \frac{3}{2}k_B T_i$ as function of cooling time. The dashed line indicates the desirable energy spread for mass measurements in TITAN's precision Penning trap. b) Corresponding evolution of the mean kinetic energy per plasma electron $E_e = \frac{3}{2}k_B T_e$. c) Survival fractions of the initial ion charge state throughout the cooling process. See text for details.

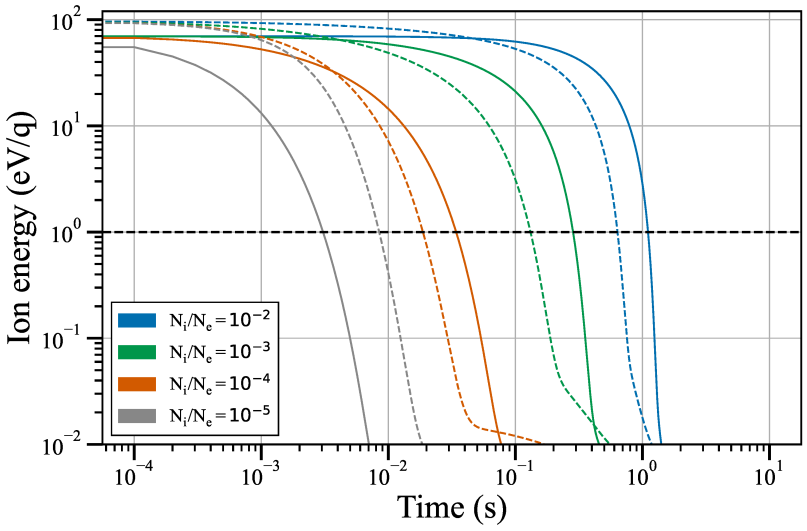

Figure 6.5. Effect of different ion-electron number ratios N_i/N_e on the ion energy evolution of C^{12+} (solid lines) and U^{92+} (dashed lines) in the two-component plasma model. For all cooling curves the ion number was fixed to $N_i = 100$. The dashed horizontal line indicates the desirable ion energy spread for precision measurements in TITAN's mass measurement Penning trap.

the cooling of short-lived, radioactive HCI [55].

Both the total number of electrons as well as the electron number density critically affect the predicted cooling timescales. This is less surprising for the electron number density which directly enters Eqn. 6.2 through τ_{ie}, resulting in a approximate scaling $\frac{dT_i}{dt} \propto n_e$. The more obscure dependence of the ion energy loss on N_e is illustrated in Fig. 6.5, which shows cooling curves of C^{6+} and U^{92+} for different ratios of N_i/N_e with N_i fixed to 100 ions. One observes that the cooling becomes increasingly slow with rising N_i/N_e. This a result of the excessive electron plasma heating arising when the dissipated ion energy is distributed over too few electrons, as an increase in T_e reduces the electron-ion temperature equilibration rate ($1/\tau_{ie}$). For the considered HCI, cooling times below 100 ms are observed for $N_i/N_e \leq 10^{-4}$. Although the roles of n_e and N_e have been investigated separately here, it should be noted that a reduced total electron number typical results in an electron plasma of lower particle density.

A few comments should be devoted to the simplifying assumptions underlying the presented model calculations. The most obvious simplification is the assumption of an unmagnetized plasma. In reality, the magnetic field will alter the collisional coupling of the longitudinal and transversal electron motions and require a description with asymmetric velocity distributions with separate temperatures for the longitudinal and transversal degrees of freedom. As we have seen, this should, however, not significantly affect the plasma self-cooling dynamics on the timescales relevant to the electron cooling process. More importantly, in his derivation of the electron-ion energy exchange time scale τ_{ie} (Eqn. 6.4), Spitzer assumed

[3] n_e additionally enters the scaling through a square-root in the Coulomb logarithm but this weak dependence changes τ_{ie} by less than 50% when varying n_e within ± 2 orders of magnitude.

non-magnetized plasma components with isotropic Maxwellian velocity components. The magnetization of the plasma will cause the electron cooling force to depend on the pitch angle between the ion velocity vector and the magnetic field axis [510]. Direct comparison of calculations with our two-component plasma model to cooling simulations based on more realistic electron cooling forces from linear-response theory [497] suggest that inclusion of the plasma magnetization extends the predicted cooling times by no more than 10% [511]. Another aspect that has been neglected in the presented calculations is the non-zero, initial centre-of-mass velocity of injected ion bunches. Additional time might have to be added to a cooling cycle to first slow down this motion and achieve a closer approximation to the thermal velocity distributions presumed here. To at least qualitatively account for this circumstance, the initial ion energy was chosen more than twice as large as typical energy spreads of charge-bred ion bunches from TITAN EBIT. Finally, the fact that trapped ions only spend part of their storage time inside the plasma, actively undergoing electron cooling, was accounted for in the calculations by multiplying τ_{ie} by a fixed overlap fraction of $\kappa = 0.5$. In a realistic nested trap potential, κ usually varies with the ion energy. Moreover, the radial particle dynamics, in particular collective plasma rotations such as the $m = 1$ diocotron mode, could add additional variation of κ over the storage time. These effects distort the shape of experimentally observable ion cooling curves, as will be detailed in section 6.4.5. Despite the inherent simplifications, the simple cooling model can be assumed to at least yield order-of-magnitude estimates of the experimentally expected cooling times.

The model calculations suggest that, at least in principle, cooling radioactive HCI with half-lives $\lesssim 100\,\mathrm{ms}$ from $100\,\mathrm{eV/q}$ to $1\,\mathrm{eV/q}$ appears possible and would require electron number densities $n_e \sim 1 \times 10^8\,\mathrm{cm}^{-3}$, plasma self-cooling times of $\tau \sim 100\,\mathrm{ms}$, plasma temperatures approaching $T_e \sim 300\,\mathrm{K}$ and electron-ion number ratios $N_i/N_e \leq 10^{-4}$. Non-neutral plasmas with such parameters have been demonstrated in earlier test measurements using preliminary configurations of the CPET setup [508]. The model calculations further illustrated that the cooling of SCI generally proceeds substantially slower than that of HCI. In order to realize electron cooling times shorter than the typical lifetime of SCI in a room-temperature Penning trap ($\sim$1–5 s), the intended proof-of-principles studies with non-radioactive SCI consequentially demanded plasmas with parameters similar to the ones given above.

6.3 The cooler Penning trap setup

This section introduces the cooler Penning trap setup used for the measurements presented later in this chapter. The construction and initial assembly of the trap electrode structure and large parts of the CPET off-line setup were documented along with early commissioning results in the PhD thesis of V.V. Simon [306]. Further, technical development of the setup, which established a viable mechanism for electron plasma generation in CPET, were described in the PhD thesis by U. Chowdhury [508]. The technical developments that ultimately facilitated the first co-confinement of ions and electrons are described

within the present thesis. Complementary information can be found in the PhD thesis of B. Kootte [512].

This section is outlined as follows. Subsections 6.3.1 and 6.3.2 discuss the Penning trap's electrode structure and the superconducting magnet that houses it, respectively, and review the corresponding technical requirements for realizing electron cooling in a Penning trap. CPET was installed in a dedicated off-line test setup that enabled test measurements and the technical development of the device without interfering with the on-line operation of the TITAN experiment. The measurements with singly charged ions and electron plasmas reported in this thesis were performed in the CPET off-line test setup. In anticipation of possible on-line tests with stable or radioactive highly charged ions (HCI) from TITAN EBIT, the test setup was located adjacent to the transport beamline to the precision Penning trap MPET and incorporated a railing system allowing for CPET to be readily inserted into the TITAN beamline for on-line tests with HCI. After giving an overview of the off-line test setup in subsection 6.3.3, the most crucial components of the setup are separately discussed in subsections 6.3.4–6.3.8. Finally, the experimental control and data acquisition system is described in subsection 6.3.9.

6.3.1 Trap assembly

The simultaneous confinement of oppositely charged particles requires a nested axial trap potential. In order to provide maximal flexibility in shaping the trap potentials during the different stages of a cooling cycle, the cooler Penning trap (CPET) consisted of a stack of 29 cylindrical trap electrodes. This type of electrode geometry is commonly referred to as a Penning-Malmberg trap [513]. The trap electrodes, each $12.7\,\mathrm{mm}$ long, had an inner diameter of $35\,\mathrm{mm}$ and were placed at a spacing of $1\,\mathrm{mm}$. They consisted of oxygen-free high-conductivity copper that was first silver and then gold coated in order to prevent patch potentials due to oxidation [306]. The trap electrodes were framed by pairs of gate electrodes and drift tubes. The entire trap assembly is shown in Fig. 6.6 (a) and further included a Lorentz steerer to aid ion injection into the trap.

A zoomed view of the trap electrode stack and the gate electrodes is shown in Fig. 6.6 (b). The trap electrode stack consisted predominantly of non-segmented ring electrodes but also includes two triplets of segmented trap electrodes that enable RF excitations of radial ion and electron motions. Each triplet was formed by an eightfold-split octupole electrode surrounded by a twofold-split dipole electrode on either end. The three different types of trap electrodes are shown in Fig. 6.6 (c).

The HV biasing of the electrodes in the trap electrode stack was realized through a sophisticated feedthrough section that was attached to the wire connectors at the end of the trap assembly. The wire connectors were in turn connected to the electrodes using oxygen-free high-conductivity copper wires that were guided through hollow ceramic insulator rods. The insulator rods were cut to appropriate lengths and supported by holes in the wire guide discs shown in Fig. 6.6 (b). Due to the spatial constraints imposed by the magnet bore, the wire guides were designed to support feeding no more than 45 different voltages to the 56

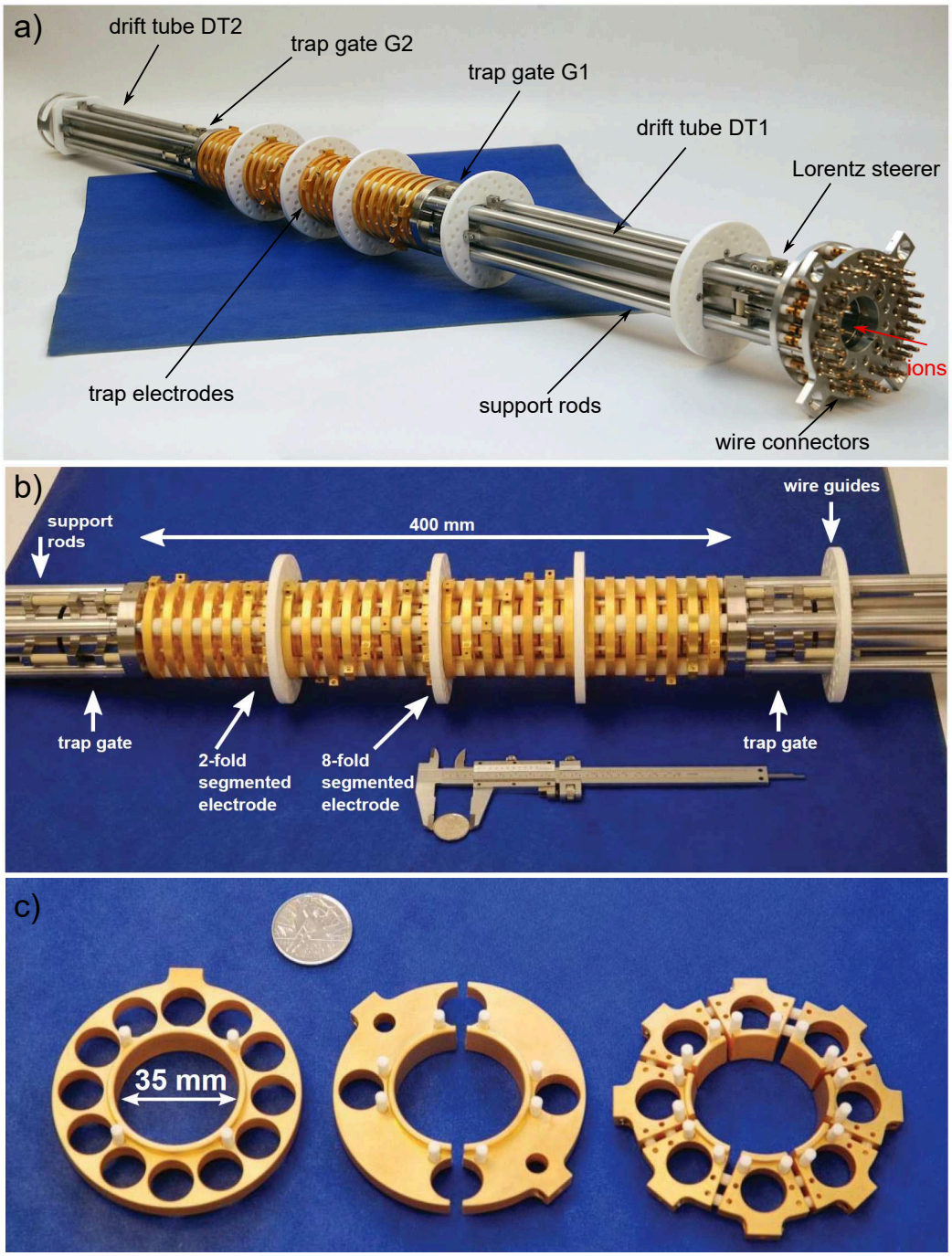

Figure 6.6. The trap assembly of the cooler Penning trap: a) Overview of the entire assembly before adding the wiring, b) zoom of the trapping region, c) the different types of ring trap electrodes (from left to right): unsegmented ring electrode, twofold-split dipole electrode & eigthfold-segmented octupole electrode. Figures from [306].

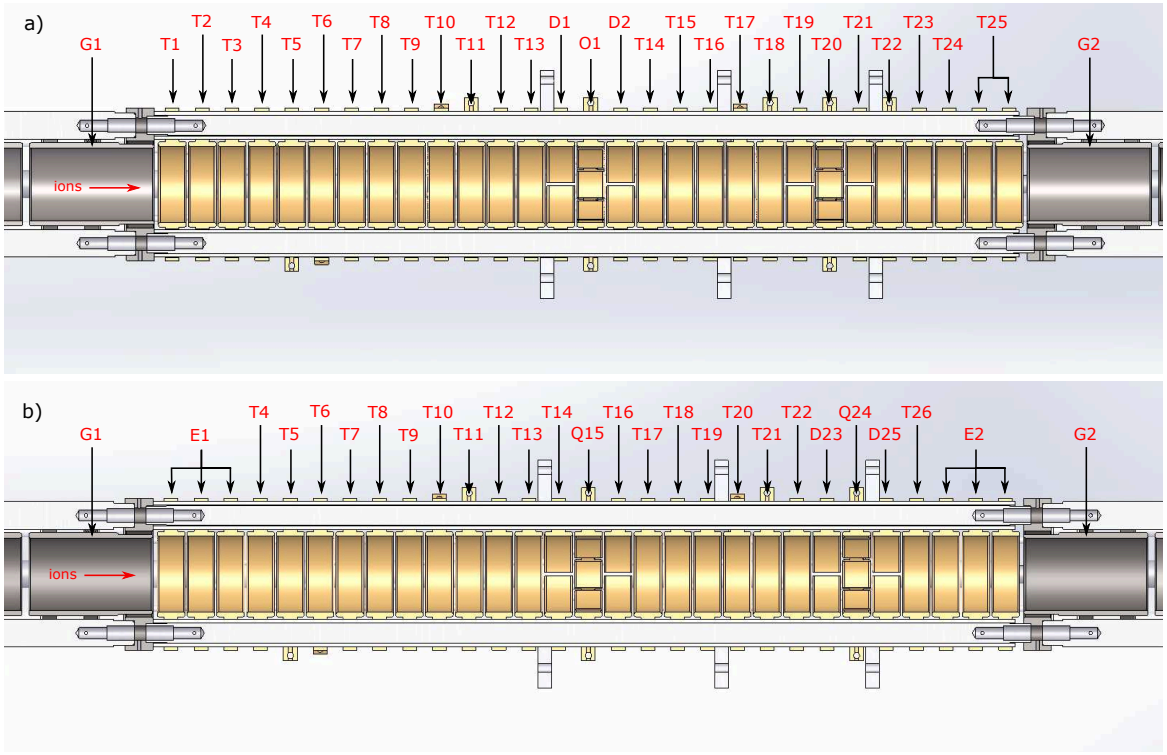

Figure 6.7. Cross sectional view of the trap electrode stack illustrating the electrode arrangement and the labelling scheme before (a) and after (b) revisions for improved strength against HV breakdown. All measurements reported in this chapter were performed with the revised wiring configuration. Shared arrows indicate electrodes shorted in vacuum. For clarity, the detailed wiring and labelling of azimuthally-segmented electrodes are not shown here. The leading letters in the electrode labels indicate the function and the wiring configuration of a given electrode: G = trap gate, E = end cap, T = ring trap electrode, D = dipole electrode, Q = quadrupole electrode, O = octupole electrode).

electrodes in the trap assembly. As a result, some electrodes necessarily had to be shorted in vacuum.

The electrode wiring and labelling schemes used for initial off-line tests with CPET are shown in Fig. 6.7 (a). Due to the limited number of feedthroughs, the segments of the dipole and octupole electrodes in the second triplet were shorted in vacuum, effectively rendering them three separate ring electrodes (T19, T20, T21). Further, during the installation of the harp electron detector (see section 6.3.8), the final two trap electrodes had to be shorted in vacuum (T25) to free up a feedthrough for the new detector. Despite acceptable performance in early studies that only involved trapped electron plasmas [508], work towards electron-ion co-trapping found this configuration to be prone to electron-induced HV breakdown (see section 6.4.2).

To increase the breakdown strength of the trap assembly and account for updated operational needs, the updated electrode arrangement and wiring scheme shown in Fig. 6.7 (b) were developed. On each end of the trap, the three outermost electrodes were shorted in vacuum to form an end cap (E1 & E2). Adjacent segments of the octupole electrodes were

shorted in vacuum to effectively form quadrupole electrodes (Q15 & Q24) and the dipole electrodes near the trap centre were shorted in vacuum, effectively making them ring electrodes (T14 & T16). The second triplet of segmented trap electrodes was shifted by one electrode towards the electron-injection side to enable RF excitation of ions accumulated near the exit end cap E2. All measurements presented in this chapter were performed with this updated trap configuration. With the updated wiring configuration conductors only had to be fed through 42 of the 45 holes in the ceramic wire guides [see Fig. 6.6 a)]. The most critical HV carrying wires (DT1, G1, G2) could thus be placed with additional spacing to other conductors. Further, special care was taken to minimize exposed wire sections by adapting the lengths of the ceramic tubes acting as wire insulators and by adding ceramic beads to bent wire sections (see appendix B for details). The aforementioned revisions to the trap electrode arrangement and wiring formed a critical part of a larger set of hardware modifications to enable electron-ion interaction studies. The full set of modifications and their motivations are described in appendix B.

6.3.2 Superconducting magnet

The radial confinement of ions and electrons in a Penning trap requires a strong axial magnetic field. At field strengths $B < 0.4\,\mathrm{T}$, the finite lifetime of a trapped electron plasma due to radial particle diffusion has been experimentally shown to scale as B^{-2} [514]. For magnetized plasmas in a regime of higher field strength, theoretical studies of cross-field particle transport predict only logarithmic modifications to this scaling [515].

The magnetic field strength further plays a key role in realizing the rapid cooling rates needed to reduce decay losses in electron cooling of radioactive ions with half-lives below $1\,\mathrm{s}$. As indicated by the simulations in section 6.2, the interaction with energetic HCI may cause a sharp initial rise of the electron plasma temperature. In order to sustain a high cooling rate, the plasma needs to rapidly re-cool towards its steady-state temperature by emission of cyclotron radiation. Since the cyclotron cooling time scales as $\tau_c \propto B^{-2}$ (see Eqn. 6.3), a strong magnetic field is essential for in-trap electron cooling of short-lived radioactive ions. To prevent negative impact on the field homogeneity of nearby ion traps, it is further desirable to minimize the cooler Penning trap's magnetic stray field.

To match these requirements, an actively-shielded superconducting magnet with a maximal field strength of $7\,\mathrm{T}$ and a room-temperature bore was chosen for CPET [511]. The solenoid and its internal shim coils provided a high-level of field homogeneity with ${}^{\delta B}/_{B} \leq 10^{-6}$ and ${}^{\delta B}/_{B} \leq 10^{-3}$ over a cylindrical volume with $25\,\mathrm{mm}$ radius and lengths of $100\,\mathrm{mm}$ and $400\,\mathrm{mm}$, respectively. A cryostat consisting of a liquid helium reservoir surrounded by a liquid nitrogen heat shield allowed to persistently keep the magnet in a superconducting state, resulting in a high temporal stability of the magnetic field strength (relative field decay rate $< 0.49\,\mathrm{ppm/h}$).

Coaxial misalignment between the symmetry axes of the magnetic and electric trapping fields can increase the radial particle loss rate [516] and trigger plasma oscillations [517]. To minimize these effects, an optical alignment procedure was performed during the early

commissioning stages of the CPET setup [306]. First, the orientation of the magnet field axis inside the magnet bore was determined through a hall-probe field mapping. When the vacuum pipe housing the trap assembly was first installed inside the magnet bore, the pipe's symmetry axis was aligned coaxially with the measured field axis using an optical level and a set of masks attached to the bore openings. See Ref.s [306] and [508] for details on the alignment procedure.

6.3.3 Off-line test setup

The measurements reported later in this chapter were performed with the cooler Penning trap installed in a dedicated off-line test setup. A cut-away rendering of the setup is shown in Fig. 6.8. Transport beamlines located on either end of the superconducting magnet enabled the injection of ion and electron beams into the trap and were correspondingly referred to as the ion-injection side (IS) and electron-injection side (ES), respectively. As detailed in section 6.3.4, a vacuum system with multiple turbomolecular pumps was used to achieve suitable pressure conditions in the beamline and the trap vacuum chambers. Bunched beams of singly charged ions were produced by an ion gun (see section 6.3.5) installed at the end of the IS beamline. Trapped electron plasmas were generated using electron beams from an electron gun situated in the ES beamline (see section 6.3.6).

A schematic overview of the optical elements and the detectors used to manipulate and monitor ion and electron beams is given in Fig. 6.9 and the corresponding acronyms are explained in table 6.2. Diagnostics chambers in the ES and IS beamlines allowed us to monitor and optimize the properties of injected ion and electron beams. Trapped electron plasmas were diagnosed using the specialized harp electron detector installed at the end of the drift tube DT1. The dynamics of trapped ions were monitored by extracting the ions onto a micro-channel plate (MCP) detector installed at the end of the ES beamline (ES MCP0). To enable unimpeded ion extraction onto the detector, the electron gun was offset from the ion optical axis. The following sections introduce the critical components of the setup in detail.

6.3.4 Vacuum system

The extended storage of HCI in an ion trap requires excellent ultra-high vacuum conditions. This is primarily due to the large cross sections for charge exchange between HCI and residual gas particles, which, at too high gas densities, would induce sizeable losses of the charge state of interest [518]. Estimates of the expected charge exchange rates in CPET have indicated [55] that storing HCI over the expected duration of the electron cooling process (a few $100\,\mathrm{ms}$) would require a vacuum level of $p < 1 \times 10^{-10}$ mbar. Achieving these conditions in the trapping region of CPET is complicated by the narrow magnet bore (12.75 cm diameter) which causes the vacuum level in the trapping region to be pump-conductance limited.

To overcome this limitation, the titanium vacuum tube housing the trap assembly was coated with a non-evaporable getter material (23% Ti, 36% Zr, 42% V) [306]. Once ac-

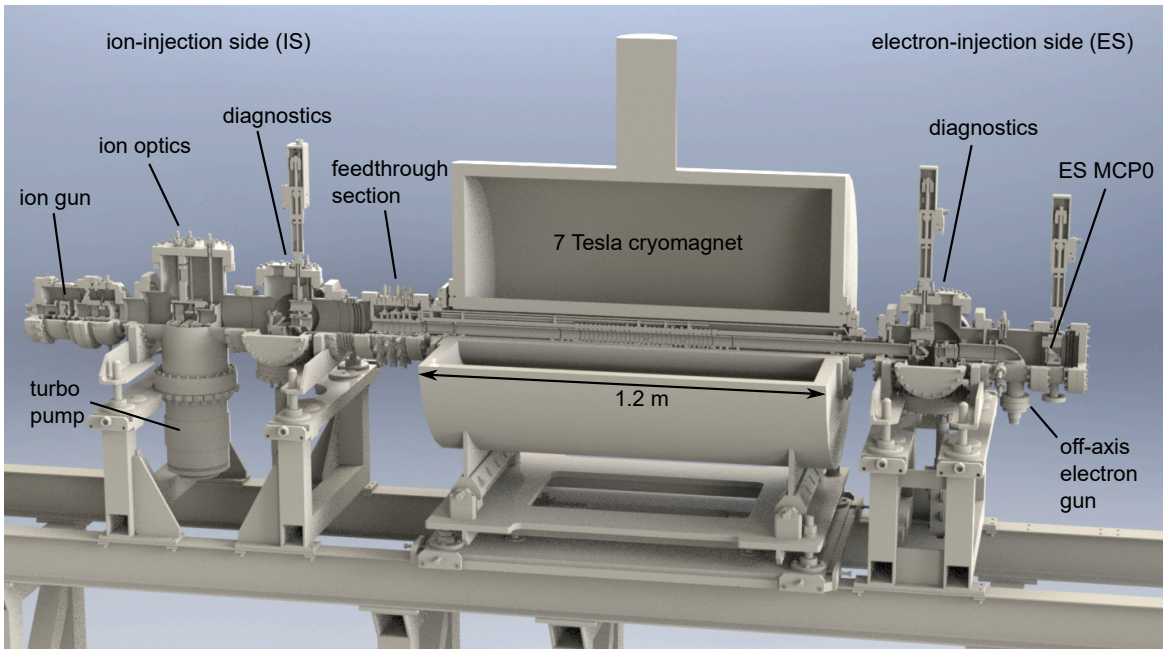

Figure 6.8. Cut-away CAD rendering of the CPET test setup.

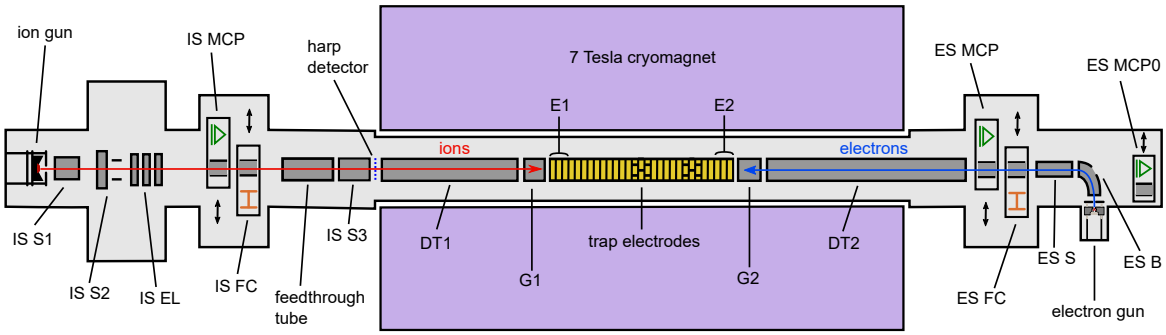

Figure 6.9. Schematic of the CPET test setup. Abbreviated electrode labels are indicated and explained in table 6.2.

Table 6.2. Explanation of the acronyms used in the labels in Fig. 6.9.

Label	Explanation
ES	electron-injection side
IS	ion-injection side
S	electrostatic steerer
EL	Einzel lens
B	4-fold segmented, electrostatic bender
DT	drift tube
G	gate electrode
E	end-cap electrode
MCP	microchannel plate
FC	Faraday cup

tivated, the getter film acts as an effective vacuum pump and can substantially reduce the ultimate pressure achievable in the trapping region. The getter coating is activated by baking the tube at a temperature $> 180\,°\mathrm{C}$ for at least $24\,\mathrm{h}$ [519]. Activation is possible at temperatures as low as $120\,°\mathrm{C}$ if the baking duration is extended appropriately. In early tests preceding this work, getter activation by baking the isolated titanium tube without the trap assembly inserted or the transport beam line chambers attached [306, 508] reduced the chamber pressure by at least two orders of magnitude, reaching pressure levels below the detection limit of the used ionization gauges ($p < 1 \times 10^{-11}\,\mathrm{mbar}$). Over a monitoring period of 30 days, no detectable saturation of the getter coating was observed [306].

Tests with SCI require less stringent vacuum conditions ($p \sim 1 \times 10^{-9}\,\mathrm{mbar}$). An operational limitation of the non-evaporable getter coating lies in the fact that air venting saturates the coating and necessitates a getter re-activation once vacuum has been reinstated. During the development work presented in this thesis, the vacuum chamber had to be regularly opened for hardware upgrades and modifications. Since the getter material only allows for a few dozen re-activation cycles [508], it was decided to avoid getter activation for measurements with SCI.

After the modifications of the trap assembly for enhanced HV breakdown strength (see section 6.4.2), a vacuum bakeout of the trap chamber was performed to remove water molecules and other adsorbed compounds from the chamber walls and the electrode surfaces. The vacuum bakeout was performed in-situ, i.e. with the trap chamber installed inside the energized magnet. In previous work [508], the trap chamber had been wrapped with flexible heating blankets and a ceramic blanket for heat insulation. A set of thermocouples interspersed between the wrapping layers provided a means to monitor the temperature at different locations inside the magnet bore. Since getter activation was not intended, the bakeout was performed over 10 days with a moderate peak temperatures of $97\,°\mathrm{C}$ on the outside of the trap chamber and $72\,°\mathrm{C}$ at the magnet bore surface. The moderate baking temperature ensured that the magnet bore was not heated beyond its maximum allowable temperature of $100\,°\mathrm{C}$, thus avoiding the risk of a magnet quench. The ultimate pressures achieved after the bakeout were $2.4 \times 10^{-9}\,\mathrm{mbar}$ in the IS diagnostics chamber and $2.5 \times 10^{-9}\,\mathrm{mbar}$ in the ES diagnostics chamber.

The vacuum system for the CPET off-line test setup is schematically depicted in Fig. 6.10. The vacuum chamber housing the trap and the charged-particle transport beam lines was evacuated using three turbomolecular pumps with a pumping speed of $500\,\mathrm{l/s}$ (TP1A, TP1B & TP1C). These pumps were in turn backed by an $80\,\mathrm{l/s}$ turbomolecular pump (TP1) and a scroll pump (BP1). The vacuum conditions in the beam line chambers and the backing lines could be monitored from atmospheric pressure down to $p \approx 1 \times 10^{-11}\,\mathrm{mbar}$ using a combination of convectron gauges (detection range $1 \times 10^{-1}\,\mathrm{mbar} \leq p \leq 1000\,\mathrm{mbar}$) and Bayard-Alpert ionization gauges (detection range $2 \times 10^{-11}\,\mathrm{mbar} \leq p \leq 1 \times 10^{-3}\,\mathrm{mbar}$).

[3] Since the vacuum section with the test ion source included Dependex fittings with Viton elastomer (instead of metal) seals, the pressure improvement from getter activation and the ultimately achievable vacuum level in the full off-line test setup used for the studies reported in this chapter would likely be significantly lower than in those early test measurements.

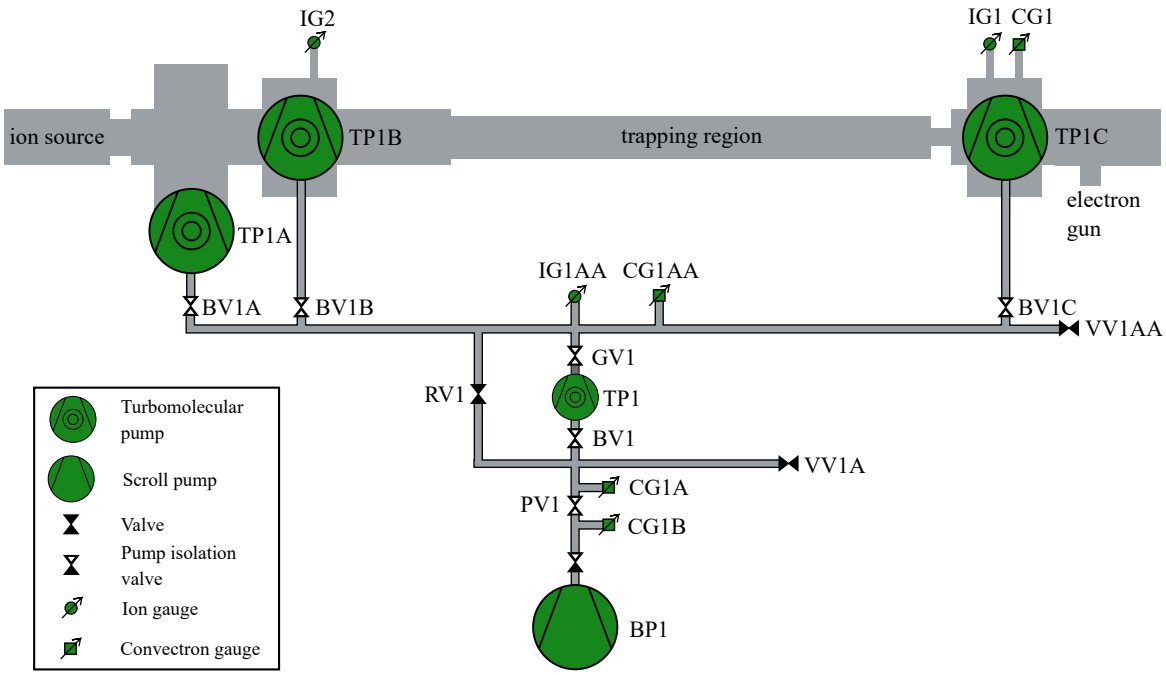

Figure 6.10. Vacuum system of the CPET off-line test setup. The beam line is evacuated by three $500\,\mathrm{l/s}$ turbomolecular pumps (TP1A, B & C) backed by a $50\,\mathrm{l/s}$ turbomolecular pump (TP1) and a scroll pump (BP1). Valves that are open in regular operation are indicated by open triangles.

With the ion and electron source heated to their operating temperatures, the ES and IS ion gauges typically recorded a pressure of $\approx 2.4 \times 10^{-9}$ mbar during the measurements reported later in this chapter.

6.3.5 Off-line ion source

Ion beams for the studies reported in this chapter were produced with an ion gun placed at the end of the ion-injection side (IS) of the test setup. The ion gun provided bunched beams of surface-ionized, singly charged alkali ions. Figure 6.11 shows a picture and a cross sectional view of the ion gun. Singly charged, non-radioactive ions were emitted from a surface ion source (HeatWave Labs #101139) [520] capable of providing stable isotopes of Na, K, Rb and Cs through thermionic emission. The ion emission current was determined by the source temperature, the ionization potential of the respective ion species and the effective work function of the aluminosilicate emission surface, the latter being a function of the applied extraction field.

The design of the ion gun resembles that of the off-line test ion source for the TITAN beamline. To aid beam focussing in the source region, the ion gun design follows a Pierce geometry [301] with both the Pierce electrode and the anode incorporating cone angles of $\approx 72°$ with respect to the ion optical axis.

The backplate, the Pierce electrode, the ion source body and one leg of the internal heater wire of the ion source were electrically shorted within the vacuum chamber, thus ensuring

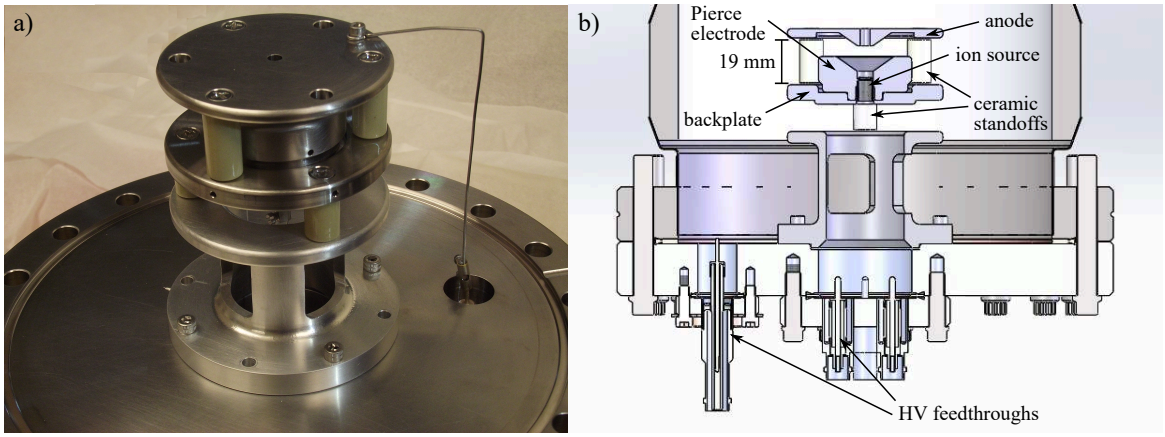

Figure 6.11. Surface ion source assembly for generation of singly-charged alkali ion beams.

identical potentials on the emission surface and the surrounding electrodes. The ion beam energy was defined by floating the aforementioned electrodes to a common high voltage that is from here on referred to as the ion source bias. To enable thermionic emission of cations from the emitter surface, the ion source was heated by driving a current of typically 1.7–1.9 A through its internal heater wire. The heater leg connected to the Pierce electrode was kept at the ion source bias. The second leg of the heater wire was insulated from the other electrodes and acquire a potential a few volts more positive than the ion source bias when a heating current was run through the wire. The heating current was provided by a regular DC lab power supply and floated to the ion source bias using a constant-current floating filament power supply (Matsusada FDC37.5-5A-30). Both the ion and electron source (see section 6.3.6) heating currents were controlled through a common LabView program. The program enabled controlled ramping of the heating currents. The anode was independently biased through a third HV line and used to adjust the extraction field and the beam focussing.

To obtain a bunched ion beam, the anode was switched between an accelerating and a repelling voltage using a Behlke HV switch box. The switch box was followed by a custom diode-bridged RC filter (effective rise/fall time $\tau \sim 100$ ns) that suppressed noise arising from the Behlke switch and the control electronics of the switch box. This setup enabled the creation of ion bunches as short as a few 100 ns. For typical ion trapping cycles, anode opening durations (and thus bunch lengths) of 1–2 µs were used.

The ion gun was followed by a set of extraction optics including skimmer plates with circular apertures. A skimmer plate with a 4 mm aperture had to be removed to achieve an acceptable ion transmission to the IS Faraday cup. Once the skimmer plate was removed, a DC ion current of ≈ 10 pA could be detected on the IS Faraday cup. As will be detailed in section 6.4.4, pulsing a steering voltage in the IS beamline provided a TOF gate that could mass separate the different elements emitted from the ion source, thus enabling electron cooling studies with different ion species.

6.3.6 Off-axis electron gun

Tests of electron cooling of ions in CPET require the creation of reproducible electron plasmas consisting of $> 10^7$ electrons. Trapped electron plasmas were created using a special loading scheme [521] that exploited the interaction of a continuous, incoming electron beam with the reflected beam and already trapped electrons. As detailed in section 6.4.3, this scheme allowed us to routinely generate non-neutral plasmas with several 1×10^8 electrons in only $100\,\mathrm{ms}$. The electron loading efficiency depended critically on the electron beam current achieved in the trapping region.

Electron beams were generated with a thermionic electron gun [522] located $\approx 1.13\,\mathrm{m}$ from the trap centre in the fringe field of the superconducting magnet. The electron gun was offset from the ion optical axis (see Fig. 6.9) to enable the extraction of trapped ions onto the MCP detector at the far end of the ES beamline (ES MCP0). An electrostatic $90°$-bender (ES B) and a Lorentz steerer (ES S), both split into four azimuthal segments, were used to steer the electron beam onto the ion-optical axis.

The off-axis electron injection introduced a number of challenges that were addressed in previous work [523]. Namely, the magnetic fringe field induced a substantial lateral beam deflection in the vertical section between the electron gun cathode and the $90°$-bender. If uncompensated, the deflection resulted in substantial beam losses against the electron gun anode and caused electrons to enter the drift tube DT2 with comparatively large pitch angles with respect to the magnetic field axis. In tests with a simplistic electron gun, whose design followed that of a planar diode, the magnetic beam deflection and insufficient compensation of space-charge forces in the beam formation region limited the electron transmission from the cathode to the ES Faraday cup (ES FC) to $< 2\%$ [523]. Moreover, the steep magnetic field gradient inside the drift tube DT2 caused any electrons entering DT2 with a pitch angle $\alpha > \alpha_m = \arcsin\left(\sqrt{B_i/B_f}\right) \approx 1.7°$ with respect to the magnetic field axis to undergo magnetic mirror reflection, where $B_i = 6\,\mathrm{mT}$ and $B_f = 7\,\mathrm{T}$ denote the magnetic field strengths at the electron gun and the trap centre, respectively. In the initial test with the simplistic electron gun magnetic mirror reflections limited the transmission from the ES FC to the harp detector (see section 6.3.8) to $< 0.6\%$. Good alignment of the electron beam with the magnetic field axis was therefore crucial to achieve appreciable electron beam currents in the trapping region and enable reproducible production of electron plasma.

These challenges were overcome through extensive charged particle simulations that resulted in the design of the specialized off-axis electron gun [523] shown in Fig. 6.12. As for the initial electron gun, a tungsten filament [524] was used as the cathode and provided typical beam currents of 10–$100\,\mu\mathrm{A}$. A Wehnelt cylinder [525] compensated the space charge in the beam formation region, resulting in well collimated beams. Switching the Wehnelt cylinder to a potential at least $50\,\mathrm{V}$ more negative than the cathode bias further provided a controlled way to deactivate the electron emission. A fourfold-segmented anode enabled electrostatic steering that helped to compensate the lateral beam deflection induced by the magnetic fringe field. These improvements increased the transmission from the cathode to the ES FC to more than 60% and raised the electron currents measured on the harp detector

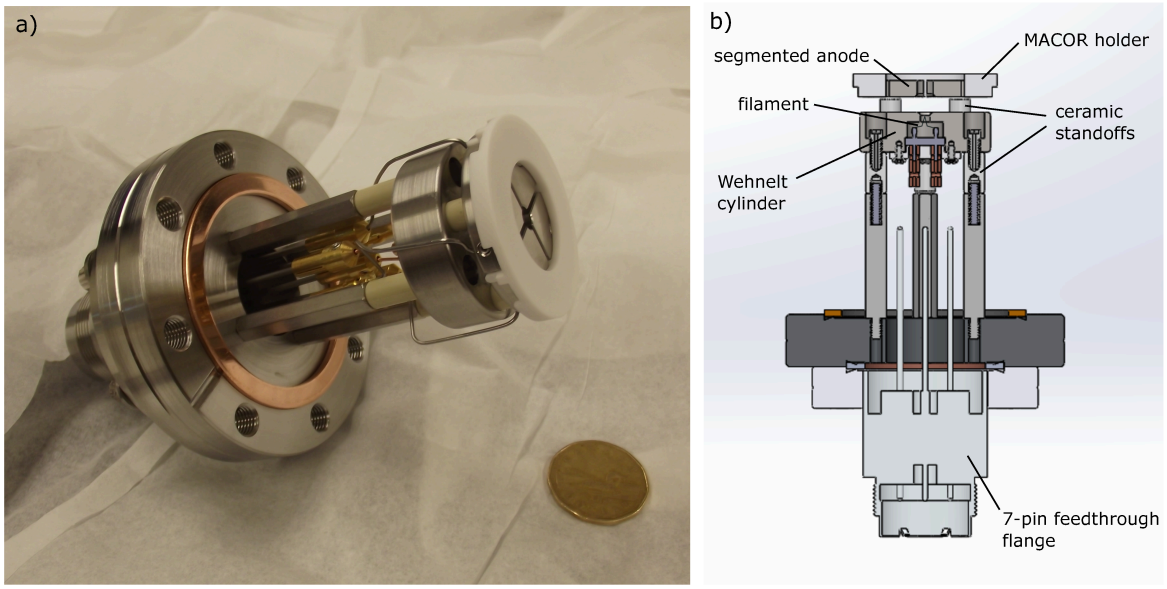

Figure 6.12. The off-axis electron gun: a) Image of the electron gun along with a Canadian one-dollar coin ($\varnothing \approx 32\,\mathrm{mm}$) for scale. (b) Cross-sectional view in a computer rendering including electrode labels.

by more than one order of magnitude to up to $5.7\,\mu\mathrm{A}$ [522]. As a result of the higher beam currents in the trap, the optimized electron gun enabled the accumulation of several 1×10^8 electrons in less than $0.5\,\mathrm{s}$ [522, 523].

The studies discussed later in this chapter were performed with the trap's ring electrodes biased to voltages between 0–$200\,\mathrm{V}$. For efficient electron transport through the magnetic field gradient, the electron gun cathode and the Wehnelt cylinder were biased to $-2\,\mathrm{kV}$. The cathode heating current was provided by a voltage-regulated DC power supply (Matsusada C37.5) that was floated on a HV platform inside a Faraday cage. The electron beam was turned on and off using a Behlke HV switch box that toggled the bias of the Wehnelt cylinder between the cathode potential ($-2\,\mathrm{kV}$) and a repulsive potential ($-2.07\,\mathrm{kV}$), respectively. The cathode was typically operated with heating currents of 2.2–$2.4\,\mathrm{A}$, resulting in emission currents of 20–$80\,\mu\mathrm{A}$ and measured electron currents of $\sim 1\,\mu\mathrm{A}$ on the harp detector.

6.3.7 HV switching

The transport and manipulation of ions and electrons throughout a cooling cycle requires more than 50 electrodes to be biased to well-chosen potentials. The concurrent transport of oppositely charged ions and electrons through shared beam line sections and the need for dynamic particle manipulations inside the trap required more than half of these electrode potentials to be switched within each cycle. All high voltage biases were derived from commercial precision power supplies (ISEG NHQ 205M and Caen A1588 & A1733SN/P), except for the trap electrodes which were biased using a custom-built programmable HV supply (see bullet 3 below). The various voltage changes occurring throughout a cooling cycle can be categorized by the required transition time τ_s [306]:

1. **Slow bi-level switching ($\tau_s \leq 10\,\text{ms}$)**:
   The injection and extraction paths of ions and electrons overlapped from the Lorentz steerer on the ion-injection end of the magnet bore (IS S3) all the way to the 90°-bender in the electron-injection beamline (ES B). In order to transport both species through these beam line sections, the respective electrode potentials had to be switched by typically several $100\,\text{V}$ up to a a few kV. The available time to switch the relevant IS transport potentials from ion injection to electron extraction and the ES potentials from electron injection to ion extraction is dictated by the shortest ion-electron interaction periods that one aims to study. Based on the simulations studies of the cooling process, the typical time scales for the processes of interest were assumed be no shorter than a few $10\,\text{ms}$, suggesting a maximal transition time of $\tau_s \approx 10\,\text{ms}$ for switching the transport potentials.

   To realize such HV switching, we built two dedicated slow switching boxes, each with 10 output channels and a common transistor-transistor logic (TTL) trigger input. The switch boxes enabled bi-level switching of arbitrary voltages between $\pm 3\,\text{kV}$ with transition times of $\approx 2\,\text{ms}$ and maximal repetition rates of $\approx 100\,\text{Hz}$. One box was used to switch the ion-injection side potentials, the other to switch the electron-injection side potentials. In comparison to typical solid-state HV switches, the relay switch boxes were not only more cost-effective but also provided more operational flexibility since the input voltage polarities could be freely changed without any circuit modifications. More details on the design of the relay switch boxes can be found in [523].

2. **Rapid bi-level switching ($\tau_s \leq 100\,\text{ns}$):**
   A number of charged-particle manipulations, such as the creation of bunched ion beams, the separation of different ion species with a TOF gate and the dynamic capture of ions, required bi-level HV switching with transition times on the order of $\tau_s \sim 100\,\text{ns}$.

   Such switching was realized using TRIUMF-built switch boxes with solid-state HV switches (Behlke HTS). Similar to the slow switching boxes, the Behlke switch boxes contained an internal logic section with a TTL trigger input. The switches were not only used for ion manipulations but also to bunch electron beams by toggling the potential of the Wehnelt cylinder between an accelerating and a reflecting state and to gate the amplification of the ES MCP0 (see section 6.3.8). Spectral analysis of the electromagnetic noise induced on the trap electrodes identified the Behlke switch boxes as the dominant source of high-frequency noise in the vacuum chamber. Further investigation showed that both the HTS switches and the trigger logic sections added sizeable levels of noise in the kHz and MHz range to the switch box outputs. Such RF noise induces an undesirable heating of trapped electron plasmas, thereby disturbing the plasma temperature relaxation and potentially hampering studies of in-trap electron cooling. To minimize the plasma heating through electrode noise, specialized diode-bridged low-pass filters were developed based on the conceptual design pre-

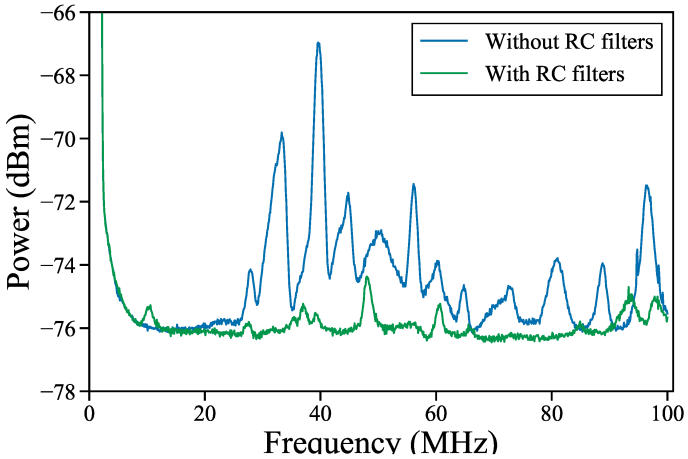

Figure 6.13. Electromagnetic noise induced on an unbiased trap electrode before (blue) and after (green) adding diode-bridged low-pass filters to the HV outputs of the Behlke switch boxes. See text for details.

sented in Ref. [526]. The second-order low-pass filters suppressed the high-frequency noise from the switch boxes while still allowing for rapid HV switching. Adding the low-pass filters to the outputs of all Behlke switch boxes yielded a substantial reduction of the noise level on the trap electrodes, as can be seen in the comparison in Fig. 6.13.

3. **Quasi-continuous multi-level switching ($\tau_s \geq 100\,\mu s$):**
While a static nested trap potential enables the simultaneous storage of ions and electrons in a Penning trap, a typical cooling cycle entails a series of particle manipulations that require dynamic changes of the trap potential. In the electron cooling studies reported in section 6.4.5, these manipulations included the controlled removal of hot electrons that did not get confined in the nested potential well after a set period for cyclotron cooling, the injection of ions into the pre-cooled electron plasma and the dump of the plasma onto the harp detector at the end of a cooling cycle. Such particle manipulations cannot readily be realized with simple bi-level switching but require a means to apply complicated sequences of voltage changes to the trap electrodes. If one aims to study the cooling of ions and electrons, heating of the particles through voltage changes should naturally be minimized. Therefore, the voltage changes should ideally proceed in a quasi-continuous or adiabatic way. More formally, this implies that any voltage changes that exceed the equivalent thermal energy of the trapped particles' should occur with transition times much longer than the particles' axial oscillation frequency. Detailed simulations of adiabatic transport of electrons trapped in CPET have been presented in [527].

   To provide the necessary flexibility in shaping the trap potentials, a custom programmable HV supply based on a multi-channel digital-to-analog converter (DAC) (Analog Devices AD5535) was developed [512]. The DAC provides voltages be-

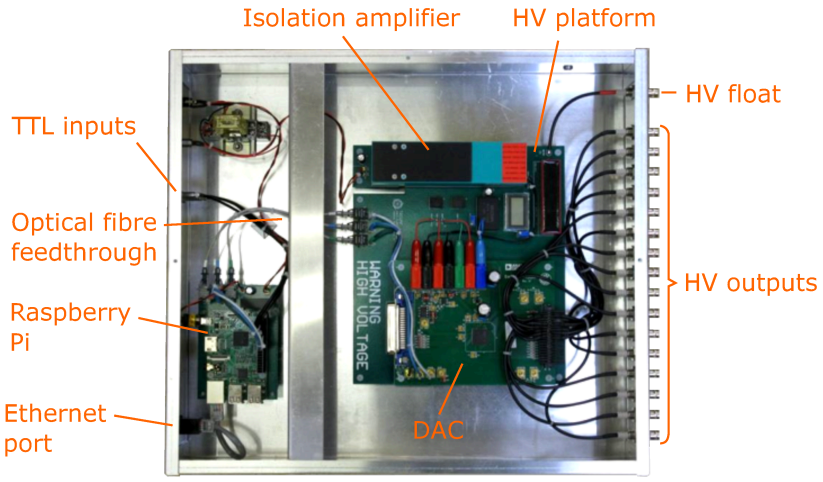

Figure 6.14. Top view of the custom programmable trap voltage supply.

tween 0–200 V with a 14-bit resolution and was mounted on a high voltage platform that could in turn be floated to voltages from 0–800 V (see Fig.6.14). The DAC is controlled through a RaspberryPi3 installed in a separate low-voltage section. The communication between the devices is established using an serial-peripheral interface (SPI) bus and optocoupling from the low- to the high-voltage section. The supply provides 16 HV output channels and 4 TTL input trigger channels. Before an experimental run, up to 4 different voltage sequences are pre-defined and stored in a JSON file on the RaspberryPi. The voltage settings are either manually set through a web interface hosted on the RaspberryPi or defined by the Maximum Integrated Data Acquisition System (MIDAS) run control. The latter also enables automatized scans of parameters such as the shape, length and depth of a potential well. Each voltage sequence may, in principle, consist of an arbitrary number of different voltages settings to be applied after defined wait times. A C program compiles the voltage settings from the JSON file at the beginning of an experimental run and then applies the different voltage sequences once a TTL logic signal is registered at the respective trigger input channel. The programmable power supply provided a reliable and cost-effective way to dynamically shape the trap potentials. However, the realization of adiabatic particle manipulations was complicated by the fact that the multi-channel DAC can by construction not apply voltage changes simultaneously to multiple output channels. Instead it sequentially steps through the channels in a user-defined order, successively changing the output voltages of individual channels. The delay in the initiation of successive voltage changes on two different channels was determined to be $\approx 20\,\mu s$.

6.3.8 Charged particle diagnostics

A set of charged particle detectors enabled beam tuning and provided indirect means to monitor the dynamics in the trap. The different types of detectors installed in the system are shown in Fig. 6.15 and described in the following subsections.

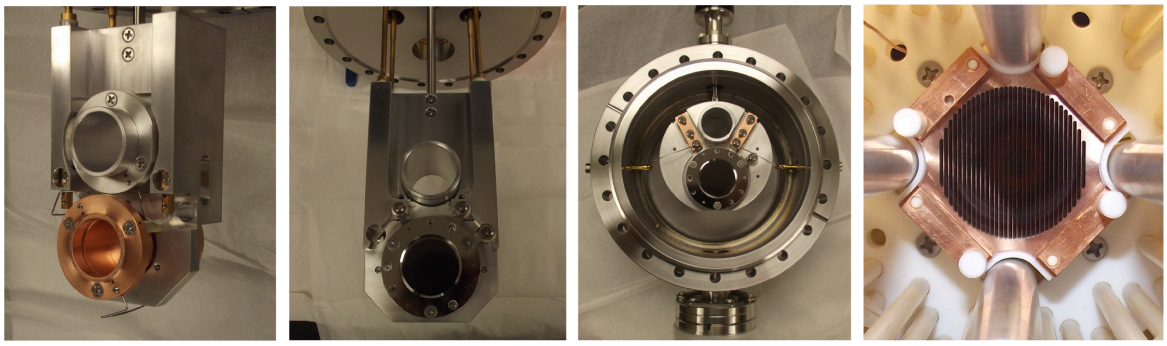

Figure 6.15. The types of charged particle diagnostics installed in the CPET test setup. From left to right: Faraday cup (IS FC & ES FC), MCP with phosphor screen (IS MCP & ES MCP), MCP with phosphor screen (ES MCP0), harp electron detector. Except for the latter, all detector assemblies were mounted on linear motion feedthroughs permitting either the respective detector or a drift tube to be inserted into the beam path.

Faraday cups (IS FC & ES FC)

Identical Faraday cups (FCs) assemblies installed inside the diagnostics chambers on the electron and ion injection side were used to optimize and monitor the transmission of (quasi-)continuous ion and electron beams. The assemblies were mounted on pneumatically operated linear motion feedthroughs that could be used to either insert a Faraday cup or a coaxial drift tube into the beam path, thus enabling quick transitions between beam diagnosis and transmission. Each Faraday cup consisted of three copper electrodes: A double-sided collector electrode with a suppression lens on either end. The suppression lenses can be used to prevent the loss of secondary electrons emitted through beam particle impact on the collector surface. For the given detector geometry, secondary electron losses were found to reduce the measured beam current to typically $80 - 90\%$ of the true beam current [523]. Biasing the suppression lenses $50\,\mathrm{V}$ more negative than the collector was found to fully suppress secondary electron losses [523]. However, since the Faraday cups were primarily used to maximize the beam transmission, secondary electron suppression was typically not necessary and the suppressor lenses were usually both kept on earth ground potential. The collector currents were monitored with time-sensitive electrometers (Keithley 6514), enabling the detection of currents $\gtrsim 1\,\mathrm{pA}$.

Microchannel plates (ES MCP, ES MCP & ES MCP0)

Bunched ion beams were monitored with micro-channel plate (MCP) detectors that allowed for ion-beam imaging, single-ion counting, time-sensitive detection (down to $\approx 10\,\mathrm{ns}$). All MCP detectors consisted of two impedance-matched MCP plates (Photonis LongLife MCP 25/12/10/12 D 60:1 MS) in Chevron configuration and a P43 phosphor screen (Photonis PS31558). The detectors were all facing the ion gun and mounted in two types of detector assemblies. The first type (center left of Fig. 6.15) was very similar to the FC assemblies and likewise installed in the ion- and electron-side diagnostics chambers (IS MCP and ES

MCP, respectively). The IS and ES MCP were primarily used to optimize the transport of bunched ion beams. A third MCP (dubbed ES MCP0) was mounted in a similar detector assembly (center right in Fig. 6.15) and installed at the far end of the electron injection side. ES MCP0 formed the primary detector used to monitor ions extracted from the trap because it allowed for counting of ions extracted from the trap but did not block the electron injection path into the Penning trap. As for the FC assemblies, all MCP assemblies were mounted on linear motion feedthroughs that either placed a detector or an adjacent drift tube in the beam path.

To achieve gains on the order of $10^5 - 10^6$ through secondary electron multiplication, the MCP front plates were biased to voltages between $-1700\,\mathrm{V}$ and $-2100\,\mathrm{V}$, while the backplates were kept at earth ground. For ion counting and arrival time measurements, the phosphor screen was biased to $200\,\mathrm{V}$. An alternating current (AC) coupling box was used to isolate the fast electron-induced voltage pulses on the phospor screen from the HV bias. The decoupled high-frequency signals were amplified with a pre-amplifier (ORTEC VT120), processed by a discriminator (LRS Model 623-B) and digitized by a multichannel scaler (MCS) (Stanford Research SR430) to obtain arrival-time spectra. The start timing of the MCS acquisition window was defined by a dedicated TTL pulse from the MIDAS controlled programmable pulse generator (PPG) (see section 6.3.9). The binning on the MCS was typically set to $320\,\mathrm{ns}$. For beam imaging, the phosphor screen was biased to $2000\,\mathrm{V}$. Mirrors mounted behind the phosphor screens reflected the emitted light by $90°$ downward through vacuum viewports. A charge-coupled device (CCD) camera placed behind the viewports recorded the light and provided images or videos of the beam spot.

At full MCP bias, the presence of the electron beam was found to induce dark-count rates in excess of $1\,\mathrm{MHz}$ on the ES MCP0, as shown in Fig. 6.16. To prevent premature aging of the microchannel plates, the ES MCP0 gain was gated by a HV switch that lowered the bias across the MCP plates from $1900\,\mathrm{V}$ to $1400\,\mathrm{V}$ whenever the electron beam was turned on. The reduced gain lowered the rate of electron-beam-induced events to a safe level.

Harp electron detector

The characterization of the electron plasma formation and the optimization of electron cooling in CPET required a reliable means to monitor the number of trapped electrons. The quantification of trapped electron plasmas was complicated by the strong axial field gradient of the actively-shielded superconducting magnet. The field gradient, which caused the magnetic field strength within the drift tubes (DT1 & DT2) to drop from $7\,\mathrm{T}$ to $< 0.1\,\mathrm{T}$, caused a transverse expansion of charged particle bunches extracted from the trapping region. The magnetic expansion is a direct consequence of the adiabatic invariance of the magnetic flux

$$\phi = BA \approx \text{const.}, \tag{6.9}$$

where $A = \pi r_c^2$ is the circular area enclosed by an electron moving around the field lines on an orbit with Larmor radius r_c. The approximate conservation of the magnetic flux implies that the Larmor radius of a charged particle moving from a region with field strength B_i to

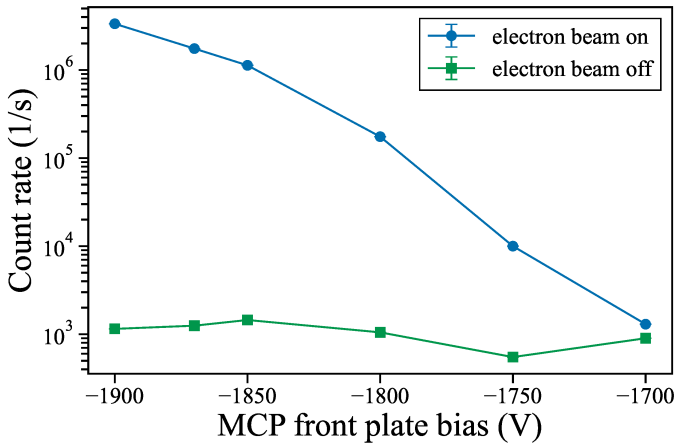

Figure 6.16. Count rate on the ES MCP0 detector with the electron beam turned on (blue circles) and off (green squares). To guide the eye, the data points were connected by lines. The unusually high dark count rate with the electron beam turned off is due to noise induced on the MCP anode and arose because a very sensitive discriminator threshold was chosen in order to not miss any electron-beam-induced events.

one with field strength $B_f < B_i$ will be widened to

$$r_f = \sqrt{\frac{B_i}{B_f}} r_i. \tag{6.10}$$

In the case of CPET's magnet, the field strength in the trapping region $B_i \approx 7\,\mathrm{T}$ dropped to $B_f \approx 80\,\mathrm{mT}$ at the IS and ES MCP, thus expanding the radial single-particle orbits by a factor $\sqrt{\frac{B_i}{B_f}} \approx 34$. In consequence, any extracted electrons starting in the trap with $r_c > 74\,\mu\mathrm{m}$ will be expanded beyond the $2.5\,\mathrm{cm}$ diameter of the MCPs. The strong transverse expansion of extracted electron bunches was further validated in earlier work [508] through trajectory tracing with the charged-particle optics simulator SIMION [528] and respective trajectories can be seen in Fig. 6.17. Since typical electron plasmas at the time exhibited radii of $r_p \approx 0.5\,\mathrm{mm}$ [508], detectors outside the magnet bore were unsuited to diagnose trapped electron plasmas and a different detector solution had to be found.

Instead of reducing the field gradient, moving the detector closer to the trap provided the most practical approach to monitor plasmas trapped in CPET. As an initial solution, Chowdhury et al. [508] inserted a phosphor screen mounted in an insulating, removable holding structure into the outer end of the DT1 drift tube. Instead of the ion source chamber, a viewport was mounted on the ion-injection end of the beam line. This setup allowed them to study the total charge, and the radial density distribution and dynamics of trapped electron plasmas created with an on-axis electron gun. These investigations have been reported in Usman Chowdhury's PhD thesis [508] and led to the observation of the $m = 1$ diocotron plasma mode in CPET [530–532]. The diocotron mode is an azimuthal $\vec{E} \times \vec{B}$-drift motion caused by the radial electric field generated by the plasma's space charge and the image charge it induces on the trap electrodes. It is the plasma equivalent of the magnetron motion

of a single charged particle in a Penning trap. The diocotron motion in CPET was found to be damped with time constants on the order 1 s, causing the entire plasma column to gradually spiral inward towards the trap's symmetry axis. Radial particle transport due to asymmetries in the trapping fields [533–535] or electron-neutral collisions [536] have been proposed as possible causes of the diocotron damping, but which damping mechanism dominates depends on the specific experimental conditions. Achieving the reproducible generation of non-neutral plasmas with number densities up to $n_e \approx 8.1 \times 10^8\,\mathrm{cm}^{-3}$ and total particle numbers of $N_e \approx 1.6 \times 10^8$ and plasma lifetimes up to 130 s [508], these preceding studies proved that plasmas suitable for electron cooling of ions can be created in CPET.

Since the phosphor screen blocked the ion injection path, a more permanent solution for electron detection had to be found for electron cooling studies. The limited space within the magnet bore prevented the installation of an actuated electron detector. Instead, Lascar et al. conceived a harp-style detector [529] that could be mounted close to the trap without preventing the injection of ions. The design of the harp was adapted from the Bradbury-Nielsen gate installed in the TITAN beamline. The harp was photochemically etched from a 0.1 mm-thin sheet of oxygen-free high-conductivity copper and mounted in a holding structure including a custom-machined MACOR® ceramic piece. After minor modifications to the trap assembly, the harp detector could be mounted between the drift tube DT1 and the adjacent Lorentz steerer IS S3 (see Fig. 6.15 far left). SIMION simulations and beam transport measurements showed that biasing the harp to a suitable potential allowed for ion transmission efficiencies of 80-90% [537]. To quantify the number of trapped electrons, the plasma was accelerated toward the harp detector by creating a monotonically increasing potential gradient with the potential maximum formed by the harp - a procedure referred to as an electron dump. Since the trap electrodes were typically biased to potentials between 0 V and 200 V with respect to earth ground, electron dumps with maximal collection efficiency required the harp to be biased to high positive voltages (typically in the range of 300–900 V).

Dumping plasmas onto the harp wires lead to a build up of charge that was dissipated through a series resistance placed between the harp detector and the corresponding HV power supply. The current flow through the resistance induced detectable voltage transients

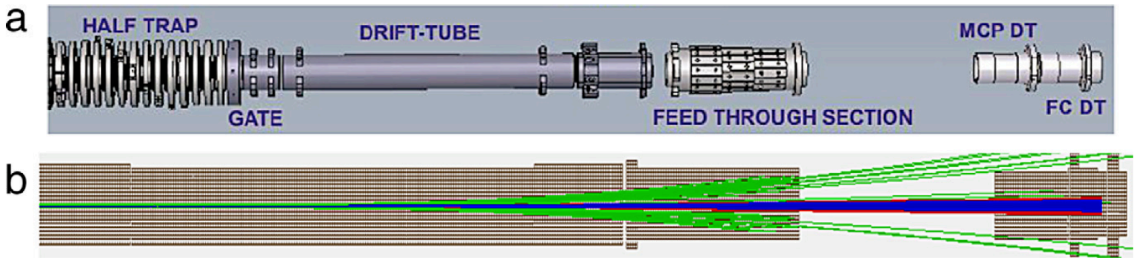

Figure 6.17. Magnetic expansion of charged particle bunches extracted from the trap toward the IS MCP. a) Electrodes along this beam line section. b) Simulated trajectories of electrons (green), protons (red) and ions with $A/q = 10$ (blue) extracted from the trap centre. Figure adapted from [529].

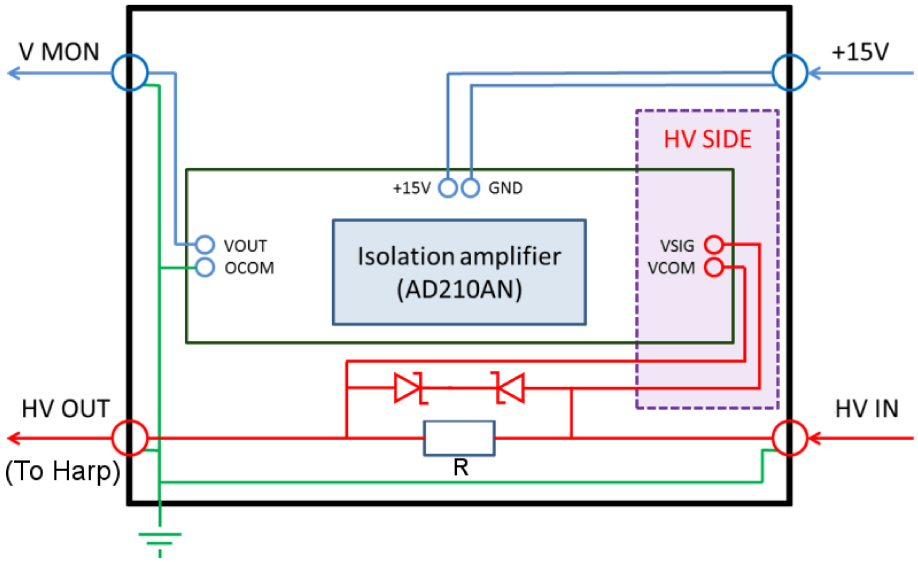

Figure 6.18. Simplified circuit schematic of the floated harp readout box. See text for details. Figure modified from [523].

that were used to estimate the number of electrons in the plasma, N_e. The voltage transients were isolated from the harp's HV bias using a dedicated readout box whose circuit diagram is shown in Fig. 6.18. The HV bias for the harp was provided by a Caen A7030SP power supply and fed to the box's HV IN terminal. Depositing a bunch with $N_e > 10^6$ electrons onto the harp wires caused a measurable voltage drop across the series resistance R. The voltage drop was shifted to earth ground using an isolation amplifier (Analog Devices AD210AN), and subsequently digitized with a 500 MHz oscilloscope (TeledyneLecroy WaveSurfer 3054) connected to the V MON output.

Typical signals recorded on the harp detector are shown in Fig. 6.19. HV switching of nearby electrodes induced switching noise on the harp detector which complicated the electron number determination. Switching the bias of the adjacent drift tube to lower the energy of injected ion bunches (switched voltage difference $\sim 1.5\,\mathrm{kV}$) was found to induce voltage pulses that exceeded the safe operating range of the isolation amplifier ($\leq 10\,\mathrm{V}$). To protect the amplifier, a pair of Zener diodes was added that truncated voltage transients to safe magnitudes ($|V| \lessapprox 9.5\,\mathrm{V}$). This modification enabled plasma detection in experimental cycles with ion injection. Due to their light mass, electrons extracted from the trap reached the harp detector within a few 100 ns. As a result, the switching noise induced on the harp when the trap potential was switched for the plasma dump overlapped with the electron signal. To enable accurate electron number determinations, a background correction was performed by alternating experimental cycles with and without electron injection and subtracting the time integrals of the respective signals, $V_{\mathrm{R,on}}(t)$ and $V_{\mathrm{R,off}}(t)$. The number of electrons impinging on the harp was then obtained by using the conversion relation

$$N_e = \frac{1}{eR}\left(\int V_{\mathrm{R,on}}(t)dt - \int V_{\mathrm{R,off}}(t)dt\right), \tag{6.11}$$

where $R = 94.3\,\mathrm{k\Omega}$ represents the load resistance in the readout box. It was further dis-

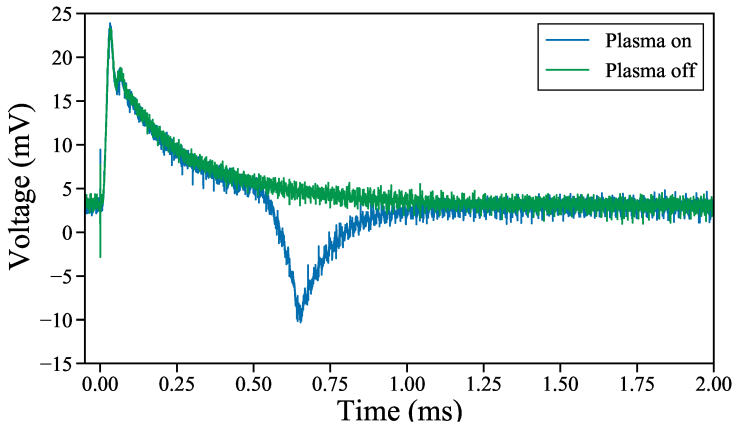

Figure 6.19. Typical voltage pulses recorded on the harp detector in a cycle with (blue) and without (green) an trapped electron plasma. The switching-noise background (green trace) was induced by switching the G1 gate electrode from $-1200\,\mathrm{V}$ to $400\,\mathrm{V}$ in order to ejected the trapped electrons towards the harp detector. The dip in the plasma-on signal (blue trace) was caused by $N_e \approx 1 \times 10^8$ ejected electrons that were initially trapped in a simple rectangular potential well formed by the gate electrodes.

covered that the leakage current of the isolation amplifier noticeably shifted the baseline of the harp voltage signals, resulting in an increased shot-to-shot fluctuation of the extracted electron numbers. Since the baseline fluctuations occurred on a time scale much longer than the length of the electron signals, this effect could be compensated by baseline-correcting each waveform before performing the integrals in Eqn. 6.11. These measures enhanced the sensitivity of the electron number detection and turned the harp detector into a powerful tool to monitor the total charge and reproducibility of electron plasmas stored in CPET.

6.3.9 Experimental control and data acquisition

The definition of electrode voltages, experimental timings and other important parameters for ion-electron interaction studies demands a versatile control and data acquisition (DAQ) system. An overview over the architecture of CPET's control and DAQ system is given in Fig. 6.20. The CPET data acquisition was based on the Maximum Integrated Data Acquisition System (MIDAS) [538]. The control system was subdivided into different subsystems (green boxes in Fig. 6.20) that separately controlled different types of hardware and were distributed over different control computers. Each subsystem could be individually controlled through a dedicated graphical user interface (orange boxes in Fig. 6.20). Network interfaces provided crosslinks between the different subsystems (dashed lines in Fig. 6.20) and turned the MIDAS run control into a master interface with write access to all relevant experimental parameters, i.e. primarily voltages and timings.

The heating currents applied to the ion and electron sources were set in a dedicated LabView Source Control program that enabled automatized ramping of heating currents at user defined rates. A DAQ unit with multiple analog-to-digital converter (ADC) and

DAC channels (Agilent 34970A) was used to convert software commands to analog control voltages and digitize current readbacks from the heating power supplies. The control voltage regulating the ion source heating current was directly connected to the floating filament power supply (Matsusada FDC37.5). Since the heating power supply for the electron gun (Matsusada C37.5) was floated on a HV platform inside a Faraday cage, the respective control and readback voltages were fed in and out of the HV cage using TRIUMF-built analog optocouplers.

All beam transport potentials, the gate and end-cap electrode potentials, and the HV biases for detectors were provided by commercial HV power supplies (ISEG NHQ205M and Caen SY4527LC HV system with Caen A1588, Caen A1733SN and Caen A1733SP modules) controlled through a different LabView control program. Communication with the Caen HV system was realized through a dedicated ethernet interface. Communication between the control computer and the serial interfaces of the ISEG NHQ modules was achieved via a USB-to-RS232 converter.

The trap electrode voltages were provided by the custom-built, multi-channel DAC HV supply (see section 6.3.7). A C program running on the RaspberryPi inside the DAC HV supply (titan-pi01) executed one of up to four different time-varying HV sequences whenever a trigger pulse was sent to the respective trigger input. The voltage sequences could be manually defined within a web interface hosted on the RaspberryPi.

A MIDAS-based run control and DAQ system with a dedicated web interface enabled the definition of experimental timings, the acquisition of harp and MCP detector signals, and served as master control interface for scans of experimental parameters. During typical runs, the user only interacted with the CPET system through the MIDAS web interface hosted on the DAQ computer (TITAN02). Before the start of an experimental run, user-defined timing sequences were compiled by the MIDAS front end running on a separate computer (lxcpet) in a Versa Module Europa (VME) crate. The compiled timing sequences were executed by a TRIUMF-built web programmable pulse generator (PPG) (purple box in Fig. 6.20), likewise housed in the VME crate. The PPG provided Nuclear Instrumentation Module standard (NIM)-logic pulses that were subsequently converted to TTL pulses and then fed to the trigger input channels of HV switch boxes, the DAC HV box and various other hardware. After pre-amplification and pulse discrimination, an MCS converted MCP signals into arrival time spectra which were recorded and further processed to summed spectra in the MIDAS DAQ. Harp electron signals were digitized and pre-processed by a digital oscilloscope. The scope provided the integrated area under harp-voltage pulses after smoothing by an internal 20 MHz-bandwidth low-pass filter and digital baseline correction. Within the MIDAS DAQ, the integrated areas were then (optionally) background-corrected and converted to corresponding electron numbers following the procedure described in section 6.3.8. The MIDAS web interface allowed for real-time monitoring and analysis of all acquired detector signals.

Network interfaces between the MIDAS run control and the LabView and DAC voltage control systems enabled automated scans of all relevant electrode voltages through a single user interface. The LabView voltage controller included a ZMQ reply server that processed

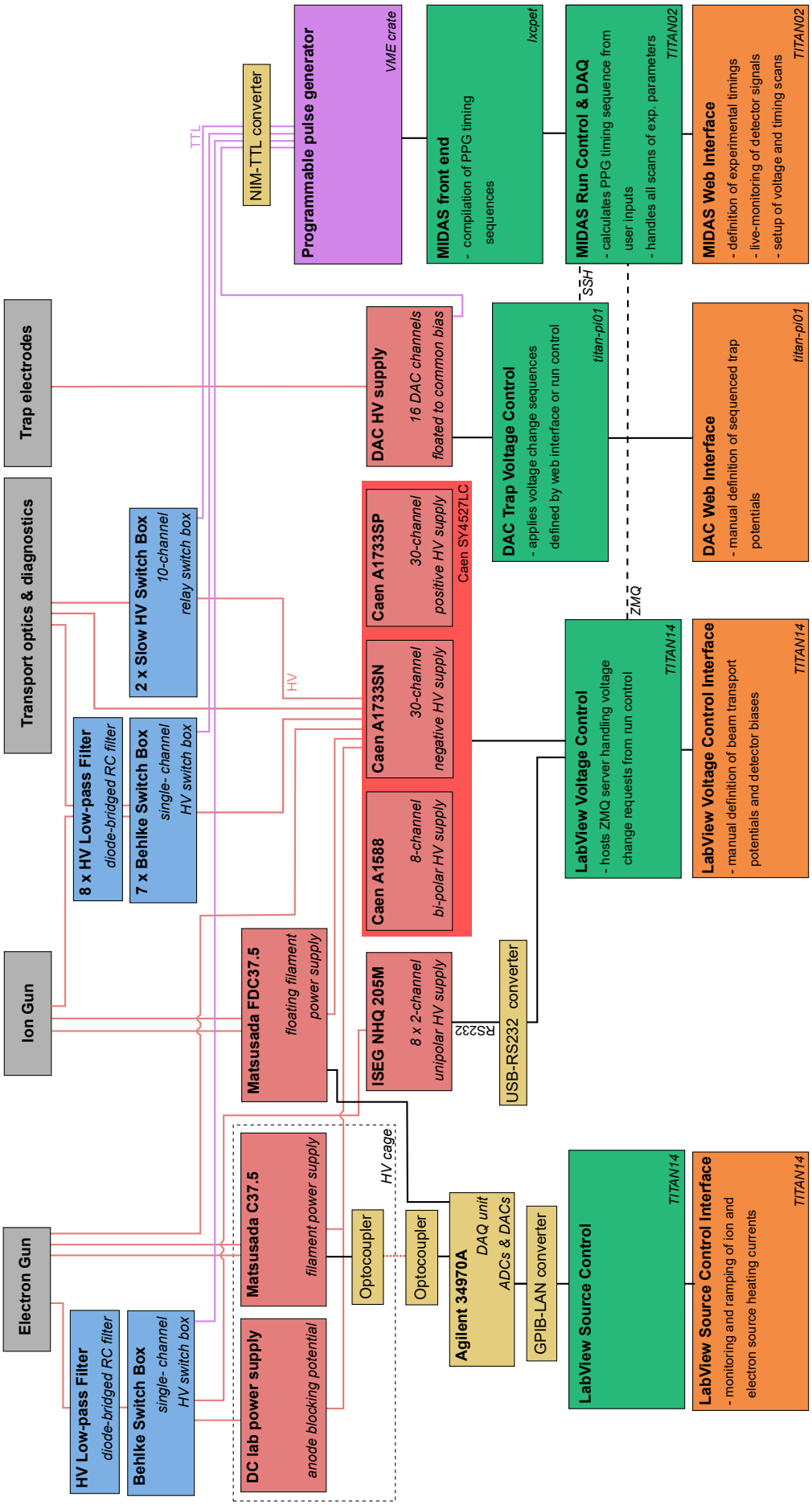

Figure 6.20. Simplified architecture of CPET's control and data acquisition (DAQ) system. Separate subsystems provide control over the source heating currents, beam line voltages, trap potentials and timings, respectively. The MIDAS run control acted as a master interface that handled the acquisition of detector signals and enabled scans of experimental timings and voltages. See text for details.

voltage change requests sent from the run control following a repeated request-and-reply pattern. Scans of trap potentials were realized through SSH communication that enabled the run control to programmatically update the trap potential sequences stored in a JSON file on the RaspberryPi prior to their execution.

6.4 Studies with the cooler Penning trap

6.4.1 Previous studies of electron plasma generation

Previous to the work reported in this thesis, experimental studies with CPET were focused on electron plasma generation. For simplicity and since the DAC trap biasing supply was then not fully developed yet, all these tests were performed with plasmas confined in non-nested, rectangular trap potentials formed by floating all trap electrodes to a common, positive high voltage and biasing the gate electrodes to a more negative potential. To provide the necessary context, I first discuss different mechanisms for electron accumulation in a Penning trap and introduce the scheme chosen for plasma formation in CPET. Subsequently, a brief review of the key results from previous plasma studies with CPET is given. This discussions forms a preface for the separate section on plasma generation in nested potentials (section 6.4.3).

Electron accumulation mechanism

The following three mechanisms for electron accumulation in a Penning trap have been presented in the literature and are exhibited in Fig. 6.21:

1. Dynamic capture: In this scheme dense, injected electron bunches are dynamically capture inside the trap by switching the potential of an initially open end cap electrode to a closed (i.e. electron-reflecting) state [see Fig. 6.21 (a)]. Assuming long electron bunches, that after reflection from the far-end gate electrode extend over twice the length of the trap $2L_T$, the maximal number of electrons that can be accumulated with this scheme can be approximated as [508, 539]:

$$N_{\text{e,max}} \approx \frac{2L_T I_e}{e\sqrt{2E_e/m_e}}, \tag{6.12}$$

where E_e is the electron energy in the trap, and m_e and e denote the electron mass and charge, respectively. Assuming typical parameters of electron beams from CPET's off-axis electron gun ($I_e = 1\,\mu\text{A}$, $E_e = 500\,\text{eV}$, $L_T = 0.4\,\text{m}$), yields $N_{\text{e,max}} \approx 5\times10^5$. This shows that this scheme is not applicable for accumulation of electrons from CPET's off-axis electron gun. Despite the conceptual simplicity of this loading mechanism, the realization of the dense bunches required to accumulate 10^8 or more electrons is a technical challenge. Ballistic electron loading is being used in HITRAP's cooler trap where a pulsed photoelectron gun provides dense bunches with up to 3×10^9 electrons and bunch lengths of $< 1\,\mu\text{s}$ [540].

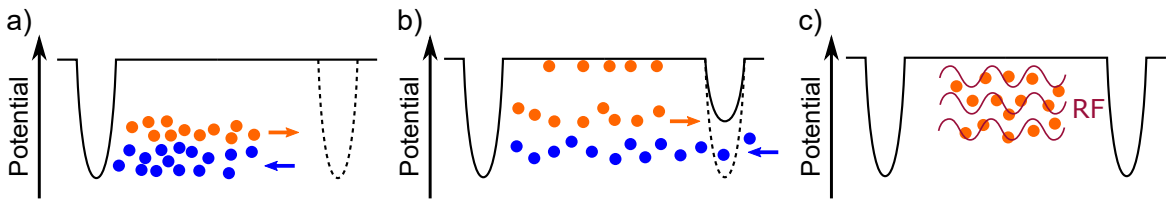

Figure 6.21. Mechanisms for electron accumulation in a Penning trap: a) Dynamic capture. b) Continuous loading. c) RF plasma generation. Incoming beam electrons are indicated in blue, reflected or trapped electrons are shown in orange. Note that electrons are high-potential seeking. See text for details.

2. Continuous electron loading: This technique was first introduced in [541] and relies on Coulomb scattering between injected electrons in a continuous beam with reflected beam electrons or already trapped electrons. The scattering transfers energy from the longitudinal into the transversal degrees of the electrons' motions. If the entrance gate electrode is biased appropriately, this energy loss can be exploited to continuously load electrons into a Penning trap [see Fig. 6.21 (b)]. The maximal number of electrons that can be accumulated with this loading scheme is, in principle, only dictated by the trapping fields, which determine the amount of electron space charge that can he held within the trap. Using this scheme, Mohamed et al. have demonstrated the production of trapped electron plasmas with up to 1.5×10^{10} electrons [542].

3. In-situ plasma generation: In this method, free electrons are created inside the Penning trap by applying RF fields to the trap electrodes that cause pre-existing charged particles to collisionally ionize residual gas particles [543]. The impact ionization events free up secondary electrons that may in turn ionize residual gas atoms, resulting in a feedback loop that can produce large numbers of trapped electrons without an external electron source. However, this scheme requires a sufficiently high neutral gas density and the initial presence of suitable charge carriers to trigger the ionization feedback loop. Since the technique has never been explored at pressures below a few 1×10^{-9} mbar [**?**], its applicability at vacuum conditions appropriate for the extended storage of HCI ($p < 1 \times 10^{-10}$ mbar) remains to be verified. Moreover, the ionization events result in the creation of positive ions. These ions can accumulate in positive wells in the nested trap potential and decrease the signal-to-contaminant ratio of ion-electron interaction studies.

As illustrated by the estimate of $N_{\mathrm{e,max}}$ deduced from Eqn. 6.12, the dynamic capture scheme was not suited to create sufficiently large electron plasma assuming the typical electron beam currents achieved within CPET (see section 6.3.6). Tests of the in-situ RF plasma generation showed that this plasma generation mechanism was not reliable enough under typical CPET vacuum conditions. Oftentimes this scheme only produced a detectable plasma after several 10 machine cycles. Electron accumulation in CPET was therefore realized using the continuous accumulation scheme. Despite the comparatively low electron currents transported into the trapping region, this scheme provided an efficient and reliable

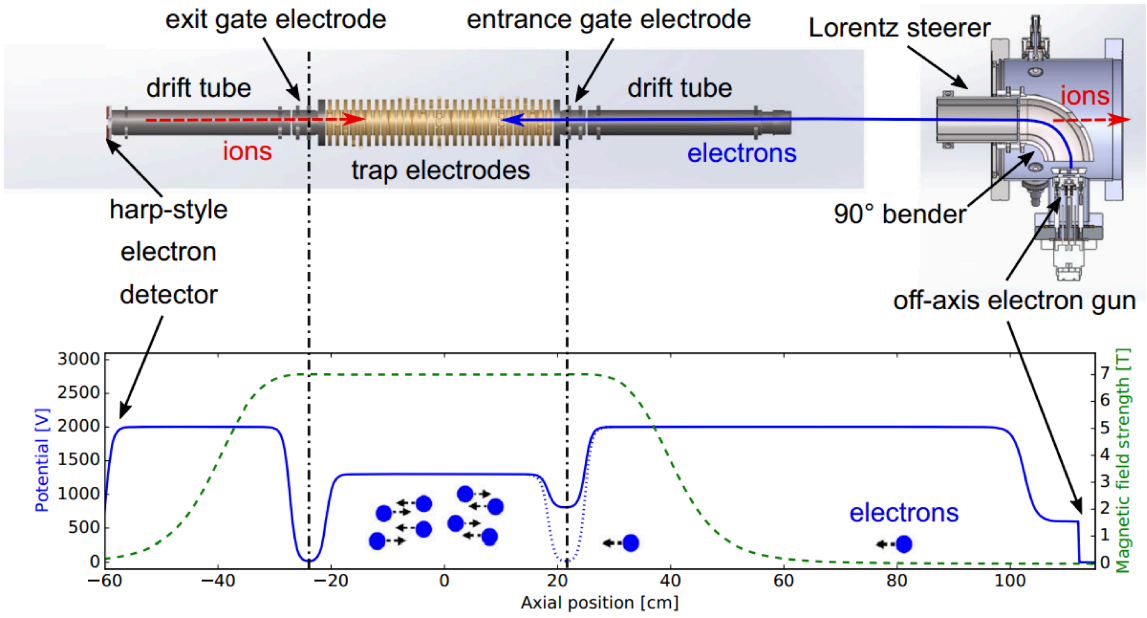

Figure 6.22. Off-axis electron injection and generation of electron plasmas in the cooler Penning trap. The most essential beamline components for creation and detection of trapped electron plasmas (top, not to scale) are shown along with typical on-axis potentials for electron loading and the magnetic field. Figure reprinted from [522].

means of loading the trap with up to several 1×10^8 electrons within less than $0.5\,\mathrm{s}$.

Previous work with electron plasmas in CPET

For initial studies of electron plasmas in CPET an on-axis electron gun was used as the electron source. As mentioned in section 6.3.8, this work revealed that the magnetic expansion of extracted electron bunches prevented electron diagnostics with a detector placed outside the magnet bore. As a temporary solution, a phosphor screen was installed within the drift tube DT1. This setup enabled Chowdhury et al. [508] to reliably create and study electron plasmas confined in rectangular potential wells formed by using the gate electrodes as end caps. The spatial resolution of the phosphor screen permitted a detailed characterization of the properties of these plasmas. Typical plasmas exhibited a length of $L_p = 400\,\mathrm{mm}$, a radius $r_p = 0.5\,\mathrm{mm}$, electron number densities of $n_e \approx 8 \times 10^8\,\mathrm{cm}^{-3}$ and consisted of $N_e = 1.6 \times 10^8$ electrons [508]. Further, it was discovered that a newly formed plasma column underwent a diocotron oscillation, an azimuthal $E \times B$-drift motion, which was found to be damped on a timescale of a few seconds [544]. These findings proved that, in principle, electron plasmas suitable for electron cooling could be created in CPET. Since the phosphor screen was blocking the ion-injection beam line, a more permanent detector solution had to be found. This lead to the development of the harp electron detector (see section 6.3.8) which provided a reliable means to monitor the number of trapped electrons while permitting ions to be injected into the trap.

As a preparation for ion-electron interaction studies, the electron gun had to be moved off

axis to allow for the unimpeded extraction of trapped ions onto an MCP detector (ES MCP0). The off-axis electron injection introduced a number of challenges which were addressed by the development of an optimized off-axis electron gun (see section 6.3.6 and ref. [523]). Initial tests with the off-axis electron gun [522] were performed with electric potentials as shown in Fig. 6.22. For simplicity, the electron gun was, at the time, operated on ground potential and the trap electrodes had to be floated to $1.3\,\mathrm{kV}$ to enable a reasonable electron transmission through the magnetic field gradient. Electrons were accumulated in non-nested rectangular potentials formed by floating the trap electrodes to $1.3\,\mathrm{keV}$ and biasing the gate electrodes to voltages between 0–$800\,\mathrm{V}$. For electron detection, the gate electrode G1 and the drift tube DT1 were used to form an extraction gradient that caused electrons to stream from the trap onto the harp detector which was biased to $2\,\mathrm{kV}$. In these tests, 2×10^8 electrons could be accumulated in only $200\,\mathrm{ms}$, thus proving that the electron accumulation was sufficiently fast for on-line cooling of radioactive HCI.

6.4.2 Initial ion trapping attempts and prevention of HV breakdown

After a suitable plasma generation mechanism had been established, we performed the first tests of ion trapping in CPET with the trap still in its original wiring configuration [Fig. 6.7 a)]. Initial plans [55] for ion and electron storage in CPET had foreseen to float the trap electrodes to voltages $\sim 1900\,\mathrm{V}$ such that ions bunches coming in at a transport energy of $2\,\mathrm{kV}$ (the typical energy for ion transport into the precision trap MPET) would be electrostatically decelerated and could be captured and released by appropriately pulsing the HV biases on the designated endcap electrodes. Although this trap biasing scheme allowed us to successfully transport ion beams from the test ion source onto the ES FC, ion trapping could not be reliably achieved since attempts to dynamically capture and release the ions by pulsing the voltages of the gate electrodes or the outermost trap electrodes regularly resulted in electrical breakdown.

The discharges lead to substantial background event rates on the MCP detectors or bright illumination of biased phosphor screens. In more severe cases, they deposited appreciable currents ($\gtrsim 10\,\mu\mathrm{A}$) onto electrodes and lead to over- or undervoltages on the respective power supply outputs. Once triggered, a discharge would often spread to multiple electrodes and sustain until the HV biases of all affected electrodes were ramped to ground potential. See appendix B for a more complete description of the observed discharge phenomena.

Since the recurring HV breakdown prevented a reliable system operation, it had to be addressed before further steps could be taken towards electron cooling studies. We performed an extensive root-cause analysis that included HV insulation tests and visual inspection of the trap structure after its removal from the vacuum chamber. The analysis revealed that multiple electrodes along the trap structure had insufficient strength against HV breakdown.

These identified issues were addressed by a set of hardware modifications for improved breakdown strength (see appendix B for details). Moreover, a new trapping scheme was devised in which the trap electrodes could be operated at voltages of $\leq 200\,\mathrm{V}$ while incoming ions would be decelerated to trappable energies by pulsing the drift tube DT1. Operating

the trap electrodes near ground potential in turn allowed us to lower the beam transport potentials applied to the surrounding electrodes along the trap structure, thus reducing the likelihood of HV breakdown between biased electrodes and grounded conductors. Biasing the trap electrodes to moderate voltages further simplified connecting sensitive electronic equipment to the trap electrodes, such as RF generators for charged particle manipulations or spectrum analyzers for noise analysis. Since the ion extraction path was well-shielded against field penetration from the grounded vacuum chamber, the new scheme permitted the extraction of trapped ions onto the ES MCP and ES MCP0 detectors without further beam energy changes by a pulsed drift tube.

The feasibility of the new ion transport procedures was verified through trajectory tracing simulations in SIMION as reported in [512, 545]. To accommodate the new operational requirements, the arrangement and wiring configuration of the trap electrodes was updated, resulting in the revised configuration already shown in Fig. 6.7 b). These changes reduced the total number of HV-carrying wires inside the magnet bore and allowed to increase the spacing between critical conductor wires, resulting in improved breakdown strength. A detailed description of the observed discharge phenomena, the associated root-cause analysis and the resulting hardware modifications is given in appendix B. Complementary information can be found in [512].

First tests of ion transport with the revised trap structure and the new trap biasing scheme verified the substantially improved breakdown strength of all critical electrodes, confirming the indications from preceding HV resistance tests. The increased robustness and reliability of the system enabled the first successful trapping of ions in CPET and allowed us to proceed with further work towards ion-electron interaction studies.

6.4.3 Preparation of trapped electron plasmas

Electron cooling studies in a Penning trap require a reproducible means to create trapped electron plasmas. The simulation studies discussed in section 6.2 indicate that plasmas with electron number densities of $n_e \sim 1 \times 10^8\,\mathrm{cm}^{-3}$ and a total electron number of $N_e > 1 \times 10^7$ are desirable. Imperfections of the trapping fields and collisions with residual gas induce a radial plasma expansion that limits the lifetime of trapped electron plasmas [546]. To obtain reproducible cooling conditions, the trap hence has to be periodically re-filled with electrons, either to replenish an existing electron plasma or to re-generate a new one entirely.

To enable rapid cooling to ion energies on the order of $1\,\mathrm{eV/q}$, the electron plasma needs to equilibrate to a temperature $T_e < 1\,\mathrm{eV}$ via cyclotron cooling. To ensure that cooled and extracted ion bunches exhibit reproducible beam properties, it is further desirable to minimize fluctuations of n_e and N_e both throughout the cooling period as well as from cycle to cycle. On-line cooling of radioactive HCI further sets tight limits on the available timescale for plasma generation. Since typical measurement cycles in TITAN's measurement Penning trap (MPET) are performed at rates of 1–10 Hz, a cooling cycle should ideally take up no more than a few 100 ms. With expected cooling durations of 100–200 ms, this limits the time available for electron plasma preparation at the beginning of a cooling cycle to 50–

300 ms. In terms of electron plasma preparation, this demand can be met in a several ways. Either a new plasma is generated in every measurement cycle (with plasma preparation taking up no more than 300 ms), or a given plasma is re-used over many cooling cycles and only occasionally replenished, leaving more time for plasma preparation.

While the demands concerning the plasma preparation and cooling time scales are crucial for work with radioactive ions, it is important to note that the cooling studies with stable singly charged ions presented here did not involve such stringent requirements. In particular, the time available for a cooling cycle was only limited by the finite lifetime of ions in the trap which results from various, non-decay-related loss mechanisms such as elastic and inelastic collisions with rest gas.

This subsection discusses the preparation of electron plasmas in CPET, with a focus on plasma generation in nested potential wells. Key findings obtained in the present work on the plasma formation in simple rectangular and more complicated, nested potential wells are presented. This work facilitated the creation of reproducible electron plasmas in nested wells and formed a critical prerequisite for the electron-ion interaction studies reported in subsection 6.4.5.

Electron trapping in non-nested potential wells

Within this thesis, initial studies of plasma generation in CPET were performed using non-nested, approximately rectangular potential wells formed by the trap gates and/or the end cap electrodes. These trap potentials resembled the ones used for the initial plasma formation tests with the optimized off-axis electron gun (see Fig. 6.22). However, to reduce the likelihood of discharges, it was decided (see section 6.4.2 for details) to operate the trap's ring electrodes at voltages near earth ground potential. To still enable electron transport through the magnetic field gradient into the trap, the electron gun cathode was floated to -2 kV using a dedicated HV cage for the cathode heating power supply (see section 6.3.6). After likewise shifting all other potentials along the electron transport beamline by -2 kV, only minor re-tuning of the beam line potentials was necessary to re-establish the original electron loading performance.

The studies with rectangular potential wells enabled a detailed characterization and optimization of the electron accumulation dynamics in CPET. As already noted in the early work by Mohamed et al. [521], the most critical parameters affecting the dynamics of the continual accumulation scheme are the electron beam current in the trap, the entrance-gate voltage and the electron loading duration. The electron accumulation and trapping in simple rectangular or harmonic potentials has already been extensively reported on in earlier work [508, 521, 523]. The description here therefore focuses on electron loading with more complicated trap potentials involving nested wells.

Electron trapping in nested potential wells

Nested trap potentials are required to simultaneously confine oppositely-charged particles such as cations and electrons. Tests of electron plasma generation in nested potential wells in

CPET's trap potential therefore formed an essential prerequisite for in-trap electron cooling studies. The electron trapping in nested potential wells proceeded in a phased approach involving an increasing technical complexity in terms of the HV biasing. First, the effect of nested potential wells on the electron loading process and the plasma formation was studied by forming simple nested wells with the end cap electrodes. Following these proof-of-principle studies, more sophisticated trap potentials were shaped using the multi-channel DAC HV supply (see section 6.3.7) to bias the ring trap electrodes. For brevity, concave potential wells that form local maxima for electron accumulation in a nested trap potential will from here on simply be referred to as *electron nests*.

Verification of electron localization in a nested potential well

The first tests of electron accumulation with nested potentials were conducted by using the E2 end cap electrode to add a nested potential well to a larger rectangular well formed by negatively biasing the gate electrodes. The resulting potential configuration allowed us to test the temperature relaxation of the electron plasma, and enabled the first demonstration of electron localization in a nested potential well in CPET.

For these tests, electrons were accumulated over $1\,\mathrm{s}$ with the E2 end cap kept at $150\,\mathrm{V}$ and the G1 and G2 gate electrodes biased to $-1200\,\mathrm{V}$ and $-600\,\mathrm{V}$, respectively. All other trap electrodes were kept on ground potential. After the loading process, the G2 bias was switched to $-1200\,\mathrm{V}$ and the electrons were held in the trap for different storage times. To probe the accumulation of electrons in the positive nest formed by the end cap, trapped electrons were dumped from the trap in two stages. First the G1 electrode was switched to an ejection voltage of $400\,\mathrm{V}$ to remove electrons that were not trapped inside the nested well. $5\,\mathrm{ms}$ later, electrons that had remained confined by the nested well were released toward the harp detector by pulsing the E2 voltage from $150\,\mathrm{V}$ to $0\,\mathrm{V}$. The corresponding electron-induced voltage pulses recorded on the harp detector are shown in Fig. 6.23 after baseline-correction and background subtraction (see section 6.3.8). Trigger pulses for the opening of the G1 gate and for the nest dump were sent at $t = 0$ and $t = 5\,\mathrm{ms}$, respectively. Delays between the trigger pulses and the electron-induced signals on the harp detector arise from electronic delays, finite HV switching times and the electron flight times to the detector.

The nest-dump signals at $t = 6\,\mathrm{ms}$ confirmed the accumulation of large quantities of electrons in the nested potential well. As the electrons entered the trap with kinetic energies $> 600\,\mathrm{eV}$, a mechanism must have been at play that efficiently cooled their longitudinal motion, causing the electrons to populate the nested well within a storage period of $500\,\mathrm{ms}$.

The presence of the voltage pulses at $t \approx 1.5\,\mathrm{ms}$ further shows that not all trapped electrons were confined inside the electron potential nest, likely because the nest was filled to its space-charge-induced storage capacity. While the amplitudes of the pulses at $t \approx 1.5\,\mathrm{ms}$ showed a measurable drop with increasing storage time, the amplitude of the nest-dump signals was found to be essentially constant for all tested storage times. This indicates that for the chosen potential configuration, the electron lifetime in the nested well was substan-

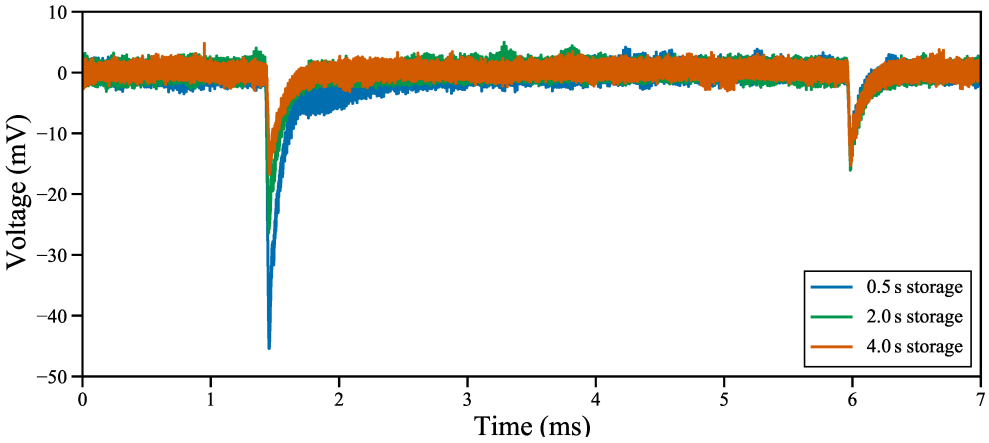

Figure 6.23. Verification of the accumulation of electrons in a nested potential well formed by the E2 end cap. Harp signals are shown after different storage times. The peaks at 1.5 ms and 6 ms correspond to electrons ejected by opening the G1 gate and electrons ejected after removing the nested well, respectively.

tially longer than that in the larger rectangular well, a promising indication for electron-ion interaction studies.

Effect of the entrance-gate voltage on the electron accumulation

Fig 6.24 shows the number of detected electrons as a function of the potential of the entrance gate (G2) for two different electron emission currents. The data was acquired with an electron loading time of 0.5 s and a subsequent storage period of 2 s. The exit-gate electrode G1 was biased to -1200 V during the loading and storage periods and pulsed to 400 V for dumping the electrons onto the harp detector. After the loading period the entrance gate G2 was switched to 1200 V. During this and all subsequent measurements, the electron emission from the cathode was normally blocked by applying a repulsive potential of -2070 V to the Wehnelt cylinder, and only unblocked during the loading period by switching the Wehnelt cylinder to the cathode potential of -2 kV. The difference between the maximal numbers of trapped electrons achieved with the different beam currents resulted from the increase of the electron loading rate with the electron current in the trap. At the given beam currents, the accumulated electron number N_e was comparatively insensitive to entrance gate voltages > -900 V. At more negative entrance-gate voltages, the number of trapped electrons quickly dropped to zero as a result of the reduced beam current permitted into the trap.

Effect of a nested potential well on the electron accumulation

After the successful accumulation of electrons in nested wells formed by the end cap electrodes, we proceeded with trapping electrons in nests formed by the DAC HV supply. These studies showed that the presence of a nested well during the electron loading stage substan-

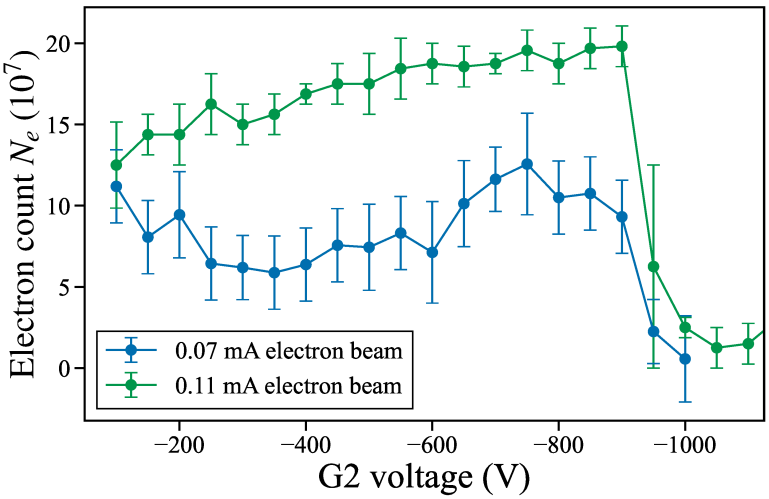

Figure 6.24. Effect of the G2 gate electrode voltage on the accumulated number of electrons for 70 µA (blue) and 110 µA (green) electron emission current. To guide the eye, data points are connected by lines.

tially increased the electron loading rate, an effect that had already been observed when forming electron nests with the end caps.

The impact of an electron nest on the number of trapped electrons is exhibited by the baseline-corrected and background-subtracted harp detector signals in Fig. 6.25. The signals were acquired by dumping the trapped electrons onto the harp after a 1 s long electron loading and a subsequent 1 s long storage period. At $t = 0$, the G1 potential was switched to 200 V to allow the electrons to stream towards the harp detector ("G1 dump"). The blue trace was obtained by dumping a plasma stored in a large rectangular potential well. The latter was formed by biasing the G1 and G2 gate electrode to -1200 V and -500 V, respectively, while keeping all other trap electrodes on ground potential. Since the electron beam was turned on and off with the Wehnelt cylinder bias, switching of the G2 voltage was not necessary to stop the electron loading process. The brown trace was obtained after adding a 100 V deep harmonic electron nest formed by the T7 to T21 trap electrodes. The green trace was acquired with an identical harmonic potential nest that was dumped 10 ms after opening the G1 gate by sequentially pulsing the ring trap electrodes to ground potential. Since the G1 gate was kept in the electron-extraction state for 100 ms, electrons ejected from the nest in secondary electron dump could freely stream to the harp detector. After the nest dump and before the beginning of a new machine cycle, the nested potential was reinstated. Average electron numbers obtained with the mentioned potential configurations are listed in table 6.3 (see section 6.3.8 for details on the electron number extraction).

The corresponding signal in Fig. 6.25 (green trace) shows a peak after the nest dump at $t = 10$ ms but exhibits no detectable electron signature after the G1 dump at $t = 0$. This indicates that essentially all electrons were successfully trapped inside the nested potential well formed by the DAC HV supply and implies that the plasma underwent a net cooling. Likely both emission of cyclotron radiation and electron-neutral collisions contributed to

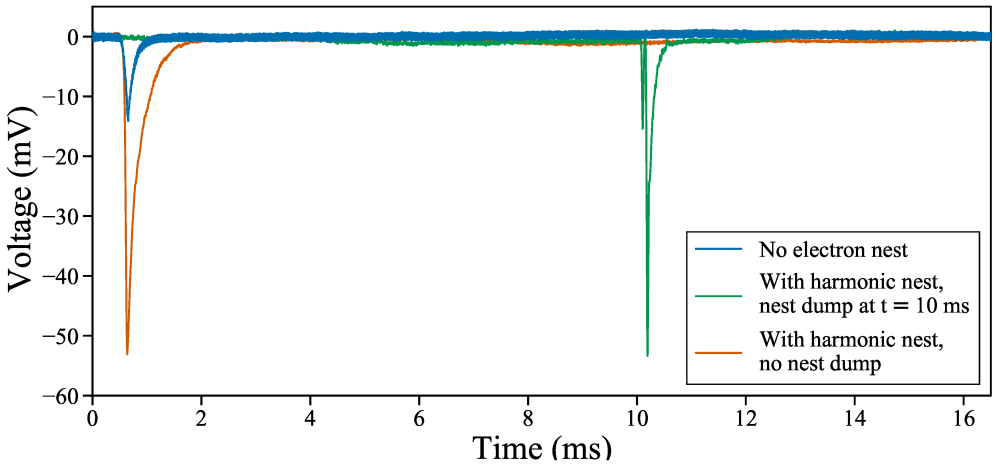

Figure 6.25. Effect of a harmonic electron nest on the electron loading efficiency. The plotted electron dump signals were baseline-corrected and background subtracted as described in section 6.3.6. The shown signals were obtained using a rectangular trap potential without an electron nest (blue trace), and with an additional 100 V deep harmonic nest that was either dumped at the end of each machine cycle (green trace) or kept static (brown trace). The large signal obtained with a static nest resulted from a successive filling of the nest with electrons over preceding cycles. See text for details.

the energy dissipation from the plasma. This observation further demonstrates that potential plasma heating induced by the HV switching of the G1 electrode bias during the G1 electron dump did not cause noteworthy quantities of electrons to escape from the nested well.

Compared to the non-nested rectangular well, the presence of the dumped electron nest produced a more than three times higher electron count. With the given electron beam conditions, the number of electrons trappable in the non-nested, rectangular potential well only saturated at $N_e \approx 6 \times 10^8$. Hence, the higher number of trapped electrons in the presence of an electron nest cannot simply be accorded to the expected increase in the trap's storage capacity but must result from an increased electron loading rate. The exact mechanism be-

Table 6.3. Electron numbers extracted for different trap potential configurations. The given electron numbers were deduced by integrating electron-dump signals as those shown in Fig. 6.25 for 10 subsequent cycles and averaging the resulting areas under the traces. Electron number uncertainties were deduced from the corresponding standard errors of the mean.

Trap potential configuration	Detected electron number N_e
No electron nest[a)]	$(1.88 \pm 1.69) \times 10^8$
Harmonic nest, with nest dump[b)]	$(5.85 \pm 1.48) \times 10^8$
Harmonic nest, no nest dump[a)]	$(8.38 \pm 0.94) \times 10^8$

a) Integrated time range corresponding to $t = 0$–6 ms in Fig. 6.25.

b) Integrated time range corresponding to $t = 10$–16 ms in Fig. 6.25.

hind this loading-rate enhancement is unclear. It can be conjectured that the higher local electron density resulting from the presence of an electron nest raised the rate of collisions between trapped electrons and beam electrons, which, in turn, increased the beam electrons' longitudinal energy loss and boosted the electron loading efficiency.

Runs with a static electron nest showed a steady increase in the electron number over the first 2–3 cycles. Subsequently, the electron signals stabilized at the signal level of the brown trace in the Fig. 6.25. The mean electron number obtained with the static nest was even higher than that with a dumped nest. This finding is in accord with the model proposed by Mohamed et al. [521] which suggests that the electron accumulation in the continuous loading scheme is not only due to interactions between electrons in the incoming and reflected beams but also due to scattering of beam particles with already trapped[4] electrons. According to their model, the electron loading rate α is given by:

$$\alpha = \frac{dN_e}{dt} = (\kappa_{\text{bb}} I_e^2 + \kappa_{\text{bp}} I_e N_e) g(N_e), \tag{6.13}$$

where I_e and N_e denote the electron beam current in the trap and the number of trapped electrons, respectively, the function $g(N_e)$ characterizes the saturation of N_e as the trap's storage capacity is approached, and the parameters κ_{bb} and κ_{bp} quantify the strength of the beam-beam and beam-plasma interaction, respectively. Assuming that in the experimental runs with a static nest, electrons remained inside the nest over multiple cycles and gradually filled it to its space-charge-induced storage capacity, the higher number of electrons observed with the static nest can be explained by an increased loading rate due to the pre-existing plasma at the beginning of a machine cycle. This hypothesis is supported by the fact that the electron number exhibited a steady increase over the first few machine cycles, before saturating at a steady level.

These findings suggest a potential mode of operation that would minimize the time "lost" to electron re-loading and permit cooling of shorter-lived isotopes. In particular, once a large plasma with $N_e > 10^7$ has been created, the number of trapped electrons could be periodically replenished by brief electron re-loading periods of less than $100\,\text{ms}$. The sketched mode of operation was not further explored within this work, since the proof-of-concept ion-electron interaction studies reported here required the plasma to be dumped onto the harp detector at the end of each cycle in order to verify the presence and shot-to-shot reproducibility of the trapped plasmas. Coupled to a non-destructive way to monitor the plasma conditions[5], such a rapid electron re-loading scheme would enable substantially faster cooling cycles. This, in turn, would make ion preparation in the cooler Penning trap more compatible with the typical repetition rates ($\geq 1\,\text{Hz}$) for mass measurements of short-lived isotopes in TITAN's measurement Penning trap and thus ensure optimal use of the rare isotope beam.

[4] An electron is regarded as a trapped rather than a beam particle, once its longitudinal energy falls below $e|V_{\text{T}}|$, where V_{T} is the trapping potential formed by the gate electrodes.

[5] Non-destructive plasma detection has been demonstrated by the pick-up of image currents induced by the plasma on the trap electrodes [547, 548]. Such a detection scheme was also being developed for CPET but was at the time of the presented measurements not available yet.

Effect of the loading time on the trapped electron number

Besides the electron beam current and the entrance-gate voltage, the third parameter that critically affected the number of trapped electrons is the electron loading time, i.e. the duration over which the electron beam was permitted into the trap. In initial studies of plasma generation in CPET, the electron beam was left continuously on and the electron accumulation in the trap was stopped by switching the entrance-gate electrode (G2) to an electron-reflecting potential. However, this procedure was found to induce a significant electron-induced background count rate on the ES MCP0 detector and made the system more prone to electron-induced HV discharges. While these effects did not hamper electron plasma studies, the electron-induced background signals on the ES MCP0 were detrimental to ion-electron interaction tests as detailed in section 6.4.5. A more appropriate mode of operation was established by pulsing the Wehnelt cylinder bias to control the electron emission from the cathode, such that the electron beam was only activated during the electron loading period. This also allowed us to keep the G2 electrode at a static bias throughout a machine cycle and prevented interactions between beam electrons and extracted ions. All measurements presented further below were performed with this mode of operation.

A rectangular electron nest was formed by biasing the 13 central trap electrodes (T9 to T21) to $20\,\mathrm{V}$. During the loading and storage periods, the G1 and G2 gate electrodes were biased to $-1200\,\mathrm{V}$ and $-200\,\mathrm{V}$, respectively. The electron gun was operated with an emission current of $\approx 75\,\mu\mathrm{A}$, resulting in a DC transmission of $\sim 1\,\mu\mathrm{A}$ to the harp detector. The loading period was followed by a $1.3\,\mathrm{s}$ long electron storage period. Subsequently, all electrons were removed from the trap via a two-stage dump. First, electrons not trapped in the nest were dumped onto the harp detector by pulsing the E1 and G1 electrode bias to $200\,\mathrm{V}$ and $220\,\mathrm{V}$, respectively. $2\,\mathrm{ms}$ later, the nest was dumped by sequentially pulsing the ring trap electrodes to ground potential. At the beginning of each machine cycle, the nested trap potential was reinitialized.

The number of electrons detected after the nest dumps is shown in Fig. 6.26 and seen to increase linearly with the electron loading time. Over the scanned range of loading times, the electron number showed no signs of saturation, indicating that the nests storage capacity was substantially larger than the maximal detected electron number of 1.1×10^8. Already after $40\,\mathrm{ms}$ of electron loading, the detected electron number had reached $N_e \approx 2 \times 10^7$, thus exceeding the smallest desirable plasma electron number suggested by the electron cooling calculations presented in section 6.2. This result verified that plasmas with sufficient electron numbers for studies of electron cooling of co-trapped ions could be rapidly and reproducibly produced in nested potential wells.

Effect of the nest depth on the trapped electron number

Throughout this work, the term *nest depth* refers to the maximal difference between the voltages applied to a set of trap electrodes that form a nested potential well[6]. Due to the

[6]Since CPET's trap electrodes were, by default, kept at ground potential, this voltage difference is equivalent to the maximal positive voltage applied to the electrodes forming an electron nest.

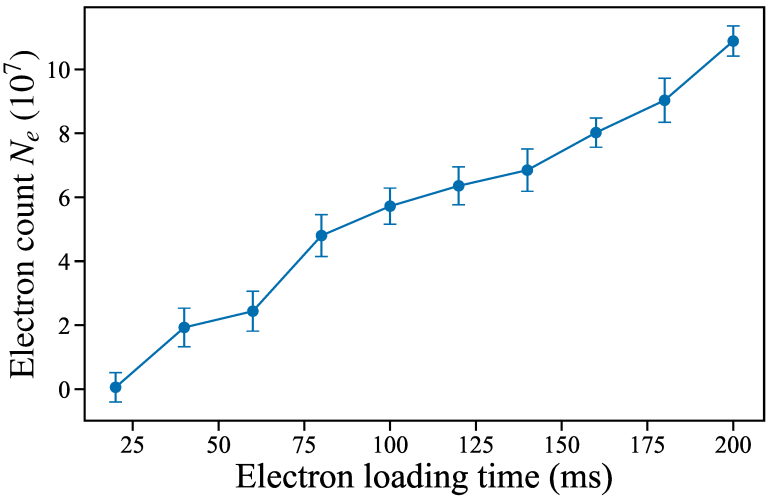

Figure 6.26. Number of electrons accumulated in a rectangular, nested well formed by biasing the central 13 trap electrodes to 20 V. The trap's other ring electrodes were grounded. Each data point is an average over 25 machine cycles. To guide the eye, data points were connected by lines.

effects of field penetration and electron space charge, even on-axis, the *effective nest depth* experienced by trapped charged particles usually differs from the externally applied nest depth. For an electron nest of fixed shape, the nest depth affects the electron cooling process in two important ways. Firstly, the nest depth determines the maximal electron line density that can be confined within the nest. Secondly, as mentioned in section 6.2, the minimal ion energy achievable through in-trap electron cooling of cations is set by the effective depth of the electron nests in the trap potential. To prevent a premature loss of cooling power, the number of trapped electrons and the applied nest depth have to be optimized with respect to each other, the general aim being to minimize the effective nest depth. This optimization can be achieved by scanning the nest depth under otherwise fixed electron loading conditions.

The number of electrons accumulated in a rectangular electron nest formed by biasing the T9 to T21 trap electrodes to a common positive potential is exhibited in Fig. 6.27 as a function of the nest depth. Electrons were again ejected using a two-stage electron dump as described above. The plotted electron numbers were extracted from the nest-dump signals recorded on the harp detector.

At nest depths ≤ 30 V, the detected electron number is seen to rise with the nest depth, indicating that the nest was filled to its storage capacity. At greater nest depths, the electron number saturates at $N_e \approx 1.75 \times 10^8$, suggesting that the number of accumulated electrons was then limited by the loading duration and could not be raised further by increasing the nest's storage capacity. The electron-ion interaction tests reported in section 6.4.5 were typically performed with similar loading conditions and a 40 V deep rectangular nest which resulted in a suitable number of trapped electrons without overfilling the nest.

Preventing an overfilling of the electron nest was later found to be crucial for ion-electron interaction tests, since excessive electron escape from a potential nest filled close to its

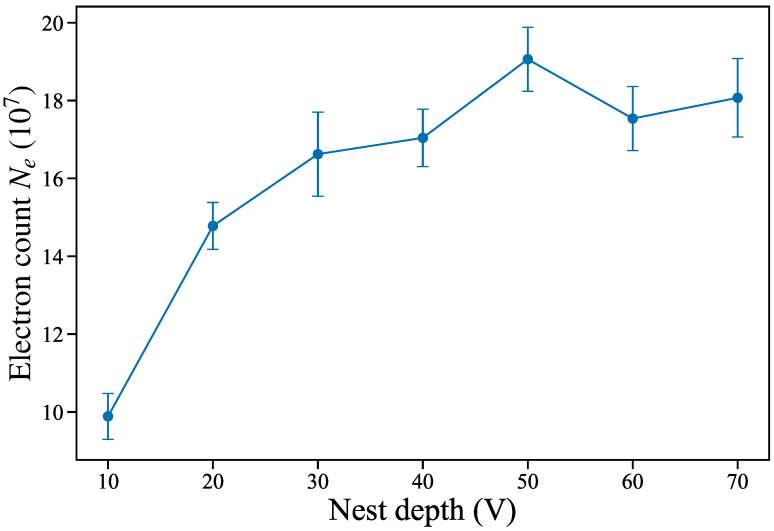

Figure 6.27. Detected number of electrons accumulated in a rectangular nest formed by 13 trap electrodes (T9-T21) as function of the nest depth. Electrons were ejected to the harp following a 250 ms long loading period and 1.15 s storage time in the trap. Each data point is an average over 50 machine cycles. To guide the eye, data points were connected by lines.

storage capacity led to substantial background event rates on the ES MCP0 detector. The background arose from secondary ions created by ionizing collisions of stray electrons with residual gas particles.

Electron plasma lifetimes

To prevent a reduction in the electron cooling power, electron losses from the trap should be minimized. This is primarily because a reduction in the trapped electron number typically results in a decrease in the electron number density n_e which, in turn, reduces the energy-exchange rate between ions and electrons (see e.g. Eqn. 6.4). The primary mechanisms that lead to electron losses, and thus limit the plasma lifetime, are radial electron transport across the magnetic field lines due to asymmetries in the confining fields [549, 550] and due to collisions with neutral rest gas particles [550, 551]. Additionally, electrons in the tail of the Boltzmann velocity distribution may evaporatively escape the axial trap potential [552]. To evaluate the extent of electron losses over a cooling cycle, we recorded the number of detected electrons as a function of the plasma storage time.

For electrons confined in a non-nested, rectangular well formed by grounding all ring electrodes and biasing the G1 and G2 gate electrodes to -1200 V and -900 V, respectively, the detected electron numbers are plotted in Fig. 6.28 (a). These plasmas were created using a 2 s long electron loading period. The rise in N_e over the first few seconds of electron storage had already been observed in earlier measurements [553] and can be attributed to the damping of the $m = 1$ diocotron mode. For plasmas with a too large radial offset from the trap's symmetry axis, the diverging magnetic field lines caused a fraction of the extracted plasma electrons to get lost against the walls of the drift tube DT1 (see section 6.3.8), pre-

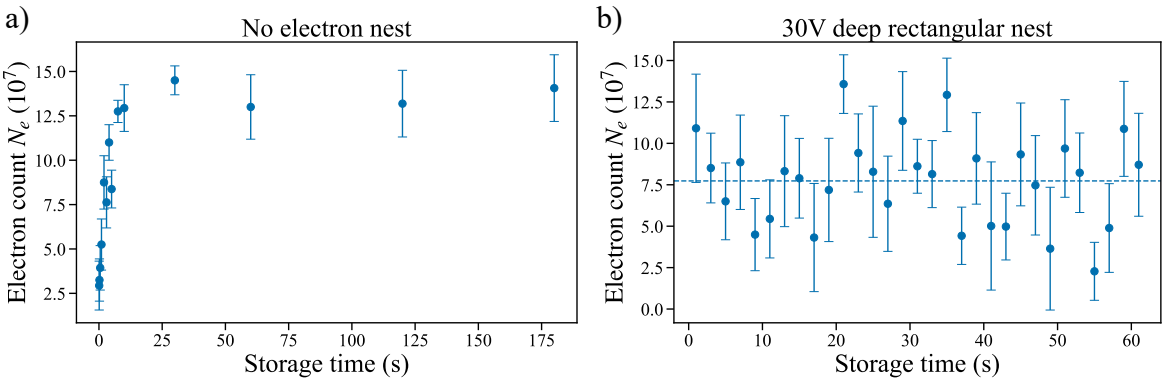

Figure 6.28. Measurements of the electron plasma lifetime in (a) a potential well formed only by the gate electrodes with all other trap electrodes at ground potential and (b) in a nested potential well formed by biasing the T13-T18 trap electrodes to 30 V. The dashed line in subfigure (b) marks the mean electron number over all storage times. See text for details.

venting them from reaching the harp detector. Once the amplitude of the $m = 1$ diocotron mode had been sufficiently damped out, the electron losses within the drift tube eventually became negligible, allowing all plasma electrons to be detected for storage times $\gtrapprox 10$ s. Subsequently, the number of detected electrons remained constant within the measurement uncertainties for storage times up to 180 s. These results indicate very stable electron trapping conditions with plasma lifetimes[7] of at least several minutes.

The data shown in Figure 6.28 (b) was obtained in a similar measurement of the number of electrons stored in a rectangular electron nest formed by biasing the trap electrodes T11 - T17 to 30 V. Due to higher electron loading rates resulting from the presence of a nested electron well, this scan could be performed with an electron loading time of only 90 ms. No initial rise in the detected electron number was observed over the covered range of storage times since, for plasmas trapped in nested potential wells, the damping of the diocotron mode was found to be significantly faster than in a large rectangular well and typically proceeded within < 400 ms [not shown within scan range of Fig. 6.28 (b)]. The increased fluctuations of N_e compared to (a) were primarily caused by uncorrected[8] baseline fluctuations of the isolation amplifier output voltage (see section 6.3.8 for details) and by a poorer signal-to-noise ratio induced by the larger switching background associated with the nest dump.

Over storage times of up to 60 s, no significant electron loss could be detected within the measurement sensitivity. This indicates that nested electron wells also provided stable trapping conditions that enabled electron plasma lifetimes of at least several minutes. Since typical ion-electron cooling measurements extended over no more than a few seconds, electron losses throughout a cooling cycle could be assumed to be negligible for the electron

[7] We define particle lifetimes in a trap as the time it takes for the trapped particle number to fall to $1/e \approx 0.37$-times the initial value.

[8] The baseline compensation procedure described in section 6.3.8 reduced the typical fluctuation of the detected electron numbers by a factor of 3–4 but was only implemented after taking the data presented in Fig. 6.28.

cooling tests reported in section 6.4.5. The observed plasma lifetimes further indicate that electron plasmas trapped in CPET could, in principle, be re-used over multiple cooling cycles, as long as care is taken to limit plasma heating due to trap potential changes.

6.4.4 Ion trapping and first co-confinement of ions and electrons

After a reliable means of electron plasma generation was established, the injection and trapping of non-radioactive singly charged ion (SCI) from the surface ion source was commissioned. For ion-electron interaction studies, a reliable mode of ion injection and trapping had to be developed. It further had to be verified that the ion lifetime in the trap was sufficiently long for the intended electron cooling studies. The following subsections separately address the creation of bunched ion beams, the capture of ion bunches and the obtained ion lifetimes in the trap, with and without co-trapped electron plasmas.

Injection of ion bunches

The typical progression used to optimize the ion transport through the system is illustrated in Fig. 6.29. The shown TOF mass spectra were recorded using the ES MCP0 detector and a MCS bin width of 80 ns. All measurements presented throughout this thesis were conducted with an ion transport energy of ≈ 1.3 keV, as defined by floating the ion source to 1.3 kV.

A bunched beam was obtained by pulsing the IS anode bias for 2.3 µs from a reflective to an accelerating potential of -80 V with respect to the ion source. A typical TOF spectrum obtained by guiding the resulting ion bunches onto the ES MCP0 is shown in Fig. 6.29 a). The relative flight times allowed us to identify the different TOF mass peaks as stable isotopes of various singly charged, alkali ions ($^{23}Na^+$, $^{39,41}K^+$, $^{85,87}Rb^+$ & $^{133}Cs^+$); however, the achieved mass resolving power ($R \approx 2$) was too low to resolve the different isotopes of these elements.

To enable systematic studies of electron cooling of different ion species, the IS S2 steerer located ≈ 35 cm downstream from the ion gun anode (see Fig. 6.9) was deployed as a TOF beam gate. By normally keeping one of the two horizontal steerer plates at a deflecting potential, the gate blocked the transmission of undesired ion species into the trap. Ions of the element of interest were transported through the trap and onto the detector by shortly pulsing the respective steerer plate back to its nominal potential. Once the time delay and duration of the TOF gate were optimized accordingly, the different ion species could be isolated with negligible amounts of contamination as illustrated for Rb^+ in Fig. 6.29 b).

To reduce the centre-of-mass energy of the (singly charged) ion bunches to a trappable level of ≤ 100 eV, the bias of the DT1 drift tube was pulsed from typically 250 V to -1100 V when the ions of interest were centred in the tube. The resulting shift of the flight times of Rb^+ ions to the ES MCP0 detector is shown in Fig. 6.29 c). Note that the peak seen in the same spectrum at $t \approx 28$ µs resulted from switching noise due to the pulsing of the drift tube bias.

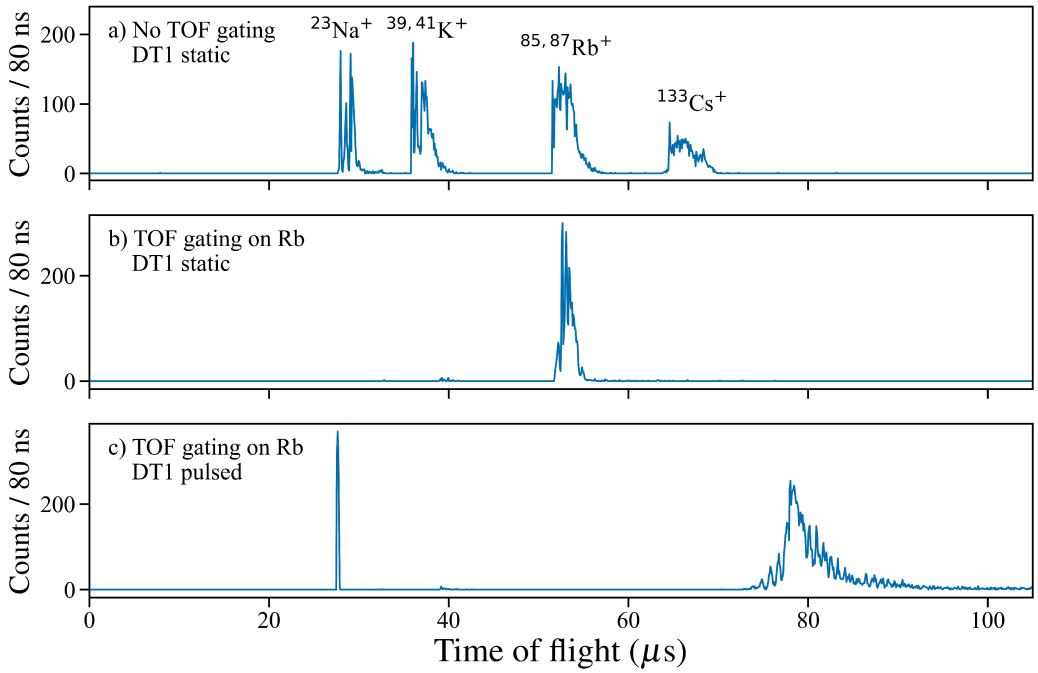

Figure 6.29. TOF spectra of stable alkali ions sent from the ion gun onto ES MCP0: a) Broadband spectrum without TOF gating. b) Isolation of Rb ions by TOF gating with a pulsed electrostatic steerer. c) Same settings as b) plus deceleration of the Rb ions by pulsing the drift tube DT1. The peak at $\approx 28\mu s$ is due to switching noise from DT1. Each spectrum shown was obtained by summing 500 machine cycles.

Ion capture and storage

The most simple scheme deployed for dynamic ion capture into CPET is illustrated by the trap potential sequence shown in Fig. 6.30 a). After suitable deceleration by the pulsed drift tube, ions entering the trap were reflected by preparing the E2 (exit) end cap voltage (or several adjacent ring trap electrodes) at a bias of 200 V. Pulsing the E1 (entrance) endcap from -50 V to 200 V before the reflected ions could leave the trap again enabled their capture [switching operation 1 in Fig. 6.30 a)]. The ring trap electrodes between the confining barriers were typically operated at voltages of 0–100 V.

By recording the ion count rate as a function of a scanned retarding potential applied to the entrance endcap, it was found that ion bunches entering the trap exhibited energy spreads of 50–100 eV, which is likely a consequence of the finite switching times of the ion-gun anode and the DT1 drift tube. Due to the substantial energy spread of the incoming ions, the lowering of the effective electron nest depth due to the plasma space charge allowed lower energy ions to penetrate deep into the trap without being reflected. This increased the likelihood for these ions to be successfully captured and altered the initial ion energy distribution. The envisioned ion-electron interaction studies, however, relied critically on consistent initial ion conditions between plasma-on and -off cycles. Consequently, a new

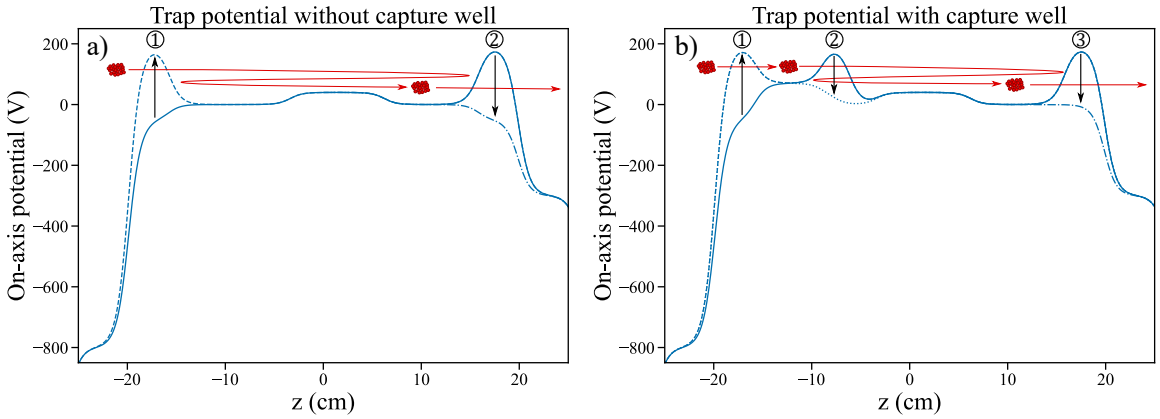

Figure 6.30. Ion captures schemes: a) Ion capture (1), storage and ejection (2) with the E1 and E2 endcap electrodes. b) Capture and prestorage of ions in a dedicated capture well (1) followed by transfer into the ion-electron interaction region (2) and ejection by opening the E2 endcap (3).

trapping scheme was developed that decoupled the ion capture stage from the mixing of ions and electrons. In this scheme, the ions were first captured into a separate potential well as illustrated in Fig. 6.30 b) formed by using the T6 & T7 electrodes as a reflective barrier. After a typically 10 ms long pre-storage period in the capture well, the ions were permitted into the interaction region including the electron nest by removing the potential barrier formed by the T6 & T7 [step 2 in Fig. 6.30 b)]. From there on, the experimental cycles proceeded identical, irrespective of the chosen ion capture scheme.

After the desired storage period, ions were extracted onto the ES MCP0 detector by removing the potential barrier at the trap exit (switching operations 2 and 3 in Fig. 6.30 a) & b), respectively). Once the timings were optimized for trapping of a given ion species of mass unit A_{ref}, trapping of a different species of mass unit A could simply be realized by scaling the time delay and duration of the TOF gate and the delays for pulsing DT1 and closing E1 with $\sqrt{A/A_{\mathrm{ref}}}$.

Typical arrival time spectra of different ion species extracted onto the ES MCP0 detector are shown in Fig. 6.31. After mass separation by the TOF gate and deceleration in the drift tube, the ions were captured by closing the E1 endcap ($-50\,\mathrm{V} \rightarrow 200\,\mathrm{V}$). After 100 ms long storage, the ions were extracted onto the ES MCP0 detector by opening the E2 endcap ($200\,\mathrm{V} \rightarrow -50\,\mathrm{V}$). The relative positions of the left peak-edges in the resulting accumulated spectra (see Fig. 6.31) again obeyed the mass scalings expected for $^{23}\mathrm{Na}^{+}$, $^{39,41}\mathrm{K}^{+}$, $^{85,87}\mathrm{Rb}^{+}$ & $^{133}\mathrm{Cs}^{+}$. This result verified the successful separation and trapping of the different alkali ions emerging from the ion source.

The absence of secondary peaks at shorter arrival times suggests that no lighter contaminant ions, e.g. created in charge exchange reactions between injected ions and residual gas particles, were present in the trap. Due to the substantial peak widths, conclusions about the presence of contaminant ions at similar or higher masses than the injected ions cannot be drawn from these spectra. A full TOF separation of the different alkali-ion peaks was also not possible due to the poor mass resolving power resulting from the ions' substantial

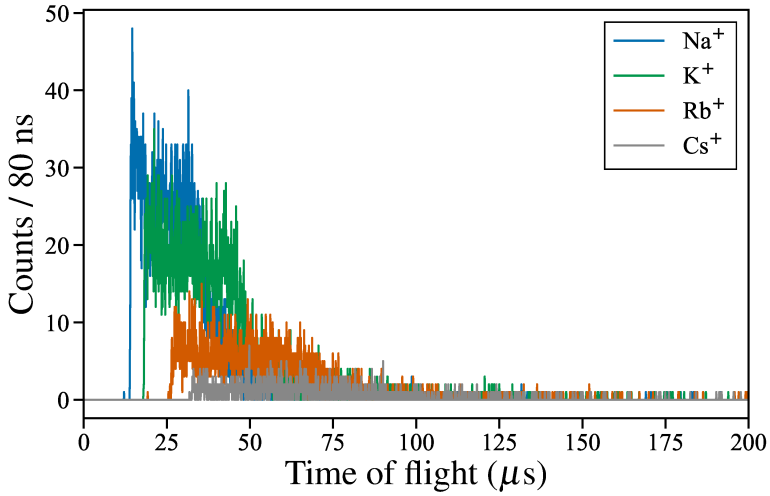

Figure 6.31. Time-of-flight spectra of different alkali ions extracted from the trap after 100 ms storage time. Each spectrum is an accumulation of 400 machine cycles. The relative positions of the left peak edges match up with the expected mass scalings for (from left to right) $^{23}Na^+$, $^{39,41}K^+$, $^{85,87}Rb^+$ & $^{133}Cs^+$. The long turn-around times in the trap and the short flight path to the detector ($\approx$1.2 m) prevent a TOF separation of the different mass peaks.

turn-around times in the $\approx$ 40 cm long trapping region. More compressed ion bunches (as needed for the transfer to downstream ion traps) could in principle be achieved by transferring cooled ions into a shorter potential well and ejecting them with a suitable potential gradient. However, great care has to be taken to prevent undesirable ion heating in such transfer operations. Since the studies presented here aimed at the first demonstration of electron cooling in CPET, trap configurations were chosen that allowed us to study the cooling dynamics in the most direct way possible. The special ion extraction schemes developed to probe the ions' kinetic energies in the trap are described in section 6.4.5.

Ion lifetimes in the trap and ion-electron co-trapping

To prevent that excessive ion losses obscure the observation of ion-electron interactions, one should aim to achieve ion lifetimes in the trap that exceed the expected timescale of the electron cooling process. Considering the several 100 ms long electron-ion energy-exchange time constants suggested by the two-component plasma model presented in 6.2, the ion lifetimes in CPET should at least be of the order of 1 s to facilitate studies of in-trap electron cooling. To verify that the ion trapping in CPET meets this criterion, we quantified the lifetimes of the singly charged alkali ions available from the surface ion source. To investigate whether the co-confinement of an electron plasma interferes with the ion storage, the ion lifetime measurements were performed in a nested trap potential and by alternating cycles with and without a co-trapped electron plasma.

The transport, co-confinement and detection of ions and electrons within a single ma-

chine cycle introduced a number of complications as compared to cycles with individual trapping of ions and electrons. To facilitate ion-electron co-trapping cycles, the following modifications and operational changes were implemented:

- The ES MCP0 bias was gated to prevent damage or aging of the detector due to high electron-beam-induced background event rates (see section 6.3.8 for details).
- Pulsing of the adjacent drift tube (DT1) for ion deceleration was found to induce voltage transients on the harp detector, whose amplitude exceeded the voltage rating of the isolation amplifier in the floating harp readout box. Harp detector signals could therefore initially only be acquired in plasma-trapping cycles without ion injection. To facilitate the concurrent detection of trapped electrons and ions within a single machine cycle, surge protection was added to protect the floating harp readout box against induced voltage transients (see section 6.3.8 for details).

The typical ion lifetimes in the trap were determined by recording the number of ions detected on the ES MCP0 detector as a function of the ion storage time. To evaluate the impact of a co-trapped electron plasma on the ion storage, machine cycles with and without a co-trapped plasma were alternated. The plasmas were confined in a 40 V deep, rectangular potential nest formed by the T13–T19 trap electrodes and exhibited electron numbers in the range $N_e = (4 \pm 1) \times 10^7$. For maximal comparability, the nest was also being applied during plasma-off machine cycles. Ions were captured into a capture well floated to 70 V above ground and after 10 ms long pre-storage injected from the capture well into the interaction region, resulting in trap potentials as shown in Fig. 6.30 b).

The ion-count evolution obtained with injected Na^+, K^+ & Rb^+ ions is shown in Fig. 6.32. Surprisingly, in the plasma-off cycles, the ion numbers detected after a 1020 ms long storage time were marginally but consistently higher than those after 20 ms storage. Other storage time scans with finer step size showed similar systematic fluctuations of the detected ion number after short storage times (see Fig. 6 in [545]). Such behaviour had also already been observed in HITRAP's cooler Penning trap, where detailed measurements revealed a periodic modulation of the ion count rate at short measurement times and simulations allowed to identify the modulation as a result of the ions $\vec{E} \times \vec{B}$ drift motion in the trap [554] (the equivalent of the magnetron motion in a harmonic axial trap potential). This mechanism is also a plausible explanation for the behaviour observed for ions trapped in CPET. In fact, SIMION simulations of the ion extraction from CPET showed that the magnetic orbit expansion along the ion extraction beamline causes any ion that leaves the trap with a radial displacement $\gtrapprox 0.8$ mm from the trap's symmetry axis to get lost against electrodes. An $\vec{E} \times \vec{B}$ drift with a large initial amplitude could therefore explain the reduced count rates at short storage times as extraction-efficiency losses. The signal increase toward longer storage times is likely a consequence of ion-neutral collisions that transfer energy from the longitudinal into the transversal ion motions. Since the $E \times B$ drift of ions in a Penning trap is a negative-energy mode (see e.g. [555]), an increase in the mode energy will drive the ions closer to the trap axis, eventually permitting them to reach the MCP detector independent of the phase of their $\vec{E} \times \vec{B}$ drift motion. In the case with a co-trapped electron

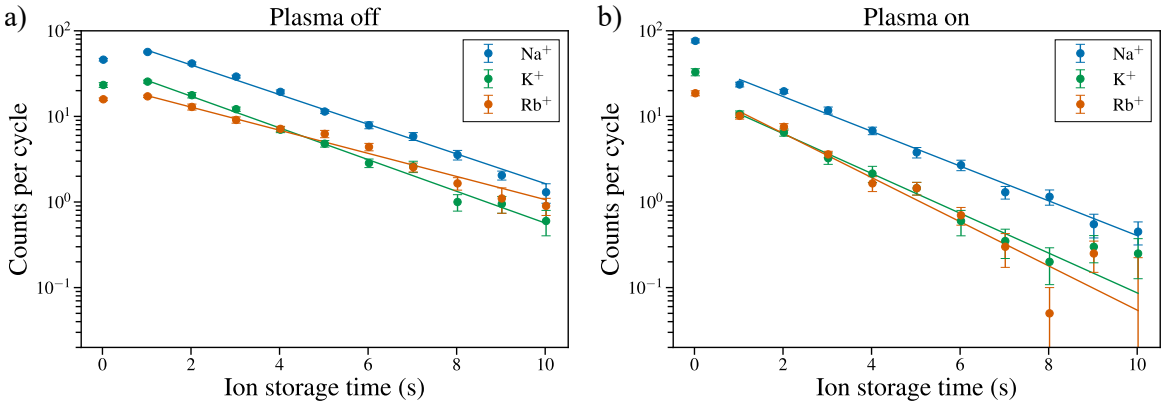

Figure 6.32. Average rate of ions counted on the ES MCP0 after different storage times with plasma off (a) and plasma on (b). The lines mark exponential fits to the data points of the same colour. The ion lifetimes extracted from the fits are listed in table 6.4.

plasma, the count rates obtained with the shortest storage time are consistently higher than in plasma-off cycles and the ion count rates exhibit a steady drop for all storage times $\leq 8\,\mathrm{s}$. A firm explanation of the discrepant ion behaviour between the plasma-on and -off cycles would have required far more detailed measurements and simulation studies. In any case, it seems plausible that the increased radial electric field arising from the plasma space charge altered the ions' $\vec{E} \times \vec{B}$ drift motion at short storage times.

To extract the respective ion lifetimes, the collected data were fitted with a simple exponential decay-law of the form

$$N_i(t) = N_{i,0} \exp\left(-t/\tau\right), \tag{6.14}$$

where the decay time constant τ is taken as the species-dependent lifetime in the trap. Due to the systematic shifts, the data points at the shortest storage times (20 ms) were excluded from the fits. The obtained fit curves are shown as lines in the logarithmic plots in Fig. 6.32 and the respective ion lifetimes are listed in table 6.4. Possible ion-loss mechanisms in the absence of an electron plasma are given by elastic or charge exchange collisions with residual gas particles, ion-ion interactions, and resonant particle transport due to field imperfections.

Resonant particle loss may occur when two eigenfrequencies of an ion's motion take an integer ratio, causing the ion to repetitively probe the same imperfections in the trapping fields. While this mechanism can, in principle, play a role for an individual ion species, it can hardly explain the rather consistent ion-loss rates observed among the different ion species in the present measurements. Ion-ion interactions are also very unlikely in sight of the large trap volume and the rather small numbers of ions (< 100) that were stored in the trap at the same time. The observed ion losses can therefore be assumed to be primarily due to interactions with residual gas particles.

In this context, it is important to realize that all ions that had, by some mechanism, become localized in the entrance-side ion well of the nested trap potential were not ejected towards the detector, and thus escaped detection. This circumstance is owed to the fact that no suitable procedures had yet been developed to combine cold, localized ions into a

Table 6.4. Ion lifetimes in CPET extracted from the exponential fits in Fig. 6.32.

Ion species	Lifetime in trap - plasma off	Lifetime in trap - plasma on
Na^+	(2.51 ± 0.07) s	(2.14 ± 0.10) s
K^+	(2.34 ± 0.07) s	(1.87 ± 0.09) s
Rb^+	(3.21 ± 0.12) s	(1.68 ± 0.12) s

single potential well. Performing such ion transfer operations in the presence of a co-trapped electron plasma poses a non-trivial task as both plasma heating due to ion-transfer operations and plasma ejection induced excessive detector background due to impact ionization of rest gas.

Elastic collisions from the dominant interaction mechanism between singly charged ions and rest gas neutrals. As will be shown in section 6.4.5, already a single elastic collision with a heavier residual gas particles (e.g. H_2O, CO, CO_2) can potentially dissipate a substantial fraction of an ion's longitudinal kinetic energy and cause the ion to become trapped in either of the two ion wells in the nested potential. Due to the non-detection of ions in the entrance-side well, the ion lifetimes extracted in the present measurements should therefore be viewed as lower limits on the true lifetimes in the trap.

A second mechanism by which ion-neutral collisions could lead to ion loss is given by collision-induced radial diffusion, as only ions with radial displacements of $\lesssim 0.8$ mm from the trap axis could be detected on the ES MCP0 detector. The primary inelastic collision process of concern in a Penning trap is charge exchange between ions and residual gas neutrals. In this process, a fast ion picks up an electron from the neutral, causing the ion to get lost from the trap. The initially neutral particle is ionized in the process and typically remains in the trap in place of the colliding ion. Charge exchange therefore does not necessarily lead to a reduced number of ions in the trap. Due to the limited TOF resolution in the ion extraction from a nested trap potential, charge exchange products could usually not be differentiated from the ions of interest and must therefore be expected to have contributed to the measured count rates. While charge exchange usually forms the dominant loss channel for HCI in a Penning trap, it is generally less relevant in the case of SCI.

The presence of an electron plasma was found to reduce the observed lifetimes for all ion species. Recalling the results from section 6.2, we can exclude ion-electron recombination losses as a relevant loss process for the singly charged ions considered here. Assuming that the plasma slowed down the longitudinal ion motion, the increased ion losses observed in plasma-on cycles could be explained by a higher rate of ion localization in the first ion well.

The plasma-induced enhancement of the ion loss rate could further result from centrifugal separation of the ions and electrons. In this phenomenon, collisions transfer angular momentum between different plasma species, resulting in a net inward transport of the lighter and a net outward transport of the heavier species. The mass-selective transport may even lead to a complete radial separation of the two plasma components [556]. Centrifugal separation has been observed in a variety of trapped multi-species plasmas with a single sign of charge such as electron-antiproton plasmas [557, 558]. The phenomenon has also been

theoretically predicted for plasmas with components of opposite charge [559], but, to the author's knowledge, this prediction still awaits experimental verification. The contributions of different ion loss processes cannot easily be disentangled from the lifetime measurement data, but the model of the cooling dynamics presented in section 6.4.5 provides additional insights into the contributing loss mechanisms.

In any case, the presented storage time scans verified that, even with static nested trap potentials and a co-trapped plasma, the ion lifetimes exceeded the demanded minimum for electron cooling tests ($\tau \geq 1\,\mathrm{s}$). This result formed an important milestone towards ion-electron interaction studies in CPET.

6.4.5 Ion-plasma interaction studies

After the plasma preparation and the ion trapping had been verified to fulfill the necessary preconditions, the first tests of ion-electron interactions in CPET could be approached. Electron-induced background on the MCP detector formed a major obstacle that initially prevented the observation of electron cooling in CPET. In the following, I therefore, first give a brief overview of the mechanisms inducing these background events and discuss the measures taken to reduce the electron-induced background on the MCP detector to a near-negligible level. The demonstration of plasma-induced cooling of ions in a Penning trap naturally requires a means to probe the ion energy evolution. Hence, I subsequently introduce the special ion extraction schemes developed for this purpose. After introducing the typical experimental cycles and the trap potentials used in the ion-electron interaction tests, experimental results for in-trap electron cooling of singly charged ions (SCI) are presented. Subsequently, the experimental results are discussed with the aid of a cooling model. Finally, the model is used to extrapolate the experimental results obtained with SCI to the expected cooling timescales for highly charged ions (HCI). Based on these model extrapolations, the chapter closes with tentative conclusions concerning the prospects of electron cooling of short-lived radioactive HCI.

Observation of electron-induced detector background

Initial attempts to probe ion and electron interactions in CPET were hampered by the re-emergence of electrical discharges and electron-induced background events on the MCP detector (ES MCP0). The spurious phenomena were usually only observed in cycles with electron injection and could be divided into three categories: (1) Discharges triggered by HV switching in the high-field region of the superconducting magnet, (2) a near-constant-rate background on the ES MCP0 detector whenever the electron beam was unblocked, and (3) background events observed on the MCP detector after opening the trap for ion extraction.

The discharges were found to occur almost exclusively in runs involving electron injection and could be accorded to so-called Penning discharges. In these discharges, energetic stray electrons became trapped in involuntarily-formed Penning traps along the trap electrode structure and ionized residual gas particles. The ionization freed up secondary ions

and electrons, thus leading into charge multiplication and electrical discharges. The discharges were usually triggered by HV switching operations that would accelerate the stray electrons to sufficient energies for impact ionization of rest gas (several $10\,\mathrm{eV}$). If the ionization occurred near the trapping region, the secondary ions could become confined and lead to excessive detector background upon ion extraction from the trap. Overfilling of the electron nest in the trap potential and incomplete dissipation of electrons during plasma dumps were also found to increase the likelihood of discharges or electron-induced background. The prompt beam-induced background could be accorded to ionization of residual gas particles that were subsequently accelerated onto the fully-biased ES MCP0 detector. In contrast to the background events upon ion extraction, beam-induced background events did not overlap temporally with any signals of interest. Nonetheless, they had to be addressed as the associated count rates ($> 1\,\mathrm{MHz}$) threatened to damage or prematurely deteriorate the detector.

To resolve the mentioned issues, the following operational changes were implemented:

- The rise and fall times of switched electrode voltages were reduced from originally $\approx 50\,\mathrm{ns}$ to $\approx 1\,\mathrm{ms}$ in the case of the G1 electrode, $\approx 2.5\,\mu\mathrm{s}$ in the case of the E1 electrode and to 100–$200\,\mathrm{ns}$ for all other switched electrodes. This measure helped to prevent the detector background due to charge multiplication and the ignition of Penning discharges by reducing the likelihood of accelerating stray electrons to ionizing energies.

- The transport energy of injected ions bunches was reduced from 2 to $1.3\,\mathrm{keV}$. This decreased both the steady-state voltages and the switched voltage differences on the drift tube DT1, the E1 and E2 endcaps and a number of other electrodes. This measure enabled a robust system operation without HV breakdown.

- Since the amount of electron-induced background counts on the ES MCP0 detector was found to correlate with the number of trapped plasma electrons, both the electron beam currents and electron loading times were reduced to a level that minimized detector background.

- The parameters of the nested potential wells, in particular their shape, length and depth, were optimized such as to minimize axial electron escape towards the Penning-like traps formed by the positively biased trap endcaps (typically the E1 and E2 electrodes).

- A second electron dump was added to experimental cycles to safely dissipate any excess electrons that had not become localized in the electron nest within the designated cyclotron cooling period prior to ion injection. This measure prevented electron accumulation in unwanted regions of the trap, such as the endcap electrodes.

- Plasma manipulation during the ion storage period was generally avoided and the plasma was only dumped once the ions had been extracted from the trap. Further, care was taken to limit plasma heating due to manipulations of trapped ions.

These adaptations enabled a stable system operation in ion-electron interaction studies and reduced the electron-induced background to a near-negligible level, thus allowing us to probe changes in the trapped ions' energies on the ES MCP0 detector.

Extraction schemes for ion energy analysis

In order to demonstrate and study electron cooling of ions in a Penning trap, special detection schemes are required that allow to unambiguously identify changes in the kinetic energy distribution of trapped ions. In principle, TOF analysis of extracted ion bunches, especially when coupled to charged particle simulations, is an appropriate tool for such diagnostics. However, as already pointed out earlier, the long turn-around times in the trap prevented detailed ion-energy diagnostics via ion TOF signals obtained after rapidly ($\tau < 200\,\mathrm{ns}$) opening of the exit endcap. Consequentially, two alternative ion extraction schemes were implemented to study ion-electron interactions in CPET.

The first extraction scheme [486] was likewise based on ion-arrival time spectra but relied on gradually opening the exit endcap, on a timescale long compared to the typical axial ion oscillation periods of several $10\,\mu\mathrm{s}$. As a result of the gradual removal of the confining barrier, the ion arrival times at the ES MCP0 detector showed a correlation with the ions' energies in the trap, with later arrival times indicating a smaller kinetic energy. To this end, the opening of the exit-endcap was not realized with a Behlke HV switch but by using a channel of the DAC HV supply, resulting in a voltage slew rate of $\approx 0.5\,\mathrm{V}/\mu\mathrm{s}$ and a total transition time of $\approx 400\,\mu\mathrm{s}$ for the linear voltage ramp from $200\,\mathrm{V}$ down to $0\,\mathrm{V}$. An even slower slew rate could have further reduced the endcap-voltage change over a typical axial ion oscillation period and thus raised the scheme's energy resolution. The chosen slew rate, however, provided a decent compromise between energy resolution and the time required to accumulate sufficient statistics.

The scheme's comparatively high data collection rate made it well suited to qualitatively check for cooling signatures under different experimental conditions. A typical measurement with this scheme only required on the order of 1–2 h to complete. Since extraction through the magnetic field gradient converted more than 99.9% of the ions transverse into longitudinal kinetic energy, this extraction scheme essentially probed the ions total kinetic energy in the trap. To enable quick changes between different extraction schemes, the E2 endcap remained biased by a Behlke HV switch for rapid endcap opening, whereas the Q24, D25 & T26 electrodes were biased by the mentioned DAC output channel and served as the endcap in runs demanding a gradually ramped endcap potential.

For more quantitative analysis of the trapped-ion energy evolution, an extraction scheme enabling retarding field analysis (RFA) of the longitudinal ion energies was developed. This scheme is illustrated by the trap potential sequence plotted in Fig. 6.33 b). Ions were either directly injected into the interaction region or pre-stored in an ion capture well and then released into the interaction region [step 1 in Fig. 6.33 b)]. The Q24, D25 & T26 electrodes again served as the exit endcap and were pulsed between a closed ($200\,\mathrm{V}$, dashed line) and open ($0\,\mathrm{V}$) state using the DAC HV supply. The E2 electrode was used to form a retarding

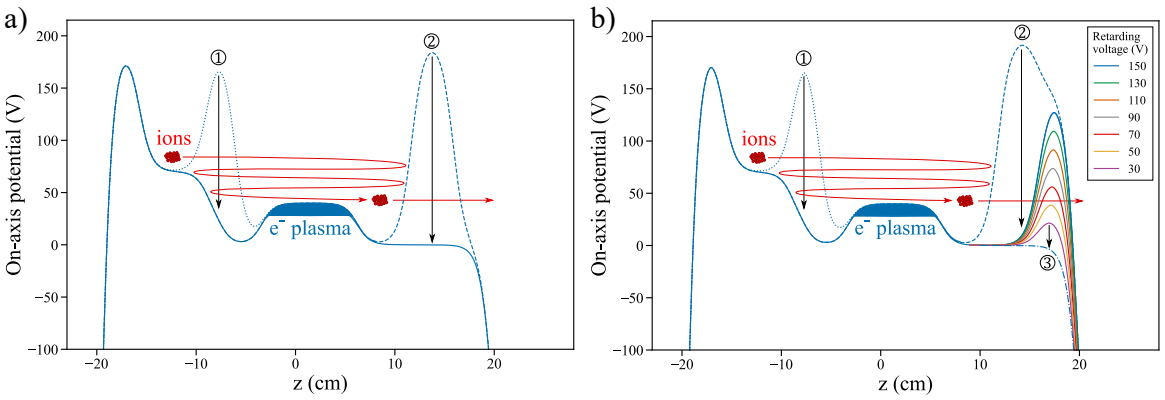

Figure 6.33. On-axis trap potentials for different analysis schemes of the trapped ions' kinetic energies: a) Extraction scheme with gradual exit-endcap opening. b) Retarding field analysis (RFA) with a variable-height retarding barrier formed by the E2 endcap (see legend). The plotted potential curves were obtained in simulations with a 40 volt deep rectangular electron nest. The dotted lines indicates the potential before ions are injected into the interaction region. The dashed lines mark the confining exit-endcap potential during the interaction period. See text for details.

barrier of a variable height ϕ_r [various coloured traces in Fig. 6.33 b)]. In each machine cycle, the E2 electrode was prepared at a given barrier voltage[9] and only allowed ions with a longitudinal kinetic energy $E_{\text{kin},\parallel} > q\phi_r$ to reach the detector once the endcap was opened (i.e. pulsed to ground potential). 3 ms after opening the endcap, the RFA barrier was likewise pulsed to ground potential, thus permitting ions that had remained confined by the RFA barrier to leave the trap towards the detector. Recording the number of ions N_i detected within the first millisecond after opening the endcap as a function of the retarding potential, the longitudinal ion energy distribution $n(E_{\text{kin},\parallel})$ could then be obtained as the derivative of the emerging RFA profile:

$$n(E_{\text{kin},\parallel}) = -\frac{dN_i(\phi_r)}{d\phi_r}. \tag{6.15}$$

The choice to use the E2 electrode as the retarding barrier was motivated by SIMION simulations which verified that applying retarding voltages of 0–150 V did not noticeably alter the ion transmission to the ES MCP0 detector. This is in contrast to the effects of other tested electrodes further downstream along the ion extraction path (e.g. the drift tubes in the ES FC and ES MCP detector assemblies). This counter-intuitive result goes back to the fact that the E2 electrode is located in the high-field region of the superconducting magnet (see Fig. 6.22) where the transverse beam dynamics are dominated by the magnetic field rather than electrostatic elements. Since the ions pass the retarding barrier before they experience the magnetic field gradient, the RFA extraction scheme only probes the ions' longitudinal kinetic energies. However, since ions were typically injected into the interaction region

[9]Note that, due to field penetration into the cylindrical E2 electrode, the on-axis barrier potential ϕ_r was always somewhat lower than the applied barrier voltage V_r. As detailed below, electrostatic field calculations were performed to correct for this effect.

from an ion capture well floated roughly 70 V above the bottom of the trap potential, they acquired longitudinal kinetic energies of 70–90 eV, which is substantially larger than the presumed initial transverse kinetic energies ($\sim$ 1 eV). Thus, the RFA extraction scheme was well-suited to study ion-electron interactions manifesting as a slowing of the ions' centre-of-mass motion or a change in the longitudinal ion energy spread.

Since each machine cycle was run with a single retarding potential, an RFA scan with a reasonable range and energy resolution (e.g. 31 steps of 5 V) typically required more than 10 hours to complete, making interaction test with this extraction scheme significantly more detailed but also much more time-consuming than the first one.[10]

Experimental cycle for ion-electron interaction tests

A typical set of experimental timings and on-axis trap potentials throughout an ion-electron interaction cycle are shown in Fig. 6.34 and Fig. 6.35, respectively. Each machine cycle can be subdivided into the following stages (corresponding to the roman numerals in Fig.s 6.34 and 6.35):

I) *Initialization:* To prepare for the electron injection, the bias of the ES MCP0 detector was lowered by several 100 V to prevent detector aging due to amplification of beam-induced background events. Further, the trap potential was reset to a configuration with an electron nest, and the ES beamline potentials were switched into electron transport mode.

II) *Electron loading:* For a fixed loading time, the electron beam was turned on by pulsing the Wehnelt cylinder to an extracting potential and electrons were continuously accumulated in the prepared trapping potential.

III) *Plasma pre-cooling:* For a fixed wait time, the trap potentials were kept static to allowed the accumulated electrons to undergo cyclotron cooling and settle into the electron nest. The waiting period also allowed for damping of the plasma's diocotron motion. Meanwhile, the ES beamline potentials were switched back into ion transport mode and ES MCP0 bias was raised again to enable ion detection.

IV) *Excess-electron dump:* Excess electrons that had not been localized in the nested potential well were ejected from the trap onto the harp detector by pulsing the G1 and E1 electrodes to a voltage of 220 V and 200 V, respectively. The 60 ms long duration of the dump period was chosen such that all excess electrons were captured by the harp wires. Ideally, at the end of the excess-electron dump the trap was only filled with electrons confined in the nested well. This stage proved crucial in preventing electron-induced background counts on the ES MCP0 detector.

[10] This extraction scheme could, in principle, have also been realized by using the DAC HV supply to sequentially stepping through various retarding voltages on every single machine cycle, thus enabling a significantly faster accumulation of statistics. However, such extended switching operations were deliberately avoided in the tests presented here as they could alter the ion energies, resulting in systematic uncertainties that are difficult to quantify.

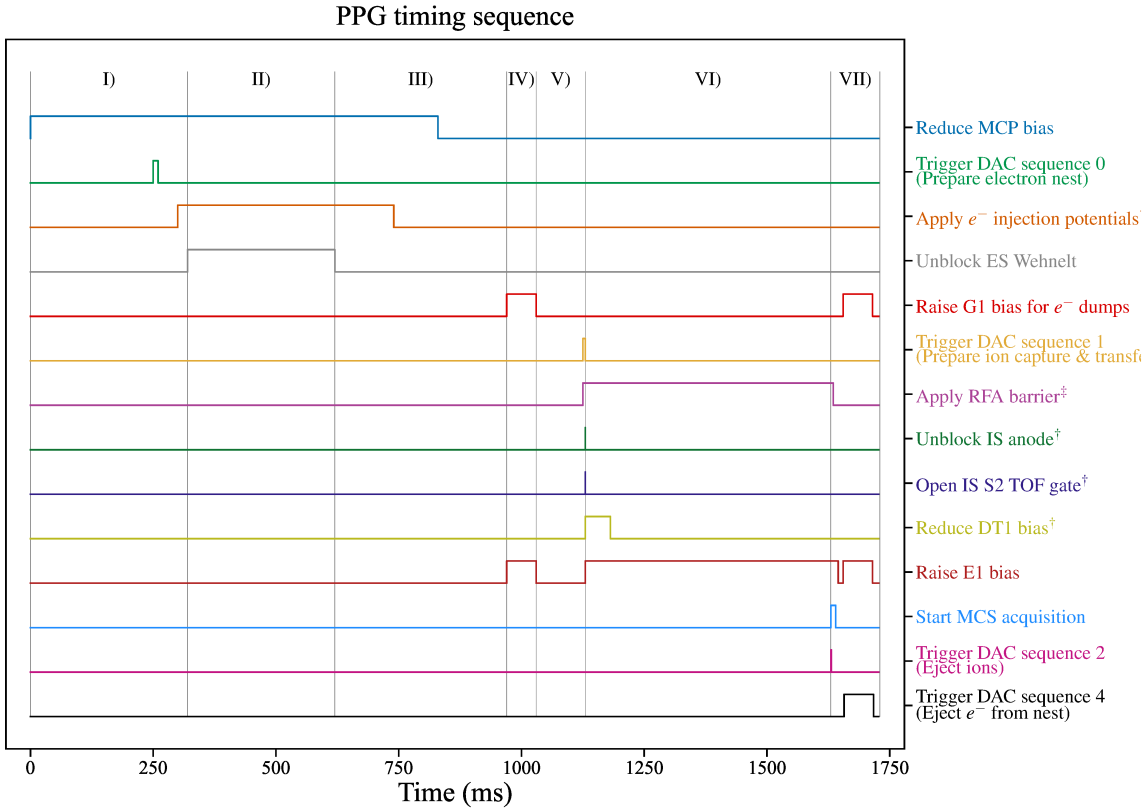

Figure 6.34. The experimental timing sequences used for the reported ion-electron interaction studies.

†Electrode biased through bi-level switched in reverse logic, i.e. positive logic pulse $\widehat{=}$ more negative electrode bias.

‡Logic pulse only relevant in runs with retarding field analysis.

V) *Final plasma pre-cooling and ion injection:* Since HV switching during the excess-electron dump re-heated the plasma, a second wait period of 90 ms duration was installed to allow for the plasma to relax back toward its equilibrium temperature. Towards the end of this stage, the ion-exit endcap potential was gradually raised to 200 V and, if applicable, an ion capture well was formed by gradually raising the respective trap electrode biases. In RFA measurements, the RFA barrier was at this point switched to its nominal retarding voltage. With the trap potentials prepared, ions were extracted from the ion gun by unblocking the IS anode, mass separated by shortly switching the IS S2 steerer potentials to a non-deflecting state and decelerated to trappable energies by pulsing down the DT1 drift tube bias. After the ions of interest had entered the trap, the E1 endcap bias was pulsed from -50 V to 200 V to confine the ions in the trap.

VI) *Ion-electron interaction:* In runs without an ion capture well, the ion-electron interaction period started as soon as the E1 endcap was closed. In runs with an ion capture well, after a 10 ms long pre-storage period, the ions were permitted into the interaction region by lowering the exit-side barrier of the capture well.

VII) *Ion extraction and plasma dump:* After the defined interaction time, the MCS acquisition window was started and the exit-side endcap was opened to extract the ions towards the MCP detector. In runs with an RFA barrier, the barrier was removed 3 ms after opening the exit endcap, thus allowing ions that remained confined by the barrier to also be registered on the MCP detector [respective potentials shown in VIIa) in Fig. 6.35]. It should be noted that, because the electron nest was kept unchanged during the ion extraction period, any ions that cooled into the entrance side ion well (centred around $z \approx -6$ cm) were not detected on the ES MCP0 detector and only got ejected during the plasma dump. Subsequently, the entire plasma was dumped from the nested well and destructively detected on the harp detector by raising the G1 electrode potential again and triggering a DAC sequence that transforms the ion-injection side of the trap into a near-linear extraction gradient [respective potentials shown in VIIb) in Fig. 6.35].

In a typical interaction tests, plasma-on and -off cycles were alternated by only unblocking the ES Wehnelt cylinder on every second cycle. All other experimental parameters, remained unchanged to ensure maximal comparability between plasma-on and -off cycles. Comparison of the ion signals acquired with and without a co-trapped plasma then provided a direct way to search for electron-ion interactions.

Cooling signatures in arrival-time spectra

Initial attempts to probe ion-electron interactions in CPET were focused on searching for a change in the arrival-time spectra of ions extracted from the trap. This technique provided a comparatively quick way to confirm electron-ion interactions since, at typical count rates of ~ 50 ions per cycle, changes in the TOF peaks became observable already after only several 10 experimental cycles (at a typical cycle duration of ≈ 2 s, translating into several minutes of data acquisition).

In order to study the ion energy evolution in the trap, the length of the ion-electron interaction period was scanned. To minimize the impact of potential system instabilities such as voltage drifts, the scan was performed in a looped fashion with alternating plasma-on and -off cycles. In each loop, the run control stepped through the defined interaction times running a successive plasma-on and -off cycle at each interaction time. To accumulate statistics, 65 scan loops were performed. Non-neutral plasmas were generated inside a 40 V deep rectangular electron nest formed by the T13–T19 trap electrodes, resulting in the on-axis potentials shown in Fig. 6.35. The electron gun cathode was operated at a heating current of ≈ 2.3 A, resulting in emission currents of $\approx 20\,\mu$A and, as detailed below, a negligible level of plasma-induced background on the MCP detector. The experimental cycle was as outlined in the previous section, with electron loading and pre-cooling periods of 300 ms and 500 ms duration, respectively. Within the statistical fluctuations, the detected electron numbers extracted from the plasma dump signals remained constant over all tested interaction times and exhibited a mean of $N_e = (4.02 \pm 0.23) \times 10^7$. $^{23}Na^+$ ions were injected and trapped on every cycle. For each interaction time, ion arrival-time spectra were

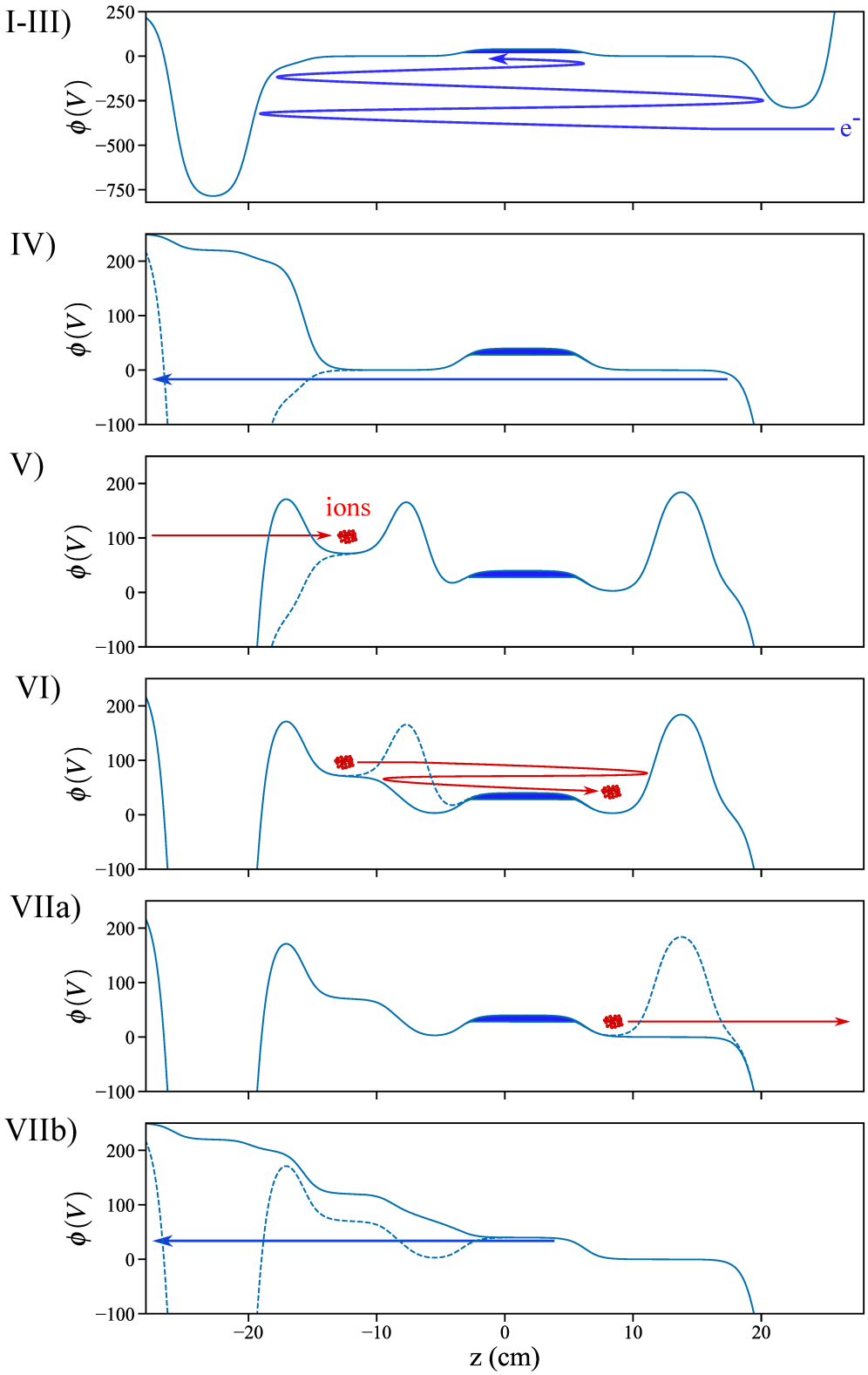

Figure 6.35. On-axis potentials throughout a typical cooling cycle with ion energy analysis by gradually opening the exit-endcap. The dark blue area indicates the lowering of the (nominally) 40 V deep, rectangular electron nest through the plasma space charge. See text for details on the different stages of the machine cycle (indicated by roman numerals). Note the different scale of the ordinate in the topmost plot.

obtained by summing the ion events accumulated over the 65 scan loops.

The resulting ion arrival time spectra are separately shown for plasma-on and -off cycles in Fig. 6.36 (b) and (c), respectively. To correct for the delayed response of the DAC HV supply to an external trigger signal, the time axes were shifted by $31\,\mu s$, such that $t = 0$ corresponded to the true start time of the endcap-voltage ramp. To provide some aid in interpreting the arrival-time spectra, the instantaneous voltage on the exit endcap is shown in Fig. 6.36 (a). With increasing ion storage times[11], both the plasma-off and plasma-on spectra exhibit a decrease in peak intensity and a shift of the peak centroids towards later arrival times.

The decreasing peak intensities are likely caused by elastic and inelastic collisions between ions and residual gas particles. Inelastic charge exchange reactions neutralize an injected ion and replace it with a ionized residual gas particle at a typically small initial kinetic energy ($< 1\,eV$). Momentum transfer in ion-neutral collisions can cause ions to escape from the trap or bring them onto larger radial orbits that cannot be projected onto the ES MCP0 detector. SIMION simulations indeed showed that the magnetic expansion of extracted ion bunches caused any ion with an initial radial displacement of $\gtrapprox 0.8\,mm$ to get lost on electrodes along the ion extraction beam path. Through this mechanism, even elastic collisions that do not cause ion loss from the trap can reduce the number of detected particles.

The peak shifts towards later arrival times clearly indicate a gradual reduction in the ions' total kinetic energy in the trap. The strongest energy loss is seen over interaction times between $20\,ms$ and $1215\,ms$. The plasma-on peaks exhibit a more rapid shift towards later arrival times, indicating a faster loss of axial ion energy. After the longest probed interaction times the plasma-off ion intensity peaks at $t \approx 320\,\mu s$, whereas the plasma-on spectra peak around $t \approx 350\,\mu s$. At interaction times of more than $2\,s$, the plasma-on spectra contain almost no events at arrival times $< 300\,\mu s$ and exhibit a significantly higher intensity at arrival times $> 500\,\mu s$ than the corresponding plasma-off spectra. This indicates that the presence of the plasma indeed cooled the ions rather than merely causing a selective loss of higher-energy ions (which could be mistaken as cooling).

To verify that the observed peak shifts in the arrival-time spectra were not caused by plasma-induced background events, a background measurement without ion injection was performed immediately after the original scan. To this end, the scan was repeated after disabling the pulsed ion extraction from the ion gun and using otherwise identical experimental settings. No counts were observed in machine cycles without electron injection. The background events accumulated in the plasma-on cycles are shown in Fig. 6.37. The observed level of plasma-induced background events is clearly negligible in comparison to the intensities observed with ion injection in Fig. 6.36. Assuming that the ion injection did not substantially raise the background level through some unknown mechanism, plasma-induced background events on the MCP detector can thus be assumed to be negligible in the interpretation of the obtained arrival time spectra. The assumption that the injected Na^+

[11] Due to the $5\,ms$ long pre-storage in the capture well, the ion-electron interaction period was only $5\,ms$ shorter than the given ion storage times.

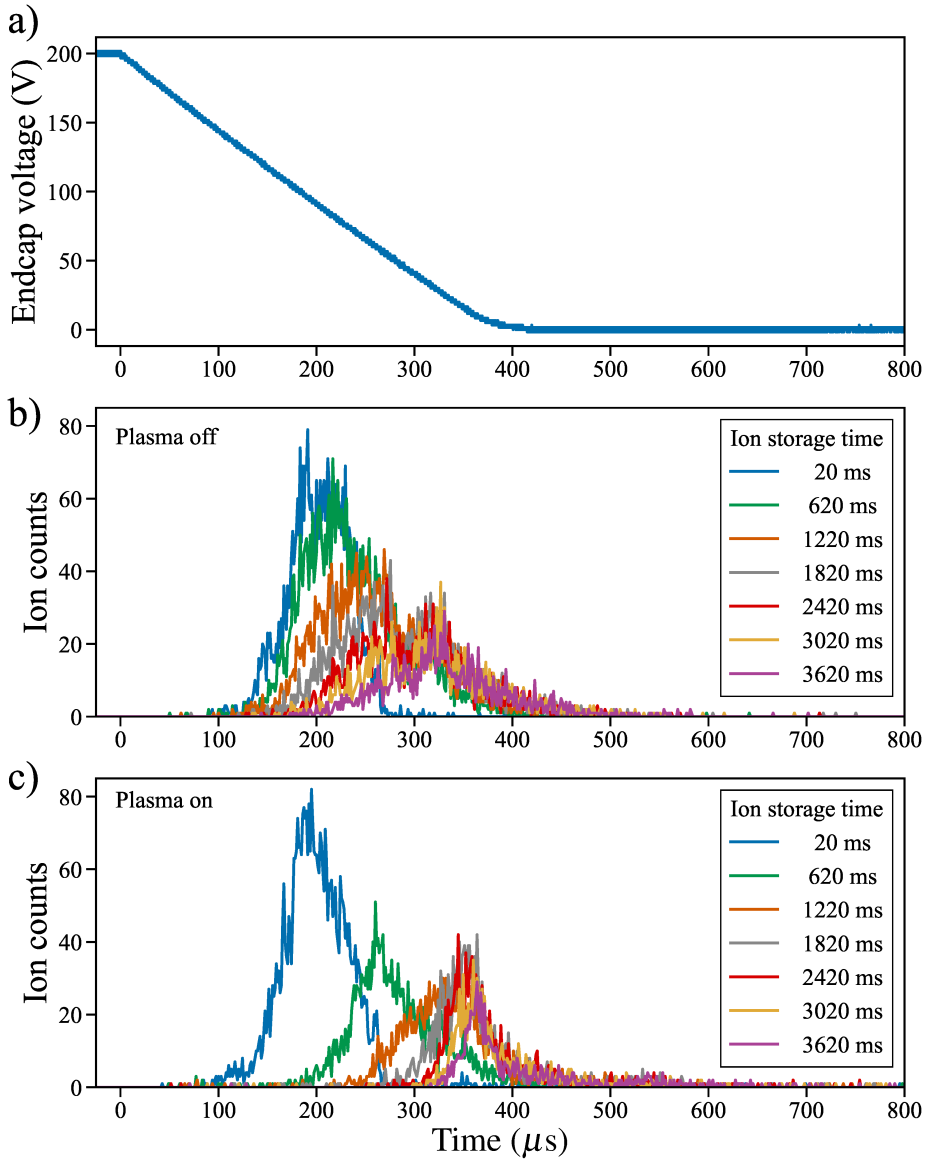

Figure 6.36. Arrival-time spectra of ions extracted from the trap after different storage times. a) Corresponding time evolution of the gradually-lowered exit-endcap potential. b) Arrival-time spectra obtained without a co-trapped electron plasma. c) Arrival-time spectra obtained with a co-trapped electron plasma.

ions did not significantly affect the plasma dynamics and the generation of plasma-induced ion counts seems plausible considering the extreme ratio of the numbers of trapped ions and electrons, $N_i/N_e \approx 100/(4\times10^7) \approx 4\times10^{-5}$. For example, if each injected ion transferred an energy of 100 eV into the plasma, the average electron energy would be raised by less than 0.3 meV, which is negligible compared to the thermal energy of electrons at $T = 300$ K (25 meV).

In summary, ion-electron interaction tests with a gradually opened exit endcap verified plasma-induced cooling of trapped ions in CPET. However, the more qualitative nature of

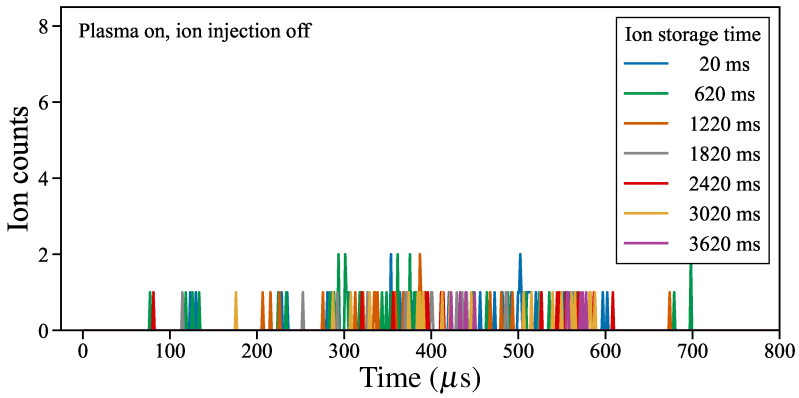

Figure 6.37. Background measurement for the data presented in Fig. 6.36. To isolate plasma-induced background events the external injection of ions from the ion gun was disabled, otherwise identical experimental settings were used. Note the 10 times enlarged scale on the vertical axis as compared to Fig. 6.36 b) and c).

this energy analysis scheme left a number of open questions. For example, a detailed extraction of the rate of the plasma-induced cooling was prevented by the background cooling due to elastic collisions between ions and residual gas. Further, a more detailed analysis was needed to identify the exact mechanism responsible for the plasma-induced cooling. While electron cooling is the most likely explanation for the increased ion energy loss in cycles with a co-trapped plasma, other plasma-related effects such as Coulomb collisions between injected ions and impurity ions in the non-neutral plasma could play a significant role in the cooling dynamics. To address these questions and enable a more quantitative analysis of the cooling dynamics, further ion-electron interaction tests were performed with the retarding-field ion energy analysis scheme introduced in the previous subsection.

Retarding field analysis (RFA) of the trapped-ion energies

For a more quantitative analysis of the ion energy evolution in the trap, measurements were performed with the retarding-field energy analysis (RFA) scheme outlined above. The results presented below were obtained with experimental conditions equivalent to those in the presented measurement with a gradually opened exit endcap. Again a 40 V deep rectangular electron nest was formed with the T13–T19 trap electrodes, resulting in the trap potential sequence shown in Fig. 6.35, with the addition of a retarding barrier potential as seen in Fig. 6.33 b). The experimental timing sequence (see Fig. 6.34) again incorporated electron loading and pre-cooling times of 300 ms and 500 ms length, respectively. To evaluate the axial ion energies in the trap as function of the ion-electron interaction duration, 2D scans of the retarding barrier voltage and the interaction time were performed. For brevity, such 2D scans will from here on simply be referred to as *RFA scans*. In all presented RFA scans, the retarding voltage was scanned from 0 V to 150 V with a step size of 5 V. Hence, 31 scan steps had to be performed per interaction time and per scan loop, making an RFA scan substantially more time-consuming than a measurement with a gradually opened exit-endcap.

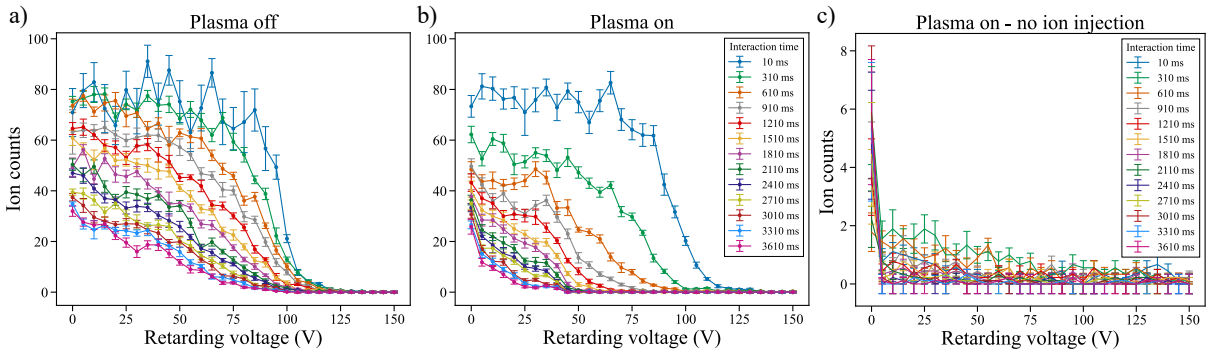

Figure 6.38. RFA count traces obtained for Na^+ in plasma-off (a) and plasma-on (b) runs. For comparison, the results of a background measurement without ion injection are likewise shown in a plot with enlarged vertical scale (c). To guide the eye, the data points were connected with straight lines.

All presented RFA scans were further performed with a total of 9 scan loops, with each scan requiring a total measurement time of $\approx 15\,\mathrm{h}$. The looped scan mode and alternated plasma-on and -off cycles again reduced the potential impact of long-term drifts of experimental parameters. As before, the ions were only permitted into the interaction region following a $5\,\mathrm{ms}$ long pre-storage in an ion capture well floated $70\,\mathrm{V}$ above ground.

In order to study the mass and atomic structure dependence of the cooling process, separate RFA scans were conducted with ions of different alkali elements. In the following, I first outline the data analysis procedure using a scan with $^{23}Na^+$ ions as an example. Subsequently, the results obtained with all studied ion species are discussed.

Analysis procedure RFA count profiles were obtained by considering all ion events at arrival times $< 1\,\mathrm{ms}$, i.e. ions escaping over the set retarding barrier once the exit-endcap was opened. The wide range of the time gate ensured that all ions with longitudinal energies larger than the barrier potential could leave the trap towards the detector (except for ions that cooled into the entrance side ion well). RFA profiles obtained in an RFA scan with injection of Na^+ ions are depicted in Fig. 6.38 a) and b). The vertical axis shows the mean number of ion counts detected per machine cycle over all scan loops and the given error bars correspond to the standard errors of the mean.

The potential impact of plasma-induced ion counts on the RFA profiles was evaluated through background measurements without ion injection. In order to shorten the measurement duration, the background measurement was conducted with plasma-on cycles only. The resulting count profile is shown with an enlarged vertical scale in Fig. 6.38 c). Again presuming that the ion injection did not substantially alter the plasma dynamics, the contribution of plasma-induced background counts to the RFA profiles obtained with ion injection was minor under the experimental conditions of all presented measurements. This result verifies the successful tuning of the experimental parameters for a suitable signal-to-background ratio. With ~ 2–6 events/cycle, the by far highest rate of background events is seen at the lowest "retarding" voltage of $0\,\mathrm{V}$. In contrast to the count rates obtained with

all non-zero retarding voltages, the background rate in this energy class did not drop with increasing storage time but fluctuated around a constant level. As detailed below, this effect can be understood by considering the impact of field penetration on the effective barrier potential. Despite the low background level, the mean plasma-induced count rates obtained in the background measurements were subtracted from the RFA count profiles acquired with ion injection.

Due to field penetration, the on-axis retarding potentials V_r experienced by the ions were somewhat lower than the retarding voltages V_r applied to the E2 electrode. To correct for this effect, the on-axis potentials resulting from various applied retarding voltages were simulated in SIMION [528] and recorded throughout the barrier region with a 1 mm resolution. The respective retarding potentials, ϕ_r, were then taken as the maximal value of the recorded on-axis potential values. Not accounting for electrode imperfections and misalignment, this procedure can be expected to yield retarding potentials to an accuracy of $< 1\,\mathrm{V}$. Field penetration further induces a radial potential gradient in the barrier region that causes ions with a larger displacement from the ion optical axis to experience a barrier potential $\phi_r(r) > \phi_r(r = 0)$. The largest radial displacement for successful transport to the ES MCP0 detector is $r \approx 0.8\,\mathrm{mm}$. For the barrier voltages used in the tests presented here ($V_r \leq 150\,\mathrm{V}$), the maximal radial barrier potential difference found in SIMION simulations was $\Delta\phi = \phi_r(r = 0.8\,\mathrm{mm}) - \phi_r(r = 0) < 1\,\mathrm{V}$. Since this contribution is negligible in comparison to the statistical measurement uncertainties, the impact of the radial barrier potential gradient could safely be neglected.

According to Eqn. 6.15 and as mentioned earlier, the longitudinal ion energy distribution can, in principle, be directly deduced from the measured count data by estimating the derivative of a given RFA count profile via finite difference methods. However, even after data smoothing, the statistical fluctuations of the acquired data prevented such deductions of the energy distributions. Therefore, the acquired RFA count profiles were instead fitted by presuming a functional form that approximates the evolving ion energy distribution reasonably well.

The choice of model function to describe the ion energy distribution is non-trivial since simple analytical expressions for particle energy distributions are typically only available for particle ensembles in thermodynamic equilibrium. The ion ensembles considered here must, however, be assumed to be far from thermodynamic equilibrium throughout most of the cooling process. Since a reduction of the energy stored in the ions' centre-of-mass motion sets in more rapidly and is thus more easily demonstrated than a reduction of their energy spread, the pre-captured ions were deliberately started with a large axial centre-of-mass velocity and a highly asymmetric velocity distribution resulting from the injection from a capture well floated to 70 V above ground. After injection into the interaction region, the ions are assumed to undergo energy-exchanging collisions among each other, and with plasma electrons (presumed temperature $T_e \approx 300$–$11\,600\,\mathrm{K}$) and residual gas particles ($T_n \approx 300\,\mathrm{K}$) that gradually drive them towards thermodynamic equilibrium. A suitable model function must therefore offer a large flexibility to account for the expected variations in the longitudinal ion energy distribution. It must further account for the fact that

the nested electric potential and the nature of the cooling process introduce two important boundaries in the longitudinal energy space accessible to trapped ions. Firstly, ion-energy loss through close-range Coulomb collisions with plasma particles ceases once an ion has been decelerated to a longitudinal energy below the effective depth of the electron nest. Once an ion has surpassed this threshold in ion-energy space, the cooling can continue but will then proceed at rate set by other energy-exchange processes such as ion-ion and ion-neutral collisions. When the energy loss rate induced by the plasma is substantially higher than that due to all other energy loss processes, ions may temporarily pile up against this threshold in energy-space until the slower energy-exchange processes transport them into lower longitudinal energy classes. In this sense, the effective nest potential can act as a quasi-boundary in the longitudinal ion-energy space. The second important boundary in the longitudinal ion-energy space is naturally given by the two local minima in the nested trap potential (both $\approx 2.75\,\mathrm{V}$ above ground) which place a hard lower bound on the energies accessible to trapped ions. The mentioned energy thresholds play an essential role in reducing the centre-of-mass energy and the energy spread of trapped ions. The cooling against these distinct (quasi-)boundaries in energy space can cause the ion-energy distribution to become bi-modal in intermediate stages of the thermalization process. In fact, RFA profiles at longer interaction times ($> 2\,\mathrm{s}$ in the case of $^{23}\mathrm{Na}^{+}$) exhibit plateaus between sloped sections that indicate such splitting into a bi-modal energy distribution.

In order to find a model function that meets the stated requirements, multiple distribution functions including a standard normal distribution, a gamma distribution and a non-central chi-squared distribution were tested to describe the axial ion energies. Bi-modal variants of these distributions were also tested but were found to result in overfitting due to the limited measurement statistics at longer interaction times. The best agreement with the experimental data, as quantified by the respective values of reduced χ^2 statistic, was obtained by assuming a uni-modal truncated normal distribution with a lower bound of $a = 0$ and an upper bound of $b = \infty$[12]. The probability density function of a truncated normal distribution is obtained from that of the standard normal distribution, $\phi_G(x; \mu_G, \sigma_G)$ with mean μ_G and standard deviation σ_G, using the relation [560]

$$f(E; \mu_G, \sigma_G, a, b) = \begin{cases} \frac{\phi_G(\frac{E-\mu_G}{\sigma_G})}{\sigma_G\left(\Phi_G(\frac{b-\mu_G}{\sigma_G}) - \Phi_G(\frac{a-\mu_G}{\sigma_G})\right)} & \text{for } E \in (a, b), \\ 0 & \text{else,} \end{cases} \tag{6.16}$$

where $\Phi_G(x)$ is the cumulative distribution function of the standard normal distribution.

The parameters of the presumed truncated normal ion energy distribution were extracted by fitting the RFA count profiles with the model function

$$N(E; \mu_G, \sigma_G) = N_i \left[1 - F(E; \mu_G, \sigma_G, 0, \infty)\right], \tag{6.17}$$

[12] Formally, it would be appropriate to also apply a finite upper bound at an energy equivalent of the trap's smallest endcap potential ($\approx 170\,\mathrm{eV}$) since ions above this threshold would escape from the trap. Since the experimental ion energies were always far below this limit, not placing a finite upper bound did not discernibly alter the fit results and simplified Eqn. 6.16 because $\Phi_G((b - \mu_G)/\sigma_G) = 1$ for $b = \infty$.

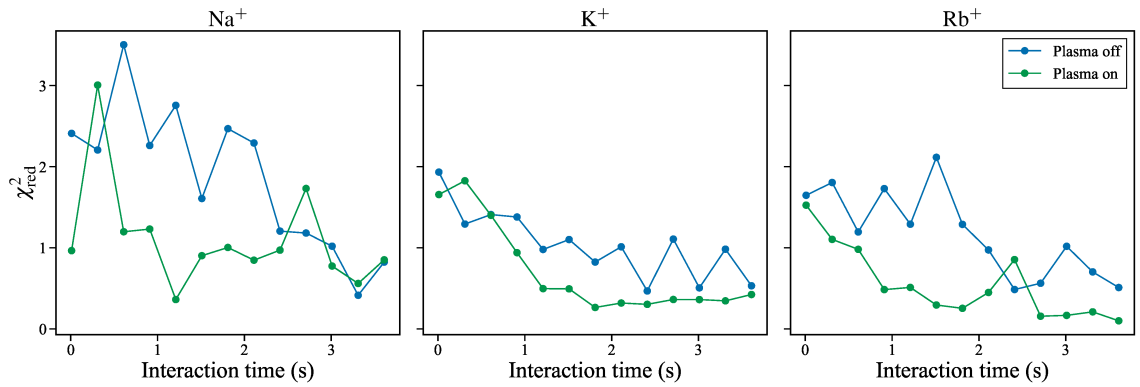

Figure 6.39. Values of the χ^2 statistic per degree of freedom obtained for the different ion species in the fits to the RFA count profiles. To guide the eye, the data points were connected by straight lines.

where N_i is the total number of trapped ions and $F(E;\mu_G,\sigma_G,0,\infty)$ is the cumulative distribution function of the truncated normal distribution (see definition in [560]). The fits were performed using a least-squares routine. The RFA count profiles acquired for various ion-electron interaction times are separately shown for Na^+, K^+ and Rb^+ in Fig. 6.40 a), b) & c), respectively. Note that, instead of the applied retarding voltage, the horizontal axes now give the effective retarding potential after correction for field penetration and the non-zero minimum of the on-axis trap potential. Solid lines denote the fit curves obtained by adjusting Eqn. 6.17 to the data points of the corresponding colour.

The values of the χ^2_{red} statistics obtained in the fits to the RFA profiles are shown in Fig. 6.39. In almost all cases, the fit model matched the plasma-on data more closely than the plasma-off data, which might point to differences in the underlying energy-exchange processes. The departures from $\chi^2_{red} \approx 1$ indicate over- and underdispersion of the measurement data, resulting from unquantified systematic uncertainties (for example deriving from the uncertainty of the retarding potentials on the abscicca) and the fitting of many zero-count bins at longer interaction times, respectively. To correct for these effects and obtain better estimates of the confidence intervals on the fit parameters, for each fit, the covariance matrix was scaled with the respective χ^2_{red}.

The mean and standard deviation of the truncated normal ion-energy distributions, denoted μ_E and σ_E respectively, were calculated from the obtained fit parameters of the underlying normal distribution (μ_G & σ_G) using the relations [560]

$$\mu_E = \mu_G - \sigma_G \frac{\phi(\beta) - \phi(\alpha)}{\Phi(\beta) - \Phi(\alpha)}, \tag{6.18}$$

and

$$\sigma_E = \sigma_G \left(1 - \frac{\beta\phi_G(\beta) - \alpha\phi_G(\alpha)}{\Phi_G(\beta) - \Phi_G(\alpha)} - \left(\frac{\phi_G(\beta) - \phi_G(\alpha)}{\Phi_G(\beta) - \Phi_G(\alpha)}\right)^2\right)^{1/2}, \tag{6.19}$$

where $\alpha = \frac{a-\mu_G}{\sigma_G}$ and $\beta = \frac{b-\mu_G}{\sigma_G}$. The respective uncertainties of μ_E and σ_E were determined using a parametric bootstrap method. Therein, both μ_G and σ_G were assumed to be nor-

mally distributed around the obtained best-fit values with a standard deviation given by the respective fit uncertainties. From these distributions, 1000 different parameter sets (μ_G,σ_G) were randomly sampled and the corresponding values for μ_E and σ_E were calculated with Eqn.s 6.18 & 6.19, respectively. The uncertainties of μ_E and σ_E were then estimated as the sample standard deviations of the obtained random samples.

RFA results and discussion Before discussing the RFA fit results, it is worth to take a second look at the acquired RFA count profiles shown in Fig. 6.40. Recalling Eqn. 6.15, we can interpret any statistically significant downward slope in the RFA count profiles as an indication for the presence of ions at the energy class corresponding to the given retarding potential. The down-sloped edges of the Na^+ RFA profiles [Fig. 6.40 a)] exhibit noticeable shifts towards lower retarding potentials as the interaction time increases. At interaction times $< 1\,\mathrm{s}$, the shifts are substantially more pronounced in the plasma-on case, indicating an increased energy loss in the presence of a co-trapped electron plasma. This behaviour is in accord with the shifts of the Na^+ arrival-time peaks observed in the measurements without a retarding barrier (see Fig. 6.36). The RFA profiles obtained for K^+ [Fig. 6.40 b)] and Rb^+ [Fig. 6.40 c)] exhibit similar shifts, but the differences between plasma-on and -off runs become less pronounced towards higher ion masses.

The best-fit parameters obtained in the fits to the RFA profiles are exhibited in Fig.s 6.41, 6.42 & 6.43. We will first discuss the emerging trends in the data. To obtain a more complete understanding of the cooling dynamics underlying the experimental data, I subsequently present a simplified model that, at least qualitatively, reproduced the observed ion energy evolutions and helped to identify the primary energy loss mechanisms.

The mean energy evolution of the Na^+ ions in Fig. 6.41 confirms the qualitative trends seen in the RFA count profiles. For all studied ion species, both in the plasma-on and -off runs, the mean ion energies drop noticeably towards longer interaction times. The energy loss in plasma-on runs is consistently more rapid than in the plasma-off runs but the respective splitting between the plasma-on and -off curves becomes progressively smaller for ions of higher mass. The observed curves clearly show an enhanced slowing-down of the longitudinal ion motions in the presence of a co-trapped electron plasma.

The imperfect vacuum conditions at the time of the measurements ($p \sim 2.2 \times 10^{-9}$ mbar measured on the ion gauges in the ES and IS diagnostics chambers, presumably $p \sim 1 \times 10^{-8}$ mbar in the trapping region) suggest elastic and inelastic collisions with residual gas particles as a plausible mechanism for the longitudinal energy loss observed in the plasma-off runs. Although elastic collisions preserve the overall kinetic energy in a collision, they may transfer substantial amounts of kinetic energy from the ion's longitudinal motion to the collision partner or into the ion's motion transversal to the magnetic field axis. In this context, it is important to recall that the RFA scheme employed here only probes the ion's longitudinal kinetic energy.

Both the Na^+ and K^+ count profiles show a particularly steep drop at interaction times $< 1\,\mathrm{s}$. Since the ion gauges outside the superconducting magnet provided no evidence for a temporary increase in the residual gas pressure during plasma-on cycles, an additional

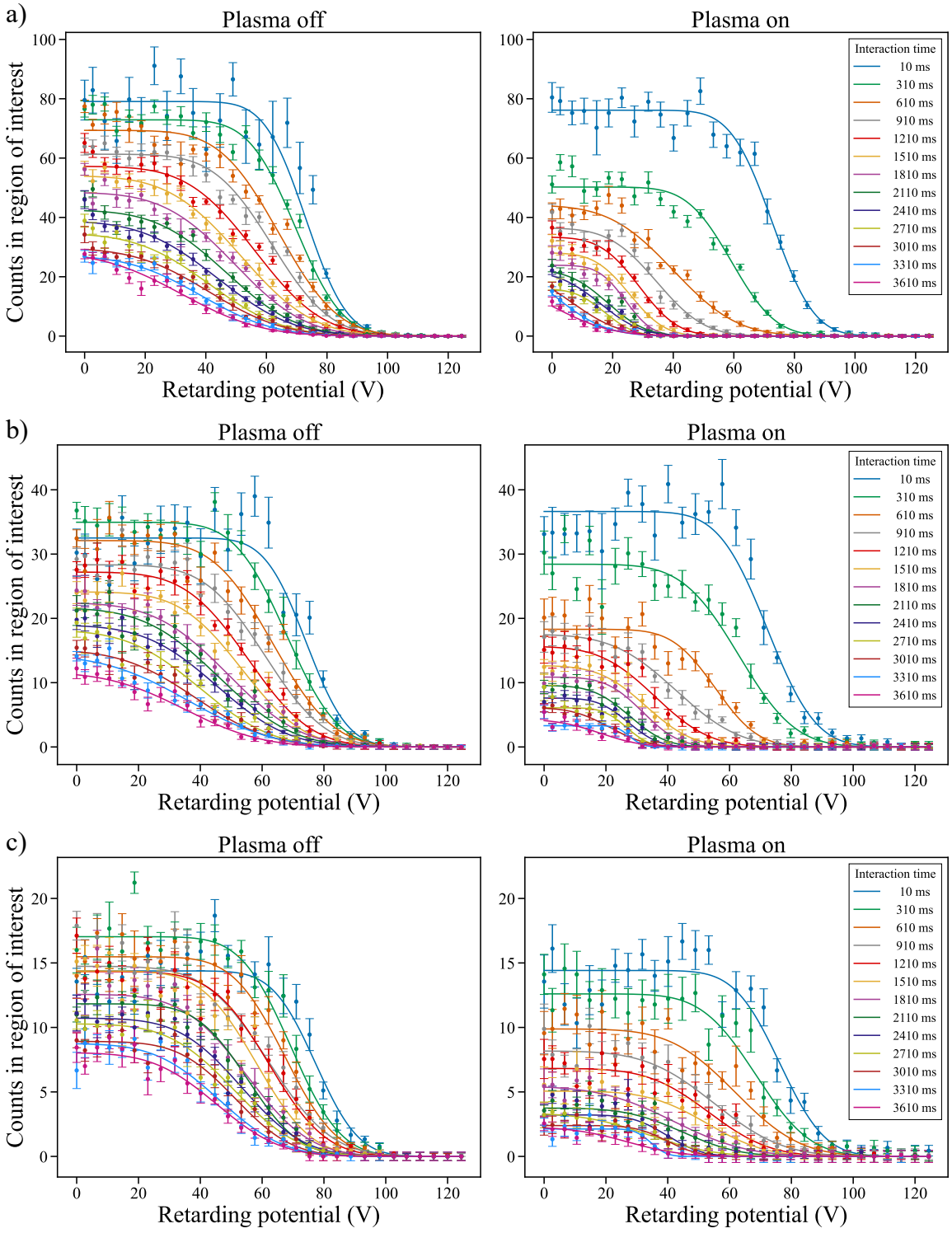

Figure 6.40. Background-subtracted RFA profiles obtained in plasma-on and -off cycles with externally injected $^{23}Na^+$ (a), $^{39,41}K^+$ (b) & $^{85,87}Rb^+$ (c). The solid lines mark least-squares fits of Eqn. 6.17 to data points of the respective colour. See text for details.

energy loss mechanism must have been at play when ions and electrons were co-confined. Further evidence for this statement can be obtained by comparing the plasma-on and -off mean energy evolution of Na^+ and K^+. In fact, the energy-loss rate in plasma-off cycles

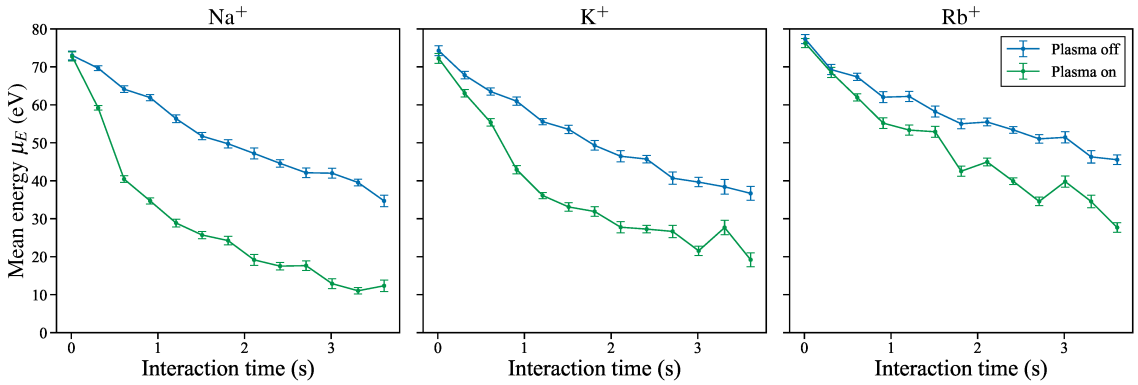

Figure 6.41. Evolution of the mean ion energies extracted from the RFA fits. The ion energies are measured with respect to the minimum of the on-axis trap potential. To guide the eye, the data points were connected by straight lines.

is near identical for Na^+ and K^+, resulting in a reduction of μ_E from $\approx 72\,\text{eV}$ to $\approx 35\,\text{eV}$ over an interaction time of $3610\,\text{ms}$. The corresponding ion energy losses in the plasma-on cycles are noticeably higher, resulting in a reduction of μ_E to $12\,\text{eV}$ and $20\,\text{eV}$ for Na^+ and K^+, respectively. The different energy loss rates seen for Na^+, K^+ and Rb^+ in plasma-on cycles are consistent with a cooling process whose collision cross section is insensitive to atomic structure properties and primarily scales with the collision velocity, resulting in a consistently higher energy loss rate for light ions. At least qualitatively such behaviour is expected for electron cooling, as evidenced by the linear increase of Spitzer's electron-ion temperature equilibration time with the ions' mass (see Eqn. 6.4). The near identical energy-loss rates seen in the plasma-off cycles cannot be explained by a simple mass scaling. However, they could be consistent with elastic or inelastic ion-atom collisions in which the average ion energy loss is not only determined by the masses of the collision partners but also by the atomic-structure-dependent collision cross sections. These aspects will be investigated more quantitatively below with the aid of the mentioned cooling model. Before extending this discussion, we will, however, first consider the time evolution of the other available obervables.

The standard deviations of the truncated Gaussian energy distributions, σ_E, plotted in Fig. 6.42 serve as a measure for the longitudinal ion energy spread. Recalling the motivation for CPET, this is the key quantity that one aims to reduce through electron cooling. In the runs without a co-trapped plasma, σ_E increases monotonically at short interaction times and eventually settles at a constant level for all studied ion species. The curves obtained from plasma-on cycles roughly follow the initial rise, but then exhibit a near-linear decrease at intermediate interaction times. The plasma-on data obtained with Na^+ ultimately settles at a roughly constant level $\approx 10\,\text{eV}$ below the plasma-off curve. Whether K^+ and Rb^+ exhibited a similar behaviour is unclear since the respective plasma-on curves show significant fluctuations at interaction times $> 2\,\text{s}$, likely as a consequence of poor fit convergence due to the strongly limited statistics for these scans values [see Fig. 6.40 b) & c)].

The evolution of total ion number parameter N_i extracted from the fits to the RFA pro-

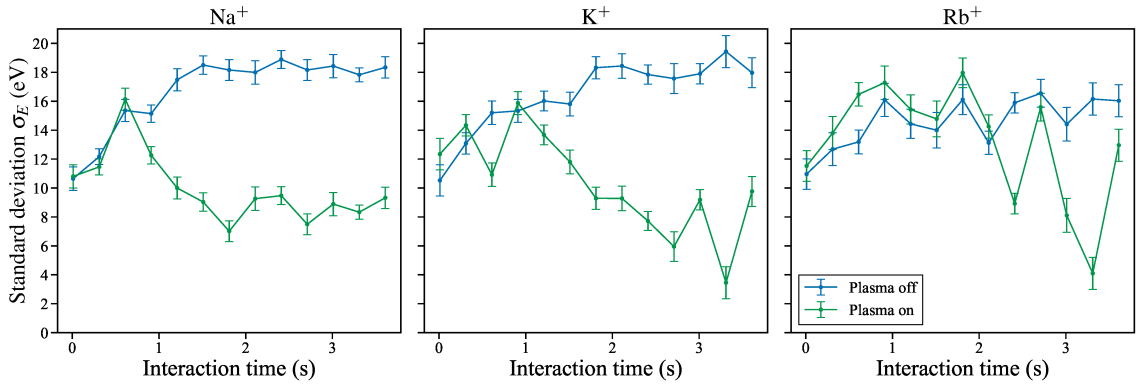

Figure 6.42. Evolution of the standard deviations of the longitudinal ion-energy distributions extracted from the RFA fits. To guide the eye, the data points were connected by straight lines.

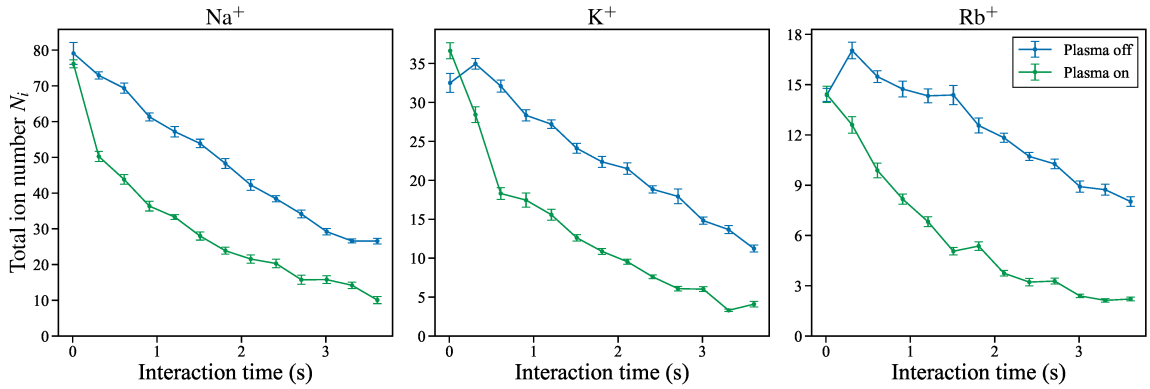

Figure 6.43. Evolution of the total ion numbers extracted from the RFA fits. To guide the eye, the data points were connected by straight lines.

files are depicted in Fig. 6.43. As already observed in earlier ion lifetime measurements, for all studied ion species the number of trapped ions declined faster with a co-trapped electron plasma. Particularly steep drops of N_i are seen in plasma-on cycles with Na^+ at $t \leq 310$ ms and with the K^+ run at $t \leq 610$ ms. In both cases, the steep initial drops are followed by a slower decline at larger interaction times (t), resulting in a kink in the N_i traces. The plasma-on data from the Rb^+ run also seems to exhibit a faster, near-linear drop up to interaction times of $t \leq 1510$ ms. However, for Rb^+ the difference between the ion loss rates at short and long interaction times is much smaller than for the other ion species, making the presence of a kink harder to verify. The sudden changes in ion loss rate indicate that different (sets of) loss processes are at play at short and long interaction times. The rapid initial loss of Na^+ and K^+ ions seems to coincide with the high, initial energy loss rates observed for these ion species. However, direct comparison of Fig.s 6.41 & 6.43 shows that the corresponding energy- and ion-loss curves do not correlate closely, since the fast initial drops continue over different time scales.

Besides the ion count signals, the electron-induced harp detector signals provided the

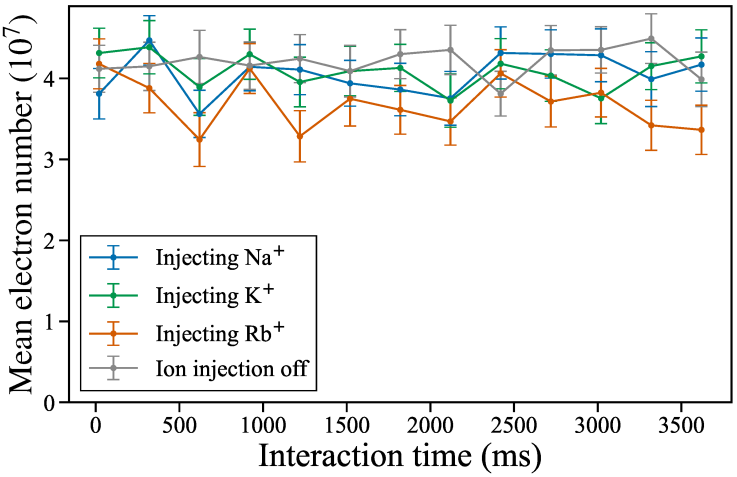

Figure 6.44. Evolution of the detected electron number N_e during RFA scans with injection of different alkali ions and during a background measurement without ion injection. To guide the eye, the data points were connected by straight lines.

second observable of the trapped-particle dynamics. Since the applied retarding potentials did not noticeably affect the electron numbers extracted from the harp signals, the electron numbers recorded at a given interaction time were averaged over all scans loops and retarding voltages. The resulting mean electron numbers are shown as function of the interaction time are shown in Fig. 6.44. The trends from the RFA runs with ion injection are compared to the electron numbers obtained in a background measurement without ion injection. To reduce the measurement duration, the background measurement was only performed with plasma-on cycles. In lieu, the plasma-off signals from the Rb^+ RFA scan were thus used to correct the harp detector signals for switching background. As expected from the plasma lifetime measurements presented in section 6.4.3, the detected electron numbers showed no noticeable drop over the considered interaction (and thus storage) times. Despite a slight reduction in the run with Rb^+ ions, the mean plasma electron number throughout all RFA scans agreed within a relative deviation of $\lessapprox 10\%$. The mean electron numbers detected in the background measurement without electron injection also agreed with those obtained in the runs with ion injection within this level, indicating that the injection of the relatively small numbers of ions ($N_i < 100$) did not induce substantial electron losses and likely had a minor impact on the overall plasma dynamics.

A simplified model of the cooling process Although the presented RFA results clearly confirmed that the presence of a co-trapped plasma induced an increased ion energy loss. A number of questions remained concerning the interpretation of the obtained data, namely: Is the enhanced energy loss indeed due to electron cooling? Which mechanism causes the ion loss in plasma-off cycles? What induces the enhanced ion-loss rates in plasma-on cycles?

To answer these questions and aid the interpretation of the obtained experimental data, a simplified model of the cooling process was constructed. As mentioned earlier, even when

the electron plasma dynamics are neglected, a three-dimensional description of the ion motion with realistic cooling forces remains a serious numerical challenge (see e.g. [561]), both due to the small time step size dictated by the fast cyclotron motion and the need to numerically solve integrals in the cooling forces. Since some critical parameters such as the electron number density as well as the pressure conditions and the residual gas composition in the trap were not well-constrained experimentally, the model had to be sufficiently efficient to enable an adjustment of the mentioned parameters to the experimental data. The plasma-off background measurements clearly demonstrated that energy-loss mechanisms other than electron cooling played an important role under the given experimental conditions. A major objective of the modelling efforts was therefore to obtain a better qualitative understanding and ideally an at least approximate theoretical description of these processes, as the latter would allow to better disentangle the electron cooling contribution from background processes in the plasma-on measurements.

Here, I only give an overview of the cooling model and its underlying assumptions. For a comprehensive description of the model, including implementation details and additional background on ion-neutral and ion-plasma collisions, the reader is referred to appendix C. The central model features and assumptions are summarized as follows:

- Due to the ions large initial centre-of-mass (COM) energy, throughout most of the cooling process, the longitudinal ion energies can be assumed to be substantially larger than the energy stored in the transversal ion motions. Consequentially, only collisional transfer of energy from the transversal into the longitudinal ion motion is simulated, whereas any energy transfer into the longitudinal ion motion is neglected. Two general mechanisms for energy loss are considered: Ion-electron collisions and ion-neutral collisions including both elastic as well as charge exchanging collisions.

- As the strong magnetic field forces ions onto helical orbits, we neglect all radial particle dynamics and assume that the ions follow the field lines like beads on a string. The high field quality of the superconducting magnet permits us to neglect magnetic field non-uniformity such that the problem of ion-orbit integration (where necessary) is effectively reduced to a single dimension given by the trap's symmetry axis. This modelling approach is equivalent to orbit integration in a guiding-centre approximation in the limit of an infinitely strong, uniform magnetic field.

- Due to their small number ($N_i < 100$) the injected ions are considered tenuous, in the sense that they do not significantly affect the plasma dynamics (e.g. by inducing noticeable electron loss or exciting plasma oscillations). The ions may, however, perturb the plasma temperature, the associated model assumption being that any energy deposited in the plasma is instantaneously (i.e. on timescales much shorter than the $1\,\mathrm{ms}$ long simulation time step) distributed among all plasma electrons. The small N_i and the comparatively large trap volume occupied by the ions further allow us to neglect ion-ion interactions.

- As for the cooling calculations in section 6.2, the energy exchange between ions and

plasma electrons is treated within the kinetic theory of unmagnetized plasmas. However, here we discard the assumption of a Maxwellian ion velocity distribution and use relations that describe the stopping of fast, monoenergetic ions in a background of plasma particles (see e.g. [484, 562]). The rate at which such ions dissipate longitudinal energy is described by the longitudinal energy-exchange frequency,

$$\nu_{E,\parallel} \doteq -\frac{\langle(\Delta v_\parallel/v)^2\rangle}{\Delta t} = \frac{8\pi q^2 e^2 n_e \ln(\Lambda)}{m^2 v_{\mathrm{e,th}}^3} G\left(\frac{v}{v_{\mathrm{e,th}}}\right)\left[2\left(1+\frac{m}{m_e}\right)\frac{v_{\mathrm{e,th}}}{v} - \frac{v_{\mathrm{e,th}}^3}{v^3}\right], \tag{6.20}$$

with

$$G(x) \doteq \frac{\Phi(x) - x\Phi'(x)}{2x^2}, \quad \text{and} \quad \ln(\Lambda) = 23 - \ln\left(\frac{q\sqrt{n_e/10^7\,\mathrm{cm}^3}}{e\,T_e^{3/2}}\right), \tag{6.21}$$

where $\Phi(x)$ denotes the error function. By tracing the trajectories of a larger set of test ions in energy space, this approach allows one to describe arbitrary ion velocity distributions. Energy fluctuations due to plasma-induced ion velocity diffusion was not taken into account as the diffusion frequencies predicted by kinetic theory are negligibly low under the considered conditions (see appendix C).

- In contrast to ion-electron collisions, ion-neutral collisions are comparatively rare events (collision frequencies $\sim 30\,\mathrm{s}^{-1}$ under CPET vacuum conditions) that may however induce significant changes of the longitudinal ion energy. Due to their low frequency, collisions between ions and gas particles are treated through a Monte Carlo collision method (see appendix C). At the beginning of each simulation time step, the probability for a collision to occur is calculated as

$$P_{\mathrm{coll}}(t) = 1 - \exp\left(-\sum_k \frac{v_{\mathrm{eff}}(t)}{l_k}\Delta t\right), \tag{6.22}$$

where l_k is the ion's mean free path with respect to the k-th neutral species, and the effective velocity $v_{\mathrm{eff}} \leq v(t)$ must be chosen such that P_{coll} correctly predicts the collision probability averaged over many axial ion oscillations. To this end, we set $v_{\mathrm{eff}} = \lambda v_{\mathrm{max}}$ with $v_{\mathrm{max}} = \sqrt{2E_\parallel/m}$ and calibrate the ion-energy- and trap-potential-dependent velocity correction factor λ as a function of ion energy. The calibration procedure is based on orbit integration of single axial ion oscillations at various energies (see appendix C for details) and is performed prior to actual simulation runs, thus greatly reducing the simulation run time.

  Once P_{coll} has been calculated, a uniformly distributed random number x between 0 and 1 is generated. If $x \leq P_{\mathrm{coll}}$, an ion-neutral collision is modelled; otherwise, no ion energy is lost due to ion-neutral interactions in the given time step.

  While the residual gas composition at the time of the measurements is unknown, based on earlier residual gas analysis in CPET, H_2, H_2O, CO and CO_2 were presumed to be a representative set of the major gas components. The respective partial pressures

were adjusted in order to best match the evolution of the observables (N_i, μ_E & σ_E) in plasma-off cycles.

- Ion-neutral collisions are described within a semi-classical model with a total collision cross section obeying the scaling $\sigma_{\text{tot}} \propto \alpha/E^{1/3}$, where α is the neutral's dipole polarizability and E_{coll} is the collision energy in the COM frame. The implemented ion-neutral collisions fall into one of the following categories [563, 564], sorted by descending cross section: (1) Small-angle elastic scattering with an induced-dipole interaction potential of the form $V(r) \propto \alpha^{2/3}/r^4$, where r is the particle spacing, (2) Langevin collisions with potentially large scattering angles (and thus large energy transfer), and (3) charge exchange reactions that effectively replace a fast ion with a thermal ($T_n \approx 300\,\text{K}$) ionized gas particle.

- Combining the mentioned energy loss mechanisms, the time evolution of the ion energies and the plasma temperature is described by the coupled equations

$$\frac{dE_{\parallel}^{j}}{dt} = -\left(E_{\parallel}^{j} - \phi_{\text{nest,eff}}\right)\,\kappa\,\nu_{E,\parallel}^{j} \; - \Delta E_{\parallel,\text{coll}}^{j}\,\delta(t - t_{\text{coll}}^{j}) \tag{6.23}$$

$$\frac{dT_e}{dt} = +\frac{2}{3k_B}\frac{\iota}{N_e}\sum_{j=1}^{N_{\text{i,sim}}}\left(E_{\parallel}^{j} - \phi_{\text{nest,eff}}\right)\,\kappa\,\nu_{E,\parallel}^{j} \; - \frac{T_e - T_{\text{e},\infty}}{\tau_e}, \tag{6.24}$$

where Eqn. 6.23 represents $N_{\text{i,sim}}$ equivalent equations, one for each simulated ion, $\iota = N_{\text{i,exp}}/N_{\text{i,sim}}$ corrects for deviations between the simulated and experimental particle number, the term with the delta distribution describes discrete jumps in energy due to ion-neutral collisions, where the collision time t_{coll}^{j} is determined by the Monte Carlo collision method, and the energy-dependent overlap factor κ measures the fraction of an axial oscillation period that an ion spends inside the plasma. For computational efficiency, both $\kappa(E_{\parallel})$ and $\lambda(E_{\parallel})$ are calibrated by performing axial ion-orbit integrations at various $E_{\parallel}$ prior to actual simulation runs (see appendix C). As all transversal particle dynamics are neglected here, the radial ion-electron overlap is assumed to be 100%.

- Except for the cyclotron cooling and small ion-induced perturbations[13] in the plasma temperature, all electron plasma dynamics are neglected. The plasma is assumed to be centred on the trap axis (implying a fully damped out diocotron motion) and sufficiently cold to acquire a uniform electron density throughout its entire extent. Based on these assumptions, the lowering of the vacuum nest potential ϕ_{nest} by the plasma space charge ϕ_p is approximated by truncating the nest potential to a user-defined upper bound, $\phi_{\text{nest,eff}} \doteq \phi_{\text{nest}} - \phi_p$. The uniform density assumption is fair since the Debye length, $\lambda_D \sim 120\,\mu\text{m}$, is much smaller than the plasma radius, $r_p \sim 1\,\text{mm}$.

[13] Due to the small numbers of injected ions, ion-induced plasma heating as described by the left term on the right-hand side of Eqn. 6.24 was essentially negligible in the present simulations as even distributing the entire kinetic energy of the ion samples among the plasma electrons would have only raised the mean electron energy by $< 1\,\text{meV}$; the term was still included to enable generalizations to large HCI samples.

Particle in-cell (PIC) simulations confirmed (see appendix C) that the assumption of a perfect flattening of the nest potential is a good approximation for plasma temperatures $T_e \lessapprox 11\,600\,\mathrm{K}$ and verified that the effect of the plasma space charge on the trap potential is indeed negligible outside the filled nest region as long as $\phi_{\text{nest,eff}} \lesssim \phi_{\text{nest}}/2$.

- Ions that have cooled into the first well do not reach the MCP detector and are discarded in the post-processing of the simulation data. As ion-ion interactions and plasma-induced ion velocity diffusion were neglected, only ion-neutral collisions could cause a simulated ion to become localized in one of the ion wells. In that case, the lack of ion-electron overlap ($\kappa = 0$) is assumed to prevent any further ion-plasma interaction, and the ion can from then on only be cooled by ion-neutral collisions.

- Ions were started with initial masses sampled such as to reproduce the given element's natural isotopic abundances (neglecting isotopes with a relative abundance $< 1\%$). The initial ion energies were sampled from truncated normal distributions with the lower bound set to the bottom of the trap potential. The parameters μ_G and σ_G were chosen only marginally different than those obtained in the fits to the RFA profiles at $10\,\mathrm{ms}$ interaction time.

The model parameters were adjusted to best match the experimental data, resulting in the parameters compiled in table 6.1. Generally, the plasma and residual gas parameters were assumed to be constant throughout all measurements and thus kept identical in simulation runs with different species. However, as the mean number of detected electrons, N_e, in the Rb^+ measurement was 10% below the (near-identical) N_e in the other runs, the electron number density, n_e, in the Rb simulation was likewise reduced by 10%, thus assuming a linear scaling of n_e with N_e. Including charge exchange was not found to improve the agreement between model and experimental observables. Hence, P_{CX} was set to zero in the presented simulations.

The energy evolution of a 30 simulated ions, obtained is illustrated in Fig. 6.45. The plasma-off data exhibits the sudden jumps in ion energy due to ion-neutral collisions; many energy jumps due to elastic collisions are too small to be visible. The plasma-on simulation results additionally show the smooth ion-energy variation due to the plasma-induced friction force. The simulation data was obtained after adjusting the neutral partial pressures, the electron number density and the initial plasma temperature to best match the experimental observables (Fig. 6.41, 6.42 & 6.43). The kinks in the steep initial drops of the experimentally observed mean energy evolutions for Na^+ and K^+ were found to partially originate from the variation of the ion-electron overlap factor, κ. To better reproduce the kinks, the plasma was initialized with a temperature 5 times above the assumed equilibrium value of $T_{e,\infty} = 300\,\mathrm{K}$. An initial increase in plasma temperature is expected in experimental reality, as the HV switching operations for ion injection into the interaction region likely heated the plasma through electrode cross talk.

The most direct comparison between model predictions and experimental data is obtained by contrasting the measured RFA profiles to their simulated equivalents. After binning the simulated ion energies with a bin resolution of $1.25\,\mathrm{V}$, the simulated RFA profiles

Table 6.5. Input parameters used to reproduce the experimental observables with the cooling model. Note that the mean ion energies $\mu_{E,\parallel}$ and the effective nest depth $\phi_{\text{nest,eff}}$ are measured with respect to the minimum of the trap potential.

Ion and electron plasma parameters:

	Na^+	K^+	Rb^+
$\mu_{E,\parallel,0}$ (eV)	77.8	77.8	81.8
$\sigma_{E,\parallel,0}$ (eV)	10.7	11.0	10.0
$N_{\text{i,exp}}$	78	37	18
$N_{\text{i,sim}}$	100	100	100
N_e	4.1×10^7	4.1×10^7	3.7×10^7
n_e (cm^{-3})	1.7×10^8	1.7×10^8	1.53×10^8
$T_{e,0}$ (K)	1500	1500	1500
$T_{e,\infty}$ (K)	300	300	300
τ_e (ms)	79	79	79
$\phi_{\text{nest,eff}}$ (V)	27.25	27.25	27.25

Residual gas parameters:

	H_2	H_2O	CO	CO_2
$\alpha/(4\pi\epsilon_0)$ (Å^3)	0.787	1.501	1.953	2.507
p (mbar)	1.4×10^{-8}	1.6×10^{-8}	9.8×10^{-9}	1.1×10^{-8}
T_n (K)	300	300	300	300
P_{CX}	0	0	0	0

were given by the complement of the cumulative ion-energy histogram. Fig. 6.46 shows measured and simulated RFA profiles for K^+ at various interaction times. As the ion losses were not well reproduced by the model, the profiles were normalized to the respective intensity in the lowest retarding potential bin for better comparison.

Despite small systematic shifts, the simulated RFA profiles are seen to reproduce the shapes of the experimental profiles reasonably well, thus validating some of the assumptions of the modelling approach. The simulations further confirmed that the sharp edge observed in the experimental RFA profiles at retarding voltages of $\approx 28\,\text{V}$ indeed arises from the plasma-induced lowering of the nest potential. As alluded to earlier, the effective nest potential depth therefore forms an important threshold that determines at which ion energy the electron cooling power ceases. This is in accord with earlier measurements [486] with much smaller electron plasmas ($N_e \sim 10^5$) that found the ultimately achievable temperature of electron cooled antiprotons to correlate with the depth of the externally applied potential. However, in that earlier work the electron space charge potential ($\sim 0.1\,\text{V}$) only constituted a minor correction to the trap potential. Similar to a study of positron cooling of antiprotons [565], our measurements probe the same effect in a regime of much higher plasma space charge ($\phi_p \approx 12\,\text{V}$ according to simulation). The edge in the measured and

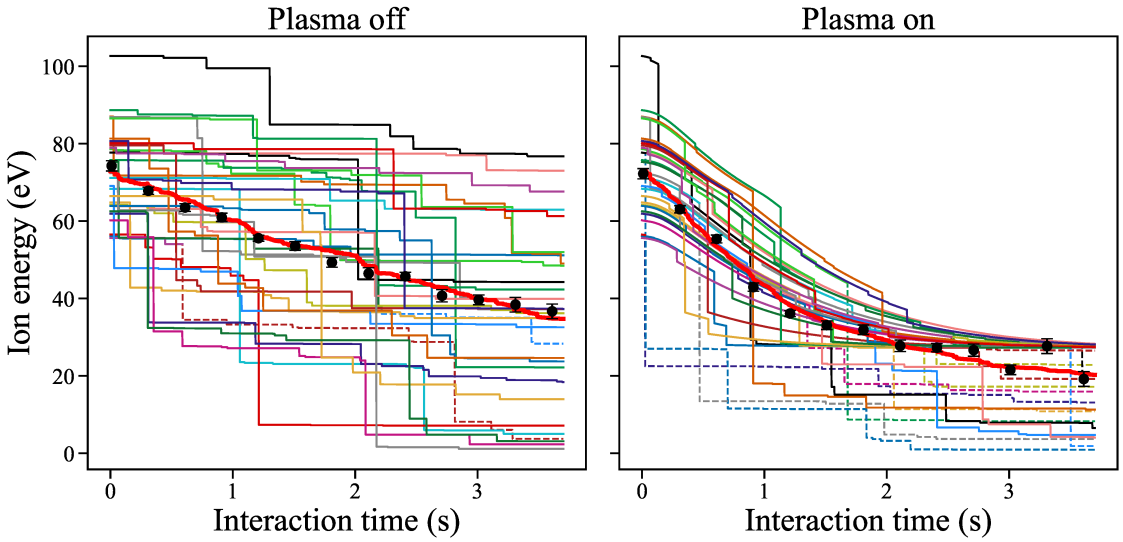

Figure 6.45. Longitudinal-energy evolution of individual $^{39,41}K^{+}$ ions (thin lines) predicted by the cooling model in simulation runs with (right) and without (left) an electron plasma. The black data points denote the mean ion energies extracted from fits to the experimental RFA data. Once an ion becomes localized in the entrance-side ion well (and thus cannot reach the detector anymore), the line indicating its energy evolution changes from solid to dashed. The thick red lines mark the respective mean of all 100 simulated energy trajectories, only 30 of which were plotted for clarity.

simulated RFA profiles in the rightmost plot of Fig. 6.46 is seen to closely match the effective nest potential specified in the simulation (dashed line). This demonstrates that the threshold at which the electron cooling ceases is indeed given by the effective nest depth, and thus strongly depends on the plasma properties, as already pointed out in [565].

If one aims to achieve ion energy spreads $\lesssim 1\,\mathrm{eV/q}$, the trap potential and plasma generation hence have to be carefully optimized in order to realize the demanded effective nest depths of $\leq 1\,\mathrm{eV}$. The implementation of such shallow nests requires a high level of control over the accumulated electron number and demands an equilibrium plasma temperature $T_e \lesssim e\phi_{\mathrm{nest,eff}}/(20k_B) \lesssim 600\,\mathrm{K}$ in order to keep evaporative electron losses from the nest at a negligible level [566]. Alternatively, the ion-electron overlap can be extended by adiabatically lowering the externally applied nest potential as the cooling process evolves. Such an adiabatic nest depth reduction has been successfully used in antihydrogen experiments to preserve the contact between co-trapped antiprotons and positrons [567].

Estimation of the electron plasma dimensions

Using the effective nest depth and electron number density obtained by matching the simulation to the experimental data, we can estimate the experimentally unconstrained dimensions of the electron plasma. The plasma length l_p is simply deduced as the distance between the two points where the vacuum on-axis nest potential $\phi(z)$ equals $\phi_{\mathrm{nest,eff}}$, resulting in

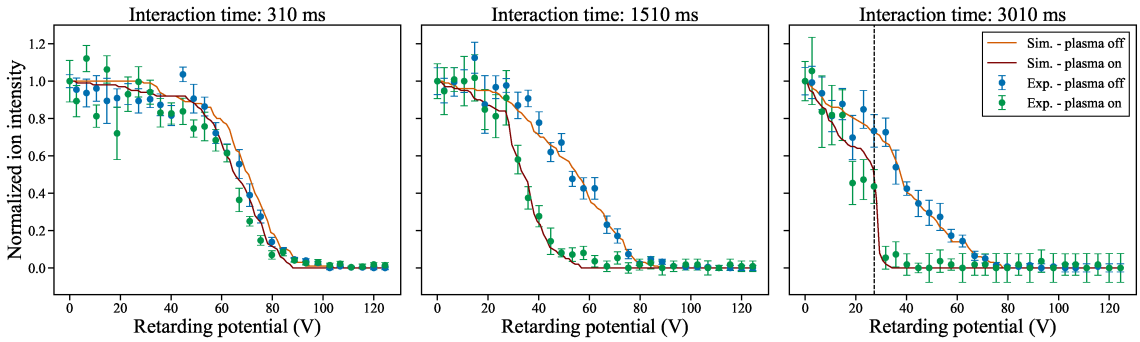

Figure 6.46. Comparison of RFA profiles (colored lines) extracted from the simulated ion energy distributions to experimental RFA profiles (data points) for $^{39,41}K^+$ at different interaction times. The overall shape of the experimental RFA profiles is fairly well reproduced by the cooling model. The dashed vertical line in the right plot indicates the pre-defined effective nest depth in the simulation, $\phi_{\text{nest,eff}} = 27.25\,\text{V}$.

$l_p \approx 8.5\,\text{cm}$. The plasma radius can be approximated from the simple analytical expression for the space charge potential along the symmetry axis of an infinitely-long cylindrical plasma [568]:

$$\phi_p = \frac{e n_e r_p^2}{4\epsilon_0}\left[1 + 2\ln\left(\frac{r_w}{r_p}\right)\right], \tag{6.25}$$

where r_w denotes the inner electrode radius (17.5 mm for CPET). Using $\phi_p = \phi_{\text{nest}} - \phi_{\text{nest,eff}} = 12\,\text{V}$ and numerically solving this equation for r_p, we find that, at the electron number density from the simulation ($n_e = 1.7 \times 10^8\,\text{cm}^{-3}$), an on-axis space charge potential of $\phi_p = 12\,\text{V}$ would be generated by a plasma with a radius $r_p \approx 1.65\,\text{mm}$. The large plasma aspect ratio of $l_p/(2r_p) \approx 25.8$ makes the assumption of an infinitely-long cylindrical plasma an acceptable approximation. The deduced plasma radius agrees within a factor of 3.5 with the measured radii of longer and denser electron plasmas ($r_p \approx 0.5\,\text{mm}$, $l_p \approx 40\,\text{cm}$, $n_e \approx 8.1 \times 10^8\,\text{cm}^{-3}$) trapped in simple rectangular potential wells in earlier studies with CPET [508]. The non-perfect agreement of these radius deductions is expected since the earlier measurements were performed at an almost five times higher electron density and using an on-axis electron gun for plasma generation. The plasma radius obtained here is more than twice as large as the radial extent of the trap volume that can be projected onto the MCP detector. Hence, for all detected ions, the presumption of 100% radial ion-electron overlap seems well justified.

Comparison of the model predictions and the experimental cooling curves

After these preparatory considerations, we may now compare the experimental evolution of the ion numbers, the mean ion energies and the standard deviations of the ion energies to the model predictions. Fig. 6.47 exhibits the simulated evolution of N_i, μ_E and σ_E in comparison to the RFA fit results already shown in the previous subsection. For comparison to the experimental observables, the model predictions for μ_E and σ_E were taken as the sample mean and sample standard deviation of the ion energies predicted at a given interaction time.

Ion number evolution The ion number evolutions shown in the top row of Fig. 6.47 qualitatively reproduce the experimental trends without a co-trapped plasma. Recalling that ion loss in the simulation is exclusively due to ion localization in the entrance-side potential well, we find that this mechanism can indeed substantially reduce the observed ion numbers over the measurement duration and might dominate the (apparent) ion loss in plasma-off cycles. Especially for the higher mass species, the simulation cannot fully reproduce the ion loss observed in plasma-off cycles, indicating that additional loss processes are needed to explain the experimental trends. The simulation also fails to describe the rapid ion loss seen at short interaction times in plasma-on cycles. However, at longer interaction times, the simulated ion loss rates in plasma-on cycles seem to match the experimental ones (despite a large vertical offset between the ion count traces).

It remains unclear how the presence of a plasma increases the ion loss rates at early stages of the ion-electron interaction period. Inelastic atomic processes such as electron ionization or excitation can hardly explain the observed ion loss as the collision energies in our measurements ($E_{\text{coll}} \approx \frac{1}{2} m_e v^2 \sim 1\,\text{meV}$) are far too small for them to become relevant.

Strikingly, the observed ion numbers in plasma-on cycles drop linearly with t at short interaction times. In order to extract the mass scaling of the plasma-enhanced ion loss rates, linear functions were fitted to the respective subsections of the experimental plasma-on ion-count evolutions using the method of least-squares [569]. The ion loss rates obtained from the slopes of the linear fits [dashed lines in Fig. 6.47 a), b) & c)] are listed in table 6.6 and scale as m^{-2}, as seen in the second row of the table. In contrast, the duration of the linear drop in ion count rate increases approximately linearly with the ion mass. It is unclear what process causes these scalings.

Considering that the cooling model cannot even qualitatively describe the plasma-enhanced ion loss, it appears likely that the underlying mechanism is to be found in the radial particle dynamics. As mentioned earlier, according to SIMION simulations, only ions with radial displacements smaller than $r_{\text{max}} \approx 0.8\,\text{mm}$ can reach the ES MCP0 detector. Thus, a temporary, plasma-induced increase in radial ion diffusion could reduce the ion count rate by driving ions onto orbits that are not projected onto the detector.

As mentioned in the discussion of the ion-lifetime measurements (section 6.4.4), a plausible mechanism that could cause the observed plasma-enhanced ion losses is centrifugal separation [556–558] of the ions and electrons. In this phenomenon, the difference in the rotation frequencies of two plasma species of different mass leads to a collisional exchange of angular momentum that drives the lighter species towards and the heavier species away from the trap axis. To the author's knowledge, centrifugal separation has so far not been experimentally demonstrated in plasmas composed of oppositely-charged species. However, calculations of test-particle trajectories [559] under the influence of drag exerted by a lepton plasma indicate that centrifugal separation should also occur in these plasmas. The same calculations predict radial ion transport rates orders of magnitude too slow to explain the experimentally observed separation rates both in the presented case as well as in other electron-antiproton plasmas [558]. In these experiments, Andresen et al. [558] injected samples of $\sim 10^4$ antiprotons into prepared electron plasmas ($n_e \approx 1.5 \times 10^9\,\text{cm}^{-3}$, $N_e \approx 1.9 \times 10^7$ &

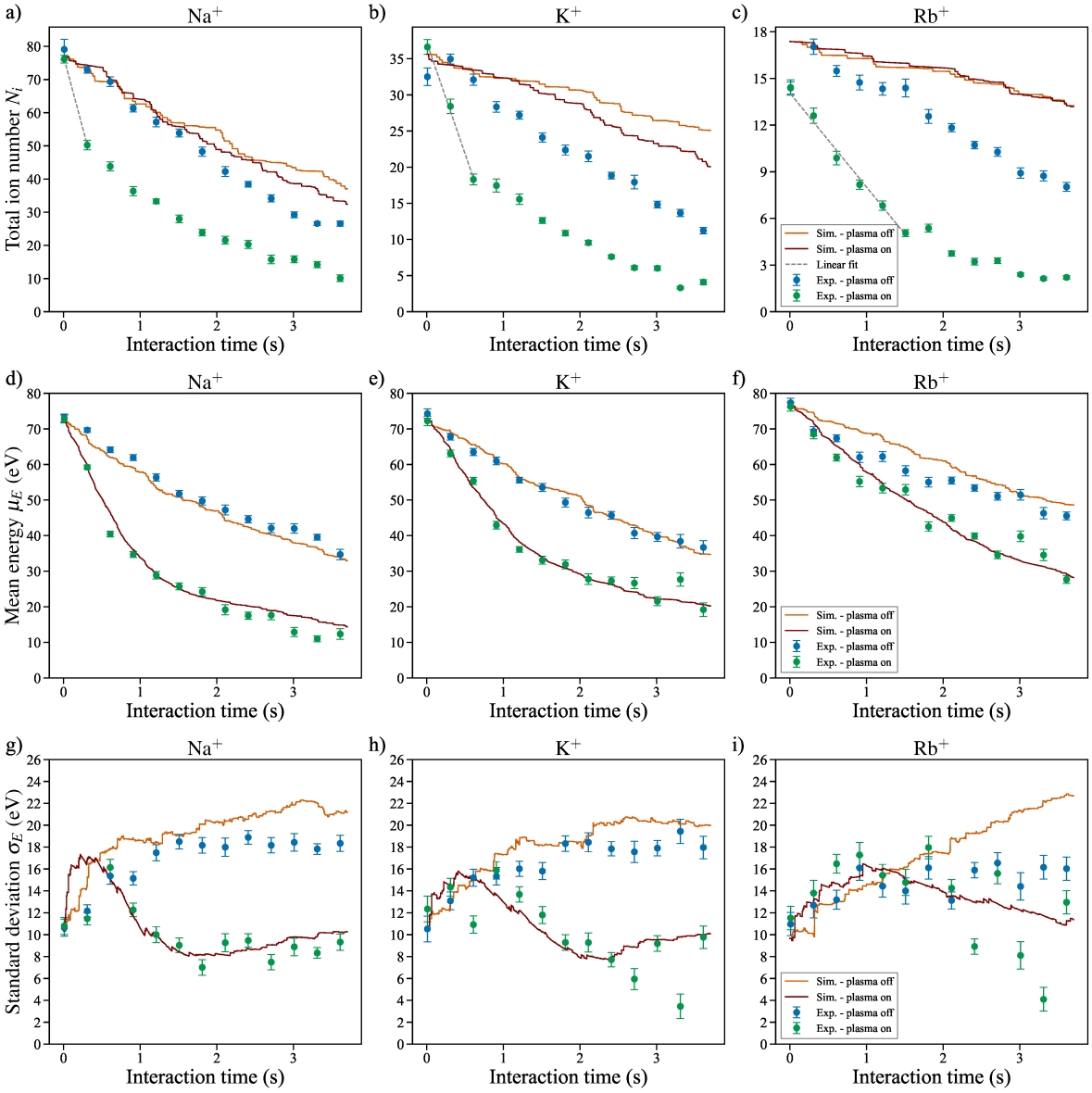

Figure 6.47. Comparison of the experimental RFA results (data points) to predictions of the simplified cooling model (solid lines). The evolution of the ion number, mean ion energy and standard deviation of the ion energies are shown for each injected ion species. See text for details.

Table 6.6. Plasma-enhanced ion-loss rates at short interaction times deduced from the slopes of the linear fits to the plasma-on ion count data in Fig. 6.47 a), b) & c). In the case of $^{23}Na^+$, only two data points were available for the fit; hence, the respective loss-rate uncertainty could not be estimated. After quadratic scaling to the mass of $^{23}Na^+$ (m_{Na}), the ion loss rates agree within their 1σ confidence intervals (see second row).

	$^{23}Na^+$	$^{39,41}K^+$	$^{85,87}Rb^+$
Ion loss rate (1/s)	-86.4	-30.8 ± 1.7	-6.1 ± 0.3
$(m/m_{Na})^2 \times$ Ion loss rate (1/s)	-86.4	-89.1 ± 4.9	-84.3 ± 4.1

$T_e \approx 120\,\mathrm{K}$) and found the separation of both species to evolve on timescales of about $80\,\mathrm{ms}$ (similar to the electron cyclotron cooling time in their system). This separation timescale is of similar order of magnitude as the plasma-enhanced ion loss rates in our measurements, suggesting that both observations might derive from the same mechanism.

With Ref. [570], the centrifugal separation rate expected from collisional drag in our plasma can be estimated to be $\sim 2 \times 10^{-3}\,\mathrm{s}^{-1}$, which is several orders of magnitude too slow to explain the observed particle losses. However, centrifugal separation may also be driven by collective plasma modes [570] such as the $m = 1$ diocotron mode. Experimental studies on electron plasma dynamics [571] have, for example, demonstrated that collective effects can enhance the radial particle transport due to asymmetries in the trapping fields. Kabantsev et al. [572] have recently observed rapid centrifugal separation in an electron-H^- plasma that correlated with a damping of the plasma's diocotron motion. A detailed theoretical explanation for the observed correlation of diocotron damping and radial ion transport is, to the authors knowledge, still outstanding. As a damping of the diocotron motion has been observed in previous work with CPET [508], it seems well possible that the same effect provided for the enhanced radial ion transport that could explain the plasma-enhanced ion losses observed in the present measurements. In fact, the trap potential switching for ion transfer into the interaction region provides a possible mechanism that could have induce a diocotron oscillation at the beginning of the ion-electron interaction periods in our measurements. Once more detailed theoretical descriptions of the radial particle dynamics in non-neutral plasmas with oppositely-charged species become available, the observed quadratic mass scaling of the ion-loss rates may help to identify the exact mechanism underlying the observed ion-loss enhancement in plasma-on cycles.

An alternative option for an explanation lies in a recently predicted transverse friction force [573, 574] that may transfer longitudinal energy into the cyclotron motion and thus gradually widen the ion's Larmor radii. A quick estimate shows that expanding a $^{23}Na^+$ ion's cyclotron orbit to a radius exceeding the critical displacement from the trap axis ($r_{max} \sim 0.8\,\mathrm{mm}$) would, however, require an energy of at least $97\,\mathrm{eV}$ to be stored in the cyclotron motion. This scenario seems highly unlikely considering that this value exceeds the ions' initial longitudinal energies in the trap.

Mean ion energy evolution The ions' longitudinal-energy evolution (central row in Fig. 6.47) is qualitatively well described by the cooling model. Despite some discrepancies, the predicted energy evolutions generally match the observed energy loss rates both in the plasma-on and -off case. Noteworthy discrepancies are seen in the plasma-off data for Rb, where the fast energy loss between the first two data points is not reproduced by model. Further, the late-time energy loss in the Na data is not well matched. This might be a sign of the expected loss of predictive power at lower longitudinal ion energies, where the radial kinetic ion energies become increasingly relevant, eventually causing the assumption of ion motion parallel to the trap axis to break down. At energies $> 20\,\mathrm{eV}$, where electron cooling dominates the energy loss, the agreement is rather impressive considering the simplicity of the model. The observed cooling rates for the different ion species are seen to follow the expected, near-linear[14] scaling with the inverse of the ion mass.

These observations confirm the expectation [575] that unmagnetized plasma theory yields a reasonable description of the electron cooling force under CPET conditions as the ions' Larmor radii are of similar or larger magnitude (e.g. $r_c = mv_\perp/(qB) \approx 99\,\mu\mathrm{m}$ for $^{23}\mathrm{Na}^+$ at $E_\perp = 1\,\mathrm{eV}$) than the Debye length of the electron plasma ($\lambda_{D,e} \approx 120\,\mu\mathrm{m}$), rendering the ions essentially unmagnetized. The fact that the plasma parameters suggested by the cooling model are compatible with those reported for comparable plasmas in other experiments [557, 558, 575] as well as with expectations based on earlier measurements of electron plasma properties in CPET [508] provides further evidence that the electron cooling force is well replicated in the present simulations.

Energy spread evolution The evolution of the ions' longitudinal energy spread (here quantified by the standard deviations, σ_E, exhibited in the bottom row of Fig. 6.47) provide additional testing grounds for the model predictions. The initial increase and the subsequent saturation seen in the experimental plasma-off data for σ_E are qualitatively well replicated by the simulated curves. However, the predicted saturation levels overestimate the experimental data by several volts. This discrepancy might either be caused by a non-optimal adjustment of the neutral partial pressures fed into the model or point to insufficiencies in the underlying ion-neutral collision model. The second option could, in principle, be explored by implementing a more complete collision model based on ion-atom interaction potentials that include terms beyond the induced-dipole interaction (see [576]). However, we refrained from this approach as, for almost all ion-atom systems of interest, no experimental or theoretical information could be found in the literature, thus preventing proper deduction of the necessary interaction strength parameters. It is further possible that inelastic collisions, which can enhance collisional energy loss by excitation of internal degrees of freedom (e.g. vibrations and rotations in rest gas molecules), would also have to be modelled to obtain an even closer agreement.

For all studied ion species, the evolution of the experimental plasma-on data for σ_E are remarkably well reproduced by the cooling model. Deviations between model and experiment are only seen at a few outliers that are predominantly found at long interaction times

[14] Neglecting terms of order $\frac{m_e}{m}$, the longitudinal energy-exchange rate from Eqn. 6.20 obeys $\nu_{E,\parallel} \propto m^{-1}$.

and derive from limited measurement statistics or the choice of the prescribed ion energy distributions in the fits of the measured RFA profiles. The fact that model and experiment agree closely in the plasma-on cases despite the discrepancies seen in the plasma-off data indicates that the overall ion-energy loss is dominated by the plasma-induced drag. Moreover, it verifies that plasma-induced diffusion of the ion velocities has indeed negligible impact on the longitudinal ion energy evolution, as presumed by the cooling model.

Stages of the cooling process Evaluation of the ensemble-averaged properties and the simulated energy trajectories of individual ions (see e.g. Fig. 6.45), allows us to explain the experimentally observed evolution of μ_E & σ_E in detail. The cooling process can be subdivided into three stages.

At short interaction times, the ions' COM energy is dissipated by ion-plasma and ion-neutral interactions as evidenced by the immediate drop in the mean ion energies. In this initial stage, the energy spread exhibits a gradual rise, since most ions are still far from reaching the energy boundaries imposed by the effective nest depth and the bottom of the ion potential wells and may lose large fractions of their kinetic energy in ion-neutral collisions.

The second stage is entered once enough COM energy has been dissipated for a sizable and gradually increasing fraction of the ions to pile up at energies just above $q\phi_{\text{nest,eff}}$. The pile up occurs since the electron cooling power ceases as the relative ion-electron velocities approach zero, and further energy loss can only be induced by slower energy-dissipation mechanisms such as ion-neutral or (not modelled) ion-ion collisions. It is the second stage that yielded the desirable reduction in ion energy spread.

The third and final stage is entered when almost all ions have been cooled to an energy $\lesssim q\phi_{\text{nest,eff}}$ (not reached in the Rb^+ measurement). At that point, the plasma-induced energy-spread reduction ends and the slower energy exchange mechanisms take over. The latter successively transport ions into the ion potential wells, causing σ_E to turn over and saturate at a slightly higher level.

The duration of the different stages are expected to depend on the rate of underlying energy-loss mechanisms, which in the case of Na^+ and K^+ was given by the plasma-induced energy exchange frequency $\nu_{E,\parallel}$. This qualitative expectation is experimentally confirmed by the increasingly stretched-out time evolutions of μ_E and σ_E for higher-mass ions.

Based on the mentioned considerations, we find that both the ion injection energy and the effective nest depth critically affect the dynamics of the cooling process and the achievable cooling timescales. As the substantial initial increase in ion energy spread is almost entirely due to ion-neutral interactions, this effect can be regarded as an artifact arising from the comparatively poor vacuum conditions during the present measurements. Under ultra-high vacuum conditions suitable for storage of HCI ($p < 1 \times 10^{-10}$ mbar), this effect would be strongly suppressed due to the smaller ion-neutral scattering rates and the energy spread reduction should set in immediately. The electron cooling limit set by the effective electron nest depth would, however, become even more important than in the present measurements as the collisional ion transport into the two wells of the nested potential would evolve considerably slower.

Identifying the mechanism driving the plasma-induced energy loss With the aid of the cooling model, we are now able to judge whether electron cooling indeed forms the dominant source of the ion stopping power exerted by the plasma. The cooling model's capability to reasonably reproduce the trends in the mean and the standard deviation of the ion energies suggests that the plasma-enhanced ion loss at early interaction times did not significantly distort the energy distribution of ions inside the detectable trap volume. The fact that the cooling model reproduces the experimental cooling curves when using realistic electron plasma parameters as model inputs therefore provides decent evidence that the observed energy-loss enhancement in plasma-on cycles was due to electron cooling.

The only other plausible mechanism that could potentially produce similar energy-loss characteristics are collisions of the ions of interest with impurity ions in the non-neutral plasma. As the implemented ion-electron collision formalism remains valid irrespective of the type of the charged background particles, we hypothetically investigated the observable features to be expected from background ions by replacing m_e, n_e and $v_{\mathrm{e,th}}$ in Eqn. 6.20 with the mass, number density and thermal velocity of potential impurity ions, respectively. Assuming protons as the background particles, the experimental mean ion energy evolution could be coarsely reproduced when using proton densities of $n_p \sim 4 \times 10^8\,\mathrm{cm}^{-3}$. The accumulation of such large numbers of impurity ions (e.g. through dissociative electron attachment to residual gas molecules) seems generally unlikely in sight of the near-negligible background event rates observed on the MCP detector. Moreover, in contrast to the case of an electron background (see Fig. C.1 in appendix C), the cooling force induced by background ions exhibits a strong velocity dependence since the fast, injected ions are initially at velocities much higher than the thermal velocities of the background ions. This in turn alters the ion energy evolution and prevented us from simultaneously matching the experimental μ_E and σ_E curves in simulation with background ions. Based on these findings, it is very unlikely that impurity ions in the plasma played a dominant role in the observed cooling dynamics.

The reported measurements can thus be regarded as the first demonstration of electron cooling in CPET. For all studied ion species, we observed cooling of the COM motion. By comparison to the simple cooling model, the underlying energy exchange times $\tau_E = \nu_{E,\parallel}^{-1}$ (which are for SCI approximately independent of the ion velocity in this regime, see Fig. C.1 in the appendix) are extracted as $\approx 300\,\mathrm{ms}$, $\approx 400\,\mathrm{ms}$ and $\approx 1000\,\mathrm{ms}$ for Na^+, Rb^+ and K^+, respectively. Considering the approximate scaling $\tau_E \propto m$, these results are consistent with an earlier experimental result [565] of $\tau_E \approx 10\,\mathrm{ms}$ obtained for cooling of antiprotons in a positron plasma with parameters comparable to those assumed in the present simulations. Although the trap potentials were not optimized for this purpose, we found a slight reduction in energy spread for $^{23}Na^+$ and $^{39,41}K^+$. However, in the present measurements, the energy spread compression was limited by the effective electron nest depth and collisions with residual gas particles. Further, optimization of the trap potential and plasma parameters could have likely still increased the obtained cooling rates. Adapting the trap potentials in order to achieve lower effective electron nest depths would have allowed to electron-cool injected ions to lower COM energies and smaller energy spreads.

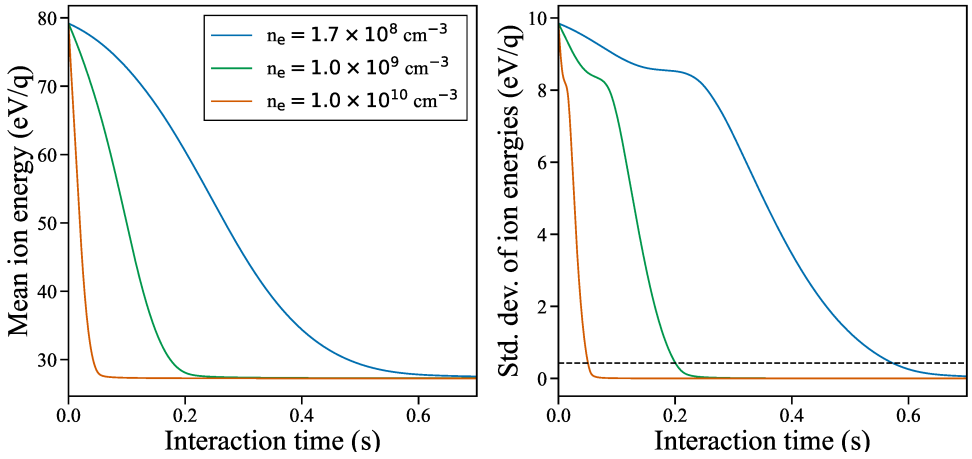

Figure 6.48. Evolution of the mean energy and standard deviation of $^{74}Rb^{37+}$ ions as predicted by the one-dimensional cooling model. The cooling of the COM motion ceases once ions approach $E_{\parallel} = q\phi_{\text{nest,eff}} = 27.25\,\text{V}$. The dashed line indicates an ion energy spread of $\Delta E_{\parallel}(\text{FWHM}) = 2\sqrt{2\ln(2)}\sigma_{E,\parallel} = 1\,\text{eV/q}$.

Expected cooling performance for HCI

Based on the gathered evidence that the relevant physics are reasonably well described, we can use the experimentally-adjusted cooling model from the previous subsection to evaluate the expected energy evolution for HCI under comparable conditions. In comparison to the estimates based on Spitzer's temperature equilibration time (see section 6.2), the present cooling model has the decisive advantage to realistically account for the ions' initial energy distribution including their non-zero COM velocity.

We adapt the calibrated plasma parameters from table 6.1 and use fully-stripped $^{74}Rb^{37+}$ ions as an example. As we are primarily interested in the timescale of the cooling process, we presume vacuum conditions suitable for storage of HCI ($p < 1 \times 10^{-10}$ mbar) and neglect ion-neutral collisions (by setting $p = 0$ in the simulation). Tracking the energies of 100 ions resulted in the mean energy and energy spread evolutions exhibited in Fig. 6.48. As expected, the cooling of fully-stripped ^{74}Rb ions proceeds substantially faster than that of the studied SCI and the initial longitudinal energy spread of $\Delta E_{\parallel}(\text{FWHM}) \approx 23.5\,\text{eV/q}$ is reduced to $\approx 1\,\text{eV/q}$ within roughly $570\,\text{ms}$. Despite the notable improvement over the observed cooling times with SCI, cooling on such timescales is clearly not compatible with the $65\,\text{ms}$-short half-life of ^{74}Rb, as only $\sim 1 \times 10^{-4}$ of the injected Rb ions would survive the cooling process.

To estimate which plasma parameters would be required for cooling of short-lived HCI, Fig. 6.48 also shows the simulated energy evolution of $^{74}Rb^{37+}$ ions for electron number densities of $n_e = 1 \times 10^9\,\text{cm}^{-3}$ and $n_e = 1 \times 10^{10}\,\text{cm}^{-3}$, respectively. In these cases, the ions are cooled to the $1\,\text{eV/q}$ level in $200\,\text{ms}$ and $50\,\text{ms}$, respectively. The respective ion survival fractions with regard to radioactive decay are 4.6% and 46.3%.

Evidently, electron number densities approaching $1 \times 10^{10}\,\text{cm}^{-3}$ would be required to

realize cooling of short-lived HCI under higher vacuum, but otherwise comparable conditions to the present measurements. This estimate is two orders of magnitude higher than the electron number density suggested by the two-component plasma model from section 6.2. This discrepancy stresses the importance to account for the ion's initial COM motion relative to the plasma, which causes the rapid reduction of the ion energy spread to set in with a delay (see right plot in Fig. 6.48). To achieve plasma densities of $n_e \sim 1 \times 10^{10}\,\mathrm{cm}^{-3}$ is an experimental challenge but, in principle, not unrealistic, as electron number densities of more than $1 \times 10^{10}\,\mathrm{cm}^{-3}$ have been demonstrated in other Penning-Malmberg traps, both with [577, 578] and in one case without [578] the use of rotating electric fields for radial plasma compression. In any case, a number of technical and procedural improvements would have to be implemented to attempt the realization of such cooling conditions in CPET, as will be detailed in the concluding remarks in the following subsection.

6.5 Conclusion

The technical developments and the experimental studies presented in this chapter resulted in the first demonstration of electron cooling of trapped ions in TITAN's cooler Penning trap (CPET).

Working up to this milestone, a number of unforeseen technical challenges had to be overcome. In analogy to technical difficulties encountered in the retardation spectrometers of the Karlsruhe Tritium Neutrino experiment (KATRIN) [579] and the Weak Interaction Trap for Charged Particles (WITCH) [580], the primary obstacles were posed by Penning discharges and stray-electron-induced detector background. These effects were suppressed by a number of hardware modifications and procedural adaptations. Special care had to be taken to avoid the accumulation of beam or plasma electrons in unwanted regions of the trap assembly. To this end, the experimental cycle was re-designed to include additional stages for excess-electron dissipation and plasma temperature relaxation. These developments enabled us to generate electron plasmas with reproducible electron numbers of typically $N_e \sim 4 \times 10^7$ and to combine them with element-separated, singly charged ions within a nested trap potential. To facilitate electron-ion interaction studies, experimental procedures were developed to achieve well-controlled initial ion conditions and to probe the ions' kinetic energies upon extraction from the cooler trap.

The reported electron cooling studies confirmed a plasma-induced energy loss for all studied ion species, namely non-radioactive isotopes of Na^+, K^+ and Rb^+. Due to the comparatively high residual gas pressure at the time of the measurements ($p > 2 \times 10^{-9}$ mbar), the interpretation of the cooling data was complicated by background energy-loss processes due to ion-neutral interactions.

A simplified, one-dimensional model of the cooling dynamics was developed and allowed to disentangle the plasma-induced cooling power from that due to ion-neutral interactions. The mass scaling of the measured energy loss rates and the overall close agreement with the model predictions verified electron cooling as the dominant energy-loss mech-

anism. The model further allowed to deduce estimates of experimentally-unconstrained plasma properties such as the electron number density ($n_e \sim 2 \times 10^8$) and the plasma dimensions. These quantities were previously inaccessible as our means to diagnose the trapped plasmas were strongly limited by the strong magnetic expansion of electron orbits upon extraction from the trap, combined with the need to leave both ends of the cooler trap unobscured for electron and ion transport. To obtain an alternative diagnostic tool, efforts were underway to pick-up image currents induced in trap electrodes by plasma oscillations [548, 575]. The deduced cooling time scales and plasma properties are consistent with an earlier experimental study on positron cooling of antiprotons [565].

The electron cooling measurements revealed a plasma-induced enhancement of the apparent ion loss rate. This enhancement evidenced as a linear decline of the detected ion number that was only observed over the first few $100\,\mathrm{ms}$ of the cooling process and the rate of decline was found to scale inversely with the square of the ions' mass. The underlying mechanism of the ion-loss enhancement and the related scalings remains unclear. It appears likely that the apparent ion losses were due to a plasma-induced enhancement of the radial ion transport that drove ions onto orbits that cannot be projected onto the MCP detector outside the superconducting magnet. The observed loss rates are orders of magnitude larger than the rates predicted for radial diffusion due to collisional drag exerted by the plasma electrons [559, 570]. However, the timescale of the ion-loss enhancement in our measurements agrees with radial ion transport rates observed in experimental studies of centrifugal separation [558, 572]. In one of these studies [572], a damped diocotron motion was suggested as the driver for the enhanced centrifugal particle separation rates. Theoretical work [570] has also pointed towards such connections between radial particle diffusion and collective plasma motions. However, to the author's knowledge, a detailed theoretical account of the mechanisms underlying the enhanced radial transport remains elusive. Clearly, further experimental and theoretical work in this direction is desirable to obtain a more comprehensive understanding of the dynamics of non-neutral plasmas composed of oppositely-charged species.

A more complete cooling simulation that also models the radial particle dynamics in CPET would be helpful to clarify whether the observed plasma-enhanced ion loss at short interaction times is indeed a result of radial ion transport. However, such simulations pose a numerical challenge that exceeds the scope of the present work. Specialized plasma codes that use the guiding-centre approximation [581] to average over the fast cyclotron motion could make a more detailed analysis of the ions' motion during the cooling process computationally tractable. A noteworthy example is the ASCOT code [582] which models the slowing down of ions in a magnetized plasma by using a guiding-centre version of the Fokker-Planck equation.

As the presented proof-of-concept measurements, were primarily intended to demonstrate electron cooling of the COM motion of ion samples in CPET, the experimental parameters were clearly not optimized for maximal cooling efficiency in regard to the ion's energy spread. Nonetheless, we used the experimentally-calibrated cooling model to tentatively assess the cooling times expected for HCI subjected to comparable electron plasmas. Using the

case of fully-stripped ^{74}Rb ions as an example, we found that the increased ion charge substantially speeds up the energy loss as compared to the presented measurements with singly charged ions. However, our model extrapolations indicate that, in order to limit decay losses to a tolerable level ($< 50\%$), electron cooling of radioactive HCI with half-lives $\leq 100\,\mathrm{ms}$ would require electron plasmas with number densities approaching $n_e \sim 1 \times 10^{10}\,\mathrm{cm}^{-3}$. Plasmas of such particle densities have been experimentally produced [577, 578] but their generation typically requires advanced plasma manipulation techniques such as a rotating wall plasma compression [556, 577, 583].

Although the present work provides important indications, a number of questions remain concerning the feasibility and practicality of in-trap electron cooling of stable and radioactive HCI. For antiprotons, electron cooling down to energies below $100\,\mathrm{meV}$ has been demonstrated in a cryogenic Penning trap [584]. Despite groundbreaking work [565, 585] within the antihydrogen community, the limits of electron (or positron) cooling of oppositely-charged ions are generally less well established. A particular challenge in electron cooling of positively-charged ions in a nested Penning trap lies in the fact that the different particle species will eventually become spatially separated, causing the cooling power to fade. The absence of a damping force that continuously drives ions towards the bottom of a potential well, as exploited in buffer gas cooling, complicates the formation of temporally compressed ion bunches upon ion extraction. It remains to be shown to which degree the ion energy reduction achieved inside the cooler trap can be translated into reproducible ion bunch properties suitable for re-capture in a downstream precision ion trap. Moreover, the potentially detrimental effect of centrifugal separation, while theoretically predicted also in these systems [565], has, to the author's knowledge, not been experimentally verified in plasmas composed of oppositely-charged species. If non-fully stripped ions are to be targeted, it would be advisable to assess the extent of potential ion loss due to dielectronic recombination more comprehensively than has been done to date [65], either in experimental studies or through atomic structure calculations. In the realm of rare isotope science, the most pressing questions to be addressed experimentally pertain to the realistically achievable cooling times and the extent of ion losses in the cooling process.

Building on the present work, some of these aspects could be explored in further studies of in-trap electron cooling. In light of the reported results, cooling studies with radioactive HCI would have demanded several technical improvements to the CPET setup. To prevent charge exchange reactions, the pressure in the trap chamber would have to be reduced by at least 1–2 orders of magnitude to a level below $1 \times 10^{-10}\,\mathrm{mbar}$. This could have been realized by baking the trap vacuum chamber to activate its non-evaporable getter coating. The in-situ low-temperature bake out performed within this thesis, however, suggests that reaching the necessary activation temperature without quenching the superconducting magnet would have been more challenging than anticipated from earlier tests in a mock setup [508]. The highest electron densities demonstrated in CPET were on the order of $\sim 8 \times 10^{8}\,\mathrm{cm}^{-3}$ [508]. Realizing the electron densities necessary for efficient cooling of short-lived HCI ($n_e \sim 1 \times 10^{-10}\,\mathrm{cm}^{-3}$, see previous subsection) would hence have required an active plasma compression by application of rotating wall fields and an increase

in the trapped electron numbers back to $N_e > 1 \times 10^8$. While the accumulation and manipulation of such electron numbers would potentially have required additional precautions to prevent Penning discharges, the improved vacuum conditions would have likely alleviated this issue (see e.g. [580]). In order to achieve cooling cycles that match the typical repetition rates for mass measurements in MPET, a single electron plasma would have had to be re-used over many successive cooling cycles to reduce the impact of wait periods for plasma generation ($\sim$ 200 ms), cyclotron pre-cooling ($\sim$ 400 ms) and rotating wall compression ($\sim$ 1–5 s [578]). In sight of these technical complications, it was decided to re-direct efforts towards cooling of radioactive HCI at TITAN to evaporative cooling within the EBIT.

The reported measurements, as well as the presented solutions to the experimental challenges encountered in the approach to them, may also provide valuable information for work towards in-trap electron cooling of non-radioactive HCI at other facilities and for experiments on non-neutral plasmas with oppositely-charged species. In particular, our results emphasize the critical impact of the ions' initial COM motion and the space-charge-induced flattening of the nested potential well on the cooling dynamics. They further indicate that the radial particle dynamics in the cooling process likely deserve additional theoretical and experimental attention, as unexpectedly fast radially-outward transport of ions could result in a premature loss of cooling power.

Chapter 7

Conclusion and outlook

The increasing amount of nuclear data becoming available from rare isotope beam facilities around the world each year provide us with important clues to answer some of the most pressing questions in modern physics. At the same time, theoretical astrophysicists are empowered by a rising availability of high-power computing resources and astronomers are leveraging a new generation of space-based observatories to acquire astronomical data of unparalleled resolution. These fruitful conditions let researchers strive to unravel some of the deepest mysteries of the known universe such as the origin of the solar element abundances or the interior structure of neutron stars. In these efforts, collaboration between fields such as astronomy, astrophysics, atomic and nuclear physics becomes increasingly important to make scientific headway. Many intriguing questions that will likely only find answers by such interdisciplinary collaboration evolve around the physics of neutron stars.

A promising way to narrow in on the parameters of accreting neutron stars in binary systems are studies of type I X-ray bursts. Since their first observation almost five decades ago [102, 120], impressive progress has been made both in terms of the astronomical observation as well as the theoretical description of these highly luminous thermonuclear explosions [39, 108]. Nuclear astrophysicists have developed a comprehensive picture of the nuclear reaction sequences that power X-ray bursts [48, 91, 109] and identified the central role played by the rapid proton capture process (*rp*-process) in shaping the burst light curve [111]. The theoretical progress enabled large-scale sensitivity studies [50, 51] that identified the most critical nuclear model inputs, thus providing guidance and motivation for targeted measurement campaigns at rare isotope beam facilities. Experimental nuclear physicists have gladly accepted the challenge to eliminate nuclear input uncertainties from X-ray burst models. While almost all relevant β-decay half-lives and most of the relevant masses have been measured, a number of crucial mass inputs and a vast set of proton capture rates remain ill-constrained by experiment [32]. Addressing these nuclear uncertainties remains a key objective on the quest to use X-ray bursts as probes of their underlying neutron star [43, 45].

The precision mass measurements of $^{60-63}$Ga [425] discussed in the first part of this thesis constrain the *rp*-process flow near the ^{60}Zn waiting point and mark a small, yet important step in this direction. Assessing the impact of the new mass data in a one-zone X-ray burst

model allowed us to exclude a hypothesized [155] secondary bypass of the ^{60}Zn waiting point through sequential two-proton capture on ^{59}Zn. We further found that the three times smaller mass uncertainty of ^{61}Ga reduces the respective uncertainty on the burst light curve by more than a factor of 2. A small mass-induced uncertainty remains on the light curve, indicating a potential need to re-measure the mass of ^{61}Ga to even higher precision in the future. However, the most critical mass uncertainty near ^{60}Zn is now given by the unmeasured mass of ^{62}Ge which limits accurate calculations of the ^{61}Ga(p,γ) rate. A precision mass measurement of ^{62}Ge is therefore urgently needed and would allow to re-assess the possible need for an even more precise ^{61}Ga mass measurement. An iterative approach of measurements followed by updated sensitivity analyses to guide further experimental efforts will provide an effective roadmap to eliminate nuclear input uncertainties from X-ray burst models.

Much of the scientific progress achieved within precision mass spectrometry over the last three decades has been owed to novel measurement schemes and technical innovations. This statement is exemplified by the presented ^{60}Ga mass measurement, which was only enabled by the drastic background suppression provided by the mass-selective retrapping technique [357]. A different technique that is unique to TITAN is its capability to charge breed radioactive ions in an electron beam ion trap (EBIT) prior to the mass measurement [58]. While this technique has led to substantial increases in mass precision and resolving power [61, 63], the full potential of mass spectrometry with highly charged ions (HCI) can currently not be accessed at TITAN as the charge breeding process increases the ion energy spread.

A potential way to counteract the charge-breeding-induced increase in ion energy spread is electron cooling in a cooler Penning trap [65]. As the second main topic of this thesis, the prospects of this technique were explored through tests of electron cooling of stable, singly charged ions in TITAN's cooler Penning trap (CPET) [55]. The injection and trapping of ions from a surface ion source and the generation of electron plasmas in nested trap potentials was commissioned. Further technical developments enabled the first co-storage of ions and electrons in CPET. Electron cooling studies were, however, initially prevented by Penning discharges and electron-induced detector background. These issues were addressed through a series of hardware modifications for improved HV breakdown strength as well as operational changes, such as the development of special procedures to remove stray electrons from the nested trap potential. These adaptations enabled the successful demonstration of in-trap electron cooling of different singly charged alkali ion species. A specialized ion extraction scheme for retarding field energy analysis facilitated quantitative studies of the ion energy evolution inside the cooler trap. The interpretation of the experimental ion energy data was aided by the development of a simplified cooling model that yielded a detailed understanding of the cooling dynamics. Isolating the electron cooling power from ion energy loss due to ion-neutral collisions, we found characteristic ion-electron energy exchange times of ≈ 300 ms, ≈ 400 ms and ≈ 1000 ms for ^{23}Na$^+$, ^{39,41}K$^+$ & ^{85,87}Rb$^+$, respectively. In cycles with a co-trapped electron plasma, the ion count rate on the detector showed a fast, linear drop over the first few 100 ms. While the cause of this behaviour remains unclear, the

most probable explanation is a plasma-induced enhancement of the radial particle transport that prevented an increasing fraction of the trapped ions from reaching the detector. Simulations with a full three-dimensional treatment of the ion trajectories during the cooling process could help to elucidate this hypothesis but are beyond the scope of this thesis. If the observed ion losses are confirmed to be due to plasma-enhanced radial transport, trapping configurations similar to the ones presented here could yield valuable information on radial transport in multi-component, non-neutral plasmas.

Extrapolating the cooling results obtained with SCI to HCI, we find that cooling of charge-bred radioactive ions with half-lives below $100\,\mathrm{ms}$ would tentatively require plasmas with electron number densities of $n_e \sim 1 \times 10^{10}\,\mathrm{cm}^{-3}$ to limit radioactive decay losses of the ions to $\leq 50\%$. While such electron densities have been realized in other Penning-Malmberg traps [577, 578], their creation is a technical challenge and would likely add several second long wait times for plasma generation, rotating wall plasma compression and cyclotron cooling to the cooling cycle. The technical complexity and the additional wait times introduced by such plasma preparation stages are not necessarily compatible with on-line mass measurements of short-lived HCI, which are typically performed at repetition rates of $\geq 1\,\mathrm{Hz}$. Although re-using a plasma over many successive cooling cycles with interleaved plasma re-generation and compression could potentially mitigate the impact of such wait times, the realization of electron cooling of short-lived radioisotopes certainly remains a considerable technical challenge. After a cost-benefit analysis, it was decided to direct the present resources available at TITAN towards evaporative cooling by injection of light, inert gases into the EBIT. If this technically less complicated and more resource-efficient approach for cooling HCI does not yield satisfactory results, the option of in-trap electron cooling could be further explored by building on the findings from the present study. The reported electron cooling studies may also provide valuable information for similar efforts towards in-trap electron cooling of stable HCI at other facilities. Our results stress the critical roles played by the ions' initial COM oscillation in the trap potential and the radial particle dynamics during the cooling process. Especially the latter aspect might need additional attention as unexpectedly fast radial ion transport could potentially result in a spatial separation of ions and electrons, and thus a premature loss of cooling power.

As a new generation of rare isotope beam facilities such as ARIEL at TRIUMF, FAIR at GSI and FRIB at Michigan State University is presently approaching day-one experiments, we are entering a new era of rare-isotope science. Coupled to innovative new measurement techniques as those highlighted in this thesis, these upcoming facilities will provide ample opportunity to expand our understanding of the structure of neutron stars and will help to address many other open questions within nuclear physics and nuclear astrophysics.

Appendix A

Development of a Python package for fitting time-of-flight mass data

This appendix gives an overview of the development of EMGFIT [426], a Python package for fitting and analysis of TOF mass data. The package was developed for the analysis of the mass data presented in this thesis and has since been used in multiple other TITAN publications [586–588]. EMGFIT wraps and heavily relies on the curve fitting package LMFIT [569]. The following, non-exhaustive description highlights key features of EMGFIT, presents selected results from accuracy tests and gives some relevant numerical implementation details. Further, potential uncertainty contributions that were evaluated but found to be negligible in the case of the presented gallium mass data are presented.

A.1 Comparison of a Gaussian and a hyper-EMG fit

The advantages of the hyper-EMG lineshape over a regular Gaussian in the case of tailed or asymmetric TOF peaks are illustrated in Fig. A.1. The exhibited mass data was taken from a $^{85}Rb^{+}$ test measurement with ≈ 1.4 million measured events. The automatic tail order determination routine described in section 5.2 identified a hyper-EMG(3,3)[1] distribution (i.e. a Gaussian with three negatively- and three positively-skewed exponential tails) as the most suited lineshape for the given data. For comparison, an MLE fit was performed both using a regular Gaussian and a hyper-EMG(3,3) distribution. Clearly, the Gaussian fails to properly describe the extended tails of the peak. As a result, in the case of the Gaussian fit, one is forced to narrow the fit range down to ≈ 1 FWHM in order to at least coarsely reproduce the data and to obtain reasonable parameter uncertainty estimates. For well-separated and fairly symmetric peaks, such fitting may yield an acceptable determination of the peak's centroid position relative to that of a reference peak. However, if one aims to deduce realistic estimates of the area of asymmetric or heavily-tailed peaks the Gaussian line shape is clearly inadequate. The same is true if one aims to obtain accurate peak area or centroid estimates in scenarios with unresolved, overlapping peaks. Considering instead the hyper-EMG(3,3) fit,

[1] The first and second number in brackets denote the number of negatively- and positively-skewed exponential tails in the distribution, respectively.

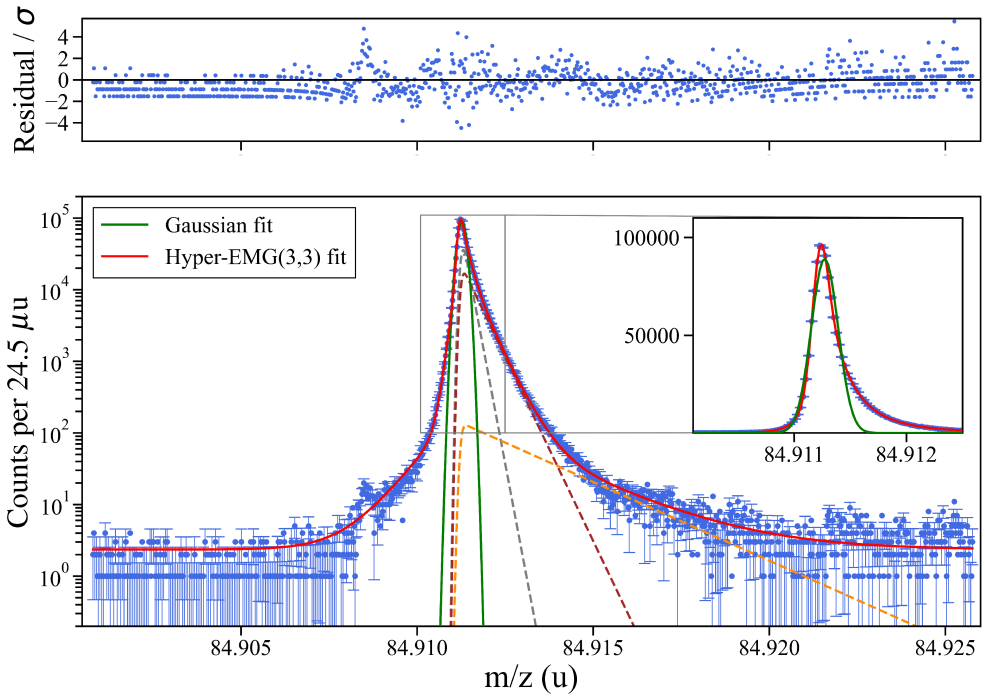

Figure A.1. Fits of a $^{85}Rb^{+}$ mass peak with ≈ 1.4 million events using a Gaussian (green) and a hyper-EMG lineshape with 3 positively- and negatively-skewed exponential tails (red). The positively-skewed EMG components underlying the hyper-EMG mixture model are indicated by dashed lines.

we find that the TOF data is well-matched down to the baseline, allowing one to make use of all measured events and to obtain realistic peak area estimates. The true power of hyper-EMG distributions, however, unfolds in situations with poorly resolved, overlapping peaks, as for example demonstrated in Ref. [350]. A more detailed and quantitative comparison between Gaussian and hyper-EMG lines shapes can be found in Ref. [427].

A.2 A robust numerical implementation of hyper-EMG distributions

The implementation of hyper-EMG distributions is a numerical challenge since some of the underlying functions are prone to over- or underflow. In order to discuss the path taken by EMGFIT to prevent numerical accuracy loss, let us recall the definition of a hyper-EMG lineshape [427] given in section 5.2. The lineshape of a multi-peak fit is defined by a uniform background of amplitude c_{bkg} and a sum over N_{peaks} single-peak lineshapes:

$$f(x) \doteq \sum_{i=1}^{N_{\text{peaks}}} a_i \cdot h_{\text{emg}}(x; \mu_i, \sigma, \eta_-, \tau_-, \eta_+, \tau_+) + c_{\text{bkg}}, \tag{A.1}$$

where a_i is the amplitude of the i-th peak and the hyper-EMG distribution is defined as

$$h_{\text{emg}}(x;\mu,\sigma,\Theta,\eta_-,\tau_-,\eta_+,\tau_+)\doteq\Theta h_{-\text{emg}}(x;\mu,\sigma,\eta_-,\tau_-)+(1-\Theta)h_{+\text{emg}}(x;\mu,\sigma,\eta_+,\tau_+), \tag{A.2}$$

with $h_{-\text{emg}}$ and $h_{+\text{emg}}$ denoting the negatively-skewed and positively-skewed hyper-EMG distributions, respectively, whose relative contributions are determined by the mixing weight $\Theta\in[0,1]$. The negatively- and positively-skewed hyper-EMG distributions are defined as

$$\begin{aligned}
h_{-\text{emg}}(x;\mu,\sigma,\eta_-,\tau_-)&\doteq\sum_{i=1}^{N_-}\frac{\eta_{-i}}{2\tau_{-i}}\exp\left(\left(\frac{\sigma}{\sqrt{2}\tau_{-i}}\right)^2+\frac{x-\mu}{\tau_{-i}}\right)\text{erfc}\left(\frac{\sigma}{\sqrt{2}\tau_{-i}}+\frac{x-\mu}{\sqrt{2}\sigma}\right),\\
h_{+\text{emg}}(x;\mu,\sigma,\eta_+,\tau_+)&\doteq\sum_{i=1}^{N_+}\frac{\eta_{+i}}{2\tau_{+i}}\exp\left(\left(\frac{\sigma}{\sqrt{2}\tau_{+i}}\right)^2-\frac{x-\mu}{\tau_{+i}}\right)\text{erfc}\left(\frac{\sigma}{\sqrt{2}\tau_{+i}}-\frac{x-\mu}{\sqrt{2}\sigma}\right),
\end{aligned} \tag{A.3}$$

where μ and σ are the standard deviation of the underlying Gaussian, respectively, $N_\pm$ denote the respective numbers of positively-skewed and negatively-skewed exponential tails, $\eta_\pm\doteq\{\eta_{\pm1},\eta_{\pm2},...,\eta_{\pm N_\pm}\}$ and $\tau_\pm\doteq\{\tau_{\pm1},\tau_{\pm2},...,\tau_{\pm N_\pm}\}$ are the sets of tail weights and exponential decay constants, respectively. Exploiting the definition of the complementary error function, $\text{erfcx}(z)\doteq\exp(z^2)\text{erfc}(z)$, $h_{-\text{emg}}$ and $h_{+\text{emg}}$ can each be expressed by two equivalent relations [589]:

$$h_{\text{emg},\pm\text{i}}=\frac{\eta_{\pm i}}{2\tau_{\pm i}}\exp(u_\pm)\text{erfc}(v_\pm), \tag{A.4}$$

$$=\frac{\eta_{\pm i}}{2\tau_{\pm i}}\exp\left(-\left(\frac{x-\mu}{\sqrt{2}\sigma}\right)^2\right)\text{erfcx}(v_\pm), \tag{A.5}$$

$$\tag{A.6}$$

where the arguments $u_\pm$ and $v_\pm$ are given by

$$u_\pm=\left(\frac{\sigma}{\sqrt{2}\tau_{\pm i}}\right)^2\mp\frac{x-\mu}{\tau_{\pm i}}, \tag{A.7}$$

$$v_\pm=\frac{\sigma}{\sqrt{2}\tau_{\pm i}}\mp\frac{x-\mu}{\sqrt{2}\sigma}. \tag{A.8}$$

The challenge in implementing hyper-EMG distribution functions numerically lies in the fact that, in double floating point precision[2], $\exp(u_\pm)$ overflows for large arguments, $u_\pm\gtrapprox 709.78$, $\text{erfc}(v_\pm)$ underflows for large positive arguments, $v_\pm\gtrapprox 26.54$, and erfcx overflows for large negative arguments, $v_\pm\lessapprox -26.54$. As a result, Eqn. A.4 and A.5, taken on their own, will at some point suffer from loss of numerical accuracy as one moves to large positive or negative arguments. In principle, this issues can be prevented by resorting to arbitrary-precision implementations of the mentioned functions (e.g. from the MPMATH Python package) but this comes at the price of a drastic increase in computation time.

[2]The stated limits for over- and underflow pertain to Python implementations of the exponential and the error functions from [590] and [591], respectively.

Fortunately, by careful consideration of the argument ranges where exp, erfc and erfcx are numerically well-defined, one finds that all mentioned over- and underflow issues in the computation of $h_{\mathrm{emg},-\mathrm{i}}$ and $h_{\mathrm{emg},+\mathrm{i}}$ can be circumvented by dynamically switching between the equivalent expressions, such that the formulation in terms of erfc (Eqn. A.4 is used for the computation whenever $v_\pm < 0$ and the formulation in terms of erfcx (Eqn. A.5) is used whenever $v_\pm \geq 0$. It should be noted that there is a certain range of values that could be selected as the threshold to switch between the different expressions, but $v_\pm = 0$ appears as the most natural choice. This is the approach adopted in EMGFIT to prevent numerical accuracy loss in calculations of $h_{\mathrm{emg},+\mathrm{i}}$ and $h_{\mathrm{emg},-\mathrm{i}}$. Essentially the same approach has been adopted in Ref. [589].

A.3 Comparison of different cost functions

In order to fit a model function to count data, one typically defines a suitable cost function and optimizes the model parameters such that the cost function becomes minimal with respect to all varied parameters. The choice of an appropriate cost function needs to include consideration of the stochastic nature of the type of data at hand. The most widely used approach to fit a model function $f(x;p)$ with a set of parameters p to a set of count data, (x_i,y_i), is likely the method of least squares[3]. In this approach to statistical inference, the best-fit model parameters $\hat{p}$ are usually determined by minimizing the *chi-squared statistic*,

$$\chi^2 = \sum_{i=1}^{N} \frac{(f(x_i) - y_i)^2}{\sigma_i^2}, \tag{A.9}$$

where σ_i^2 is the variance of the i-th datum and N is the number of fitted data. As one usually does not have knowledge of the true variance of each datum, σ_i has to be estimated directly or indirectly from the data. Assuming the data to be created by a Poisson process, one oftentimes takes $\sigma_i = \sqrt{y_i + 1}$, which avoids a divergence for $y_i = 0$ and leads to *Neyman's chi squared* statistic[4]

$$\chi_N^2 = \sum_{i=1}^{N} \frac{(f(x_i) - y_i)^2}{y_i + 1}. \tag{A.10}$$

Alternatively, one may use the model prediction at each iteration of the optimization to estimate σ_i, as is done in *Pearson's chi squared* statistic [432]

$$\chi_P^2 = \sum_{i=1}^{N} \frac{(f(x_i) - y_i)^2}{f(x_i)} \tag{A.11}$$

It has been known for a while that the aforementioned cost functions have shortfalls in cases of Poisson-distributed data with low statistics. For example, χ_N^2 has been shown to underestimate the true area of a peak, and χ_P^2 has been shown to overestimate the true peak

[3] Note all considerations and the expression given here presume that the data are uncorrelated.

[4] Alternatively, this statistics is also often defined using $\sigma_i^2 = (\min(\sqrt{y_i}, 1))^2$ as the denominator.

area [430, 432]. In order to address some of these shortfalls, further variants of χ^2 have been proposed in the literature, namely the *chi-squared gamma* statistic [430],

$$\chi^2_\gamma = \sum_{i=1}^{N} \frac{(f(x_i) - \min(y_i, 1) - y_i)^2}{y_i + 1}. \tag{A.12}$$

and the *modified chi-squared gamma* statistic [592]

$$\chi^2_{\gamma M} = \sum_{i=1}^{N} \left[(\chi^2_{\gamma,i} - \langle \chi^2_{\gamma i} \rangle) \sqrt{\frac{2}{\sigma_{\langle \chi^2_{\gamma i} \rangle}}} + 1 \right], \tag{A.13}$$

where $\chi^2_{\gamma,i} = [y_i + \min(y_i, 1) - f(x_i)]^2/(y_i + 1)$ and the corresponding mean, $\langle \chi^2_{\gamma i} \rangle$, and standard deviation, $\sigma_{\langle \chi^2_{\gamma i} \rangle}$, are explicitly given in Ref. [592].

A known shortcoming of the χ^2 statistic lies in the fact that the model parameters inferred with it become biased at low statistics. This is because the derivation of the chi-squared distribution presumes the data in each bin to be normally distributed, which, for Poisson-distributed data, is only a fair approximation for large y_i. A proper description of the Poisson nature of counting data, even in case of many low-statistics bins, can be obtained by performing a binned maximum likelihood estimation (MLE) with a Poisson likelihood as the cost function. Here, we consider the following (negative, doubled) log-likelihood ratio[5] [432, 433]

$$\mathcal{L} = 2 \sum_{i=1}^{N} \left[f(x_i) - y_i + y_i \ln \left(\frac{y_i}{f(x_i)} \right) \right]. \tag{A.14}$$

The so-defined Poisson log-likelihood ratio yields results identical to those from a regular Poisson log-likelihood but, according to Wick's theorem, has the convenient feature to asymptotically (i.e. for large N) approach the χ^2 statistic, thereby providing a convenient measure of the absolute goodness-of-fit [433] and enabling the deduction of confidence intervals as in a χ^2 fit [432].

An additional feature of the log-likelihood ratio is that all its summands $L_i = f(x_i) - y_i + y_i \ln \left(\frac{y_i}{f(x_i)} \right)$ are semipositive definite (i.e. non-negative). This property can be exploited to express Eqn. A.14 as a sum of squares,

$$\mathcal{L} = \sum_{i=1}^{N} \left(\sqrt{2L_i} \right)^2, \tag{A.15}$$

effectively converting the minimization of the scalar $\mathcal{L}$ into a least-squares problem. Hence, $\mathcal{L}$ can not only be minimized using scalar optimization methods (such as the Powell method) but also by use of algorithms optimized for least squares problems (e.g. Scipy's "least_squares" optimizer). Tests showed that the latter typically yield substantially faster computation times than scalar optimizers, which is relevant for some of the Monte Carlo methods implemented in EMGFIT. This aspect will be addressed in more detail in the subsequent section.

[5] A derivation of this quantity can be be found in Ref. [593].

The performance of the aforementioned cost functions in terms of the accuracy of the inferred peak centroids and peak areas was evaluated in a Monte Carlo study with synthetic TOF mass spectra. The spectra were taken to be background-free and to consist of a single hyper-EMG(2,1) peak. The events in the synthetic spectra were randomly generated by sampling from the reference distribution using a simple rejection sampling method. Various different total numbers of events, N_{ions}, were considered. For each predefined event number, 1000 spectra were created. Comparison to the true parameter values of the generating distribution provided a way to judge the accuracy of the parameter estimates obtained with the different cost functions. The generated spectra were fitted with a hyper-EMG distribution whose shape was fixed to that of the reference distribution used to sample events. All cost functions including the log-likelihood ratio were minimized using the "least_squares" optimizer of the SciPy library [591]. After each fit, the obtained peak centroids and areas were collected.

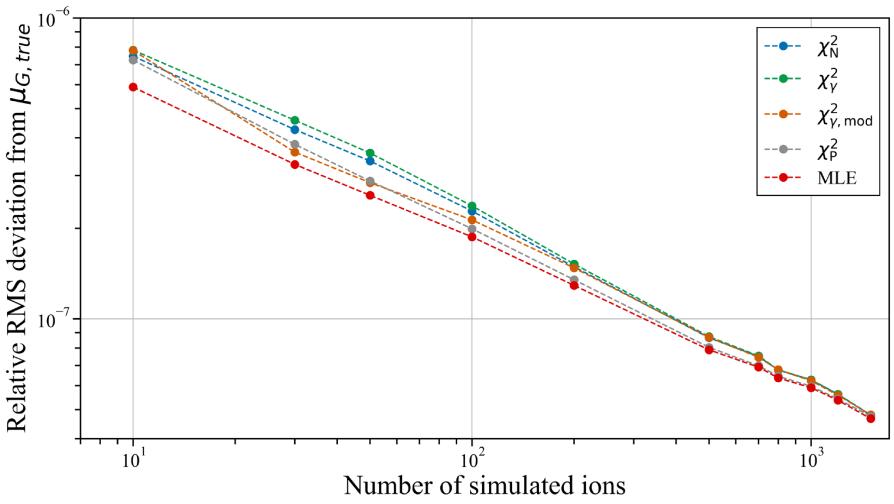

Figure A.2. Relative RMS deviation from the true peak centroid as function of the simulated number of events and for different cost functions. Each data point was derived from fits to 1000 synthetic mass spectra.

Fig. A.2 exhibits the RMS deviations of the obtained peak centroids from the true peak centroid as a function of the total number of simulated events. At high event numbers, all cost functions yield rather similar results, but towards low statistics the results diverge and, for $N_{\text{ions}} < 50$, the MLE with the Poisson log-likelihood ratio clearly outperforms the other cost functions. Towards higher event numbers, the χ^2_P cost function is seen to yield results that converge with the MLE predictions the fastest and, for $N_{\text{ions}} > 500$, both curves essentially overlap whereas the other cost functions still produce slightly higher RMS deviations.

As the second quantity of interest, the accuracy of the predicted peak areas was studied. To better illustrate the differing signs of the deviations between predicted and true peak area, the mean deviations from the true peak area were taken as the figure of merrit. The

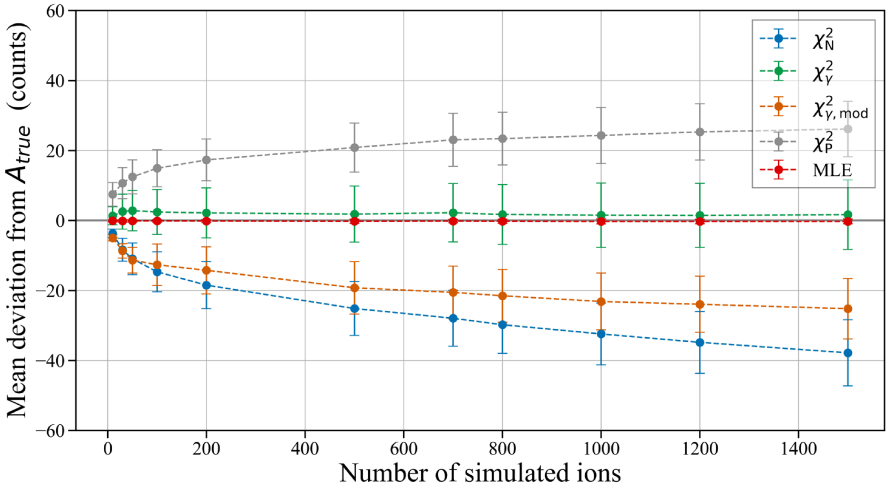

Figure A.3. Relative RMS deviation from the true peak area as function of the simulated number of events and for different cost functions.

mean deviations from the true peak area are shown as a function of N_{ions} in Fig. A.3. As is theoretically expected for the background-free case [432], the peak areas inferred with the MLE are seen to perfectly agree with the number of events in the spectrum. Only a slight systematic overestimation is seen for χ^2_γ predictions. While χ^2_P consistently overestimates the true peak area, $\chi^2_{\gamma,\mathrm{mod}}$ and χ^2_N are seen to consistently underestimate it.

Based on these results, the log-likelihood ratio and the χ^2_P statistics were selected as cost functions for EMGFIT. The choice to use χ^2_P over the other χ^2-type cost functions was based on its performance in terms of peak-centroid estimation, as that is clearly the most relevant parameter for mass measurement applications.

A.4 Accuracy validation of single-peak fits

After the full implementation of the log-likelihood ratio and the χ^2_P cost functions in EMGFIT, the accuracy of single-peak fits was validated using a similar Monte Carlo approach as in the preliminary tests described above. For more efficient event sampling, a hyper-EMG generalization[6] of the EMG random sampling method from [591] (SciPy's "exponnorm" method) was developed and validated through comparison between histograms of sampled events and their generating distribution. A hyper-EMG(2,2) distribution with a FWHM of 226.2 μu that had been obtained from fits to experimental mass data was used as the reference distribution. The sampled events were uniformly binned with a bin width of 31.6 μu.

To test whether the aforementioned re-formulation of the MLE with the log-likelihood ratio into a least-squares problem (see previous section) yields the same results as scalar optimization, Eqn. A.14 was minimized using both the scalar Powell optimizer (SciPy's

[6]See `https://robbenroll.github.io/emgfit/v0.4.1/modules.html?highlight=sample#module-emgfit.sample` for details.

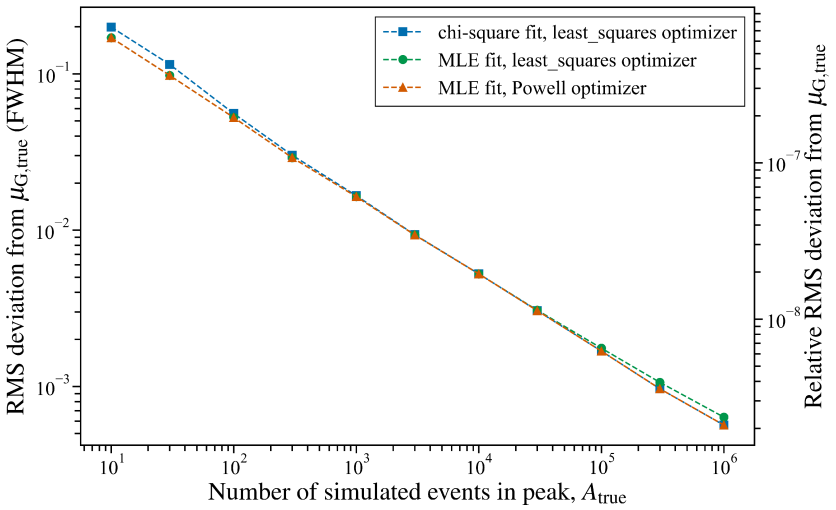

Figure A.4. Accuracy of the peak areas obtained from fits to synthetic single-peak mass spectra with different cost functions and optimizers (see legend). Each data point is based on 1000 fits to synthetic spectra.

"Powell" method) and a least-squares optimizer (SciPy's "least_squares" method). At various total event numbers, 1000 synthetic spectra were generated and fitted with different cost function and optimizer combinations. The resulting RMS deviations from the true peak centroid are displayed in Fig. A.4. At low statistics, the superior centroid accuracy of MLE fits is seen again. At event numbers up to 3×10^4, the scalar and least-squares minimization of the log-likelihood ratio yield essentially identical results. Only at higher event numbers, the minimization results are seen to diverge.

The same effect is even more obvious in the relative RMS deviations from the true peak area shown in Fig. A.5. The cause of this evolving discrepancy is unclear. However, most mass spectra of interest for TITAN exhibit measurement statistics where the scalar and the least-squares optimizer yield essentially identical results. In case of doubt, it is always advisable to perform a quick cross check if the results for the different optimizers agree. If so, one may take advantage of the improved performance of the least-squares optimization which is especially helpful when subsequently using the computationally-demanding, optional Monte Carlo methods for evaluation of the statistical and the peak-shape uncertainty. This approach was followed during the analysis of the gallium data presented in chapter 5. For all reported cases, both optimizers yielded essentially identical mass results ($\delta m/m \leq 5 \times 10^{-10}$).

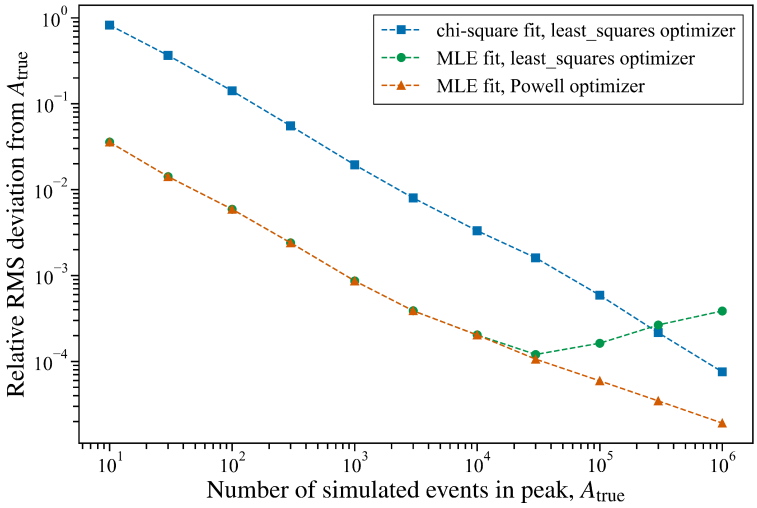

Figure A.5. Accuracy of the peak centroids obtained from fits to synthetic single-peak mass spectra with different cost functions and optimizers (see legend). Each data point is based on 1000 fits to synthetic spectra.

A.5 Monte-Carlo evaluation of the peak-shape uncertainty

A drawback of the peak-shape uncertainty evaluation by $\pm 1\sigma$-variation of the shape parameters (see section 5.2.6 for details) is that it neglects correlations between shape parameters. However, the latter are non-negligible in most practical cases. Consequentially, the estimates from the $\pm 1\sigma$-variation method may overestimate the true mass uncertainty resulting from the uncertainty of the shape parameters. Additionally, in the rare case of hyper-EMG distributions with three or more negatively- or positively-skewed tails, the variation of the respective tail weight factors $\eta_{\pm i}$ becomes ambiguous, as once one $\eta_{\pm i}$ is varied, the other two have to be re-adjusted (in a then ambiguous way) in order to preserve the normalization, $\sum_i \eta_{\pm i} = 1$. In order to overcome these limitation, within this thesis, a Monte-Carlo peak-shape uncertainty evaluation method was developed that can properly account for correlations in the shape calibration parameters. The following describes the main steps of the routine and how it was used in the analysis of the $^{60-63}$Ga mass data:

1. *Explore the parameter space of the peak-shape calibration with MCMC sampling:* The Markov-chain Monte Carlo (MCMC) sampling was performed with the affine invariant sampler implemented in the EMCEE Python package [435]. MCMC sampling has become a powerful tool for Bayesian analysis and related applications; for a general introduction to the topic the reader is referred to Ref. [594]. For each varying fit parameter, 20 MCMC walkers were sent out to explore the parameter space. The walkers were randomly initialized, assuming for each parameter a Gaussian distribution whose mean and standard deviation equalled the best-fit values obtained for the respective parameter in the peak-shape calibration.

2. *Discard burn-in period and thin Markov chains:* To ensure sampling results independent of the initialization, the first 500 MCMC steps were discarded ("burn-in"). The random samples in a MCMC chain are not independent but exhibit a degree of autocorrelation that decreases with the number of sampling steps between two samples in the chain. The autocorrelation time of a parameter provides a measure of the characteristic number of sampling steps after which two Markov samples for the parameter can be assumed to be independent. In order to ensure independent sampling results, the MCMC chain was "thinned" by discarding all but every n-th sample, where n was chosen to be similar to the parameter's autocorrelation times in the given Markov chain. As an example, MCMC samples after burn-in and thinning are displayed in the correlation map in Fig. A.6.

3. *Randomly draw 1000 shape parameter sets from the sampling results.*

4. *Re-perform the IOI fits for each of the 1000 selected peak shapes. Calculate new final mass values and peak areas.*

5. *Estimate the peak-shape uncertainty of the peak's mass and area as the RMS error of the resulting set of mass values and peak areas (see example histograms in Fig. A.7).*

In all studied cases, including both measured and simulated spectra, the Monte Carlo routine resulted in smaller peak-shape uncertainties as compared to those from the $\pm 1\sigma$-variation procedure. The latter can therefore be assumed to yield conservative upper limits on the peak-shape uncertainty; the Monte Carlo routine, in turn, yields more accurate uncertainty estimates at the price of a higher (but, with typical computation times of ≈ 1 h, manageable) computational expense. Confirming the general expectation for cases where both the mass calibrant and the IOI peaks are well resolved, the peak-shape uncertainties obtained for $^{60-63}$Ga with the Monte Carlo routine were all on a negligible level, $(\delta m/m)_{\mathrm{PS}} < 3 \times 10^{-8}$. However, in cases where IOI peaks reside in the tails of peaks with substantially higher intensity, the Monte Carlo peak-shape uncertainty has been found to become relevant.

A.6 Uncertainty due to the finite bin width

In fits to binned spectroscopic data with limited statistics, the finite bin size can induce systematic uncertainties in peak centroid determinations. The recorded TOF data comes inherently binned due to the finite time resolution of the time-to-digital converter (TDC). During the mass measurements presented in this thesis, the TDC bin width was set to 1.6 ns, which for the ^{61}Ga mass measurement corresponded to a mass bin width[7] of $\Delta m \approx 31.6$ µu. The peak fitting was performed with the original mass bins as calculated in the MAc software [423] based on the TDC time resolution of the raw data; no re-binning was performed.

[7] Due to the scaling $m \propto t^2$, a uniform binning in time results in mass bins of non-uniform width. However, for the isobaric mass spectra considered here, the differential non-linearity was only on the order of DNL $= \frac{\max(\Delta m) - \min(\Delta m)}{\max(\Delta m) + \min(\Delta m)} \approx 0.037\%$, where Δm are the widths of the mass bins. Hence, the present analysis assumed uniform mass binning.

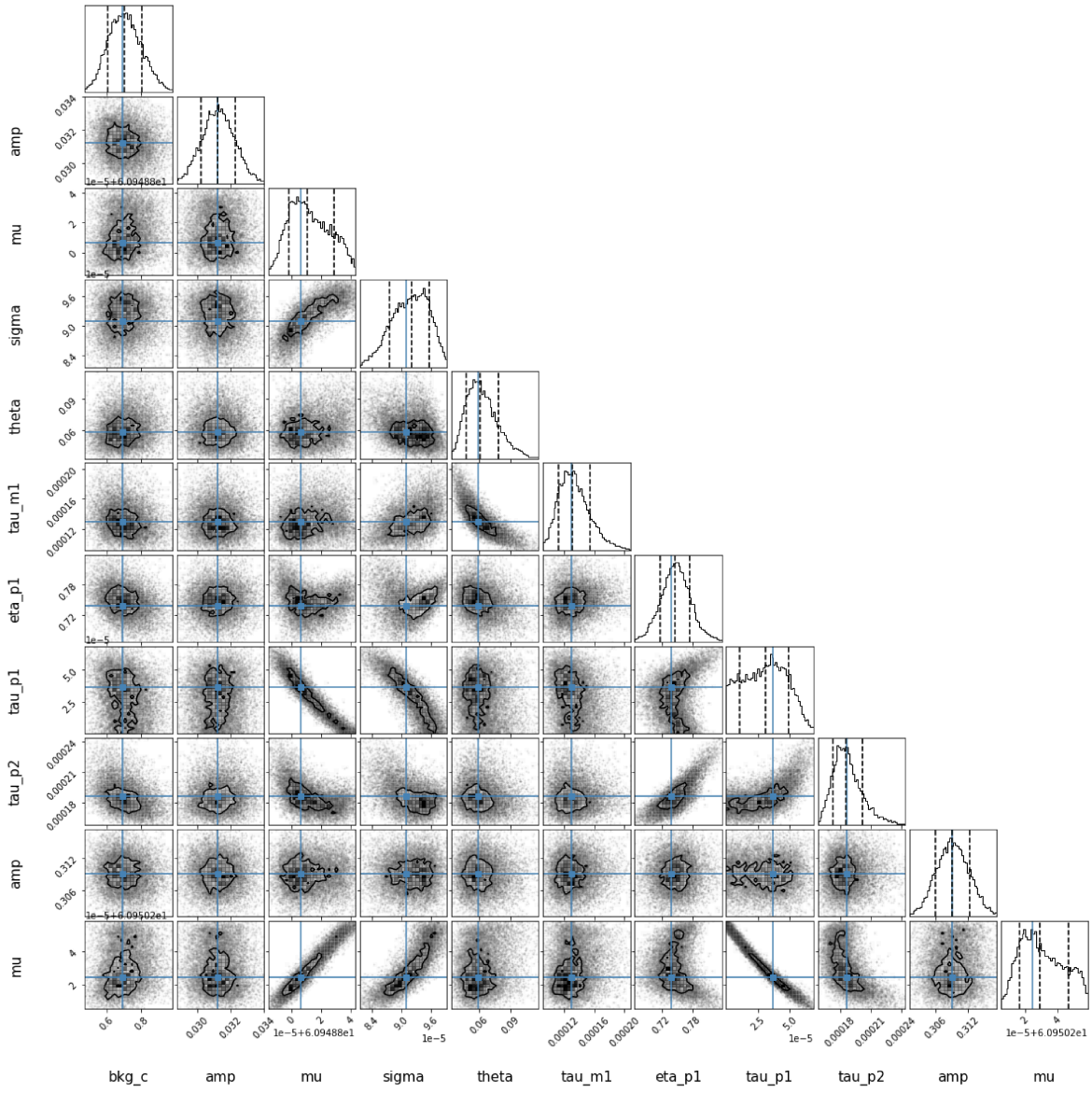

Figure A.6. Correlation map obtained by exploring the parameter space of the peak-shape calibrant fit at $A = 61$ through MCMC sampling. Only samples that remained after burn-in and thinning are shown. Black lines in the 2D scatter plots of the MCMC samples enclose 1σ confidence regions. Diagonal ellipses indicate parameter correlations. The histograms approximate the posterior probability distributions of the fit parameters and the respective 32%, 50% & 68% quantiles are indicated by dashed lines. Blue lines and dots indicate the best-fit values obtained in the peak-shape calibration.

As has been demonstrated in Ref. [595], the accuracy of a centroid determination from binned count data depends on the available statistics in the given peak, and on the ratio of the peak's FWHM and the bin width. The effect of the finite bin size on the peak centroid determination in MR-TOF mass spectra was evaluated through a Monte Carlo study. Synthetic spectra were generated by randomly sampling events from a single hyper-EMG(1,2) peak with identical shape parameters as those obtained in the fit to the experimental ^{61}Ga mass spectrum and with a mean of $\mu_{\text{true}} = 60.948\,872\,42\,\mu\text{u}$. The initially unbinned mass

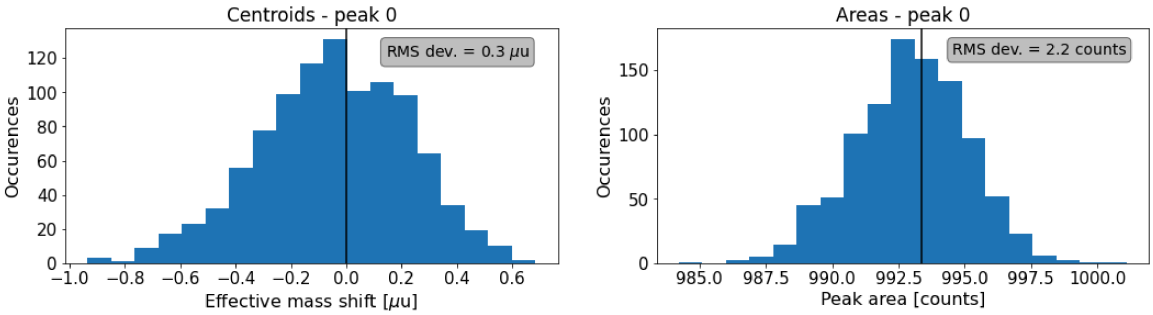

Figure A.7. Mass and peak area variations obtained in the Monte Carlo peak-shape uncertainty evaluation for ^{61}Ga. Black vertical lines indicate the best-fit values obtained in the IOI fit.

events were then uniformly binned over the range [60.93 u, 60.97 u] using a bin width of $\Delta m = 31.6\,\mu\text{u}$. In the worst case scenario for this bin width, the binning may shift a mass event by $\pm 31.6/2\,\mu\text{u}$ away from its true position. While for high statistics, these binning-induced shifts average out and become irrelevant, in cases of low statistics these stochastic mass shifts may shift the inferred peak centroid away from the true value. To quantify this effect, the simulated mass data were fitted after binning with different bin positions. Fits were performed through maximum likelihood estimation with the Poisson log-likelihood ratio (Eqn. A.14). In the fits, the peak shape was fixed to the true shape of the reference peak used for the event sampling. The mean centroid variations (and thus mass variations) resulting from bin position shifts were evaluated through the following procedure:

1. *Generate* $N_{\text{spec}} = 1000$ *synthetic spectra by sampling events from the reference distribution.*

2. *For each spectrum:* Perfom $N_{\text{steps}} = 20$ fits after binning the data, after each fit shifting the bin positions by the increment $\Delta m / N_{\text{steps}}$. Calculate the standard deviation of the peak positions μ_i relative to the true centroid: $\delta m_j = \sqrt{\sum_i^{N_{\text{steps}}} (\mu_i - \mu_{\text{true}})^2 / N_{\text{steps}}}$

3. *Estimate the mass variation due to the finite bin size,* δm_b*, as the mean of the obtained* δm_j*:* $\delta m_b = \sum_{j=1}^{N_{\text{spec}}} \delta m_j$.

4. *Repeat all steps above for different total event numbers.*

5. *Repeat all steps above for different bin widths.*

The resulting relative mass variations are shown in Fig. A.8. The error bars on the data points were taken as the standard deviations of the δm_j. One observes the increase of the mass variations towards low statistics and towards larger bin widths. For the binning in the presented gallium mass measurements (31.6 μu), the mass uncertainty from binning is seen to be negligible compared to the statistical uncertainties. Even for the comparatively low statistics of the ^{60}Ga measurement, with $N_{\text{ions}} = 41$, the relative mass uncertainty due to the finite bin size is only about $(\delta m/m)_b \approx 3 \times 10^{-8}$ — more than an order of magnitude below the relative statistical mass uncertainty of 5.1×10^{-7}.

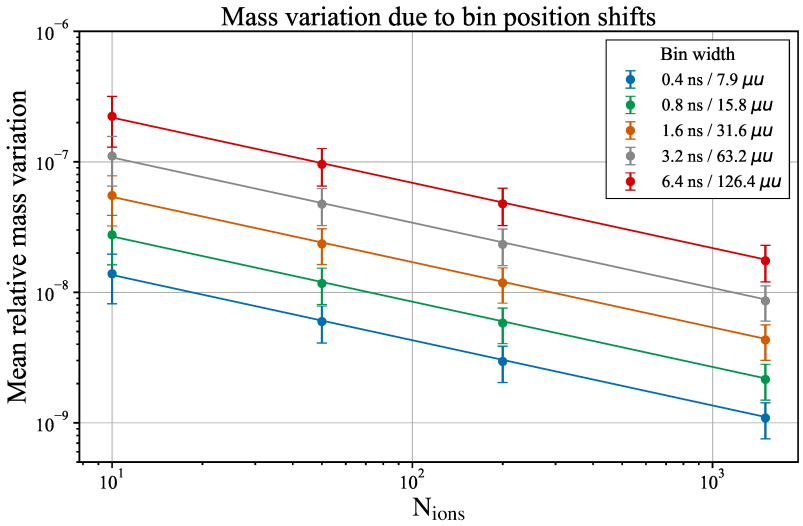

Figure A.8. Relative mass uncertainty due to the finite bin size taken as the mean relative mass variations $(\delta m/m)_b = \delta m_b/\mu_{\text{true}}$ obtained from the bin position scans.

A.7 Uncertainty due to the choice of the fit ranges

The choice of the fit ranges in the peak-shape calibration and the IOI fits can potentially induce shifts in the final mass values. To quantify this potential source of mass uncertainty, the spectrum analyses were re-performed varying the peak-shape calibration by between $\pm 20\%$ and $\pm 50\%$ and the IOI fit ranges by between 10% and $\pm 25\%$ around the nominal values, respectively. The resulting mass shifts were found to be on a negligble level of $\frac{\delta m}{m} \leq 8 \times 10^{-9}$ in all cases.

Appendix B

Hardware modifications for improved HV breakdown strength

Initial attempts of ion trapping in CPET were hampered by HV discharges. This appendix gives a more detailed description of the observed discharge phenomena and reports the hardware modifications applied to improve the HV breakdown strength of the trap assembly.

The discharges encountered during early ion-trapping tests were typically observed as background events on the ES MCP0 detector. With the detector's phosphor screen biased to $\gtrapprox 1\,\mathrm{keV}$, the discharges could be observed as bright flashes (indicating a spark discharge) or in more severe cases as steady illumination of the screen (indicating a sustained discharge). These MCP signals were generally insensitive to the voltages applied along the electron-injection beamline, suggesting UV- or X-ray radiation emitted in the discharges as the primary signal origin. However, since stronger discharges also deposited measurable currents ($> 1\,\mu\mathrm{A}$) onto various electrodes along the trap structure, we avoided using the MCP detectors for extensive studies of the observed discharge phenomena in order to not risk detector damage through excessive current deposition. Once ignited, a discharge often spread and, within a few seconds, produced detectable discharge currents on multiple power supply channels, oftentimes resulting in over- or undervoltages. These more severe discharges could typically only be stopped by ramping the HV biases of all affected electrodes to zero.

At the time of these tests, the pressure in the ES diagnostics chamber (as measured with the ionization gauge IG1, see Fig. 6.10) was elevated from the typical level of $\approx 2\times10^{-9}$ mbar to 5.3×10^{-8} mbar. Installing an ionization gauge on the IS diagnostics chamber (IG2) later revealed that the pressure in the IS diagnostics chamber was even higher, at a level of $\approx 6.5\times10^{-6}$ mbar, indicating a vacuum leak in this beamline section. A subsequent search with a He leak checker confirmed that the elevated chamber pressure originated from a faulty feedthrough in the IS diagnostics chamber. At the time of the above ion trapping tests, the pressure level in the trapping region can therefore be assumed to have been elevated to somewhere between 1×10^{-6}–1×10^{-8} mbar. The elevated pressure very likely exacerbated the observed discharges. However, electrical breakdown due to switching of the gate electrode voltages had already been observed in earlier ion trapping tests with better

vacuum conditions ($\approx 3 \times 10^{-10}$ mbar measured on IG1 and presumably $\lesssim 1 \times 10^{-9}$ mbar in the trapping region).

Since the discharges prevented stable electrode biasing and increased the risk of detector damage, they had to be addressed to enable a reliable system operation. In order to identify the mechanisms triggering the discharges, an extensive root-cause analysis was conducted.

In a first stage, the system was operated while only biasing a single or a few selected electrodes at a time. These tests identified a number of electrodes with insufficient HV breakdown strength. HV insulation resistance tests were performed with a $2.5\,\mathrm{kV}$ megaohmmeter while the trap assembly was under high vacuum and installed inside the superconducting magnet. Subsequently, the trap assembly was removed from the superconducting magnet and the trap-vacuum housing for further HV insulation tests at atmospheric pressure visual inspection. Since, according to Paschen's law [596], the breakdown voltage for a gas discharge between two conductors is generally a function of the product of the ambient pressure and the gap length, the tests at atmospheric pressure should be interpreted with caution. Nonetheless, they turned out to be particularly helpful to pinpoint potential areas with insufficient breakdown strength as the electrode structure could be visually monitored during HV insulation tests without obstruction by enclosing vacuum chambers. Insulation resistance was tested with negative and positive polarity between electrodes and grounded conductors (i.e. chamber walls, and metal components in the support structure) as well as among adjacent electrodes. The minimal obtained insulation resistances between the different electrodes with respect to grounded conductors are listed in table B.1. Resistances between different electrodes are not listed, since only between the DT1 and harp electrodes, a measurable resistance of $0.3\,\mathrm{M\Omega}$ was observed in the initial tests at atmospheric pressure. The insulation strength of the detached feedthrough section was likewise tested under atmospheric pressure and all terminals reached the meter's sensitivity limit of $\sim 1000\,\mathrm{G\Omega}$. Generally, any insulation resistance above $100\,\mathrm{M\Omega}$ is considered *excellent* and was therefore assumed to be sufficient for our purposes. The visual inspection and the HV insulation tests identified the following issues:

- Most electrodes in the trap assembly became prone to breakdown at high voltages between 1–$2.5\,\mathrm{kV}$. In vacuum, electrodes generally exhibited a lower breakdown voltage when negatively biased. Since field emission is the primary cause of electrical breakdown under high vacuum [597], this pointed to electrode surface non-uniformity or sharp wire bends as potential sources of breakdown.

- Sparking was observed between the DT1 drift tube and stainless steel screws in the harp detector assembly.

- A ceramic insulator in the wire connector assembly that attaches to the feedthrough section was cracked, likely compromising the breakdown voltage for the G1 electrode bias.

- For multiple electrodes, sparking was observed in the wire connector assembly. The sparking was likely caused by copper wires not being well-centred inside the holes of

Table B.1. Comparison of insulation resistances between various electrodes and earth ground measured with a $2.5\,\mathrm{kV}$ megaohmmeter under different ambient pressures (p) before and after the modifications for increased breakdown strength (see text). For each electrode, the minimal resistance obtained in measurements with both positive and negative polarity is reported. In cases listed as OL (for open loop) the sensitivity limit of the meter was reached, indicating a resistance $\gtrsim 1000\,\mathrm{G\Omega}$.

Electrode	Before modifications		After modifications	
	$p = 1\,\mathrm{atm}$	$p \approx 10^{-6}$–$10^{-8}\,\mathrm{mbar}$	$p = 1\,\mathrm{atm}$	$p \approx 10^{-8}$–$10^{-9}\,\mathrm{mbar}$
Harp	$49\,\mathrm{G\Omega}$	OL	$131\,\mathrm{G\Omega}$	OL
DT1	$0.6\,\mathrm{M\Omega}$	$4.6\,\mathrm{M\Omega}$	$118\,\mathrm{G\Omega}$	OL
G1	$88.3\,\mathrm{M\Omega}$	$300\,\mathrm{M\Omega}$	$277\,\mathrm{G\Omega}$	OL
Trap electrodes	Not tested	$6.1\,\mathrm{M\Omega}^{\dagger}$	$> 120\,\mathrm{G\Omega}$	$240\,\mathrm{G\Omega}^{\ddagger}$
G2	$700\,\mathrm{G\Omega}$	$0.4\,\mathrm{M\Omega}$	$77.4\,\mathrm{G\Omega}$	OL
DT2	$113\,\mathrm{G\Omega}$	$104\,\mathrm{M\Omega}$	$149\,\mathrm{G\Omega}$	$91\,\mathrm{G\Omega}$

†Listed resistance measured with all trap electrodes shorted outside the vacuum chamber.

‡Listed resistance measured on one segment of the D25 electrode; all other trap electrodes yielded OL.

the aluminum end plate of the connector assembly [see Fig. B.1 (a)], thus reducing the spacing between the wires and the grounded end plate.

- Dark discoloration was seen on the exposed end section of the copper wire leading to the DT2 drift tube, likely resulting from a discharge in this region.

Informed by these observations, a number of operational changes and hardware upgrades were applied to ensure a stable system operation. A new trapping scheme was devised that foresaw the operation of the trap electrodes at voltages near earth ground (to within -100–$200\,\mathrm{V}$) rather than the original floating voltages of 0.8–$1.2\,\mathrm{keV}$. This implied that most electrodes along the trap assembly could be operated at substantially lower voltages, thus reducing the likelihood of electrical breakdown. Working with trapping potentials near earth ground also allowed to connect trap electrodes to laboratory equipment such as spectrum analyzers and frequency generators, thereby greatly simplifying excitation and image-current detection of plasma oscillations or diagnostics of ambient noise in the trapping region.

A complication of the new trapping scheme lay in the fact that injected ion bunches had to be decelerated to trappable energies by pulsing the voltage bias of the DT1 drift tube. Since field penetration from grounded conductors was essentially negligible along the electron beampath, the electron transport potentials could simply be shifted by a fixed voltage offset to accommodate the new trap bias and only required minor re-tuning to re-establish electron transmission into the trap. The ion-injection beamline, however, included the grounded drift tube inside the feedthrough section as well as other transport sections prone to field penetration from the grounded vacuum chamber. Therefore, the viability of the new ion injection and extraction schemes was verified through SIMION [528] trajectory simulations as reported in [512, 545].

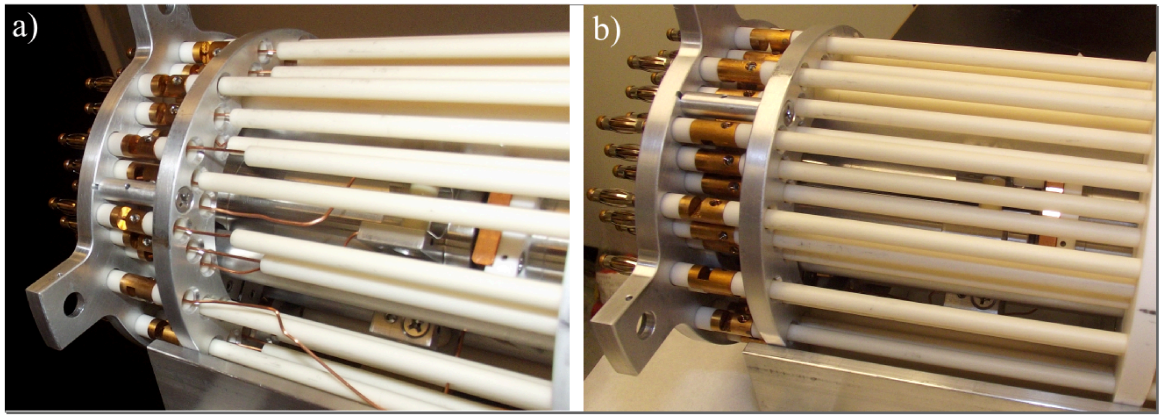

Figure B.1. The ceramic wire shielding at the transition to the wire connectors before (a) and after (b) the modifications for improved HV breakdown strength.

In order to improve the HV breakdown strength of the trap assembly and to accommodate the requirements of the new trapping scheme, the following hardware modifications were applied:

- The arrangement and electrical wiring of electrodes within the trap assembly was adapted for increased HV breakdown strength (see section 6.3.1 for details). The new biasing scheme reduced the number of electrical connections between the feedthrough section and trap assembly. In distributing the wires over the various terminals in the connector assembly, this provided the necessary flexibility to increase the spacing between the most critical HV-carrying wires.

- Special care was taken to minimize exposed sections on the copper wires that connected the electrodes to the terminals in the connector assembly. To this end, the ceramic tubes shielding the copper wires were cut to the appropriate length for each wire. The copper wires were carefully centred inside the holes of the connector assembly end plate and subsequently covered by sliding the ceramic tubes all the way into the larger diameter insulators in the connector assembly [see Fig. B.1 (b)]. Where possible, the bent wire end sections leading to the electrodes were shielded with smaller ceramic tubes of < 1 cm length, thus preserving the necessary flexibility (see Fig. B.2).

- To prevent HV breakdown between the harp detector and the DT1 drift tube, a set of holes was removed from the MACOR® ceramic holder of the harp detector and the stainless steel screws inserting into it were replaced with ceramic screws (see Fig. B.3).

After the modifications, another set of HV insulation tests under atmospheric pressure verified the substantial improvements in breakdown strength, with all electrodes exhibiting insulation resistances above $70\,\mathrm{G\Omega}$ at $\pm 2.5\,\mathrm{kV}$ (see table B.1). Subsequently, the trap was re-installed inside the vacuum chamber and tested for HV insulation under high vacuum conditions with the ES and IS ionization gauge reading pressures $2.1 \times 10^{-9}\,\mathrm{mbar}$ and

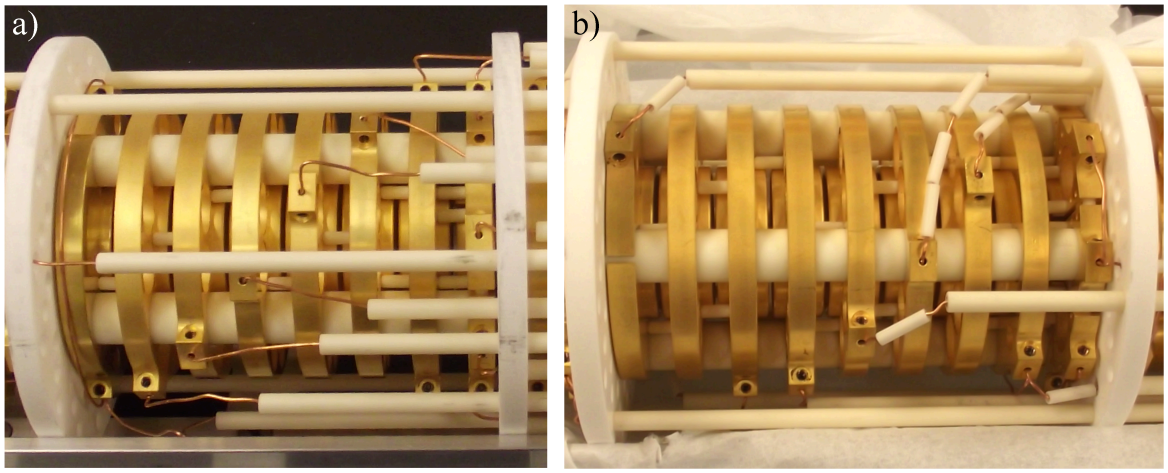

Figure B.2. The electrode wiring before (a) and after (b) the modifications for improved HV breakdown strength.

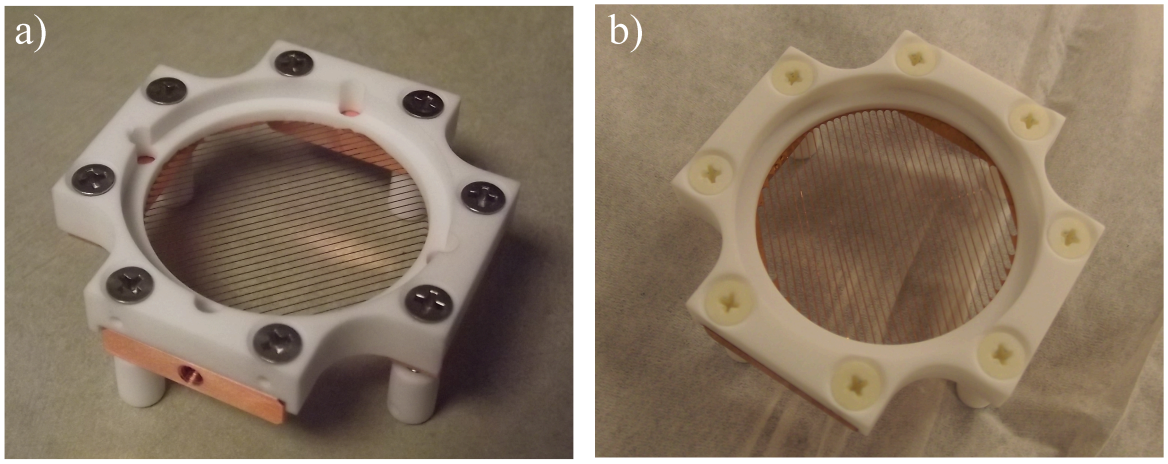

Figure B.3. The harp detector before (a) and after (b) the modifications for improved HV breakdown strength.

2.4×10^{-9} mbar, respectively. For almost all electrodes in the trap assembly, the insulation resistance exceeded the sensitivity limit of the megaohmmeter (see table B.1); only for one segment of the D25 dipole electrode and for the DT2 drift tube the tests yielded finite resistance readings of $240\,\mathrm{G\Omega}$ and $91\,\mathrm{G\Omega}$, respectively. Since even those values are more than sufficient, no further hardware changes were deemed necessary and work towards electron-ion interaction studies could proceed. The mentioned hardware changes were found to significantly reduce the likelihood of electrical breakdown and enabled the first successful trapping of ions in CPET.

Appendix C

Detailed description of the cooling model

The following gives a more comprehensive description of the one-dimensional cooling model that aided the interpretation of the measurements presented in section 6.4.5. After an overview of the simulation approach, the underlying ion-electron and ion-neutral collision models are introduced and their computational implementations are discussed. Finally, an overview of the full procedural flow of a simulation is given.

C.1 Simulation approach and separation of timescales

Using an appropriate expression for the electron-induced friction force acting on an ion, in principle the electron cooling process could be modelled by tracing the full threedimensional trajectories of a swarm of ions orbiting within the trap potential. However, since we are interested in the evolution of the longitudinal ion energies, care has to be taken to ensure energy conservation over the entire simulation time (i.e. $3710\,\mathrm{ms}$ when aiming to reproduce the experimental cooling cycles). This demand prohibited the use of standard trajectory tracing tools with Runge-Kutta orbit integration such as SIMION, because the Runge-Kutta method is known to be prone to numerical energy drift [582] and would have required prohibitively small time steps to conserve the ion energies. Due to the fast cyclotron gyration (e.g. with an orbital period of $T_c = 214\,\mathrm{ns}$ for $^{23}\mathrm{Na}^+$ in a $7\,\mathrm{T}$ field), tracing of the ions' full orbital motion becomes numerically expensive if one seeks to follow the ion motion over $\sim 10^7$ cyclotron gyrations. However, when assuming that the fields and dissipative forces acting on an ion only vary appreciable over many successive cyclotron periods, the ions gyromotion becomes redundant and can be "averaged out" through a so-called guiding centre approximation [582].

As we are anyhow only interested in the ion's longitudinal energy evolution, the simulations of the cooling process were carried out employing a guiding centre approximation in the limit of an infinitely strong and perfectly uniform magnetic field. In this case, tracing the ion motion is reduced to a one dimensional problem and the ions can be considered to move like beads on a string. However, even in this approximation, the axial ion motion, with typical periods $\sim 10\,\mu\mathrm{s}$, has to be integrated over several 10^5 oscillations. Combined with the small time step size ($\Delta t \leq 100\,\mathrm{ns}$) required to conserve the ions' total energy, this

circumstance still resulted in unpractically long computation times when aiming to integrate the orbits of several 10 ions on a personal computer.

To make tracing of the longitudinal ion energy evolution computationally more tractable, the problem was de-composed into the well-separated time scales of the different processes of interest. All considered processes inducing ion energy loss, namely the ion-electron energy exchange, elastic ion-neutral collisions and charge exchange between ions and rest gas neutrals, evolved on characteristic timescales $> 10\,\mathrm{ms}$. Therefore, these processes could be modelled separately from the axial ion motion ($T_z \sim 10\,\mu\mathrm{s}$). Similar as in the two-component plasma model from section 6.2, the ions' longitudinal energies, as the main observable of interest, could be modelled with a set of rate equations and a time step of $\Delta t \approx 1\,\mathrm{ms}$.

However, as the ion-neutral collision frequencies vary with the ion velocity, a correct reproduction of the ion-neutral collision dynamics would require a simulation time step small enough to resolve changes in the ion velocity. To overcome this limitation, the respective collision probabilities were bounce-averaged[1] by precalibrating all relevant quantities on a grid of ion energies through ion orbit integrations before a simulation run. Thereby, during a simulation run, the computationally-expensive ion orbit integrations could be avoided and the average collision frequencies remained correctly described although the simulation time step was 2 orders of magnitude larger than the typical axial ion oscillation period. Ion-neutral collisions were then handled in an event-based Monte Carlo approach that only demanded expensive orbit integrations in the comparatively rare time steps where an ion-neutral collision occurred. In conjunction, these procedures reduced the required simulation run times from many days to a few hours on a standard personal computer, thereby enabling repeated simulation runs without the need for high-power computing. The following sections describe the briefly mentioned procedures in more detail.

C.2 Integration of axial ion oscillation

The asymmetric and anharmonic nested trap potential used for the electron cooling studies reported in section 6.4.5 prevented an analytical treatment of the motions of trapped ions. A more realistic theoretical description of some of the relevant physical processes, such as collisions between ions and neutral rest gas particles (see details below), therefore required the numerical integration of the ion orbits. The vacuum trap potential for the integration of the axial ion motion was based on SIMION field calculations with CPET's realistic electrode geometry. The on-axis potential was pre-calculated in SIMION and recorded on an uniformly-spaced grid $[z_0, z_0 + \delta z, ..., z_N]$ with a resolution of $\delta z = 1\,\mathrm{mm}$. The vacuum trap potential $\phi_{\mathrm{vac}}(z)$ at an arbitrary position z was then obtained by a cubic spline interpolation of the pre-calculated potential array $[\phi(z_0), \phi(z_0 + dz), ..., \phi(z_N)]$. The lowering of the electron-nest potential by the plasma-space-charge potential ϕ_p was approximated by truncating the vacuum nest potential to a user-defined effective nest depth $\phi_{\mathrm{nest,eff}} = \phi_{\mathrm{nest}}(z) - \phi_p(z) \approx \mathrm{const.}$

[1] Bounce-averaging refers to an average over the axial ion oscillation in the trap potential.

Any impact of the plasma space charge on the trap potential outside the filled nest region was neglected. This approach yields fair approximations of the true trap potential as long as $\phi_p \lesssim \phi_{\text{nest}}/2$ and $k_B T_e \ll \phi_{\text{nest}}$. Simulations of CPET's effective trap potential performed with the particle in-cell code WARP [598] and following the methodology outlined in [599] verified the assumed flattening of the trap potential and confirmed that the plasmas of interest here only marginally perturbed the trap potential outside the nest region filled with electrons (see Fig. 6.33). Outside the plasma, the axial ion acceleration at a given position was then calculated from the smoothed vacuum potential data using first-order finite differences, resulting in the following combined relation:

$$\frac{dv_z}{dt}(z) = \frac{q}{m}E_z(z) = -\frac{q}{m}\frac{\partial\phi(z)}{\partial z} \approx \begin{cases} 0 & , \text{ for } z_l < z < z_r \\ -\frac{q}{m}\frac{\phi_{\text{int}}(z+\Delta z)-\phi_{\text{int}}(z)}{\Delta z} & , \text{ else} \end{cases} \tag{C.1}$$

where Δz was taken as $1\,\mu\text{m}$ and the two plasma endpoints z_l and z_r are defined by the relation $\phi_{\text{int}}(z_l) = \phi_{\text{int}}(z_r) = \phi_{\text{nest,eff}}$. Since, under all studied conditions, the relative ion energy loss per pass through the plasma was $\frac{\Delta E}{E} \leq 10^{-4}$, the ion slowing-down due to ion-electron collisions could be neglected when integrating over a single half-oscillation in the axial trap potential. The same goes for ion-neutral collisions which exhibited collision frequencies several orders of magnitude lower than the axial ion oscillation frequencies. The ion's equations of motion in the trap potential were integrated using a Python implementation [591] of the explicit 8$^{\text{th}}$ order Runge-Kutta integrator DOP853 [600].

C.3 Electron-ion collisions

Based on the results from section 6.2, plasma-induced ion-loss processes such as radiative, dielectronic and three-body recombination can be considered irrelevant for singly charged ions under the given measurement conditions and were not implemented in the present simulations. Consequentially, only ion-electron interactions through elastic Coulomb collisions were simulated.

As for the cooling simulations in section 6.2, Coulomb collisions between ions and electrons were described based on the kinetic theory of unmagnetized plasma [484, 562]. Since the ion samples in our measurements started with a large centre-of-mass motion and were presumably far from thermal equilibrium throughout most of the interaction period, the assumption of a Maxwellian ion energy distribution was discarded and the cooling process was described by considering the energy loss of individual, non-interacting ions. Considering the large trap volume, as well as the low charge ($q = 1e$) and the rather small quantities of the trapped ions (on average < 100 ions per cycle), the assumption of negligible ion-ion interactions certainly seems appropriate in the presented measurements[2]. This scheme, in

[2]Assuming for example, that $N_i = 100$ ions trapped in CPET uniformly occupy a cylindrical volume $0.8\,\text{mm}$ radius and $20\,\text{cm}$ length results in an ion number density $n_i = 2.5 \times 10^2\,\text{cm}^{-3}$. The respective ion self-collision frequency can be estimated as [601] $\nu_{ii} = 4.8 \times 10^{-8}(q/e)^4(m/m_p)^{-0.5} n_i \ln(\lambda)$, where $\ln(\lambda) \approx 23 - \ln(q^2 m/(e^2 m_p T_i)\sqrt{(2n_i Z^2/T_i)}))$, T_i is in units of eV and m_p denotes the proton mass. For

principle, allows one to model the evolution of arbitrary ion velocity distributions by tracing the energy evolution of many individual ions with initial velocities sampled from a given velocity distribution. An obvious drawback compared to Maxwellian-averaged plasma descriptions is the typically much higher numerical cost of this approach.

According to kinetic plasma theory (see e.g. [562]), the deceleration of initially monoenergetic ions passing through a Maxwellian background of plasma electrons at velocity v is described by the slowing-down frequency

$$\nu_s \doteq -\frac{\langle \Delta v_\parallel / v \rangle}{\Delta t} = 2\nu_0 \left(1 + \frac{m}{m_e}\right) \frac{v_{\text{e,th}}}{v} G\left(\frac{v}{v_{\text{e,th}}}\right), \tag{C.2}$$

where $v_{\text{e,th}} = \sqrt{k_B T_e / m_e}$ is the thermal electron velocity, the pre-factor

$$\nu_0 \doteq \frac{4\pi q^2 e^2 n_e \ln(\Lambda)}{m^2 v_{\text{e,th}}^3} \tag{C.3}$$

is a characteristic collision frequency of importance to various transport processes and

$$G(x) = \frac{\Phi(x) - x\Phi'(x)}{2x^2}, \tag{C.4}$$

where Φ denotes the error function,

$$\Phi(x) = \frac{2}{\sqrt{2}} \int_0^x du \exp\left(-u^2\right). \tag{C.5}$$

The Coulomb logarithm in Eqn. C.3 is given by [601]

$$\ln(\Lambda) = 23 - \ln\left(\frac{q\sqrt{n_e}}{e\, T_e^{3/2}}\right), \tag{C.6}$$

where n_e is taken in units of cm^{-3}. Since $G(x)$ peaks at $x = 1$, the slowing-down rate is largest for ions with velocities $v \approx v_{\text{e,th}}$.

According to the fluctuation-dissipation theorem, the drag force exerted by the electrons must be accompanied by velocity diffusion that gradually spreads out the initially monoenergetic ion velocity distribution. The rate of this spreading is described by the longitudinal velocity diffusion frequency

$$\nu_\parallel \doteq -\frac{\langle (\Delta v_\parallel / v)^2 \rangle}{\Delta t} = 2\nu_0 \frac{v_{\text{e,th}}^3}{v^3} G\left(\frac{v}{v_{\text{e,th}}}\right) \tag{C.7}$$

and the perpendicular velocity diffusion frequency

$$\nu_\perp \doteq -\frac{\langle (\Delta v_\perp / v)^2 \rangle}{\Delta t} = 2\nu_0 \frac{v_{\text{e,th}}^3}{v^3} \left(\Phi\left(\frac{v}{v_{\text{e,th}}}\right) + G\left(\frac{v}{v_{\text{e,th}}}\right)\right), \tag{C.8}$$

Na^+ ions with $n_i = 2.5 \times 10^2$ cm^{-3}, $T_i = 10$ eV and $m \approx 23 m_p$, one obtains $\nu_{ii} \approx 1.6 \times 10^{-6}$ s^{-1}, which indicates that the rate of energy exchange by ion-ion collisions is indeed negligible compared to the timescales of other energy exchange processes in the system.

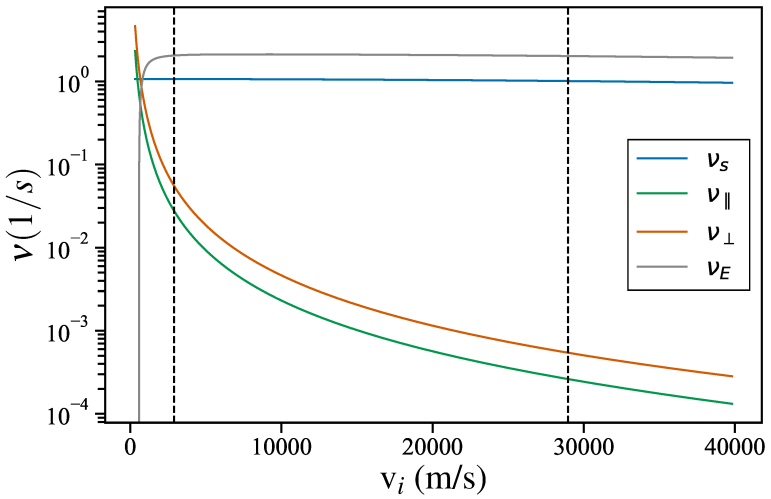

Figure C.1. The plasma collision frequencies for Na^+ and an electron plasma with $n_e = 1 \times 10^8\,\mathrm{cm}^{-3}$ & $T_e = 300\,\mathrm{K}$ as function of the ion velocity. The dashed vertical lines correspond to ion energies of 1 eV and 100 eV, respectively, and mark the energy range of interest for the measurements presented in section 6.4.5.

respectively. Generally, when evaluating the rate of ion-energy dissipation, both drag and diffusion have to be considered. The total energy exchange between test ions and the background of plasma electrons is characterized by the (total) energy-loss frequency

$$\nu_E \doteq -\frac{\langle \Delta E/E \rangle}{\Delta t} = 2\nu_s - \nu_\parallel - \nu_\perp. \tag{C.9}$$

Here however, we are only interested in the evolution of the longitudinal ion energy, $E_\parallel \doteq E - \frac{m}{2}v_\perp^2$, for which we can define the longitudinal energy-loss rate

$$\nu_{E,\parallel} \doteq -\frac{\langle \Delta E_\parallel/E \rangle}{\Delta t} = 2\nu_s - \nu_\parallel. \tag{C.10}$$

Fig. C.1 depicts the trends of the different plasma collision frequencies as function of the ion velocity under typical CPET plasma conditions. Over the ion energy range of interest here (marked by dashed lines), the velocity diffusion frequencies are negligible compared to the slowing-down frequency such that $\nu_{E,\parallel} \approx \nu_E \approx 2\nu_D$. This indicates that, at least when neglecting plasma magnetization, the collisions between fast ions and electrons in a plasma with $n_e = 1 \times 10^8\,\mathrm{cm}^{-3}$ should only slowly deflect ions away from the trap axis, as implicitly assumed in our one-dimensional model.

C.4 Ion-neutral collisions

In order to describe the ion energy loss in interactions with residual gas particles, elastic atom-ion collisions and charge exchange reactions were modelled following a direct simulation Monte Carlo approach [602]. Other inelastic ion-atom collisions such as rotational or vibrational excitation of residual gas molecules could in principle also be modelled by this

method, but were not included due to the unknown residual gas composition in the trap and the lack of readily available cross sections for these atomic processes.

In the direct simulation Monte Carlo method, ion-neutral collisions are modelled as occasional, instantaneous events that may induce substantial jumps in an ions' energy. The probability for a collision to occur in a given simulation time step spanning the interval $[t, t+\delta t]$ is given by [603]

$$P_{\text{coll}}(t) = 1 - \exp\left(-\frac{v(t)}{l}\delta t\right), \tag{C.11}$$

where the ion-neutral collision frequency $\nu_{\text{in}} = \frac{v(t)}{l}$ in the exponential is determined by the respective particle velocity and the mean free path, $l = 1/(n_n\sigma)$, which in turn depends on the neutral number density n_n and the collision cross section σ. Generally, the mean free path l is also dependent on the ion velocity, as the collision cross sections usually vary with the collision energy. For Eqn. C.11 to yield realistic estimates of the collision probability, the time step δt has to be chosen small compared to ν_{in}^{-1} and should be small enough to resolve changes of the ion velocity $v(t)$.

The elastic ion-atom collisions and the charge exchange reactions were described by means of a semiclassical scattering model adapted from those presented in [564, 604]. The interaction between the ion and atom arises from the dipole moment the ion induces in the neutral and gives rise to an interaction potential of the form $V(r) = -C_4/(2r^4)$, where r is the particle spacing and $C_4 = \frac{\alpha q^2}{4\pi\epsilon_0}$ is a strength parameter that depends on the neutral's dipole polarizability α and the ion charge q. All experimental dipole polarizabilities used in the simulations were adopted from Ref. [605]. The probability for an ion to undergo an elastic collision or a charge exchange reaction was deduced based on the total cross section [604]

$$\sigma_{\text{tot}} = \pi\left(\frac{\mu C_4^2}{\hbar^2}\right)^{1/3}\left(1+\frac{\pi^2}{16}\right)E_{\text{coll}}^{-1/3}, \tag{C.12}$$

where μ is the reduced mass and E_{coll} is the collision energy in the COM frame.

Based on the impact parameter, elastic collisions in this intermediate energy regime ($1\times10^{-4}\,\text{eV} \lesssim E_{\text{coll}} \lesssim 30\,\text{eV}$) can be grouped into two categories [563].

The dominant category are *glancing collisions* that occur for large impact parameters and only lead to a small deflection with minor momentum and energy exchange. The COM scattering angle for a glancing collision characterized by a r^{-4} interaction potential is given by [564]

$$\theta = \pi - 2\tilde{b}\sqrt{2}\sqrt{\tilde{b}^2 - \sqrt{\tilde{b}^4-1}}K\left(2\tilde{b}^4 - 2\tilde{b}^2\sqrt{\tilde{b}^4-1} - 1\right) \tag{C.13}$$

$$\text{with}\quad K(y) = \int_0^{\pi/2}\frac{1}{\sqrt{1-y\sin^2(x)}}dx, \tag{C.14}$$

where $K(y)$ is the complete elliptic integral of the first kind and $\tilde{b} = b/b_{\text{max}}$ is the impact parameter normalized by the largest relevant impact parameter, $b_{\text{max}} = \sqrt{\sigma_{\text{tot}}/\pi}$.

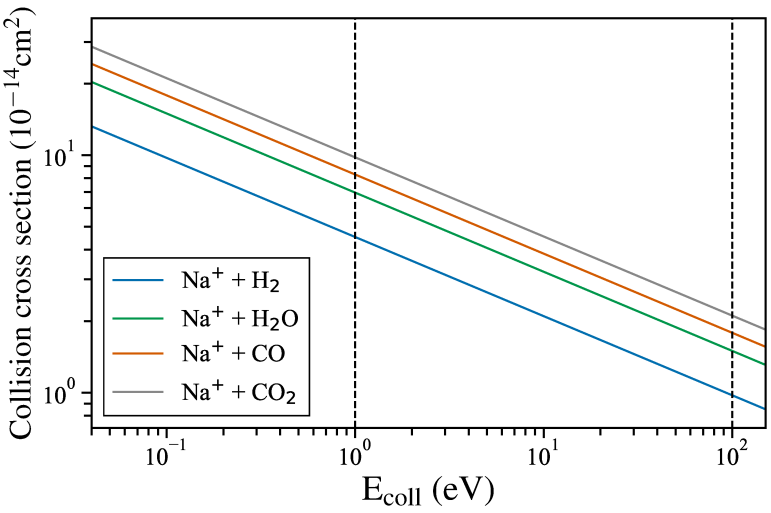

Figure C.2. Semiclassical collision cross sections, σ_{tot}, for $^{23}Na^+$ and the different residual gases used in the cooling simulations.

Collisions of the second category occur at impact parameters below a critical value that Langevin theory predicts as $b_c = (2C_4/E_{\text{coll}})^{1/4}$. In this case, the projectile ion is thought to be sent onto a spiraling orbit around the target atom that eventually leads into a hard collision with large momentum transfer. The COM scattering angle in such *Langevin collisions* is isotropically distributed [564] and the associated Langevin cross section is given by $\sigma_L = \pi b_c^2$. Due to the scaling $\sigma_L \propto E_{\text{coll}}^{-1/2}$, the rate of Langevin collisions is independent of the collision energy and velocity.

Collisions with impact parameters $b \leq b_c$ can not only lead to momentum transfer but may also induce *charge exchange* [563]. Scattering experiments at energies $< 1\,\text{eV}$ have confirmed that resonant charge exchange cross sections of ions immersed in their parent gas (e.g. $Rb^+ + Rb$) follow the $E^{-1/2}$ scaling of the Langevin cross section at these low energies, such that $\sigma_{\text{CX}} = P_{\text{CX}}\sigma_L$, where P_{CX} may take a wide range of values between $10^{-3} - 0.7$ [606]. At higher energies, $\gtrsim 1\,\text{meV}$, charge exchange cross sections transition from the low- into the intermediate-velocity regime where the exact cross sections become dependent on the potential energy difference between the initial and final atomic states [607]. For the collisions partners and energies ($E_{\text{coll}} \sim 1$–$50\,\text{eV}$) of interest here, no theoretical or experimental cross sections were available in the literature. Further, the model of asymmetric charge exchange in the intermediate-velocity regime from Ref. [607] was found inapplicable in the transition regime of interest here. In lieu, we crudely model charge exchange reactions by assuming that 10% of the collisions with $b \leq b_c$ result in charge exchange, which implies $\sigma_{\text{CX}} = 0.1\sigma_{\text{L}}$.

The type of a given collision is determined by calculating the impact parameter as $b = b_{\text{max}}\sqrt{y}$ [564], where $y \in \mathcal{U}(0,1)$ is a random number between 0 and 1, sampled from the uniform distribution, $\mathcal{U}(0,1)$. If $b \leq b_c$, a second random number $x \in \mathcal{U}(0,1)$ is drawn to decide whether the collision was a regular Langevin collision ($x > P_{\text{CX}}$) or a charge exchange reaction ($x \leq P_{\text{CX}}$). In the case of a charge exchange reaction, the ion is neutralized

and leaves the trap volume, whereas the neutral collision target is ionized and typically remains confined in place of the projectile ion. Neglecting the thermal motion of residual gas particles, an ion undergoing charge exchange in the simulation is thus replaced by a neutral ($m \to m_n$) with a total energy defined by the effective trap potential at the collision location, z_{coll}, and the neutral's (typically negligible) thermal energy ($E_\parallel \to q\phi_{\text{eff}}(z_{\text{coll}}) + k_B T_n$). The energy loss of an ion undergoing a glanzing or a regular Langevin collision, is calculated from the COM angle θ as

$$\Delta E_{\parallel,\text{coll}} = E_{\text{coll}} \left[\frac{m}{m+m_n} + \left(1 - \frac{m}{m+m_n} \cos(\theta) \right)^2 - 1 \right]. \tag{C.15}$$

C.5 Ion-energy and plasma-temperature evolution

Taking into account both ion-electron and ion-neutral interactions, the time evolution of individual ion energies and of the plasma temperature were determined by the coupled differential equations,

$$\frac{dE_\parallel^j}{dt} = -\left(E_\parallel^j - \phi_{\text{nest,eff}} \right) \kappa \, \nu_{E,\parallel}^j - \Delta E_{\parallel,\text{coll}}^j \, \delta(t - t_{\text{coll}}^j), \tag{C.16}$$

$$\frac{dT_e}{dt} = +\frac{2}{3k_B} \frac{\iota}{N_e} \sum_{j=1}^{N_{\text{i,sim}}} \left(E_\parallel^j - \phi_{\text{nest,eff}} \right) \kappa \, \nu_{E,\parallel}^j - \frac{T_e - T_{\text{e},\infty}}{\tau_e}, \tag{C.17}$$

where $N_{\text{i,sim}}$ is the number of simulated ions, Eqn. C.16 represents the $N_{\text{i,sim}}$ equivalent equations for all simulated ions, $\iota = N_{\text{i,exp}}/N_{\text{i,sim}}$ enables runs with different simulated and experimental ion numbers, $\Delta E_{\parallel,\text{coll}}^j$ quantifies the instantaneous energy loss due to ion-neutral collisions occurring at randomly sampled collision times t_{coll}, the overlap factor κ measures the fraction of an axial oscillation period that ions spend inside the plasma, $T_{e,\infty}$ is the equilibrium plasma temperature and τ_e is the effective cyclotron cooling time introduced in section 6.2.

Upon first inspection, these equations appear quite similar to those of the two-component plasma model used in section 6.2. However, the following two complications make numerical integration of Eqn.s C.16 & C.17 substantially more elaborate:

1. The ion-plasma overlap factor is a non-trivial function of the longitudinal ion energy and the effective nest depth: $\kappa = \kappa(E_\parallel, \phi_{\text{nest,eff}})$.
   While under the given measurement conditions, $\nu_{\text{E},\parallel}$ is essentially constant over all relevant ion velocities (see Fig. C.1), the energy dependence of κ will cause the effective energy transfer frequency $\kappa\nu_{\text{E},\parallel}$ to vary throughout the cooling process. As the variation of κ in the anharmonic nested trap potential did not follow a simple functional form, κ was calibrated by integrating the axial motion of test ions. To this end, ions were started on an equidistant grid of energies spanning the energy range from 0–120 V in steps of 0.5 V. At each energy, the ion motion was integrated over half an axial oscillation and κ was set to the obtained fraction of the integration time that

an ion spent inside the plasma. To allow for variation of the experimentally unknown plasma space charge potential, this procedure was repeated for various values of the effective nest depth ($10\,\mathrm{V} \leq \phi_{\mathrm{nest,eff}} \leq 40\,\mathrm{eV}$ in $0.5\,\mathrm{V}$ steps). A subset of the $\kappa(E_{\parallel})$ curves obtained by integrating over axial oscillations of $^{23}Na^{+}$ ions is shown in the left subplot of Fig. C.3. By linear, two-dimensional interpolation of these pre-calculated values, κ could then be obtained at arbitrary points within the covered range of the ($E_{\parallel}$,$\phi_{\mathrm{nest,eff}}$)-plane. As κ also weakly depends on the ions' mass-to-charge ratio, separate overlap factors were pre-calculated for each ion species. Using the pre-calculated values circumvented the need to perform repeated, numerically-expensive orbit integration in the numerical integration of Eqn.s C.16 & C.17, and thus substantially reduced the computation times.

2. As already mentioned, the standard Monte Carlo approach for modelling ion-neutral collisions requires time steps sufficiently small to resolve variations in the ion velocity. As the ions in CPET underwent axial oscillations with periods T_z on the order of a few $10\,\mu\mathrm{s}$, the latter condition would require the axial ion motion to be integrated over the full simulation time ($3710\,\mathrm{ms}$) in fine steps of $< 1\,\mu\mathrm{s}$ in order to properly treat ion-neutral collisions by means of Eqn. C.11. Such fine-grained orbit integration was found to result in unpractically-long execution times (multiple hours to propagate a single ion when performing the integration in the compiled Julia programming language) on a standard notebook. The important realization for overcoming this limitation lies in the fact that, like all observables of interest, both the ion-electron and the ion-neutral collisions times vary on timescales $> 10\,\mathrm{ms}$. The ion energy thus remains nearly constant over many successive axial oscillation periods and it seems appropriate to average over the ions' axial bounce motion. However, in choosing time steps $\Delta t \gg T_z$ care must be taken to retain a correct description of the ion-neutral collision frequency, ν_{in}. In particular, the collision probability per time step P_{coll} must be averaged over the ions' axial bounce motion. Rewriting Eqn. C.11 in the infinitesimal limit $\Delta t \to dt$, we obtain

$$dP_{\mathrm{coll}} = 1 - \exp\left(-\sum_k \frac{|v|}{l_k} dt\right) \approx -\sum_k \frac{|v|}{l_k} dt. \tag{C.18}$$

If the mean free path, l_k, was independent of ion velocity, averaging over dP_{coll} would be trivial and the bounce-averaged collision probability would simply be obtained from Eqn. C.11 by replacing v with an effective velocity given by the mean (i.e. bounce-averaged) ion velocity. The mean free path in our collision model, however, scales as $l_k \propto \sigma_{\mathrm{tot,k}}^{-1} \propto v^{2/3}$, where the second step assumes the neutral velocity to be negligible compared to v. In this case, integration over Eqn. C.18 reveals that the bounce-averaged collision probability is obtained from Eqn. C.11 by the transformation $v \to v_{\mathrm{eff}} = \lambda v_{\mathrm{max}}$, where the velocity scale factor λ is given by

$$\lambda = \left(\frac{1}{T_z}\int_0^{T_z} |v(t)|^{1/3} dt\right)^3 / v_{\mathrm{max}} \tag{C.19}$$

and $v_{\text{max}} = \sqrt{2E_{\parallel}/m}$ is the ions maximal velocity during an axial oscillation. To calculate the bounce-averaged collision probability at a given time step, one therefore needs to determine the velocity scale factor λ at the given longitudinal ion energy by evaluating $v(t)$ over an axial (half-)oscillation. To avoid having to re-perform this orbit integration on each time step in a cooling simulation, $\lambda(E_{\parallel}, \phi_{\text{nest,eff}})$ was pre-calculated on a grid of $(E_{\parallel}, \phi_{\text{nest,eff}})$ pairs that spanned all values relevant to the present simulations. A subset of the pre-calculated λ traces is exhibited in the right subplot of Fig. C.3. Within a given simulation run, λ could then be obtained at arbitrary E_{parallel} & $\phi_{\text{nest,eff}}$ through (numerically much less intensive) linear, two-dimensional interpolation of the pre-calculated grid values.

By supporting substantially larger time steps without a relevant loss of accuracy and by minimizing the number of orbit integrations necessary throughout a simulation run, the introduction of pre-calibrated, bounce-averaged correction factors reduced the execution times by several orders of magnitude. This facilitated simulation of ≥ 100 ion-energy trajectories within computation times of only a few hours on a regular personal computer.

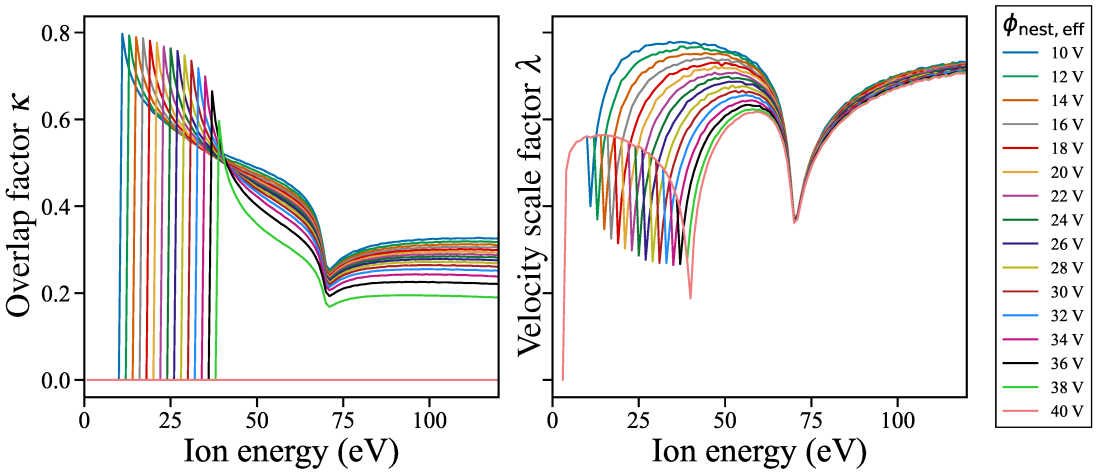

Figure C.3. Bounce-averaged ion-plasma overlap factors and velocity scale factors for $^{23}Na^{+}$ at various effective nest depths. All curves were deduced for a vacuum nest depth $\phi_{\text{nest}} \approx 40\,\text{V}$. For clarity, curves are only shown in 2 V-increments of $\phi_{\text{nest,eff}}$. Without a plasma ($\phi_{\text{nest,eff}} = \phi_{\text{nest}}$), the overlap fraction is zero at all ion energies, as expected.

C.6 Overview of the simulation procedure

The procedural flow of a cooling simulation is illustrated by the flow charts in Fig. C.4 and will be outlined in the following paragraphs.

At the beginning of a simulation run initial ion energies $E_{\parallel}$ are sampled from a truncated normal distribution with a user-defined mean and standard deviation, and the lower bound of the distribution fixed to the minimum of the trap potential. In the case of K^{+} and Rb^{+},

the ion masses were randomly selected from the respective naturally-occurring isotopes, with probability weights chosen to respect the natural isotopic abundances. Isotopes with a natural abundance $< 1\%$ were not considered.

The main program then iterates the simulation time with a fixed step size of typically $\Delta t = 1\,\text{ms}$. Within each time step, the following procedures are executed for each ion:

1. *Check if an ion-neutral collision occurred in the time interval* $[t,t+\Delta t)$: To this end, a random number $x \in \mathcal{U}(0,1)$ is drawn and compared to the bounce-averaged collision probability,

$$P_{\text{coll}}(\Delta t) = 1 - \exp\left(-\sum_k v_{\text{eff}}\, n_k\, \sigma(v_{\text{eff}})\, \Delta t\right), \tag{C.20}$$

   where the $\sigma_{\text{tot,k}}$ are given by Eqn. C.12, and the velocity scale factor in $v_{\text{eff}} = \lambda v_{\text{max}}$ is interpolated from the pre-calculated λ values. Only a single collisions per time step is permitted which is a fair simplification as $\nu_{\text{in}}^{-1} \gg \Delta t$. If $x \leq P_{\text{coll}}(\Delta t)$, an ion-neutral collision is to be modelled. Otherwise, the simulation directly advances to step 3.

2. *Model ion-neutral collision:* If an ion-neutral collision is to be modelled, the program proceeds as shown in the right flow chart of Fig. C.4. First, the type of the collision target is randomly selected from the user-specified residual gas components. To ensure that random selection correctly represents the relative collision frequencies, each neutral species (indexed by k) is probability-weighted with a factor $P_{\text{coll}} \propto 1 - \exp(-v_{\text{eff}}\, n_k \sigma_{\text{tot,k}} \delta t)$, where the adaptive orbit integration time step was typically $\delta t \leq 0.5\,\mu\text{s}$.

   Subsequently, the ions' axial position and velocity at the time of collision are determined by starting single ions from one of their turning-points in the trap potential and integrating over one axial half-oscillation. The time of collision is then randomly selected from all integration time steps with each step, t_j, probability-weighted by a factor $P_{\text{coll}}(t_j) = 1 - \exp(n_n \sigma_{\text{tot,n}} v(t_j)\, t_j)$, where the index n now refers to the pre-selected target species.

   Next, a linearly distributed impact parameter is generated from the relation $b = b_{\text{max}}\sqrt{y}$, with a random number $y \in \mathcal{U}(0,1)$. For $b > b_c$ the collision is modelled as a glanzing collision, otherwise as a Langevin collision. If the collision is of Langevin-type, another random number $x \in \mathcal{U}(0,1)$ is drawn to decide whether the collision is a regular Langevin collision ($x > P_{\text{CX}}$) or a charge exchange reaction ($x \leq P_{\text{CX}}$).

   For glanzing collisions, the COM collision angle θ is calculated from the impact parameter according to Eqn. C.13. For Langevin collisions, θ is drawn from the uniform distribution $\mathcal{U}(0,\pi)$. In the case of a glanzing or a regular Langevin collision, the ion's longitudinal energy loss $\Delta E_{\parallel,\text{coll}}$ is then calculated from Eqn. C.15. To simulate a charge exchange event, the ion is replaced with the ionized collision target ($m \to m_n$) and the energy loss is set to $\Delta E_{\parallel,\text{coll}} = E_\parallel - q\phi_{\text{eff}}(z_{\text{coll}}) - k_B T_n$. With

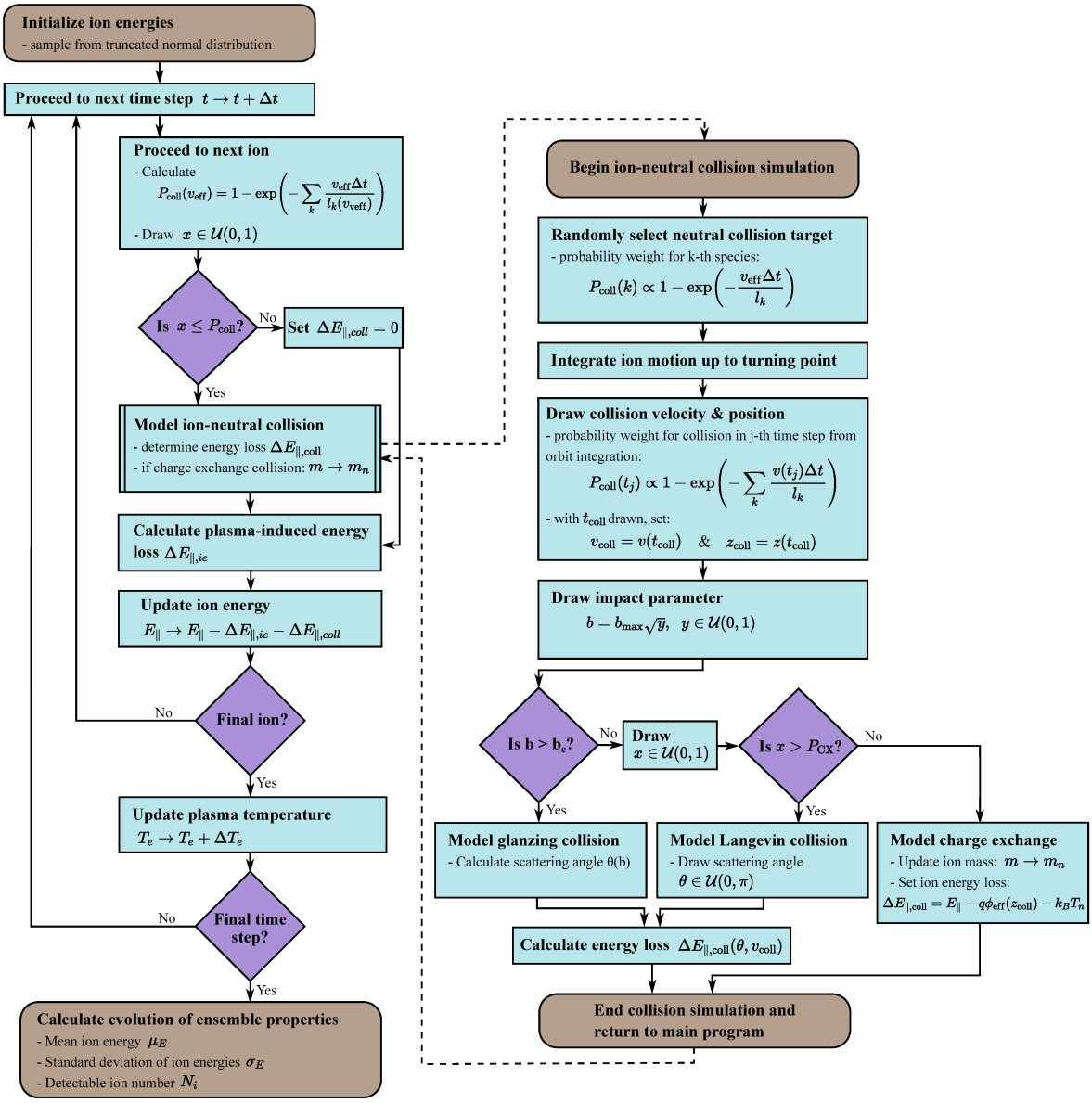

Figure C.4. Flow chart of the cooling simulations. The left half of the chart corresponds to the main program that loops over all simulated ions and time steps. Individual ion-neutral collisions are modelled by the subprogram shown in the right half of the chart. See text for details.

$\Delta E_{\parallel,\mathrm{coll}}$ determined, the simulation proceeds in the main program (left flow chart in Fig. C.4).

3. *Calculate plasma-induced energy loss and update ion energy:* After interpolating the pre-calculated ion-electron overlap factor κ to the given ion energy $E_\parallel$, the plasma-induced energy loss $\Delta E_{\parallel,ie}$ is calculated from a discretized version of Eqn. C.16. Subsequently, the obtained ion-neutral and ion-electron energy loss are subtracted from the total longitudinal energy, $E_\parallel$. Then the next ion is treated.

4. *Once the last ion has been processed, the plasma temperature is updated according to Eqn. C.17 and the simulation time is advanced.*

The listed steps are iterated until the specified simulation end time is reached. Then evolution of ensemble properties such as the ensemble-average and the standard deviation of the longitudinal ion energy are calculated and prepared for visualization.

Record of publications

Part of the material discussed in this thesis has been published in the articles labelled O1, O2 and O3. The other publications listed below report experimental results and technical developments that I contributed to over the course of my PhD work, but they did not form a central part of this thesis.

[O1] S. F. Paul, B. Kootte, D. Lascar, A. A. Kwiatkowski, G. Gwinner, J. Dilling, and the TITAN collaboration. Off-axis electron injection into a cooler Penning trap. *Hyperfine Interactions*, 240(1):50, 2019.

[O2] S. F. Paul, J. Bergmann, J. D. Cardona, K. A. Dietrich, E. Dunling, Z. Hockenbery, C. Hornung, C. Izzo, A. Jacobs, A. Javaji, B. Kootte, Y. Lan, E. Leistenschneider, E. M. Lykiardopoulou, I. Mukul, T. Murböck, W. S. Porter, R. Silwal, M. B. Smith, J. Ringuette, T. Brunner, T. Dickel, I. Dillmann, G. Gwinner, M. MacCormick, M. P. Reiter, H. Schatz, N. A. Smirnova, J. Dilling, and A. A. Kwiatkowski. Mass measurements of $^{60-63}$Ga reduce x-ray burst model uncertainties and extend the evaluated $T = 1$ isobaric multiplet mass equation. *Phys. Rev. C*, 104:065803, 12 2021. doi:10.1103/PhysRevC.104.065803.

[O3] R. Silwal, S. F. Paul, B. K. Kootte, T. Joseph, R. Simpson, A. A. Kwiatkowski, G. Gwinner, J. Dilling, and the TITAN collaboration. Ion simulations, recent upgrades and tests with TITAN's cooler Penning trap. In *24th Int. Workshop on ECR Ion Sources (ECRIS2020)*, 2020.

[O4] M. A. Blessenohl, S. Dobrodey, C. Warnecke, M. K. Rosner, L. Graham, S. Paul, T. M. Baumann, Z. Hockenbery, R. Hubele, T. Pfeifer, F. Ames, J. Dilling, and J. R. Crespo López-Urrutia. An electron beam ion trap and source for re-acceleration of rare-isotope ion beams at TRIUMF. *Review of Scientific Instruments*, 89, 05 2018. doi:10.1063/1.5021045.

[O5] C. Babcock, R. Klawitter, E. Leistenschneider, D. Lascar, B. R. Barquest, A. Finlay, M. Foster, A. T. Gallant, P. Hunt, B. Kootte, Y. Lan, S. F. Paul, M. L. Phan, M. P. Reiter, B. Schultz, D. Short, C. Andreoiu, M. Brodeur, I. Dillmann, G. Gwinner, A. A. Kwiatkowski, K. G. Leach, and J. Dilling. Mass measurements of neutron-rich indium isotopes toward the $N = 82$ shell closure. *Phys. Rev. C*, 97:024312, 2 2018. doi:10.1103/PhysRevC.97.024312.

[O6] M. P. Reiter, S. Ayet San Andrés, E. Dunling, B. Kootte, E. Leistenschneider, C. Andreoiu, C. Babcock, B. R. Barquest, J. Bollig, T. Brunner, I. Dillmann, A. Finlay, G. Gwinner, L. Graham, J. D. Holt, C. Hornung, C. Jesch, R. Klawitter, Y. Lan, D. Lascar, J. E. McKay, S. F. Paul, R. Steinbrügge, R. Thompson, J. L. Tracy, M. E. Wieser, C. Will, T. Dickel, W. R. Plaß, C. Scheidenberger, A. A. Kwiatkowski, and J. Dilling. Quenching of the $N = 32$ neutron shell closure studied via precision mass measurements of neutron-rich vanadium isotopes. *Phys. Rev. C*, 98:024310, 8 2018. doi:10.1103/PhysRevC.98.024310.

[O7] E. Leistenschneider, M. P. Reiter, S. Ayet San Andrés, B. Kootte, J. D. Holt, P. Navrátil, C. Babcock, C. Barbieri, B. R. Barquest, J. Bergmann, J. Bollig, T. Brunner, E. Dunling, A. Finlay, H. Geissel, L. Graham, F. Greiner, H. Hergert, C. Hornung, C. Jesch, R. Klawitter, Y. Lan, D. Lascar, K. G. Leach, W. Lippert, J. E. McKay, S. F. Paul, A. Schwenk, D. Short, J. Simonis, V. Somà, R. Steinbrügge, S. R. Stroberg, R. Thompson, M. E. Wieser, C. Will, M. Yavor, C. Andreoiu, T. Dickel, I. Dillmann, G. Gwinner, W. R. Plaß, C. Scheidenberger, A. A. Kwiatkowski, and J. Dilling. Dawning of the $N = 32$ shell closure seen through precision mass measurements of neutron-rich titanium isotopes. *Phys. Rev. Lett.*, 120:062503, 2 2018. doi:10.1103/PhysRevLett.120.062503.

[O8] I. Mukul, C. Andreoiu, M. Brodeur, T. Brunner, K. Dietrich, T. Dickel, I. Dillmann, E. Dunling, D. Fusco, G. Gwinner, C. Izzo, A. Jacobs, B. Kootte, Y. Lan, E. Leistenschneider, M. Lykiardopoulou, S. F. Paul, M. P. Reiter, J. L. Tracy, J. Dilling, and A. A. Kwiatkowski. Measuring the half-life of n-rich ^{100}Rb with the TITAN MR-TOF-MS. *Journal of Physics: Conference Series*, 1643:012057, dec 2020. doi:10.1088/1742-6596/1643/1/012057.

[O9] I. Mukul, C. Andreoiu, J. Bergmann, M. Brodeur, T. Brunner, K. A. Dietrich, T. Dickel, I. Dillmann, E. Dunling, D. Fusco, G. Gwinner, C. Izzo, A. Jacobs, B. Kootte, Y. Lan, E. Leistenschneider, E. M. Lykiardopoulou, S. F. Paul, M. P. Reiter, J. L. Tracy, J. Dilling, and A. A. Kwiatkowski. Examining the nuclear mass surface of Rb and Sr isotopes in the $A \approx 104$ region via precision mass measurements. *Phys. Rev. C*, 103:044320, 4 2021. doi:10.1103/PhysRevC.103.044320.

[O10] M. P. Reiter, S. Ayet San Andrés, S. Nikas, J. Lippuner, C. Andreoiu, C. Babcock, B. R. Barquest, J. Bollig, T. Brunner, T. Dickel, J. Dilling, I. Dillmann, E. Dunling, G. Gwinner, L. Graham, C. Hornung, R. Klawitter, B. Kootte, A. A. Kwiatkowski, Y. Lan, D. Lascar, K. G. Leach, E. Leistenschneider, G. Martínez-Pinedo, J. E. McKay, S. F. Paul, W. R. Plaß, L. Roberts, H. Schatz, C. Scheidenberger, A. Sieverding, R. Steinbrügge, R. Thompson, M. E. Wieser, C. Will, and D. Welch. Mass measurements of neutron-rich gallium isotopes refine production of nuclei of the first r-process abundance peak in neutron-star merger calculations. *Phys. Rev. C*, 101:025803, 2 2020. doi:10.1103/PhysRevC.101.025803.

[O11] M. P. Reiter, F. Ames, C. Andreoiu, S. A. San Andrés, C. Babcock, B. Barquest, J. Bergmann, J. Bollig, T. Brunner, T. Dickel, J. Dilling, I. Dillmann, E. Dunling, A. Finlay, G. Gwinner, L. Graham, C. Hornung, B. Kootte, R. Klawitter, P. Kunz, Y. Lan, D. Lascar, J. Lassen, E. Leistenschneider, R. Li, J. McKay, M. Mostamand, S. F. Paul, W. R. Plaß, C. Scheidenberger, B. Schultz, R. Steinbrügge, A. Teigelhöfer, R. Thompson, M. Wieser, C. Will, and A. A. Kwiatkowski. Improved beam diagnostics and optimization at ISAC via TITAN's MR-TOF-MS. *Nuclear Instruments and Methods in Physics Research Section B: Beam Interactions with Materials and Atoms*, 463:431–436, 2020. doi:https://doi.org/10.1016/j.nimb.2019.04.034.

[O12] M. B. Smith, T. Murböck, E. Dunling, A. Jacobs, B. Kootte, Y. Lan, E. Leistenschneider, D. Lunney, E. M. Lykiardopoulou, I. Mukul, S. F. Paul, M. P. Reiter, C. Will, J. Dilling, and A. A. Kwiatkowski. High-precision mass measurement of neutron-rich ^{96}Kr. *Hyperfine Interactions*, 241(1):1 – 8, 2020. URL `https://doi.org/10.1007/s10751-020-01722-2`.

[O13] M. P. Reiter, S. A. San Andrés, J. Bergmann, T. Dickel, J. Dilling, A. Jacobs, A. A. Kwiatkowski, W. R. Plaß, C. Scheidenberger, D. Short, C. Will, C. Babcock, E. Dunling, A. Finlay, C. Hornung, C. Jesch, R. Klawitter, B. Kootte, D. Lascar, E. Leistenschneider, T. Murböck, S. F. Paul, and M. Yavor. Commissioning and performance of TITAN's multiple-reflection time-of-flight mass-spectrometer and isobar separator. *Nuclear Instruments and Methods in Physics Research Section A: Accelerators, Spectrometers, Detectors and Associated Equipment*, 1018:165823, 2021. doi:https://doi.org/10.1016/j.nima.2021.165823.

[O14] C. Izzo, J. Bergmann, K. A. Dietrich, E. Dunling, D. Fusco, A. Jacobs, B. Kootte, G. Kripkó-Koncz, Y. Lan, E. Leistenschneider, E. M. Lykiardopoulou, I. Mukul, S. F. Paul, M. P. Reiter, J. L. Tracy, C. Andreoiu, T. Brunner, T. Dickel, J. Dilling, I. Dillmann, G. Gwinner, D. Lascar, K. G. Leach, W. R. Plaß, C. Scheidenberger, M. E. Wieser, and A. A. Kwiatkowski. Mass measurements of neutron-rich indium isotopes for r-process studies. *Phys. Rev. C*, 103:025811, 2 2021. doi:10.1103/PhysRevC.103.025811.

[O15] S. Beck, B. Kootte, I. Dedes, T. Dickel, A. A. Kwiatkowski, E. M. Lykiardopoulou, W. R. Plaß, M. P. Reiter, C. Andreoiu, J. Bergmann, T. Brunner, D. Curien, J. Dilling, J. Dudek, E. Dunling, J. Flowerdew, A. Gaamouci, L. Graham, G. Gwinner, A. Jacobs, R. Klawitter, Y. Lan, E. Leistenschneider, N. Minkov, V. Monier, I. Mukul, S. F. Paul, C. Scheidenberger, R. I. Thompson, J. L. Tracy, M. Vansteenkiste, H.-L. Wang, M. E. Wieser, C. Will, and J. Yang. Mass measurements of neutron-deficient Yb isotopes and nuclear structure at the extreme proton-rich side of the $N = 82$ shell. *Phys. Rev. Lett.*, 127:112501, Sep 2021. doi:10.1103/PhysRevLett.127.112501.

[O16] W. S. Porter, E. Dunling, E. Leistenschneider, J. Bergmann, G. Bollen, T. Dickel, K. A. Dietrich, A. Hamaker, Z. Hockenbery, C. Izzo, A. Jacobs, A. Javaji, B. Kootte,

Y. Lan, I. Miskun, I. Mukul, T. Murböck, S. F. Paul, W. R. Plaß, D. Puentes, M. Redshaw, M. P. Reiter, R. Ringle, J. Ringuette, R. Sandler, C. Scheidenberger, R. Silwal, R. Simpson, C. S. Sumithrarachchi, A. Teigelhöfer, A. A. Valverde, R. Weil, I. T. Yandow, J. Dilling, and A. A. Kwiatkowski. Investigating nuclear structure near $N = 32$ and $N = 34$: Precision mass measurements of neutron-rich Ca, Ti, and V isotopes. *Phys. Rev. C*, 106:024312, Aug 2022. doi:10.1103/PhysRevC.106.024312.

[O17] A. Jacobs, C. Andreoiu, J. Bergmann, T. Brunner, T. Dickel, I. Dillmann, E. Dunling, J. Flowerdew, L. Graham, G. Gwinner, Z. Hockenbery, B. Kootte, Y. Lan, K. G. Leach, E. Leistenschneider, E. Lykiardopoulou, V. Monier, I. Mukul, S. F. Paul, W. R. Plaß, M. P. Reiter, C. Scheidenberger, R. Thompson, J. Tracy, C. Will, M. Wieser, M. Yavor, J. Dilling, and A. A. Kwiatkowski. Collision-induced dissociation at TRIUMF's Ion Trap for Atomic and Nuclear science. *International Journal of Mass Spectrometry*, 482:116931, 2022. doi:https://doi.org/10.1016/j.ijms.2022.116931.

Bibliography

[1] K. Blaum. High-accuracy mass spectrometry with stored ions. *Physics Reports*, 425, 2006. doi: 10.1016/j.physrep.2005.10.011.

[2] K. Blaum, J. Dilling, and W. Nörtershäuser. Precision Atomic Physics Techniques for Nuclear Physics with Radioactive Beams. *Phys. Scripta*, T152:014017, 2013. doi: 10.1088/0031-8949/2013/T152/014017.

[3] J. Dilling, K. Blaum, M. Brodeur, and S. Eliseev. Penning-trap mass measurements in atomic and nuclear physics. *Annual Review of Nuclear and Particle Science*, 68(1): 45–74, 2018. doi: 10.1146/annurev-nucl-102711-094939. URL https://doi.org/10.1146/annurev-nucl-102711-094939.

[4] J. C. Hardy and I. S. Towner. Superallowed $0^+ \rightarrow 0^+$ nuclear β decays: 2020 critical survey, with implications for V_{ud} and CKM unitarity. *Phys. Rev. C*, 102:045501, 10 2020. doi: 10.1103/PhysRevC.102.045501. URL https://link.aps.org/doi/10.1103/PhysRevC.102.045501.

[5] H. Schatz. Nuclear masses in astrophysics. *International Journal of Mass Spectrometry*, 349-350:181 – 186, 2013. ISSN 1387-3806. doi: https://doi.org/10.1016/j.ijms.2013.03.016. URL https://www.sciencedirect.com/science/article/pii/S1387380613001073. 100 years of Mass Spectrometry.

[6] K. Langanke and H. Schatz. The role of radioactive ion beams in nuclear astrophysics. *Physica Scripta*, 2013(T152):014011, 2013.

[7] K. Blaum, S. Eliseev, T. Eronen, and Yu. Litvinov. Precision mass measurements for nuclear astro- and neutrino physics. *Journal of Physics Conference Series*, 381, 09 2012. doi: 10.1088/1742-6596/381/1/012013.

[8] E. P. Wigner. *in: Proc. Robert A. Welch Found. Conf. 1*, pages pp. 67 – 91, 1957. reproduced in: D. Robson, J. D. Fox (Eds.), Nuclear Analogue States, in: Benchmark Papers in Nuclear Physics, vol. 1, John Wiley & Sons, 1976, p. 39.

[9] P. Van Isacker, D. D. Warner, and D. S. Brenner. Test of Wigner's spin-isospin symmetry from double binding energy differences. *Phys. Rev. Lett.*, 74:4607 – 4610, 6 1995. doi: 10.1103/PhysRevLett.74.4607. URL https://link.aps.org/doi/10.1103/PhysRevLett.74.4607.

[10] D. Lunney, J. M. Pearson, and C. Thibault. Recent trends in the determination of nuclear masses. *Rev. Mod. Phys.*, 75:1021–1082, 8 2003. doi: 10.1103/RevModPhys.75.1021. URL https://link.aps.org/doi/10.1103/RevModPhys.75.1021.

[11] Y. Y. Cheng, M. Bao, Y. M. Zhao, and A. Arima. Wigner energy and nuclear mass relations. *Physical Review C*, 91(2):024313, 2015.

[12] P. J. Woods and C. N. Davids. Nuclei beyond the proton drip-line. *Annual Review of Nuclear and Particle Science*, 47(1):541 – 590, 1997. doi: 10.1146/annurev.nucl.47.1.541. URL https://doi.org/10.1146/annurev.nucl.47.1.541.

[13] J. Erler, N. Birge, M. Kortelainen, et al. The limits of the nuclear landscape. *Nature*, 486(7404):509 – 512, 2012.

[14] M. Thoennessen and B. Sherrill. From isotopes to the stars. *Nature*, 473(7345):25–26, 2011. ISSN 1476-4687. URL https://doi.org/10.1038/473025a.

[15] Y. Blumenfeld, T. Nilsson, and P. Van Duppen. Facilities and methods for radioactive ion beam production. *Physica Scripta*, T152:014023, 1 2013. doi: 10.1088/0031-8949/2013/t152/014023. URL https://doi.org/10.1088/0031-8949/2013/t152/014023.

[16] A. Chakrabarti, V. Naik, and S. Dechoudhury. *Rare Isotope Beams: Concepts and Techniques*. CRC Press, 2021. doi: https://doi.org/10.1201/9780429185885.

[17] M. Thoennessen. Reaching the limits of nuclear stability. *Reports on Progress in Physics*, 67(7):1187 – 1232, June 2004. doi: 10.1088/0034-4885/67/7/r04. URL https://doi.org/10.1088/0034-4885/67/7/r04.

[18] F. Wienholtz, D. Beck, K. Blaum, et al. Masses of exotic calcium isotopes pin down nuclear forces. *Nature*, 498(7454):346, 2013.

[19] E. Leistenschneider, M. P. Reiter, S. Ayet San Andrés, et al. Dawning of the $N = 32$ shell closure seen through precision mass measurements of neutron-rich titanium isotopes. *Phys. Rev. Lett.*, 120:062503, 2 2018. doi: 10.1103/PhysRevLett.120.062503. URL https://link.aps.org/doi/10.1103/PhysRevLett.120.062503.

[20] M. Goeppert Mayer. The shell model. *Science*, 145(3636):999–1006, 1964.

[21] T. Baumann, A. Spyrou, and M. Thoennessen. Nuclear structure experiments along the neutron drip line. *Reports on Progress in Physics*, 75(3):036301, Feb 2012. doi: 10.1088/0034-4885/75/3/036301. URL https://dx.doi.org/10.1088/0034-4885/75/3/036301.

[22] R. D. Page, P. J. Woods, R. A. Cunningham, et al. Radioactivity of neutron deficient isotopes in the region $N > 82 > Z$. *Phys. Rev. C*, 53:660–670, Feb 1996. doi: 10.1103/PhysRevC.53.660. URL https://link.aps.org/doi/10.1103/PhysRevC.53.660.

[23] C. Rauth, D. Ackermann, K. Blaum, et al. First Penning trap mass measurements beyond the proton drip line. *Phys. Rev. Lett.*, 100:012501, Jan 2008. doi: 10.1103/PhysRevLett.100.012501. URL https://link.aps.org/doi/10.1103/PhysRevLett.100.012501.

[24] J. A. Nolen and J. P. Schiffer. Coulomb energies. *Annual Review of Nuclear Science*, 19(1):471–526, 1969. doi: 10.1146/annurev.ns.19.120169.002351. URL https://doi.org/10.1146/annurev.ns.19.120169.002351.

[25] G. A. Miller, A. K. Opper, and E. J. Stephenson. Charge symmetry breaking and QCD. *Annual Review of Nuclear and Particle Science*, 56(1):253–292, 2006. doi: 10.1146/annurev.nucl.56.080805.140446. URL https://doi.org/10.1146/annurev.nucl.56.080805.140446.

[26] J. M. Dong, Y. H. Zhang, W. Zuo, et al. Generalized isobaric multiplet mass equation and its application to the Nolen-Schiffer anomaly. *Phys. Rev. C*, 97:021301, Feb 2018. doi: 10.1103/PhysRevC.97.021301. URL https://link.aps.org/doi/10.1103/PhysRevC.97.021301.

[27] W. E. Ormand and B. A. Brown. Empirical isospin-nonconserving Hamiltonians for shell-model calculations. *Nuclear Physics A*, 491(1):1 – 23, 1989. ISSN 0375-9474. doi: https://doi.org/10.1016/0375-9474(89)90203-0. URL https://www.sciencedirect.com/science/article/pii/0375947489902030.

[28] Y. H. Lam, N. A. Smirnova, and E. Caurier. Isospin nonconservation in sd-shell nuclei. *Phys. Rev. C*, 87:054304, May 2013. doi: 10.1103/PhysRevC.87.054304. URL https://link.aps.org/doi/10.1103/PhysRevC.87.054304.

[29] I. S. Towner and J. C. Hardy. Improved calculation of the isospin-symmetry-breaking corrections to superallowed Fermi β decay. *Phys. Rev. C*, 77:025501, 2 2008. doi: 10.1103/PhysRevC.77.025501. URL https://link.aps.org/doi/10.1103/PhysRevC.77.025501.

[30] A. D. MacLean, A. T. Laffoley, C. E. Svensson, et al. High-precision branching ratio measurement and spin assignment implications for ^{62}Ga superallowed β decay. *Phys. Rev. C*, 102:054325, Nov 2020. doi: 10.1103/PhysRevC.102.054325. URL https://link.aps.org/doi/10.1103/PhysRevC.102.054325.

[31] H. Schatz. The importance of nuclear masses in the astrophysical rp-process. *International Journal of Mass Spectrometry*, 251(2-3):293 – 299, 2006.

[32] A. Arcones, D. W. Bardayan, T. C. Beers, et al. White paper on nuclear astrophysics and low energy nuclear physics part 1: Nuclear astrophysics. *Progress in Particle and Nuclear Physics*, 94:1–67, 2017. ISSN 0146-6410. doi: https://doi.org/10.1016/j.ppnp.2016.12.003. URL https://www.sciencedirect.com/science/article/pii/S014664101630076X.

[33] Z. Meisel and A. Deibel. Constraints on bygone nucleosynthesis of accreting neutron stars. *The Astrophysical Journal*, 837(1):73, Mar 2017. doi: 10.3847/1538-4357/aa618d. URL https://doi.org/10.3847/1538-4357/aa618d.

[34] A. W. Steiner, J. M. Lattimer, and E. F. Brown. The equation of state from observed masses and radii of neutron stars. *The Astrophysical Journal*, 722(1):33–54, 9 2010. doi: 10.1088/0004-637x/722/1/33. URL https://doi.org/10.1088/0004-637x/722/1/33.

[35] James M. Lattimer. The nuclear equation of state and neutron star masses. *Annual Review of Nuclear and Particle Science*, 62(1):485–515, 2012. doi: 10.1146/annurev-nucl-102711-095018. URL https://doi.org/10.1146/annurev-nucl-102711-095018.

[36] J. M. Lattimer. Neutron stars and the nuclear matter equation of state. *Annual Review of Nuclear and Particle Science*, 71(1):433–464, 2021. doi: 10.1146/annurev-nucl-102419-124827. URL https://doi.org/10.1146/annurev-nucl-102419-124827.

[37] N. Chamel and P. Haensel. Physics of neutron star crusts. *Living Reviews in Relativity*, 11(1):1 – 182, 2008. URL https://doi.org/10.12942/lrr-2008-10.

[38] C.A. Bertulani and T. Kajino. Frontiers in nuclear astrophysics. *Progress in Particle and Nuclear Physics*, 89:56–100, 2016. ISSN 0146-6410. doi: https://doi.org/10.1016/j.ppnp.2016.04.001. URL https://www.sciencedirect.com/science/article/pii/S0146641016300011.

[39] D. K. Galloway and L. Keek. *Thermonuclear X-ray Bursts*, pages 209–262. Springer Berlin Heidelberg, Berlin, Heidelberg, 2021. ISBN 978-3-662-62110-3. doi: 10.1007/978-3-662-62110-3_5. URL https://doi.org/10.1007/978-3-662-62110-3_5.

[40] A. Heger, A. Cumming, D. K. Galloway, and S. E. Woosley. Models of type I X-ray bursts from GS 1826-24: A probe of rp-process hydrogen burning. *The Astrophysical Journal*, 671(2):L141–L144, 11 2007. doi: 10.1086/525522. URL https://doi.org/10.1086/525522.

[41] M. Zamfir, A. Cumming, and D. K. Galloway. Constraints on neutron star mass and radius in GS 1826–24 from sub-Eddington X-ray bursts. *The Astrophysical Journal*, 749(1):69, 3 2012. doi: 10.1088/0004-637x/749/1/69. URL https://doi.org/10.1088/0004-637x/749/1/69.

[42] Z. Meisel. Consistent modeling of GS 1826-24 X-ray bursts for multiple accretion rates demonstrates the possibility of constraining rp-process reaction rates. *The Astrophysical Journal*, 860(2):147, 6 2018. doi: 10.3847/1538-4357/aac3d3. URL https://doi.org/10.3847%2F1538-4357%2Faac3d3.

[43] Z. Meisel, G. Merz, and S. Medvid. Influence of nuclear reaction rate uncertainties on neutron star properties extracted from X-ray burst model–observation comparisons. *The Astrophysical Journal*, 872(1):84, 2 2019. doi: 10.3847/1538-4357/aafede. URL https://doi.org/10.3847%2F1538-4357%2Faafede.

[44] C. A. Raithel. Constraints on the neutron star equation of state from GW170817. *The European Physical Journal A*, 55(5):80, 2019. ISSN 1434-601X. URL https://doi.org/10.1140/epja/i2019-12759-5.

[45] C. Wolf, C. Langer, F. Montes, et al. Constraining the neutron star compactness: Extraction of the ^{23}Al(p,γ) reaction rate for the rp process. *Phys. Rev. Lett.*, 122: 232701, 6 2019. doi: 10.1103/PhysRevLett.122.232701. URL https://link.aps.org/doi/10.1103/PhysRevLett.122.232701.

[46] L. van Wormer, J. Görres, C. Iliadis, et al. Reaction Rates and Reaction Sequences in the rp-Process. *The Astrophysical Journal*, 432:326, 9 1994. doi: 10.1086/174572.

[47] H. Schatz, A. Aprahamian, J. Görres, et al. rp-process nucleosynthesis at extreme temperature and density conditions. *Physics Reports*, 294(4):167 – 263, 1998. ISSN 0370-1573. doi: https://doi.org/10.1016/S0370-1573(97)00048-3. URL https://www.sciencedirect.com/science/article/pii/S0370157397000483.

[48] H. Schatz, A. Aprahamian, V. Barnard, et al. End point of the *rp* process on accreting neutron stars. *Phys. Rev. Lett.*, 86:3471 – 3474, 4 2001. doi: 10.1103/PhysRevLett.86.3471. URL https://link.aps.org/doi/10.1103/PhysRevLett.86.3471.

[49] in 't Zand, J. J. M., Visser, M. E. B., Galloway, D. K., et al. Neutron star cooling and the rp process in thermonuclear X-ray bursts. *Astronomy & Astrophysics*, 606: A130, 2017. doi: 10.1051/0004-6361/201731281. URL https://doi.org/10.1051/0004-6361/201731281.

[50] R. H. Cyburt, A. M. Amthor, A. Heger, et al. Dependence of X-ray burst models on nuclear reaction rates. *The Astrophysical Journal*, 830(2):55, 10 2016. doi: 10.3847/0004-637x/830/2/55. URL https://doi.org/10.3847%2F0004-637x%2F830%2F2%2F55.

[51] H. Schatz and W.-J. Ong. Dependence of X-ray burst models on nuclear masses. *The Astrophysical Journal*, 844(2):139, 2017.

[52] J. Dilling, P. Bricault, M. Smith, and H.-J. Kluge. The proposed TITAN facility at ISAC for very precise mass measurements on highly charged short-lived isotopes. *Nuclear Instruments and Methods in Physics Research Section B: Beam Interactions with Materials and Atoms*, 204:492 – 496, 2003. ISSN 0168-583X. doi: https://doi.org/10.1016/S0168-583X(02)02118-3. URL http://www.sciencedirect.com/science/article/pii/S0168583X02021183. 14th International Conference on Electromagnetic Isotope Separators and Techniques Related to their Applications.

[53] A. A. Kwiatkowski, T. D. Macdonald, C. Andreoiu, et al. Precision mass measurements at TITAN with radioactive ions. *Nuclear Instruments and Methods in Physics Research Section B: Beam Interactions with Materials and Atoms*, 317, Part B:517 – 521, 2013. ISSN 0168-583X. doi: http://dx.doi.org/10.1016/j.nimb.2013.05.087. URL `http://www.sciencedirect.com/science/article/pii/S0168583X13007064`. XVIth International Conference on Electromagnetic Isotope Separators and Techniques Related to their Applications, December 27, 2012 at Matsue, Japan.

[54] C. Jesch, T Dickel, W. R. Plaß, et al. The MR-TOF-MS isobar separator for the TITAN facility at TRIUMF. In Michiharu Wada, Peter Schury, and Yuichi Ichikawa, editors, *TCP 2014*, pages 175 – 184, Cham, 2017. Springer International Publishing. ISBN 978-3-319-61588-2.

[55] V. V. Simon, U. Chowdhury, P. Delheij, et al. A cooler Penning trap for the TITAN on-line trapping facility. *Journal of Physics: Conference Series*, 312(5):052024, 2011. URL `http://stacks.iop.org/1742-6596/312/i=5/a=052024`.

[56] Erich Leistenschneider. *Dawning of nuclear magicity in $N = 32$ seen through precision mass spectrometry*. PhD thesis, University of British Columbia, 2019.

[57] E. M. Lykiardopoulou, C. Izzo, E. Leistenschneider, et al. Towards high precision mass measurements of highly charged ions using the phase-imaging ion-cyclotron-resonance technique at TITAN. *Hyperfine Interactions*, 241(1):1–7, 2020.

[58] J. Dilling, R. Baartman, P. Bricault, et al. Mass measurements on highly charged radioactive ions, a new approach to high precision with TITAN. *International Journal of Mass Spectrometry*, 251(2-3):198–203, 2006.

[59] A. Lapierre, M. Brodeur, T. Brunner, et al. The TITAN EBIT charge breeder for mass measurements on highly charged short-lived isotopes—first online operation. *Nuclear Instruments and Methods in Physics Research Section A: Accelerators, Spectrometers, Detectors and Associated Equipment*, 624, 2010. doi: 10.1016/j.nima.2010.09.030.

[60] M. Brodeur, V.L. Ryjkov, T. Brunner, et al. Verifying the accuracy of the TITAN Penning-trap mass spectrometer. *International Journal of Mass Spectrometry*, 310, 2012. doi: 10.1016/j.ijms.2011.11.002.

[61] S. Ettenauer, M. C. Simon, A. T. Gallant, et al. First use of high charge states for mass measurements of short-lived nuclides in a Penning trap. *Physical Review Letters*, 107, 12 2011. doi: 10.1103/PhysRevLett.107.272501.

[62] M. C. Simon, T. D. Macdonald, J. C. Bale, et al. Charge breeding rare isotopes for high precision mass measurements: Challenges and opportunities. *Physica Scripta*, 2013 (T156):014098, 2013. URL `http://stacks.iop.org/1402-4896/2013/i=T156/a=014098`.

[63] A. T. Gallant, M. Brodeur, T. Brunner, et al. Highly charged ions in Penning traps: A new tool for resolving low-lying isomeric states. *Physical Review C*, 85, 4 2012. doi: 10.1103/PhysRevC.85.044311.

[64] R. Schupp. Determination of beam properties of highly charged ions extracted from TITAN's electron beam ion trap. Master's thesis, Ruprecht-Karls-Universität Heidelberg, 2016.

[65] Z. Ke, W. Shi, G. Gwinner, et al. A cooler ion trap for the TITAN on-line trapping facility at TRIUMF. *Hyperfine Interactions*, 173(1):103–111, 2006. ISSN 1572-9540. doi: 10.1007/s10751-007-9548-x. URL http://dx.doi.org/10.1007/s10751-007-9548-x.

[66] A. Parikh, J. José, G. Sala, and C. Iliadis. Nucleosynthesis in type I X-ray bursts. *Progress in Particle and Nuclear Physics*, 69:225 – 253, 2013. ISSN 0146-6410. doi: https://doi.org/10.1016/j.ppnp.2012.11.002. URL https://www.sciencedirect.com/science/article/pii/S0146641012001354.

[67] Z. Meisel, A. Deibel, L. Keek, et al. Nuclear physics of the outer layers of accreting neutron stars. *Journal of Physics G: Nuclear and Particle Physics*, 45(9):093001, 7 2018. doi: 10.1088/1361-6471/aad171. URL https://doi.org/10.1088/1361-6471/aad171.

[68] Z. Johnston. *Modelling Thermonuclear X-ray Bursts on Accreting Neutron Stars*. PhD thesis, Monash University, 2020.

[69] D. K. Galloway, A. Cumming, E. Kuulkers, et al. Periodic thermonuclear X-ray bursts from gs 1826–24 and the fuel composition as a function of accretion rate. *The Astrophysical Journal*, 601(1):466, 2004.

[70] C. J. Hansen and H. M. Van Horn. Steady-state nuclear fusion in accreting neutron-star envelopes. *The Astrophysical Journal*, 195:735–741, 1975.

[71] H. Schatz and K. E. Rehm. X-ray binaries. *Nuclear Physics A*, 777:601 – 622, 2006. ISSN 0375-9474. doi: https://doi.org/10.1016/j.nuclphysa.2005.05.200. URL https://www.sciencedirect.com/science/article/pii/S0375947405008791. Special Issue on Nuclear Astrophysics.

[72] S. Bhattacharyya. Measurement of neutron star parameters: A review of methods for low-mass X-ray binaries. *Advances in Space Research*, 45(8):949–978, 2010. ISSN 0273-1177. doi: https://doi.org/10.1016/j.asr.2010.01.010. URL https://www.sciencedirect.com/science/article/pii/S0273117710000451.

[73] K.-L. Kratz, B. Pfeiffer, M. Hannawald, et al. Nuclear physics far from stability and explosive nucleosynthesis processes. *Il Nuovo Cimento A (1971-1996)*, 111(8-9):1043 – 1054, 1998. URL https://link.springer.com/article/10.1007/BF03035991.

[74] T. Rauscher, N. Dauphas, I. Dillmann, et al. Constraining the astrophysical origin of the p-nuclei through nuclear physics and meteoritic data. *Reports on Progress in Physics*, 76(6):066201, 5 2013. doi: 10.1088/0034-4885/76/6/066201. URL https://doi.org/10.1088/0034-4885/76/6/066201.

[75] N. Degenaar and V. F. Suleimanov. *Testing the Equation of State with Electromagnetic Observations*, pages 185–253. Springer International Publishing, Cham, 2018. ISBN 978-3-319-97616-7. doi: 10.1007/978-3-319-97616-7_5. URL https://doi.org/10.1007/978-3-319-97616-7_5.

[76] M. Zamfir. *Probing neutron star interiors with type I x-ray bursts*. McGill University (Canada), 2015.

[77] D. K. Galloway, Z. Johnston, A. Goodwin, and A. Heger. High-energy transients: Thermonuclear (Type-I) X-ray bursts: Invited talk. *Proceedings of the International Astronomical Union*, 14(S339):121–126, 2017. doi: 10.1017/S1743921318002363.

[78] A. J. Goodwin, D. K. Galloway, A. Heger, et al. A Bayesian approach to matching thermonuclear X-ray burst observations with models. *Monthly Notices of the Royal Astronomical Society*, 490(2):2228–2240, 9 2019. ISSN 0035-8711. doi: 10.1093/mnras/stz2638. URL https://doi.org/10.1093/mnras/stz2638.

[79] Z. Johnston, A. Heger, and D. K. Galloway. Multi-epoch X-ray burst modelling: MCMC with large grids of 1D simulations. 2020. doi: https://doi.org/10.48550/arXiv.1909.07977.

[80] J. M. Lattimer. Introduction to neutron stars. *AIP Conference Proceedings*, 1645(1):61–78, 2015. doi: 10.1063/1.4909560. URL https://aip.scitation.org/doi/abs/10.1063/1.4909560.

[81] A. Yu. Potekhin. Atmospheres and radiating surfaces of neutron stars. *Physics-Uspekhi*, 57(8):735–770, 8 2014. doi: 10.3367/ufne.0184.201408a.0793. URL https://doi.org/10.3367/ufne.0184.201408a.0793.

[82] P. Braun-Munzinger, V. Koch, T. Schäfer, and J. Stachel. Properties of hot and dense matter from relativistic heavy ion collisions. *Physics Reports*, 621:76–126, 2016. ISSN 0370-1573. doi: https://doi.org/10.1016/j.physrep.2015.12.003. URL https://www.sciencedirect.com/science/article/pii/S0370157315005013. Memorial Volume in Honor of Gerald E. Brown.

[83] J. M. Lattimer. Neutron star mass and radius measurements. *Universe*, 5(7), 2019. ISSN 2218-1997. doi: 10.3390/universe5070159. URL https://www.mdpi.com/2218-1997/5/7/159.

[84] A. W. Steiner, C. O. Heinke, S. Bogdanov, et al. Constraining the mass and radius of neutron stars in globular clusters. *Monthly Notices of the Royal Astronomical Society*,

476(1):421–435, 01 2018. ISSN 0035-8711. doi: 10.1093/mnras/sty215. URL https://doi.org/10.1093/mnras/sty215.

[85] G. Fiorella Burgio and Isaac Vidaña. The equation of state of nuclear matter: From finite nuclei to neutron stars. *Universe*, 6(8), 2020. ISSN 2218-1997. doi: 10.3390/universe6080119. URL https://www.mdpi.com/2218-1997/6/8/119.

[86] F. Özel, D. Psaltis, T. Güver, et al. The dense matter equation of state from neutron star radius and mass measurements. *The Astrophysical Journal*, 820(1):28, 3 2016. doi: 10.3847/0004-637x/820/1/28. URL https://doi.org/10.3847/0004-637x/820/1/28.

[87] J. R. Stone. Nuclear physics and astrophysics constraints on the high density matter equation of state. *Universe*, 7(8), 2021. ISSN 2218-1997. doi: 10.3390/universe7080257. URL https://www.mdpi.com/2218-1997/7/8/257.

[88] J. M. Lattimer. Neutron star masses and radii. *AIP Conference Proceedings*, 2127(1):020001, 2019. doi: 10.1063/1.5117791. URL https://aip.scitation.org/doi/abs/10.1063/1.5117791.

[89] I. Goldman. General relativistic effects and the radius and mass of X-ray bursters. *Astronomy and Astrophysics*, 78:L15, 1979.

[90] J. Van Paradijs. Possible observational constraints on the mass-radius relation of neutron stars. *The Astrophysical Journal*, 234:609–611, 1979.

[91] R. E. Taam. X-ray bursts from thermonuclear runaways on accreting neutron stars. *The Astrophysical Journal*, 241:358–366, 1980.

[92] T. Güver and F. Özel. The mass and the radius of the neutron star in the transient low-mass x-ray binary SAX j1748.9–2021. *The Astrophysical Journal*, 765(1):L1, 2 2013. doi: 10.1088/2041-8205/765/1/l1. URL https://doi.org/10.1088/2041-8205/765/1/l1.

[93] A. Parikh, J. José, C. Iliadis, et al. Impact of uncertainties in reaction Q values on nucleosynthesis in type I x-ray bursts. *Phys. Rev. C*, 79:045802, 4 2009. doi: 10.1103/PhysRevC.79.045802. URL https://link.aps.org/doi/10.1103/PhysRevC.79.045802.

[94] S. E Woosley, A. Heger, A. Cumming, et al. Models for type I X-ray bursts with improved nuclear physics. *The Astrophysical Journal Supplement Series*, 151(1):75, 2004.

[95] L. Keek, A. Heger, and J. J. M. in 't Zand. Superburst models for neutron stars with hydrogen- and helium-rich atmospheres. *The Astrophysical Journal*, 752(2):150, 6 2012. doi: 10.1088/0004-637x/752/2/150. URL https://doi.org/10.1088/0004-637x/752/2/150.

[96] D. Yakovlev and K. Levenfish. Pycnonuclear reactions and the physics of neutron star interiors. *PoS*, page 152, 2008.

[97] H. Schatz, S. Gupta, P. Müller, et al. Strong neutrino cooling by cycles of electron capture and β^- decay in neutron star crusts. *Nature*, 505(7481):62–65, 2014. ISSN 1476-4687. URL https://doi.org/10.1038/nature12757.

[98] A. Deibel, Z. Meisel, H. Schatz, et al. Urca cooling pairs in the neutron star ocean and their effect on superbursts. *The Astrophysical Journal*, 831(1):13, 10 2016. doi: 10.3847/0004-637x/831/1/13. URL https://doi.org/10.3847/0004-637x/831/1/13.

[99] R. Lau, M. Beard, S. S. Gupta, et al. Nuclear reactions in the crusts of accreting neutron stars. *The Astrophysical Journal*, 859(1):62, 5 2018. doi: 10.3847/1538-4357/aabfe0. URL https://doi.org/10.3847/1538-4357/aabfe0.

[100] A. Dohi, N. Nishimura, M. Hashimoto, et al. Effects of the nuclear equation of state on type I x-ray bursts: Interpretation of the x-ray bursts from GS 1826–24. *The Astrophysical Journal*, 923(1):64, 12 2021. doi: 10.3847/1538-4357/ac2821. URL https://doi.org/10.3847/1538-4357/ac2821.

[101] M. E. Caplan and C. J. Horowitz. Colloquium: Astromaterial science and nuclear pasta. *Rev. Mod. Phys.*, 89:041002, 10 2017. doi: 10.1103/RevModPhys.89.041002. URL https://link.aps.org/doi/10.1103/RevModPhys.89.041002.

[102] J. Grindlay, H. Gursky, H. Schnopper, et al. Discovery of intense x-ray bursts from the globular cluster NGC 6624. *The Astrophysical Journal*, 205:L127–L130, 1976.

[103] D. K. Galloway, M. P. Muno, J. M. Hartman, et al. Thermonuclear (Type I) X-ray bursts observed by the Rossi X-ray timing explorer. *The Astrophysical Journal Supplement Series*, 179(2):360 – 422, 12 2008. doi: 10.1086/592044. URL https://doi.org/10.1086/592044.

[104] F. A. Harrison, W. W. Craig, F. E. C., et al. The Nuclear Spectroscopic Telescope Array (NuSTAR) high energy X-ray mission. *The Astrophysical Journal*, 770(2):103, 5 2013. doi: 10.1088/0004-637x/770/2/103. URL https://doi.org/10.1088/0004-637x/770/2/103.

[105] J. V. Chauhan, J. S. Yadav, R. Misra, et al. AstroSat/LAXPC detection of millisecond phenomena in 4U 1728-34. *The Astrophysical Journal*, 841(1):41, 5 2017. doi: 10.3847/1538-4357/aa6d7e. URL https://doi.org/10.3847/1538-4357/aa6d7e.

[106] Z. Arzoumanian, K. C. Gendreau, C. L. Baker, et al. The neutron star interior composition explorer (NICER): mission definition. In Tadayuki Takahashi, Jan-Willem A. den Herder, and Mark Bautz, editors, *Space Telescopes and Instrumentation 2014: Ultraviolet to Gamma Ray*, volume 9144, pages 579 – 587. Interna-

tional Society for Optics and Photonics, SPIE, 2014. doi: 10.1117/12.2056811. URL https://doi.org/10.1117/12.2056811.

[107] D. K. Galloway, A. J. Goodwin, and L. Keek. Thermonuclear burst observations for model comparisons: A reference sample. *Publications of the Astronomical Society of Australia*, 34:E019, 2017. doi: 10.1017/pasa.2017.12.

[108] D. K. Galloway, J. in 't Zand, J. Chenevez, et al. The Multi-INstrument burst ARchive (MINBAR). *The Astrophysical Journal Supplement Series*, 249(2):32, 8 2020. doi: 10.3847/1538-4365/ab9f2e. URL https://doi.org/10.3847/1538-4365/ab9f2e.

[109] R. K. Wallace and S. E. Woosley. Explosive hydrogen burning. *The Astrophysical Journal Supplement Series*, 45:389 – 420, 1981.

[110] W. H. G. Lewin, J. Van Paradijs, and R. E. Taam. X-ray bursts. *Space Science Reviews*, 62(3):223–389, 1993. ISSN 1572-9672. URL https://doi.org/10.1007/BF00196124.

[111] J. J. M. in 't Zand, M. E. B. Visser, D. K. Galloway, et al. Neutron star cooling and the rp process in thermonuclear X-ray bursts. *Astronomy & Astrophysics*, 606: A130, 2017. doi: 10.1051/0004-6361/201731281. URL https://doi.org/10.1051/0004-6361/201731281.

[112] E. Kuulkers, M. H. van Kerkwijk, R. Cornelisse, et al. A half-a-day long thermonuclear X-ray burst from KS 1731-260. *Astronomy & Astrophysics*, 382(2):503–512, 2002.

[113] Andrew Cumming. Superbursts: A new probe of the rp-process. *Nuclear Physics A*, 758:439–446, 2005. ISSN 0375-9474. doi: https://doi.org/10.1016/j.nuclphysa.2005.05.081. URL https://www.sciencedirect.com/science/article/pii/S0375947405007335. Nuclei in the Cosmos VIII.

[114] N. Degenaar, R. Wijnands, and R. Kaur. Swift detection of an intermediately long x-ray burst from the very faint X-ray binary XMMU J174716. 1-281048. *Monthly Notices of the Royal Astronomical Society: Letters*, 414(1):L104–L108, 2011.

[115] J. J. E. Kajava, J. Nättilä, J. Poutanen, et al. Detection of burning ashes from thermonuclear X-ray bursts. *Monthly Notices of the Royal Astronomical Society: Letters*, 464(1):L6–L10, 8 2016. ISSN 1745-3925. doi: 10.1093/mnrasl/slw167. URL https://doi.org/10.1093/mnrasl/slw167.

[116] J. A. Hoffman, L. Cominsky, and W. H. G. Lewin. Repeatable, multiple-peaked structure in type I X-ray bursts. *The Astrophysical Journal Letters*, 240:L27–L31, August 1980. doi: 10.1086/183317.

[117] V. Suleimanov, J. Poutanen, and K. Werner. X-ray bursting neutron star atmosphere models using an exact relativistic kinetic equation for Compton scattering. *Astronomy & Astrophysics*, 545:A120, 9 2012. doi: 10.1051/0004-6361/201219480.

[118] J. Poutanen, J. Nättilä, J. J. E. Kajava, et al. The effect of accretion on the measurement of neutron star mass and radius in the low-mass X-ray binary 4U 1608-52. *Monthly Notices of the Royal Astronomical Society*, 442(4):3777–3790, 8 2014. doi: 10.1093/mnras/stu1139.

[119] J. Nättilä, V. F. Suleimanov, J. J. E. Kajava, and J. Poutanen. Models of neutron star atmospheres enriched with nuclear burning ashes. *Astronomy & Astrophysics*, 581: A83, 2015.

[120] R. D. Belian, J. P. Conner, and W. D. Evans. The discovery of X-ray bursts from a region in the constellation Norma. *The Astrophysical Journal*, 206:L135–L138, 1976.

[121] P. C. Joss. Helium-burning flashes on an accreting neutron star - A model for X-ray burst sources. *The Astrophysical Journal*, 225:L123–L127, 1978.

[122] T. Hanawa, D. Sugimoto, and M.-A. Hashimoto. Nucleosynthesis in explosive hydrogen burning and its implications in ten-minute interval of X-ray bursts. *Publications of the Astronomical Society of Japan*, 35:491–506, 1983.

[123] S. E. Woosley and T. A. Weaver. Repeated thermonuclear flashes on an accreting neutron star. *AIP Conference Proceedings*, 115(1):273–297, 1984. doi: 10.1063/1.34531. URL `https://aip.scitation.org/doi/abs/10.1063/1.34531`.

[124] O. Koike, M. Hashimoto, K. Arai, and S. Wanajo. Rapid proton capture on accreting neutron stars-effects of uncertainty in the nuclear process. *Astronomy and Astrophysics*, 342:464 – –473, 1999.

[125] T. A. Weaver, G. B. Zimmerman, and S. E. Woosley. Presupernova evolution of massive stars. *The Astrophysical Journal*, 225:1021–1029, 1978.

[126] J. Hu, H. Yamaguchi, Y. H. Lam, et al. Advancement of photospheric radius expansion and clocked type-I X-ray burst models with the new $^{22}\mathrm{Mg}(\alpha, p)^{25}\mathrm{Al}$ reaction rate determined at the Gamow energy. *Phys. Rev. Lett.*, 127:172701, 10 2021. doi: 10.1103/PhysRevLett.127.172701. URL `https://link.aps.org/doi/10.1103/PhysRevLett.127.172701`.

[127] L. Keek and A. Heger. Multi-zone models of superbursts from accreting neutron stars. *The Astrophysical Journal*, 743(2):189, 12 2011. doi: 10.1088/0004-637x/743/2/189. URL `https://doi.org/10.1088/0004-637x/743/2/189`.

[128] A. Spitkovsky, Y. Levin, and G. Ushomirsky. Propagation of thermonuclear flames on rapidly rotating neutron stars: Extreme weather during type I X-ray bursts. *The*

Astrophysical Journal, 566(2):1018–1038, 2 2002. doi: 10.1086/338040. URL https://doi.org/10.1086/338040.

[129] A. Parikh, J. José, and G. Sala. Classical novae and type I X-ray bursts: Challenges for the 21st century. *AIP Advances*, 4(4):041002, 2014. doi: 10.1063/1.4863946. URL https://doi.org/10.1063/1.4863946.

[130] A. Parikh, J. José, F. Moreno, and C. Iliadis. The effects of variations in nuclear processes on type I X-ray burst nucleosynthesis. *The Astrophysical Journal Supplement Series*, 178(1):110 – 136, 9 2008. doi: 10.1086/589879. URL https://doi.org/10.1086/589879.

[131] S. Guillot, M. Servillat, N. A. Webb, and R. E. Rutledge. Measurement of the radius of neutron stars with high signal-to-noise quiescent low-mass X-ray bunaries in globular clusters. *The Astrophysical Journal*, 772(1):7, Jun 2013. doi: 10.1088/0004-637x/772/1/7. URL https://doi.org/10.1088/0004-637x/772/1/7.

[132] A. Bauswein, O. Just, H.-T. Janka, and N. Stergioulas. Neutron-star radius constraints from GW170817 and future detections. *The Astrophysical Journal*, 850(2):L34, 11 2017. doi: 10.3847/2041-8213/aa9994. URL https://doi.org/10.3847/2041-8213/aa9994.

[133] F. J. Fattoyev, J. Piekarewicz, and C. J. Horowitz. Neutron skins and neutron stars in the multimessenger era. *Phys. Rev. Lett.*, 120:172702, 4 2018. doi: 10.1103/PhysRevLett.120.172702. URL https://link.aps.org/doi/10.1103/PhysRevLett.120.172702.

[134] S. Koranda, N. Stergioulas, and J. L. Friedman. Upper limits set by causality on the rotation and mass of uniformly rotating relativistic stars. *The Astrophysical Journal*, 488(2):799–806, 10 1997. doi: 10.1086/304714. URL https://doi.org/10.1086/304714.

[135] R. H. Cyburt, A. M. Amthor, R. Ferguson, et al. The JINA REACLIB database: Its recent updates and impact on type-I X-ray bursts. *The Astrophysical Journal Supplement Series*, 189(1):240 – 252, 7 2010. doi: 10.1088/0067-0049/189/1/240.

[136] A. Kankainen, Yu. N. Novikov, H. Schatz, and C. Weber. *Mass measurements of neutron-deficient nuclei and their implications for astrophysics*, pages 345–363. Springer Netherlands, Dordrecht, 2014. ISBN 978-94-007-5555-0. doi: 10.1007/978-94-007-5555-0_27. URL https://doi.org/10.1007/978-94-007-5555-0_27.

[137] H. Schatz. Rare isotopes in thermonuclear explosions on neutron stars. *Progress in Particle and Nuclear Physics*, 66(2):277–282, 2011. ISSN 0146-6410. doi: https://doi.org/10.1016/j.ppnp.2011.01.020. URL https://www.sciencedirect.com/science/article/pii/S0146641011000214. Particle and Nuclear Astrophysics.

[138] J. L. Fisker, H. Schatz, and F.-K. Thielemann. Explosive hydrogen burning during type I X-ray bursts. *The Astrophysical Journal Supplement Series*, 174(1):261–276, 1 2008. doi: 10.1086/521104. URL https://doi.org/10.1086/521104.

[139] M. Wiescher, G. P. A. Berg, M. Couder, et al. Astrophysical nuclear reactions and the break-out from the hot CNO cycles. *Progress in Particle and Nuclear Physics*, 59(1):51–65, 2007. ISSN 0146-6410. doi: https://doi.org/10.1016/j.ppnp.2007.01.021. URL https://www.sciencedirect.com/science/article/pii/S0146641007000221. International Workshop on Nuclear Physics 28th Course.

[140] J. Görres, M. Wiescher, and F.-K. Thielemann. Bridging the waiting points: The role of two-proton capture reactions in the rp process. *Phys. Rev. C*, 51:392–400, 1 1995. doi: 10.1103/PhysRevC.51.392. URL https://link.aps.org/doi/10.1103/PhysRevC.51.392.

[141] W. Hauser and H. Feshbach. The inelastic scattering of neutrons. *Phys. Rev.*, 87:366–373, 7 1952. doi: 10.1103/PhysRev.87.366. URL https://link.aps.org/doi/10.1103/PhysRev.87.366.

[142] T. Rauscher and F.-K. Thielemann. Astrophysical reaction rates from statistical model calculations. *Atomic Data and Nuclear Data Tables*, 75(1):1–351, 2000. ISSN 0092-640X. doi: https://doi.org/10.1006/adnd.2000.0834. URL https://www.sciencedirect.com/science/article/pii/S0092640X00908349.

[143] J. L. Fisker, V. Barnard, J. Görres, et al. Shell model based reaction rates for rp-process nuclei in the mass range $A = 44 - 63$. *Atomic Data and Nuclear Data Tables*, 79(2):241–292, 2001. ISSN 0092-640X. doi: https://doi.org/10.1006/adnd.2001.0867. URL https://www.sciencedirect.com/science/article/pii/S0092640X01908678.

[144] Y. H. Lam, J. J. He, A. Parikh, et al. Reaction rates of ^{64}Ge(p,γ)^{65}As and ^{65}As(p,γ)^{66}Se and the extent of nucleosynthesis in type I X-ray bursts. *The Astrophysical Journal*, 818(1):78, Feb 2016. doi: 10.3847/0004-637x/818/1/78. URL https://doi.org/10.3847/0004-637x/818/1/78.

[145] S.-B. Ma, L.-Y. Zhang, and J. Hu. Stellar reaction rate of ^{55}Ni(p, γ)^{56}Cu in type I X-ray bursts. *Nuclear Science and Techniques*, 30(9):1 – 9, 2019.

[146] A. J. Koning and D. Rochman. Modern nuclear data evaluation with the TALYS code system. *Nuclear Data Sheets*, 113(12):2841 – 2934, 2012. ISSN 0090-3752. doi: https://doi.org/10.1016/j.nds.2012.11.002. URL https://www.sciencedirect.com/science/article/pii/S0090375212000889. Special Issue on Nuclear Reaction Data.

[147] H. Schatz, C. A. Bertulani, B. A. Brown, et al. Revised result for the ^{32}Cl$(p,\gamma)^{33}$Ar reaction rate for astrophysical rp-process calculations. *Phys. Rev. C*, 72:065804, 12

2005. doi: 10.1103/PhysRevC.72.065804. URL https://link.aps.org/doi/10.1103/PhysRevC.72.065804.

[148] W.-J. Ong, C. Langer, F. Montes, et al. Low-lying level structure of ^{56}Cu and its implications for the *rp* process. *Phys. Rev. C*, 95:055806, 5 2017. doi: 10.1103/PhysRevC.95.055806. URL https://link.aps.org/doi/10.1103/PhysRevC.95.055806.

[149] C. R. Brune and B. Davids. Radiative capture reactions in astrophysics. *Annual Review of Nuclear and Particle Science*, 65(1):87–112, 2015. doi: 10.1146/annurev-nucl-102014-022027. URL https://doi.org/10.1146/annurev-nucl-102014-022027.

[150] T. Rauscher. The path to improved reaction rates for astrophysics. *International Journal of Modern Physics E*, 20(05):1071–1169, 2011.

[151] M. Wang, W. J. Huang, F. G. Kondev, et al. The AME 2020 atomic mass evaluation (II). Tables, graphs and references. *Chinese Physics C*, 45(3):030003, 3 2021. doi: 10.1088/1674-1137/abddaf. URL https://doi.org/10.1088/1674-1137/abddaf.

[152] W. J. Huang, M. Wang, F. G. Kondev, et al. The AME2020 atomic mass evaluation (I). Evaluation of input data, and adjustment procedures. *Chinese Physics C*, 45 (3):030002, 3 2021. doi: 10.1088/1674-1137/abddb0. URL https://doi.org/10.1088/1674-1137/abddb0.

[153] N. N. Duy, P.-T. Ho, and N. K. Uyen. Examination of the astrophysical-rate variations of the key reactions in the rp-process due to mass uncertainties. *Journal of the Korean Physical Society*, 76:881 – 888, 2020. URL https://doi.org/10.3938/jkps.76.881.

[154] M. Saxena, W.-J. Ong, Z. Meisel, et al. ^{57}Zn β-delayed proton emission establishes the ^{56}Ni rp-process waiting point bypass. *Physics Letters B*, 829:137059, 2022. ISSN 0370-2693. doi: https://doi.org/10.1016/j.physletb.2022.137059. URL https://www.sciencedirect.com/science/article/pii/S0370269322001939.

[155] B. Blank, S. Andriamonje, S. Czajkowski, et al. New isotopes from ^{78}Kr fragmentation and the ending point of the astrophysical rapid-proton-capture process. *Phys. Rev. Lett.*, 74:4611–4614, Jun 1995. doi: 10.1103/PhysRevLett.74.4611. URL https://link.aps.org/doi/10.1103/PhysRevLett.74.4611.

[156] C. Mazzocchi, Z. Janas, J. Döring, et al. First measurement of β-decay properties of the proton drip-line nucleus ^{60}Ga. *The European Physical Journal A-Hadrons and Nuclei*, 12(3):269–277, 2001.

[157] B. Blank, C. Borcea, G. Canchel, et al. Production cross-sections of proton-rich ^{70}Ge fragments and the decay of ^{57}Zn and ^{61}Ge. *The European Physical Journal A*, 31(3): 267 – 272, 2007.

[158] C. F. v. Weizsäcker. Zur Theorie der Kernmassen. *Zeitschrift für Physik*, 96(7):431–458, 1935. ISSN 0044-3328. URL https://doi.org/10.1007/BF01337700.

[159] H. A. Bethe and R. F. Bacher. Nuclear physics A. stationary states of nuclei. *Rev. Mod. Phys.*, 8:82–229, 4 1936. doi: 10.1103/RevModPhys.8.82. URL https://link.aps.org/doi/10.1103/RevModPhys.8.82.

[160] P. R. Chowdhury, C. Samanta, and D. N. Basu. Modified Bethe-Weizsäcker mass with isotonic shift and new driplines. *Modern Physics Letters A*, 20(21):1605–1618, 2005. doi: 10.1142/S021773230501666X. URL https://doi.org/10.1142/S021773230501666X.

[161] M. W. Kirson. Mutual influence of terms in a semi-empirical mass formula. *Nuclear Physics A*, 798(1):29–60, 2008. ISSN 0375-9474. doi: https://doi.org/10.1016/j.nuclphysa.2007.10.011. URL https://www.sciencedirect.com/science/article/pii/S0375947407007531.

[162] V. M. Strutinsky. Shell effects in nuclear masses and deformation energies. *Nuclear Physics A*, 95(2):420–442, 1967. ISSN 0375-9474. doi: https://doi.org/10.1016/0375-9474(67)90510-6. URL https://www.sciencedirect.com/science/article/pii/0375947467905106.

[163] Peter Möller. Essentials of the macroscopic-microscopic folded-Yukawa approach and examples of its record in providing nuclear-structure data for simulations. In *EPJ Web of Conferences*, volume 184, page 01013. EDP Sciences, 2018.

[164] P. Möller, A. J. Sierk, T. Ichikawa, and H. Sagawa. Nuclear ground-state masses and deformations: FRDM(2012). *Atomic Data and Nuclear Data Tables*, 109-110:1–204, 2016. ISSN 0092-640X. doi: https://doi.org/10.1016/j.adt.2015.10.002. URL https://www.sciencedirect.com/science/article/pii/S0092640X1600005X.

[165] N. Wang, M. Liu, X. Wu, and J. Meng. Surface diffuseness correction in global mass formula. *Physics Letters B*, 734:215–219, 2014. ISSN 0370-2693. doi: https://doi.org/10.1016/j.physletb.2014.05.049. URL https://www.sciencedirect.com/science/article/pii/S037026931400358X.

[166] P. Möller, W. D. Myers, W. J. Swiatecki, and J. Treiner. Nuclear mass formula with a finite-range droplet model and a folded-Yukawa single-particle potential. *Atomic Data and Nuclear Data Tables*, 39(2):225–233, 1988. ISSN 0092-640X. doi: https://doi.org/10.1016/0092-640X(88)90023-X. URL https://www.sciencedirect.com/science/article/pii/0092640X8890023X.

[167] W. D. Myers and W. J Swiatecki. Average nuclear properties. *Annals of Physics*, 55(3):395–505, 1969. ISSN 0003-4916. doi: https://doi.org/10.1016/0003-4916(69)90202-4. URL https://www.sciencedirect.com/science/article/pii/0003491669902024.

[168] N. Wang, M. Liu, and X. Wu. Modification of nuclear mass formula by considering isospin effects. *Phys. Rev. C*, 81:044322, Apr 2010. doi: 10.1103/PhysRevC.81.044322. URL https://link.aps.org/doi/10.1103/PhysRevC.81.044322.

[169] A. Sobiczewski, Yu. A. Litvinov, and M. Palczewski. Detailed illustration of the accuracy of currently used nuclear-mass models. *Atomic Data and Nuclear Data Tables*, 119:1 – 32, 2018. ISSN 0092-640X. doi: https://doi.org/10.1016/j.adt.2017.05.001. URL http://www.sciencedirect.com/science/article/pii/S0092640X17300323.

[170] J. M. Pearson, S. Goriely, and N. Chamel. Microscopic mass models for astrophysics. *International Journal of Mass Spectrometry*, 349-350:57–62, 2013. ISSN 1387-3806. doi: https://doi.org/10.1016/j.ijms.2013.04.003. URL https://www.sciencedirect.com/science/article/pii/S1387380613001292. 100 years of Mass Spectrometry.

[171] P. Navrátil, S. Quaglioni, G. Hupin, et al. Unified ab initio approaches to nuclear structure and reactions. *Physica Scripta*, 91(5):053002, 4 2016. doi: 10.1088/0031-8949/91/5/053002. URL https://doi.org/10.1088/0031-8949/91/5/053002.

[172] H. Hergert. A guided tour of ab initio nuclear many-body theory. *Frontiers in Physics*, 8, 2020. ISSN 2296-424X. doi: 10.3389/fphy.2020.00379. URL https://www.frontiersin.org/article/10.3389/fphy.2020.00379.

[173] T. H. R. Skyrme. The effective nuclear potential. *Nuclear Physics*, 9(4):615–634, 1958.

[174] S. Goriely, S. Hilaire, M. Girod, and S. Péru. First Gogny-Hartree-Fock-Bogoliubov nuclear mass model. *Phys. Rev. Lett.*, 102:242501, 6 2009. doi: 10.1103/PhysRevLett.102.242501. URL https://link.aps.org/doi/10.1103/PhysRevLett.102.242501.

[175] D. Peña-Arteaga, S. Goriely, and N. Chamel. Relativistic mean-field mass models. *The European Physical Journal A*, 52(10):320–, 2016. ISSN 1434-601X. URL https://doi.org/10.1140/epja/i2016-16320-x.

[176] M. Bender, P.-H. Heenen, and P.-G. Reinhard. Self-consistent mean-field models for nuclear structure. *Rev. Mod. Phys.*, 75:121–180, 1 2003. doi: 10.1103/RevModPhys.75.121. URL https://link.aps.org/doi/10.1103/RevModPhys.75.121.

[177] J. Erler, N. Birge, M. Kortelainen, et al. Microscopic nuclear mass table with high-performance computing. *Journal of Physics: Conference Series*, 402:012030, 12 2012. doi: 10.1088/1742-6596/402/1/012030. URL https://doi.org/10.1088/1742-6596/402/1/012030.

[178] M. Stoitsov, W. Nazarewicz, and N. Schunck. Large-scale mass table calculations. *International Journal of Modern Physics E*, 18(04):816–822, 2009. doi: 10.1142/S0218301309012914. URL https://doi.org/10.1142/S0218301309012914.

[179] J. Bartel, P. Quentin, M. Brack, et al. Towards a better parametrisation of Skyrme-like effective forces: A critical study of the SkM force. *Nuclear Physics A*, 386(1):79 – 100, 1982. ISSN 0375-9474. doi: https://doi.org/10.1016/0375-9474(82)90403-1. URL https://www.sciencedirect.com/science/article/pii/0375947482904031.

[180] S. Goriely, N. Chamel, and J. M. Pearson. Further explorations of Skyrme-Hartree-Fock-Bogoliubov mass formulas. XVI. Inclusion of self-energy effects in pairing. *Phys. Rev. C*, 93:034337, Mar 2016. doi: 10.1103/PhysRevC.93.034337. URL https://link.aps.org/doi/10.1103/PhysRevC.93.034337.

[181] S. Goriely, N. Chamel, and J. M. Pearson. HFB mass models for nucleosynthesis applications. *Journal of the Korean Physical Society*, 59(2):2100–2105, 2011.

[182] J. M. Pearson, N. Chamel, A. F. Fantina, and S. Goriely. Symmetry energy: nuclear masses and neutron stars. *The European Physical Journal A*, 50(2):43–, 2014. ISSN 1434-601X. URL https://doi.org/10.1140/epja/i2014-14043-8.

[183] R. N. Wolf, F. Wienholtz, D. Atanasov, et al. ISOLTRAP's multi-reflection time-of-flight mass separator/spectrometer. *International Journal of Mass Spectrometry*, 349-350:123–133, 2013. ISSN 1387-3806. doi: https://doi.org/10.1016/j.ijms.2013.03.020. URL https://www.sciencedirect.com/science/article/pii/S1387380613001115. 100 years of Mass Spectrometry.

[184] A. Sobiczewski and Yu. A. Litvinov. Accuracy of theoretical descriptions of nuclear masses. *Phys. Rev. C*, 89:024311, 2 2014. doi: 10.1103/PhysRevC.89.024311. URL https://link.aps.org/doi/10.1103/PhysRevC.89.024311.

[185] G. Audi and A. H. Wapstra. The 1993 atomic mass evaluation: (I) Atomic mass table. *Nuclear Physics A*, 565(1):1–65, 1993. ISSN 0375-9474. doi: https://doi.org/10.1016/0375-9474(93)90024-R. URL https://www.sciencedirect.com/science/article/pii/037594749390024R.

[186] G. T. Garvey and I. Kelson. New nuclidic mass relationship. *Phys. Rev. Lett.*, 16:197 – 200, 1 1966. doi: 10.1103/PhysRevLett.16.197. URL https://link.aps.org/doi/10.1103/PhysRevLett.16.197.

[187] I. Kelson and G. T. Garvey. Masses of nuclei with $Z > N$. *Physics Letters*, 23(12):689 – 692, 1966. ISSN 0031-9163. doi: https://doi.org/10.1016/0031-9163(66)91102-4. URL https://www.sciencedirect.com/science/article/pii/0031916366911024.

[188] J. Jänecke and P. J. Masson. Mass predictions from the Garvey-Kelson mass relations. *Atomic Data and Nuclear Data Tables*, 39(2):265 – 271, 1988. ISSN 0092-640X. doi: https://doi.org/10.1016/0092-640X(88)90028-9. URL https://www.sciencedirect.com/science/article/pii/0092640X88900289.

[189] G. J. Fu, Y. Lei, H. Jiang, et al. Description and evaluation of nuclear masses based on residual proton-neutron interactions. *Phys. Rev. C*, 84:034311, Sep 2011. doi: 10.1103/PhysRevC.84.034311. URL https://link.aps.org/doi/10.1103/PhysRevC.84.034311.

[190] H. Jiang, G. J. Fu, B. Sun, et al. Predictions of unknown masses and their applications. *Phys. Rev. C*, 85:054303, May 2012. doi: 10.1103/PhysRevC.85.054303. URL https://link.aps.org/doi/10.1103/PhysRevC.85.054303.

[191] Y. Y. Cheng, Y. M. Zhao, and A. Arima. Reconstitution of local mass relations. *Phys. Rev. C*, 90:064304, Dec 2014. doi: 10.1103/PhysRevC.90.064304. URL https://link.aps.org/doi/10.1103/PhysRevC.90.064304.

[192] E. Tiesinga, P. J. Mohr, D. B. Newell, and B. N. Taylor. CODATA Recommended values of the fundamental physical constants: 2018. *Journal of Physical and Chemical Reference Data*, 50(3):033105, 2021. doi: 10.1063/5.0064853. URL https://doi.org/10.1063/5.0064853.

[193] Y. H. Lam, B. Blank, N. A. Smirnova, et al. The isobaric multiplet mass equation for $A \leq 71$ revisited. *Atomic Data and Nuclear Data Tables*, 99(6):680 – 703, 2013. ISSN 0092-640X. doi: https://doi.org/10.1016/j.adt.2012.11.002. URL https://www.sciencedirect.com/science/article/pii/S0092640X13000569.

[194] S. Shlomo. Nuclear coulomb energies. *Reports on Progress in Physics*, 41(7):957 – 1026, jul 1978. doi: 10.1088/0034-4885/41/7/001. URL https://doi.org/10.1088/0034-4885/41/7/001.

[195] W. E. Ormand. Mapping the proton drip line up to $A = 70$. *Phys. Rev. C*, 55:2407 – 2417, May 1997. doi: 10.1103/PhysRevC.55.2407. URL https://link.aps.org/doi/10.1103/PhysRevC.55.2407.

[196] B. A. Brown, W. A. Richter, and R. Lindsay. Displacement energies with the Skyrme Hartree–Fock method. *Physics Letters B*, 483(1-3):49 – 54, 2000.

[197] O. Klochko and N. A. Smirnova. Isobaric-multiplet mass equation in a macroscopic-microscopic approach. *Phys. Rev. C*, 103:024316, Feb 2021. doi: 10.1103/PhysRevC.103.024316. URL https://link.aps.org/doi/10.1103/PhysRevC.103.024316.

[198] M.S. Antony, A. Pape, and J. Britz. Coulomb displacement energies between analog levels for $3 \leq A \leq 239$. *Atomic Data and Nuclear Data Tables*, 66(1):1–63, 1997.

ISSN 0092-640X. doi: https://doi.org/10.1006/adnd.1997.0740. URL https://www.sciencedirect.com/science/article/pii/S0092640X97907403.

[199] B. A. Brown, R. R. C. Clement, H. Schatz, et al. Proton drip-line calculations and the rp process. *Phys. Rev. C*, 65:045802, 3 2002. doi: 10.1103/PhysRevC.65.045802. URL https://link.aps.org/doi/10.1103/PhysRevC.65.045802.

[200] K. Kaneko, Y. Sun, T. Mizusaki, and S. Tazaki. Variation in displacement energies due to isospin-nonconserving forces. *Phys. Rev. Lett.*, 110:172505, Apr 2013. doi: 10.1103/PhysRevLett.110.172505. URL https://link.aps.org/doi/10.1103/PhysRevLett.110.172505.

[201] K. Kaneko, Y. Sun, T. Mizusaki, and S. Tazaki. Probing isospin-symmetry breaking with the modern storage rings and other advanced facilities. *Physica Scripta*, T166: 014011, Nov 2015. doi: 10.1088/0031-8949/2015/t166/014011. URL https://doi.org/10.1088/0031-8949/2015/t166/014011.

[202] M. A. Bentley and S. M. Lenzi. Coulomb energy differences between high-spin states in isobaric multiplets. *Progress in Particle and Nuclear Physics*, 59 (2):497 – 561, 2007. ISSN 0146-6410. doi: https://doi.org/10.1016/j.ppnp.2006.10.001. URL https://www.sciencedirect.com/science/article/pii/S0146641006000743.

[203] M. MacCormick and G. Audi. Evaluated experimental isobaric analogue states from $T = 1/2$ to $T = 3$ and associated IMME coefficients. *Nuclear Physics A*, 925:61 – 95, 2014. ISSN 0375-9474. doi: https://doi.org/10.1016/j.nuclphysa.2014.01.007. URL http://www.sciencedirect.com/science/article/pii/S0375947414000220.

[204] W. A. Richter, B. Alex Brown, A. Signoracci, and M. Wiescher. Properties of ^{26}Mg and ^{26}Si in the *sd* shell model and the determination of the ^{25}Al(p,γ)^{26}Si reaction rate. *Phys. Rev. C*, 83:065803, 6 2011. doi: 10.1103/PhysRevC.83.065803. URL https://link.aps.org/doi/10.1103/PhysRevC.83.065803.

[205] W. Richter and A. Brown. Application of the isobaric mass multiplet equation to the rp process in nuclear astrophysics. *Proceedings of Science*, Bormio 2013:022, 2013. doi: 10.22323/1.184.0022.

[206] Y. H. Lam, N. Lu, A. Heger, et al. The regulated NiCu cycles with the new ^{57}Cu(p,γ)^{58}Zn reaction rate and its influence on type I X-ray bursts: the GS 1826-24 clocked burster. *The Astrophysical Journal*, 929(1):73, 4 2022. doi: 10.3847/1538-4357/ac4d89. URL https://doi.org/10.3847/1538-4357/ac4d89.

[207] B. E. Glassman, D. Pérez-Loureiro, C. Wrede, et al. Revalidation of the isobaric multiplet mass equation for the $A = 20$ quintet. *Phys. Rev. C*, 92:042501, 10 2015.

doi: 10.1103/PhysRevC.92.042501. URL https://link.aps.org/doi/10.1103/PhysRevC.92.042501.

[208] J. Su, W. P. Liu, N. T. Zhang, et al. Revalidation of the isobaric multiplet mass equation at $A = 53$, $T = 3/2$. *Physics Letters B*, 756:323–327, 2016. ISSN 0370-2693. doi: https://doi.org/10.1016/j.physletb.2016.03.024. URL https://www.sciencedirect.com/science/article/pii/S0370269316001957.

[209] D. A. Nesterenko, A. Kankainen, L. Canete, et al. High-precision mass measurements for the isobaric multiplet mass equation at $A = 52$. *Journal of Physics G: Nuclear and Particle Physics*, 44(6):065103, apr 2017. doi: 10.1088/1361-6471/aa67ae. URL https://doi.org/10.1088/1361-6471/aa67ae.

[210] M. B. Bennett, C. Wrede, B. A. Brown, et al. Isobaric multiplet mass equation in the $A = 31$, $T = 3/2$ quartets. *Phys. Rev. C*, 93:064310, 6 2016. doi: 10.1103/PhysRevC.93.064310. URL https://link.aps.org/doi/10.1103/PhysRevC.93.064310.

[211] C. Y. Fu, Y. H. Zhang, M. Wang, et al. Mass measurements for the $T_z = -2$ fp-shell nuclei ^{40}Ti, ^{44}Cr, ^{46}Mn, ^{48}Fe, ^{50}Co, and ^{52}Ni. *Phys. Rev. C*, 102:054311, Nov 2020. doi: 10.1103/PhysRevC.102.054311. URL https://link.aps.org/doi/10.1103/PhysRevC.102.054311.

[212] M. Kamil, S. Triambak, A. Magilligan, et al. Isospin mixing and the cubic isobaric multiplet mass equation in the lowest $T = 2$, $A = 32$ quintet. *Phys. Rev. C*, 104: L061303, 12 2021. doi: 10.1103/PhysRevC.104.L061303. URL https://link.aps.org/doi/10.1103/PhysRevC.104.L061303.

[213] N. Auerbach. Coulomb effects in nuclear structure. *Physics Reports*, 98(5): 273–341, 1983. ISSN 0370-1573. doi: https://doi.org/10.1016/0370-1573(83)90008-X. URL https://www.sciencedirect.com/science/article/pii/037015738390008X.

[214] J. M. Dong, J. Z. Gu, Y. H. Zhang, et al. Beyond wigner's isobaric multiplet mass equation: Effect of charge-symmetry-breaking interaction and coulomb polarization. *Phys. Rev. C*, 99:014319, Jan 2019. doi: 10.1103/PhysRevC.99.014319. URL https://link.aps.org/doi/10.1103/PhysRevC.99.014319.

[215] W. A. Richter, B. A. Brown, R. Longland, et al. Shell-model studies of the astrophysical rp-process reactions ^{34}S$(p,\gamma)^{35}$Cl and ^{34g,m}Cl$(p,\gamma)^{35}$Ar. *Phys. Rev. C*, 102: 025801, 8 2020. doi: 10.1103/PhysRevC.102.025801. URL https://link.aps.org/doi/10.1103/PhysRevC.102.025801.

[216] Y. H. Lam, Z. X. Liu, A. Heger, et al. Impact of the new ^{65}As(p,$\gamma)^{66}$Se reaction rate on the two-proton sequential capture of ^{64}Ge, weak GeAs cycles, and type I X-ray bursts such as the clocked burster GS 1826-24. *The Astrophysical Journal*, 929(1):

72, 4 2022. doi: 10.3847/1538-4357/ac4d8b. URL https://doi.org/10.3847/1538-4357/ac4d8b.

[217] E. Caurier, G. Martínez-Pinedo, F. Nowacki, et al. The shell model as a unified view of nuclear structure. *Rev. Mod. Phys.*, 77:427–488, Jun 2005. doi: 10.1103/RevModPhys.77.427. URL https://link.aps.org/doi/10.1103/RevModPhys.77.427.

[218] P. Ring and P. Schuck. *The nuclear many-body problem*. Springer Science & Business Media, 1980.

[219] R. F. Casten. *Nuclear structure from a simple perspective*. Oxford University Press, 1990.

[220] B. A. Brown. The nuclear shell model towards the drip lines. *Progress in Particle and Nuclear Physics*, 47(2):517–599, 2001. ISSN 0146-6410. doi: https://doi.org/10.1016/S0146-6410(01)00159-4. URL https://www.sciencedirect.com/science/article/pii/S0146641001001594.

[221] L. Coraggio, A. Covello, A. Gargano, et al. Shell-model calculations and realistic effective interactions. *Progress in Particle and Nuclear Physics*, 62(1):135–182, 2009. ISSN 0146-6410. doi: https://doi.org/10.1016/j.ppnp.2008.06.001. URL https://www.sciencedirect.com/science/article/pii/S0146641008000410.

[222] S. R. Stroberg, H. Hergert, S. K. Bogner, and J. D. Holt. Nonempirical interactions for the nuclear shell model: An update. *Annual Review of Nuclear and Particle Science*, 69(1):307–362, 2019. doi: 10.1146/annurev-nucl-101917-021120. URL https://doi.org/10.1146/annurev-nucl-101917-021120.

[223] A. Magilligan and B. A. Brown. New isospin-breaking "USD" Hamiltonians for the sd shell. *Phys. Rev. C*, 101:064312, Jun 2020. doi: 10.1103/PhysRevC.101.064312. URL https://link.aps.org/doi/10.1103/PhysRevC.101.064312.

[224] B. H. Wildenthal. Empirical strengths of spin operators in nuclei. *Progress in Particle and Nuclear Physics*, 11:5–51, 1984. ISSN 0146-6410. doi: https://doi.org/10.1016/0146-6410(84)90011-5. URL https://www.sciencedirect.com/science/article/pii/0146641084900115.

[225] M. Honma, T. Otsuka, B. A. Brown, and T. Mizusaki. New effective interaction for pf-shell nuclei and its implications for the stability of the $N = Z = 28$ closed core. *Phys. Rev. C*, 69:034335, 3 2004. doi: 10.1103/PhysRevC.69.034335. URL https://link.aps.org/doi/10.1103/PhysRevC.69.034335.

[226] M. A. Bentley, S. M. Lenzi, S. A. Simpson, and C. A. Diget. Isospin-breaking interactions studied through mirror energy differences. *Phys. Rev. C*, 92:024310, 8 2015. doi: 10.1103/PhysRevC.92.024310. URL https://link.aps.org/doi/10.1103/PhysRevC.92.024310.

[227] N. A. Smirnova, B. Blank, B. A. Brown, et al. Isospin mixing from β-delayed proton emission. *Phys. Rev. C*, 95:054301, May 2017. doi: 10.1103/PhysRevC.95.054301. URL https://link.aps.org/doi/10.1103/PhysRevC.95.054301.

[228] W. E. Ormand and B. A. Brown. Isospin-mixing corrections for fp-shell Fermi transitions. *Phys. Rev. C*, 52:2455–2460, Nov 1995. doi: 10.1103/PhysRevC.52.2455. URL https://link.aps.org/doi/10.1103/PhysRevC.52.2455.

[229] L. Xayavong and N. A. Smirnova. Radial overlap correction to superallowed $0^+ \rightarrow 0^+$ β decay reexamined. *Phys. Rev. C*, 97:024324, 2 2018. doi: 10.1103/PhysRevC.97.024324. URL https://link.aps.org/doi/10.1103/PhysRevC.97.024324.

[230] J. C. Hardy and I. S. Towner. Superallowed $0^+ \rightarrow 0^+$ nuclear β decays: 2014 critical survey, with precise results for V_{ud} and CKM unitarity. *Phys. Rev. C*, 91:025501, 2 2015. doi: 10.1103/PhysRevC.91.025501. URL https://link.aps.org/doi/10.1103/PhysRevC.91.025501.

[231] A. Signoracci and B. A. Brown. Effects of isospin mixing in the $A = 32$ quintet. *Phys. Rev. C*, 84:031301, Sep 2011. doi: 10.1103/PhysRevC.84.031301. URL https://link.aps.org/doi/10.1103/PhysRevC.84.031301.

[232] A. Magilligan. *Isospin-symmetry breaking interactions in the nuclear shell modeL*. PhD thesis, Michigan State University, 2021.

[233] K. Kaneko, S. Tazaki, T. Mizusaki, et al. Isospin symmetry breaking at high spins in the mirror pair ^{67}Se and ^{67}As. *Phys. Rev. C*, 82:061301, Dec 2010. doi: 10.1103/PhysRevC.82.061301. URL https://link.aps.org/doi/10.1103/PhysRevC.82.061301.

[234] K. Kaneko, T. Mizusaki, Y. Sun, et al. Coulomb energy difference as a probe of isospin-symmetry breaking in the upper fp-shell nuclei. *Phys. Rev. Lett.*, 109:092504, Aug 2012. doi: 10.1103/PhysRevLett.109.092504. URL https://link.aps.org/doi/10.1103/PhysRevLett.109.092504.

[235] J. Henderson, D. G. Jenkins, K. Kaneko, et al. Spectroscopy on the proton drip-line: Probing the structure dependence of isospin nonconserving interactions. *Phys. Rev. C*, 90:051303, 11 2014. doi: 10.1103/PhysRevC.90.051303. URL https://link.aps.org/doi/10.1103/PhysRevC.90.051303.

[236] A. Gadea, S. M. Lenzi, S. Lunardi, et al. Observation of ^{54}Ni: Cross-conjugate symmetry in $f_{7/2}$ mirror energy differences. *Phys. Rev. Lett.*, 97:152501, Oct 2006. doi: 10.1103/PhysRevLett.97.152501. URL https://link.aps.org/doi/10.1103/PhysRevLett.97.152501.

[237] W. E. Ormand, B. A. Brown, and M. Hjorth-Jensen. Realistic calculations for c coefficients of the isobaric mass multiplet equation in 1p0f shell nuclei. *Physical Review C*, 96(2):024323, 2017.

[238] K. Kaneko, Y. Sun, T. Mizusaki, and S. Tazaki. Isospin nonconserving interaction in the $T = 1$ analogue states of the mass-70 region. *Phys. Rev. C*, 89:031302, Mar 2014. doi: 10.1103/PhysRevC.89.031302. URL https://link.aps.org/doi/10.1103/PhysRevC.89.031302.

[239] P. Baczyk, J. Dobaczewski, M. Konieczka, et al. Isospin-symmetry breaking in masses of $N \simeq Z$ nuclei. *Physics Letters B*, 778:178 – 183, 2018. ISSN 0370-2693. doi: https://doi.org/10.1016/j.physletb.2017.12.068. URL http://www.sciencedirect.com/science/article/pii/S0370269318300170.

[240] D. Puentes, G. Bollen, M. Brodeur, et al. High-precision mass measurements of the isomeric and ground states of ^{44}V: Improving constraints on the isobaric multiplet mass equation parameters of the $A = 44$, 0^+ quintet. *Phys. Rev. C*, 101:064309, Jun 2020. doi: 10.1103/PhysRevC.101.064309. URL https://link.aps.org/doi/10.1103/PhysRevC.101.064309.

[241] M. Honma, T. Otsuka, B. A. Brown, and T. Mizusaki. Shell-model description of neutron-rich pf-shell nuclei with a new effective interaction GXPF 1. *The European Physical Journal A - Hadrons and Nuclei*, 25(1):499–502, 2005. ISSN 1434-601X. URL https://doi.org/10.1140/epjad/i2005-06-032-2.

[242] M. Wang, G. Audi, F. G. Kondev, et al. The AME2016 atomic mass evaluation (II). Tables, graphs and references. *Chinese Physics C*, 41(3):030003, 2017. URL http://stacks.iop.org/1674-1137/41/i=3/a=030003.

[243] R. Sandler, G. Bollen, J. Dissanayake, et al. Direct determination of the ^{138}La β-decay Q value using Penning trap mass spectrometry. *Phys. Rev. C*, 100:014308, 7 2019. doi: 10.1103/PhysRevC.100.014308. URL https://link.aps.org/doi/10.1103/PhysRevC.100.014308.

[244] J. Van Schelt, D. Lascar, G. Savard, et al. Mass measurements near the r-process path using the Canadian penning trap mass spectrometer. *Phys. Rev. C*, 85:045805, 4 2012. doi: 10.1103/PhysRevC.85.045805. URL https://link.aps.org/doi/10.1103/PhysRevC.85.045805.

[245] E. Roeckl. Decay experiments on $N \sim Z$ nuclei: The role of masses, Q values and separation energies. *Hyperfine Interactions*, 132(1):153–161, 2001. ISSN 1572-9540. URL https://doi.org/10.1023/A:1011906108641.

[246] R. C. Greenwood and M. H. Putnam. Measurement of β^- end-point energies using a Ge detector with Monte Carlo generated response functions. *Nuclear Instruments and Methods in Physics Research Section A: Accelerators, Spectrometers, Detectors and Associated Equipment*, 337(1):106–115, 1993. ISSN 0168-9002. doi: https://doi.org/10.1016/0168-9002(93)91142-A. URL https://www.sciencedirect.com/science/article/pii/016890029391142A.

[247] A. Kankainen, L. Batist, S. A. Eliseev, et al. Mass measurements of neutron-deficient nuclides close to $A = 80$ with a Penning trap. *The European Physical Journal A - Hadrons and Nuclei*, 29(3):271–280, 2006. ISSN 1434-601X. URL https://doi.org/10.1140/epja/i2006-10088-6.

[248] S. Rahaman, U. Hager, V. V. Elomaa, et al. Precise atomic masses of neutron-rich Br and Rb nuclei close to the r-process path. *The European Physical Journal A*, 32(1):87–96, 2007. ISSN 1434-601X. URL https://doi.org/10.1140/epja/i2006-10297-y.

[249] U. Hager, T. Eronen, J. Hakala, et al. First precision mass measurements of refractory fission fragments. *Phys. Rev. Lett.*, 96:042504, 2 2006. doi: 10.1103/PhysRevLett.96.042504. URL https://link.aps.org/doi/10.1103/PhysRevLett.96.042504.

[250] A. Kankainen, J. Hakala, T. Eronen, et al. Isomeric states close to doubly magic ^{132}sn studied with the double Penning trap JYFLTRAP. *Phys. Rev. C*, 87:024307, 2 2013. doi: 10.1103/PhysRevC.87.024307. URL https://link.aps.org/doi/10.1103/PhysRevC.87.024307.

[251] B. Franzke. The heavy ion storage and cooler ring project ESR at GSI. *Nuclear Instruments and Methods in Physics Research Section B: Beam Interactions with Materials and Atoms*, 24-25:18–25, 1987. ISSN 0168-583X. doi: https://doi.org/10.1016/0168-583X(87)90583-0. URL https://www.sciencedirect.com/science/article/pii/0168583X87905830.

[252] T. Dickel, W. R. Plaß, A. Becker, et al. A high-performance multiple-reflection time-of-flight mass spectrometer and isobar separator for the research with exotic nuclei. *Nuclear Instruments and Methods in Physics Research Section A: Accelerators, Spectrometers, Detectors and Associated Equipment*, 777:172–188, 2015. ISSN 0168-9002. doi: https://doi.org/10.1016/j.nima.2014.12.094. URL https://www.sciencedirect.com/science/article/pii/S0168900214015629.

[253] B. Schlitt, K. Beckert, F. Bosch, et al. Schottky mass spectrometry at the ESR: A novel tool for precise direct mass measurements of exotic nuclei. *Nuclear Physics A*, 626(1):315–325, 1997. ISSN 0375-9474. doi: https://doi.org/10.1016/S0375-9474(97)00552-6. URL https://www.sciencedirect.com/science/article/pii/S0375947497005526. Proceedings of the Third International Conference on Nuclear Physics at Storage Rings.

[254] W. R. Plaß, T. Dickel, and C. Scheidenberger. Multiple-reflection time-of-flight mass spectrometry. *International Journal of Mass Spectrometry*, 349-350:134–144, 2013. ISSN 1387-3806. doi: https://doi.org/10.1016/j.ijms.2013.06.005. URL https://www.sciencedirect.com/science/article/pii/S138738061300239X. 100 years of Mass Spectrometry.

[255] K. Blaum, S. Eliseev, and S. Sturm. Perspectives on testing fundamental physics with highly charged ions in Penning traps. *Quantum Science and Technology*, 6(1): 014002, 11 2020. doi: 10.1088/2058-9565/abbc75. URL https://doi.org/10.1088/2058-9565/abbc75.

[256] P. G. Bricault, F. Ames, M. Dombsky, et al. Rare isotope beams at ISAC–target & ion source systems. *Hyperfine Interactions*, 225(1):25–49, 2014. ISSN 1572-9540. URL https://doi.org/10.1007/s10751-013-0880-z.

[257] D. J. Morrissey and B. M. Sherrill. *In-Flight Separation of Projectile Fragments*, pages 113–135. Springer Berlin Heidelberg, Berlin, Heidelberg, 2004. ISBN 978-3-540-44490-9. doi: 10.1007/978-3-540-44490-9_4. URL https://doi.org/10.1007/978-3-540-44490-9_4.

[258] G. Münzenberg. The separation techniques for secondary beams. *Nuclear Instruments and Methods in Physics Research Section B: Beam Interactions with Materials and Atoms*, 70(1):265–275, 1992. ISSN 0168-583X. doi: https://doi.org/10.1016/0168-583X(92)95942-K. URL https://www.sciencedirect.com/science/article/pii/0168583X9295942K.

[259] H. Geissel, P. Armbruster, K. H. Behr, et al. The GSI projectile fragment separator (frs): A versatile magnetic system for relativistic heavy ions. *Nuclear Instruments and Methods in Physics Research Section B: Beam Interactions with Materials and Atoms*, 70(1):286–297, 1992. ISSN 0168-583X. doi: https://doi.org/10.1016/0168-583X(92)95944-M. URL https://www.sciencedirect.com/science/article/pii/0168583X9295944M.

[260] M. Hausmann, J. Stadlmann, F. Attallah, et al. Isochronous mass measurements of hot exotic nuclei. *Hyperfine Interactions*, 132(1):289–295, 2001. ISSN 1572-9540. URL https://doi.org/10.1023/A:1011911720453.

[261] H. Geissel, H. Weick, M. Winkler, et al. The Super-FRS project at GSI. *Nuclear Instruments and Methods in Physics Research Section B: Beam Interactions with Materials and Atoms*, 204:71–85, 2003. ISSN 0168-583X. doi: https://doi.org/10.1016/S0168-583X(02)01893-1. URL https://www.sciencedirect.com/science/article/pii/S0168583X02018931. 14th International Conference on Electromagnetic Isotope Separators and Techniques Related to their Applications.

[262] G. Bollen, C. Campbell, S. Chouhan, et al. Manipulation of rare isotope beams – from high to low energies. *Nuclear Instruments and Methods in Physics Research Section B: Beam Interactions with Materials and Atoms*, 266(19):4442–4448, 2008. ISSN 0168-583X. doi: https://doi.org/10.1016/j.nimb.2008.05.058. URL https://www.sciencedirect.com/science/article/pii/S0168583X08007532. Proceedings of the XVth International Conference on Electromagnetic Isotope Separators and Techniques Related to their Applications.

[263] M. Wada, Y. Ishida, T. Nakamura, et al. Slow RI-beams from projectile fragment separators. *Nuclear Instruments and Methods in Physics Research Section B: Beam Interactions with Materials and Atoms*, 204:570–581, 2003. ISSN 0168-583X. doi: https://doi.org/10.1016/S0168-583X(02)02151-1. URL https://www.sciencedirect.com/science/article/pii/S0168583X02021511. 14th International Conference on Electromagnetic Isotope Separators and Techniques Related to their Applications.

[264] S. Purushothaman, M. P. Reiter, E. Haettner, et al. First experimental results of a cryogenic stopping cell with short-lived, heavy uranium fragments produced at 1000 MeV/u. *EPL (Europhysics Letters)*, 104(4):42001, 11 2013. doi: 10.1209/0295-5075/104/42001. URL https://doi.org/10.1209/0295-5075/104/42001.

[265] M. Facina, C. Bachelet, M. Block, et al. Charged particle transport and extraction studies in the NSCL gas cell for stopping radioactive fragments. *Nuclear Instruments and Methods in Physics Research Section B: Beam Interactions with Materials and Atoms*, 266(19):4471–4474, 2008. ISSN 0168-583X. doi: https://doi.org/10.1016/j.nimb.2008.05.052. URL https://www.sciencedirect.com/science/article/pii/S0168583X08007581. Proceedings of the XVth International Conference on Electromagnetic Isotope Separators and Techniques Related to their Applications.

[266] P. Kienle. Physics and present status of the GSI-SIS/ESR project. *Nuclear Physics A*, 478:847–860, 1988.

[267] H. G. Blosser. Superconducting cyclotrons at Michigan State University. *Nuclear Instruments and Methods in Physics Research Section B: Beam Interactions with Materials and Atoms*, 24-25:752–756, 1987. ISSN 0168-583X. doi: https://doi.org/10.1016/S0168-583X(87)80239-2. URL https://www.sciencedirect.com/science/article/pii/S0168583X87802392.

[268] T. Kubo, M. Ishihara, N. Inabe, et al. The RIKEN radioactive beam facility. *Nuclear Instruments and Methods in Physics Research Section B: Beam Interactions with Materials and Atoms*, 70(1):309–319, 1992. ISSN 0168-583X. doi: https://doi.org/10.1016/0168-583X(92)95947-P. URL https://www.sciencedirect.com/science/article/pii/0168583X9295947P.

[269] W. Henning. FAIR — an international accelerator facility for research with ions and antiprotons. *AIP Conference Proceedings*, 773(1):3–5, 2005. doi: 10.1063/1.1949487. URL https://aip.scitation.org/doi/abs/10.1063/1.1949487.

[270] G. Bollen. FRIB—Facility for Rare Isotope Beams. *AIP Conference Proceedings*, 1224(1):432–441, 2010. doi: 10.1063/1.3431449. URL https://aip.scitation.org/doi/abs/10.1063/1.3431449.

[271] P. Van Duppen. *Isotope Separation On Line and Post Acceleration*, pages 37–77. Springer Berlin Heidelberg, Berlin, Heidelberg, 2006. ISBN 978-3-540-33787-4. doi: 10.1007/3-540-33787-3_2. URL https://doi.org/10.1007/3-540-33787-3_2.

[272] A. Gottberg. Target materials for exotic ISOL beams. *Nuclear Instruments and Methods in Physics Research Section B: Beam Interactions with Materials and Atoms*, 376:8–15, 2016. ISSN 0168-583X. doi: https://doi.org/10.1016/j.nimb.2016.01.020. URL https://www.sciencedirect.com/science/article/pii/S0168583X16000689. Proceedings of the XVIIth International Conference on Electromagnetic Isotope Separators and Related Topics (EMIS2015), Grand Rapids, MI, U.S.A., 11-15 May 2015.

[273] P. Bricault, R. Baartman, M. Dombsky, et al. TRIUMF-ISAC target station and mass separator commissioning. *Nuclear Physics A*, 701(1):49–53, 2002. ISSN 0375-9474. doi: https://doi.org/10.1016/S0375-9474(01)01546-9. URL https://www.sciencedirect.com/science/article/pii/S0375947401015469. 5th International Conference on Radioactive Nuclear Beams.

[274] U. Köster, P. Carbonez, A. Dorsival, et al. (Im-)possible ISOL beams. *The European Physical Journal Special Topics*, 150(1):285–291, 11 2007. ISSN 1951-6401. doi: 10.1140/epjst/e2007-00326-1. URL https://doi.org/10.1140/epjst/e2007-00326-1.

[275] J. Dilling, R. Krücken, and G. Ball. ISAC overview. *Hyperfine Interactions*, 225(1):1–8, 2014.

[276] R. Catherall, W. Andreazza, M. Breitenfeldt, et al. The ISOLDE facility. *Journal of Physics G: Nuclear and Particle Physics*, 44(9):094002, 8 2017. doi: 10.1088/1361-6471/aa7eba. URL https://doi.org/10.1088/1361-6471/aa7eba.

[277] A. C. C. Villari. The accelerated ISOL technique and the SPIRAL project. *Nuclear Physics A*, 693(1):465–476, 2001. ISSN 0375-9474. doi: https://doi.org/10.1016/S0375-9474(01)01107-1. URL https://www.sciencedirect.com/science/article/pii/S0375947401011071. Radioactive Nuclear Beams.

[278] M. J. G. Borge and K. Riisager. HIE-ISOLDE, the project and the physics opportunities. *The European Physical Journal A*, 52(11):334–, 2016. ISSN 1434-601X. URL https://doi.org/10.1140/epja/i2016-16334-4.

[279] S. Gales. GANIL-SPIRAL2: a new era. *Journal of Physics: Conference Series*, 267:012009, 1 2011. doi: 10.1088/1742-6596/267/1/012009. URL https://doi.org/10.1088/1742-6596/267/1/012009.

[280] J. Dilling, R. Krücken, and L. Merminga. *ARIEL overview*, pages 253–262. Springer Netherlands, Dordrecht, 2014. ISBN 978-94-007-7963-1. doi: 10.1007/

978-94-007-7963-1_30. URL https://doi.org/10.1007/978-94-007-7963-1_30.

[281] B. Franzke, H. Geissel, and G. Münzenberg. Mass and lifetime measurements of exotic nuclei in storage rings. *Mass Spectrometry Reviews*, 27(5):428–469, 2008. doi: https://doi.org/10.1002/mas.20173. URL https://analyticalsciencejournals.onlinelibrary.wiley.com/doi/abs/10.1002/mas.20173.

[282] F. Bosch and Yu. A. Litvinov. Mass and lifetime measurements at the experimental storage ring of GSI. *International Journal of Mass Spectrometry*, 349-350:151–161, 2013. ISSN 1387-3806. doi: https://doi.org/10.1016/j.ijms.2013.04.025. URL https://www.sciencedirect.com/science/article/pii/S1387380613001528. 100 years of Mass Spectrometry.

[283] Y. H. Zhang, Yu. A. Litvinov, T. Uesaka, and H. S. Xu. Storage ring mass spectrometry for nuclear structure and astrophysics research. *Physica Scripta*, 91(7):073002, 6 2016. doi: 10.1088/0031-8949/91/7/073002. URL https://doi.org/10.1088/0031-8949/91/7/073002.

[284] J. W. Xia, W. L. Zhan, B. W. Wei, et al. The heavy ion cooler-storage-ring project (HIRFL-CSR) at Lanzhou. *Nuclear Instruments and Methods in Physics Research Section A: Accelerators, Spectrometers, Detectors and Associated Equipment*, 488(1):11–25, 2002. ISSN 0168-9002. doi: https://doi.org/10.1016/S0168-9002(02)00475-8. URL https://www.sciencedirect.com/science/article/pii/S0168900202004758.

[285] S. Naimi, H.F. Li, Y. Abe, et al. Experimental challenges of the first mass measurement campaign at the rare-RI ring. *Journal of Physics: Conference Series*, 1643(1):012058, 12 2020. doi: 10.1088/1742-6596/1643/1/012058. URL https://doi.org/10.1088/1742-6596/1643/1/012058.

[286] M. Grieser, Yu. A. Litvinov, R. Raabe, et al. Storage ring at HIE-ISOLDE. *The European Physical Journal Special Topics*, 207(1):1–117, 2012. ISSN 1951-6401. URL https://doi.org/10.1140/epjst/e2012-01599-9.

[287] P. Woods, K. Blaum, F. Bosch, et al. Nuclear astrophysics experiments at storage rings: midterm perspectives at GSI. *Physica Scripta*, T166:014002, 11 2015. doi: 10.1088/0031-8949/2015/t166/014002. URL https://doi.org/10.1088/0031-8949/2015/t166/014002.

[288] J. Glorius, C. Langer, Z. Slavkovská, et al. Approaching the Gamow window with stored ions: Direct measurement of ^{124}Xe(p,γ) in the ESR storage ring. *Phys. Rev. Lett.*, 122:092701, 3 2019. doi: 10.1103/PhysRevLett.122.092701. URL https://link.aps.org/doi/10.1103/PhysRevLett.122.092701.

[289] F. Herfurth, T. Beier, L. Dahl, et al. Precision measurements with highly charged ions at rest: The HITRAP project at GSI. *International Journal of Mass Spectrometry*, 251(2):266–272, 2006. ISSN 1387-3806. doi: https://doi.org/10.1016/j.ijms.2006.02.012. URL https://www.sciencedirect.com/science/article/pii/S1387380606001357. Ultra-accurate mass spectrometry and related topics - Dedicated to H.-J. Kluge on the occasion of his 65th birthday anniversary.

[290] M. Hausmann, F. Attallah, K. Beckert, et al. First isochronous mass spectrometry at the experimental storage ring ESR. *Nuclear Instruments and Methods in Physics Research Section A: Accelerators, Spectrometers, Detectors and Associated Equipment*, 446(3):569–580, 2000. ISSN 0168-9002. doi: https://doi.org/10.1016/S0168-9002(99)01192-4. URL https://www.sciencedirect.com/science/article/pii/S0168900299011924.

[291] B. Franzke, K. Beckert, H. Eickhoff, et al. Schottky mass spectrometry at the experimental storage ring ESR. *Physica Scripta*, T59:176–178, 1 1995. doi: 10.1088/0031-8949/1995/t59/021. URL https://doi.org/10.1088/0031-8949/1995/t59/021.

[292] M. Steck, P. Beller, K. Beckert, et al. Electron cooling experiments at the ESR. *Nuclear Instruments and Methods in Physics Research Section A: Accelerators, Spectrometers, Detectors and Associated Equipment*, 532(1):357–365, 2004. ISSN 0168-9002. doi: https://doi.org/10.1016/j.nima.2004.06.065. URL https://www.sciencedirect.com/science/article/pii/S0168900204012689. International Workshop on Beam Cooling and Related Topics.

[293] H. Poth. Electron cooling: Theory, experiment, application. *Physics Reports*, 196(3):135 – 297, 1990. ISSN 0370-1573. doi: http://dx.doi.org/10.1016/0370-1573(90)90040-9. URL http://www.sciencedirect.com/science/article/pii/0370157390900409.

[294] P. M. Walker, Yu. A. Litvinov, and H. Geissel. The ILIMA project at FAIR. *International Journal of Mass Spectrometry*, 349-350:247–254, 2013. ISSN 1387-3806. doi: https://doi.org/10.1016/j.ijms.2013.04.007. URL https://www.sciencedirect.com/science/article/pii/S1387380613001334. 100 years of Mass Spectrometry.

[295] J. Borer, P. Bramham, W. Schnell, et al. Non-destructive diagnostics of coasting beams with Schottky noise. Technical report, CM-P00063743, 1974.

[296] F. Nolden, P. Hülsmann, Yu.A. Litvinov, et al. A fast and sensitive resonant schottky pick-up for heavy ion storage rings. *Nuclear Instruments and Methods in Physics Research Section A: Accelerators, Spectrometers, Detectors and Associated Equipment*, 659(1):69–77, 2011. ISSN 0168-9002. doi: https://doi.org/10.1016/j.nima.

2011.06.058. URL https://www.sciencedirect.com/science/article/pii/S016890021101182X.

[297] F. Nolden, K. Beckert, P. Beller, et al. Experience and prospects of stochastic cooling of radioactive beams at GSI. *Nuclear Instruments and Methods in Physics Research Section A: Accelerators, Spectrometers, Detectors and Associated Equipment*, 532(1):329–334, 2004. ISSN 0168-9002. doi: https://doi.org/10.1016/j.nima.2004.06.062. URL https://www.sciencedirect.com/science/article/pii/S016890020401263X. International Workshop on Beam Cooling and Related Topics.

[298] F. Bosch. Schottky mass- and lifetime-spectrometry of unstable, stored ions. *Journal of Physics B: Atomic, Molecular and Optical Physics*, 36(3):585–597, 1 2003. doi: 10.1088/0953-4075/36/3/316. URL https://doi.org/10.1088/0953-4075/36/3/316.

[299] X. L. Tu, H. S. Xu, M. Wang, et al. Direct mass measurements of short-lived $A = 2Z-1$ nuclides ^{63}Ge, ^{65}As, ^{67}Se, and ^{71}Kr and their impact on nucleosynthesis in the rp process. *Phys. Rev. Lett.*, 106:112501, 3 2011. doi: 10.1103/PhysRevLett.106.112501. URL https://link.aps.org/doi/10.1103/PhysRevLett.106.112501.

[300] F. M. Penning. Verzögerungen bei der Zündung von gasgefüllten Photozellen im Dunkeln. *Physica*, 3(6):563–568, 1936.

[301] J. R. Pierce. *Theory and design of electron beams*, chapter 3. D. van Nostrand Co., New York, 1949.

[302] K. Blaum, Yu. N. Novikov, and G. Werth. Penning traps as a versatile tool for precise experiments in fundamental physics. *Contemporary Physics*, 51, 03 2010. doi: 10.1080/00107510903387652.

[303] G. Bollen. *Traps for Rare Isotopes*, pages 169–210. Springer Berlin Heidelberg, Berlin, Heidelberg, 2004. ISBN 978-3-540-44490-9. doi: 10.1007/978-3-540-44490-9_6. URL https://doi.org/10.1007/978-3-540-44490-9_6.

[304] C. Smorra, A. Mooser, K. Franke, et al. A reservoir trap for antiprotons. *International Journal of Mass Spectrometry*, 389:10–13, 2015. ISSN 1387-3806. doi: https://doi.org/10.1016/j.ijms.2015.08.007. URL https://www.sciencedirect.com/science/article/pii/S1387380615002560.

[305] G. Bollen, R. B. Moore, G. Savard, and H. Stolzenberg. The accuracy of heavy ion mass measurements using time of flight ion cyclotron resonance in a Penning trap. *Journal of Applied Physics*, 68(9):4355–4374, 1990. doi: http://dx.doi.org/10.1063/1.346185. URL http://scitation.aip.org/content/aip/journal/jap/68/9/10.1063/1.346185;jsessionid=M8_M2fHJRlwMPbmwodAhVMYS.x-aip-live-02.

[306] V. V. Simon. *Penning-Trap Mass Spectrometry of Radioactive, Highly Charged Ions: Measurements of neutron-rich Rb and Sr nuclides for nuclear astrophysics and the development of a novel Penning trap for cooling highly charged ions*. PhD thesis, Ruprecht-Karls-Universität Heidelberg, 2012.

[307] M. Kretzschmar. Particle motion in a Penning trap. *European Journal of Physics*, 12 (5):240, 1991. URL http://stacks.iop.org/0143-0807/12/i=5/a=010.

[308] L. S. Brown and G. Gabrielse. Geonium theory: Physics of a single electron or ion in a Penning trap. *Rev. Mod. Phys.*, 58:233–311, 1 1986. doi: 10.1103/RevModPhys.58.233. URL http://link.aps.org/doi/10.1103/RevModPhys.58.233.

[309] M. Brodeur, T. Brunner, C. Champagne, et al. New mass measurement of ^{6}Li and ppb-level systematic studies of the Penning trap mass spectrometer TITAN. *Phys. Rev. C*, 80:044318, 10 2009. doi: 10.1103/PhysRevC.80.044318. URL https://link.aps.org/doi/10.1103/PhysRevC.80.044318.

[310] M. Brodeur. *First direct mass measurement of the two and four neutron halos ^{6}He and ^{8}He using the TITAN Penning trap mass spectrometer*. PhD thesis, University of British Columbia, 2010.

[311] G. Gabrielse. Why is sideband mass spectrometry possible with ions in a Penning trap? *Phys. Rev. Lett.*, 102:172501, 4 2009. doi: 10.1103/PhysRevLett.102.172501. URL https://link.aps.org/doi/10.1103/PhysRevLett.102.172501.

[312] M. König, G. Bollen, H.-J. Kluge, et al. Quadrupole excitation of stored ion motion at the true cyclotron frequency. *International Journal of Mass Spectrometry and Ion Processes*, 142, 1995. doi: 10.1016/0168-1176(95)04146-c.

[313] A. A. Valverde, G. Bollen, M. Brodeur, et al. First direct determination of the superallowed β-decay Q_{EC} value for ^{14}O. *Phys. Rev. Lett.*, 114:232502, 6 2015. doi: 10.1103/PhysRevLett.114.232502. URL https://link.aps.org/doi/10.1103/PhysRevLett.114.232502.

[314] G. Savard, St. Becker, G. Bollen, et al. A new cooling technique for heavy ions in a Penning trap. *Physics Letters A*, 158(5):247 – 252, 1991. ISSN 0375-9601. doi: http://dx.doi.org/10.1016/0375-9601(91)91008-2. URL http://www.sciencedirect.com/science/article/pii/0375960191910082.

[315] G. Gräff, H. Kalinowsky, and J. Traut. A direct determination of the proton electron mass ratio. *Zeitschrift für Physik A Atoms and Nuclei*, 297(1):35–39, 1980. ISSN 0939-7922. URL https://doi.org/10.1007/BF01414243.

[316] R. Ringle, G. Bollen, A. Prinke, et al. A "Lorentz" steerer for ion injection into a Penning trap. *International Journal of Mass Spectrometry*, 263, 2007. doi: 10.1016/j.ijms.2006.12.008.

[317] K. Blaum, Sz. Nagy, and G. Werth. High-accuracy Penning trap mass measurements with stored and cooled exotic ions. *Journal of Physics B: Atomic, Molecular and Optical Physics*, 42(15):154015, 7 2009. doi: 10.1088/0953-4075/42/15/154015. URL https://doi.org/10.1088/0953-4075/42/15/154015.

[318] S. Eliseev, K. Blaum, M. Block, et al. A phase-imaging technique for cyclotron-frequency measurements. *Applied Physics B*, 114(1-2):107–128, 2014.

[319] F. Herfurth, J. Dilling, A. Kellerbauer, et al. Breakdown of the isobaric multiplet mass equation at $A = 33$, $T = 3/2$. *Phys. Rev. Lett.*, 87:142501, 9 2001. doi: 10.1103/PhysRevLett.87.142501. URL https://link.aps.org/doi/10.1103/PhysRevLett.87.142501.

[320] M. Smith, M. Brodeur, T. Brunner, et al. First Penning-trap mass measurement of the exotic halo nucleus ^{11}Li. *Physical Review Letters*, 101, 11 2008. doi: 10.1103/PhysRevLett.101.202501.

[321] G. Bollen, H.-J. Kluge, M. König, et al. Resolution of nuclear ground and isomeric states by a Penning trap mass spectrometer. *Physical Review C*, 46, 12 1992. doi: 10.1103/PhysRevC.46.R2140.

[322] S. George, S. Baruah, B. Blank, et al. Separated oscillatory fields for high-precision Penning trap mass spectrometry. *Phys. Rev. Lett.*, 98:162501, 2007. doi: 10.1103/PhysRevLett.98.162501.

[323] M. Vilen, J. M. Kelly, A. Kankainen, et al. Exploring the mass surface near the rare-earth abundance peak via precision mass measurements at JYFLTRAP. *Phys. Rev. C*, 101:034312, 3 2020. doi: 10.1103/PhysRevC.101.034312. URL https://link.aps.org/doi/10.1103/PhysRevC.101.034312.

[324] S. Eliseev, K. Blaum, M. Block, et al. Phase-imaging ion-cyclotron-resonance measurements for short-lived nuclides. *Phys. Rev. Lett.*, 110:082501, 2 2013. doi: 10.1103/PhysRevLett.110.082501. URL https://link.aps.org/doi/10.1103/PhysRevLett.110.082501.

[325] R. Orford, J. A. Clark, G. Savard, et al. Improving the measurement sensitivity of the Canadian Penning trap mass spectrometer through PI-ICR. *Nuclear Instruments and Methods in Physics Research Section B: Beam Interactions with Materials and Atoms*, 463:491–495, 2020. ISSN 0168-583X. doi: https://doi.org/10.1016/j.nimb.2019.04.016. URL https://www.sciencedirect.com/science/article/pii/S0168583X19302009.

[326] G. Eitel, M. Block, A. Czasch, et al. Position-sensitive ion detection in precision Penning trap mass spectrometry. *Nuclear Instruments and Methods in Physics Research Section A: Accelerators, Spectrometers, Detectors and Associated Equipment*, 606(3):475–483, 2009. ISSN 0168-9002. doi: https://doi.org/10.1016/j.nima.

2009.04.046. URL https://www.sciencedirect.com/science/article/pii/S0168900209008249.

[327] D. A. Nesterenko, T. Eronen, A. Kankainen, et al. Phase-imaging ion-cyclotron-resonance technique at the JYFLTRAP double Penning trap mass spectrometer. *The European Physical Journal A*, 54(9):154–, 2018. ISSN 1434-601X. URL https://doi.org/10.1140/epja/i2018-12589-y.

[328] A. G. Marshall. Fourier transform ion cyclotron resonance mass spectrometry. *Accounts of Chemical Research*, 18(10):316–322, 1985.

[329] W. M. Itano, J. C. Bergquist, J. J. Bollinger, and D. J. Wineland. Cooling methods in ion traps. *Physica Scripta*, 1995(T59):106, 1995. URL http://stacks.iop.org/1402-4896/1995/i=T59/a=013.

[330] R. X. Schüssler, H. Bekker, M. Braß, et al. Detection of metastable electronic states by Penning trap mass spectrometry. *Nature*, 581(7806):42–46, 2020. ISSN 1476-4687. URL https://doi.org/10.1038/s41586-020-2221-0.

[331] E. G. Myers, A. Wagner, H. Kracke, and B. A. Wesson. Atomic masses of tritium and helium-3. *Phys. Rev. Lett.*, 114:013003, 1 2015. doi: 10.1103/PhysRevLett.114.013003. URL https://link.aps.org/doi/10.1103/PhysRevLett.114.013003.

[332] J. Dilling, D. Ackermann, J. Bernard, et al. The SHIPTRAP project: A capture and storage facility at GSI for heavy radionuclides from SHIP. *Hyperfine Interactions*, 127(1):491–496, 2000. ISSN 1572-9540. URL https://doi.org/10.1023/A:1012638322226.

[333] M. Block, D. Ackermann, K. Blaum, et al. Mass measurements of exotic nuclides at SHIPTRAP. *AIP Conference Proceedings*, 912(1):423–430, 2007. doi: 10.1063/1.2746619. URL https://aip.scitation.org/doi/abs/10.1063/1.2746619.

[334] F. Giacoppo, K. Blaum, M. Block, et al. Recent upgrades of the SHIPTRAP setup: On the finish line towards direct mass spectroscopy of superheavy elements. *Acta Physica Polonica B*, 48(3):423–429, 2017.

[335] A. Hamaker, G. Bollen, M. Eibach, et al. SIPT - an ultrasensitive mass spectrometer for rare isotopes. *Hyperfine Interactions*, 240(1):34–, 2019. ISSN 1572-9540. URL https://doi.org/10.1007/s10751-019-1576-9.

[336] W. R. Plaß, T. Dickel, S. A. San Andrés, et al. High-performance multiple-reflection time-of-flight mass spectrometers for research with exotic nuclei and for analytical mass spectrometry. *Physica Scripta*, T166:014069, 11 2015. doi: 10.1088/0031-8949/2015/t166/014069. URL https://doi.org/10.1088/0031-8949/2015/t166/014069.

[337] T. Dickel, W. R. Plaß, J. Lang, et al. Multiple-reflection time-of-flight mass spectrometry for in situ applications. *Nuclear Instruments and Methods in Physics Research Section B: Beam Interactions with Materials and Atoms*, 317:779–784, 2013. ISSN 0168-583X. doi: https://doi.org/10.1016/j.nimb.2013.08.021. URL https://www.sciencedirect.com/science/article/pii/S0168583X1300880X. XVIth International Conference on ElectroMagnetic Isotope Separators and Techniques Related to their Applications, December 2–7, 2012 at Matsue, Japan.

[338] S. Kimura, Y. Ito, D. Kaji, et al. Atomic masses of intermediate-mass neutron-deficient nuclei with relative uncertainty down to 35-ppb via multireflection time-of-flight mass spectrograph. *International Journal of Mass Spectrometry*, 430:134 – 142, 2018. ISSN 1387-3806. doi: https://doi.org/10.1016/j.ijms.2018.05.001. URL http://www.sciencedirect.com/science/article/pii/S1387380617304220.

[339] M. P. Reiter, S. Ayet San Andrés, J. Bergmann, et al. Commissioning and performance of TITAN's multiple-reflection time-of-flight mass-spectrometer and isobar separator. *Nuclear Instruments and Methods in Physics Research Section A: Accelerators, Spectrometers, Detectors and Associated Equipment*, 1018:165823, 2021. ISSN 0168-9002. doi: https://doi.org/10.1016/j.nima.2021.165823. URL https://www.sciencedirect.com/science/article/pii/S0168900221008081.

[340] M. P. Reiter, F. Ames, C. Andreoiu, et al. Improved beam diagnostics and optimization at ISAC via TITAN's MR-TOF-MS. *Nuclear Instruments and Methods in Physics Research Section B: Beam Interactions with Materials and Atoms*, 463:431–436, 2020. ISSN 0168-583X. doi: https://doi.org/10.1016/j.nimb.2019.04.034. URL https://www.sciencedirect.com/science/article/pii/S0168583X19302186.

[341] P. Schury, M. Wada, Y. Ito, et al. A multi-reflection time-of-flight mass spectrograph for short-lived and super-heavy nuclei. *Nuclear Instruments and Methods in Physics Research Section B: Beam Interactions with Materials and Atoms*, 317:537–543, 2013. ISSN 0168-583X. doi: https://doi.org/10.1016/j.nimb.2013.06.025. URL https://www.sciencedirect.com/science/article/pii/S0168583X13006563. XVIth International Conference on ElectroMagnetic Isotope Separators and Techniques Related to their Applications, December 2–7, 2012 at Matsue, Japan.

[342] T. Y. Hirsh, N. Paul, M. Burkey, et al. First operation and mass separation with the CARIBU MR-TOF. *Nuclear Instruments and Methods in Physics Research Section B: Beam Interactions with Materials and Atoms*, 376:229–232, 2016. ISSN 0168-583X. doi: https://doi.org/10.1016/j.nimb.2015.12.037. URL https://www.sciencedirect.com/science/article/pii/S0168583X15012835. Proceedings of the XVIIth International Conference on Electromagnetic Isotope Separators and Related Topics (EMIS2015), Grand Rapids, MI, U.S.A., 11-15 May 2015.

[343] P. Chauveau, P. Delahaye, G. De France, et al. PILGRIM, a multi-reflection time-of-flight mass spectrometer for Spiral2-S3 at GANIL. *Nuclear Instruments*

and Methods in Physics Research Section B: Beam Interactions with Materials and Atoms, 376:211–215, 2016. ISSN 0168-583X. doi: https://doi.org/10.1016/j.nimb.2016.01.025. URL https://www.sciencedirect.com/science/article/pii/S0168583X16000732. Proceedings of the XVIIth International Conference on Electromagnetic Isotope Separators and Related Topics (EMIS2015), Grand Rapids, MI, U.S.A., 11-15 May 2015.

[344] C. Jesch. *The Multiple-Reflection Time-of-Flight Isobar Separator for TITAN and Direct Mass Measurements at the FRS Ion Catcher*. PhD thesis, Justus-Liebig-Universität Gießen, 2016.

[345] W. C. Wiley and I. H. McLaren. Time-of-flight mass spectrometer with improved resolution. *Review of Scientific Instruments*, 26(12):1150–1157, 1955. doi: 10.1063/1.1715212. URL https://doi.org/10.1063/1.1715212.

[346] M. Yavor. Time-of-flight mass analyzers. In *Optics of Charged Particle Analyzers Volume 157*, Advances in Imaging and Electron Physics. Elsevier, 2009. ISBN 9780123747686; 0123747686. doi: 10.1016/S1076-5670(09)01608-5. URL libgen.li/file.php?md5=bc5934b40a169730fb55a494a2ed8232.

[347] W. R. Plaß, T. Dickel, S. Purushothaman, et al. The FRS Ion Catcher – A facility for high-precision experiments with stopped projectile and fission fragments. *Nuclear Instruments and Methods in Physics Research Section B: Beam Interactions with Materials and Atoms*, 317:457–462, 2013. ISSN 0168-583X. doi: https://doi.org/10.1016/j.nimb.2013.07.063. URL https://www.sciencedirect.com/science/article/pii/S0168583X13008823. XVIth International Conference on ElectroMagnetic Isotope Separators and Techniques Related to their Applications, December 2–7, 2012 at Matsue, Japan.

[348] B. A. Mamyrin, V. I. Karataev, D. V. Shmikk, and V. A. Zagulin. The mass-reflectron, a new nonmagnetic time-of-flight mass spectrometer with high resolution. *Zh. Eksp. Teor. Fiz*, 64(1):82–89, 1973.

[349] R. J. Cotter. Time-of-flight mass spectrometry, instrumentation and applications in biological research. *Instrumentation Science & Technology*, 26(4):433–434, 1998. doi: 10.1080/10739149808001910. URL https://doi.org/10.1080/10739149808001910.

[350] Samuel Ayet San Andrés, Christine Hornung, Jens Ebert, et al. High-resolution, accurate multiple-reflection time-of-flight mass spectrometry for short-lived, exotic nuclei of a few events in their ground and low-lying isomeric states. *Phys. Rev. C*, 99:064313, Jun 2019. doi: 10.1103/PhysRevC.99.064313. URL https://link.aps.org/doi/10.1103/PhysRevC.99.064313.

[351] W. Paul. Electromagnetic traps for charged and neutral particles. *Rev. Mod. Phys.*, 62:531–540, 7 1990. doi: 10.1103/RevModPhys.62.531. URL https://link.aps.org/doi/10.1103/RevModPhys.62.531.

[352] R. N. Wolf, G. Marx, M. Rosenbusch, and L. Schweikhard. Static-mirror ion capture and time focusing for electrostatic ion-beam traps and multi-reflection time-of-flight mass analyzers by use of an in-trap potential lift. *International Journal of Mass Spectrometry*, 313:8–14, 2012. ISSN 1387-3806. doi: https://doi.org/10.1016/j.ijms.2011.12.006. URL https://www.sciencedirect.com/science/article/pii/S1387380611004775.

[353] B. E. Schultz, J. M. Kelly, C. Nicoloff, et al. Construction and simulation of a multi-reflection time-of-flight mass spectrometer at the University of Notre Dame. *Nuclear Instruments and Methods in Physics Research Section B: Beam Interactions with Materials and Atoms*, 376:251–255, 2016. ISSN 0168-583X. doi: https://doi.org/10.1016/j.nimb.2016.02.043. URL https://www.sciencedirect.com/science/article/pii/S0168583X16001737. Proceedings of the XVIIth International Conference on Electromagnetic Isotope Separators and Related Topics (EMIS2015), Grand Rapids, MI, U.S.A., 11-15 May 2015.

[354] T. Dickel, M. I. Yavor, J. Lang, et al. Dynamical time focus shift in multiple-reflection time-of-flight mass spectrometers. *International Journal of Mass Spectrometry*, 412:1–7, 2017. ISSN 1387-3806. doi: https://doi.org/10.1016/j.ijms.2016.11.005. URL https://www.sciencedirect.com/science/article/pii/S1387380616302664.

[355] N. E. Bradbury and R. A. Nielsen. Absolute values of the electron mobility in hydrogen. *Phys. Rev.*, 49:388–393, 3 1936. doi: 10.1103/PhysRev.49.388. URL https://link.aps.org/doi/10.1103/PhysRev.49.388.

[356] F. Wienholtz, S. Kreim, M. Rosenbusch, et al. Mass-selective ion ejection from multi-reflection time-of-flight devices via a pulsed in-trap lift. *International Journal of Mass Spectrometry*, 421:285–293, 2017. ISSN 1387-3806. doi: https://doi.org/10.1016/j.ijms.2017.07.016. URL https://www.sciencedirect.com/science/article/pii/S1387380617301987.

[357] T. Dickel, W. R. Plaß, W. Lippert, et al. Isobar separation in a multiple-reflection time-of-flight mass spectrometer by mass-selective re-trapping. *Journal of The American Society for Mass Spectrometry*, 28(6):1079–1090, 2017.

[358] M. I. Yavor, W. R. Plaß, T. Dickel, et al. Ion-optical design of a high-performance multiple-reflection time-of-flight mass spectrometer and isobar separator. *International Journal of Mass Spectrometry*, 381-382:1 – 9, 2015. ISSN 1387-3806. doi: https://doi.org/10.1016/j.ijms.2015.01.002. URL https://www.sciencedirect.com/science/article/pii/S1387380615000202.

[359] D. Short. Nuclear isobar separation for Penning trap mass measurements at TRIUMF. Master's thesis, Simon Fraser University, 2018.

[360] I. Mardor, S. Ayet San Andrés, T. Dickel, et al. Mass measurements of As, Se, and Br nuclei, and their implication on the proton-neutron interaction strength toward the $N = Z$ line. *Phys. Rev. C*, 103:034319, 3 2021. doi: 10.1103/PhysRevC.103.034319. URL https://link.aps.org/doi/10.1103/PhysRevC.103.034319.

[361] G. C. Ball, G. Hackman, and R. Krücken. The TRIUMF-ISAC facility: two decades of discovery with rare isotope beams. *Physica Scripta*, 91(9):093002, 2016. URL http://stacks.iop.org/1402-4896/91/i=9/a=093002.

[362] I. Bylinskii and M. K. Craddock. The TRIUMF 500 MeV cyclotron: the driver accelerator. *Hyperfine Interactions*, 225(1):9–16, 2014. ISSN 1572-9540. URL https://doi.org/10.1007/s10751-013-0878-6.

[363] M. Dombsky and P. Kunz. ISAC targets. *Hyperfine Interactions*, 225(1):17–23, 2014. ISSN 1572-9540. URL https://doi.org/10.1007/s10751-013-0879-5.

[364] P. Bricault, F. Ames, T. Achtzehn, et al. An overview on TRIUMF's developments on ion source for radioactive beams (invited). *Review of Scientific Instruments*, 79(2): 02A908, 2008. doi: 10.1063/1.2801344. URL https://aip.scitation.org/doi/abs/10.1063/1.2801344.

[365] J. Lassen, P. Bricault, M. Dombsky, et al. Laser ion source operation at the TRIUMF radioactive ion beam facility. In *4th International Conference on Laser Probing-LAP 2008*, volume 1104, pages 9 – 15. 2009. doi: https://doi.org/10.1063/1.3115616. URL https://aip.scitation.org/doi/abs/10.1063/1.3115616.

[366] M. Mostamand, R. Li, J. Romans, et al. Production of clean rare isotope beams at TRIUMF ion guide laser ion source. *Hyperfine Interactions*, 241(1), 3 2020. ISSN 1572-9540. doi: 10.1007/s10751-020-1704-6. URL http://dx.doi.org/10.1007/s10751-020-1704-6.

[367] K. Jayamanna. Off-line ion source terminal. *Hyperfine Interactions*, 225(1):51–62, 2014.

[368] R. Baartman. *ISAC LEBT*, pages 69–77. Springer Netherlands, Dordrecht, 2014. ISBN 978-94-007-7963-1. doi: 10.1007/978-94-007-7963-1_7. URL https://doi.org/10.1007/978-94-007-7963-1_7.

[369] R. E. Laxdal and M. Marchetto. The ISAC post-accelerator. *Hyperfine Interactions*, 225(1):79–97, 2014. ISSN 1572-9540. URL https://doi.org/10.1007/s10751-013-0884-8.

[370] J. Dilling and R. Krücken. *The experimental facilities at ISAC*, pages 111–114. Springer Netherlands, Dordrecht, 2014. ISBN 978-94-007-7963-1. doi: 10.1007/978-94-007-7963-1_10. URL https://doi.org/10.1007/978-94-007-7963-1_10.

[371] G. C. Ball, L. Buchmann, B. Davids, et al. Physics with reaccelerated radioactive beams at TRIUMF-ISAC. *Journal of Physics G: Nuclear and Particle Physics*, 38(2): 024003, 2011. URL http://stacks.iop.org/0954-3899/38/i=2/a=024003.

[372] M. Marchetto, R. E. Laxdal, and Fang Yan. Decelerating heavy ion beams using the ISAC DTL. In *Proceedings of HIAT09*, 2009.

[373] ISAC yield database - gallium yields, 2022. URL https://mis.triumf.ca/science/planning/yield/beam/Ga.

[374] M. Brodeur, T. Brunner, S. Ettenauer, et al. Precision mass measurements of neutron halo nuclei using the TITAN Penning trap. *Hyperfine Interactions*, 199(1-3):167–173, 2011.

[375] V. L. Ryjkov, M. Brodeur, T. Brunner, et al. Direct mass measurement of the four-neutron halo nuclide ^{8}He. *Phys. Rev. Lett.*, 101:012501, 7 2008. doi: 10.1103/PhysRevLett.101.012501. URL https://link.aps.org/doi/10.1103/PhysRevLett.101.012501.

[376] R. Ringle, M. Brodeur, T. Brunner, et al. High-precision Penning trap mass measurements of ^{9,10}Be and the one-neutron halo nuclide ^{11}Be. *Physics Letters B*, 675(2):170–174, 2009. ISSN 0370-2693. doi: https://doi.org/10.1016/j.physletb.2009.04.014. URL https://www.sciencedirect.com/science/article/pii/S0370269309004067.

[377] M. Brodeur, T. Brunner, C. Champagne, et al. First direct mass measurement of the two-neutron halo nucleus ^{6}He and improved mass for the four-neutron halo ^{8}He. *Phys. Rev. Lett.*, 108:052504, 1 2012. doi: 10.1103/PhysRevLett.108.052504. URL https://link.aps.org/doi/10.1103/PhysRevLett.108.052504.

[378] M. P. Reiter, S. Ayet San Andrés, E. Dunling, et al. Quenching of the $N = 32$ neutron shell closure studied via precision mass measurements of neutron-rich vanadium isotopes. *Phys. Rev. C*, 98:024310, 8 2018. doi: 10.1103/PhysRevC.98.024310. URL https://link.aps.org/doi/10.1103/PhysRevC.98.024310.

[379] M. P. Reiter, S. Ayet San Andrés, S. Nikas, et al. Mass measurements of neutron-rich gallium isotopes refine production of nuclei of the first r-process abundance peak in neutron-star merger calculations. *Phys. Rev. C*, 101:025803, 2 2020. doi: 10.1103/PhysRevC.101.025803. URL https://link.aps.org/doi/10.1103/PhysRevC.101.025803.

[380] I. Mukul, C. Andreoiu, J. Bergmann, et al. Examining the nuclear mass surface of Rb and Sr isotopes in the $A \approx 104$ region via precision mass measurements. *Phys. Rev. C*, 103:044320, 4 2021. doi: 10.1103/PhysRevC.103.044320. URL https://link.aps.org/doi/10.1103/PhysRevC.103.044320.

[381] C. Izzo, J. Bergmann, K. A. Dietrich, et al. Mass measurements of neutron-rich indium isotopes for r-process studies. *Phys. Rev. C*, 103:025811, 2 2021. doi: 10.1103/PhysRevC.103.025811. URL https://link.aps.org/doi/10.1103/PhysRevC.103.025811.

[382] S. Ettenauer, M. C. Simon, T. D. Macdonald, and J. Dilling. Advances in precision, resolution, and separation techniques with radioactive, highly charged ions for Penning trap mass measurements. *International Journal of Mass Spectrometry*, 349-350:74 – 80, 2013. ISSN 1387-3806. doi: https://doi.org/10.1016/j.ijms.2013.04.021. URL http://www.sciencedirect.com/science/article/pii/S1387380613001486. 100 years of Mass Spectrometry.

[383] T. Brunner, M. J. Smith, M. Brodeur, et al. TITAN's digital RFQ ion beam cooler and buncher, operation and performance. *Nuclear Instruments and Methods in Physics Research Section A: Accelerators, Spectrometers, Detectors and Associated Equipment*, 676:32–43, 2012. doi: 10.1016/j.nima.2012.02.004.

[384] F. Herfurth, J. Dilling, A. Kellerbauer, et al. A linear radiofrequency ion trap for accumulation, bunching, and emittance improvement of radioactive ion beams. *Nuclear Instruments and Methods in Physics Research Section A: Accelerators, Spectrometers, Detectors and Associated Equipment*, 469(2):254–275, 2001. ISSN 0168-9002. doi: https://doi.org/10.1016/S0168-9002(01)00168-1. URL https://www.sciencedirect.com/science/article/pii/S0168900201001681.

[385] A. Kellerbauer, G. Bollen, J. Dilling, et al. A linear radiofrequency quadrupole ion trap for the cooling and bunching of radioactive ion beams. *Nuclear Physics A*, 701(1):565–569, 2002. ISSN 0375-9474. doi: https://doi.org/10.1016/S0375-9474(01)01645-1. URL https://www.sciencedirect.com/science/article/pii/S0375947401016451. 5th International Conference on Radioactive Nuclear Beams.

[386] A. Nieminen, J. Huikari, A. Jokinen, et al. Beam cooler for low-energy radioactive ions. *Nuclear Instruments and Methods in Physics Research Section A: Accelerators, Spectrometers, Detectors and Associated Equipment*, 469(2):244–253, 2001. ISSN 0168-9002. doi: https://doi.org/10.1016/S0168-9002(00)00750-6. URL https://www.sciencedirect.com/science/article/pii/S0168900200007506.

[387] M. Mukherjee, D. Beck, K. Blaum, et al. Isoltrap: An on-line penning trap for mass spectrometry on short-lived nuclides. *The European Physical Journal A*, 35(1):1–29,

2008. ISSN 1434-601X. doi: 10.1140/epja/i2007-10528-9. URL http://dx.doi.org/10.1140/epja/i2007-10528-9.

[388] T. Eronen, V. S. Kolhinen, V.-V. Elomaa, et al. *JYFLTRAP: a Penning trap for precision mass spectroscopy and isobaric purification*, pages 61–81. Springer Netherlands, Dordrecht, 2014. ISBN 978-94-007-5555-0. doi: 10.1007/978-94-007-5555-0_3. URL https://doi.org/10.1007/978-94-007-5555-0_3.

[389] J. Äystö, A. Jokinen, and The EXOTRAPS Collaboration. Ion beam coolers in nuclear physics. *Journal of Physics B: Atomic, Molecular and Optical Physics*, 36(3): 573–584, 1 2003. doi: 10.1088/0953-4075/36/3/315. URL https://doi.org/10.1088/0953-4075/36/3/315.

[390] G. Savard, R. C. Barber, C. Boudreau, et al. The Canadian Penning trap spectrometer at Argonne. In *Atomic Physics at Accelerators: Mass Spectrometry*, pages 223–230, Dordrecht, 2001. Springer Netherlands.

[391] S. Schwarz, G. Bollen, R. Ringle, et al. The LEBIT ion cooler and buncher. *Nuclear Instruments and Methods in Physics Research Section A: Accelerators, Spectrometers, Detectors and Associated Equipment*, 816:131–141, 2016. ISSN 0168-9002. doi: https://doi.org/10.1016/j.nima.2016.01.078. URL https://www.sciencedirect.com/science/article/pii/S0168900216001194.

[392] E. Haettner, W. R. Plaß, U. Czok, et al. A versatile triple radiofrequency quadrupole system for cooling, mass separation and bunching of exotic nuclei. *Nuclear Instruments and Methods in Physics Research Section A: Accelerators, Spectrometers, Detectors and Associated Equipment*, 880:138–151, 2018. ISSN 0168-9002. doi: https://doi.org/10.1016/j.nima.2017.10.003. URL https://www.sciencedirect.com/science/article/pii/S0168900217310409.

[393] A. Nieminen, P. Campbell, J. Billowes, et al. On-line ion cooling and bunching for collinear laser spectroscopy. *Phys. Rev. Lett.*, 88:094801, 2 2002. doi: 10.1103/PhysRevLett.88.094801. URL https://link.aps.org/doi/10.1103/PhysRevLett.88.094801.

[394] E. Mané, J. Billowes, K. Blaum, et al. An ion cooler-buncher for high-sensitivity collinear laser spectroscopy at ISOLDE. *The European Physical Journal A*, 42 (3):503–507, 2009. ISSN 1434-601X. URL https://doi.org/10.1140/epja/i2009-10828-0.

[395] E Mané, J. A. Behr, J. Billowes, et al. Collinear laser spectroscopy with reverse-extracted bunched beams at TRIUMF. *Hyperfine Interactions*, 199(1-3):357, 2011.

[396] B. A. Thomson. 1997 McBryde Medal Award lecture radio frequency quadrupole ion guides in modern mass spectrometry. *Can. J. Chem.*, 76(5):499–505, May 1998. ISSN 0008-4042. doi: 10.1139/v98-073. URL https://doi.org/10.1139/v98-073.

[397] A. Kellerbauer, T. Kim, R.B. Moore, and P. Varfalvy. Buffer gas cooling of ion beams. *Nuclear Instruments and Methods in Physics Research Section A: Accelerators, Spectrometers, Detectors and Associated Equipment*, 469(2):276 – 285, 2001. ISSN 0168-9002. doi: http://dx.doi.org/10.1016/S0168-9002(01)00286-8. URL http://www.sciencedirect.com/science/article/pii/S0168900201002868.

[398] F. G. Major and H. G. Dehmelt. Exchange-collision technique for the rf spectroscopy of stored ions. *Phys. Rev.*, 170:91–107, 6 1968. doi: 10.1103/PhysRev.170.91. URL https://link.aps.org/doi/10.1103/PhysRev.170.91.

[399] S. Schwarz. *Simulations for Ion Traps Buffer Gas Cooling*, pages 1–21. Springer Berlin Heidelberg, Berlin, Heidelberg, 2008. ISBN 978-3-540-77817-2. doi: 10.1007/978-3-540-77817-2_4. URL https://doi.org/10.1007/978-3-540-77817-2{_}4.

[400] B. Höltkemeier, P. Weckesser, H. López-Carrera, and M. Weidemüller. Buffer-gas cooling of a single ion in a multipole radio frequency trap beyond the critical mass ratio. *Phys. Rev. Lett.*, 116:233003, 6 2016. doi: 10.1103/PhysRevLett.116.233003. URL https://link.aps.org/doi/10.1103/PhysRevLett.116.233003.

[401] M. Smith, L. Blomeley, P. Delheij, and J. Dilling. First tests of the TITAN digital RFQ beam cooler and buncher. *Hyperfine Interactions*, 173(1):171–180, 2006. ISSN 1572-9540. URL https://doi.org/10.1007/s10751-007-9554-z.

[402] M. Froese, C. Champagne, J. R. Crespo López-Urrutia, et al. A high-current electron beam ion trap as an on-line charge breeder for the high precision mass measurement TITAN experiment. *Hyperfine Interactions*, 173(1):85–92, 2006. ISSN 1572-9540. URL https://doi.org/10.1007/s10751-007-9546-z.

[403] R. Klawitter, A. Bader, M. Brodeur, et al. Mass measurements of neutron-rich Rb and Sr isotopes. *Phys. Rev. C*, 93:045807, 4 2016. doi: 10.1103/PhysRevC.93.045807. URL https://link.aps.org/doi/10.1103/PhysRevC.93.045807.

[404] M. Foster. An upgrade of the TITAN-EBIT high voltage operation for investigations into decay rate modifcations by highly charged ions. Master's thesis, University of Surrey, 2017.

[405] T. Brunner, A.R. Mueller, K. O'Sullivan, et al. A large Bradbury Nielsen ion gate with flexible wire spacing based on photo-etched stainless steel grids and its characterization applying symmetric and asymmetric potentials. *International Journal of Mass Spectrometry*, 309:97–103, 2012. ISSN 1387-3806. doi: https://doi.org/10.1016/j.ijms.2011.09.004. URL https://www.sciencedirect.com/science/article/pii/S1387380611003770.

[406] T. Brunner, M. Brodeur, P. Delheij, et al. In-trap decay spectroscopy for 2νββ decay experiments. *Hyperfine Interactions*, 199(1):191–, 2011. ISSN 1572-9540. URL https://doi.org/10.1007/s10751-011-0313-9.

[407] T. Brunner, A. Lapierre, C. Andreoiu, et al. Trapped-ion decay spectroscopy towards the determination of ground-state components of double-beta decay matrix elements. *The European Physical Journal A*, 49(11):142–, 2013. ISSN 1434-601X. URL https://doi.org/10.1140/epja/i2013-13142-4.

[408] A. Lennarz, A. Grossheim, K. G. Leach, et al. In-trap spectroscopy of charge-bred radioactive ions. *Phys. Rev. Lett.*, 113:082502, 8 2014. doi: 10.1103/PhysRevLett.113.082502. URL https://link.aps.org/doi/10.1103/PhysRevLett.113.082502.

[409] K. G. Leach, A. Grossheim, A. Lennarz, et al. The TITAN in-trap decay spectroscopy facility at TRIUMF. *Nuclear Instruments and Methods in Physics Research Section A: Accelerators, Spectrometers, Detectors and Associated Equipment*, 780:91 – 99, 2015. ISSN 0168-9002. doi: http://dx.doi.org/10.1016/j.nima.2014.12.118. URL http://www.sciencedirect.com/science/article/pii/S0168900215001023.

[410] E. Leistenschneider, R. Klawitter, A. Lennarz, et al. Diversifying beam species through decay and recapture ion trapping: a demonstrative experiment at TITAN-EBIT. *Journal of Physics G: Nuclear and Particle Physics*, 47(4):045113, 3 2020. doi: 10.1088/1361-6471/ab6ee1. URL https://doi.org/10.1088/1361-6471/ab6ee1.

[411] D. Frekers, M. C. Simon, C. Andreoiu, et al. Penning-trap Q-value determination of the ^{71}Ga(ν,e$^-$)^{71}Ge reaction using threshold charge breeding of on-line produced isotopes. *Physics Letters B*, 722(4):233 – 237, 2013. ISSN 0370-2693. doi: http://dx.doi.org/10.1016/j.physletb.2013.04.019. URL http://www.sciencedirect.com/science/article/pii/S0370269313002980.

[412] J. Bollig. Longitudinal energy spread and transverse emittance measurements of TITAN's radio frequency quadrupole cooler and buncher (RFQ). Bachelor's thesis, Ruprecht-Karls-Universität Heidelberg, 2017.

[413] J. Ladislas Wiza. Microchannel plate detectors. *Nuclear Instruments and Methods*, 162(1):587–601, 1979. ISSN 0029-554X. doi: https://doi.org/10.1016/0029-554X(79)90734-1. URL https://www.sciencedirect.com/science/article/pii/0029554X79907341.

[414] K. Fehre, D. Trojanowskaja, J. Gatzke, et al. Absolute ion detection efficiencies of microchannel plates and funnel microchannel plates for multi-coincidence detection. *Review of Scientific Instruments*, 89(4):045112, 2018. doi: 10.1063/1.5022564. URL https://doi.org/10.1063/1.5022564.

[415] G. W. Fraser. The ion detection efficiency of microchannel plates (MCPs). *International Journal of Mass Spectrometry*, 215(1):13–30, 2002. ISSN 1387-3806. doi: https://doi.org/10.1016/S1387-3806(01)00553-X. URL https://www.sciencedirect.com/science/article/pii/S138738060100553X. Detectors and the Measurement of Mass Spectra.

[416] RoentDek Handels GmbH. The DLD delay line detectors, October 2022. URL http://www.roentdek.com/info/RoentDek_DLD_description.pdf.

[417] A. Finlay. Integration of a multi-reflection time-of-flight isobar separator into the TITAN experiment at TRIUMF. Master's thesis, University of British Columbia, 2017.

[418] C. Will. TITAN's multiple-reflection time-of-flight mass spectrometer and isobar separator - characterization and first experiments. Bachelor's thesis, Justus-Liebig Universität Gießen, 2017.

[419] ETP Electron Multipliers. MagneTOF: A new class of robust sub-nanosecond TOF detectors with exceptional dynamic range. Product Data Sheet. URL https://www.etp-ms.com/file-repository/8. Accessed January 2022.

[420] FASTComTec GmbH. FAST ComTec MCS6A-5T8. Product data sheet. URL https://www.fastcomtec.com/fwww/datashee/photon/mcs6.pdf. Accessed February 2022.

[421] S. A. San Andrés. *Developments for Multiple-Reflection Time-of-Flight Mass Spectrometers and their Application to High-Resolution Accurate Mass Measurements of Short-Lived Exotic Nuclei*. PhD thesis, Justus-Liebig-Universität Gießen, 2018.

[422] iseg Spezialelektronik GmbH. iseg EHS high precision HV modules. Data sheet. URL https://iseg-hv.com/files/media/iseg_datasheet_EHS_en_20210607111806.pdf. Accessed February 2022.

[423] J. Bergmann. Datenaufnahme und Systemsteuerung eines Flugzeitmassenspektrometers mit Anwendungen. Master's thesis, Justus-Liebig-Universität Gießen, 2015.

[424] A. Jacobs. Collision induced dissociation and mass spectrometry with the TITAN multiple-reflection time-of-flight mass-spectrometer. Master's thesis, Univeristy of British Columbia, 2019.

[425] S. F. Paul, J. Bergmann, J. D. Cardona, et al. Mass measurements of $^{60-63}$Ga reduce x-ray burst model uncertainties and extend the evaluated $T = 1$ isobaric multiplet mass equation. *Phys. Rev. C*, 104:065803, 12 2021. doi: 10.1103/PhysRevC.104.065803. URL https://link.aps.org/doi/10.1103/PhysRevC.104.065803.

[426] S. F. Paul. emgfit - Fitting of time-of-flight mass spectra with hyper-EMG models, March 2021. URL https://doi.org/10.5281/zenodo.4731018.

[427] S. Purushothaman, S. A. San Andrés, J. Bergmann, et al. Hyper-emg: A new probability distribution function composed of exponentially modified gaussian distributions to analyze asymmetric peak shapes in high-resolution time-of-flight mass spectrometry. *International Journal of Mass Spectrometry*, 421:245 – 254, 2017. ISSN 1387-3806. doi: https://doi.org/10.1016/j.ijms.2017.07.014. URL http://www.sciencedirect.com/science/article/pii/S1387380616302913.

[428] P. J. Naish and S. Hartwell. Exponentially modified Gaussian functions—a good model for chromatographic peaks in isocratic HPLC? *Chromatographia*, 26(1):285–296, 1988.

[429] S. Pommé and B. Caro Marroyo. Improved peak shape fitting in alpha spectra. *Applied Radiation and Isotopes*, 96:148 – 153, 2015. ISSN 0969-8043. doi: https://doi.org/10.1016/j.apradiso.2014.11.023. URL http://www.sciencedirect.com/science/article/pii/S0969804314004175.

[430] K. J. Mighell. Parameter estimation in astronomy with Poisson-distributed data. I. The χ^2_γ statistic. *The Astrophysical Journal*, 518(1):380–393, jun 1999. doi: 10.1086/307253. URL https://doi.org/10.1086%2F307253.

[431] H. Dembinski, M. Schmelling, and R. Waldi. Application of the iterated weighted least-squares fit to counting experiments. *Nuclear Instruments and Methods in Physics Research Section A: Accelerators, Spectrometers, Detectors and Associated Equipment*, 940:135–141, 2019.

[432] S. Baker and R. D. Cousins. Clarification of the use of chi-square and likelihood functions in fits to histograms. *Nuclear Instruments and Methods in Physics Research*, 221(2):437–442, 1984. ISSN 0167-5087. doi: https://doi.org/10.1016/0167-5087(84)90016-4. URL https://www.sciencedirect.com/science/article/pii/0167508784900164.

[433] J. S. Kaastra. On the use of C-stat in testing models for X-ray spectra. *Astronomy & Astrophysics*, 605:A51, 2017. URL https://doi.org/10.1051/0004-6361/201629319.

[434] M. B. Smith, T. Murböck, E. Dunling, et al. High-precision mass measurement of neutron-rich ^{96}Kr. *Hyperfine Interactions*, 241(1):1 – 8, 2020. URL https://doi.org/10.1007/s10751-020-01722-2.

[435] D. Foreman-Mackey, D. W. Hogg, D. Lang, and J. Goodman. emcee: The MCMC hammer. *Publications of the Astronomical Society of the Pacific*, 125(925):306–312, mar 2013. doi: 10.1086/670067. URL https://doi.org/10.1086/670067.

[436] E. Dunling. *Exploring magicity around N = 32 & 34 in Z = 20 isotopes via precision mass measurements and developments with the TITAN MR-TOF mass spectrometer*. PhD thesis, University of York, 2021.

[437] L. Weissman, J. Cederkall, J. Äystö, et al. β^+ decay of ^{61}Ga. *Phys. Rev. C*, 65: 044321, Mar 2002. doi: 10.1103/PhysRevC.65.044321. URL https://link.aps.org/doi/10.1103/PhysRevC.65.044321.

[438] X. L. Tu, M. Wang, Yu. A. Litvinov, et al. Precision isochronous mass measurements at the storage ring CSRe in Lanzhou. *Nuclear Instruments and Methods in Physics Research Section A: Accelerators, Spectrometers, Detectors and Associated Equipment*, 654(1):213–218, 2011. ISSN 0168-9002. doi: https://doi.org/10.1016/j.nima.2011.07.018. URL https://www.sciencedirect.com/science/article/pii/S0168900211014471.

[439] T. Eronen, V. Elomaa, U. Hager, et al. Q-value of the superallowed β decay of ^{62}Ga. *Physics Letters B*, 636(3):191–196, 2006. ISSN 0370-2693. doi: https://doi.org/10.1016/j.physletb.2006.03.062. URL https://www.sciencedirect.com/science/article/pii/S0370269306004023.

[440] C. Guénaut, G. Audi, D. Beck, et al. High-precision mass measurements of nickel, copper, and gallium isotopes and the purported shell closure at $N = 40$. *Phys. Rev. C*, 75:044303, Apr 2007. doi: 10.1103/PhysRevC.75.044303. URL https://link.aps.org/doi/10.1103/PhysRevC.75.044303.

[441] S. E. A. Orrigo, B. Rubio, W. Gelletly, et al. β decay of the very neutron-deficient ^{60}Ge and ^{62}Ge nuclei. *Phys. Rev. C*, 103:014324, Jan 2021. doi: 10.1103/PhysRevC.103.014324. URL https://link.aps.org/doi/10.1103/PhysRevC.103.014324.

[442] C. N. Davids, C. A. Gagliardi, M. J. Murphy, and E. B. Norman. Superallowed Fermi decay of ^{62}Ga. *Phys. Rev. C*, 19:1463–1466, Apr 1979. doi: 10.1103/PhysRevC.19.1463. URL https://link.aps.org/doi/10.1103/PhysRevC.19.1463.

[443] B. Hyland, C. E. Svensson, G. C. Ball, et al. Precision branching ratio measurement for the superallowed β^+ emitter ^{62}Ga and isospin-symmetry-breaking corrections in $A \geq 62$ nuclei. *Phys. Rev. Lett.*, 97:102501, Sep 2006. doi: 10.1103/PhysRevLett.97.102501. URL https://link.aps.org/doi/10.1103/PhysRevLett.97.102501.

[444] P. Finlay, G. C. Ball, J. R. Leslie, et al. High-precision branching ratio measurement for the superallowed β^+ emitter ^{62}Ga. *Phys. Rev. C*, 78:025502, Aug 2008. doi: 10.1103/PhysRevC.78.025502. URL https://link.aps.org/doi/10.1103/PhysRevC.78.025502.

[445] B. J. Cole. Predicted proton and two-proton decay energies for nuclei in the upper fp shell. *Phys. Rev. C*, 59:726 – 730, Feb 1999. doi: 10.1103/PhysRevC.59.726. URL https://link.aps.org/doi/10.1103/PhysRevC.59.726.

[446] G. Audi, A. H. Wapstra, and C. Thibault. The Ame2003 atomic mass evaluation: (ii). tables, graphs and references. *Nuclear Physics A*, 729(1):337–676, 2003.

ISSN 0375-9474. doi: https://doi.org/10.1016/j.nuclphysa.2003.11.003. URL https://www.sciencedirect.com/science/article/pii/S0375947403018098. The 2003 NUBASE and Atomic Mass Evaluations.

[447] M. Del Santo, Z. Meisel, D. Bazin, et al. β-delayed proton emission of ^{69}kr and the ^{68}se rp-process waiting point. *Physics Letters B*, 738:453 – 456, 2014. ISSN 0370-2693. doi: https://doi.org/10.1016/j.physletb.2014.10.023. URL https://www.sciencedirect.com/science/article/pii/S0370269314007461.

[448] S. E. A. Orrigo, B. Rubio, Y. Fujita, et al. Observation of the β-delayed γ-proton decay of ^{56}Zn and its impact on the Gamow-Teller strength evaluation. *Phys. Rev. Lett.*, 112:222501, Jun 2014. doi: 10.1103/PhysRevLett.112.222501. URL https://link.aps.org/doi/10.1103/PhysRevLett.112.222501.

[449] S. E. A. Orrigo, B. Rubio, Y. Fujita, et al. β decay of the exotic $T_z = -2$ nuclei ^{48}Fe,^{52} Ni, and ^{56}Zn. *Phys. Rev. C*, 93:044336, Apr 2016. doi: 10.1103/PhysRevC.93.044336. URL https://link.aps.org/doi/10.1103/PhysRevC.93.044336.

[450] A. Zdeb, M. Warda, C. M. Petrache, and K. Pomorski. Proton emission half-lives within a Gamow-like model. *The European Physical Journal A*, 52(10):1–6, 2016.

[451] E. Browne and J. K. Tuli. Nuclear data sheets for $A = 60$. *Nuclear Data Sheets*, 114(12):1849 – 2022, 2013. ISSN 0090-3752. doi: https://doi.org/10.1016/j.nds.2013.11.002. URL https://www.sciencedirect.com/science/article/pii/S0090375213000823.

[452] P. Möller, W. D. Myers, H. Sagawa, and S. Yoshida. New finite-range droplet mass model and equation-of-state parameters. *Phys. Rev. Lett.*, 108:052501, 1 2012. doi: 10.1103/PhysRevLett.108.052501. URL https://link.aps.org/doi/10.1103/PhysRevLett.108.052501.

[453] W. Satula, D.J. Dean, J. Gary, et al. On the origin of the Wigner energy. *Physics Letters B*, 407(2):103–109, 1997. ISSN 0370-2693. doi: https://doi.org/10.1016/S0370-2693(97)00711-9. URL https://www.sciencedirect.com/science/article/pii/S0370269397007119.

[454] Z. M. Niu and H. Z. Liang. Nuclear mass predictions based on Bayesian neural network approach with pairing and shell effects. *Physics Letters B*, 778:48 – 53, 2018. ISSN 0370-2693. doi: https://doi.org/10.1016/j.physletb.2018.01.002. URL http://www.sciencedirect.com/science/article/pii/S0370269318300091.

[455] L. Neufcourt, Y. Cao, S. A. Giuliani, et al. Quantified limits of the nuclear landscape. *Phys. Rev. C*, 101:044307, Apr 2020. doi: 10.1103/PhysRevC.101.044307. URL https://link.aps.org/doi/10.1103/PhysRevC.101.044307.

[456] M. Shelley and A. Pastore. A new mass model for nuclear astrophysics: Crossing 200 kev accuracy. *Universe*, 7(5):131, 2021. ISSN 2218-1997. doi: 10.3390/universe7050131. URL https://www.mdpi.com/2218-1997/7/5/131.

[457] Léo Neufcourt, Yuchen Cao, Samuel Giuliani, et al. Beyond the proton drip line: Bayesian analysis of proton-emitting nuclei. *Phys. Rev. C*, 101:014319, Jan 2020. doi: 10.1103/PhysRevC.101.014319. URL https://link.aps.org/doi/10.1103/PhysRevC.101.014319.

[458] P. Möller, J. R. Nix, W. D. Myers, and W. J. Swiatecki. Nuclear ground-state masses and deformations. *Atomic Data and Nuclear Data Tables*, 59(2):185 – 381, 1995. ISSN 0092-640X. doi: https://doi.org/10.1006/adnd.1995.1002. URL https://www.sciencedirect.com/science/article/pii/S0092640X85710029.

[459] D. Rodrıguez, V. S. Kolhinen, G. Audi, et al. Mass measurement on the rp-process waiting point ^{72}Kr. *The European Physical Journal A-Hadrons and Nuclei*, 25(1):41 – 43, 2005. URL https://doi.org/10.1140/epjad/i2005-06-164-3.

[460] A. Stolz, T. Baumann, N. H. Frank, et al. First observation of ^{60}Ge and ^{64}Se. *Physics Letters B*, 627(1):32 – 37, 2005. ISSN 0370-2693. doi: https://doi.org/10.1016/j.physletb.2005.08.130. URL https://www.sciencedirect.com/science/article/pii/S0370269305012748.

[461] Y. H. Zhang, P. Zhang, X. H. Zhou, et al. Isochronous mass measurements of $T_z = -1$ fp-shell nuclei from projectile fragmentation of ^{58}Ni. *Phys. Rev. C*, 98:014319, 7 2018. doi: 10.1103/PhysRevC.98.014319. URL https://link.aps.org/doi/10.1103/PhysRevC.98.014319.

[462] A. A. Valverde, M. Brodeur, G. Bollen, et al. High-precision mass measurement of ^{56}Cu and the redirection of the rp-process flow. *Phys. Rev. Lett.*, 120:032701, Jan 2018. doi: 10.1103/PhysRevLett.120.032701. URL https://link.aps.org/doi/10.1103/PhysRevLett.120.032701.

[463] Evaluated nuclear structure datafile (ENSDF), 2021. URL http://www.nndc.bnl.gov/ensdf.

[464] M. B. Greenfield, C. R. Bingham, E. Newman, and M. J. Saltmarsh. (^{3}He, n) reaction at 25 MeV. *Phys. Rev. C*, 6:1756 – 1769, Nov 1972. doi: 10.1103/PhysRevC.6.1756. URL https://link.aps.org/doi/10.1103/PhysRevC.6.1756.

[465] R. B. Schubank, J. A. Cameron, and V. P. Janzen. Gamma-ray spectroscopy of ^{60,61}Zn and ^{59,60}Cu. *Phys. Rev. C*, 40:2310 – 2319, Nov 1989. doi: 10.1103/PhysRevC.40.2310. URL https://link.aps.org/doi/10.1103/PhysRevC.40.2310.

[466] F. Pougheon, P. Roussel, P. Colombani, et al. Two-nucleon stripping reactions induced by ^{16}O in ^{54}Fe and ^{58}Ni at 80 MeV. *Nuclear Physics A*, 193(1):305 – 322, 1972.

ISSN 0375-9474. doi: https://doi.org/10.1016/0375-9474(72)90255-2. URL https://www.sciencedirect.com/science/article/pii/0375947472902552.

[467] F. G. Kondev, M. Wang, W. J. Huang, et al. The NUBASE2020 evaluation of nuclear physics properties. *Chinese Physics C*, 45(3):030001, mar 2021. doi: 10.1088/1674-1137/abddae. URL https://doi.org/10.1088/1674-1137/abddae.

[468] B. A. Brown and W. D. M. Rae. The shell-model code NuShellX@MSU. *Nuclear Data Sheets*, 120:115–118, 2014. ISSN 0090-3752. doi: https://doi.org/10.1016/j.nds.2014.07.022. URL https://www.sciencedirect.com/science/article/pii/S0090375214004748.

[469] K. Zuber and B. Singh. Nuclear data sheets for A = 61. *Nuclear Data Sheets*, 125:1 – 200, 2015. ISSN 0090-3752. doi: https://doi.org/10.1016/j.nds.2015.02.001. URL https://www.sciencedirect.com/science/article/pii/S0090375215000022.

[470] Y. Okuma, T. Motobayashi, K. Takimoto, et al. Ann. rept. 1984. RCNP (Osaka), 1985.

[471] D. J. Weber, G. M. Crawley, W. Benenson, et al. Study of ^{60}Zn and ^{61}Zn. *Nuclear Physics A*, 313(3):385–396, 1979. doi: https://doi.org/10.1016/0375-9474(79)90508-6.

[472] S. Ulmer, C. Smorra, A. Mooser, et al. High-precision comparison of the antiproton-to-proton charge-to-mass ratio. *Nature*, 524(7564):196–199, 2015. ISSN 1476-4687. URL https://doi.org/10.1038/nature14861.

[473] H. Häffner, T. Beier, S. Djekić, et al. Double Penning trap technique for precise g factor determinations in highly charged ions. *The European Physical Journal D - Atomic, Molecular, Optical and Plasma Physics*, 22(2):163–182, 2003. ISSN 1434-6079. URL https://doi.org/10.1140/epjd/e2003-00012-2.

[474] G. Werth, J. Alonso, T. Beier, et al. Highly charged ions, quantum-electrodynamics, and the electron mass. *International Journal of Mass Spectrometry*, 251(2):152–158, 2006. ISSN 1387-3806. doi: https://doi.org/10.1016/j.ijms.2006.01.046. URL https://www.sciencedirect.com/science/article/pii/S1387380606000790. ULTRA-ACCURATE MASS SPECTROMETRY AND RELATED TOPICS Dedicated to H.-J. Kluge on the occasion of his 65th birthday anniversary.

[475] R. Becker and O. Kester. Electron beam ion source and electron beam ion trap (invited). *Review of Scientific Instruments*, 81(2):02A513, 2010. doi: 10.1063/1.3303820. URL https://doi.org/10.1063/1.3303820.

[476] P. Sortais, J. F. Bruandet, J. L. Bouly, et al. Electron cyclotron resonance charge breeder (invited). *Review of Scientific Instruments*, 71(2):617–622, 2000. doi: 10.1063/1.1150331. URL https://doi.org/10.1063/1.1150331.

[477] W. Barth, A. Fomichev, L. Grigorenko, et al. Charge stripping at high energy heavy ion Linacs. In *Journal of Physics: Conference Series*, volume 1350, page 012096. IOP Publishing, 2019.

[478] Z. Andelkovic, R. Cazan, W. Nörtershäuser, et al. Laser cooling of externally produced Mg ions in a Penning trap for sympathetic cooling of highly charged ions. *Phys. Rev. A*, 87:033423, Mar 2013. doi: 10.1103/PhysRevA.87.033423. URL https://link.aps.org/doi/10.1103/PhysRevA.87.033423.

[479] D. J. Larson, J. C. Bergquist, J. J. Bollinger, et al. Sympathetic cooling of trapped ions: A laser-cooled two-species nonneutral ion plasma. *Phys. Rev. Lett.*, 57:70–73, Jul 1986. doi: 10.1103/PhysRevLett.57.70. URL http://link.aps.org/doi/10.1103/PhysRevLett.57.70.

[480] L. Schmöger, O. O. Versolato, M. Schwarz, et al. Coulomb crystallization of highly charged ions. *Science*, 347(6227):1233–1236, 2015.

[481] V. S. Kolhinen, M. Bussmann, D. Habs, et al. MLLTRAP: A Penning trap facility for high-accuracy mass measurements. *Nuclear Instruments and Methods in Physics Research Section B: Beam Interactions with Materials and Atoms*, 266 (19):4547 – 4550, 2008. ISSN 0168-583X. doi: http://dx.doi.org/10.1016/j.nimb.2008.05.100. URL http://www.sciencedirect.com/science/article/pii/S0168583X08007738. Proceedings of the XVth International Conference on Electromagnetic Isotope Separators and Techniques Related to their Applications.

[482] S. Schmidt, T. Murböck, Z. Andelkovic, et al. Sympathetic cooling in two-species ion crystals in a Penning trap. *Journal of Modern Optics*, 65(5-6):538–548, 2018. doi: 10.1080/09500340.2017.1342877. URL https://doi.org/10.1080/09500340.2017.1342877.

[483] M. Vogel, H. Häffner, K. Hermanspahn, et al. Resistive and sympathetic cooling of highly-charged-ion clouds in a Penning trap. *Phys. Rev. A*, 90:043412, Oct 2014. doi: 10.1103/PhysRevA.90.043412. URL http://link.aps.org/doi/10.1103/PhysRevA.90.043412.

[484] L Spitzer. *Physics of Fully Ionized Gases*. Interscience, New York, 1956.

[485] G. Gabrielse, L. Haarsma, and S. L. Rolston. Open-endcap Penning traps for high precision experiments. *International Journal of Mass Spectrometry and Ion Processes*, 88(2):319 – 332, 1989. ISSN 0168-1176. doi: https://doi.org/10.1016/0168-1176(89)85027-X. URL http://www.sciencedirect.com/science/article/pii/016811768985027X.

[486] D. S. Hall and G. Gabrielse. Electron cooling of protons in a nested Penning trap. *Physical Review Letters*, 77(10):1962, 1996.

[487] Guo-Zhong Li, Shenheng Guan, and Alan G. Marshall. Sympathetic cooling of trapped negative ions by self-cooled electrons in a fourier transform ion cyclotron resonance mass spectrometer. *Journal of the American Society for Mass Spectrometry*, 8(8):793–800, Aug 1997. ISSN 1879-1123. doi: 10.1016/S1044-0305(97)84131-1. URL https://doi.org/10.1016/S1044-0305(97)84131-1.

[488] C. Amole, G.B. Andresen, M.D. Ashkezari, et al. The alpha antihydrogen trapping apparatus. *Nuclear Instruments and Methods in Physics Research Section A: Accelerators, Spectrometers, Detectors and Associated Equipment*, 735:319 – 340, 2014. ISSN 0168-9002. doi: http://dx.doi.org/10.1016/j.nima.2013.09.043. URL http://www.sciencedirect.com/science/article/pii/S0168900213012771.

[489] M. Ahmadi, B. X. R. Alves, C. J. Baker, et al. Antihydrogen accumulation for fundamental symmetry tests. *Nature Communications*, 8(1):681–, 2017. ISSN 2041-1723. URL https://doi.org/10.1038/s41467-017-00760-9.

[490] F. Herfurth, T. Beier, L. Dahl, et al. Highly charged ions at rest: The HITRAP project at GSI. *AIP Conference Proceedings*, 793(1):278–292, 2005. doi: 10.1063/1.2121990. URL https://aip.scitation.org/doi/abs/10.1063/1.2121990.

[491] W. Quint, J. Dilling, S. Djekic, et al. HITRAP: A facility for experiments with trapped highly charged ions. *Hyperfine Interactions*, 132(1):453–457, 2001. ISSN 1572-9540. URL https://doi.org/10.1023/A:1011908332584.

[492] H.-J. Kluge, T. Beier, K. Blaum, et al. HITRAP: A facility at GSI for highly charged ions. In S. Salomonson and E. Lindroth, editors, *Current Trends in Atomic Physics*, volume 53 of *Advances in Quantum Chemistry*, chapter 7, pages 83–98. Academic Press, 2008. doi: https://doi.org/10.1016/S0065-3276(07)53007-8. URL https://www.sciencedirect.com/science/article/pii/S0065327607530078.

[493] M. Vogel, Z. Andelkovic, G. Birkl, et al. Penning-trap experiments for spectroscopy of highly-charged ions at HITRAP. *Physica Scripta*, T166:014066, nov 2015. doi: 10.1088/0031-8949/2015/t166/014066. URL https://doi.org/10.1088/0031-8949/2015/t166/014066.

[494] Z. Andelkovic, G. Birkl, S. Fedotova, et al. Status of deceleration and laser spectroscopy of highly charged ions at HITRAP. *Hyperfine Interactions*, 235(1):37–44, Nov 2015. ISSN 1572-9540. doi: 10.1007/s10751-015-1199-8. URL https://doi.org/10.1007/s10751-015-1199-8.

[495] G. Zwicknagel H. B. Nersisyan, C. Toepffer. *Interactions Between Charged Particles in a Magnetic Field: A Theoretical Approach to Ion Stopping in Magnetized Plasmas*. Springer, 1st edition, 2007. ISBN 3540698531,9783540698531,9783540698548.

[496] H. B. Nersisyan, M. Walter, and G. Zwicknagel. Stopping power of ions in a magnetized two-temperature plasma. *Phys. Rev. E*, 61:7022–7033, Jun 2000. doi: 10.1103/PhysRevE.61.7022. URL https://link.aps.org/doi/10.1103/PhysRevE.61.7022.

[497] G. Zwicknagel. Electron cooling of highly charged ions in Penning traps. *AIP Conference Proceedings*, 862(1):281–291, 2006. doi: 10.1063/1.2387934. URL https://aip.scitation.org/doi/abs/10.1063/1.2387934.

[498] H. B. Nersisyan and G. Zwicknagel. Cooling force on ions in a magnetized electron plasma. *Phys. Rev. ST Accel. Beams*, 16:074201, Jul 2013. doi: 10.1103/PhysRevSTAB.16.074201. URL https://link.aps.org/doi/10.1103/PhysRevSTAB.16.074201.

[499] S. Cohen, E. Sarid, and M. Gedalin. Fokker-Planck coefficients for a magnetized ion-electron plasma. *Physics of Plasmas*, 25(1):012311, 2018. doi: 10.1063/1.5009284. URL https://doi.org/10.1063/1.5009284.

[500] S. Cohen, E. Sarid, and M. Gedalin. Collisional relaxation of a strongly magnetized ion-electron plasma. *Physics of Plasmas*, 26(8):082105, 2019. doi: 10.1063/1.5109965. URL https://doi.org/10.1063/1.5109965.

[501] S. L. Rolston and G. Gabrielse. Cooling antiprotons in an ion trap. *Hyperfine Interactions*, 44(1):233–245, 1989. ISSN 1572-9540. doi: 10.1007/BF02398673. URL http://dx.doi.org/10.1007/BF02398673.

[502] J. Bernard, J. Alonso, T. Beier, et al. Electron and positron cooling of highly charged ions in a cooler Penning trap. *Nuclear Instruments and Methods in Physics Research Section A: Accelerators, Spectrometers, Detectors and Associated Equipment*, 532, 2004. doi: 10.1016/j.nima.2004.06.049.

[503] C. Amsler, H. Breuker, S. Chesnevskaya, et al. Reducing the background temperature for cyclotron cooling in a cryogenic Penning–Malmberg trap. *Physics of Plasmas*, 29 (8):083303, 2022. doi: 10.1063/5.0093360. URL https://doi.org/10.1063/5.0093360.

[504] M. E. Glinsky, T. M. O'Neil, M. N. Rosenbluth, et al. Collisional equipartition rate for a magnetized pure electron plasma. *Physics of Fluids B: Plasma Physics*, 4(5):1156–1166, 1992. doi: 10.1063/1.860124. URL https://doi.org/10.1063/1.860124.

[505] R. E. Cohen, D. Lide, and G. Trigg. *Physicist's Desk Reference*. Springer Science & Business Media, 3rd ed. edition, 2003. ISBN 0387989730.

[506] N. R. Badnell. Atomic data from AUTOSTRUCTURE. Online database, 2022. URL http://amdpp.phys.strath.ac.uk/tamoc/DATA/.

[507] A. Müller and A. Wolf. Production of antihydrogen by recombination of $\bar{p}$ with e^+: What can we learn from electron–ion collision studies? *Hyperfine Interactions*, 109(1):233–267, 1997. ISSN 1572-9540. URL https://doi.org/10.1023/A:1012617803666.

[508] U. Chowdhury. *A cooler Penning trap to cool highly charged radioactive ions and mass measurement of ^{24}Al*. PhD thesis, University of Manitoba, 2016.

[509] M. Amoretti, C. Amsler, G. Bonomi, et al. Production and detection of cold antihydrogen atoms. *Nature*, 419(6906):456–459, 2002.

[510] B. Möllers, C. Toepffer, M. Walter, et al. Cooling of ions and antiprotons with magnetized electrons. *Nuclear Instruments and Methods in Physics Research Section A: Accelerators, Spectrometers, Detectors and Associated Equipment*, 532 (1):279 – 284, 2004. ISSN 0168-9002. doi: http://dx.doi.org/10.1016/j.nima.2004.06.057. URL http://www.sciencedirect.com/science/article/pii/S0168900204012550. International Workshop on Beam Cooling and Related Topics.

[511] Z. Ke. *A cooler ion trap for the TITAN on-line trapping facility at TRIUMF*. PhD thesis, University of Manitoba, 2008.

[512] B. Kootte. In preparation. PhD thesis, University of Manitoba, To be published 2023.

[513] J. H. Malmberg and J. S. deGrassie. Properties of nonneutral plasma. *Phys. Rev. Lett.*, 35:577–580, Sep 1975. doi: 10.1103/PhysRevLett.35.577. URL https://link.aps.org/doi/10.1103/PhysRevLett.35.577.

[514] C. F. Driscoll, K. S. Fine, and J. H. Malmberg. Reduction of radial losses in a pure electron plasma. *The Physics of Fluids*, 29(6):2015–2017, 1986. doi: 10.1063/1.865580. URL http://aip.scitation.org/doi/abs/10.1063/1.865580.

[515] D. H. E. Dubin. Collisional transport in non-neutral plasmas. *Physics of Plasmas*, 5 (5):1688–1694, 1998.

[516] A. Narimannezhad, J. Jennings, M. H. Weber, and K. G. Lynn. Arrays of micro Penning-Malmberg traps: An approach to fabricate very high aspect ratios. In *2014 IEEE 27th International Conference on Micro Electro Mechanical Systems (MEMS)*, pages 453–456, 2014. doi: 10.1109/MEMSYS.2014.6765674.

[517] Grant W. Hart. The effect of a tilted magnetic field on the equilibrium of a pure electron plasma. *Physics of Fluids B Plasma Physics*, 3, 11 1991. doi: 10.1063/1.859777.

[518] D. A. Church. Toward storage and cooling of highly-charged ions in a Penning trap. *Physica Scripta*, 46(3):278–281, sep 1992. doi: 10.1088/0031-8949/46/3/012. URL https://doi.org/10.1088/0031-8949/46/3/012.

[519] C. Benvenuti, P. Chiggiato, P. Costa Pinto, et al. Vacuum properties of TiZrV non-evaporable getter films. *Vacuum*, 60(1):57–65, 2001. ISSN 0042-207X. doi: https://doi.org/10.1016/S0042-207X(00)00246-3. URL https://www.sciencedirect.com/science/article/pii/S0042207X00002463. The Sixth European Vacuum Conference.

[520] HeatWave Labs. Tb-118 aluminosilicate ion sources, model 101139. Technical report, HeatWave Labs, Inc., 2002. URL https://www.cathode.com/.

[521] T. Mohamed, H. Imao, N. Oshima, et al. Fast electron accumulation and its mechanism in a harmonic trap under ultrahigh vacuum conditions. *Physics of Plasmas*, 18 (3):032507, 2011.

[522] S. F. Paul, B. Kootte, D. Lascar, et al. Off-axis electron injection into a cooler Penning trap. *Hyperfine Interactions*, 240(1):50, 2019.

[523] Stefan Felix Paul. Off-axis electron injection into a cooler Penning trap. Master's thesis, Ruprecht-Karls-Universität Heidelberg, 2017.

[524] Technical report, 8 2017. URL https://www.kimballphysics.com/cathode-specs-w. https://www.kimballphysics.com/cathode-specs-w.

[525] J. B. Le Poole. Electron guns, state of the art. *Nuclear Instruments and Methods in Physics Research*, 187(1):241–244, 1981. ISSN 0167-5087. doi: https://doi.org/10.1016/0029-554X(81)90494-8. URL https://www.sciencedirect.com/science/article/pii/0029554X81904948.

[526] S. Koszudowski. *Developments for the HITRAP Cooler Trap and mass measurements around A = 96 at SHIPTRAP*. PhD thesis, Ruprecht-Karls Universität Heidelberg, 2009.

[527] B. Eberhardt. The TITAN cooler Penning trap for short-lived highly charged ions; investigations for nested trap applications and fast electrode switching. Diploma, Johannes Gutenberg-Universität Mainz, 2011.

[528] D. A. Dahl. SIMION for the personal computer in reflection. *International Journal of Mass Spectrometry*, 200(1):3 – 25, 2000. ISSN 1387-3806. doi: https://doi.org/10.1016/S1387-3806(00)00305-5. URL http://www.sciencedirect.com/science/article/pii/S1387380600003055. Volume 200: The state of the field as we move into a new millenium.

[529] D. Lascar, B. Kootte, B. R. Barquest, et al. A novel transparent charged particle detector for the CPET upgrade at TITAN. *Nuclear Instruments and Methods in Physics Research Section A: Accelerators, Spectrometers, Detectors and Associated Equipment*, 2017. ISSN 0168-9002. doi: http://dx.doi.org/10.1016/j.nima.2017.07.003. URL http://www.sciencedirect.com/science/article/pii/S0168900217307143.

[530] R. H. Levy. Diocotron instability in a cylindrical geometry. *The Physics of Fluids*, 8(7):1288–1295, 1965. doi: 10.1063/1.1761400. URL https://aip.scitation.org/doi/abs/10.1063/1.1761400.

[531] K. S. Fine and C. F. Driscoll. The finite length diocotron mode. *Physics of Plasmas*, 5(3):601–607, 1998. doi: 10.1063/1.872752. URL https://doi.org/10.1063/1.872752.

[532] G. W. Mason and R. L. Spencer. Simulations of the instability of the m=1 self-shielding diocotron mode in finite-length non-neutral plasmas. *Physics of Plasmas*, 9 (8):3217–3224, 2002. doi: 10.1063/1.1488600. URL https://doi.org/10.1063/1.1488600.

[533] B. P. Cluggish and C. F. Driscoll. Transport and damping from rotational pumping in magnetized electron plasmas. *Phys. Rev. Lett.*, 74:4213–4216, May 1995. doi: 10.1103/PhysRevLett.74.4213. URL https://link.aps.org/doi/10.1103/PhysRevLett.74.4213.

[534] E. Sarid, E. P. Gilson, and J. Fajans. Decay of the diocotron rotation and transport in a new low-density asymmetry-dominated regime. *Phys. Rev. Lett.*, 89:105002, Aug 2002. doi: 10.1103/PhysRevLett.89.105002. URL https://link.aps.org/doi/10.1103/PhysRevLett.89.105002.

[535] C. Y. Chim and T. M. O'Neil. Flux-driven algebraic damping of $m = 1$ diocotron mode. *Physics of Plasmas*, 23(7):072113, 2016.

[536] Chao, E. H. and Davidson, R. C. and Paul, S. F. and Morrison, K. A. Effects of background gas pressure on the dynamics of a nonneutral electron plasma confined in a Malmberg-Penning trap. *Physics of Plasmas*, 7, 2000. doi: 10.1063/1.873879.

[537] D. Lascar, R. Klawitter, C. Babcock, et al. Precision mass measurements of $^{125-127}$Cd isotopes and isomers approaching the $N = 82$ closed shell. *Phys. Rev. C*, 96:044323, Oct 2017. doi: 10.1103/PhysRevC.96.044323. URL https://link.aps.org/doi/10.1103/PhysRevC.96.044323.

[538] S. Ritt and P. A. Amaudruz. New components of the MIDAS data acquisition system. In *1999 IEEE Conference on Real-Time Computer Applications in Nuclear Particle and Plasma Physics. 11th IEEE NPSS Real Time Conference. Conference Record (Cat. No.99EX295)*, pages 116–118, 1999. doi: 10.1109/RTCON.1999.842578.

[539] G. Bettega, F. Cavaliere, M. Cavenago, et al. Active control of the ion resonance instability by ion removing fields. *Physics of Plasmas*, 13, 2006. doi: 10.1063/1.2363175.

[540] C. Krantz. *Intense electron beams from GaAs photocathodes as a tool for molecular and atomic physics*. PhD thesis, Ruprecht-Karls-Universität, Heidelberg, 2009.

[541] T. Mohamed, N. Oshima, A. Mohri, and Y. Yamazaki. Fast accumulation of electron plasma in a multi-ring trap (MRT) under ultra-high vacuum condition. *AIP Conference Proceedings*, 862(1):56–61, 2006. doi: 10.1063/1.2387908. URL https://aip.scitation.org/doi/abs/10.1063/1.2387908.

[542] T. Mohamed, A. Mohri, and Y. Yamazaki. Comparison of non-neutral electron plasma confinement in harmonic and rectangular potentials in a very dense regime. *Physics of Plasmas*, 20(1):012502, 2013. doi: http://dx.doi.org/10.1063/1.4773900. URL http://scitation.aip.org/content/aip/journal/pop/20/1/10.1063/1.4773900.

[543] B. Paroli, F. De Luca, G. Maero, et al. Broadband radio frequency plasma generation in a Penning–Malmberg trap. *Plasma Sources Science and Technology*, 19(4):045013, jun 2010. doi: 10.1088/0963-0252/19/4/045013. URL https://doi.org/10.1088%2F0963-0252%2F19%2F4%2F045013.

[544] U. Chowdhury, M. Good, B. Kootte, et al. A cooler Penning trap for the TITAN mass measurement facility. In *AIP Conference Proceedings*, volume 1640, pages 120–123. AIP, 2015.

[545] R. Silwal, S. F. Paul, B. K. Kootte, et al. Ion simulations, recent upgrades and tests with TITAN's cooler Penning trap. In *24th Int. Workshop on ECR Ion Sources (ECRIS2020)*, 2020.

[546] B. M. Dyavappa, D. Datar, P. Ananthamurthy, and S. Ananthamurthy. Dependence of the confinement time of an electron plasma on the magnetic field in a quadrupole Penning trap. *EPJ Techniques and Instrumentation*, 4(1):4, Aug 2017. ISSN 2195-7045. doi: 10.1140/epjti/s40485-017-0039-4. URL https://doi.org/10.1140/epjti/s40485-017-0039-4.

[547] M. Amoretti, C. Amsler, G. Bonomi, et al. Positron plasma diagnostics and temperature control for antihydrogen production. *Phys. Rev. Lett.*, 91:055001, Jul 2003. doi: 10.1103/PhysRevLett.91.055001. URL https://link.aps.org/doi/10.1103/PhysRevLett.91.055001.

[548] G. Bettega, B. Paroli, R. Pozzoli, et al. Low-noise techniques for electrostatic diagnostics on a pure electron plasma. *Measurement Science and Technology*, 19(8):085703, 2008. URL http://stacks.iop.org/0957-0233/19/i=8/a=085703.

[549] J. Notte and J. Fajans. The effect of asymmetries on non-neutral plasma confinement time. *Physics of Plasmas*, 1(5):1123–1127, 1994. doi: 10.1063/1.870762. URL https://doi.org/10.1063/1.870762.

[550] E. M. Hollmann, F. Anderegg, and C. F. Driscoll. Confinement and manipulation of non-neutral plasmas using rotating wall electric fields. *Physics of Plasmas*, 7(7):2776–2789, 2000.

[551] E. H. Chao, R. C. Davidson, and S. F. Paul. Non-neutral plasma expansion induced by electron-neutral collisions in a Malmberg–Penning trap. *Journal of Vacuum Science & Technology A*, 17(4):2050–2055, 1999. doi: 10.1116/1.581724. URL https://doi.org/10.1116/1.581724.

[552] Y. Chang, J. R. Correa, and C. A. Ordonez. Loss rate of an electrically trapped non-neutral plasma. *Physics of Plasmas*, 11(7):3360–3367, 2004. doi: 10.1063/1.1752932. URL https://doi.org/10.1063/1.1752932.

[553] B. Kootte, M. Alanssari, C. Andreoiu, et al. Quantification of the electron plasma in TITAN's cooler Penning trap. In *Int. Workshop on Beam Cooling and Related Topics (COOL'15), Newport News, VA, USA, September 28-October 2, 2015*, pages 39–42. JACOW, Geneva, Switzerland, 2016.

[554] S. Fedotova. *Experimental characterization of the HITRAP Cooler trap with highly charged ions*. PhD thesis, Ruprecht-Karls-Universität Heidelberg, 2013.

[555] M. Kretzschmar. Calculating damping effects for the ion motion in a Penning trap. *The European Physical Journal D*, 48(3):313–319, 2008. ISSN 1434-6079. URL https://doi.org/10.1140/epjd/e2008-00125-0.

[556] T. M. O'Neil. Centrifugal separation of a multispecies pure ion plasma. *The Physics of Fluids*, 24(8):1447–1451, 1981. doi: 10.1063/1.863565. URL http://aip.scitation.org/doi/abs/10.1063/1.863565.

[557] G. Gabrielse, W. S. Kolthammer, R. McConnell, et al. Centrifugal separation of antiprotons and electrons. *Phys. Rev. Lett.*, 105:213002, Nov 2010. doi: 10.1103/PhysRevLett.105.213002. URL https://link.aps.org/doi/10.1103/PhysRevLett.105.213002.

[558] G. B. Andresen, M. D. Ashkezari, M. Baquero-Ruiz, et al. Centrifugal separation and equilibration dynamics in an electron-antiproton plasma. *Phys. Rev. Lett.*, 106:145001, Apr 2011. doi: 10.1103/PhysRevLett.106.145001. URL http://link.aps.org/doi/10.1103/PhysRevLett.106.145001.

[559] M. Amoretti, C. Canali, C. Carraro, et al. Centrifugal separation of ions and an oppositely charged non-neutral plasma. *Physics of Plasmas*, 13(1):012308, 2006. doi: 10.1063/1.2164992. URL https://doi.org/10.1063/1.2164992.

[560] N. L. Johnson, S. Kotz, and N. Balakrishnan. *Continuous univariate distributions, volume 2*, volume 289. John Wiley & Sons, 1995.

[561] B. Möllers. *Elektronenkühlung hochgeladener Ionen in Penningfallen*. PhD thesis, Friedrich-Alexander-Universiät Erlangen-Nürnberg, 2007.

[562] M. W. Kunz. Lecture notes on irreversible processes in plasmas, November 2021. URL https://www.astro.princeton.edu/~kunz/Site/AST554/AST554_lecture_notes_Kunz.pdf.

[563] A. Härter and J. Hecker Denschlag. Cold atom–ion experiments in hybrid traps. *Contemporary Physics*, 55(1):33–45, 2014. doi: 10.1080/00107514.2013.854618. URL https://doi.org/10.1080/00107514.2013.854618.

[564] A. Mahdian, A. Krükow, and J. Hecker Denschlag. Direct observation of swap cooling in atom–ion collisions. *New Journal of Physics*, 23(6):065008, 2021.

[565] M. Amoretti, C. Amsler, G. Bonomi, et al. Dynamics of antiproton cooling in a positron plasma during antihydrogen formation. *Physics Letters B*, 590 (3):133 – 142, 2004. ISSN 0370-2693. doi: https://doi.org/10.1016/j.physletb.2004.03.073. URL http://www.sciencedirect.com/science/article/pii/S037026930400557X.

[566] C. A. Ordonez, D. D. Dolliver, Y. Chang, and J. R. Correa. Possibilities for achieving antihydrogen recombination and trapping using a nested Penning trap and a magnetic well. *Physics of Plasmas*, 9(8):3289–3302, 2002. doi: 10.1063/1.1494822. URL https://doi.org/10.1063/1.1494822.

[567] G. Gabrielse, P. Larochelle, D. Le Sage, et al. Antihydrogen production within a Penning-Ioffe trap. *Phys. Rev. Lett.*, 100:113001, 3 2008. doi: 10.1103/PhysRevLett.100.113001. URL https://link.aps.org/doi/10.1103/PhysRevLett.100.113001.

[568] J. R. Danielson, D. H. E. Dubin, R. G. Greaves, and C. M. Surko. Plasma and trap-based techniques for science with positrons. *Rev. Mod. Phys.*, 87:247–306, Mar 2015. doi: 10.1103/RevModPhys.87.247. URL https://link.aps.org/doi/10.1103/RevModPhys.87.247.

[569] M. Newville, R. Otten, A. Nelson, et al. lmfit/lmfit-py:, February 2021. URL https://doi.org/10.5281/zenodo.4516644.

[570] D. H. E. Dubin. Equilibrium and dynamics of multispecies nonneutral plasmas with a single sign of charge. *AIP Conference Proceedings*, 1521(1):26–34, 2013. doi: 10.1063/1.4796058. URL https://aip.scitation.org/doi/abs/10.1063/1.4796058.

[571] D. L. Eggleston, T. M. O'Neil, and J. H. Malmberg. Collective enhancement of radial transport in a nonneutral plasma. *Phys. Rev. Lett.*, 53:982–984, Sep 1984. doi: 10.1103/PhysRevLett.53.982. URL https://link.aps.org/doi/10.1103/PhysRevLett.53.982.

[572] A. A. Kabantsev, K. A. Thompson, and C. F. Driscoll. First experiments with e^-/H^- plasmas: Enhanced centrifugal separation from diocotron mode damping. *AIP Conference Proceedings*, 1928(1):020008, 2018. doi: 10.1063/1.5021573. URL https://aip.scitation.org/doi/abs/10.1063/1.5021573.

[573] T. Lafleur and S. D Baalrud. Transverse force induced by a magnetized wake. *Plasma Physics and Controlled Fusion*, 61(12):125004, Oct 2019. doi: 10.1088/1361-6587/ab45d4. URL https://doi.org/10.1088/1361-6587/ab45d4.

[574] D. J. Bernstein, T. Lafleur, J. Daligault, and S. D. Baalrud. Friction force in strongly magnetized plasmas. *Phys. Rev. E*, 102:041201, Oct 2020. doi: 10.1103/PhysRevE.102.041201. URL https://link.aps.org/doi/10.1103/PhysRevE.102.041201.

[575] N. Kuroda, S. Ulmer, D. J. Murtagh, et al. A source of antihydrogen for in-flight hyperfine spectroscopy. *Nature communications*, 5, 2014.

[576] S. Schwarz. IonCool—a versatile code to characterize gas-filled ion bunchers and coolers (not only) for nuclear physics applications. *Nuclear Instruments and Methods in Physics Research Section A: Accelerators, Spectrometers, Detectors and Associated Equipment*, 566(2):233–243, 2006. ISSN 0168-9002. doi: https://doi.org/10.1016/j.nima.2006.07.004. URL https://www.sciencedirect.com/science/article/pii/S016890020601254X.

[577] J. R. Danielson and C. M. Surko. Plasma compression using rotating electric fields — the strong drive regime. *AIP Conference Proceedings*, 862(1):19–28, 2006. doi: 10.1063/1.2387903. URL https://aip.scitation.org/doi/abs/10.1063/1.2387903.

[578] T. Mohamed. Compression features of high density electron plasma in a long harmonic trap using a rotating wall technique. *Physics Letters A*, 382(35):2459 – 2463, 2018. ISSN 0375-9601. doi: https://doi.org/10.1016/j.physleta.2018.07.012. URL http://www.sciencedirect.com/science/article/pii/S0375960118307369.

[579] F. M. Fränkle, F. Glück, K. Valerius, et al. Penning discharge in the KATRIN pre-spectrometer. *Journal of Instrumentation*, 9(07):P07028–P07028, jul 2014. doi: 10.1088/1748-0221/9/07/p07028. URL https://doi.org/10.1088%2F1748-0221%2F9%2F07%2Fp07028.

[580] Michaël Tandecki. *Progress at the WITCH experiment towards weak interaction studies*. PhD thesis, Katholieke Universiteit Leuven, Apr 2011. URL https://cds.cern.ch/record/1642846. Presented 27 May 2011.

[581] T. G. Northrop. The guiding center approximation to charged particle motion. *Annals of Physics*, 15(1):79–101, 1961. ISSN 0003-4916. doi: https://doi.org/10.

1016/0003-4916(61)90167-1. URL https://www.sciencedirect.com/science/article/pii/0003491661901671.

[582] E. Hirvijoki, O. Asunta, T. Koskela, et al. ASCOT: Solving the kinetic equation of minority particle species in tokamak plasmas. *Computer Physics Communications*, 185(4):1310–1321, 2014. ISSN 0010-4655. doi: https://doi.org/10.1016/j.cpc.2014.01.014. URL https://www.sciencedirect.com/science/article/pii/S0010465514000277.

[583] F. Anderegg, E. M. Hollmann, and C. F. Driscoll. Rotating field confinement of pure electron plasmas using Trivelpiece-Gould modes. *Phys. Rev. Lett.*, 81:4875–4878, Nov 1998. doi: 10.1103/PhysRevLett.81.4875. URL https://link.aps.org/doi/10.1103/PhysRevLett.81.4875.

[584] G. Gabrielse, X. Fei, L. A. Orozco, et al. Cooling and slowing of trapped antiprotons below 100 meV. *Phys. Rev. Lett.*, 63:1360–1363, Sep 1989. doi: 10.1103/PhysRevLett.63.1360. URL http://link.aps.org/doi/10.1103/PhysRevLett.63.1360.

[585] G. Gabrielse, J. Estrada, J. N. Tan, et al. First positron cooling of antiprotons. *Physics Letters B*, 507(1):1–6, 2001. ISSN 0370-2693. doi: https://doi.org/10.1016/S0370-2693(01)00450-6. URL https://www.sciencedirect.com/science/article/pii/S0370269301004506.

[586] W. S. Porter, E. Dunling, E. Leistenschneider, et al. Investigating nuclear structure near $N = 32$ and $N = 34$: Precision mass measurements of neutron-rich Ca, Ti, and V isotopes. *Phys. Rev. C*, 106:024312, Aug 2022. doi: 10.1103/PhysRevC.106.024312. URL https://link.aps.org/doi/10.1103/PhysRevC.106.024312.

[587] W. S. Porter, B. Ashrafkhani, J. Bergmann, et al. Mapping the $N = 40$ island of inversion: Precision mass measurements of neutron-rich Fe isotopes. *Phys. Rev. C*, 105:L041301, Apr 2022. doi: 10.1103/PhysRevC.105.L041301. URL https://link.aps.org/doi/10.1103/PhysRevC.105.L041301.

[588] R. Silwal, C. Andreoiu, B. Ashrafkhani, et al. Summit of the $N = 40$ island of inversion: Precision mass measurements and ab initio calculations of neutron-rich chromium isotopes. *Physics Letters B*, 833:137288, 2022. ISSN 0370-2693. doi: https://doi.org/10.1016/j.physletb.2022.137288. URL https://www.sciencedirect.com/science/article/pii/S0370269322004221.

[589] Y. Kalambet, Y. Kozmin, K. Mikhailova, et al. Reconstruction of chromatographic peaks using the exponentially modified Gaussian function. *Journal of Chemometrics*, 25(7):352–356, 2011. doi: 10.1002/cem.1343. URL https://onlinelibrary.wiley.com/doi/abs/10.1002/cem.1343.

[590] C. R. Harris, K. J. Millman, S. J. van der Walt, et al. Array programming with NumPy. *Nature*, 585(7825):357–362, September 2020. doi: 10.1038/s41586-020-2649-2. URL https://doi.org/10.1038/s41586-020-2649-2.

[591] P. Virtanen, R. Gommers, T. E. Oliphant, et al. SciPy 1.0: Fundamental algorithms for scientific computing in Python. *Nature Methods*, 17:261–272, 2020. doi: 10.1038/s41592-019-0686-2.

[592] K. J. Mighell. Parameter estimation in astronomy with Poisson-distributed data. II. The modified chi-square-gamma statistic, 2000.

[593] M. Thomson. Statistics lecture 3 : Fitting and hypothesis testing. Online Lecture Notes, Accessed October 2022, 2015. URL https://indico.cern.ch/category/6015/attachments/192/631/Statistics_Fitting_II.pdf.

[594] D. van Ravenzwaaij, P. Cassey, and S. D. Brown. A simple introduction to Markov Chain Monte-Carlo sampling. *Psychonomic Bulletin & Review*, 25(1):143–154, 2018. ISSN 1531-5320. URL https://doi.org/10.3758/s13423-016-1015-8.

[595] D. A. Gedcke. How histogramming and counting statistics affect peak position precision. Application note AN58, Ortec, Accessed October 2022. URL https://www.ortec-online.com/-/media/ametekortec/application-notes/an58.pdf?la=en&revision=4a94e5c4-a8c3-4955-8760-595610345e0b&hash=D57AE6A30882539409E0A40A456392F0.

[596] F. Paschen. Über die zum Funkenübergang in Luft, Wasserstoff und Kohlensäure bei verschiedenen Drucken erforderliche Potentialdifferenz. *Annalen der Physik*, 273 (5):69–96, 1889. doi: https://doi.org/10.1002/andp.18892730505. URL https://onlinelibrary.wiley.com/doi/abs/10.1002/andp.18892730505.

[597] F. M. Charbonnier, C. J. Bennette, and L. W. Swanson. Electrical breakdown between metal electrodes in high vacuum. I. Theory. *Journal of Applied Physics*, 38(2):627–633, 1967. doi: 10.1063/1.1709385. URL https://doi.org/10.1063/1.1709385.

[598] J.-L. Vay, D. P. Grote, R. H. Cohen, and A. Friedman. Novel methods in the particle-in-cell accelerator code-framework WARP. *Computational Science & Discovery*, 5(1): 014019, 2012. URL http://stacks.iop.org/1749-4699/5/i=1/a=014019.

[599] K. Gomberoff, J. Wurtele, A. Friedman, et al. A method for obtaining three-dimensional computational equilibrium of non-neutral plasmas using WARP. *Journal of Computational Physics*, 225(2):1736 – 1752, 2007. ISSN 0021-9991. doi: https://doi.org/10.1016/j.jcp.2007.02.029. URL http://www.sciencedirect.com/science/article/pii/S0021999107000848.

[600] E. Hairer, S. P. Nørsett, and G. Wanner. Solving ordinary differential equations I: Nonstiff problems. 2000. 2000. URL https://profs.info.uaic.

ro/~{}fliacob/An2/2014-2015/Resurse_MCM_2015/Hairer,%20Norsett,%20Wanner_Solving%20Ordinary%20Differential%20Equations%20I.pdf.

[601] J. D. Huba. NRL plasma formulary 2016. Supported by the Office of Naval Research, Naval Research Laboratory, Washington, D.C., 2016.

[602] C. K. Birdsall. Particle-in-cell charged-particle simulations, plus Monte Carlo collisions with neutral atoms, PIC-MCC. *IEEE Transactions on Plasma Science*, 19(2): 65–85, 1991. doi: 10.1109/27.106800.

[603] C. K. Birdsall and A. B. Langdon. *Plasma Physics via Computer Simulation*. Series in Plasma Physics and Fluid Dynamics. CRC Press, 2004. ISBN 978-1-4822-6306-0,1482263068,277-277-277-2.

[604] R. Côté and A. Dalgarno. Ultracold atom-ion collisions. *Physical Review A*, 62(1): 012709, 2000.

[605] Experimental polarizabilities - computational chemistry comparison and benchmark database release 22. Standard Reference Database 101, May 2022. URL https://cccbdb.nist.gov/pollistx.asp.

[606] R. Saito, S. Haze, M. Sasakawa, et al. Characterization of charge-exchange collisions between ultracold ^{6}Li atoms and $^{40}Ca^{+}$ ions. *Phys. Rev. A*, 95:032709, Mar 2017. doi: 10.1103/PhysRevA.95.032709. URL https://link.aps.org/doi/10.1103/PhysRevA.95.032709.

[607] D. Rapp and W. E. Francis. Charge exchange between gaseous ions and atoms. *The Journal of Chemical Physics*, 37(11):2631–2645, 1962. doi: 10.1063/1.1733066. URL https://doi.org/10.1063/1.1733066.

Acknowledgements

As my PhD journey comes to an end, there are many people that I'm indebted to and that I would like to express my gratitude to at this point.

First of all, I would like to thank my local supervisors at TRIUMF, Ania Kwiatkowski and Jens Dilling. Thank you both for the continual guidance, trust and leadership over the last years. Your encouragement and help to connect with leading experts around the world were instrumental to the success of my PhD work. Your own paths and the work environment you have built at TITAN prove that forefront research and family need not be incompatible. I am especially grateful to Jens for staying invested in my progress, irrespective of his move from TRIUMF to ORNL. Your mentorship and the countless helpful remarks during the thesis writing process are greatly appreciated. I am also grateful to Gerald Gwinner for many valuable physics discussions and all the advice both remotely from Manitoba and in person at TRIUMF.

Next, I would like to thank my primary PhD supervisor, Klaus Blaum, for his contagious enthusiasm and optimism, and all the rapid e-mail replies that greatly helped to resolve any organizational matters that came up along the way. Once having attended the lecture as a Bachelor student myself, it was a fun and rewarding experience to switch roles and serve as the tutor for your and Sebastian George's Stored Charged Particles lectures – thanks for the opportunity. Many thanks to you, Sergey Eliseev, Gabi Weese and all ion trappers at the MPIK for welcoming me into your ion trapping family during my stay in Heidelberg. Temporarily joining the PENTRATRAP team and seeing the ultra-high precision end of mass spectrometry was an enrichment to my doctoral studies. The diverse skill sets of the students I had the pleasure to work alongside at the MPIK taught me valuable lessons and motivated me to take on electronics and programming projects that turned out to be critical for the success of my thesis work.

I would like to express my gratitude to Prof. Dr. Ulrich Uwer for agreeing to act as the second referee for this thesis and to Prof. Dr. Björn Malte Schäfer und Prof. Dr. Peter Bachert for serving as the additional examiners.

I am also thankful to Brian Kootte, Zach Hockenberry, Stephanie Rädel and Gerald Gwinner for the thorough reading and the helpful edits and comments to various parts of this thesis.

I am indebted to a diverse set of external collaborators that connected with me across borders in order to forge the gallium publication and, in the process, graciously taught me about

their respective fields of specialization. In a challenging time where public health measures often hampered direct communication with other researchers, this correspondence proved invaluable to the progress of my studies. Many thanks to Hendrik Schatz for running the X-ray burst simulations and for willingly sharing his vast expertise on the *rp*-process. Further thanks to Marion MacCormick for the fruitful and motivating exchange throughout our IMME evaluation for the gallium paper; I learned a lot about what true literature detective work looks like. Moreover, I'm grateful to Nadya Smirnova for contributing the shell model calculations to the paper and adding valuable comments during the writing stage.

Thanks to all CPET team members over the years, Brian Kootte, Roshani Silwal, Dan Lascar, Duane Byer, Tigris Joseph, Solbee Seo and Rane Simpson, for their hard work, the creative problem solving and many fun physics and non-physics related discussions. During my PhD studies, I was glad to be given the chance to take on the day-to-day supervision of two Coop-Students: Rane and Solbee – thank you for your trust in my guidance and for all your valuable contributions to the project. My gratitude also extends to Ben Smith and Andrea Teigelhöfer who reinforced the CPET team during the pandemic and who both proved instrumental in enabling the electron cooling measurements. I'd also like to acknowledge Mel Good's excellent support in all hardware and vacuum related matters. Thank you to Hubert Hui and Daryl Bishop for the great support and many enlightening discussions concerning electronics.

Thanks to all TITAN students and post-docs for the camaraderie in- and outside the lab. I felt honoured to work within such a diverse group of bright and driven young researchers. Especially, in pre-pandemic times, our lunch room conversations, which regularly involved people of more than 5 nationalities, were often high notes of my days. Special thanks to Pascal for the inspiring discussions about MR-TOF peak fitting that eventually lead to the development of EMGFIT. Brian, Erich, Leigh, Pascal, John, Eleanor, Julian, Marilena, Andrew, Sam, Zach, Jon, Chris, Abhilash, Kilian, Tobias and many others were not only excellent companions in the counting room but also on various hikes and other outings. The TITAN weekend on Vancouver Island will remain a highlight of my PhD years :)

Thanks to Rob Watt and the entire TRIUMF running team for the companionship in many lunch runs in Pacific Spirit Park and at multiple Vancouver Sun Runs!

Zum Abschluss gilt mein Dank meiner Familie. Vielen Dank an Tina, Lutz, Anna und Jonathan für die wertvollen und energiespendenden gemeinsamen Zeiten während unseres Heidelbergaufenthalts und Eurer Besuche in Kanada. Herzlichen Dank an meine Eltern und Großeltern für die ideelle, finanzielle und tatkräftige Unterstützung meiner Promotion. Ich freue mich drauf, den Abschluss dieses Kapitels mit Euch gemeinsam feiern zu können! Der größte Dank gilt meiner fantastischen Partnerin Stephi – danke für die bedingunglose Unterstützung, insbesondere während meiner Schreibphase. Du und Jasper waren stets die beste Ablenkung and der beste Ansporn, wenn Dinge im Labor oder im Home-Office nicht ganz gelingen wollten!